Measuring Fundamental Symmetry Violation
in Polyatomic Molecules

Thesis by

Arian Jadbabaie

In Partial Fulfillment of the Requirements for the

Degree of

Doctor of Philosophy

Caltech

CALIFORNIA INSTITUTE OF TECHNOLOGY

Pasadena, California

2023

Defended May 23, 2023

ACKNOWLEDGEMENTS

vii

visiting New York, including Reza, Framerz, Nikta, Yosi, Tara, Sam, Tim, Sohum, and many others. Thanks to the folks at Equinunk for making my birthday memorable in 2021. And to Laila and Arian, thank you for the philosophical and mystical discussions during COVID.

A special thanks to the crew at Rumi's Tea House in the summer of 2016, including Sheida, Justin, Reza, Sep, Arash, Ish, Sina, Ruth, Behrooz, Parhom, Ashoka, James, Nima, Melda, Matt, Annalyse, and others. That was an unbelievable experience I will always treasure. Also, thanks to the folks who listened to me talk about physics and philosophy during a sandstorm.

I'm grateful for the communities where I found a home during my undergraduate years. To my friends in the Rodriguez Scholars program, including Paolo, Daniel, Annie, Victor, Ana Paula, Adrian, Claudia, Alicia, and more, thank you for unofficially adopting me into your community.

I have to thank all of the communities where I found a home in undergrad. Thanks to all of my friends in the Rodriguez Scholars program who unofficially adopted me into their community: Paolo, Daniel, Annie, Victor, Ana Paula, Adrian, Claudia, Alicia, and more. Thanks to Erin for your companionship in my senior year. Thanks the Beta Sigma chapter of Kappa Sigma for showing me the meaning of brotherhood, with special thanks to the folks I lived with at Wash Ave. Thanks to Justin Au for hosting me in Hong Kong, to Himmel for taking me under his wing, and to Yannic and SheShe for so many great memories in London and SF. I am very grateful to Will Rogers for his support and understanding me on a deep level. To all the friends who joined me in reading books, thank you for the knowledge we gained together.

I want to extend my gratitude to my friends from high school and earlier, who continue to support me. I will forever be grateful to have such long lasting friendships. Thanks to Greg, Sam, Matt, Evan, Louie, Steven, Nick, Justin, Chris, Jon, Derek, Frank, Alex, Julia, and many others for all the memories. Special thanks to Greg for being my first friend in elementary school at Beecher, Sam for understanding my passion for Star Wars, Matt and Evan for sharing the experience of Mrs. Smith's class, Nick for DnDing during COVID, Louie for visiting me in Boston, Steven andJustin for always hosting, and everybody who was a part of the Berkshires getaways.

Thanks also to all of the influences that inspired my passion for physics and philosophy. In particular, thanks to George Lucas for creating Star Wars; Joanna Cole, for creating the Magic School Bus and Ms. Frizzle; Sid Meier, for creating the Civilization games; Fritjof Capra, for inspiring me with the Tao of Physics; and thanks to all the authors of all the non-fiction and fiction books that inspired me as a curious child. Special thanks to Marissa Smith, who mentored me in high school and opened my eyes to the world of philosophy.

I must thank my family for their constant support. Thank you to my grandparents for laying the foundations for our family to prosper. This thesis is dedicated to them and the sacrifices they made.

Everytime I speak Farsi, I embody their spirit. Living in LA, I had the good fortune of being supported my my aunt, uncle, cousins, and extended family, to whom I am grateful for always providing me a home away from home. Thanks also to my uncle Ali for providing a role model in academia. Immense thanks to my parents, Forugh and Farid, who always encouraged my curiosity and raised me to be compassionate. Because of your support, I have been able to follow my dreams, and for that I will be forever grateful. And thanks to my sister, Sara, who has taught me so much about life and healing. You are so cool, amazing, brilliant, and I am so lucky to be able to call you my sister.

Finally, thank you to my partner, Shima, for all of the love we have shared. I am blessed to have you in my life and I cannot believe we found each other. Your support and care during the thesis writing in particular has been absolutely essential. You see me so clearly and allow me to be myself. You understand the passion I have for bringing together art and physics. With you in my heart, I am never alone.

I want to acknowledge the privilege I have had that has allowed me to pursue my passion for physics. I hope that one day, studying the universe is accessible to anyone. Finally, I must provide thanks to the universe, for being so wonderful and sublime. I am but a drop in an ocean, and even this tiny drop is full of so much meaning. I will be forever grateful to be a part of this grand tapestry.

For my grandparents, who made this all possible:
Dr. Mohammad Jafar Jadbabaie and Goli Safavi
Habib Homayounrooz and Sedigheh Shakour Nezami

ABSTRACT

Open questions in fundamental physics, such as the cosmological origins of the observed imbalance of matter and antimatter, motivate the search for fundamental symmetry violating physics beyond the Standard Model (BSM). Recent measurements of heavy, polar, diatomic molecules constrain the existence of new, Parity (P) and Time-reversal (T) violating physics at ~10 TeV energy scales, exceeding the reach of particle colliders. The power of existing molecular measurements motivates us to pursue the next-generation of searches for symmetry violation. By adopting polyatomic molecules as an experimental platform, we can generically combine laser-cooling and trapping, BSM sensitivity, and exquisite quantum control over P and/or T violating energy shifts. These improvements are projected to increase the sensitivity of measurements to the PeV energy scale. In this thesis, we develop the foundations for new physics searches using cold and ultracold, linear triatomic molecules. These molecules have long-lived vibrational bending modes with closely spaced, opposite parity doublets, a key structure that aids polarizability, molecule control, state engineering, and systematic suppression. We produce a cryogenic buffer gas beam of cold YbOH molecules, using laser-enhanced chemical reactions to increase molecular yield by an order of magnitude. As a prerequisite for precision measurements, we perform high-resolution spectroscopic characterization of both the ground and excited bending modes of YbOH. Next, we present detailed tests of quantum state preparation and readout protocols in a YbOH beam, successfully demonstrating Ramsey interferometry using two-photon transitions. Finally, as part of the PolyEDM collaboration, we illustrate the power of polyatomic molecules by combining laser cooling and optical trapping with quantum state engineering to perform proof-of-principle measurements of P, T violating physics in magnetically-insensitive states of ultracold CaOH molecules at Harvard University. Our results open the door to a wide range of quantum-enhanced symmetry violation searches benefiting from the unique structural features of polyatomic molecules.

Published Content and Contributions

[1]L. Anderegg, N. B. Vilas, C. Hallas, P. Robichaud, A. Jadbabaie, J. M. Doyle, and N. R. Hutzler, *Quantum Control of Trapped Polyatomic Molecules for eEDM Searches*, (Jan. 20, 2023) `http://arxiv.org/abs/2301.08656`,
A. J. participated in the conception of the project, performed calculations and modeling of molecular structure, helped develop experimental methods, provided feedback, and participated in the writing of the manuscript.

[2]A. Jadbabaie, Y. Takahashi, N. H. Pilgram, C. J. Conn, Y. Zeng, C. Zhang, and N. R. Hutzler, *Characterizing the Fundamental Bending Vibration of a Linear Polyatomic Molecule for Symmetry Violation Searches*, (Jan. 10, 2023) `http://arxiv.org/abs/2301.04124`,
A. J. participated in the conception of the project, constructed significant portion of the experiment, participated in data taking and analysis, developed models and performed fits, led the writing of the manuscript, and responded to editors.

[3]A. Jadbabaie, N. H. Pilgram, J. Kłos, S. Kotochigova, and N. R. Hutzler, "Enhanced molecular yield from a cryogenic buffer gas beam source via excited state chemistry," New Journal of Physics **22**, 022002 (2020) `10.1088/1367-2630/ab6eae`,
A.J. participated in the conception of the project, helped construct the experiment, and led the data taking, analysis, modeling, manuscript writing, and response to the editors.

TABLE OF CONTENTS

LIST OF ILLUSTRATIONS

LIST OF TABLES

C H A P T E R

1

INTRODUCTION

Luminous beings are we, not this
crude matter.

–Yoda

1.1 Overview

Fundamental physics research currently lies at a paradoxical juncture. On one hand, the last 50 years have seen the development and validation of the most successful description thus far of Nature's fundamental building blocks—the Standard Model of particle physics. Built on the mathematical foundations of quantum field theory (QFT), the Standard Model has consistently demonstrated its accuracy in experimental tests, such as the discovery of the Higgs boson particle at the Large Hadron Collider (LHC) [1, 2], or the one part per trillion agreement of theoretical predictions with experimental measurements of the electron's magnetic moment [3].

On the other hand, the Standard Model is a deeply incomplete theory. First, though we observe four fundamental forces in nature[1], the Standard Model only describes three—gravity is missing. Second, the Standard Model has major inaccuracies when compared to cosmological observations, failing to provide an origin for dark matter or dark energy. Third, the Standard Model does not explain the observed imbalance of matter and antimatter in the universe [4]. Fourth, while experiments have determined neutrinos have finite mass, the Standard Model describes them as

---
[1]The strong nuclear force, the weak nuclear force, electromagnetism, and gravity.

massless. Finally, the Standard Model has 19 free parameters² that must be provided as an input to the model. These parameters are not derived, can only be obtained experimentally, and their origin is not understood, giving rise to the flavor [5] and hierarchy problems [6]. To address these issues and more, we require new physics beyond the Standard Model (BSM).

The silver lining is that the new physics is out there; we simply have to discover it. The experimental program searching for new physics has two complimentary approaches—one can either precisely measure properties of exotic objects, or one can take a magnifying glass to so-called ordinary matter, and precisely search for exotic properties. The former approach motivates experiments detecting gravitational waves or colliding particles at high energy, while the latter approach motivates tabletop experiments performing measurements on our ubiquitous constituents, atoms and molecules. In this thesis, we focus on the low energy, tabletop approach, though we emphasize that both approaches are complimentary, and their combination is necessary to cover the vast parameter space of possible BSM physics.

A fruitful approach to searching for new physics is to perform a "background-free" measurement. To ensure a low energy observable is background-free, we can look for violations of *fundamental symmetries* that are expected to be very weak in the Standard Model. Fundamental symmetry violation can generically manifest as "exotic" electromagnetic moments that have not yet been observed in Nature [7]. A textbook example is the permanent electric dipole moment (EDM) of a fundamental particle, which would violate fundamental Parity (P) and Time-reversal (T) symmetries, and is highly suppressed in the Standard Model [8]. In general, vacuum fluctuations of symmetry violating BSM particles at high energy scales can interact with fundamental particles, such as the electron, and induce permanent EDMs at the atomic or molecular scale. Any nonzero measurement of an EDM would constitute an exciting new realm of exploration in physics, while a null result can place tighter bounds on proposed theories of BSM physics, such as models of supersymmetry or extra dimensions [9]. As an example, current state-of-the-art searches for the electron's EDM in diatomic molecules [10, 11] have sensitivity to symmetry violating new physics at ~50 TeV energy scales, beyond the current reach of particle colliders [12].

It may seem odd that measurements of atoms or molecules at low energies can provide us information on the inner-workings of high energy particle physics [13–15]. After all, the center of mass energies of LHC experiments are at ~13 TeV, while the temperature of the cold molecules in our experiments are orders-of-magnitude away at ~100 µeV. However, the electromagnetic environment *inside* an atom or molecule is actually quite extreme. For example, electrons orbiting a heavy nucleus can travel at near light speed through the inside of the nucleus. These electrons

---

²Without neutrino masses and mixing, we get: 6 quark masses, 4 angles for the CKM matrix, 3 lepton masses, 3 gauge coupling constants, 2 Higgs constants, and the QCD vacuum angle. Neutrinos add 4 angles for the PMNS matrix and 3 masses.

experience relativistically-enhanced electric fields, on the order ~30 GV/cm, that are 10^5 times stronger than what we can produce in a lab! Measurements of these relativistic, core-penetrating orbits can have amplified sensitivity to the subtle effects of permanent EDMs. Core-penetrating electrons can also provide sensitive probes of Standard Model nuclear properties, and we direct the curious reader to Ref. [16] for more details.

The powerful reach of existing molecular EDM measurements motivates us to pursue the next-generation of BSM searches. By adopting polyatomic molecules as an experimental platform, we can generically combine laser-cooling and trapping, BSM sensitivity, and exquisite quantum control over EDM interactions [17]. This will enable significant synergy with the toolbox of atomic physics techniques developed for quantum information, simulation, and metrology [18]. However, before we can reach the promised land of quantum-enhanced measurements, we must first understand and control the additional complexity present in polyatomics molecules.

The work described in this thesis develops the foundations for precision measurements of symmetry violating physics in polyatomic molecules. While the majority of this work focuses on YbOH molecules, the results are extendable to other linear triatomic molecules of the M-OH form (M=Ca, Sr, Ba, Yb, Ra). Before presenting results, we provide useful background in the introduction. In Section 1.2, we introduce fundamental symmetries, motivate searches for their violation, and discuss their manifestation as exotic electromagnetic moments. Then, in Section 1.3, we discuss symmetry violation in atoms and molecules, including mechanisms for their enhancement, and connections to high energy theory. Finally, in Section 1.4, we conclude the introduction by answering the question, "Why *polyatomic* molecules?"

The rest of the thesis is divided as follows. Chapter 2 provides a foundational understanding of molecules and the electromagnetic interactions used to control them. In Chapter 3, we describe our beam source used to generate high fluxes of cold YbOH molecules, and we present a novel scheme for enhancing molecule production using laser light. In Chapter 4, we present results on spectroscopy of YbOH, in particular the study of the molecule's fundamental bending mode, unique to polyatomics. In Chapter 5, we discuss methods for performing precision measurements in polyatomic molecules, including results from prototype measurements in both a cold YbOH beam and a trap of ultracold CaOH molecules. We conclude with an outlook on an ongoing search for symmetry violation in ^{173}YbOH, and discuss the future of polyatomic molecules for precision measurements.

1.2 Fundamental Symmetry Violation

1.2.1 Background

A *symmetry* describes a transformation of an object that leaves the physical properties of the object unchanged. The study of symmetry can simplify a complex problem and classify emergent behavior. Symmetries help us understand what properties are redundancies of our reference frame, and what properties have physical consequences independent of our basis. For example, the rotational states of polyatomic molecules can be very complicated, as we will see. However, in the language of symmetry, we can understand and classify the many states of a molecule in terms of their behavior under transformations (rotations, reflections) performed in the molecule's rotating frame. If we further understand the symmetries of interactions, we can develop an accurate theory of the molecule's physical behavior in external electric and magnetic fields. Further, we can use our understanding of molecular symmetry to predict emergent behaviors and to engineer specific quantum states with favorable properties. Ironically, we use our understanding of symmetries in molecules to look for violations of fundamental symmetries in physics!

The same principles of symmetry classification can be found all over physics, including at the fundamental level in describing subatomic particles. The laws of physics as we construct them are imbued with various spacetime symmetries. Theories of fundamental physics can trace a lineage to Copernicus's insight that as observers, we do not occupy a privileged position in the universe. In other words, the law of physics should be independent of our frame of reference in in space and time. Of course, there is a program of new physics looking for violations of even these symmetries [14]. However, to date, we have not found evidence for variation of the laws of physics in different regions of space or different points in time.

The complete group of spacetime symmetries is the Poincare group [19], consisting of the following transformations: translations, rotations, and Lorentz boosts. Particles in our theories are defined as objects that retain characteristic physical properties even when we transform our reference frame. Wigner put this concept on mathematical grounds in 1939 [20] by defining particles as the irreducible representations of the Poincare group, classified by two properties: an intrinsic spin that must take on integer or half-integer values, $S = 0, \frac{1}{2}, 1, \frac{3}{2}, \ldots$ and an intrinsic mass $m \geq 0$. For $m > 0$, what we call a particle is a collection of $2S + 1$ spin orientation states that transform into each other upon rotations of physical space. This is just a statement of angular momentum conservation: while the spin of an electron may point in different directions in different reference frames, its magnitude $S = \frac{1}{2}$ must be conserved. The transformation properties of an arbitrary spin S under rotations are given by the Wigner D-matrices, $\mathcal{D}^{(S)}$, which we will repeatedly encounter later in this thesis in the context of the symmetric top eigenstates that describe molecular rotation. Finally, Wigner also showed for $m = 0$, we can only have 2 orientations, which correspond to the

two polarizations of light. We do not observe $m < 0$ states in nature.

So far, the spacetime symmetries we have discussed are continuous in nature. We can also investigate the behavior of physical systems under discrete symmetries, essentially generalizations of the concept of a reflection. In QFT, dynamic quantities such as momenta or currents are described in terms of relativistic four-vectors. For example, we can consider the electromagnetic current $j_\mu = (\rho, \vec{j})$, where ρ is the charge density and $\vec{j}$ describes standard three dimensional charge currents. We consider a generalized reflection operation, consisting of $j_\mu \to -j_\mu$. This turns out to be a deep symmetry transformation that is connected to Lorentz invariance, and it is known as Charge-Parity-Time (CPT) symmetry. CPT is postulated to be an exact symmetry of the universe by the CPT theorem, a cornerstone of QFT. Observations of CPT violation would require major reworkings of the theoretical framework underpinning the Standard Model. Of course, there are experiments searching for CPT violation, detailed in a recent review [14]. But as with Lorentz invariance, no evidence has yet to be discovered for the violation of CPT, and we take it to be an exact symmetry in this thesis.

As the name suggests, a CPT transformation can be factored into three separate discrete symmetry operations: Charge reversal (C), Parity reversal (P), and Time reversal[3] (T). The effect of these transformations in QFT is derived in textbooks, and here we simply provide an intuitive physical explanation. Performing a C transformation reverses electromagnetic charges, swapping matter with antimatter. Performing a P transformation inverts spatial coordinates, $\vec{r} = (x, y, z) \to -\vec{r} = (-x, -y, -z)$. This operation is equivalent to a mirror reflection, followed by a 180° rotation along an axis perpendicular to the mirror plane. Finally, performing a T transformation reverses the sign of all motion, such as momenta or currents, swaps initial and final states, and performs complex conjugation, i.e. takes $i \to -i$. For convenience, we have provided a table of the C, P, T symmetry properties of various common physical quantities in 1.1.

Intriguingly, while the combination of CPT is a good symmetry, all three individual symmetries have been found to be violated separately in Nature. The details depend on the specific fundamental force in question. Gravity is expected to be fully symmetric under C, P, and T, though only recently are gravitational wave experiments able to place bounds. Thus far, electromagnetism and the strong nuclear force have been observed to be fully symmetric under any of C, P, or T, applied together or individually, but as we shall see, there could still be symmetry violation at scales we have yet to probe. On the other hand, the weak nuclear force explicitly violates P, T, and CP symmetries [21], and we note the various violations are all in agreement with the CPT theorem[4]. To date, the weak

[3]We note that we are discussing microscopic T-symmetry—while we observe a clear asymmetry in the flow of time in our everyday life, this applies only to macroscopic phenomena that statistically will always evolve from low entropy initial states to high entropy final states.
[4]Technically, if $CPT = -1$, then $T = -CP$, but overall phases are not distinguishable.

Table 1.1: Table of useful symmetry relations. To be explicit, we have included spin in its own row, but there is no reason for it to behave differently from an ordinary angular momentum J.

Symbol	Description	C	P	T
$\vec{r}$	Position	+	−	+
$\vec{p}$	Momentum	+	−	−
$\vec{J}$	Angular momentum	+	+	−
$\vec{S}$	Spin	+	+	−
$\vec{E}$	Electric field	−	−	+
$\vec{B}$	Magnetic field	−	+	−
$\vec{j}$	Electric current	−	−	−
ρ	Charge density	−	+	+

nuclear force is the only fundamental force that has been observed to violate discrete symmetries[5].

1.2.2 Cosmological Motivation

Is there any reason to expect Nature to violate fundamental symmetries? Originally, scientists believed that Nature should be symmetric by principle. However, fundamental symmetry violation can have drastic consequences for Cosmology, the study of the origins of the universe. In this section, we motivate the existence of fundamental symmetry violation on cosmological grounds.

Astronomical observations indicate the universe is dominated by matter, with virtually no free antimatter [4, 22]. While antimatter is produced in physical processes, such as radioactive decays or high energy collisions, once antimatter encounters its equivalent ordinary matter partner, both masses annihilate into photons. This is indeed how we know the universe is matter dominated— if there were a region of antimatter in the universe, the boundary of interstellar space would generate enough annihilation events to be observable [4, 22]. A special region of antimatter in the universe would also violate the cosmological isotropy principle, which states the universe should be statistically homogeneous on large scales [23–25]. The observed imbalance of matter and antimatter is known as the Baryon[6] Asymmetry of the Universe (BAU). The BAU is often parameterized in terms of the asymmetry parameter $\eta_B = \frac{n_B - n_{\bar{B}}}{n_\gamma} \sim 10^{-10}$, where n_B ($n_{\bar{B}}$) is the number density of baryons (antibaryons) observed in the universe, and n_γ is the number density of cosmic microwave background (CMB) photons, which represent the photons produced by matter/antimatter annihilation in the early universe[7]. The asymmetry parameter η_B can be obtained

---

[5]Curiously, the weak force is also the only force that violates flavor symmetry. Among other things, flavor violation is essential for the proton-proton chain, the dominant fusion reaction in the sun and other stars with similar or smaller mass.

[6]Baryons are composite particles, in particular protons and neutrons, which are made of three quarks.

[7]Since the CMB photon density changes over time in an expanding universe, some authors prefer instead to normalize by the total entropy density of the universe s, which remains constant. We note s and n_γ are proportional to

experimentally from many sources, such as analysis of studies of the CMB, or the observed abundances of light elements [21, 22, 26]. Interestingly, the asymmetry we see now actually began as a relatively small one in the early universe.

In 1967, Sakharov showed [27] that three conditions must be satisfied to generate the BAU: 1) The existence of C and CP ($= T$) violation; 2) The violation of baryon number; and 3) Departure from thermal equilibrium. As it turns out, the Standard Model can have all three ingredients, though not at sufficient scales for the latter two. The violation of baryon number can occur via non-perturbative processes known as sphaleron transitions [4, 7, 19] that violate baryon number but preserve the difference of baryon number minus lepton number. The Standard Model can also satisfy departure from thermal equilibrium if the electroweak phase transition of the Higgs vacuum is a first order transition. However, the measurement of the Higgs mass at $m_H \approx 125$ GeV indicates the electroweak phase transition is likely a second order transition [28], which cannot generate sufficient deviation from equilibrium [7, 22], requiring new physics. Finally, we mentioned earlier that the electroweak force violates CP and C symmetries. However, it turns out this violation is too weak to physically cause the BAU [4, 7, 22], even if we had sufficient departure from thermal equilibrium. Essentially, the processes that result in CP violation happen at many loops in perturbation theory that must involve all three quark generations[8], suppressing their dynamical contribution. Typically, the "strength" of CP violation is parameterized by the Jarlskog determinant [22, 29], in invariant product of quark masses and mixing angles. The Jarlskog determinant is much smaller than the energy scale of sphaleron processes, making it difficult to develop a model for electroweak baryogenesis [22].

In general, electroweak baryogenesis models require new physics to explain the BAU. There are of course other possible explanations, such as leptogenesis [9, 30–32], where CP violation in neutrinos first generates a lepton asymmetry, and sphaleron transitions convert this to a baryon asymmetry. Another possible explanation is violations of CPT symmetry [33], though this would have drastic consequences on the rest of our understanding of nature. Further details on the baryon asymmetry of the universe can be found in Refs. [4, 7, 22], as well as the pedagogical review given in Ref. [34].

1.2.3 P, T Violating Moments

Since we know Nature can violate symmetries, and we have cosmological motivations for symmetry violation, we have reason to expect electromagnetism and/or the strong force have their discrete symmetries broken on a a subatomic scale. Generically, both forces can admit interactions and terms that violate P and T symmetries, but so far no such interactions have been observed

---

each other.

[8]If fewer than 3 generations are invovled, the CKM phase is trivial can be transformed away by a unitary operation.

in Nature. In this section we provide a discussion of how such symmetry violation manifests in electromagnetic interactions.

P and T-violation can can result in symmetry violating electromagnetic moments of fundamental particles. These moments can be derived generally, either from a standard multipole expansion of charge and current, or from a decomposition of the electromagnetic current operator, j_μ, into Lorentz invariant form factors. The latter approach is detailed in Refs. [35–38], and we outline it here schematically. Consider the matrix element of j_μ connecting generic initial and final particle states with a given spin S and momenta k, k'. The matrix element $\langle k', S | j_\mu | k, S \rangle$ can be factored into its Lorentz invariant constituents, known as form factors, labeled as $F_1(q^2), F_2(q^2), \ldots$, and parameterized in terms of the 4-momentum transfer $q^2 = (k' - k)^2$. There are generically $6S + 1$ form factors for a given spin S.

For now, we consider the case of a fundamental spin-$\frac{1}{2}$ particle, such as the electron, giving us four separate terms. In the non-relativistic rest frame, $q^2 \to 0$, and the form factors can be identified[9] with various properties of our spin-$\frac{1}{2}$ particle, some more familiar than others:

$$F_1(0) = Q \quad \text{(charge)} \tag{1.1}$$

$$\frac{1}{2m}\left(F_1(0) + F_2(0)\right) = \mu \quad \text{(magnetic dipole moment)} \tag{1.2}$$

$$-\frac{1}{2m}F_3(0) = d \quad \text{(electric dipole moment)} \tag{1.3}$$

$$\frac{1}{m^2}F_4(0) = a \quad \text{(anapole moment)}. \tag{1.4}$$

The first two quantities, the charge Q and magnetic moment μ, are familiar properties of all subatomic particles, including electrons. The electric dipole moment has a clear classical analogue, and the anapole moment describes a "torodial" magnetic moment. We note all of these quantities are intrinsic. Of these quantities, only Q is invariant under rotations. While the magnitude of the moments (including the anapole) are fixed, they are vector observables that must be oriented along the same axis as the spin: $\vec{\mu} = \mu\vec{S}$, $\vec{d} = d\vec{S}$, and $\vec{a} = a\vec{S}$. We now give some reasons for such a constraint.

First, recall our spin-$\frac{1}{2}$ particle transforms under rotations according to the Wigner D-matrices, $\mathcal{D}^{(S=\frac{1}{2})}$, and this was obtained by demanding our particle properties remain invariant under changes to our reference frame. Imagine we were to add another, second physical axis to describe our particle, describing $2S' + 1$ hypothetical orientations of some dipole moment $\vec{d}$. To maintain invariance under rotations, we demand this second axis also transform according to the D-matrices[10], and our

---

[9]For composite particles such as protons or neutrons, the form factors besides F_1 are generally hard to compute.

[10]If we did not do this, then $\vec{d}$ would pick out an absolute direction in space, which is Lorentz violating.

particle's rotation properties are now given by $\mathcal{D}^{(\frac{1}{2})} \oplus \mathcal{D}^{(S')} = \mathcal{D}^{(|S'-\frac{1}{2}|)} \otimes \mathcal{D}^{(|S'-\frac{1}{2}+1|)} \otimes \ldots \mathcal{D}^{(S'+\frac{1}{2})}$. Our simple spin-$\frac{1}{2}$ particle has turned into a coupled angular momentum problem consisting of $(2(\frac{1}{2}) + 1)(2S' + 1)$ orientations, contradicting our initial classification of the particle's rotational symmetries. If we tried to use this two-axis state to describe a wavefunction of identical electrons in the same spatial state, we would conclude that we have $(2S'+1)$ times *more* configurations available than what we physically observe with electrons under the Pauli exclusion principle. Furthermore, we run into a deeper issue—by the spin-statistics theorem, if S' is half-integer, then our combined two-axis particle is now a boson, and Pauli exclusion does not apply at all! In Nature, we observe spin-$\frac{1}{2}$ electrons that only have 2-fold internal degrees of freedom, which is only consistent with the case that $\vec{d} \propto \vec{S}$.

For the sake of argument, let us proceed as if $\vec{d}$ can point at an arbitrary angle relative to $\vec{S}$. If we try to measure $\vec{d}$, we will run into problems. Since our particle has angular momentum, any components of $\vec{d}$ perpendicular to $\vec{S}$ will be averaged away by the spin, leaving only the projection $\vec{d} \cdot \vec{S}$. Since $\vec{S}$ only has S_z defined due to the commutation relationships of angular momenta, the transverse components of $\vec{S}$ and $\vec{d}$ vanish, and we can only measure $d_z \propto S_z$. This argument can be generalized to angular momenta larger than $S = \frac{1}{2}$ via the Wigner-Eckart theorem, presented in Sec. 2.1.2. In the language of spherical tensor operators [39], all electromagnetic moments of a given rank are therefore proportional to the angular momentum tensor of the same rank, which classifies the rotational symmetries of our particle.

Now we move on to considering the symmetry behaviors of these moments interacting with external fields. One approach is to consider the coupling of j_μ to the photon field in the QED Lagrangian [35]. Instead, we pursue the low energy equivalent, considering the Hamiltonian derived from the non-relativistic limit of the Lagrangian [19, 38]. If the Hamiltonian is left changed by our symmetry operation, then the symmetry is broken. First, we consider the charge Q. While $Q \xrightarrow{C} -Q$, the Coulomb interaction scales as $H_Q \propto Q\phi$, where ϕ is the charge-dependent electric potential, and therefore $H_Q \xrightarrow{C} H_Q$. Similarly, for the magnetic moment, we have $\mu \xrightarrow{C} -\mu \xrightarrow{T} \mu$, recalling that $\vec{\mu} \propto Q\vec{S}$. But also, the interaction Hamiltonian is $H_\mu = -\vec{\mu} \cdot \vec{B}$, and magnetic fields are generated by currents which are C- and T-odd (see Table 1.1), so we have $H_\mu \xrightarrow{T} H_\mu$, and a similar argument shows H_μ is also C-symmetric.

The anapole moment a has a non-relativistic interaction Hamiltonian given by [37, 38] $H_a \propto a\vec{S} \cdot (\nabla \times \vec{B} - \frac{\partial E}{\partial t})$. Note the anapole only interacts with electromagnetic sources or sinks, which means it is only nonzero in matter. Since ∇ is P-odd and ∂t is T-odd, we see the term in the parentheses is C-odd, P-odd and T-odd. The spin is T-odd as well, so the resulting anapole Hamiltonian is C-odd, P-odd, and T-even, and satisfies CPT invariance as expected. The C-odd nature of the anapole means it cannot have long-distance effects [35]. Finally, we consider the

Table 1.2: Table denoting the C, P, T symmetry properties of the $6S + 1$ electromagnetic moments obtained from the form factor decomposition of the electromagnetic current. When two values are given separated by the semi-colon, the left value refers to half-integer S; the right refers to integer S. Table reproduced from Ref. [35].

C	P	T	Number of moments
$+$	$+$	$+$	$2S + 1$
$-$	$-$	$+$	$S + \frac{1}{2}; S$
$-$	$+$	$-$	$S - \frac{1}{2}; S$
$+$	$-$	$-$	$2S$

electric dipole moment, given by $H_d = -d\vec{S} \cdot \vec{E}$. The spin S is T-odd, while the electric field, generated by charge distributions, is P-odd and C-odd. By intuition (and by CPT) d is C-odd, and we therefore have that H_d is P-odd, T-odd, C-even.

We emphasize that in the above discussion, d refers to a permanent moment, and is not taken to be P-odd, though often it is presented as such when hand-waving. The permanent dipole moment $\vec{d} \propto \vec{S}$ of a point particle is not the same as a composite dipole moment $\vec{D} \propto \vec{r}$ that we will encounter in atoms and molecules, distinguished by capital D. Since $\vec{D}$ is explicitly P-odd and T-even, its interaction with the P-odd E field is P-even, T-even. Further, one can show that $\langle D \rangle$ must vanish for states with well-defined parity [40, 41], and therefore there are no permanent dipole moments of atoms and molecules at zero field, which are good parity eigenstates. For an atom this makes sense given its spherical symmetry. For a simple diatomic molecule, the spherical symmetry is reduced to cylindrical symmetry, with $\vec{D}$ pointing along the symmetry axis. However, the molecule eigenstate still has well-defined parity. We can think of the molecule as constantly rotating, causing $\langle \vec{D} \rangle = 0$ in the lab frame. As we shall see later, only by applying an external field and breaking the P symmetry of the molecule do we begin to an induce a dipole moment in the system. The total dipole moment can then be decomposed into T-even contributions and T-odd contributions, and we search for the latter.

We finally return to the case of an arbitrary spin-S particle, with $6S + 1$ total invariant form factors. In Ref. [35], these form factors are tabulated according to their total interaction symmetry under C, P, and T, and we reproduce their results in Table 1.2. For this thesis, we will only focus on the P, T-odd moments. The C-odd moments are discussed further in Refs. [42–44].

If we have a particle with spin $S \geq 1$, we can now support additional P, T-violating moments, which correspond to higher order multipoles. Of particular interest is the magnetic quadrupole moment (MQM) $\mathcal{M}$, which is P, T-odd and has never been observed, in contrast to the electric quadrupole moment (EQM) Q, which is P, T-even, and a commonly observed property of nuclei.

Similar to how d and μ have analogous mathematical forms, so too can we draw comparisons between $\mathcal{M}$ and $\mathcal{Q}$.

The EQM and MQM are both rank 2 moments, which means they are described by two spatial indices, and referred to as tensors. To obtain a rotationally invariant interaction Hamiltonian, these moments must be contracted with tensor quantities that also have two indices. The EQM naturally interacts with electric field gradients, $H_Q \propto Q_{ij} \nabla_i E_j$, while the MQM interacts with magnetic field gradients, $H_\mathcal{M} \propto \mathcal{M}_{ij} \nabla_i B_j$. As with the EDM, the MQM must point along the spin S, but since it is a tensor quantity, we must construct a rank 2 representation of S. The common choice is the irreducible, traceless tensor, given by:

$$\mathcal{M}_{ij} = \mathcal{M}\frac{3}{2S(2S-1)}T_{ij}. \tag{1.5}$$

Here, we have defined the tensor $T_{ij} = \{S_i, S_j\} - \frac{2}{3}\delta_{ij}S(S+1)$, where $\{A, B\} = AB + BA$ is the anti-commutator, and δ_{ij} is the Kronecker delta, with $\delta_{ij} = 1$ if $i = j$ and 0 otherwise. The $2S - 1$ factor in the denominator means the MQM is only well-defined for $S \geq 1$. The quantity $\mathcal{M} := \mathcal{M}_{zz}$ is the "magnitude" of the MQM, which can be seen by evaluating eq. 1.5 for a polarized spin, $S_z = S$. The $\mathcal{M}_{ij}$ form is given in Cartesian coordinates. In the language of spherical tensor operators (discussed in Sec. 2.1.2 and Ch. 5 of Ref. [39]), we can write the MQM as:

$$T_p^2(\mathcal{M}) = \frac{\sqrt{6}}{S(2S-1)}T_p^2(S, S) \tag{1.6}$$

where p is the index labeling the 5 components in the spherical basis, running from $p = -2, -1, 0, 1, 2$. Returning to the form of $H_\mathcal{M}$, we have an odd number of T-odd quantities (2 spin components in $\mathcal{M}$, and one from the magnetic field B), and the dependence on the gradient results in P-odd behavior as well, and therefore the MQM interaction is P, T-odd, C-even.

Classically, we can think of an MQM as two opposite current loops, with magnetic moments $\pm ja$, separated by a distance r, where j is electric current and a is area. Using atomic units, the MQM is given by $\mathcal{M} \propto \mu_B a_0$, or alternatively with nuclear units, $\mu_N \text{fm}$. Clearly, the MQM is the mangetic dipole analogue of the EDM, with units of dipole $\times$ distance instead of charge $\times$ distance. The SI units of the MQM are current $\times$ volume, or A m^3. We note some papers write the MQM by factoring out the speed of light and setting $c = 1$, resulting in the same units for MQMs and EQMs, charge $\times$ area.

Finally, for completeness, we provide the classical formula for the MQM. The classical form of the MQM multipole is given by [45, 46]:

$$\overleftrightarrow{M} = \frac{1}{2}\int d\vec{r} \left(\vec{r}(\vec{r} \times \vec{J}) + (\vec{J} \times \vec{r})\vec{r}\right) \tag{1.7}$$

where the notation $\overset{\leftrightarrow}{\mathcal{M}}$ indicates we are dealing with a tensor quantity. Like the previous forms we provided of the MQM, this form is also traceless and symmetric. Further, classical vector potential generated by $\overset{\leftrightarrow}{\mathcal{M}}$ is given by:

$$\vec{A}(\vec{r}) = \frac{\mu_0}{4\pi} \frac{\hat{r} \times \overset{\leftrightarrow}{\mathcal{M}} \times \hat{r}}{r^3} \tag{1.8}$$

and the magnetic field can be obtained by the usual relation, $\vec{B} = \nabla \times \vec{A}$. A generalization to higher order moments can be found in Jackson [47].

So far, our discussion has focused on permanent P, T violating moments of fundamental particles. Early on, physicists realized that these permanent moments can also manifest in composite systems. The first example was the work of Ramsey and Purcell in 1957 [48], where they placed the first limits on the EDM of the neutron ($d_n < 10^{-20}\, e$ cm). We might naively expect a nonzero neutron EDM, given the neutron is made up of oppositely charged quarks. However, no EDM has been found so far, with current experimental bounds limiting the neutron EDM to $d_n < 1.8 \times 10^{-26}\, e$ cm, and even more sensitive experiments currently underway [49]. The neutron EDM is explicitly a probe of P, T violation in the strong force, which manifests in the quantum chromodynamics (QCD) vacuum angle, parameterized by the θ parameter. The experimental neutron EDM bound translates to a limit of $\theta \lesssim 10^{-10}$ [7], though the exact value can vary in the literature as the calculation is challenging. The question of the small or zero value of θ constitutes the strong-CP problem, a rich field of physics that has given rise to the theory of axion-like particles, a potential dark matter candidate. We do not discuss this further, but direct the reader to the excellent review in Ref. [50] for more information.

1.3 Atoms and Molecules

1.3.1 Electronic Enhancements

Permanent P, T violating moments can also arise in atoms and molecules. An excellent and comprehensive discussion is given in Ch. 5 of Ref. [14] as well as Refs. [7, 51, 52]. Furthermore, the white paper in Ref. [12] describes the state of the field at the time of this thesis.

The existence of P, T violation in composite systems actually non-trivial—in a neutral, non-relativistic collection of point charges, Schiff's theorem [53] states that there can be no permanent EDM of the composite system, as the constituent charges will re-arrange themselves to "screen" EDMs. However, Schiff also showed this screening breaks down for magnetic interactions [54] (there are no magnetic charges to screen with) and if there is a finite charge distribution that is offset from the spin distribution (as can happen in generically a nucleus with different proton and neutron distributions). This gives rise to the following nuclear P, T violating nuclear moments: the nuclear Schiff moment (NSM) [55, 56], which is a partially screened dipole moment, and the nuclear

magnetic quadrupole moment (NMQM) [57, 58], which is essentially the composite equivalent of the MQM discussed earlier. We note there is also an electric octupole moment [59], but this effect is supressed in atoms and molecules and is usually not considered. Further, Sandars [60] first showed that relativistic effects can also result in evasion of Schiff's theorem, adding the electron EDM (eEDM) as another possible observable in a composite atom or molecule. Ref. [61] explains the relativistic evasion directly in terms of the Lorentz contraction of the eEDM (which has units of charge distance) when viewed from the frame of the stationary nucleus. An additional result is that for both electrons and nuclei, P, T violation can actually be *amplified* by relativistic effects compared to the bare particle value [14]. For example, the eEDM is enhanced by a factor of roughly Z^3, while the NMQM is enhanced by roughly Z^2, where Z is the number of protons in the heavy nucleus. These scalings motivate us to perform measurements in systems with high Z and core-penetrating, relativistic electron orbitals with s character.

There are many different enhancement factors at play in measurements of P, T violation in atoms and molecules. First we discuss "electronic" enhancement. Since the P, T violating effects are strongest near the heavy nucleus, we can think of their effect as causing mixing between opposite parity electronic orbitals, i.e. mixing $s_{1/2}$ and $p_{1/2}$ orbitals[11], where the letter denotes the orbital angular momentum l, and the subscript labels total spin and orbital angular momentum j. For example, with the eEDM, the mixing is generated by the relativistic interaction [63] of the spin with the electric field inside the atom or molecule. As a result, the eEDM interaction scales like $\sim \alpha^2 Z^3$, originating from the overlap integral of the $s_{1/2}$ and $p_{1/2}$ wavefunctions near the nucleus [14, 51, 57, 58, 60].

For the NMQM, the interaction is now between the nucleus and the gradient of the magnetic field generated by the electron spin [35, 52, 57]. Imagining the NMQM as two opposite current loops oriented along the nuclear spin, we see a traveling electron will either be deflected upwards or downwards depending on its spin, generating a spin-dependent charge distribution (manifestly P, T odd) of the whole system. Because the NMQM interacts with the electron spin, it is only observable in systems with unpaired valence electrons (paramagnetic). Additionally, since the NMQM is a tensor operator, it only arises in nuclei with $I \geq 1$. Further, by the Wigner-Eckart theorem, the rank 2 NMQM mixes the $s_{1/2}$ and $p_{3/2}$ relativistic electron wavefunctions, resulting in $\sim Z^2$ scaling [57, 58]. This is also why the rank 3 electric octupole moment is so small [64], as it must now mix $s_{1/2}$ and $f_{5/2}$, or $p_{1/2}$ and $d_{5/2}$, all which have small mutual overlap at the nucleus.

Finally, considering the NSM, the offset of charge and spin distributions results in an effective electric field that is nonzero inside the nucleus, and points collinear with the nuclear spin [51,

---

[11]If the mixing coefficient is imaginary, we obtain a P odd, T even effect, and if the coefficient is real, we obtain a P, T violating effect, see Ref. [62].

55]. The NSM distribution arises at third order in the nuclear radius [51, 56], similar to the octupole [64], though the NSM is still a rank 1 moment. Similar to the case of the NMQM, the internal field caused by the NSM deflects electrons dependent on the nuclear orientation, generating a P, T odd charge distribution. However, now the interaction is independent of electron spin, and so the NSM can be measured in systems with paired off valence electrons (diamagnetic). Due to the partial cancellation of the NSM and the strong relativistic enhancement of the eEDM and NMQM interactions, the electronic enhancement of the NSM is typically weaker than the paramagnetic moments by an order-of-magnitude or more [51, 57].

1.3.2 Atoms

The manifestation of P, T violation has significant differences between the atomic and molecular case. In the case of atoms, the s and p wavefunctions are well separated in energy by ~eV or more. As a result, in free-field, the P, T violating interaction, H_{PT}, will only slightly mix the opposite parity levels, inducing a small dipole moment along the direction of the total atomic angular momentum $\vec{J}$. We should always remember the orientation of a spatial vector (dipole) along an angular momentum vector (J) is manifestly P, T violating. Continuing, if we evaluate the dipole moment $\vec{D} = e\vec{r}$ of the atom in perturbation theory, we find the induced P, T violating EDM in free-field as [51]:

$$\langle \vec{D}_{PT} \rangle_{\text{atom}} = 2 \frac{\langle s|\vec{D}|p \rangle \langle p|H_{PT}|s \rangle}{E_s - E_p} \propto \frac{\vec{J}}{\sqrt{J(J+1)}} \tag{1.9}$$

If we apply an external electric field, $\vec{E}_{\text{lab}}$, we expect to observe very small first-order Stark shifts from $\vec{D}_{PT} \cdot \vec{E}_{\text{lab}}$. Crucially, in atoms the P, T violating effect scales with E_{lab}, motivating the use of very large fields [65]. In atoms, there will also be a P, T even effect resulting from the ordinary induced dipole moment, $\vec{D} = \alpha \vec{E}_{\text{lab}}$, where α is the DC polarizability. This results in quadratic Stark shifts on top of the hypothetical linear Stark shifts. Of course, these two effects can be disentangled by comparing their shifts for T-reversed states.

In the literature, the concept of an internal electric field of the atom, $\mathcal{E}_{\text{eff}}$, is provided as heuristic picture for the P, T violating effects of the eEDM [14, 35]. We can see that in free-field, the atom is spherically symmetric, and so the interaction of $\mathcal{E}_{\text{eff}}$ with the eEDM, d_e, will mostly average away. As we show in eq. 1.9, any intrinsic P, T violation will result in a slight orientation of $\mathcal{E}_{\text{eff}}$ along J, suppressed by the separation of atomic opposite parity levels. By applying an external field E_{lab}, we polarize the atom ever so slightly, shifting the electron cloud center slightly relative to the positive nucleus. This provides a preferential axis for orienting $\mathcal{E}_{\text{eff}}$. Unfortunately, even with 100 kV/cm external electric fields, atoms always remain in the induced dipole moment regime, limiting the orientation of $\mathcal{E}_{\text{eff}}$ in the lab frame, which limits our ability to access the full enhancement of EDM effects. Molecules, however, have their spherical symmetry broken down to cylindrical symmetry,

which naturally provides an orientation for $\mathcal{E}_{\text{eff}}$. This has very important consequences that make molecules significantly more sensitive than atoms to P, T violating effects.

1.3.3 Molecules

In molecules, the electronic wavefunctions localized on the heavy nucleus are now strongly modified by the electric field from the ligand. For polar molecules in particular, the molecule now has a molecule frame electric dipole moment $\vec{D}_{\text{mol}}$, indicating a separation of charge across the molecule. This dipole moment is on the order of $ea_0 \approx 2.54$ D, where D is the preferred unit of dipole moment, the Debye. The dipole moment lies along the axis drawn from the heavy nucleus to the ligand, which defines the internuclear axis[12] $\hat{n}$. Often $\hat{n}$ is taken to lie along the $\hat{z}$ axis of the molecule frame coordinate system. We note that D_{mol} is not symmetry violating, as it reverses under P and remains invariant under T, and therefore the overall interaction $\vec{D}_{\text{mol}} \cdot \vec{E}_{\text{lab}}$ is P, T even. Since the ligand field causes Stark mixing of states with different orbital angular momenta l, only the projection of l given by $\lambda = \vec{l} \cdot \hat{n}$ is well-defined. As a result, the molecular electronic state can be expressed as a combination of atomic orbitals, for example $a_s s\sigma + a_p p\sigma + \ldots$, where the a values are wavefunction amplitudes. Here, we use molecular orbital notation, where σ means $\lambda = 0$. Therefore, in the molecule frame, P, T violating interactions can directly connect the s and p orbitals, without suppression by the ΔE_{sp}^{-1} factor we encountered in atoms [35]. Connecting to the atomic picture, we can think of $\vec{\mathcal{E}}_{\text{eff}} \propto \hat{n}$ in the molecule.

However, since molecular eigenstates still have well-defined parity to very good degree, there are still no P, T violating shifts in free-field[13], in other words $\langle \hat{n} \rangle = 0$. We can think of this as the molecular rotation averaging away D_{mol} in the lab frame, such that $\vec{\mathcal{E}}_{\text{eff}}$ has no preferred orientation. More rigorously, free-field molecular eigenstates are always written as symmetric or anti-symmetric combinations: $|\psi_{\text{mol}}\rangle \propto |\eta, \hat{n}\rangle \pm |\eta', -\hat{n}\rangle$, where $\pm$ is connected to the parity of the molecular state, and $\eta^{(\prime)}$ encodes additional quantum numbers. The key strength of molecules is that the opposite parity levels arise from molecular rotation, with energy separations of $\Delta E \lesssim 50$ μeV $\sim h \times 10$ GHz. As a result, compared to atoms, polarizing a molecule and orienting $\hat{n}$ in the lab frame is a manageable task, achieved with $E_{\text{lab}} \gtrsim 10$ kV/cm fields by mixing rotational states. As we shall see, certain molecules can have nearly degenerate opposite parity levels, known as parity doublets [17], separated by $\Delta E \lesssim 50$ neV $\sim h \times 10$ MHz, which can be polarized in fields $E_{\text{lab}} \lesssim 100$ V/cm. In parity doublets, the states $|\psi_{\text{mol}}\rangle$ are written with $\eta = \eta'$, that is all the quantum numbers are the same in parity doublet superpositions except for the direction of the internuclear axis. A good discussion of polarization by mixing opposite parity levels is given in Ch. 2 of Ref. [41], as well

---

[12]We take $\hat{n}$ to point along $\vec{D}_{mol}$, that is pointing from $- \rightarrow +$. In M-OH molecules, $\vec{D}_{\text{mol}}$ points from O to M in the physics convention for dipole moment.

[13]Technically, similar to atoms, there will be a small, induced P, T violating dipole moment [52, 66], but we can do much better than this as we shall see.

as in Ch. 2 of Ref. [67]. Sandars was the first to realize [68] that by orienting the molecule in the lab frame, we have effectively aligned $\vec{\mathcal{E}}_{\text{eff}}$, allowing us to access the full relativistic EDM enhancements available. Indeed, modern molecular EDM experiments have shown the power of this enhancement, setting very strong limits on the eEDM [10, 11], $|d_e| < 4.1 \times 10^{-30}\, e$ cm.

Fundamentally, in molecular experiments searching for P,T violating moments, we are measuring an interaction Hamiltonian of the form:

$$H_{PTV} = \xi_{PTV}\, W_{\text{elec}}\, (\vec{J}_{\text{odd}} \cdot \hat{n}). \qquad (1.10)$$

Here $\cdot$ indicates the dot-product. The quantity ξ_{PTV} represents the magnitude of the P,T violating electromagnetic moment, which can be connected to the high-energy physics scale. For example, this could be the eEDM, d_e. For nuclear observables, there can be additional enhancements in ξ_{PTV}, discussed later. The quantity W_{elec} encodes the aforementioned relativistic enhancement of P,T violating observables in the electromagnetic environment near a heavy nucleus. This quantity must be calculated from electronic structure theory, and the calculation accuracy can be gauged by also calculating hyperfine interaction parameters and comparing against experiment. For the eEDM, W_{elec} can be directly related to the notion of an internal effective field, $\mathcal{E}_{\text{eff}}$. Continuing, the quantity $\vec{J}_{\text{odd}}$ represents the rank 1 operator formed by coupling together an odd number of angular momenta in the atom or molecule, which is explicitly T-odd. The form of $\vec{J}_{\text{odd}}$ varies for different moments. However, regardless of the interaction, ξ_{PTV} must lie along $\vec{J}_{\text{odd}}$, as we discussed earlier. Finally, we measure the projection of $\vec{J}_{\text{odd}}$ onto the internuclear axis of the molecule, $\hat{n}$. The dependence on $\hat{n}$ explicitly makes the interaction P odd, and requires us to apply an external field to polarize the system. Since our goal is to measure the shifts from H_{PTV}, we can go about measuring frequency differences between states with various orientations of J_{odd} relative to $\hat{n}$. In an atom experiment, we can use a similar Hamiltonian, just replacing $\hat{n}$ with the applied field $\vec{E}_{\text{lab}}$. Finally, we note there are proposed schemes to measure P,T violating *couplings* between opposite parity states by using AC fields, see Ref. [69], however we do not discuss the details here.

We now discuss the form of $\vec{J}_{\text{odd}}$ for different P,T violating interactions. For the eEDM, we have $\vec{J}_{\text{odd}} = \vec{S}$, which means the EDM shift is just the projection of the electron spin on the internuclear axis of the molecule, as expected. For the NSM, we recall that the physical mechanism of the interaction results in an electric field internal to the nucleus that points along the spin I. Therefore, for the NSM we have $\vec{J}_{\text{odd}} = \vec{I}$. Finally, for the NMQM, the situation is more complicated because we are dealing with a rank 2 tensor, $\mathcal{M}$, interacting with a rank 1 vector, the electron spin S. Since J_{odd} must be rank 1 in order to be contracted with $\hat{n}$, we surmise the form of J_{odd} is obtained by coupling I to itself, and then coupling with S. Indeed, up to some constants, this gives us the

effective the form of the NMQM interaction [57, 58, 70]:

$$H_{\mathrm{MQM}} = W_M \mathcal{M} \vec{J}_{\mathrm{odd}} \cdot \hat{n} = -\frac{\mathcal{M}}{2I(2I-1)} \vec{S} \cdot \overleftrightarrow{T} \cdot \hat{n}$$
$$= \frac{\mathcal{M}}{2I(2I-1)} \sqrt{\frac{20}{3}} T^1(S, T^2(I,I)) \cdot \hat{n}.$$

(1.11)

Here, W_M is the electronic enhancement factor, and $\mathcal{M} := \mathcal{M}_{zz}$, where $\hat{z} = \hat{n}$. In the second line we have written the interaction in terms of spherical tensor operators (see Ch.5 of Ref. [39] for details). The tensor $\overleftrightarrow{T}$ is the same as T_{ij} in eq. 1.5, and is written as $T_{ij} = \{I_i, I_j\} - \frac{2}{3}\delta_{ij}I(I+1) = 2T^2(I,I)$. Using the same arguments, we see that the effective interaction of an electric octupole moment should be written as $\vec{J}_{\mathrm{odd}} \cdot \hat{n} \propto T^1(I, I, I) \cdot \hat{n}$.

1.3.4 Nuclear Enhancements

Finally, we discuss the nuclear enhancements of ξ_{PTV}, which are relevant for the nuclear moments. The enhancements of nuclear moments have been discussed in many references [51, 57, 70–84], though we caution that nuclear structure calculations are intrinsically challenging. Of these, Refs. [81] treats the nuclear theory with particular care. Fundamentally, all of the nuclear enhancement mechanisms relate to the existence of deformed nuclei [85], which arise from collective proton-neutron interactions[14] [86]. The collective states of deformed nuclei are described by the Nilsson model [86], and the wavefunctions describing the rotation of the deformed nucleus are the same symmetric top wavefunctions that we use to describe rotating molecules.

In general, there are two types of relevant nuclear deformations: quadrupole and octupole deformations. A quadrupole deformed nucleus is shaped like an ellipse, with the deformation either along I (prolate) or perpendicular to I (oblate). Quadrupole deformed nuclei can be though of like a homonuclear linear molecule, as the deformation is symmetric upon reflection through a plane perpendicular to I. Just like homonuclear molecules, quadrupole deformed nuclei have rotational ladders of same parity states. In quadrupole deformed nuclei, there are many nucleons in the valence shell, and the total NMQM is enhanced by an order-of-magnitude by summing all of the individual nucleon contributions [57, 70, 80]. Note, however, these estimates tend to ignore configuration mixing effects, which could modify the overall NMQM magnitude [80].

On the other hand, octupole deformed nuclei are pear-shaped with a cylindrical symmetry axis, and have intrinsic reflection asymmetry when reflected about a plane perpendicular to the symmetry axis [85, 87–89]. Several nuclei, including isotopes of Thorium [90] and Radium [91], have been observed[15] to exhibit octupole deformations, which are classified as either static (intrinsic

---

[14]It is interesting to observe that the simplest proton-neutron system, deuterium, has a quadrupole deformation.

[15]In Thorium, Ref. [90] observes the E1 (electric dipole) matrix elements, a sign of reflection asymmetry, and uses that to estimate the octupole deformation. In Radium, the E3 (octupole) matrix elements are directly observed.

deformation) or dynamic (arising via vibrations). Their reflection asymmetry means they are the nuclear analogue of heteronuclear molecular states, which naturally have rotational ladders containing opposite parity states. In fact, because the nucleus can have angular momentum projected on the cylindrical symmetry axis, octupole deformed nuclei are actually analogues of parity doublet states in heteronuclear molecules. As a result, octupole deformed nuclei can have closely spaced opposite parity levels that split due to Coriolis interactions. For example, ^{223}Ra and ^{225}Ra have parity doublets separated by 50 keV [92] and 55 keV [93], respectively, which are "close" by nuclear standards. Similar to the earlier discussion of P, T violation in atoms, any interaction H_{PT} in the nucleus can mix these opposite parity levels, inducing a small overall orientation (dipole moment) of the nuclear pear shape along the nuclear spin I. Such a correlation of orientation with angular momentum is P, T odd. The mixing of opposite parity nuclear states is expected to significantly increase the value of the NSM and NMQM by over an order-of-magnitude [74–78, 81, 83]. Further, the NSM receives an additional increase from the r^3 nuclear radius dependence of the NSM, which correlates with the octupole matrix element [81] (recall an octupole deformation is proportional to rank 3 spherical harmonics). As a result, NMQMs can be 1-2 orders-of-magnitude higher in octupole deformed nuclei, while the NSM can be 2-3 orders-of-magnitude higher [83]. This provides strong motivation for performing P, T violation measurements on molecules containing Radium nuclei [94].

1.3.5 Connection to High Energy Physics

Interpreting EDM bounds in terms of high energy physics requires the framework of the Standard Model effective field theory (SMEFT) [7, 15, 95–97]. Theorists can use the SMEFT to match low energy observable to high energy models, deriving model-dependent constraints. Ref. [98] provides an excellent example by interpreting the high energy consequences of recent molecule EDM experiments. The basic idea of SMEFT is similar to the effective Hamiltonians we use later for modeling molecular physics. Further, one of the first examples of an EFT is the Fermi electroweak theory, which was developed before the discovery of the W and Z bosons. Fermi used an effective constant G_F (equivalent to a Wilson operator) to encode all of the unknown physics at high energy scales, and was able to write an effective model for beta decay that only invovled particles known at the time.

In SMEFT, the Standard Model is taken to be an effective theory that is only accurate at "low energies" below a cut-off scale, Λ, which encodes the high energy scale of new physics beyond the Standard Model (BSM). The new physics effects are accounted for at low energies using a series of effective operators that only involve the Standard Model degrees of freedom. The coefficients that scale these operators are known as Wilson coefficients, and they encode all of the new physics information. To construct the effective theory, in addition to the Standard Model, we write down

any additional terms that satisfy physically relevant constraints. Examples of such constraints include Lorentz invariance, gauge symmetry, T symmetry (=CP), and locality. For searches for P, T violation, we can relax the T symmetry constraint. The terms encoding BSM physics are written as:

$$\mathcal{L}_{BSM} = \sum_{k,d} \alpha_k^{(d)} \left(\frac{1}{\Lambda}\right)^2 O_k^{(d)}. \tag{1.12}$$

Here, the $O_k^{(d)}$ are the k different operators of a given dimension[16] d that satisfy our constraints. The operators essentially describe a vertex of the Lagrangian, with certain particles going into the vertex and certain particles coming out. The d sum begins at $d \geq 4$. The $\alpha_k^{(d)}$ are the Wilson coefficients that encode all the BSM physics we have integrated out. And Λ is the scale of the new physics. We note these effective operators are not renormalizable, and are only meant to be applied to low energy scales.

For T violating observables, the only relevant term at $d = 4$ is the θ QCD vacuum angle. At dimension $d = 5$ we have the operators that generate fermion EDMs in the electroweak force via the CKM matrix. We will return to the EDMs generated by CKM later. Then, at $d = 6$, we have a host of 15 operators that encode T violating effective interactions between the first-generation Standard Model fermions and bosons. Typically other generations of particles are not considered. These operators are listed in Refs. [7, 95, 96]. The T violating terms can be grouped into the following categories: fermion EDMs, four-quark couplings, three gluon couplings, quark Higgs couplings, lepton quark couplings, and quark chromo-EDMs. An example is the operator encoding a fermion EDM d_f, given by:

$$\mathcal{L}_{\text{EDM}} = -i\frac{d_f}{2}\bar{\psi}\sigma^{\mu\nu}\gamma^5 F_{\mu\nu}\psi. \tag{1.13}$$

Here, $d_f = \alpha_f \Lambda^{-2}$ is the fermion EDM Wilson coefficient including the high energy mass scaling, $\sigma^{\mu\nu} = \frac{i}{2}[\gamma^\mu, \gamma^\nu]$ represents the fermion spin, sums are performed over repeated indices, γ^μ are Dirac gamma matrices, γ^5 causes P-odd behavior, $F_{\mu\nu}$ is the electromagnetic field strength tensor, and the combination of $\bar{\psi}$ and ψ encode the fermion wavefunction, indicating the operator vertex has the fermion ψ in both the initial and final states.

To connect from the SMEFT scale to our low energy atomic and molecular scale, theorists must go from working with quarks to working with hadrons, which are bound states of the strong force with no color charge. This involves the application of further EFTs, such as chiral EFT, which we will not discuss. In the end, the result is a series of contributions to our low energy P, T violating moments of interest. In general, multiple Wilson coefficients will contribute to interpreting any P, T violating moment. The nuclear P, T violating moments in particular receive

---

[16]In high energy physics, energy = mass = length^{-1}, so we can think of everything as having energy dimension.
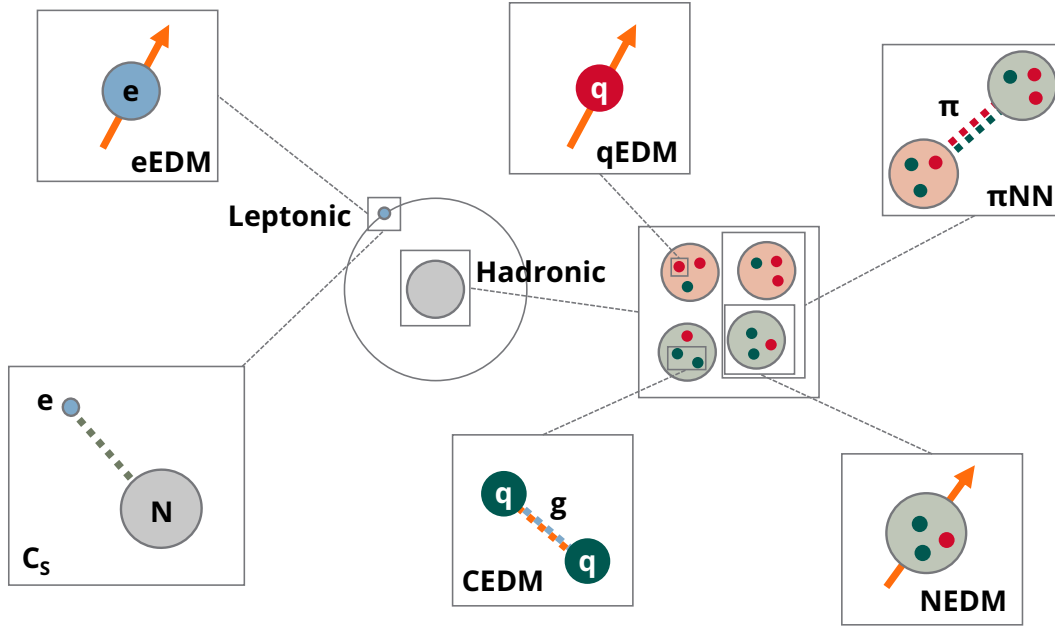
Figure 1.1: Schematic diagram illustrating some sources, not exhaustive, of P, T violating physics in atoms and molecules. The interactions displayed are: the electron electric dipole moment (EDM), the electron-nucleon scalar-pseudoscalar coupling C_S, quark EDMs, quark chromo-EDMs (CEDM), overall nucleon EDMs (NEDM), and P, T violating pion exchange (πNN), representing internal nuclear forces. Figure created by N. Hutzler.

numerous contributions. This would make it not possible to determine the source of P, T violation from one positive measurement alone, requiring measurements in many different systems. In Figure 1.1, we show the various contributions to T violation in atomic and molecular systems at the hadronic scale.

Even the electron EDM receives multiple contributions in EFT. At the hadronic scale, the $\vec{S} \cdot \vec{\mathcal{E}}_{\text{eff}}$ eEDM interaction receives contribtuions from both the fermion EDM of the electron, d_e, and from the scalar-pseudoscalar nucleon-electron coupling, denoted C_S. In the hadronic picture, the C_S interaction given by $\bar{e} i \gamma_5 e \bar{N} N$, where N is a nucleon wavefunction, e is the electron wavefunction, and $i\gamma^5$ is P, T odd. This is essentially an interaction of the electron spin with the scalar nucleon density that arises from the quark-lepton interactions in the SMEFT. Essentially, when we interpret an eEDM experiment as a constraint on d_e, we are performing a single-source assumption, and setting $C_S = 0$ implicitly. Technically, an EDM constraint from a single experiment consists of bounding P, T violation to a diagonal line of some width in the entire 2-D parameter space spanned by C_S and d_e. Only by performing measurements in multiple systems, which naturally have different slopes in the C_S, d_e space, can we obtain a finite constraint region. For example, only by combining the EDM constraint from the JILA experiment in Ref. [10] and the constraint from the ACME experiment in Ref. [11], do we obtain tight bound on both variables: $|d_e| < 2.1 \times 10^{-29}$ e cm
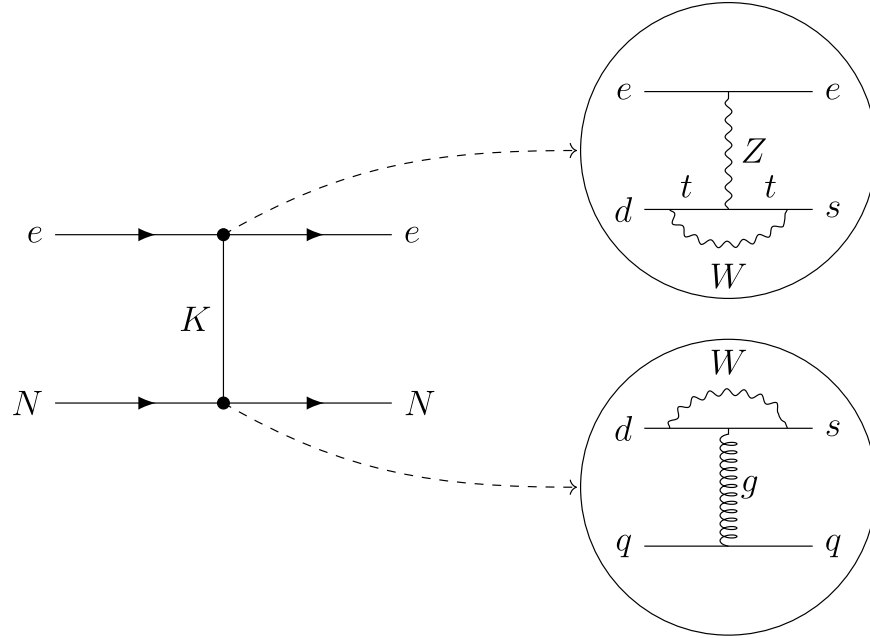
Figure 1.2: Diagram of the leading order contributions to the C_S interaction resulting in an equivalent eEDM of $\sim 10^{-35}$ e cm, adapted from Ref. [99]. The interaction is a 3rd order electroweak interaction involving all three quark generations, which is necessary to generate a non-trivial CKM phase. The particle exchanged between the electron and neutron is a Kaon. The upper electron vertex is T-odd, P-even, while the lower nulceon vertex is T-even, P-odd, resulting in an overall P, T-odd interaction. Thanks to Jane Panangaden for creating this figure.

and $|C_S| < 1.9 \times 10^{-9}$ e cm [10]. This is a reason why having many different EDM searches is complimentary.

We must also consider multiple eEDM sources when we ask the very relevant question, "What is the eEDM prediction of the Standard Model?" The Standard Model is known to violate T symmetry in the electroweak force via the complex phase of the CKM matrix that converts quark mass eigenstates to electroweak eigenstates. It turns out the Standard Model contributions to d_e are considerably weaker than the contribtions to C_S. While the pure d_e contribution is estimated at $\sim 6 \times 10^{-40}$ e cm, the C_S term was previously estimated to contribute at the $\sim 10^{-38}$ e cm [8] equivalent scale. A very recent calculation from Ref. [99] has considered a novel mechanism that contributes to C_S at third order in the electroweak force. The Feynman diagram for this interaction is reproduced in Figure 1.2. The interaction results in $C_S \sim 7 \times 10^{-16}$, corresponding to an an equivalent Standard Model eEDM at the 10^{-35} e cm scale, much larger than any previous estimate. While this is still $\sim 5 - 6$ orders-of-magnitude smaller than the current best eEDM bounds, it raises the possibility that future order-of-magnitude improvements in EDM experiments could measure the Standard Model value. While this would mean eEDM measurements would no longer be background-free, is an exciting prospect nonetheless. Measurements of the eEDM in different

systems could be used to extensively benchmark our theoretical understanding of nature, all the way from the high energy scale to the nuclear scale to the atomic scale.

Finally, we note that by using dimensional arguments, we can estimate model-independent constraints on high energy physics [7, 12, 98]. These estimates are expected to be accurate to within an order-of-magnitude. This allows us to connect an experimental EDM bound to the high energy scale in a simple manner. For example, for the eEDM, the estimate is given by [10, 11, 98]:

$$\frac{d_e}{e} \sim (\hbar c) \sin \phi_{TV} \left(\frac{\alpha_{\text{BSM}}}{4\pi}\right)^n \frac{m_e c^2}{\Lambda^2}. \tag{1.14}$$

Here, e is the electron charge, ϕ_{TV} is the T violating phase angle, α_{BSM} is the coupling strength of BSM physics to the electron, n is the number of loops involved in generating the eEDM, m_e is the electron mass, and Λ is the energy scale of the BSM physics. Typically, estimates set $\alpha_{BSM} \sim \alpha_{EM}$, and $\phi_{TV} \sim \pi/2$. For example, the constraint of Ref. [10] corresponds to a limit of $\Lambda \gtrsim 40$ TeV for 1-loop processes and $\Lambda \gtrsim 1$ TeV for 2-loop processes. Even if we introduce additional caveats that pull these constraints down by a factor of 10, we see they are still competative with the direct constraints from the LHC. Furthermore, regardless of our caveats, order-of-magnitude improvements in EDM bounds result in order-of-magnitude increases in high-energy physics.

1.4 Why Polyatomic Molecules?

1.4.1 Long Term Vision

So far, we have provided an overview of searches for fundamental symmetry violation in atoms and molecules. We have shown why molecules with heavy nuclei are extremely sensitive probes of new physics. We now provide the final motivation for why we seek to perform EDM measurements in polyatomic molecules.

Current state-of-the-art eEDM experiments are broadly sensitive to T-violating physics at energies much greater than 1 TeV [10–12, 100, 101]. Molecular beam experiments have achieved high statistical sensitivity by measuring a large number of molecules over a ≈ 1 ms coherence time [11, 100]. While there are further improvements that can increase sensitivity, beams of neutral molecules are ultimately limited by their interaction time. To achieve orders-of-magnitude improvement in sensitivity, we must slow, cool, and trap the molecules. Already, molecular ion experiments obtain seconds long coherence times [10, 101, 102], though the number of ions in their traps are limited by Coloumb repulsion. Measurements with trapped neutral polyatomic molecules can potentially combine the best features of each approach to achieve orders-of-magnitude improved statistical sensitivity [17].

Additionally, precision measurements in trapped atoms and molecules have significant synergy with the toolbox of techniques developed for studies of quantum information, quantum simulation,

and quantum metrology. In these fields, state-of-the-art quantum control techniques allow for bottom-up control of quantum states, their interactions, and their entanglement. Precise entanglement control in atoms has already been demonstrated to provide metrological advantages. By harnessing these techniques for EDM searches, we can push the energy reach of EDM experiments to PeV energy scales or higher.

The starting point for ground-up quantum control of neutral atoms is laser cooling and trapping. While atomic laser cooling is now decades old, molecular laser cooling was first demonstrated in 2010 with SrF molecules [103], with the first magneto-optical trap following a few years later [104]. Since then, the field has made significant strides, with laser cooling and/or trapping having been demonstrated for many diatomic species. Further, laser cooling and/or trapping has recently extended to several species of polyatomic molecules [105–111]. These advances have been made possible by the development of a recipe of the primary ingredients necessary for molecular laser cooling [112, 113]. Most importantly, the molecule must be chosen such that the laser cooling valence electron is decoupled from chemical bonds. This decoupling is achieved by choosing molecules formed by an alkaline-earth(-like) atom with two valence electrons, designated M, that is single-bonded to an electronegative ligand. The ligand can be a halogen (F, Cl, etc.) in the case of diatomic molecules, or, in the case of polyatomic molecules, can have the form -O-R, with R serving as a placeholder ranging from a simple H atom to complicated functional groups [112]. We can think of the bond in the ionic picture, where the metal atom readily gives up an electron that bonds with the ligand, giving us a simple picture of the charge distribution in the molecule: M^+-O^--R. The remaining un-bonded electron on the metal atom is pushed away from the bonding region, and is described as having atomic character. Though the M-O-R motif may not be absolutely necessary for laser cooling [114], it certainly guarantees, to good degree, that the valence electron of the molecule is largely independent of of the bond. This allows for many photon scatters with minimal vibrational repumping lasers [115].

On the other hand, the success of existing molecule EDM experiments has demonstrated the power of parity doublets. When polarized, parity doublets allow for reversal of P, T violating interactions without modifying laboratory fields. This is a huge aid for systematic error rejection in precision measurements [10, 11]. Further, parity doublets allow for coherent control of the orientation of the internuclear axis in the lab frame. It is difficult to generically find a diatomic molecule that satisfies all three of the following constraints: laser-coolable, containing parity doublets, and containing core-penetrating orbitals centered on a heavy nucleus. The difficulty is largely because we are relying on the electronic structure of the molecule to satisfy three requirements at once, resulting in conflicting demands. This motivates moving toward polyatomic molecules for the future of molecular EDM experiments.

Polyatomic molecules generically have parity doublets arising from internal rotations of nuclei about the molecule axis. Since this structure results from rotations of nuclei, and since we have chosen a molecule with an electron decoupled from the bonds, the electronic structure for laser-cooling can generically co-exist with the parity doublet structure for EDM measurements. This lays the foundation for a future vision of laser cooled and trapped polyatomic atomic molecules, entangled together to perform an EDM measurement with quantum enhanced metrology [18].

1.4.2 Molecular Orientation Control

Molecules with parity doublets have free-field eigenstates with parity $\mathcal{P}$ that can be generically written as:

$$|\psi, \mathcal{P} = \pm\rangle = \frac{1}{\sqrt{2}} \left(\left|J, K, M\right\rangle \pm \left|J, -K, M\right\rangle \right). \tag{1.15}$$

Here, $\pm$ represents the state parity (up to a J dependent phase for simplicity), J is the total angular momentum of the state, $M = \vec{J} \cdot \hat{Z}$ is the projection of J on the lab $\hat{Z}$ axis, and $K = \vec{J} \cdot \hat{n}$ is the projection of J on the intermolecular axis. For a given value of J, we see that molecular eigenstates are labeled by two projection quantum numbers, M and K, that desribe the orientation of J in both the lab and molecule frames. The separation of the $\pm$ parity states can vary depending on the choice of polyatomic molecule, allowing for some tuning. In the bending modes of linear triatomic molecules, the parity states can be separated by ~10 MHz, while in symmetric top molecules, the splitting can be even smaller, ~300 kHz [116].

While ordinary angular momentum states, $|J, M\rangle$, have $2J+1$ degeneracy in free field, describing the different orientations of J, we see molecular eigenstates have $2(2J + 1)$ near-degenerate states, describing both the orientations of J and the two orientations $\pm K$ of the internuclear axis. For certain molecules, like bending modes of linear triatomics, we are restricted to have a single value of $|K|$ in a given electronic and vibrational state. However, if we generalize our consideration to asymmetric rotors, we find there are actually $(2J + 1)(2J + 1)$ states, though they are no longer necessarily near degenerate. One factor corresponding to the spatial orientations of J on $\hat{Z}$, and the other factor corresponds to the internal orientations of J on the molecular axis $\hat{n} = \hat{z}$. However, we note we are typically interested in the maximally projected states, $J = |K|$.

Regardless of the specific polyatomic molecule, by creating superpositions of different M and K states, we have available to us many different orientations of the molecular axis in space. The orientation of the molecule axis in the lab frame is given by $\langle \hat{n} \rangle \propto \langle MK \rangle$, with $\langle \hat{n} \rangle = 0$ at free field. However, since parity doublet states in polyatomic molecules are separated by $\lesssim 10$ MHz, and since them have $D_{\mathrm{mol}} \sim ea_0$, we can mix these states and polarize the molecule by applying an external field $E_{\mathrm{lab}} \sim 100$ V/cm. In Figure 1.3, as a function of the applied electric field, we compare the orientation $\langle \hat{n} \rangle$ of a linear triatomic molecule with parity doubling with the orientation
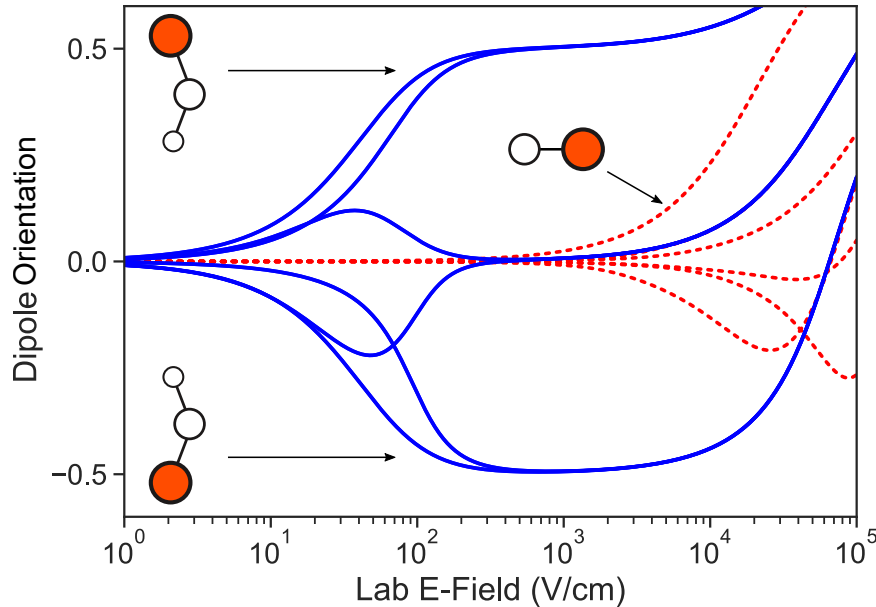
Figure 1.3: Plot of $\langle \hat{n} \rangle$, labeled "Dipole Orientation," as a function of the applied electric field (note the log scale), in a polyatomic molecule with parity doubling (blue lines) with $N = 1$ (N labels rotational quanta), compared to a diatomic molecule without parity doubling (dashed red lines) with $N = 0, 1, 2$. Not only do parity doublets polarize at order-of-magnitude lower fields, but they generically provide states with collinear orientation and transverse alignment with respect to the electric field. We note the orientation for parity doublets saturates at $|\hat{n}| = 0.5$ because the projection on the laboratory axis is given by $\ell M_N / (N(N+1)) = 1/2$ for a Hund's case (b) (see Ch. 2) molecule with $N = M_N = \ell = 1$ [117]. We can think of this as the molecular rotation being split between overall rotation and rotation about the $\hat{n}$ axis. At large fields, the parity doublet in $N = 1$ mixes with higher N, causing an overall orientation behavior of the polyatomic similar to the diatomic.

of a diatomic molecule without parity doublets. Not only does the polyatomic molecule polarize more quickly, it also has states available that correspond three possible lab orientations: aligned with the applied field, perpendicular to the applied field, and anti-aligned to the applied field. Here, we only have 3 orientations as we considered a $J = 1$ state. In general, when the molecule is fully polarized, we have $2J + 1$ orientations of the internuclear axis, corresponding to the different values of M in the expectation value $\langle MK \rangle$.

In molecules with parity doublets, we can provide a simple intuitive picture of such states in the fully polarized limit. For now, we consider just a space of four states, formed by the combinations of $\pm M$ with $\pm K$, given by $|J, M, K\rangle$. These states are shown in Figure 1.4, which encapsulates the basic idea of any molecule EDM experiment with parity doublets. Recall from eq. 1.10, we can think of any P, T violating interaction as $H_{PTV} \propto \vec{J}_{\mathrm{odd}} \cdot \hat{n}$. For this discussion, we will use J to generically represent J_{odd}, such that $H_{PTV} \propto K$, as the basic picture is agnostic about the specific P, T violating interaction in question. Each $|J, M, K\rangle$ state has a unique set of shifts under
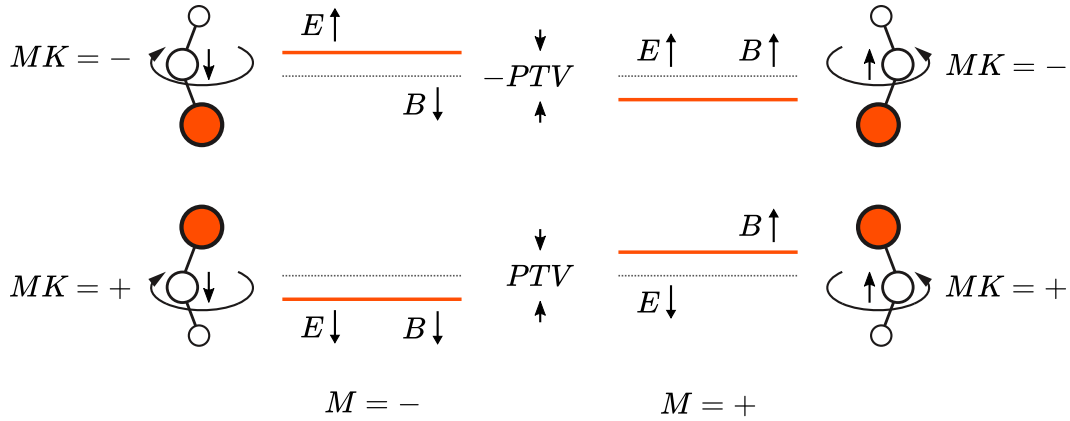
Figure 1.4: Diagram showing schematic energy shifts for measurements of P, T violation (PTV) in a fully polarized molecule with parity doublets. Dotted lines show energies in absence of PTV. $M = \pm$ describes the lab frame projection of J_{odd} (see main text), while $MK = \pm$ describes the lab frame orientation of the internuclear axis $\hat{n}$. The PTV shift is given by $H_{PTV} \propto K$, where K is the projection of J_{odd} on $\hat{n}$. Energy shifts from external E and B fields are also indicated.

E fields, B fields, and P, T violating interactions. When comparing the energy shifts of states with $\pm M$ and fixed MK, we are probing T violation, which can result from either B or H_{PTV}. On the other hand, if we compare $\pm MK$ states with fixed M, we are probing P violation, which can result from either E or H_{PTV}. By comparing both $\pm M$ and $\pm MK$ states, we can uniquely distinguish H_{PTV} from E or B effects. Since this manifold of four states exists generically at any value of E_{lab} that polarizes the molecules, we see we have access to all combinations of P and T violation *without* changing the orientation of any laboratory fields! In reality, the electric and magnetic sensitivities of the upper and lower MK manifolds will not be exactly identical, which can mimic an EDM. However, we can then perform additional reversals of laboratory fields to help disentangle real EDM shifts from differential sensitivities. Therefore, a major goal of any EDM experiment is to reduce systematics and false signals that can arise from interactions with external fields, particularly non-reversing fields. In this regard, the near-complete reversal of P, T violating effects afforded by parity doublets have proved to be an extremely useful tool for systematic error rejection in molecular eEDM searches [10, 11].

As we have seen, not only do parity doublets allow for easy molecular polarization, they allow for exquisite control of the orientation of both T odd angular momenta and the P odd internuclear axis vector $\hat{n}$. It should come as no surprise that such a structure is very desirable for experiments seeking to measure P, T violation. Furthermore, if we can one day harness quantum entanglement for a metrological advantage, it will be very useful to have the toolbox of $|J, M, K\rangle$ states available to develop novel EDM measurement techniques that evade sources of noise and systematic errors that typically plague experiments.

1.4.3 Quantum Projection Noise

Fundamentally, the precision of an EDM measurement is limited by quantum projection noise (QPN), which is a quantum mechanical effect arising from non-commutation of operators. In this section, we discuss how QPN limits EDM experiments, motivating us to move toward trapped neutral molecules for precision measurements.

For detailed discussion on QPN, see Refs. [118, 119]. Consider repeated measurements of the phase of a two level superposition state, $|\psi(\tau)\rangle \propto |0\rangle + e^{i\phi}|1\rangle$. If we project this state onto the $|0\rangle \pm |1\rangle$ basis, we obtain a spread of results with some width. For N independent measurements of a phase ϕ, irrespective of other noise sources, the QPN limit is given by [119]:

$$\delta\phi = \frac{1}{2C\sqrt{N}}. \tag{1.16}$$

Here, $C \leq 1$ is the contrast of our measurement, which encapsulates deviations resulting from decoherence as well as imperfect state preparation and readout.

The QPN limit can be recast into a limit on our ability to measure a frequency ω, by scaling it by the measurement interaction time τ. For experiments that operate in a pulsed fashion, we can also expand N as $N = N_p R_p T_{tot}$, where N_p is the number of measurements obtained in a pulse, R_p is the rate of pulses per time, and T_{tot} is the total time that we run the experiment. We then obtain:

$$\delta\omega = \frac{1}{2C\tau\sqrt{N_p R_p T_{\text{tot}}}}. \tag{1.17}$$

We can make some rough estimates for a beam source. With $\tau = 1$ ms, $C = 0.5$, $N_p = 10^6$, $R_p = 10$ Hz, we obtain a frequency QPN limit of $\delta\omega = 2\pi \times 1$ mHz for $T_{\text{tot}} = 1$ day.

The scaling of $\delta\omega \propto \tau^{-1}$ motivates us to consider the effect of extending the interaction time by using a trap. Consider now the value $\tau = 1$ s, limited by the lifetime of a bending mode in a polyatomic molecule, and a trapped number of $N_p = 10^4$ molecules[17]. We note that we can no longer run at 10 Hz, however, as the entire experiment takes at minimum 1 second. To encapsulate the connection between increasing measurement time and decreasing measurement rate, we write $N = N_p D\tau^{-1}T$, where D is the duty cycle of the experiment. The full frequency QPN limit for a duty cycle limited experiment is given by:

$$\delta\omega = \frac{1}{2C\sqrt{\tau}\sqrt{N_p D T_{\text{tot}}}}. \tag{1.18}$$

Continuing with our estimate, for a 10^4 trapped molecules, 1 s coherence, and a $D = 50\%$ duty cycle, we obtain $\delta\omega = 2\pi \times 0.02$ mHz for $T_{\text{tot}} = 1$ day.

---

[17]A factor of 2 higher number was trapped in a CaOH MOT in Ref. [108]. While the EDM measurement cannot proceed in a MOT, we use this as an initial estimate.

While two orders-of-magnitude is already quite good, we provide further discussion on why traps are the future of molecular EDM experiments. First, there is a pathway towards increasing both the number of trapped molecules [120–122] and toward increasing the lifetime of the species [123]. Next, an experiment may not always be quantum projection noise limited. If other noise sources are not adequately controlled, we will have to contend with them first. Therefore it is attractive to develop methods for suppressing sensitivity to external noise.

Noise reduction can be classified as passive, active, or "quantum." Magnetic shielding is an example of passive noise cancellation, whereby we redirect ambient magnetic fields away from the experiment. It is certainly easier to shield a small trapped volume compared to a large beamline. We can also use active compensation to measure and feedback on the ambient field to cancel its fluctuations, which is also easier to perform for a small volume.

We use "quantum" to refer to techniques that utilize quantum control to improve sensitivity to noise. An example of this is state engineering in molecules, where we tune the noise sensitivities of measurement states using external control fields. We demonstrate this technique in trapped CaOH molecules in Ch. 5, Sec. 5.4. Further, in Ref. [124], it was shown that transitions between molecular states can also be tuned with external fields to have suppressed noise sensitivity. All of these techniques are more easily implemented in a trap, where we can precisely control applied fields. Finally, we note that there are protocols that achieve metrological gain in isotope shifts of trapped ions by using entangled states in a decoherence free subspace [125, 126]. Generalization of these techniques to EDM measurements would be very useful.

Finally, we add that quantum control can also be used to make a state *more* sensitive to the interaction of interest, by going beyond the QPN limit. Using *spin-squeezed states* [127], measurements can approach the ultimate Heisenberg limit, $\propto 1/N$, instead of $1/N^{-1/2}$ [18]. A spin-squeezed state is essentially an ensemble of entangled spins. For an un-entangled state, the minimum uncertainty noise is symmetric in all observables. For a spin squeezed state, the noise from an observable of interest, is transferred to another observable. For example, spin-squeezing of a superposition along the XY plane of the bloch sphere can reduce quantum uncertainty of the XY phase observable, which is sensitive to Z rotations, at the expense of increased uncertainty in the phase along the XZ or YZ planes. However, the observable with reduced uncertainty will be more sensitive to noise from other sources that were previously unresolved, for example from stray magnetic fields. Furthermore, entangled states are difficult to produce and keep coherent, necessitating the use of a trap. Nonetheless, quantum metrology is the final frontier for achieving significant EDM sensitivity gains in the future, with many different entangled states available that can offer unique advantages [128].

2

MOLECULES

This is where the fun begins.

–Anakin Skywalker

2.1 Molecular Structure

Most atomic and molecular systems, beyond hydrogen and H_2^+, constitute a many-body quantum Hamiltonian that is too complicated to be described analytically, and requires extensive theoretical tools to approach from a purely computational perspective. How then are we to perform a precision measurement in such a complicated system? We rely on the fact that atomic and molecular systems have degrees of freedom that remain relatively well-conserved as the system state evolves. We refer to these conserved or approximately conserved quantities as *good quantum numbers*.

Quantum numbers are eigenvalues of a state associated with the action of an operator of interest on the state. A perfect quantum number is associated with an operator that commutes with the Hamiltonian. Since the Hamiltonian generates time evolution, a commuting operator corresponds to a conserved quantity. By Noether's theorem, perfect quantum numbers correspond to symmetries of the Hamiltonian. In the matrix representation of the Hamiltonian, these conserved quantities allow us to represent the Hamiltonian in a diagonal basis. Examples of quantum numbers in free space, which, as far as we know, are perfect, include: the total energy E, which is the eigenvalue of the operator H; the total angular momentum F, associated with the operator F^2 with eigenvalue $F(F + 1)$; and the projection of F on the lab Z-axis, $\vec{M}_F = \langle \vec{F} \cdot Z \rangle$. These operators are conserved by virtue of time-reversal symmetry and 3D rotational invariance of the atomic or molecular

Hamiltonian.

Now, imagine we break the spherical symmetry of space by applying an electromagnetic field along the $\hat{Z}$ axis. If this field couples to the atom or molecule, we no longer have F as a perfect quantum number, as the system can exchange momentum with the field. However, there still exists cylindrical symmetry around the applied field vector, and therefore M_F is conserved. If the applied field interaction is weak compared to the energy separation of different F levels, then the coupling of different F levels is perturbatively small, and we say F is an approximately good quantum number.

Of course, this discussion need not be restricted to interactions with an external field, as the notion of approximately good quantum numbers can apply to individual operators in a constituent system as well. If there is a separation of energy scales, then we can have approximately good quantum numbers that are only slightly mixed by off-diagonal matrix elements of the Hamiltonian. These good quantum numbers are only good to some approximation, and the collection of good quantum numbers can vary among eigenstates separated by large energy scales (i.e., large in the atomic scale, ~ eV). A given collection of good quantum numbers can be used to construct a basis to describe the molecule or atom. In the systems we study, there are often electronic states with internal structure that is well described with a single basis.

There are also poor quantum numbers, associated with operators with completely undefined expectation values. This can apply when there are strong interactions between angular momenta that make them indistinguishable from each other. For example, the intuitive end-over-end rotation of the molecule, R, interacts with the angular momentum of the electrons, L, and as a result only their combination is well-defined. The separation of energy scales and perturbative treatments of off-diagonal operators is essential to make the molecular problem tractable. Connecting various physical scenarios to a choice of a quantum number basis is at the heart of the effective Hamiltonian treatment of molecular states. We will discuss the effective Hamiltonian in Sec. 2.2 in detail, along with Hund's cases (Sec. 2.1.5), which correspond to different bases used to describe molecules in different physical regimes. However, first we will establish the foundations of describing with molecules, which is first describing atoms.

2.1.1 Angular Momentum and Spherical Tensors

There are many good references on angular momentum algebra, such as Brown and Carrington Ch. 5 [39], Hirota [129], or Zare [130]. Here we simply present a few foundational concepts. We define the lab frame with axes written as $\hat{X}, \hat{Y}, \hat{Z}$, and we note these are unit vectors, not

operators. In quantum mechanics, the angular momentum vector[1] $\vec{J}$ has lab-frame components (i.e., $J_X = \vec{J} \cdot \hat{X}$) that satisfy the essential commutation relations $[J_i, J_j] = i\epsilon_{ijk}J_k$, where ϵ_{ijk} is the Levi-Civita symbol, and the index i, j, k runs over X, Y, Z.

The total angular momentum magnitude $\vec{J}^2$ commutes with any of its components. Picking J_Z as is convention, we can define quantum states of angular momentum, written as $|J, M\rangle$. These states are eigenstates of the the the operators $\vec{J}^2$ and $J_Z = \vec{J} \cdot \hat{Z}$, with respective eigenvalues $J(J + 1)$ and M. Each of the $2J + 1$ values of M specifies an *orientation* of the vector $\vec{J}$, with M running from $-J, -J + 1, \ldots, J$. The remaining components, J_X and J_Y, are written in terms of raising and lowering operators: $J_\pm = J_X \pm iJ_Y$. As the name implies, $J_\pm$ can change the orientation of the angular momentum vector, $M \to M \pm 1$, while preserving the magnitude J. The matrix elements of $J_\pm$ can be found in the literature. These definitions encode an accepted phase convention choice, the Condon and Shorltey phase, such that the matrix elements of J_X are real.

All of the atoms and molecules we are interested in consist of multiple composite angular momenta coupled together by internal interactions. Mathematically, different angular momenta, J_1 and J_2, belong to different Hilbert spaces, and the combined state is written $|J_1, M_1\rangle \otimes |J_2, M_2\rangle$, though often we and others abbreviate this as $|J_1, M_1\rangle|J_2, M_2\rangle$. Under interactions coupling two or more angular momenta, the combined angular momentum is conserved, and written as $\vec{J} = \vec{J_1} \otimes I_2 + I_1 \otimes \vec{J_2}$, with $I_{1/2}$ representing the identity operator, and once again often the tensor product notation is usually dropped in practice. Mathematically, one can show that J can take on quantity $2 \times \min(J_1, J_2) + 1$ values, given by $|J_1 - J_2|, |J_1 - J_2| + 1, \ldots, J_1 + J_2$. Much like the individual angular momentum eigenstates, each J value has $2J + 1$ orientations with well-defined lab frame projection $M = \vec{J} \cdot \hat{Z}$.

We can therefore define a new basis, defined by eigenstates of the coupled angular momentum J. The change of basis is given by:

$$
\begin{aligned}
|J, M\rangle &= \sum_{M_1, M_2} |J_1, M_1\rangle|J_2, M_2\rangle \langle J_1, M_1; J_2, M_2|J, M\rangle \\
&= (-1)^{J_1 - J_2 + M} \sqrt{2J + 1} \sum_{M_1, M_2} \begin{pmatrix} J_1 & J_2 & J \\ M_1 & M_2 & -M \end{pmatrix} |J_1, M_1; J_2, M_2\rangle.
\end{aligned}
\tag{2.1}
$$

Here, $\langle J, M|J_1, M_1; J_2, M_2|J, M\rangle$ is a real number known as a Clebsch-Gordan coefficient, and will show up very often in manipulations of angular momenta. In the second line, we have written the Clebsch-Gordan coefficient in terms of the symbol in parentheses, known as the Wigner 3j symbol. The 3j symbol encodes all of the information in the Clebsch-Gordan coefficient, and has

---

[1]Note, in this entire thesis, we work with dimensionless angular momentum operators, and the physical value of an angular momentum is given in the correct units by $\vec{J}\hbar$.

certain selection rules. Namely, the symbol is zero unless J_2, J_2, J_3 satisfy a triangle inequality and $M_1 + M_2 + M_3 = 0$. Further symmetry details and identities of the 3j symbol are given in Ref. [39].

This procedure can be generalized to sequentially couple multiple angular momenta, labeled $J_1, J_2, J_3, \ldots$ etc. We note there is a choice of coupling sequence–we can either couple J_1 and J_2 to form J_{12}, which we then couple to J_3 to obtain J_{tot}, or we can follow another path. These different coupling schemes represent different bases that span the same space, and are related by unitary transformations to each other. Further information on coupling schemes of multiple angular momenta can be found in Ref. [39]. We will write coupled states with the following notation: $|(J_1, J_2)J_{12}\rangle$. In the case where we have multiple sequential couplings, we will write the states as: $|(J_1, J_2)J_{12}; (J_{12}, J_3)J_{\text{tot}}\rangle$. This can be extended for arbitrary number of couplings.

We note that it is typically convenient to begin by coupling the angular momenta that interact most strongly and incorporating the more weakly coupled angular momenta after. This allows us to express the Hamiltonian of interest with larger on-diagonal elements compared to off-diagonal elements, and to effectively encapsulate the effects of the off-diagonal elements via perturbation theory.

2.1.2 Spherical Tensors and the Wigner-Eckart Theorem

We are often interested in the behavior of angular momentum states and operators under rotations. This is certainly the case in molecules, where various molecular properties, such as the molecule frame dipole moment, are most naturally defined in the frame rotating with the nuclear framework. Further, because the physics of interest remains invariant under coordinate frame rotations, considering a physical problem in multiple frames can provide helpful insights. In this section we provide an overview of angular momentum rotations, culminating in the presentation of the Wigner-Eckart theorem, which will be indispensable for the work in this thesis.

We can parameterize a rotation about an axis $\hat{n}$ by an angle θ as $R_{\hat{n}}(\theta)$. We note that rotations can either be *active*, applied to the angular momentum state, or *passive*, applied to the coordinate frame. Any active rotation by an angle θ can be written as a passive rotation by the inverse angle $-\theta$. In this thesis, we follow the rotation conventions in Ref. [39], where angular momenta J_X, J_Y, J_Z are generators of active rotations[2]. Therefore a rotation about a single axis is written as $R_{\hat{n}}(\theta) = e^{-i\theta J_{\hat{n}}}$, where $J_{\hat{n}}$ generates rotations about the $\hat{n}$ axis.

We require three angles, known as *Euler angles*, to fully parameterize arbitrary rotations of the coordinate axes. In this thesis, we denote the Euler angles as $\omega = (\phi, \theta, \chi)$, following the definitions of Ref. [39]. The full rotation that relates one coordinate frame ("the lab frame") to a

---

[2]We note that this is opposite of the convention followed by Ref. [131].

second frame ("the molecule frame") is given by:

$$R(\omega) = R_Z(\phi)R_Y(\theta)R_Z(\chi) = e^{-i\phi J_Z}e^{-i\theta J_Y}e^{-i\chi J_Z}. \tag{2.2}$$

We emphasize all of the above rotations are defined by the lab frame axes. We note the operations are performed from right to left, and the rotation angles have the ranges $0 \leq \phi \leq 2\pi$, $0 \leq \theta \leq \pi$, and $0 \leq \chi \leq 2\pi$. Since the angular momentum states are diagonal under J_Z, we see that the J_Y rotation is the operation that couples different M states. We also note the inverse rotation is given by $R^{-1}(\phi, \theta, \chi) = R(-\chi, -\theta, -\phi)$.

We may write the effect of the rotation $R(\omega)$ of an angular momentum state as a unitary operator $\mathcal{D}(\omega)$ that acts on Hilbert space. Physically, a rotation should preserve the length of the angular momentum J, so the matrix representation of $\mathcal{D}(\omega)$ for all angular momentum states will be block diagonal in J, and we can denote a single J block as $\mathcal{D}^{(J)}(\omega)$. We expect the $\mathcal{D}^{(J)}(\omega)$ matrices to mix the M values for a given J, because we rotations generically change the orientation of J relative to $\hat{Z}$. The angular momentum states transform under rotations as follows:

$$|J, M\rangle \xrightarrow{R(\omega)} \mathcal{D}^{(J)}(\omega)|J, M\rangle \tag{2.3}$$

$$\mathcal{D}^{(J)}(\omega)|J, M\rangle = \sum_{M'} |J, M'\rangle \mathcal{D}^{(J)}_{M',M}(\omega). \tag{2.4}$$

Here, $\mathcal{D}^{(J)}_{M',M}(\omega) = \langle J, M'|\mathcal{D}^{(J)}(\omega)|J, M\rangle$ are the matrix elements of the unitary operator representing rotations, known as the *Wigner rotation matrix* or Wigner D-matrix. It turns out these D-matrices are very useful, being the irreducible representations of both the group of 3D rotations, SO(3), and the group of unitary 2x2 matrices, SU(2), which are used to describe spins and two level systems. We shall see the D-matrices again again in our section discussing of molecular states, which can have angular momentum about both lab and molecule axes.

Finally, we also summarize the concept of spherical tensor operators. The decomposition of vectors and operators into the spherical basis is extremely convenient for performing calculations with angular momentum states. Essentially, spherical tensor operators transform under rotations akin to angular momentum states, as described by the D-matrices. For any vector operator $\vec{A}$ with rank k, we write the *spherical tensor components* of A as $T^k_p(A)$. These transform under coordinate rotations as:

$$T^k_p(A) = \sum_{p'} T^k_{p'}(A)\mathcal{D}^{(k)}_{p',p}(\omega) \tag{2.5}$$

The properties of spherical tensor operators are summarized in the literature [39]. We can draw an intuitive analogy with angular momentum states. The rank k corresponds to the magnitude J, and encodes the number of possible orientations as $2k + 1$. We note that unlike J, the rank of a

spherical tensor k must be an integer. The orientations of the operator are denoted by p, in analogy to the M projection of an angular momentum.

We can now introduce a very important theorem known as the *Wigner-Eckart Theorem*. This theorem allows us to write the matrix elements of spherical tensor operators on angular momentum states as:

$$\langle \eta, J, M | T_p^k(A) | \eta', J', M' \rangle = (-1)^{J-M} \begin{pmatrix} J & k & J' \\ -M & p & M' \end{pmatrix} \langle \eta, J || T^k(A) || \eta', J' \rangle. \qquad (2.6)$$

We use η to denote all other quantum numbers, for example those related to the electronic or vibrational state of a molecule. The box is for emphasis, as we will use this eq. 2.6 over and over again.

The Wigner-Eckart theorem essentially factorizes the matrix element into a factor dependent on orientations M, which we can look up in a table or on a computer, and a factor independent of orientation in physical space, known as the reduced matrix element $\langle \eta, J || T^k(A) || \eta', J' \rangle$. If the operator A is an angular momentum operator, then the reduced matrix element can be obtained analytically [39]. Otherwise, calculating the reduced matrix element is typically a hard problem, and often one actually compares to experiment to obtain the value of the reduced matrix element as a fit to data. This is the case for example when $\vec{A} = \vec{r}$, the position operator acting on the electronic wavefunction.

Using the Wigner-Eckart theorem and the theory of angular momentum coupling, we can effectively evaluate the matrix elements of any operator acting on a composite molecular angular momentum state. In Appendix A, we provide a recipe for evaluating matrix elements in molecules. Many important formulae, identities, and results are provided in Refs. [39, 129]. Chapter 2 of Ref. [132] is also an excellent introduction to evaluating angular momentum matrix elements. Now, with basic angular momentum machinery in hand, we now proceed to describing the physical content of atomic and molecular states.

2.1.3 Atomic States

There are many fantastic textbooks detailing the atomic Hamiltonian, so here we just mention some relevant aspects that have parallels in molecules. First and foremost, the energy scales of the atomic problem are far smaller than those involved in the nucleus. Therefore the nuclear degrees of freedom are frozen out, and we only deal with the nuclear ground state. This is a somewhat trivial example of using separations of energy scales to simplify a problem, which we will encounter later with molecules. By the same logic, when working with multi-electron atoms, we typically only care about the valence electron, as the lower shells are tightly bound and not accessed by our energy scales of interest.

In multi-electron atoms, the "Hydrogenic" quantum numbers (particularly the orbital angular momenta l and spins s) are coupled, and we must introduce new quantum numbers. The quantum numbers used depend on the basis that renders the Hamiltonian most diagonal, which depends on the scale of the physical interactions present. We can categorize the energy scales of interest as ΔE_{elec}, representing the electrostatic separation of states due to the central Coloumb potential, and ΔE_{SO}, representing the scale of the splitting of spin-orbit states. We note that the ratio between relativistic E_{SO} interaction and the electrostatic energy is given by $E_{\text{SO}}/E_{\text{elec}} \sim \alpha^2 Z^2$ [133], where α is the fine structure constant, and Z is the atomic number of the nucleus. Therefore we expect spin orbit to dominate for heavy atoms. A similar situation will hold in molecules as well.

In the regime with $\Delta E_{\text{elec}} > \Delta E_{\text{SO}}$, we are dominated by the central field potential, and we use the Russell-Saunders coupling scheme. In this coupling scheme, all the electron orbital angular momenta first couple together to form the total electronic orbital angular momentum $\vec{L} = \sum_i \vec{l}_i$, where i runs over electrons in the valence orbital. Similarly, the electron spins also initially couple to each other first, forming the total electron spin angular momentum $\vec{S} = \sum_i \vec{s}_i$. Finally, spin-orbit interactions couple the L and S together to form the total angular momentum $\vec{J} = \vec{L} + \vec{S}$. If the atom has non-zero nuclear spin, it couples to J at the very end to obtain the grand total angular momentum, $\vec{F} = \vec{J} + \vec{I}$.

To succinctly describe the good quantum numbers describing a system of interest, we use *term symbols*. The notation of these symbols dates back to the early days of quantum mechanics, and initially they may seem difficult to interpret. However, after becoming familiar with term symbols, they can be used to succinctly label different electronic states of an atom or molecule. For Russell-Saunders coupling in atoms, the term symbol is given by:

$$^{2S+1}L_J \tag{2.7}$$

where we have already defined the angular momenta L, S, amd J. For historical reasons, the spin S is labeled by its multiplicity of M_S orientations (i.e., singlet, doublet, triplet,...), while the orbital angular momentum $L = 0, 1, 2, 3, 4, \ldots$ is represented by the capital letters $S, P, D, F, G, \ldots$. We note sometimes the term symbol is also written with a $^\circ$ subscript to denote a state of opposite parity from the ground state.

In the other regime, $\Delta E_{\text{SO}} > \Delta E_{\text{elec}}$, and we are dominated by spin-orbit coupling. The Hamiltonian now contains large off-diagonal matrix elements in the basis denoted by the Russell-Saunders coupling scheme. Instead of the orbital and spin angular momenta initially coupling separately amongst themselves, we now first couple each electron's orbit and spin together first, before coupling all the electrons together. We therefore have the good quantum number $\vec{j}_i = \vec{l}_i + \vec{s}_i$ defined for each electron indexed by i. Then the individual j_i are coupled together to form the total

angular momentum $\vec{J} = \sum_i \vec{j}_i$. Essentially, J is the only good quantum number, with L and S so strongly coupled that they are indistinguishable. This is known as the jj-coupling scheme, and is particularly relevant for heavy atoms where spin-orbit interactions cannot be treated perturbatively. We note there are further variations on atomic coupling schemes related to configurations where multiple valence shells may be active.

We shall soon see that while we have more degrees of freedom to contend with in molecules, the description of their states follows as a natural generalization of atomic term symbols.

2.1.4 The Simplest Molecule

Now we move on to adding another nucleus to the atom and forming a diatomic molecule. By no means will we give a comprehensive discussion of the chemical bonds holding the molecule together. For details, we direct the curious reader to Pauling's introduction on the subject [134].

Just as we turn to the hydrogen atom initially to gain insight in the case of atoms, so too can we turn to the H_2^+ cation to gain insight into molecules. The case of infinitely rigid H_2^+, fixed in place, can be solved analytically by introducing elliptical coordinates [39, 135], allowing the wavefunction to be separated, much like the case with the hydrogen atom. We simply quote the result: the eigenstates $\psi_{n,l,\lambda}$ are now labeled by three good quantum numbers, n, l, λ. The first two quantum numbers are familiar from the atomic case, and have similar interpretations–n describes the "radial" wavefunction, now in terms of constant ellipsoidal surfaces, while l describes the electronic angular momentum. The quantum number $\lambda = l \cdot \hat{n}$ can be interpreted as the projection of l on the internuclear axis $\hat{n}$ pointing from one nucleus to the other. Given the cylindrical symmetry of the problem, it is natural that the projection λ can be defined.

In an approach known as Ligand Field Theory (LFT) [136–138], we can consider constructing the $\psi_{n,l,\lambda}$ states by beginning with an isolated H atom, and bringing closer a proton initially separated at infinite distance. Here, the proton represents a "ligand." The electric field between the orbiting electron and the distant proton creates an interaction analogous to the Stark effect in atoms and molecules. Essentially, the states of the isolated atom, designated by n and l, with degenerate orientations m_l, are now split by the ligand according to different projections of m_l along $\hat{n}$, which is the definition of λ.

Indeed, we note the eigenvalues depend only on λ^2, and therefore we have a double degeneracy of $\pm\lambda$. Additional interactions, such as molecular rotation, will inevitably couple $\pm\lambda$ states, causing them to split into states written as symmetric and anti-symmetric combinations of $\pm\lambda$. Such combinations are actually necessary to preserve parity symmetry, as we shall see. Indeed, the weak mixing of nominally degenerate projection states is the mechanism behind parity doubling, which is present in certain diatomic molecules, generic in polyatomic molecules, and absent in atoms.

Though our molecule neither rotates nor vibrates thus far, we have already seen the emergence of key properties in considering the simplest case. Similar to atoms, we have $n \geq l \geq \lambda$. The molecular quantum numbers can be written in terms of molecular orbitals, with n designated by an integer, l designated by lowercase Latin characters ($s, p, d, f, \ldots$) and $|\lambda|$ designated by lower Greek characters ($\sigma, \pi, \delta, \phi, \ldots$). In general, lowercase symbols are used to designate single electron properties.

As we add more electrons and possibly more nuclei, the molecular problem rapidly increases in complexity. In general, we sidestep a great deal of the multi-electron complexity in molecules by working with systems with one valence electron. The molecules we focus on follow a motif that has been identified to produce laser coolable molecules, by engineering favorable vibrational decays, discussed further in Sec. 2.1.7. A good discussion of the electronic structure of laser-coolable molecules is given in Ch. 2.2 of Ref. [139].

2.1.5   Separation of Energy Scales and Hund's Cases

Molecules can vibrate and rotate, in addition to their electronic degrees of freedom. We provide a sense of the energy scales involved. In molecular spectroscopy, it is customary to describe energy as a wavenumber, $E = hck$, with k given in units of cm^{-1}. While these units may seem odd, they encapsulate the many orders-of-magnitude of energy scales present in molecules. For the molecules we consider here, electronic energies are typically order $\sim 10^4$ cm^{-1}, vibrational energies are on the scale of $100 - 1000$ cm^{-1}, rotational splittings are on the $0.1 - 1$ cm^{-1} scale, and rotational fine and hyperfine structure (encoding interactions of rotation with other angular momenta) are on the scale of ≤ 0.1 cm^{-1}.

The significant variation of the energy scales of the problem translates to significant differences in the timescales of molecular dynamics. The electronic dynamics are the fastest in the problem, followed by vibration, then rotation. As a result, we are motivated to perform an approximate separation of the wavefunction, known as the *Born-Oppenheimer* approximation, which is treated in detail in many textbooks. Here we provide a brief summary, following Refs. [39, 135].

We denote the full molecular wavefunction as Ψ_{rve}, which is a function of the electron spatial coordinates $\vec{r}_i$ with electron index i, the electronic spins $\vec{s}_i$, the nuclear coordinates $\vec{R}_k$ with nuclear index k, and the Euler angles $\omega := (\phi, \theta, \chi)$ describing the orientation of the molecular frame relative to the lab frame. Prior to performing the approximations, the total Hamiltonian can be written as:

$$(H_{\text{elec}} + H_{\text{nucl}})\Psi_{rve} = E_{rve}\Psi_{rve}. \tag{2.8}$$

Here, H_{elec} has been factored such that it does not contain any effects of nuclear motion. On the other hand, H_{nucl} contains angular momentum operators that can couple different electronic states.

The first step, not yet an approximation, is to expand the total wavefunction in a complete basis spanned by products of electronic and nuclear wavefunctions:

$$\Psi_{rve} = \sum_n \psi_e^n(\vec{r}_i, \vec{R}_k)\psi_{rv}^n(\vec{R}_k, \omega). \tag{2.9}$$

Here, n is an index labeling different wavefunctions correlated with electronic states of the rigid molecule, and we have dropped the spin interactions for convenience, as they will be very weak in comparison. At this point, we note the electronic wavefunctions are defined as eigenstates of the electronic Hamiltonian, $H_{\text{elec}}\psi_e^n(\vec{r}_i, R_k) = E_e^n(R_k)\psi_e^n(\vec{r}_i, R_k)$.

We now perform the adiabatic approximation, writing the wavefunction as:

$$\Psi_{rve}^0 = \psi_e^n(\vec{r}_i, R_k)\phi_{rv}^n(R_k, \omega). \tag{2.10}$$

Here, ϕ_{rv}^n is an appoximation of a single ψ_{rv}^n vibrational state, which means we are neglecting terms that mix different n states. As the name "adiabatic" implies, in this approximation the electrons instantaneously adjust their dynamics to track the vibrating and rotating nuclei, which move slowly in comparison. This approximation is motivated by the separation of electronic and nuclear timescales observed in molecules. The electronic wavefunction depends parametrically on the nuclear coordinates, $\vec{R}_k$, but is independent of the nuclear momenta or operators. We imagine we can fix the nuclei in place, solve for the electronic Hamiltonian, then vary the fixed nuclear position, re-solve the electronic energies, and so on, obtaining a potential energy surface describing the electronic state as a function of the nuclear coordinates. For diatomic molecules, this potential energy surface is one dimensional, as there is only one nuclear "coordinate," the relative separation of the nuclei R. For polyatomic molecules, the potential energy surface is multi-dimensional, which can have consequences such as allowing certain crossings known as conical intersections, where the approximations discussed break down completely, though we do not discuss the matter further in this work.

Finally, to complete the Born-Oppenheimer (BO) approximation, we neglect all couplings of electronic and nuclear motions when determining ϕ_{rv}^n. By using Euler angles to describing the molecular rotation in relation to the molecule body-fixed axes, we can further separate the rotation-vibration wavefunction into separate vibrational and rotation parts. For the complete molecular wavefunction in the BO approximation, we therefore have completed a full separation of electronic, vibrational, and rotational degrees of freedom:

$$\Psi_{rve}^0 = \psi_e\psi_v\psi_r. \tag{2.11}$$

We note that the procedure of quantizing the molecule rotation in terms of the body-fixed axes will have consequences for how we handle ψ_r, discussed in the next section. This separation of the

molecular wavefunction is at the heart of how we can perform physics experiments with molecules in a tractable manner. In essence, the BO approximation expands the molecular energy E in terms of the BO parameter, $\kappa = (m/M)^{1/4}$, where m is the electron mass, and M is the nuclear mass. Very approximately, we have $E_{mol} \approx E_{\text{elec}}(\kappa^0) + E_{vib}(\kappa^2) + E_{\text{Rot}}(\kappa^4)$. However, we shall see that even in the molecules we consider, we will encounter breakdowns of the approximations we have introduced. For example, we shall see later that vibration-rotation couplings will be relevant for bending polyatomic molecules. Nonetheless, we will be able to treat the relevant interactions perturbatively in the case of the variations from BO wavefunctions that we encounter.

2.1.6 Rotation and Symmetric Top States

In this section we provide a detailed discussion the rotational states of the molecule, denoted ψ_r in eq. 2.11. In this section we will denote the total rotational angular momentum of the molecule generically as $\vec{J}$. In later sections, we will discuss the specific composition of this rotation in terms of spin, nuclear framework, etc., but for this discussion we remain agnostic about the specifics. We introduce the notion of the molecular frame, labeled by axes $\hat{x}, \hat{y}, \hat{z}$. We use lowercase letters to denote the molecule frame components, while we reserve the uppercase letters $\hat{X}, \hat{Y}, \hat{Z}$ to denote the lab frame components. In a linear molecule, $\hat{z}$ is taken along the axis of cylindrical symmetry, and often referred to as the internuclear axis $\hat{n}$. For symmetric and asymmetric rotors, we follow the convention of aligning $\hat{z}$ to the principal axis with the largest moment of inertia.

We discuss further what we meant in the previous section by "quantizing" the rotational angular momentum in the molecule body-fixed frame. We can convert back and forth between the lab and molecule frames by using rotations parameterize by the Euler angles, defined in eq. 2.2. The rotations that transforms lab frame vector to the molecule frame and vice versa can be written as a unitary matrix U that acts on 3D vectors. That is, if $\vec{V}_L$ is in the lab frame and $\vec{v}_m$ is in the molecule frame, $\vec{V}_L = U\vec{v}_m$. The matrix U is always 3x3, resulting from the dimension of physical space. The matrix elements of U are referred to as the direction cosines in the literature [39, 129], and the explicit form of U is given in eq. 2.39 of Ref. [39].

We can use the direction cosines to define the rotational angular momentum of the molecule, J, in the molecule frame, which allows us to separate ψ_r and ψ_v. The body-fixed angular momenta J_x, J_y, J_z generate rotations in the molecule frame. Further, it can be shown that the space-fixed Euler rotation in eq. 2.2 is equivalent to a series of body-fixed rotations performed in the reverse order:

$$R_Z(\phi)R_Y(\theta)R_Z(\chi) = R_z(\chi)R_y(\theta)R_z(\phi). \tag{2.12}$$

The rotations on the right hand side are generated by the angular momenta quantized along the

molecule frame axes[3]. While rotations of the molecule body may be easier to conceptualize, the associated angular momenta are difficult to work with as the molecule axes are changing in space as we perform the rotations, causing complications.

The biggest issue with the molecule rotation J being quantized in the molecule frame is that the components J_x, J_y, J_z have *anomalous* commutation relations. Explicitly, we have $[J_a, J_b] = -iJ_c\epsilon_{abc}$, where a, b, c are indices for the molecule axes, and the sign of $-i$ is anomalous. This means if, in analogy with the lab frame, we were to naively construct a "raising" $J_+^{(m)} = J_x + iJ_y$ operator in the molecule frame and act it on the molecule state, it would actually lower the projection J_z in the molecule frame! This means we cannot apply the machinery of spherical tensor operators presented earlier. We note the anomalous commutation *only* applies to operators that contain the molecule body rotation, which will either be denoted by J or N, depending on the coupling scheme. Other operators such as L and S are not anomalous in either the lab or molecule frame [39].

To deal with the anomalous commutation relations, we always transform operators coupled with the molecule rotation from the molecule frame to the lab frame. We consider an operator A represented in the lab frame with spherical tensor form $T_p^k(A)$. We use p to refer lab frame components. We can also define the same operator A in the molecule frame as $T_q^k(A)$, where we use q to refer to molecule frame components. Using the D-matrices, we can transform the operator A between the two frames as follows:

$$T_p^k(A) = \sum_q \mathcal{D}_{p,q}^{(k)}(\omega)^* T_q^k(A) \tag{2.13}$$

$$T_q^k(A) = \sum_p (-1)^{p-q} \mathcal{D}_{-p,-q}^{(k)}(\omega)^* T_p^k(A). \tag{2.14}$$

The advantage of this approach is that the matrix elements of the D-matrix can be found in the literature [39, 129, 130]. Essentially, when we calculate matrix elements involving $\mathcal{D}_{p,q}^{(k)}(\omega)$, we are integrating over the space of all possible molecular orientations with a measure given by $d\omega = sin\theta \, d\phi \, d\theta \, d\chi$. For more details on matrix element calculations, see Appendix A.

We now introduce the eigenstates that generically describe the molecular rotation J in both the molecule and lab frames. The rotational Hamiltonian can take many forms, depending on the symmetries of the principal axes that diagonalize the moment of inertia matrix, which is constructed from the nuclear masses and bond geometries. On one hand, the simplest rotational Hamiltonian is that of a diatomic molecule with zero angular momentum about the internuclear axis $\hat{n}$, that is $J_z = J \cdot \hat{n} = 0$. Such a molecule has infinite rotational symmetry about $\hat{n} = \hat{z}$, and is described by only one moment of inertia, I, describing rotation perpendicular to $\hat{n}$ (i.e., only J_x and J_y are

---

[3]Technically the angular momenta are quantized along lab frame axes that are always rotated to be instantaneously coincident with the molecule body axes, see Ref. [39] and references therein.

non-zero). The Hamiltonian is referred to as the rigid rotor Hamiltonian, given by:

$$H = B\vec{J}^2. \tag{2.15}$$

Here, $B \propto I^{-1}$ is the energy scaling of the moment of inertia in wavenumber units. The eigenstates of the rigid rotor Hamiltonian are described by spherical harmonics, with eigenvalue $J(J+1)$, and degenerate $M = \vec{J} \cdot \hat{Z}$ sublevels.

On the other end of the rotational complexity scale, we have an asymmetric rotor, which is a molecule without any symmetry axis. Here, $\vec{J}$ is described by three unique moments of inertia, one for each component. The Hamiltonian is given by:

$$H = AJ_a^2 + BJ_b^2 + CJ_c^2. \tag{2.16}$$

Here, A, B, and C denote the three principle axes of the moment of inertia, and the usual convention[4] has $I_a < I_b < I_c$ ($A > B > C$), with the a, b, c identified with $\hat{z}, \hat{x}, \hat{y}$. The eigenstates of this Hamiltonian are typically complicated, with the rotation Hamiltonian mixing states with by $\Delta J_z = \pm 2$. Therefore J_z is not well-defined, and only J and its lab frame projection M are good quantum numbers. More information can be found in Refs. [39, 135, 140, 141].

It turns out that we can describe the molecular rotation eigenstates in a single basis that will let us interpolate between the asymmetric rotor on one hand, and the diatomic molecule on the other hand. This basis is referred to as the *symmetric top* basis, which describes rotors with two equal moments of inertia. For example, setting $B = C$ equal in eq. 2.16, we obtain the symmetric top Hamiltonian:

$$H = B(\vec{J}^2 - J_z^2) + AJ_z^2. \tag{2.17}$$

This is specifically the Hamiltonian for a *prolate* symmetric top, with $I_a < I_b = I_c$ (and therefore $A > B = C$), and $\hat{z}$ identified with the a axis. Pictorally, such a system can be thought of as a football or an egg like shape[5]. A symmetric top can also be oblate, and convention then is to label $\hat{z}$ with the c axis, with $I_c > I_b = I_a$ (and therefore $C < A = B$). Pictorally, oblate rotors are shaped like a disk or frisbee. Given we often have a heavy atomic mass on the symmetry axis, we consider only prolate tops.

The Hamiltonian in eq. 2.17 can be shown to commute with $\vec{J}^2$, $J_z := K$, and $J_Z := M$. The symmetric top eigenstates are therefore labeled with three quantum numbers, written as $|J, K, M\rangle$. In the basis of Euler angles, the normalized wavefunction can be written in terms of the D-matrix:

$$\Psi_{JKM} = \langle \omega | JKM \rangle = \sqrt{\frac{2J+1}{8\pi^2}} \mathcal{D}_{M,K}^{(J)}(\omega)^* \tag{2.18}$$

---

[4]The convention we present for identifiying a, b, c with z, x, y is known as I^r.
[5]The mass quadrupole is positive for prolate and negative for oblate.

where the normalization is defined such that $\int d\omega \Psi = 1$. The eigenvalues of the three good operators have their usual values. The spherical harmonics are a special case of the symmetric top wavefunction when $K = 0$.

We can intuitively understand the symmetric top wavefunctions as describing the amplitude for finding the molecule fixed angular momentum state $|J, K\rangle$ projected onto the lab-frame state $|J, M\rangle$. Indeed, using the properties of the D-matrices, we can write:

$$
\begin{aligned}
\mathcal{D}_{M,K}^{(J)}(\omega)^* &= \langle J, M | \mathcal{D}^{(J)}(\omega) | J, K \rangle^* \\
&= \langle J, K | \mathcal{D}^{(J)}(\omega^{-1}) | J, M \rangle
\end{aligned}
\tag{2.19}
$$

Where $\omega^{-1} = (-\chi, -\theta, -\phi)$ denotes the Euler rotation inverse to ω. Alternatively, ω^{-1} denotes the passive rotation of the axes equivalent to the active rotation ω of the body. We therefore see the symmetric top wavefunctions describe a rotation of the lab-frame angular momentum state into the molecule frame given by an Euler rotation ω^{-1} of the lab-frame coordinates. We finally note that $|JKM\rangle$ can also describe half integer J, which can occur if J contains contributions from the electron spin. We also note that the symmetric top wavefunction can have significant impact on the matrix elements of operators evaluated in the molecule frame, for example causing hyperfine shifts to differ between $K = 0$ and $K = 1$ states.

2.1.7 Vibrational States

In this section, we discuss the vibrational part of the molecule wavefunction, denoted ψ_v in eq. 2.11. In the discussion of rotation, we considered the molecule as being rigid. However, in reality the bond distances can deform as the molecule vibrates. Large molecules can have large amplitude, "floppy" vibrations, and we do not consider them here. Instead, we work with molecules where the vibrational displacements can be considered as small variations of the equilibrium nuclear framework.

For a diatomic molecule, the vibration is relatively simple, with the only vibrational coordinate being the variation of the bond distance R about the equilibrium value R_e. The potential for $R - R_e$ can be approximated as that of a simple harmonic oscillator, with anharmonicities being included perturbatively, either with additional higher order terms or with the Morse potential. The vibrational energy for a single vibrational mode is written as [39]:

$$
E_{vib} = \omega_e \left(v + \frac{1}{2} \right) - \omega_e x_e \left(v + \frac{1}{2} \right)^2 + \omega_e y_e \left(v + \frac{1}{2} \right)^3 + \ldots
\tag{2.20}
$$

Here, v is the number of vibrational quanta, x_e and y_e are small corrections representing deviations from the harmonic oscillator potential, and ω_e is the equilibrium vibrational constant. We note the vibration contributes zero point energy to the total molecular energy.

Since the rotation of the molecule is much slower than the vibration, we can consider the rotational constant as averaged over the vibrational motion. Therefore, the rotational constant measured in a given vibrational level v can be written as [129]:

$$B_v = B_e - \alpha \left(v + \frac{1}{2} \right) + \dots \tag{2.21}$$

Here, B_e is the rotational constant obtained from the equilibrium bond distance, and α represents the correction to the rotational constant from vibration.

Often, we are interested in electronic transitions between different molecular states. Such transitions can also be accompanied by a change in the vibrational coordinates, $\Delta v = v' - v''$. In the Condon approximation, we assume the electronic transition happens instantaneously compared to vibrational timescales, and so the ground vibrational wavefunction $|v''\rangle$ is projected onto the excited state wavefunction $|v'\rangle$. The strength of the electronic transition for a given Δv is scaled by the overlap integral of the two states, known as the Franck-Condon Factor (FCF), given by $|\langle v'|v''\rangle|^2$. We note the FCFs must be scaled by the electronic transition frequency ω_{eg}^3 to obtain branching ratios for the transition, see Ch. 3, Sec. 3.2.4.1 for details.

We can imagine writing the FCFs as a matrix where the diagonal entries of the matrix denote $\Delta v = 0$ transitions. For a generic molecule, we expect large values off-diagonal elements of the FCF matrix. However, for a class of carefully selected molecules, the FCF matrix is dominated by the on-diagonal entries. In a so-called "diagonal" molecule, the majority of spontaneous decays for a given excited state have $\Delta v = 0$, with increasingly smaller branching ratios for transitions with $|\Delta v| = 1, 2, \ldots$.

Molecules that have diagonal FCFs can be laser-coolable, requiring only a modest number[6] of additional of lasers to address all relevant vibrational decays from the excited state. The number of vibrational states that need addressing depend on the number of photons we would like to scatter. In general, scattering N_{ph} photons requires addressing all vibrational decays that occur at the $\sim N_{ph}^{-1}$ branching level. For example, to scatter $N_{ph} = 10^4$, we must ensure the sum of all unaddressed branching is $< 10^{-4}$. At this point there is an established motif for choosing molecules with near-diagonal FCFs by bonding an alkaline-earth (like) metal atom with an electronegative ligand, such has OH [112, 113, 123]. We discussed some relevant details earlier in Ch. 1, Sec. 1.4. The details of weak vibrational branching and establishing nearly closed optical cycles in polyatomic molecules are discussed further in Refs. [139, 143, 144].

In this thesis, we are interested in polyatomic molecules, which have additional vibrational degrees of freedom. For a molecule with N nuclei, we will have $3N - 6$ vibrational degrees

---

[6]~3 lasers for a diatomic [142], ~10 lasers for a linear triatomic [108].

of freedom ($3N - 5$ for a linear molecule[7]). We note the cartesian vibrational coordinates will generically be coupled to each other. This motivates the transformation into orthogonal vibrational coordinates, known as normal modes denoted Q_i. The procedure to obtain normal modes is known as the GF matrix approach, and is detailed in Refs. [145, 146]. We do not discuss the GF matrix approach, and merely assume that we begin with a series of normal modes for the molecule.

For a linear triatomic molecule such as YbOH, the normal modes of vibration associated with two stretching vibrations, denoted v_1 to describe the Yb-O stretch and v_3 to describe the O-H stretch, and one bending vibration, denoted v_2. Owing to the large mass asymmetry of Yb compared to H, the bend can be interpreted physically as the bending of the H atom off the axis defined by the Yb-O bond [146, 147]. The stretching modes are treated similarly to the case of vibrations in a diatomic molecule. The total vibrational wavefunction is written as a product of the individual wavefunctions for the v_i, and often we will designate the vibrational state as (v_1, v_2^ℓ, v_3). Here, ℓ is the angular momentum associated with the doubly-degenerate bending mode, which we will investigate further.

We concern ourselves with the normal coordinate Q_2 describing the bending mode of the molecule, which is *doubly-degenerate*. In a non-rotating molecule, there is no difference between displacements along Q_{2x} and Q_{2y}, and so the eigenstates are linear combinations of the two motions, resulting in the emergence of vibrational angular momentum $\vec{G}_\ell$ with projection $\vec{G}_\ell \cdot \hat{z} = \ell$ on the symmetry axis. Physically, we can picture the molecule in a bent configuration, rotating around its former symmetry axis. The degeneracy of ℓ then refers to a degeneracy in the direction of the molecule axis orientation. Of course, higher order electron-vibration couplings and Coriolis effects will lift this degeneracy, resulting in small splittings of opposite parity levels in doubly-degenerate bending modes.

The vibrational eigenstates of the bending mode are denoted $|v_2, \ell\rangle$, where v_2 is the number of vibrational quanta, and ℓ is the angular momentum projection. The possible eigenvalues of ℓ are obtained by considering aligned or anti-aligned combinations of the vibrational quanta. For example, $v_2 = 1$ only has $\ell = 1$, while $v_2 = 2$ can support an aligned, $\ell = 2$ configuration, and an-antialigned, $\ell = 0$ configuration. Continuing, $v_2 = 3$ will have available $\ell = 1, 3$, $v_2 = 4$ has $\ell = 0, 2, 4$, and so on.

To obtain a form of $|v_2, \ell\rangle$, we consider the case of a two-dimensional harmonic oscillator discussed in detail in the Appendix of Ref. [145]. We can write the normal mode in dimensionless units as $q_2 = \gamma^{1/2} Q_2$, where $\gamma = 2\pi c \omega_2 / \hbar$, with ω_2 the harmonic bending frequency. The

---

[7]N nuclei have $3N$ degrees of freedom. We subtract 3 for translational motion and 3 for rotation for non-linear molecules, or 2 for rotation in a linear molecule.

eigenstates of the two dimensional harmonic oscillator can be written as [145, 148, 149]:

$$|v_2, \ell\rangle = \frac{1}{\sqrt{2\pi}} e^{i\ell\phi} \Psi_{v_2,\ell}(q). \tag{2.22}$$

Here, $q = q_2 = \sqrt{q_{2x}^2 + q_{2y}^2}$, where (q_{2x}, q_{2y}) are the dimensionless normal coordinates of the bending mode, and $\phi = \tan^{-1}(q_2/q_1)$ is the bending angle associated with the normal mode[8]. The function $\Psi_{v_2,\ell}$ is given by [148]:

$$\Psi_{v,\ell}(q) = (-1)^{(v+|\ell|)/2} N_{v,\ell} q^{|\ell|} e^{-q^2/2} L_{(v+|\ell|)/2}^{|\ell|}(q^2). \tag{2.23}$$

Here, $N_{v,\ell}$ is a normalization factor defined up to an overall phase, i.e., $N_{v,\ell} = e^{i2\delta_\ell}|N_{v,\ell}|$, and $L_n^k(x)$ is an associated Laguerre polynomial. The phase δ_ℓ can be chosen according to two conventions; either $\delta_\ell = 0$, and $|v, \ell\rangle = |v, -\ell\rangle$, or $\delta_\ell = \pi/2$, and $|v, \ell\rangle = -|v, -\ell\rangle$. While this sign is just a convention and cannot affect the eigenstate energies, differences in phase can result in disagreements over the sign of off-diagonal matrix elements in the Hamiltonian. We discuss phase conventions in detail in Appendix A, Sec. A.2, where we discuss parity symmetries of molecular states.

Further, we can also define ladder operators for the bending mode as $q_\pm = q_2 e^{\pm i\phi} = q_{2x} \pm iq_{2y}$. The matrix elements of these operators is given in Refs. [129, 148, 151], all using the $\delta_\ell = 0$ phase convention. The result is:

$$q_\pm|v_2, \ell\rangle = \sqrt{\frac{v_2 + 2 \pm l}{2}}|v_2 + 1, \ell \pm 1\rangle + \sqrt{\frac{v_2 \mp \ell}{2}}|v_2 - 1, \ell \pm 1\rangle. \tag{2.24}$$

Interestingly, q_+ must raise ℓ, but it can either raise or lower v_2, and vice versa for q_-. This is because the "true" ladder operators of both v_2 and ℓ involve not just q but also p, the momenta conjugate to the bending normal coordinate [148, 149, 152, 153]. If we analogously define $p_\pm = p_{2x} \pm ip_{2y}$, then we can write total ladder operators $F^{\pm(\pm)} = q_{(\pm)} \mp ip_{(\pm)}$, which cause $\Delta v_2 = \pm 1$ and $\Delta\ell = (\pm)1$, and have matrix elements provided in Ref. [148, 152]. We note Ref. [149] defines their ladder operators $R^{\pm(\pm)}$ with an additional factor of $\mp i$, such that $F^{\pm(\pm)} = \mp iR^{\pm(\pm)}$.

We often do not consider p, but it shows up in the Coriolis couplings of the vibrational angular momentum. We also note that both q and p are used to define the bending angular momentum $\vec{G}_\ell$, according to [129]:

$$\vec{G}_\ell = \sum_i \sum_j \zeta_{ij} Q_i P_j \tag{2.25}$$

where the indices i and j run over all normal modes, including both modes for a degenerate vibration (i.e., Q_{2x} and Q_{2y} in the linear triatomic case), Q_i and P_i are pairs of conjugate position and momenta, and ζ_{ij} are the Coriolis coupling constants defined in Refs. [129, 154], which satisfy

---

[8]It is not so simple to interpret this as the physical bending coordinate. See Ref. [150]

$\zeta_{ij} = -\zeta_{ji}$ in general, and specifically for linear molecules we have the relation $\sum_i \zeta_{ij}^2 = 1$ [154]. These Coriolis coupling constants arise when we write the bending rotation in the molecule frame [155].

We now return to the total vibrational energy of the polyatomic molecule. In general, the vibrations will have anharmonic corrections, and there will also be anharmonic cross-couplings between different vibrational modes. The total vibrational energy for a polyatomic molecule with $n = s + t$ total vibrational modes, with s symmetric stretching modes and t degenerate bending modes, is given by [135, 145, 155]:

$$E(v_s; v_t, \ell_t, \ldots) = \sum_i^n \omega_i \left(v_i + \frac{d_i}{2} \right) + \sum_{i \leq j}^n \left(v_i + \frac{d_i}{2} \right) \left(v_j + \frac{d_j}{2} \right) + \sum_{k \leq k'}^t g_{kk'} \ell_k \ell_{k'} + \ldots \quad (2.26)$$

Here, d_i is the degeneracy of a vibrational mode, with $d_s = 1$ and $d_t = 2$. The sums over i are taken for all modes, while the sums over k are only taken for the t degenerate modes. The term $g_{kk'} \ell_k \ell_{k'}$ generates the anharmonic splitting between the different values of ℓ possible for a degenerate bending mode v_k, and can also include cross couplings of v_k and v'_k. The ellipses indicate we can always add higher order terms to the expansion. Similar to a diatomic molecule, the vibrations also affect the rotational constant of a polyatomic molecule [129, 135]:

$$B_v = B_e - \sum_i \alpha_i \left(v_i + \frac{d_i}{2} \right) + \ldots \quad (2.27)$$

Many higher order corrections are discussed in Hirota [129].

2.1.8   Electronic States and Hund's Cases

We now follow the same path as our discussion of atoms, and define bases of good quantum numbers that can label molecules in different regimes of competing physical interactions. Once we have a basis, we can write the term symbols for molecules. The different bases for representing molecular states are known as *Hund's cases* [39, 129]. The relevant physical interactions we consider are ΔE_{elec}, ΔE_{SO}, and ΔE_{Rot}, representing the energy of the electrostatic interaction with the ligand field, spin-orbit interactions, and the rotation of the molecule. Once again, we refer to the molecule frame, labeled by axes $\hat{x}, \hat{y}, \hat{z}$. In a linear molecule, $\hat{z}$ is taken along the axis of cylindrical symmetry, and often referred to as the internuclear axis $\hat{n}$. For symmetric and asymmetric rotors, we follow the convention of aligning $\hat{z}$ to the principal axis with the smallest moment of inertia.

We now write down all of the angular momenta of a linear polyatomic molecule; some quantities will end up being well-defined, while others will be poor quantum numbers. Similar to the atomic case, we define $\vec{L} = \sum_i \vec{\lambda}_i$ and $\vec{S} = \sum_i \vec{\sigma}_i$, where i is a sum over valence electrons, and λ and σ represent values associated with molecular orbitals. Novel in the molecular case, we can also define

an operator $\vec{R}$ to describe the end-over-end rotation or tumbling motion of the bare nuclei. Further, in the case of polyatomic molecules, as we discussed earlier the nuclei can exhibit vibrational bending motions that constitute orbits about the molecular symmetry axis, and we will denote this angular momentum as $\vec{G}_\ell$ with projection ℓ on the internuclear axis. We will see that none of L, R, or G_ℓ are well-defined, and so instead we introduce the combined electronic and nuclear rotation without spin, $\vec{N} = \vec{L} + \vec{R} + \vec{G}_\ell$. Depending on the molecule, if spin-orbit interactions are large, N may also be a poor quantum number, with the well-defined quantity being the total electronic and nuclear angular momentum including spin, $\vec{J} = \vec{N} + \vec{S}$. Finally, as in the case of atoms, if we have a nuclear spin I, then we must form the grand total angular momentum $\vec{F} = \vec{J} + \vec{I}$. The various symbols are summarized in Table 2.1.

The Hund's cases are first classified according to the coupling scheme of the electron spin, and then subclassified according to the hyperfine coupling scheme of the nuclear spin. Beginning with the electron spin $\vec{S}$, we can describe the spin components in the molecule frame, which describes Hund's case (a) and (c), or in the lab frame, which describes Hund's case (b). Cases (a) and (c) are distinguished from one another by the strength of spin-orbit coupling. As we shall see, in case (c) we cannot even separate the electron's spin from its orbital angular momentum L. Meanwhile, the hyperfine subclassifications are added as subscripts and denote how strong the electron spin-nuclear spin coupling is compared to the electron spin-rotation or electron spin-orbit couplings. Often the case of strong hyperfine coupling only arises in case (b), and by default when we omit subscripts we describe weak hyperfine coupling. We now present the cases in more detail.

First, we consider Hund's case (a), which corresponds to the hierarchy $\Delta E_{\text{elec}} \gg \Delta E_{\text{SO}} \gg \Delta E_{\text{Rot}}$. The strong electrostatic interaction couples the angular momenta to the internuclear axis $\hat{n}$, and therefore only the projections on $\hat{n}$ are good quantum numbers, denoted by $\Lambda = L \cdot \hat{n}$ and $\Sigma = S \cdot \hat{n}$. Semiclassically, we can think of the angular momenta L and S as precessing around the internuclear axis, a result of the torque exerted by electrostatic forces. Conversely, the operators $\vec{L}$ and $\vec{R}$ are poorly-defined in case (a), and we do not use their eigenvalues to label the states. Instead we write $\vec{R} = \vec{J} - \vec{L} - \vec{S}$, first considering diatomic molecules. States with different magnitudes of $|\Lambda|$ are split in energy by the electrostatic interaction ΔE_{elec}. At smaller energy scale, on-diagonal spin-orbit terms cause splittings of states with the same value $|\Lambda|$ but different orientations of Σ. The off-diagonal terms can also cause small mixings of Λ. Overall, the spin-orbit interaction preserves the magnitude of $\Omega = \Lambda + \Sigma$, and this is therefore a good quantum number as well that can be used to label the states. In Hund's case (a), we label electronic states with term symbols using the following notation:

$$^{2S+1}\Lambda_\Omega^{(\pm)}. \tag{2.28}$$

We note that the values of Ω and Λ are taken to be unsigned for the term symbol. As in the case

Table 2.1: The various angular momenta relevant to the linear polyatomic molecules we consider. The column "Anomalous?" indicates if the angular momentum has anomalous commutation relationships. The columns labeled (a), (b$_{\beta J}$), (b$_{\beta S}$), (c) each correspond to the respective Hund's case. A checkmark ✓ indicates the angular momentum is a good quantum number in this basis. An x-mark ✗ indicates the angular momentum is not well-defined in this basis, and must be written in terms of good angular momenta. For example, in case (a), we must write $\vec{N} = \vec{J} - \vec{S}$.

Symbol	Description	Anomalous?	a	b$_{\beta J}$	b$_{\beta S}$	c
$\vec{R}$	Rotation of the nuclear framework	Yes	✗	✗	✗	✗
$\vec{G}_\ell$	Vibrational angular momentum	No	✗	✗	✗	✗
$\ell = \vec{G}_\ell \cdot \hat{n}$	Projection of G	–	✓	✓	✓	✓
$\vec{L}$	Electronic orbital angular momentum	No	✗	✗	✗	✗
$\Lambda = \vec{L} \cdot \hat{n}$	Projection of L	–	✓	✓	✓	✗
$\vec{N} = \vec{R} + \vec{L} + \vec{G}_\ell$	Nuclear and electronic rotation	Yes	✗	✓	✓	✗
$K = \Lambda + \ell$	Projection of N	–	✓	✓	✓	✗
$\vec{S}$	Total electron spin	No	✓	✓	✓	✗
$\Sigma = S \cdot \hat{n}$	Projection of S	–	✓	✗	✗	✗
$\Omega = \Lambda + \Sigma$	Projection of electronic momentum	–	✓	✗	✗	✓
$\vec{J} = \vec{N} + \vec{S}$	Total angular momentum	Yes	✓	✓	✗	✓
$P = \Lambda + \ell + \Sigma$	Projection of J	–	✓	✗	✗	✓
$\vec{I}$	Nuclear spin	No	✓	✓	✓	✓
$\vec{G}_I = \vec{S} + \vec{I}$	Total hyperfine spin	No	✗	✗	✓	✗
$\vec{F} = \vec{J} + \vec{I} = \vec{N} + \vec{G}_I$	Grand total angular momentum	Yes	✓	✓	✓	✓

Table 2.2: The various Hund's cases relevant to this work and their corresponding basis states. Here we include hyperfine interactions with a nuclear spin I, and we have defined the total spin quantum number $\vec{G}_I = \vec{S} + \vec{I}$. The second column indicates the energy hierarchy implied by the basis of interest, where E_{SO}, E_{SR}, and E_{Hyp} are scale of the spin-orbit, spin-rotation, and hyperfine interactions, respectively. A full list of Hund's cases, including other hyperfine coupling scenarios, can be found in Ref. [39] and Ref. [129].

Hund's Case	Energy Scales	Basis States[1,2]
(a$_\beta$)	$E_{\text{SO}} > E_{\text{SR}} > E_{\text{Hyp}}$	$\lvert v, \ell \rangle \, \lvert \eta, \Lambda \rangle \, \lvert S, \Sigma \rangle \, \lvert J, P; (J, I)F, M_F \rangle$
(b$_{\beta J}$)	$E_{\text{SR}} > E_{\text{Hyp}} > E_{\text{SO}}$	$\lvert v, \ell \rangle \, \lvert \eta, \Lambda \rangle \, \lvert N, K; (N, S)J; (J, I)F, M_F \rangle$
(b$_{\beta S}$)	$E_{\text{Hyp}} > E_{\text{SR}} > E_{\text{SO}}$	$\lvert v, \ell \rangle \, \lvert \eta, \Lambda \rangle \, \lvert N, K; (S, I)G_I; (N, G_I)F, M_F \rangle$

[1] We use the notation $\lvert (J_1, J_2)J_{12} \rangle$ to denote coupled angular momenta.
[2] η represents all other possible quantum numbers labeling the electronic state.

of atoms, $2S + 1$ labels the spin multiplicity. The values of Λ are designated with capital Greek letters[9], with $\Lambda = 0, 1, 2, 3, 4, \ldots \ldots$ corresponding to $\Sigma, \Pi, \Delta, \Phi, \ldots$. States with $\Lambda > 0$ exhibit a double degeneracy of $\pm\Lambda$ states, which is lifted by higher order Coriolis couplings in the molecule, resulting in parity doubling. The $\pm$ superscript is only used for Σ states ($\Lambda = 0$) to denote the symmetry of the electronic wavefunction upon reflection in a plane containing $\hat{n}$. Practically, this has the consequence of determining the parity of the lowest rotational state. For example, in a state where two $\lambda = \pi$ molecular orbitals anti-align to form a $\Lambda = 0$ state, the electronic state is an anti-symmetric singlet state designated Σ^-. It is also conventional to drop the Ω value when writing the term symbol for a Σ state.

The above discussion can be easily generalized to linear polyatomic molecules. Here, the only addition we need to consider is the vibrational angular momentum $\vec{G}_\ell$ that can result from doubly degenerate bending modes. The bending motion has well-defined projection angular momentum $\ell = \vec{G}_\ell \cdot \hat{n}$. The projection ℓ can be added to Λ to form the combined orbital and bending angular momentum $K = \Lambda + \ell$. Interactions in the molecule between the bending vibration and the electronic angular momentum can cause "vibronic" splittings for different values of K. These interactions are known as Renner-Teller interactions and we discuss them in Sec. 2.2.4. Continuing, in Hund's case (a) we can combine Σ with K to obtain the total projection quantum number $P = \Lambda + \Sigma + \ell$. This allows us to describe the molecular state using a vibronic term symbol:

$$^{2S+1}K_P^{(\pm)}. \tag{2.29}$$

We can see this term symbol is the polyatomic analogue to the electronic term symbol for diatomic molecules. In a similar fashion, K is given by $\Sigma, \Pi, \ldots$, and $\pm$ only applies to Σ vibronic states. Now, we will have parity doubling interaction from both the degeneracy of $\pm\Lambda$ and the degeneracy of $\pm\ell$. Their combination can result in very rich and interesting molecular structure, as we shall see in Ch. 4, Sec. 4.3.2.

We do not consider Hund's case (a) for more complicated molecules (symmetric tops, asymmetric rotors) in detail, other than to comment on two effects that occur as the molecule deviates further from cylindrical symmetry. First, anisotropic spin-orbit and rotational interactions result in a reduction (a.k.a quenching) of the electronic orbital angular momentum, such that $\langle L_z \rangle = \zeta_e$ obtains a fractional value [123]. The increase in molecular asymmetry means the internal projection axis is no longer fully well-defined. Furthermore, symmetric tops we can have rotational angular momenta about the top axis, and in Hund's case (a), this quantity is denoted $K = N = P - \Sigma$. For asymmetric rotors, we can have angular momentum about all three axes: K_a, K_b, and K_c. Typically

---

[9]There is an unfortunate overuse of notation. We use italic Σ to denote the spin projection in the molecule frame, and upper case Σ to denote the electronic value of the term symbol.

one picks one axis as a basis to help write the asynmmetric rotor states as mixtures of symmetric top wavefunctions [141].

In case (c), we have the hierarchy $\Delta E_{\text{SO}} \gg \Delta E_{\text{elec}} \gg \Delta E_{\text{Rot}}$. The spin-orbit interaction overpowers all the other splittings in the molecule, causing mixing of Λ and Σ. Hund's case (c) is similar to the jj-coupling scheme in atoms, as now we cannot talk about L or S separately, but must discuss J_e, the total electronic angular momentum. Further, because of strong coupling to the internuclear axis, only the projection of J_e is well-defined, given by $\Omega = \Lambda + \Sigma = \vec{J}_e \cdot \hat{n}$. Case (c) is the most general approach one can take to a molecular state, only labeling the state in terms of Ω. The total angular momentum of the molecule is still given by J, we just cannot divide it among N and S.

Finally, we now consider Hund's case (b), corresponding to the hierarchy $\Delta E_{\text{elec}} \gg \Delta E_{\text{Rot}} \gg \Delta E_{\text{SO}}$. Here, the spin-orbit interaction is weak or non-existent, and case (b) is valid either for Σ electronic states or light molecules with very strong rotational couplings. In Hund's case (b), the spin S is not strongly coupled to the molecule frame, and so we write it in the lab frame with projection M_S. In terms of Σ, the M_S eigenstates can be written as symmetric or anti-symmetric superpositions, and vice versa. Further, the combined orbital and rotational angular momentum, excluding spin, is a good quantum number, given by $\vec{N} = \vec{L} + \vec{R} + \vec{G}_\ell$. However, we note the individual angular momenta that make up $\vec{N}$ are not well-defined. Finally, the spin-rotation interaction couples the spin to the molecule rotation to form well-defined $\vec{J} = \vec{N} + \vec{S}$.

We note that J is a good quantum number in both case (a) and (b), even though they describe very different coupling schemes. We can go back and forth between the two bases using a unitary transformation, derived by Brown in Ref. [156], and also provided in Hirota [129]. The change of basis is given by:

$$|N, K; (N, S)J, M\rangle = \sum_{\Sigma, P} (-1)^{N-S+P} \sqrt{2N+1} \begin{pmatrix} J & S & N \\ P & -\Sigma & -K \end{pmatrix} |S, \Sigma\rangle |J, P, M\rangle. \qquad (2.30)$$

Here, $P = \Lambda + \Sigma + \ell$, and $K = \Lambda + \ell$. We note the formula in Ref. [39] has a typo. We use this formula extensively to calculate transition dipole moments in molecules by expressing all states in Hund's case (a) for convenience.

We now consider the hyperfine subdivisisions, provided in Table 2.2. We focus on Hund's case (b) subdesignations, denoted ($b_{\beta J}$) and ($b_{\beta S}$). The βJ case describes the situation when the hyperfine energy splittings from nuclear spin interactions, ΔE_{Hyp}, are smaller than the spin-rotation splittings ΔE_{SR} between different J states. As a result we couple the nuclear spin I to J as the last step in our coupling scheme to obtain the grand total angular momentum F. This is the "default"

case in atoms and molecules, and the equivalent scenario in case (a) is denoted (a_β)[10].

Meanwhile, the βS coupling scheme describes the hierarchy $\Delta E_{\text{Hyp}} > \Delta E_{\text{SR}}$. This coupling scheme can arise with core-penetrating orbitals, and is particularly relevant for precision measurement searches in odd-isotopes of molecules. In case βS, we first couple I and S together to form the total hyperfine spin $\vec{G}_I = \vec{S} + \vec{I}$, where we use the subscript to distinguish this quantity from $\vec{G}_\ell$. Then, the rotation N is coupled to G to form the grand total angular momentum $\vec{F} = \vec{N} + \vec{I}$. We note J is not well-defined, in contrast to the other cases. Finally, if there are multiple spins, they can be coupled sequentially according to the hierarchy of their interaction strengths. For example, in the $^2\Sigma^+$ ground state of $^{171/173}$YbOH, we first couple $\vec{G}_{\text{Yb}} = \vec{S} + \vec{I}_{Yb}$, where I_{Yb} is the nuclear spin of the Yb atom, then we couple $\vec{F}_1 = \vec{N} + \vec{G}_{\text{Yb}}$, and then finally we couple $\vec{F} = \vec{F}_1 + \vec{I}_{\text{H}}$, where I_{H} is the hydrogen nuclear spin.

The unitary change of basis to convert from $(b_{\beta J})$ to $(b_{\beta S})$ is given by the Clebsch-Gordan coefficients. We may write this in terms of Wigner 6j-symbols as follows [39]:

$$
\begin{aligned}
|N, K; (N, S)J; (J, I)F, M_F\rangle &= \sum_{G_I} (-1)^{I+S+F+N} \sqrt{(2G_I + 1)(2J + 1)} \\
&\times \begin{Bmatrix} I & S & G_I \\ N & F & J \end{Bmatrix} |N, K; (S, I)G_I; (N, G_I)F, M_F\rangle
\end{aligned}
\tag{2.31}
$$

where the quantity in curly brackets is the Wigner 6j-symbol [39]. We include this formula for completeness, noting that throughout this thesis, we use Hund's case $(b_{\beta J})$, which we simply abbreviate to case (b), or Hund's case (a_β), which we abbreviate to case (b).

2.2 Effective Hamiltonians

2.2.1 Basic Principle

The effective Hamiltonian arises out of the need to model the complicated quantum states of molecules with high precision, in a self-contained, modular fashion. In fact the effective Hamiltonians we use for molecules are very similar to the effective field theories (EFTs) in high energy physics, discussed in Ch. 1. The goal of the effective Hamiltonian program in molecules is to reduce the effects of electronic, vibrational, and rotational interactions to a single, finite Hamiltonian, expressed within a basis of good quantum numbers that specify the relevant angular momenta present in the molecule. Regardless of the interaction present in the molecule, we can always encapsulate its effects in the effective Hamiltonian. Crucially for precision measurements, effective Hamiltonians can also be used to accurately model the behavior of molecules in applied electric and magnetic fields, aiding much of the work on measurement protocols for polyatomic molecules presented in Ch. 5.

---

[10]The (a_α) coupling describes strong coupling of I to $\hat{n}$, which is not common.

However, there is a price to be paid for this level of accuracy and precision—we require a series of experimentally determined parameters to construct the effective Hamiltonian. Essentially, these parameters are obtained from fits to the spectral data, and the resulting effective Hamiltonian is only as accurate as the residuals of the fit. These parameters are like the Wilson coefficients in EFTs, in that they encode all of the complicated physics that we have "integrated out" in order to obtain a simple model. Therefore, the measured effective Hamiltonian parameters provide a connection to the theory describing the underlying molecular dynamics, allowing us to gain intuition for the molecule's behavior. Furthermore, effective parameters are crucial for benchmarking theory computations. For example, the hyperfine parameters are used to gauge the accuracy of calculations determining molecular sensitivities to symmetry violation [157]. The experimental process of determining effective Hamiltonian parameters from data is the work of molecular spectroscopy, the topic of Ch. 4. In this section, we lay out some foundations for modeling molecules with effective Hamiltonians.

Effective Hamiltonians are discussed extensively in Brown and Carrington [39], particularly Ch. 7. While the textbook is quite comprehensive, it also suffers from the fact that useful and relevant information is scattered throughout the book. Another good textbook is Hirota [129], particularly when dealing with polyatomic molecules. Brown originally derived effective Hamiltonians for diatomic molecules in Ref. [158], and included the vibronic interaction of triatomic molecules in Refs. [151, 156, 159]. Furthermore, there is good discussion of how to deal with anomalous commutation of molecule rotation operators in Ref. [160], Hirota [129], and Brown and Carrington [39]. There is also good discussion of effective Hamiltonians and matrix element calculations in Nick Hutzler's thesis [41] and Nick Pilgram's thesis [161]. Finally, in Ref. [141], Sears provides the effective Hamiltonian for an asymmetric top molecule, including Zeeman effects from an applied magnetic field.

2.2.2 Details of the Effective Hamiltonian

We wish to study and model the rotational states belonging to a single vibrational and electronic configuration of the molecule. We generically denote this state $|\psi^{(0)}, i\rangle = |P^{(0)}; v^{(0)}; \eta, J\rangle$. Here, i is simply an index labeling the quantum numbers defining our state. We use $P^{(0)}$ to denote the collection of projection quantum numbers relevant to our state. For example, for a diatomic molecule in Hund's case (a), $P^{(0)} = (\Lambda, \Sigma)$, while for Hund's case (b), $P^{(0)} = (\Lambda)$. Since we are most interested in interactions internal to the molecule frame, it is easier to use case (a) representations, though we will try to keep the discussion as generic as possible. Continuing, we use $v^{(0)}$ to denote the vibrational state of the molecule, for example $v^{(0)} = (v_1, v_2, v_3)$ in a triatomic molecule. Finally, we use J to characterize the total angular momentum of our state, and η to represent all other relevant quantum numbers, such electronic or nuclear spins, which we will

often suppress for brevity. Since total angular momentum is conserved by internal interactions, we will consider dynamics that re-orient J and change its projections, but never that change the magnitude of J. Of course, when we apply an external electromagnetic field, the total molecule angular momentum will no longer be conserved, as the interaction with the field can exchange angular momenta.

There are many interactions in the molecule that will necessarily couple our state of interest to other vibronic states. We use the index α to label the space of all states not within our vibronic manifold of interest, characterized by their own values of $P^{(\alpha)}$ and $v^{(\alpha)}$. In reality, the true molecular state $|\psi, i\rangle$ is actually a mixture of $|\psi^{(0)}, i\rangle$ and many other contributions $|\psi^{(\alpha)}, k\rangle$, with potentially different quantum numbers represented by the index k. When the admixtures of other states are comparable to the admixture for $\psi^{(0)}$, it is an indication that we have not used a good basis of approximate quantum numbers. However, it is often the case that the mixtures of other states are perturbative, owing to the large separation of electronic and vibrational energy scales from the rotational energy scale. In such a case, to deal with mixings outside of our vibronic state, we do not have to consider the whole, "true" wavefunction. Instead, we work only with $|\psi^{(0)}, i\rangle$, and we incorporate the effects of interactions external to our subspace in a source-agnostic manner by simply adding additional, effective terms to the Hamiltonian. These effective terms must be consistent with the symmetries of our Hamiltonian (rotation, parity), so in free-field they are written as scalar products of possibly many angular momenta. There is also the constraint from the Wigner-Eckart theorem that any operator involving the spin S can only be allowed if its rank k satisfies $2S \geq k$ [39]. For example, when working with a state with a single unpaired valence electron spin, we do not need to worry about considering spin-spin interactions. We caution this may not be the case if there is strong configuration mixing (for example, strong mixing with state that has extra valence spin excitation). As a related point, the situation is also quite complicated in multi-electron systems, which must be written in terms of Slater determinants [39]. However, in the single valence electron molecules we consider (often the case for laser coolable molecules), the effective Hamiltonian approach is applicable and quite powerful.

The primary interactions that we would like to "integrate out" are those that involve the electronic angular momentum L. Later, we will also discuss the very similar procedure for dealing with operators that couple the vibrational angular momentum G_ℓ present in triatomic molecules. Returning to L, we specifically do not want to deal with the transverse components $L_\perp = L_{x,y}$, which can be written in terms of raising and lowering operators $L_\pm$. Determining the matrix elements of these ladder operators is a hard computational task, as L is not well-defined in the molecule due to the breaking of spherical symmetry. We can see that two essential molecular interactions will have

$L_\pm$ operators: spin-orbit (H_{SO}) and rotation H_{Rot}. Writing these out in Hund's case (a), we have:

$$
\begin{aligned}
H_{Rot} &= B\left(\vec{J} - \vec{L} - \vec{S}\right)^2 \\
&= B\left(\vec{J}^2 + \vec{L}^2 + \vec{S}^2 - 2\vec{J}\cdot\vec{L} - 2\vec{J}\cdot\vec{S} - 2\vec{L}\cdot\vec{S}\right) \\
&= B\left(\vec{J}^2 + \vec{L}^2 + \vec{S}^2 - 2J_z(L_z + S_z) - 2L_zS_z \right. \\
&\quad \left. - J_+L_- - J_-L_+ - J_+S_- - J_-S_+ - L_+S_- - L_-S_+\right)
\end{aligned}
\tag{2.32}
$$

$$
\begin{aligned}
H_{Rot} &= A(\vec{L}\cdot\vec{S}) \\
&= A\left(L_zS_z + \frac{1}{2}(L_+S_- + L_-S_+)\right).
\end{aligned}
\tag{2.33}
$$

Here, we have written the nuclear rotation as $\vec{R} = \vec{J} - \vec{L} - \vec{S}$, and B and A are "bare" constants that will not be the parameters we fit in the effective Hamiltonian. We note this can be generalized to a triatomic molecule by writing $\vec{R} = \vec{J} - \vec{L} - \vec{G}_\ell - \vec{S}$, as was done in Ref. [162], for example. The dot products have been expanded in the molecular frame, and we emphasize that the matrix elements of $J_\pm$ have anomalous commutation relations, and care must be taken to transform them to the lab frame before evaluation [39, 160]. Keeping this in mind, the operators $S_\pm$ and $J_\pm$ can be dealt with using the Wigner-Eckart theorem, but the $L_\pm$ and L^2 operators, as we mentioned before, are not easy to compute. We note there is an approximate method for estimating their matrix elements, described further in Appendix A.3.2.

The effective Hamiltonian approach actually does not require us to evaluate any matrix elements of $L_\perp$ or L^2. Instead, we recognize that the operators in eqs. 2.32 and 2.33 can be grouped into three classes. First, we have operators that are well-defined to act among two states i and j belonging to $\psi^{(0)}$, for example the operators $\vec{J}^2 = J(J+1)$ or J_+S_-. Their matrix elements can be calculated within $\psi^{(0)}$ using angular momentum algebra [39]. Then we have operators whose form is identical for all the different states in $\psi^{(0)}$, for example $\vec{S}^2$. These operators are simply absorbed into an overall energy offset of the electronic state, known as the "origin." We note the distinction between which operators are diagonal shifts and which operators are origin contributions is somewhat arbitrary—for example, L_zS_z can be taken as a diagonal energy shift if our basis of interest contains multiple Ω states, or it can just be taken as a contribution to the origin if we consider just a single Ω state. Further, here we have shown rotational contributions to the origin, but we note that there are also vibrational contributions, such as the zero point energy.

Continuing, we have operators that contain $L_\pm$ and connect us to different electronic states $|\psi^{(0)}, i\rangle \rightarrow \|\psi^{(\alpha)}, k\rangle$. These operators only have an impact on the energies of $\psi^{(0)}$ state when they connect back, that is when we also consider $|\psi^{(\alpha)}, k\rangle \rightarrow |\psi^{(0)}, j\rangle$ at some higher order of perturbation theory. For example, separate terms in the spin-orbit and rotational Hamiltonians can
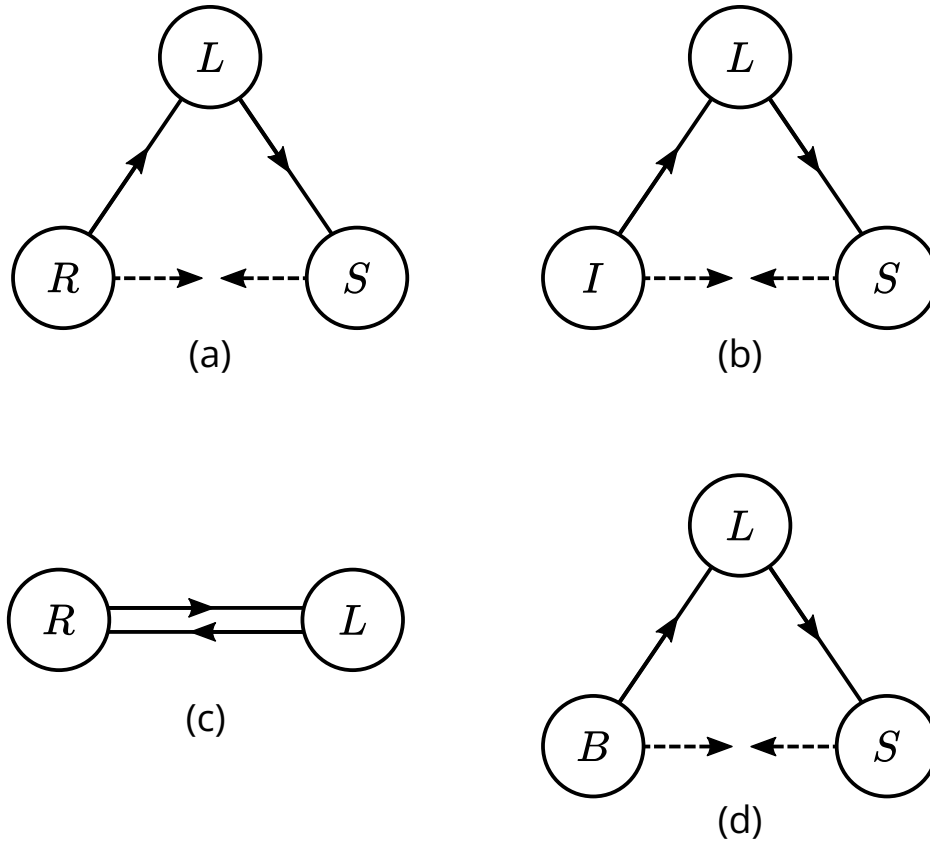
Figure 2.1: Diagram of second order interactions that arise in the effective Hamiltonian when we trace out L, the electronic orbital angular momentum. (a) This diagram describes contributions to an effective spin-rotation interaction. We note that depending on the states involved, this interaction can either generate parity doubling, or be parity preserving, see main text for details. (b) Effective contribution to the electron spin-nuclear spin interaction. (c) Effective contribution to the R^2 rotational interaction, showing how even the rotational constant becomes an effective parameter. (d) An applied magnetic field B can also couple to the orbital angular momentum L, and when we form the effective Hamiltonian we can end up with additional interactions between B and S. See main text for further details.

take us to another state and back—if we combine J_+L_- with L_+S_-, we obtain an overall interaction that looks like J_+S_-. This term looks like a term in the rotational Hamiltonian, and the two effects are actually indistinguishable. We note we have swept under the rug the possibility of combining J_+L_- and L_-S_+. Such a possibility is allowed, but can result instead in parity doubling interactions, where the signs of the projections in $P^{(0)}$ are flipped. We discuss parity doubling more later on. In general, once we begin to consider the effective Hamiltonian expansion, the original parameters of the theory, such as B and A, are mixed up, and all we can determine are effective parameters that receive contributions at various orders of perturbation theory. In Appendix A.3.3, we provide further information about the mathematical formulation of the effective Hamiltonian.

To gain an intuition, we illustrate the situation diagrammatically in Figure 2.1. We consider four relevant angular momenta of the molecule, L, the electronic orbit, S, the electronic spin, R, the molecular rotation, and I, the nuclear spin. We also consider the possible coupling of an external magnetic field B, which we elaborate on soon. In the effective Hamiltonian, we are free to write down symmetry conserving terms involving interactions of any of these angular momenta. However, once we reduce the Hamiltonian to act only within the subspace of a given vibronic state by "tracing out" L, we may end up with different effective interactions, shown at second order in Fig. 2.1. If the traced out interactions involve flips of Λ, they will result in parity doubling, which we discuss in Sec. 2.2.3.

As a further concrete example, we consider the contributions to the spin-rotation operator, $\gamma \vec{J} \cdot \vec{S}$ in case (a), and $\gamma \vec{N} \cdot \vec{S}$ in case (b)[11]. In the effective Hamiltonian approach, the spin-rotation parameter receives contributions from various orders of perturbation theory, $\gamma = \gamma^{(1)} + \gamma^{(2)} + \cdots$ [39]. The first order term $\gamma^{(1)}$ results from the magnetic interaction between the electron spin and the magnetic dipole moment of the rotating molecule [163]. In heavy molecules, the first order term is small compared to the dominant second order contribution $\gamma^{(2)}$, arising from off-diagonal spin-orbit and rotational perturbations, i.e., combinations of BJ_+L_- and AL_+S_-. The resulting contribution to $\gamma^{(2)}$ is provided in 7.122 of Ref. [39], and more discussion can be found in Ref. [161].

If we now consider the application of a magnetic field to the molecule, we will have terms that look like $\vec{B} \cdot \vec{L}$. The evaluation of this operator requires rotating $\vec{B}$ into the molecule frame, where L_z is good and $L_\perp$ is undesirable. We deal with the $L_\perp$ terms by using the effective Hamiltonian approach. We can now obtain effective interactions of the form $B_x S_x + B_y S_y$, where x, y are defined in the molecule frame. This term encodes electronic mixing of Λ, and the interaction represents the anisotropic response of the electron g-factor in a molecule, compared to the usual isotropic response in an atom. See Ref. [164] for an excellent discussion of magnetic effects in molecules. We can also obtain parity dependent Zeeman effects, which we will return to when discussing parity doubling. Curiously, there are no effective Stark terms in the effective Hamiltonian. However, we can understand why simply; such terms would involve a coupling of the internuclear axis $\hat{n}$, which is P-odd T-even, to an angular momentum of the molecule, $\vec{L}$, which P-even T-odd. This would be a P, T violating effect—exactly what we are searching for!

Finally, as was mentioned earlier, the effective Hamiltonian approach can also be generalized for polyatomic molecules, eliminating the components of $\vec{G}_\ell$ that couple outside of our vibronic subspace to other vibrational states. When tracing out $G_\perp$, we obtain additional effective terms that can contribute just like the effective operators obtained by tracing out $L_\perp$. However, the scale of

---

[11] See Appendix A.3.1 for the use of N vs. R in effective Hamiltonians.

the contribution from $\vec{G}_\ell$ effects is typically smaller compared to spin-orbit effects. For example, there is usually not a strong coupling of ℓ and Σ. However, this is not always the case, particularly if ℓ is actually mixed with Λ, resulting in effective spin-orbit interactions, as we shall see in the bending mode of YbOH in Ch. 4. Finally, we note different effective Hamiltonians are useful for different molecular states and bases. For example, we will use a different Hamiltonian to describe a Hund's case (b) molecule with little to no spin-orbit interactions, compared to a Hund's case (a) molecule with strong spin-orbit. Further, we will have additional terms when dealing with bending modes of polyatomics, or spin-spin interactions in triplet systems.

2.2.3 Parity Doubling

Many molecules contain states of both parities, $\mathcal{P} = \pm$, with the same values of rotational angular momenta. As we saw in Ch. 1, in Hund's case (a) these states can be written as:

$$\left|J, M, \mathcal{P} = \pm\right\rangle = \frac{1}{\sqrt{2}} \left(\left|J, P, M\right\rangle \pm (-1)^p \left|J, -P, M\right\rangle\right). \tag{2.34}$$

Here, $(-1)^p$ represents a J dependent phase factor, given by the action of the parity operator $\mathcal{P}|J, P, M\rangle = (-1)^p|J, -P, M\rangle$. We discuss this phase factor in Appendix A, Sec. A.2, and in this thesis we take $p = J - S - \ell$ for Hund's case (a) and $p = N - \ell$ for Hund's case (b).

We now provide an explanation for how such eigenstates arise from the effective Hamiltonian constructed in the un-symmetrized case (a) or case (b) basis states given in Table 2.2. Recall that in the construction of the effective Hamiltonian, we traced out terms involving $L_\pm$. While doing so, we saw that terms like J_+L_- and L_+S_- can combine to give us J_+S_- terms, which really are just the spin-rotation interaction, $\vec{J} \cdot \vec{S}$. In the full Hamiltonian, such a term encodes the combined effect of an operator proportional to $J_+L_+L_-S_-$. However, we also saw that we could combine J_+L_- and L_-S_+ terms. This now gives us the combined effect of $J_+L_-^2S_+$. For a state i in $\psi^{(0)}$ with $\Lambda = 1$, such an operator would connect us back to a state j in $\psi^{(0)}$ with $\Lambda' = -\Lambda = -1$. We see the interaction has flipped Λ! If all the other terms in the Hamiltonian respect the degeneracy $\pm\Lambda$, it is clear that the off-diagonal matrix elements that connect $\Lambda \leftrightarrow -\Lambda$ will therefore lift the $\pm\Lambda$ degeneracy, and the resulting eigenstates will be symmetric and anti-symmetric superpositions of $\pm\Lambda$. If we generalize $\Lambda \to P$, we see this is exactly the sort of mechanism that can give us the symmetrized parity state shown earlier. These states are also referred to as Wang combinations in the literature.

Therefore, the breaking of projection degeneracy, the degeneracy of $\pm P$, $\pm\Lambda$, $\pm\ell$, $\pm\Sigma, \ldots$, is caused by parity doubling terms in the effective Hamiltonian that mix the opposite projections with each other. These effective operators are actually encoding mixings with *other* electronic or vibrational states outside of our subspace. At second order, we will always get interactions that

can flip an integer projection, i.e., we can take $P = 1 \rightarrow -1$. However, the situation can be more complicated if we consider for example $P = 2$, as now we require four effective operators to connect with $P' = -2$. Therefore, the parity doubling is much weaker in higher magnitudes of projection quantum numbers. Furthermore, the situation is complicated when Σ is half integer. In a $^2\Pi_{1/2}$ electronic state, we can connect $P = \Omega = 1/2 \rightarrow -1/2$ by interactions that flip $\Lambda = 1 \rightarrow -1$ and also flip $\Sigma = -1/2 \rightarrow 1/2$. These interactions involve spin-orbit interactions with nearby $^2\Sigma$ perturbing states. However, if we now consider a $^2\Pi_{3/2}$ state, we see such an interaction cannot take us from $\Omega = 3/2 \rightarrow -3/2$. Instead, we actually require the combination of two effective Hamiltonian terms. The first is an effective $\Delta\Lambda = 2$, $\Delta\Sigma = 0$ interaction that is generated by rotational terms coupling outside of our subspace, and within our subspace has the effect of coupling $^2\Pi_{3/2}$ and $^2\Pi_{1/2}$ states. The second is the parity-preserving $\vec{J} \cdot \vec{S}$ term of the rotational Hamiltonian in eq. 2.32, which has $\Delta\Sigma = 1$ and $\Delta\Lambda = 0$. As a result, through two effective Hamiltonian terms, effectively a four operator interaction, we can mix $\Delta\Omega = 3$, causing a much smaller parity splitting in the $\Omega = 3/2$ states compared to the $\Omega = 1/2$ states.

Parity doubling is discussed further in Ref. [39], in particular Sections 7.4.5 and 9.7.1. Additionally, Ref. [165] discusses parity doubling in $^3\Pi$ states, Ref. [166] discusses parity doubling in Δ electronic states, and Refs. [162, 167] have some discussion of parity doubling effects that combine from rotation and vibrational angular momenta. We also discuss vibrational angular momenta doubling in Ch. 4, Sec. 4.2.

Finally, in the same way we generate parity doubling from the effective Hamiltonian, so too can we generate parity-dependent Zeeman interactions. These terms are manifestations of $\vec{B} \cdot \vec{L}$ terms that combine in the effective Hamiltonian with various internal interactions involving $\vec{L}$, from spin-orbit to rotation to hyperfine. Such parity dependent magnetic effects result in a g-factor that depends on parity. A similar effect can be achieved from parity dependent spin-rotation terms in the effective Hamiltonian, which we will encounter in Ch. 4, Sec. 4.2. Refs. [39, 164] discuss parity dependent magnetic interactions further.

We make a note on the phase convention of the $(-1)^p$ term introduced at the beginning of this section. We discuss phase conventions in detail in Appendix A, Sec. A.2. Essentially, parity doubling is generated by off-diagonal matrix elements, and the phase of off-diagonal matrix elements does not impact the eigenvalues we obtain from diagonalization. However, what the phase does control is the phase of the symmetric and anti-symmetric parity combinations of the case (a) or case (b) states. One can see this very simply by diagonalizing a 2×2 toy Hamiltonian with degenerate diagonal terms and non-zero off-diagonal terms. When the off-diagonal terms are *positive*, the lower-energy eigenvector is the *anti-symmetric* combination of our basis states. Continuing, this means the phase factor of $(-1)^p$ in the symmetrized parity states is connected to

the phase factor of the parity doubling operators that flip angular momentum projections. With the phase $p = J - S - \ell$ in case (a) and $p = N - \ell$ in case (b), the operators that flip $\Lambda \to -\Lambda$ and $\ell \to -\ell$ have opposite phase conventions [151, 159, 168, 169]:

$$\langle \Lambda = \pm 1 | e^{\pm 2i\theta} | \Lambda = \mp 1 \rangle = -1 \tag{2.35}$$

$$\langle \ell = \pm 1 | e^{\pm 2i\phi} | \ell = \mp 1 \rangle = 1. \tag{2.36}$$

Here, θ is the azimuthal electronic angle, with $|\Lambda\rangle \propto e^{i\Lambda\theta}$, and ϕ is the azimuthal bending angle, with $|v, \ell\rangle \propto e^{i\ell\phi}$. By writing the wavefunctions in terms of their phase angles, we see how the operators above flip angular momenta. We derive these relations in Appendix A.

2.2.4 Renner-Teller Effects

In linear molecules with both $\ell \neq 0$ and $\Lambda \neq 0$, there will be couplings between the bending motion and the electronic angular momentum, referred to as Renner-Teller interactions. These interactions are discussed extensively in Refs. [129, 135, 140, 151, 155], which is not an exhaustive list by any means. We will discuss Renner-Teller interactions further in Ch. 4, Sec. 4.3.2. In this section, we provide a heuristic overview on how these interactions arise physically.

Intuitively, Renner-Teller (RT) couplings can be understood as arising from the electrostatic interaction between the electron charge distribution and the electric dipole moment induced by the bending molecule [129, 151, 170, 171]. We restrict our consideration to a single electron, with azimuthal angle θ, orbiting a bending molecule, with bending azimuthal angle ϕ defining the plane that the bent molecule lies in. The interaction between the electron and the molecule depends on the relative angle $(\theta - \phi)$. For small displacements of the bending normal coordinate q_2, it is standard to perform a double Taylor expansion in q_2 and $\cos \theta - \phi$. Often the terms with only q_2 depedence are dropped, as they are the same for all rotational states, and are absorbed into the overall vibrational energy origin. The remaining Hamiltonian is then given by [129, 151]:

$$H_{RT} = V_{11} q_2 \cos (\theta - \phi) + V_{22} q_2^2 \cos^2 (\theta - \phi) + \ldots \tag{2.37}$$

Here, we have introduce the dipolar RT parameter, V_{11}, and the quadrupolar RT parameter, V_{22}. In Hirota [129], these parameters are given in terms of the physical electron coordinates, such as distance from $\hat{n}$, nuclear charge, etc. Meanwhile, Brown [151, 156] provides interpretations of these constants in terms of effective Hamiltonian parameters. We note that while we have presented RT effects as electrostatic effects in the linear molecule limit, the RT effect was considered as arising from Coriolis interactions in the bent molecule limit in Ref. [172], and both approaches are identical.

To better understand the above Hamiltonian, we can rewrite it as follows:

$$H_{RT} = \frac{V_{11}}{2} q_2 (e^{i(\theta-\phi)} + e^{-i(\theta-\phi)}) + \frac{V_{22}}{4} q_2^2 (e^{i2(\theta-\phi)} + e^{-i2(\theta-\phi)}) + \ldots \tag{2.38}$$

We now immediately recognize the exponential operators that raise and lower ℓ and Λ. We see that the dipolar interaction has operators of the form $L_\pm q_\mp$, while the quadrupolar interaction has operators of the form $L_\pm^2 q_\mp^2$. The quadrupolar Hamiltonian can directly act within our effective Hamiltonian subspace, acting as a parity doubling term. Meanwhile, the dipolar term encodes mixings of ℓ and Λ, such that only their combination K is conserved. If we consider a bending mode in a $^2\Pi$ electronic state, we see the dipolar operator connects us to $^2\Sigma$ and $^2\Delta$ states. As the molecule bends, Λ is no longer integer valued, and instead our electronic wavefunction is mixed with other Λ states by the electrostatic interaction with the dipole moment of the bending molecule. This is what provides weak transition strength to $\Delta\ell \neq 0$ transitions, as we will see in Ch. 4, Sec. 4.2. Finally, we note that since the dipolar terms take us out of the effective Hamiltonian subspace, they must be traced out. The result is that the dipolar interaction V_{11} will also contribute to an effective Hamiltonian operator that looks just like the quadrupolar term. Therefore, the overall Renner-Teller effect in the effective Hamiltonian is a combination of both dipolar and quadrupolar effects.

The resulting contribution of RT effects to the effective Hamiltonian is given by [151, 159]:

$$
\begin{aligned}
H_{RT} = {} & \frac{1}{2}\epsilon\omega_2 \left(q_+^2 e^{-2i\theta} + q_-^2 e^{2i\theta} \right) + g_K(G_z + L_z)L_z \\
& + \frac{1}{2}\epsilon\omega_{2,D} \left(q_+^2 e^{-2i\theta} + q_-^2 e^{2i\theta} \right) \vec{N}^2 .
\end{aligned}
\tag{2.39}
$$

Here, θ is the electronic azimuthal coordinate, and $q_\pm$ are dimensionless raising and lowering operators for the vibrational angular momentum $\vec{G}_\ell$, with matrix elements available in the literature [129, 143, 151, 173]. The term $\epsilon\omega_2$ is the Renner-Teller coupling strength, which can be related to V_{11} and V_{22}, g_K is a correction derived by Brown [156] that encodes the change in Λ caused by bending-induced mixing with other electronic states, and we note $G_z = \ell$ and $L_z = \Lambda$. Finally, $\epsilon\omega_{2,D}$ is the centrifugal correction to the Renner-Teller interaction, derived by Brown [159], which we do not consider further but have included for completeness.

We now discuss RT effects from a symmetry perspective. For a linear molecule in the C_∞ symmetry group, the electronic wavefunction is symmetric under all rotations around the molecule z axis. This is natural for the cylindrical symmetry of the molecule, and this enforces the conservation of Λ as a good quantum number (in the absence of spin-orbit). When $\Lambda \neq 0$, the wavefunction is doubly degenerate between the values $\pm\Lambda$. However, once the molecule bends, the cylindrical symmetry is broken, lifting the electronic degeneracy. For a bent XYZ triatomic molecule, the symmetry group is now C_s, and the electronic state splits into two electronic states of differing symmetries. In the language of group theory, the two electronic states have A' and A'' symmetry, corresponding to the electronic wavefunction being symmetric and anti-symmetric, respectively, about reflection in the x, z plane (i.e., the plane of the bending molecule). The splitting of the

electronic degeneracy corresponds to a splitting of the harmonic bending potential into two curves, V' and V''.

For small displacements of the bending normal coordinate q_2, the bending potential remains harmonic, and the Renner-Teller interactions are in the $10 - 100$ cm^{-1} scale. The two curves are degenerate at $q = 0$, when cylindrical symmetry is restored. We can write the harmonic bending potential in the absence of RT effects as $V_0 = \frac{1}{2}k_2 q_2$, with k_2 a harmonic force constant. Upon turning on RT interactions, this curve is split into two potentials, written as $V', V'' = V_0(1 \pm \epsilon)$, with ϵ the RT parameter given above, and $1 \pm \epsilon$ corresponding to the symmetric (V') and anti-symmetric (V'') electronic states. Each potential now has its own force constant, k' and k''. In terms of these force constants, we can write the ϵ RT parameter as:

$$\epsilon = \frac{k' - k''}{k' + k''}. \tag{2.40}$$

We see that when $\epsilon < 0$, as it is in the triatomic molecules we consider, it means the electronic state that is symmetric upon reflection in the bending plane is lower in energy.

Finally, we provide relations for ϵ, k', and k'', in terms of the 2nd order RT contribution[12], ϵ_1, form the dipolar V_{11} parameter, and the first order contribution ϵ_2 from the quadrupolar V_{22} parameter. These relations are given in Refs. [129, 151, 172]. We reproduce them here, noting that our form H_{RT} is expressed in terms of dimensionless coordinates q. Furthermore, In terms of the harmonic bending frequency ω_2 we have:

$$\epsilon \omega_2 = (\epsilon_1 + \epsilon_2)\omega_2 \tag{2.41}$$

$$\epsilon_2 \omega_2 = \langle \eta | V_{22} | \eta \rangle \tag{2.42}$$

$$\epsilon_1 \omega_2 = -\sum_{\eta \subset \Sigma} (-1)^s \frac{|\langle \eta | V_{11} | \eta' \rangle|^2}{2\Delta E} \left(1 + \left(\frac{\omega_2}{\Delta E}\right)^2\right) \tag{2.43}$$

$$g_K = \frac{\omega_2}{4} \sum_{\eta \subset \Sigma, \Delta} (-1)^p \frac{|\langle \eta | V_{11} | \eta' \rangle|^2}{(\Delta E)^2}. \tag{2.44}$$

Here η and η' represent different electronic states. We have defined $\Delta E = E(\eta') - E(\eta)$. In the sum over Σ states, $s = 0$ for Σ^+ states and $s = 1$ for Σ^- states. Further, in the sum over Σ, Δ states, $p = 0$ for Σ states and $p = 1$ for Δ states. We note that Ref. [172] disagrees on the form of eq. 2.42 compared to Refs. [129, 151]. In Ref. [172], the authors write $\epsilon = (\epsilon_1 + \epsilon_2)(1 + \epsilon_1)^{-1}$. Ref. [172] also has slightly different forms for the other equations as well. They do, however, provide a form for the anharmonic correction g_{22} in terms of ϵ_1 and ϵ_2.

---

[12]There can be some confusion as to the use of ϵ_1 vs. $\epsilon^{(1)}$ in the literature. The subscript version represents the dipolar contribtuion, while the superscript version represents the 1st order contribution, which is actually the quadrupolar term, i.e., $\epsilon_2 = \epsilon^{(1)}$ and vice versa.

CHAPTER

3

Producing Cold Molecules

There's always a bigger fish.

–Qui-Gon Jinn

3.1 Introduction

This chapter overviews the production, study, control, and applications of cold molecular beams. First, we motivate the need to produce cold samples of molecules. Then, in Section 3.2, we discuss the primary workhorse of our experiments, the cryogenic buffer gas beam (CBGB). We provide both specific details on the beam source used for much of this thesis, as well as providing an overview of relevant information on cryogenic buffer gas cooling. We also provide a discussion of beam diagnostics, namely absorption and fluorescence spectroscopy, including relevant equations.

Then, in Section 3.3, we discuss novel work performed in this thesis on driving chemical reactions with laser excitation. This results in an order of magnitude enhancement of the molecular yield in our CBGBs. We characterize the chemical enhancement in detail, and discuss applications. Optically driven chemical enhancement is an invaluable tool in our lab and in other labs working with cold alkaline-earth (like) metal hydroxide molecules.

3.1.1 Molecules are Entropically Hard

The presence of molecular degrees of freedom, namely rotation and vibration, mean that molecules typically have more entropy than atoms, by virtue of having a higher density of states. This introduces the need for additional steps to remove entropy from the molecular system to
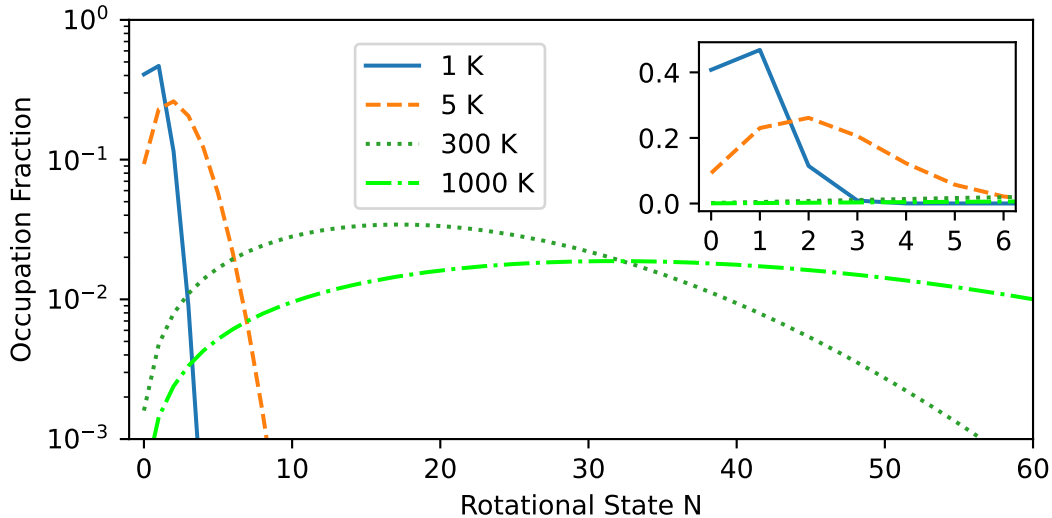
Figure 3.1: Visualization of rigid rotor Botlzmann probabilities at various temperatures. The rotor energy is given by $BN(N+1)$ with $B = 10$ GHz, and the occupation fraction is the fraction of the total population in a given N, taking into account the $2N + 1$ degeneracy of each level. The inset in the upper left is a zoom in on the lowest rotational states with population plotted on a linear scale. By cooling down to 5 K, we have order unity population in the lowest rotational levels.

concentrate population and enable coherent quantum manipulation. For example, experiments with cold atoms typically begin with an oven source or dispenser, which is heated to $\sim 500 - 1,000$ K to produce an effusive source of hot atoms. Since electronic degrees of freedom in atoms are typically at energy scales of order $\sim h \times 10,000$ K, the majority of the atoms produced are in the absolute ground state, allowing for the now standard pipeline of laser cooling, slowing, and magneto-optical trapping to proceed.

In contrast, a molecular oven source will produce molecules distributed among numerous rotational states and a few vibrational states. For example, we can consider a sample of rigid rotors at 1,000 K, with a rotational constant $B \sim h \times 10$ GHz $\sim k_B \times 0.5$ K. We calculate occupation probabilities using the standard Boltzmann probability distribution, $P(N) = g(N)e^{-BN(N+1)/(k_B T)}/Z$, where Z is the partition function, and $g(N) = 2N + 1$ is the orientation degeneracy for a given N level. Neglecting vibration, a 1,000 K sample would have peak occupation of around $N = 44$ and a large tail occupation up to $N = 100$. In general, a sample with population distributed from $N = 0$ to $N = N_{\text{max}}$ will occupy $\sum_{N=0}^{N_{\text{max}}}(2N+1) = (N_{\text{max}}+1)^2$ sublevels. When population is spread amongst so many levels, i.e., the entropy is high, it becomes difficult to perform state resolved quantum operations with adequate signal to noise ratio. For $T = 1,000$ K, population is spread amongst quantity $\sim 10^4$ levels; for $T = 300$ K, $\sim 10^3$ levels; and for $T = 5$ K, ~ 50 levels. A comparison of Boltzmann populations for cryogenic, room temperature, and oven temperatures is given in Fig. 3.1.

Furthermore, when producing molecules, we must contend with chemistry. Many species of

interest for optical cycling and precision measurements involve molecules with unpaired valence electrons in anti-bonding orbitals, referred to as free radicals by chemists. These molecules will have very low vapor pressure in equilibrium and cannot be easily sourced, for example from a commercial gas cylinder. Instead, free radicals must be formed by chemical reactions.

Older spectroscopy papers studied molecules in a heated oven, boiling off a solid reactant while simultaneously introducing reagent gas for reactions. Subsequent chemistry typically exhibits chemiluminiscence, sometimes at atomic transition wavelengths. Spectroscopists realized that chemistry can be made more favorable by introducing a high-voltage discharge, or by using laser excitation on an atomic transition. This concept of excited state chemistry formed the basis for techniques for improving molecule production that we will describe later in this chapter.

An alternative technique to oven chemistry is to produce the molecules in a high temperature ($T > 1,000$ K) plasma formed by focusing a nanosecond pulsed laser onto a solid target, known as laser ablation. The targets are typically either a solid piece of metal ablated in the presence of a reagent gas, or a pressed powder target containing all molecular constituents. This is the approach we will use to produce molecules in all subsequent discussions and chapters. However, after formation, the molecules must be cooled further, both for high-resolution spectroscopy, and for coherent quantum control.

There are currently two primary methods for producing cold (~$1 - 10$ K) samples of free radicals: supersonic expansion and cryogenic buffer gas cooling. Both methods are typically used to produce cold molecular beams as a starting point for a wide variety of experiments, from spectroscopy to quantum control. In this thesis, we will be concerned primarily with cryogenic buffer gas cooling. Though we will only review it briefly, supersonic expansion is an effective method for producing cold beams of free radicals [174–176], and is the method of choice for many spectroscopists[1].

A great deal of science has been done using supersonic beams, such as molecular spectroscopy and collisional studies. Supersonic beams are formed by pulsing a vacuum valve in a vacuum chamber, with the line upstream of the valve filled with (usually) room temperature gas at some pressure. Often the pulse of gas is an inert, monatomic carrier gas, i.e., a Noble gas, and the expansion occurs presence of laser ablation to produce free radicals of interest. If the valve diameter is much larger than the mean free path of the expanding gas, there will be many collisions during the expansion, forming a supersonic jet. This process has three consequences: 1) the velocity is boosted to ~$300 - 500$ m/s and the velocity distribution narrows, as a result of the

---

[1]For example, our collaborator Tim Steimle has used supersonic sources to characterize countless numbers of small molecules.

quadratic velocity scaling of kinetic energy[2], 2) A majority of the gas is directed along the center line, resulting in much higher intensity than an effusive beam, and 3) The supersonic expansion is approximately isentropic, meaning the internal degrees of freedom are in equilibrium with the translational degrees of freedom, which are cooled by expansion and boosting. Supersonic beams operating at room temperature achieve rotational temperatures in the $5-20$ K range and vibrational temperatures in the $30-100$ K range. Vibrational cooling is less efficient, a fact that we will encounter again with cryogenic buffer gas beams.

Supersonic beams require good electronics timing and the right pulsed valve, but can have the advantage of rapid prototyping, owing to the room temperature beam line and modest vacuum requirements. This makes them ideally suited to spectroscopy, including high-resolution and/or dispersed laser-induced fluorescence studies, double-resonance rf/microwave/optical techniques, and Stark/Zeeman spectroscopy. Nonetheless, their fast forward velocity and ~10 K internal temperature means they are not the best suited for precision measurements, molecular laser-cooling, and coherent quantum manipulation. To produce slow and bright beams of free radicals, we instead work with cryogenic buffer gas beams.

3.2 Cryogenic Buffer Gas Beam Sources

Cryogenic buffer gas beam (CBGB) sources are a versatile and essential starting point for many cold molecule experiments [178], including precision measurements [11, 100, 179] and ultracold molecule production through direct laser cooling [104, 108, 180–185]. While CBGBs are reviewed in detail in the literature [178, 184], I will provide a brief summary here.

CBGB sources produce bright, slow molecular beams that are both translationally (T) and internally cold (T_{int}), typically with temperatures of $T \approx T_{int} \approx 4$ K. In such sources, the molecular species of interest is introduced into a cryogenic cell containing a density-tuned, inert buffer gas (nearly always He or Ne). The species of interest is introduced via either a heated fill-line or laser ablation of a solid target. The resulting hot molecules, typically introduced at $T > 1,000$ K, are subsequently cooled by collisions with the buffer gas. Once thermalized, the molecular species is entrained within the cell in the buffer gas flow, and carried out of the cell through an aperture, forming a beam. Alternatively, the cell can be completely closed, allowing for long interaction times and isolation of the molecular sample, which can be useful when dealing with a radioactive species or when trying to recapture gas, i.e., ^{3}He. The cryogenic buffer gas cooling method is quite generic and can be applied to many species, from atoms to small bio-molecules [186], including highly reactive or refractory species.

---

[2]The same energy (temperature) distribution will have a much narrower velocity width at higher velocities: $\delta E \approx mv\delta v$, which was recently used to perform spectroscopy on hot and fast radioactive beams of molecules [177].
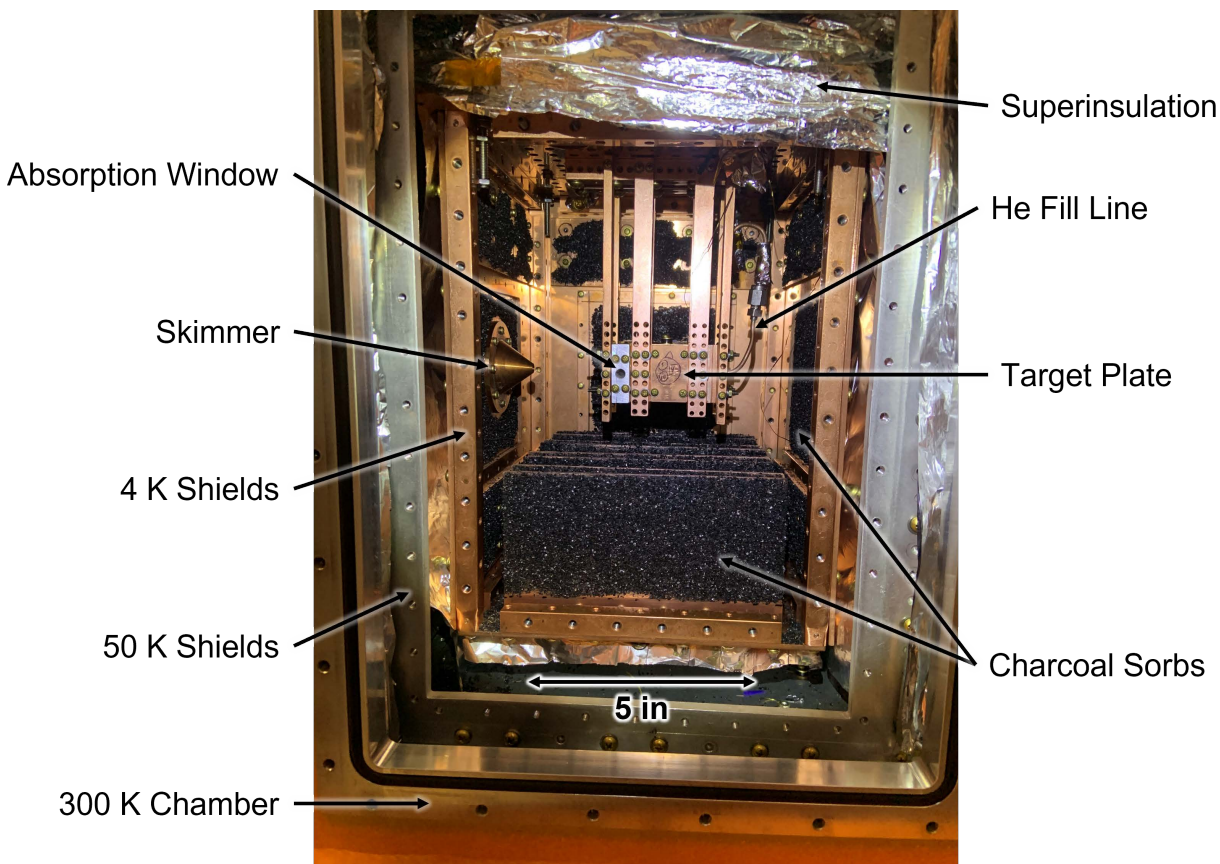
Figure 3.2: A photo of the 4 K CBGB source with labeled components. This photo was taken after the cryo-pumping upgrades described in the section on cryopumping. The cell sits in the middle of the photo, anchored with vertical bars to the top of the 4 K shields, which is connected to the cold head (not visible). See main text for more details.

In the lab we have two CBGB sources, the 4 K (a.k.a. "orange") beam source and the 1 K (a.k.a. "red") beam source, as well as a closed cryogenic buffer gas cell, known as the "mini-fridge." The work in this thesis performed at Caltech was primarily performed in the 4 K source. Details of the source design and construction, including technical drawings, are presented in Nick Pilgram's thesis [161]. My main focus here will be on providing a heuristic discussion of the 4 K source and its operation.

3.2.1 The 4 K Source

A photo of the 4 K CBGB source is shown in Fig. 3.2, with relevant components labeled. The source is inspired by the ACME experiment [41], and follows general design principles that are reasonably well established for CBGBs. The 4 K source consists of a copper[3] cell that is cryogenically cooled[4] to ~4 K, and surrounded by radiation shields. The shields provide insulation

---

[3]The alloy should be C10100 for optimal thermal conductivity at cryogenic temperatures.
[4]We use a Cryomech PT415 pulse tube cooler, with a cooling capacity of 1.5 W/K at 4 K and 40 W/K at 45 K.

from blackbody radiation at 300 K, which generates a 460 W/m^2 heat load. The entire 300 K vacuum chamber is mounted to an aluminum 80-20 structure. To help reduce vibration noise from the top-heavy structure, we fill the legs of the 3×1.5-in^2 80-20 struts with copper-coated lead shot. This improved the vibration noise of the experiment considerably.

From outside in, after the 300 K vacuum chamber, we have the 50 K aluminum shields, which are hung from the 300 K top plate via stainless steel threaded rods to help isolate from the mechanical vibrations of the cold head. To provide a thermal connection, the 50 K shields are connected via copper braids to the 50 K cold head[5]. This cooling stage has over an order of magnitude more cooling power compared to the 4 K stage, and can sink the blackbody heat load. To increase reflectivity and reduce thermal loads, the radiation shields are covered in a layer of aluminized mylar superinsulation. The 50 K shields have windows on the side plates that allow for optical access to the cell, and the front 50 K plate has a 3/8-in diameter hole that collimates the molecular beam exiting the source. Inside the 50 K shields, we have the 4 K copper[6] shields, which are also suspended from the 50 K shields via threaded stainless steel rods, and thermally anchored to the 4 K cold head via copper braids. The 4 K side plates (removed for the photo) do not have windows, but instead have a 3×2-in^2 open area for optical access. To deal with the issue of differential thermal contraction, all parts that cool down to cryogenic temperatures are held together with brass screws and Belleville washers. The copper threads are helicoiled to prevent them from stripping.

The cell was designed in a modular fashion, which allows for design changes and length adjustments. Here we describe the "final" iteration that was used for much of the work in Chapters 4 and 5. The cell is essentially an 0.5-in diameter bore inside a series of modular copper blocks connected together to form a single cylindrical volume. The cell parts are sandwiched together with Belleville washers and brass nuts on stainless steel threaded rods running down the cell length. From back to front, the cell components are as follows, with each part characterized by the length it adds to the cell volume. First, we have the gas inlet, consisting of a 0.125-in diameter copper tube braised on to a copper plate with a matching entrance hole for the gas. Then there is a 0.125-in spacer, followed by a 0.125-in diffuser plate that helps even the He flow distribution. Then we have a 0.5-in spacer, followed by a 1-in long ablation stage, which also has 0.75-in diameter ports on the sides. On one side port, we mount the targets, which are glued onto a copper plate with Stycast 2850 FT Black with catalyst 24 LV, and are described in detail in a later section. The reverse port from the targets provides optical access for the pulsed laser used to ablate the targets. Ablation is described later, and for now we simply mention the ablation laser enters through a non-AR coated window, mounted on a copper tube ("snorkel") that helps reduce the amount of material deposited

---

[5]Not the most accurate name, as it actually cools down to 40 K.
[6]Also C10100.

on the window. Following the ablation stage, we have a 0.5-in spacer, and then a 0.5-in wide absorption window stage, which has 0.25-in diameter ports for optical access, where we mount 0.5-in diameter windows. Finally, there is the front plate, which adds 0.1875-in of length to the cell, and terminates in a 5-mm diameter aperture. The total length of the cell, excluding the He diffuser stage, is nominally 2.6875 in.

We are able to run the source cold for months at a time without needing to warm up. When the targets are sufficiently spent, we warm up the source. Once warm, we replace the targets, as well as the ablation window, as it becomes opaque and coated with ablated material over the course of normal operation, in spite of the snorkel. The absorption windows can be cleaned with solvent and re-used a few times before needing replacement. We also perform a simple clean the inside of the cell, which is often covered in powder resulting from target ablation. Using heaters to warm up, if all the parts are ready in advance, the entire warmup and cooldown procedure can take a few days at most.

3.2.1.1   The Beam Extension

After the molecules leave the cell, they encounter a 4 K conical skimmer 1.875 in downstream, with a 0.25-in diameter collimating hole. Following the skimmer, the molecules travel another 2.625 in before encountering the 50 K collimating hole, with 0.375-in diameter. Then the molecules travel another ≈ 2 in before exiting the 300 K vacuum chamber entirely. The front plate of the 300 K chamber has a KF50 port for a 70 L/s turbo pump to pump out background gas. After the work described in this thesis, we installed an ion-sweeper at the exit of the 300 K chamber[7]. Following the 300 K vacuum chamber, there is a gate valve that can be used to isolate the CBGB source from the downstream beamline, also known as the beam extension.

The beam extension is where much of the work described in Chs. 4 and 5 was performed. A photo of the beam extension is shown in Fig. 3.3. The molecules travel ballistically down the beam extension through a series of vacuum chambers assembled by KF50 connections. The ability to probe the molecules upstream and downstream in the beam is very useful for both spectroscopy and coherent control. The beam extension is modular and has undergone multiple iterations over the course of the experiment. Here we describe the setup used for much of the work described in Chs. 4 and 5. We note that at the time of writing, the beam extension has been disassembled, to be replaced with an upstream pumping region (using the KF50 octagon described below) followed by the MQM science chamber.

After the gate valve, the molecules encounter a six-way KF50 cross, with the cross center at a distance of ≈ 42 cm downstream from the cell aperture. The cross has optical axis with AR-coated

---

[7]Essentially a pair of wires with a voltage applied across them used to deflect ions.
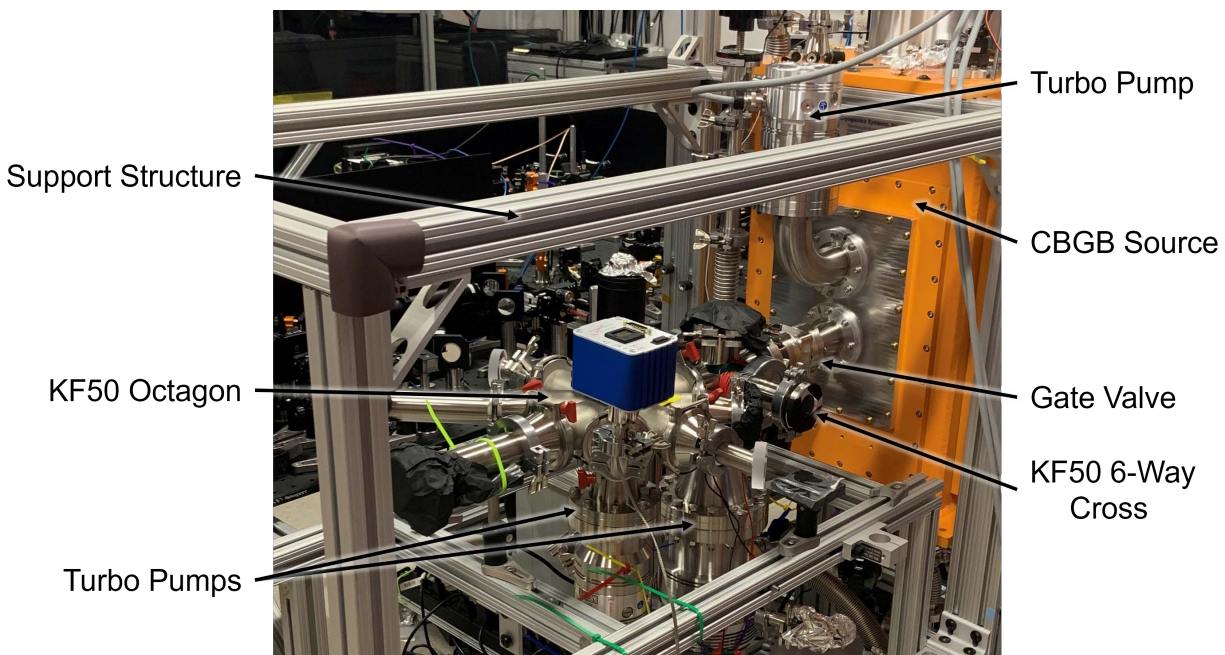
Figure 3.3: The beam extension downstream from the CBGB source. This photo was taken with many electronics, optics, and detectors removed.

windows along one of the arm axes transverse to the molecule beam. The windows are mounted with a custom mount[8]. The final arm axis (up/down) has a window on the top for fluorescence collection, and the bottom is connected to a 300 L/s turbo[9].

Following the six-way cross, the molecules then enter the octagon, essentially an 8-way KF50 cross[10]. The octagon center is located ≈60 cm downstream from the cell. The octagon has 4 arm axes transverse to the molecule beam, with one of the arm axes in the up/down direction, and the other 3 axes contained in a plane orthogonal to the up/down axis. The bottom port is connected to a 70 L/s turbo pump, and the top port has a feedthrough for a 19-mm diameter light pipe for fluorescence collection. The remaining 3 arms provide optical access for perpendicular probing of the molecule beam as well as 45°probes, which are useful for Doppler measurements.

The entire beam extension is supported by an aluminum 80-20 structure, which is secured to the 80-20 structure holding up the source via connections at two points. This structure is also useful for mounting optical breadboards, mounting equipment, and securing the vacuum chamber when performing modifications.

---

[8]The windows sit on an aluminum flange, essentially a KF50 stub with a hole in the center. The flange also has a radial o-ring groove that houses an o-ring that creates a seal against the window glass. The window is pressed down onto the o-ring by a 3-D printed plastic clamp held with fasteners that screws into the aluminum flange.

[9]Agilent TwisTorr 304 FS

[10]The part was made by ANCORP

3.2.2 Buffer Gas Dynamics

The buffer gas dynamics inside and in front of the cell can have drastic effects on the properties and yield of a CBGB source. In this thesis, we will focus on the use of helium buffer gas in sources near 4 K. We note that CBGB sources have also been operated with neon, for example in the ACME experiment. Refs. [41, 179] have detailed discussions on the difference between helium and neon sources. For our purposes, the primary differences are two-fold: 1) helium CBGB sources can achieve lower temperatures and forward velocities, and 2) while neon simply freezes when contacting a cold surfaces, helium gas does not freeze, and instead can be adsorbed by porous materials.

As a function of the gas flow through the cell, CBGB sources can operate in three flow regimes: nearly effusive, intermediate, and hydrodynamic. These regimes are characterized by the number of collisions within roughly one aperture diameter distance from the aperture. For on few (<1) collisions on average, the beam produced from the aperture is effusive, and samples the thermal velocity of the molecules inside the cell. While such beams are slow, the fraction of molecules exiting the cell can be low, and the subsequent beam has large divergence. Meanwhile, when there are many (≫1) collisions, the gas flow is fluid-like, and the beam is hydrodynamic. In this regime, the beam velocity is boosted by collisions at the aperture, and saturates at a supersonic velocity of ~200 m/s. This boosting can also result in expansion cooling [179], which can further cool the rotational distribution of the molecules. This expansion cooling is what allows neon sources that run at hotter temperatures (i.e., ~15 K) to achieve cold rotational temperatures, comparable to helium sources (i.e., ~5 K). Finally, in the intermediate regime, there are ~1 − 10 buffer gas collisions on average near the aperture, and the flow cannot be easily modeled. There has been some progress in using computational simulations to model gas flow in this intermediate regime [187]. In this work, we typically operate with intermediate regime gas flows.

For a cell with an exit aperture, the helium density can be approximated by making a steady state assumption, see Ref. [178] for equations. Typically we operate with gas flows in the regime of 3 standard cubic centimeters per minute (SCCM) (1 SCCM = 4.5×10^{17} atoms/sec [178]), and with a 5 mm diameter aperture, resulting in typical He densities on the order of $\sim 10^{15}/cm^3$. At this density, the mean free path of the species of interest is ~0.1 mm, and after about ~100 collisions, the molecules thermalize translationally and rotationally. Therefore the buffer gas cell dimensions are typically at least ~1 cm.

The helium density inside the cell must be high enough to thermalize the molecules after ablation. If the density is too low, the majority of molecules formed by ablation will rapidly expand without stopping, eventually colliding with the cell walls. The few molecules that survive will be hot and fast. Conversely, if the density is too high, a few undesired dynamics occur. First, the

focused ablation laser can form a plasma that dissipates energy and shields the target from ablation, known as plasma shielding [188, 189]. Second, the high helium density prevents the expansion of the initial ablation plume, limiting the spatial extent of the molecules. Detailed investigation of ablation and thermalization dynamics in a closed buffer gas cell were performed in Ref. [190].

Finally, with too much helium gas, the ablation energy can "ring up" the cell, causing the propagation of helium pressure waves. A quick estimate indicates that the speed of sound of helium at 4 K is ~118 m/s. For a 3-in long cell, this results in a fundamental longitudinal mode with a ~1 ms period. This sloshing of the helium gas can result in a modulation of the output beam intensity at roughly this timescale. We have observed this multi-pulse behavior when ablating at energies > 30 mJ/pulse. Typically, the first molecular pulses that exit are fastest, and the last pulse to exit is the slowest, having interacted with the buffer gas for longer time.

We note the assumption of steady state does not hold in helium based CBGBs operating with porous targets, for example pressed powder targets. In such sources, it has been observed that helium can be cryo-pumped, a.k.a. adsorbed, by the target. This is supported by two pieces of evidence: 1) in open buffer gas cells (that is, cells with an exit aperture), if helium is flowed for some time, and then stopped, molecular beams may still be produced when ablating without gas flow [41, 184]. In our source, such beams without gas flow persist for ~10 shots or so before the signal degrades significantly. This effect is not observed if, after flowing gas, the cell is heated up to above the desorption temperature of helium (~10 K) before being cooled back down and ablated. 2) In experiments with closed buffer gas cells, when the cell is loaded with helium gas in the presence of porous targets, the pressure will drop as the helium gas is adsorbed by the target. Subsequent ablation of the target liberates the adsorbed helium. This has been observed in Ref. [190] and in experiments in our lab with the mini-fridge.

The cell geometry and aperture characterize an extraction time, roughly the time scale for molecules to leave the cell. The net flow of the buffer gas inside our 0.5-in diameter cell has a velocity on the order of ~30 m/s, which can be estimated from conservation of flux inside the cell compared to flux outside by the aperture, where the velocity is ~200 m/s. We can then approximate the extraction time as the time it takes the molecules to travel down the cell to the aperture, roughly ~1 ms for the dimensions of our cell (~1.5-in distance from ablation to aperture). We can also use the extraction time to characterize the spatial extent of the CBGB. Assuming a 200 m/s velocity upon leaving the cell, this gives a spatial extent of ~20 cm, possibly more if the extraction time is increased. We note for larger cells, the extraction time can be longer, ~ 10 ms or more, which can result in ~1 m long beams.

The extraction rate must be balanced with the thermalization and diffusion times of the molecules. The diffusion time refers to the timescale for diffusion to the walls, which results

in loss. If the diffusion time is too short, the molecules will hit the cell wall before being extracted. But if the extraction time is too short, the molecules may not properly thermalize. For our cell geometry, the extraction fraction is roughly on the order of $10 - 20\%$. We note all of these estimates are subject to caveats and deviations, given the complicated nature of the buffer gas dynamics.

We now consider the divergence and velocity distribution of the molecules exiting the cell. These quantities are discussed in detail in Ref. [178, 179, 191], here we simply provide estimates and values. The forward velocity distribution can be characterized as a 1D Maxwell-Boltzmann distribution, with an estimated FWHM of $\Delta v_\parallel \approx 30$ m/s for YbOH at 4 K. Meanwhile, the transverse velocity spread can be larger as a result of collisions by the aperture, with $\Delta v_\perp \approx 60 - 80$ m/s in the flow regimes we consider. Finally a crucial figure of merit is the angular spread and divergence of the beam, which, in the intermediate flow regime, can be less than an effusive or supersonic beam. We expect an angular FWHM of $\Delta\theta \approx 35°$, resulting in a solid angle of $\Delta\Omega \approx 0.3$ sr. We can use this quantity to estimate the loss from beam divergence downstream as follows. We model the aperture as a point source, and we estimate the distance to the "science region" of the beamline as 0.5 m. Then a 1 cm laser beam will probe a solid angle that is approximately 10^{-3} times smaller than that at the aperture, resulting in roughly 3 orders of magnitude of loss from beam divergence.

Finally, the molecule-helium collision process is characterized by the cross-section for elastic and inelastic collisions. However, vibrational degrees of freedom have significantly smaller inelastic cross-section, and therefore vibrational thermalization occurs inefficiently and slowly [192]. In CBGB sources, the molecules are often extracted out of the cell by the helium flow before the vibration can thermalize, and the vibrational populations are therefore athermal, with distributions on the order of 300 K or more. The existence of excited vibrational population can be beneficial for the study and spectroscopy of vibrational states in molecules.

3.2.2.1 Background Gas and Cryopumping

The brightness of a CBGB source is strongly dependent on the vacuum environment after leaving the cell. Since we are flowing buffer gas constantly, residual gas atoms present after the cell can knock molecules out of the beam. This was investigated in simulations [193], where it was found that this effect particularly harms slow velocity classes, which take longer to travel the same distance. To deal with this problem, in helium CBGB sources the region outside the cell is filled with charcoal surfaces at 4 K. The charcoal is epoxied to sanded copper plates using Stycast 2850 FT. The charcoal is very porous, and serves as a reservoir that can adsorb and trap helium gas, acting as a pump at cold temperatures. Eventually, these charcoal "sorbs" can fill up with helium, and must then be heated to above ~10 K. At such temperatures the sorbs will release their trapped helium, which can be pumped out with standard vacuum pumps. This procedure is known as desorbing, and must be
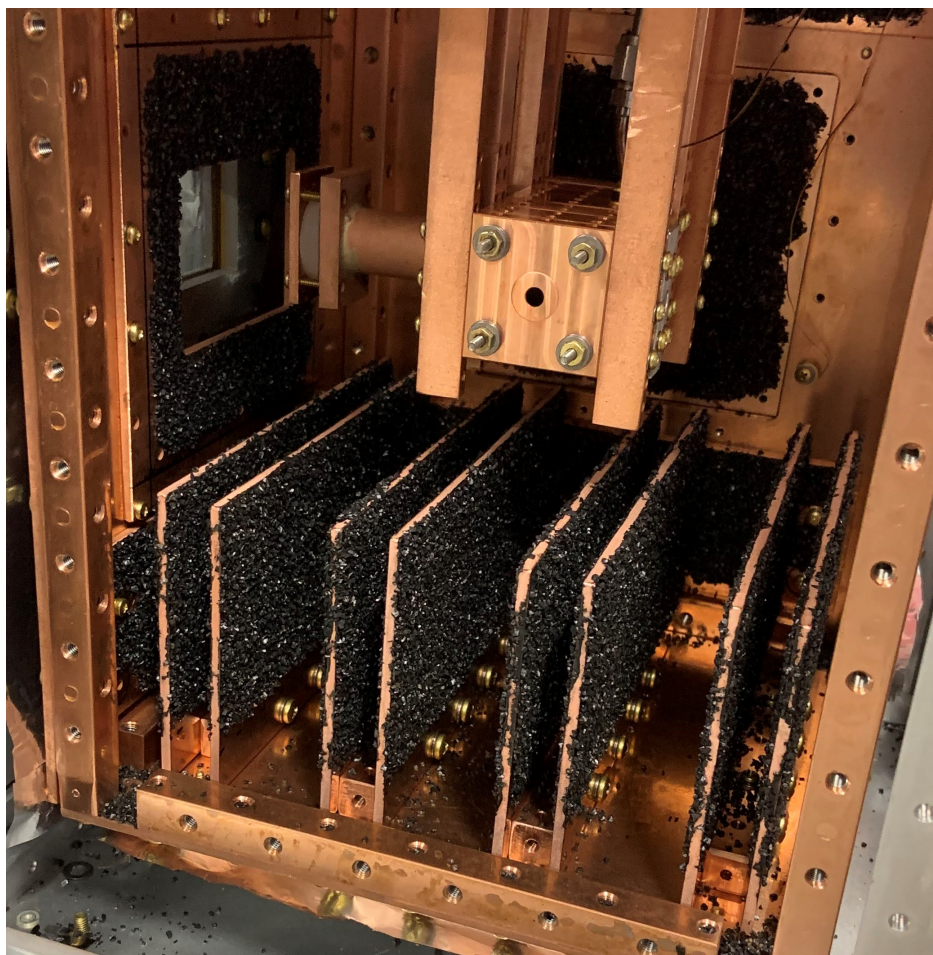
Figure 3.4: A photo of the charcoal sorb fins after installation. The fins are mounted to the bottom of the 4 K radiation shields. The cell is visible, along with the exit aperture and the ablation snorkel, which is used to prevent the ablation plume from coating the ablation window. Charcoal sorbs on the sides of the 4 K chamber are also visible.

performed occasionally to refresh the cryo-pumping capacity of the sorbs.

As we continued to work on the 4 K source, we realized the importance of background gas collisions on beam signals downstream. When operating with approximately 280 in^2 of charcoal surfaces, a 70 L/s turbo pump[11] downstream in the beamline, and a gauge in the beamline reading a pressure of $1 - 7 \times 10^{-7}$ Torr when flowing $1 - 9$ SCCM in the cell, we saw loss of molecule fluorescence $\sim$50 cm downstream that scaled linearly with the increased gas flow. An increase in gas flow from 1 to 3 SCCM roughly resulted in a factor of 2 loss in fluorescence signal downstream.

As a result, we performed a significant upgrade on our CBGB source. We first installed a series of 8 sorb fins, shown in Fig. 3.4. These copper fins are covered with charcoal on both sides (attached with Stycast), significantly increasing both the surface area for cryo-pumping and

---

[11]Agilent TwisTorr 84 FS.

the overall capacity for storing helium. The installed fins represent an additional surface area of ≈ 312 in^2. The fins are mounted such that the charcoal faces are parallel to the molecular beam axis. Finally, we replaced the sorbs by the 4 K collimator with a skimmer (a metal cone facing toward the buffer gas cell). The sorbs had been completely coated in dust that we could not remove; instead of constantly replacing the collimator sorbs, we instead opted for a skimmer, which has no charcoal, and simply provides an angled surface to redirect gas[12].

Additionally, we must efficiently pump out helium that makes it out of the 4 K stage, as it no longer experiences cryo-pumping. If this helium is trapped between the beam box layers and the vacuum chamber, it can collide with and attenuate the molecular beam. Therefore, we installed an additional 70 L/s turbo pump on the front plate of our 300 K stage. This turbo has the added benefit of preventing back-flow into the vacuum chamber when cryo-pumping is active. Prior to the installation of this turbo, the vacuum chamber was pumped on with a dry scroll pump[13]. Because cryo-pumping is extremely effective at pulling vacuum, the scroll was exposed to a very low vacuum, and was unable to maintain the compression ratio with the exhaust at atmosphere. Air would back-flow through the scroll pump into the vacuum, causing ice to form on our windows. Installing a turbo, backed by the scroll pump, directly on the source, solved this problem, as the turbo can maintain the compression ratio between the cryo-pumped chamber and the scroll inlet.

After performing the sorb upgrade and turbo upgrade, the molecular signals in the beamline no longer degraded with increased gas flow. The pressure gauge on the beam extension reads $\sim 1 \times 10^{-7}$ Torr, even when flowing up to 9 SCCM of gas. Not only did our overall fluorescence signals increase, but we can now vary the gas flow, which impacts properties such as buffer gas density inside the cell, extraction of molecules out of the cell, and beam velocity.

3.2.3 Ablation Targets and Chemistry

Modeling cryogenic buffer gas sources with laser ablation is a hard problem. The plasma dynamics alone are an active field of research [188, 189, 195–198], with shockwave speeds reaching up to 50 km/s and plasma energies on the order of 10^4 K. In our source, we ablate with a pulsed, nanosecond Nd:YAG laser[14], frequency doubled to 532 nm. The pulse energy can be varied from 1 mJ up to $\sim 50 - 100$ mJ, with a repetition rate as high as 50 Hz, though we often operate with < 10 Hz, both to avoid excess heating of the cell from the ablation, and due to constraints of other equipment, such as mechanical shutters. We typically focus the laser from a ~ 6-mm collimated beam using a $300 - 400$-mm lens, resulting in a ~ 100-µm spot size, limited primarily by aberrations.

---

[12]Note that Helium surface dynamics are non-trivial at low temperatures. There is a high change the incident Helium adsorbs to the cryogenic surface [194], and can later be desorbed with a non-trivial angular distribution [194].

[13]Agilent IDP-10.

[14]Big-Sky/Quantel YAG laser from Anderson Lasers.

For molecular beam production, optimizing ablation targets can result in significantly improved yield and consistency. Typically, metals, sintered ceramics, and high-density targets ablate well, while soft or crumbly targets tend to rapidly degrade in ablation yield [193, 199, 200]. Yb metal is a great ablation target and often used to characterize CBGB performance. Other metals, like Sr or Ba, can oxidize quickly, which can result in rapid target deterioration. Ablation yield typically increases with pulse energy, up to a point. Further, targets with lower melting and/or boiling points experience more melting/boiling in the wings of the intensity distribution of the ablation laser. This can result in more material removed per pulse [189]. However, ablation yield eventually plateaus due to plasma shielding effects, where the focused laser creates a plasma in front of the target that reduces the efficiency of energy transfer from the laser to the surface [188, 189].

To produce YbOH molecules, we ablate pressed powder targets containing Yb, O, and H atoms. The targets are formed by first mixing Yb powder (200 mesh, ground and passed through 230 mesh) with $Yb(OH)_3$ powder (ground/milled and passed through 230 mesh). The powders are combined, often with the addition of 4% polyethylene glycol (PEG 8000) by mass acting as a binder, and pressed in an 8-mm hydraulic die press with 6 metric tons of pressing force for $\gtrsim$15 minutes. The press and the target are lubricated with dry molybdenum spray. We found YbOH target yield improved by nearly an order of magnitude when mixing Yb and $Yb(OH)_3$ to achieve a stoichiometric Yb:OH ratio, compared to targets that are predominantly $Yb(OH)_3$. Ablation yield can exhibit significant variation from shot to shot on the same targe location, as well as when comparing different locations. Overall, the ablation signal decays over time, with pressed powder targets decaying more quickly (each spot provides $\sim$ 1,000 shots) compared to metal targets. In another experiment in the lab, the addition of Yb powder improved the ablation consistency of potassium salt targets used to produce K atoms, suggesting Yb metal can be used to stabilize target performance.

We have experimented with various recipes, and typically find similar results amongst different targets. To produce YbOH, we have tested targets with polyvinyl alcohol, telluric acid, D-sorbital, aluminum hydroxide, and epsom salt, and all have worked to some degree. Some photos of targets are shown in Fig. 3.5. Target testing can be challenging due to the slow turn around with cryogenic sources and the large parameter space for investigation, including target composition, pulse energy, repetition rate, ablation focus, etc. We have found that for our pressed Yb targets, there is typically an onset of YbOH production after an energy threshold of ~15 mJ/pulse. This is possibly tied to the energy threshold required to produce significant energized excited states in the ablation plume, and/or possibly related to the melting dynamics of the ablated surface.
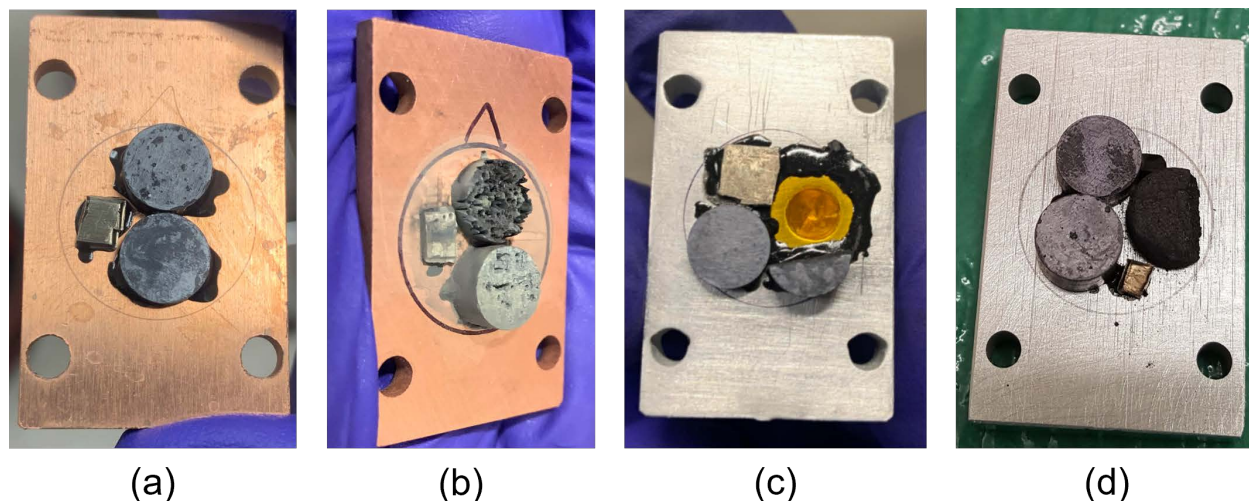
Figure 3.5: Some examples of targets we have used for ablation. (a) Yb metal target with stoichiometric Yb+Yb(OH)$_3$ targets, the bottom one having been cold sintered (see main text for details). (b) Targets after ablation. Pale coloration occurs from oxidization. (c) Target used for double ablation tests. In addition to the Yb and Yb + Yb(OH)$_3$ targets, this plate has a well sealed off with kapton and stycast. Inside the well is water containing gold nanoparticles that possibly help with 532 nm absorption. (d) In addition to the usual Yb and Yb + Yb(OH)$_3$ targets, this plate had a mixture of Yb + polyvinyl alcohol, the target on the right.

3.2.3.1 Heated Fill Line

Metal ablation is generally superior to pressed target ablation [193, 200], motivating the introduction of reagents not via laser ablation, but via a heated fill line. The ablation yield and consistency of metal targets is excellent, particularly for Yb metal. Further, with metal targets the ablation energy can be lowered to $5 - 10$ mJ/pulse, which can help reduce the beam velocity for applications such as laser cooling. To produce molecules, a heated fill line can be connected to the cell and used to flow in reagent gases that must be held at high temperature to have sufficient vapor pressure. Examples include water [108, 200] and methanol [106, 139] for hydroxide production, or SF$_6$ [184, 193] for fluoride production.

There are a few drawbacks to use of a heated fill line. Difficulties include the thermal engineering challenges of having a >250 K gas line running through <50 K cryogenic regions. It is therefore helpful to have the heated fill line follow a path that is separate from the rest of the gas lines and electronics. The heated fill line must have heaters along its length, used to keep the temperature high. Some thermal engineering is required to make sure the rigid connection of the cell to the heated fill line is thermally insulating, and this is typically achieved with teflon spacers. Nonetheless, operation of a heated fill line typically raises cell temperatures by ~1 K. This can also be a challenge for systems designed to reach 1 K or lower, which can be sensitive to added

heat loads. The heated fill line nozzle is inserted through a hole in the cell that has a much wider diameter and does not contact the fill line. The nozzle must not stick too far into the cell such that its tip freezes over, but also not be too recessed such that an ice bridge can form from the nozzle to the hole in the cell. Diagnosing such issues at cryogenic temperatures is also difficult, requiring constant warmup and cooldown cycles. Finally, the reagents that are flowed into the cell coat the walls of the cell, creating a layer of ice or snow after a week or so of operation [139, 184]. This ice is correlated with a speed up of the molecular beam, requiring a warmup and cooldown cycle to remove the ice and return the beam to its original properties.

We attempted to install a heated fill line in our source, but it ended up being less effective in our source compared to working with pressed targets instead. Briefly, we designed an 0.75-in diameter cell, with the inner bore expanded to allow for the introduction of both a heated fill line and a helium gas line into the cell. Around this time, we ran into significant cell failures that caused the production of both YbOH molecules and Yb atoms to be uncharacteristically weak. For example, our Yb absorption signals, which typically are optically thick when probing the $^3P_1$ line (~99% absorption, see Sec. 3.2.4.2), were noticeably weaker with $10-50\%$ absorption, depending on ambient conditions. YbOH signals, which are ~10% or more (depending on the rotational line) in our 0.5-in cell, were $\lesssim 1\%$ in size with the 0.75-in cell. Some possible failure mechanisms were investigated, and we did indeed find braise joint leaks in the He gas line, but even still we were unable to make the 0.75-in diameter cell work.

We suspect the issue was related to insufficient Helium gas density. It is possible we had a leak at the connection of the He line to the cell, which we could not leak test. Furthermore, it is possible there were additional leaks at cell connections or the windows that resulted in loss of He density. In all of our cell designs on the 4 K source, the windows are mounted to the cell by pressing the glass against a kapton "gasket" on the copper surface, and the modular cell parts are "sealed" by pressing them together with nuts and Belleville washers on threaded rods, with apiezon grease applied between the surfaces. We note that leak tests on closed cells in our lab have shown that these sealing methods are inadequate to hold vacuum, and can be leaky at the $>10^{-6}$ mbar L/s level. Only by using indium seals can we lower this leak rate to $\lesssim 10^{-9}$ mbar L/s. Though there have been no detailed studies of the effect of leaky vs sealed cells, there is anecdotal evidence that the puff of desorbed He liberated by ablation has an impact on the cell dynamics, and such a puff could have different non-equilibrium densities depending on how leak-tight the cell is. It is also possible that a He film forms on the surfaces at low temperature, further increasing sensitivity to leaks. Unfortunately we can offer no conclusions from our experience with the 0.75-in cell, only conjectures.

When we returned to the 0.5-in cell design, we were able to recover our typical Yb and YbOH

signals. To install a heated fill line, we then replaced the spacer upstream of the ablation region with an inlet for the heated fill line, with the nozzle spraying gas into the cell at an angle. We tested this configuration with methanol reagent, and we were able to observe molecule production. However, the signals were noticeably weaker than those from the mixed powder targets, so we abandoned the heated fill line. The reason for weaker signals could be due to issues with our heated fill line design. For example, the heated fill line passed through much of the 4 K and 50 K stages, causing 1 K additional heat load when operated, which can reduce signals. Furthermore, due to space constraints, our heated fill line had a large bend right before the cell, instead of coming in straight, which could affect the flow. Finally, we note the aspect ratio of our cell design ($\approx 1 \times 5$) is quite different from those in other experiments using heated fill lines (closer to 1×1) [106, 139, 193, 200].

3.2.3.2   Cold Sintering

Target density is correlated with improved yield and target consistency. Some experiments have had success in creating ceramic targets for ablation via sintering [201]. Typically, sintering involves raising the temperature of a sample to ~1,000 K or higher to transform a pressed powder into a dense ceramic. We attempted sintering tests[15] of YbOH early on, but after heating beyond 300° C, the targets showed some weight loss, with one target dissolving slightly. X-ray diffraction analysis indicated one target formed a new Yb_2O_3 phase. We surmised that the hydroxide breaks apart at high temperatures and is driven off, resulting in weight loss and the formation of oxide phases. Therefore, high temperature sintering is not useful for M-OH targets.

Recently, a technique has been developed in materials science called cold sintering [202–208]. The basic idea of cold sintering is to heat the target to $\lesssim 300°$ C while applying pressure either in an open or closed environment. Often an aqueous solution is added to promote diffusion and re-arrangement, such as water. There are also variants, such as flash sintering which utilizes electric current [209, 210], or hydroflux sintering using ionic salts with sparing quantities of water to depress their melting point [211]. A recent demonstration of cold sintering produced a dense pellet of γ-AlOOH after starting with aluminum hydroxide percursor [212].

We have experimented with cold sintering by adding ~$10 - 40\%$ by mass of water to the target mixture before pressing, and wrapping the die press in heating tape to bring the temperature to $150 - 200$ °C when pressing. If the pressed material is sufficiently aqueous, we use tape to cover the cracks in the press and prevent the liquid from spilling out. The resulting targets have improved density compared to the un-sintered case, and anecdotally have better ablation yield consistency,

---

[15]Thanks to Xiaomei Zeng and Katherine Faber for assistance with the sintering tests and subsequent analysis.

particularly at high ($\gtrsim$40 mJ/pulse) ablation energies. More investigation is needed to determine optimal target recipes and techniques.

3.2.3.3   Double Ablation

Another approach is to ablate two separate targets containing constituents of the molecule of interest, known as "double ablation." For example, instead of using a heated fill line to introduce water and produce YbOH, one can co-ablate a Yb metal target and another target containing hydroxides. This can be useful if the metal is difficult to obtain in powder form to make mixed targets with, for example for trace or radioactive species. In our lab, tests in other experiments show that co-ablation of metal and solid hydroxide targets is effective at producing molecules, with similar yields compared to ablation of a single mixed target. Separating metal and reagant targets can also be useful for studying reaction dynamics, for example by varying relative ablation powers, or delaying one shot relative to the other if they are sourced from separate lasers. Alternatively, double ablation can be performed with a single YAG laser, split with a beam splitter into two paths with different alignments. For optimal molecular yield, the power balance in double ablation must be adjusted by monitoring production signals.

We have also experimented with frozen ice targets to produce water in the cell for double ablation. If water can be sealed in a well in the target plate, then when the plate is cooled down, the water freezes and can be ablated. The target well was formed by drilling a hole in a copper plate, sanding it down, filling it with water containg gold nanoparticles that absorb 532 nm light[16], and sealing the hole with a combination of kapton (polyamide) tape and stycast 2850 FT at the edges of the tape. The target is shown in Fig. 3.5. Though this maintained a seal that retained water even after pulling a modest vacuum, the kapton did slightly buldge, and the target was not weighed to assess material loss.

We were able to successfully produce YbOH molecules when co-ablating a Yb metal target and the frozen water target. The overall yield was a factor of $\sim 5-10\times$ worse for water + metal ablation, compared to typical stochiometric pressed powder abaltion yields. Nonetheless the scheme worked, and has potential room for improvement; for example, the water can be covered with gold foil to create a stronger seal, and the target can be frozen in advance, before pulling a vacuum. A thermo-electric cooler (TEC) mounted to the back of the target plate could be used to keep the water frozen during pump out and initial cooldown. Further testing is needed to improving ablation yield and consistency with frozen liquid targets.

---

[16]Water has poor absorption at 532 nm otherwise.

3.2.4 Diagnostics

When operating a CBGB source, we want to monitor and study molecule production and beam properties. There are two primary ways of obtaining signals from the CBGB—absorption and fluorescence spectroscopy. Here we provide a brief overview of these two approaches. Absorption measurements are most useful in the cell or in front of the cell, and can be related to molecule density in a relatively straightforward manner. Fluorescence spectroscopy, on the other hand, is better suited for measurements downstream in the beam, and can have excellent signal-to-noise ratio (SNR).

All of our diagnostic tools involve studying the interaction of light with the atoms or molecules. Therefore it is useful to first introduce some relevant quantities related to excitation and decay rates, and cross sections.

3.2.4.1 Decay Rates, Branching Ratios, and Cross Sections

This section will follow Refs. [131, 213, 214]. We note that Ref. [131] is in cgs units[17], while Ref. [213] uses a different reduced matrix element convention[18]. Throughout this section, we discuss orientation averaging, which consists of averaging over initial state orientations (a.k.a. M sublevels) and summing over final state orientations. We use double primes to indicate ground state quantum numbers, and single primes to indicate the excited state. We will denote orientation averaged quantities with a tilde, e.g., $\tilde{\sigma}$. This is in contrast to quantities without a tilde, e.g., σ, which refer to a situation where we do not assume spherical symmetry and therefore perform no additional sums or averages.

In the dipole (a.k.a. E1) approximation for describing the light-matter interaction, the spatial gradient of the light field over the extent of the atom or molecule is neglected. As a result, the interaction operator can be written as $H_{int} = -\vec{d} \cdot \vec{E}$, where d is the transition dipole moment operator and E is the ambient or applied oscillating electric field. Technically, the interaction is $-\vec{d} \cdot \vec{E}$ for photon emission, and $-\vec{d} \cdot \vec{E}^*$ for photon absorption [67, 215, 216].

We begin by considering a single component of the dipole operator, written $T_p^1(d)$ in spherical tensor notation, which couples to a single spherical component of the light polarization vector. This situation corresponds to polarized emission, $|e, J', M'\rangle \rightsquigarrow |g, J'', M''\rangle$, where we do not perform any averages or sums over initial or final M sublevels. In this case, the decay rate for the polarization component p is given by [131, 213, 215–217]:

$$\gamma_{ij} = \frac{\omega_0^3}{3\pi\epsilon_0 \hbar c^3} |\langle g, i|T_p^1(d)|e, j\rangle|^2 \tag{3.1}$$

---

[17]To convert to SI, we take $d_{\text{cgs}}^2 \rightarrow d_{\text{SI}}^2/(4\pi\epsilon_0)$

[18]We follow the definition in Ref. [39].

where we have introduced the abbreviated labels $i = g, J'', M''$ and $j = e, J', M'$. Here, ω_0 represents the transition frequency of the decay in question.

We can also define the branching ratio specific to the M sublevels of interest as follows:

$$r_{ij} = \frac{|\langle g, i|T_p^1(d)|e, j\rangle|^2}{|\langle g||T^1(d)||e\rangle|^2} = \frac{|\langle g, i|T_p^1(d)|e, j\rangle|^2}{D_{ge}^2}. \tag{3.2}$$

The factor in the denominator is the J-independent reduced matrix element[19] for $T^1(d)$ that couples g and e, which we have written as D_{ge}. This is related to the J-dependent reduced matrix element by $\langle g, J''||T^1(d)||e, J'\rangle = c(J'', J')D_{ge}$, where $c(J'', J')$ is a coefficient obtained from angular momentum algebra (see Appendix A for details). For molecules, D_{ge} corresponds to the reduced matrix element in the molecule frame, $T_q^1(d)$. The quantity r_{ij} describes the branching for $i \leftarrow j$, although since the matrix element is squared, the order of the label makes little difference.

We now consider performing an *orientation average* by averaging over initial states (M' for emission), summing over final states (M''), and summing over all polarizations (p). This corresponds to spontaneous emission for an excited, unpolarized atom or molecule emitting in all directions, $|e, J'\rangle \rightsquigarrow |g, J''\rangle$. Though we do not consider hyperfine structure for now, the approach in this section can be generalized. We expand eq. 3.1 using the Wigner-Eckart theorem, and the subsequent sum over M, M', and p allows us to simplify the Wigner 3j-symbols using their orthogonality relations [39]. We therefore have:

$$\tilde{\gamma}_{J'',J'} = \sum_{M'',M',p} \frac{\gamma_{ij}}{2J'+1} = \frac{\omega_0^3}{3\pi\epsilon_0\hbar c^3} \frac{|\langle g, J''||T^1(d)||e, J'\rangle|^2}{2J'+1}. \tag{3.3}$$

This form agrees with Refs. [131, 213, 215, 216]. Here we have assumed $\omega_{ij}^3 \approx \omega_0^3$ for all ground and excited states in consideration. The orientation averaged quantity $\tilde{\gamma}_{J''J'}$ is often referred to as the *partial width* of a transition. The factor of $(2J'+1)^{-1}$ arises from the average over initial states. Alternatively, we can derive eq. 3.3 in the following way: we fix a given initial state M', and sum γ_{ij} over the final state M'' and the polarizations p. The orthogonality of the 3j-symbols then gives $1/(2J'+1)$, and since there is no preferred excited state orientation for spontaneous emission, this applies equally to all excited M' levels, and we obtain the same result as eq. 3.3. Finally, we note that the quantity $S = \sum_{M'',M',p} |\langle g, i|T_p^1(d)|e, j\rangle|^2$ is often referred to as the "line strength" of a transition.

Often in the case of molecules and CBGBs, there are multiple J'' states, and we are interested in unpolarized branching ratios. Analogous to eq. 3.2, we define the *orientation averaged* rotational

---

[19]Note the reduced matrix element satisfies the property $(D_{ge})^* = (-1)^{J'-J''}D_{eg}$, see Ref. [131] and Ref. [130].

branching ratio, $\tilde{r}$, as:

$$\tilde{r}_{J'',J'} = \frac{|\langle g, J_i''||d||e, J'\rangle|^2}{(2J'+1)D_{ge}^2}. \tag{3.4}$$

The orientation averaged branching ratios are normalized such that $\sum_{J''} \tilde{r}_{J',J''} = 1$. In terms of $\tilde{r}$ and D_{ge}, we may rewrite the partial width as:

$$\tilde{\gamma}_{J'J''} = \frac{\omega_0^3}{3\pi\epsilon_0\hbar c^3}\tilde{r}_{J',J''}D_{ge}^2. \tag{3.5}$$

If we now take the sum over all J'', we obtain the following formula for the total radiative decay rate of the excited state, in the absence of vibrational branching:

$$\gamma = \sum_{J''} \tilde{\gamma}_{J'J''} = \frac{\omega_0^3}{3\pi\epsilon_0\hbar c^3}D_{ge}^2. \tag{3.6}$$

This also agrees with Refs. [131, 213], as well as Ref. [217], where TDMs were determined for YbOH. After summing over all ground states, we see the total decay rate looks like that of a two-level system with transition dipole moment D_{ge}. The individual rates can therefore be parameterized in as $\gamma_{ij} = r_{ij}\gamma$, and similarly for $\tilde{\gamma}_{J'J''}$. This means we can treat our multi-level system as a two-level system scaled by the appropriate branching ratio.

If we expand our discussion to include multiple vibrational states as well then we must scale $\tilde{r}$ by the Franck-Condon factors of the vibrational transitions involved. We note that if the vibrational transitions have very different frequencies, the approximation $\omega_{ij}^3 \approx \omega_0^3$ may no longer hold[20], and we have to consider a sum over ω_{ij}^3 values. If we are just interested in a partial width, we can simply scale the partial width of interest by the vibrational branching ratio. If we want the total width, the sum in eq. 3.6 must be expanded to include a sum over vibrational ground states v'' as well. An example of calculations with vibronic TDMs can be found in Ref. [217].

Now that we have discussed emission, we consider absorption when applying resonant light onto the atom or molecule in question. We can describe the light as having intensity $I = \frac{1}{2}\epsilon_0 c E_0^2$, where E_0 is the amplitude of the applied field. We wish to describe the interaction between the light and the species in terms of an interaction cross section $\sigma(\omega)$. We first consider the case of resonance. The cross section can be written as follows [131]:

$$\sigma = \frac{W_{eg}}{\Phi}. \tag{3.7}$$

Here, W_{eg} is the excitation rate for stimulated absorption and $\Phi = I/(\hbar\omega_0)$ is flux of photons. From time-reversal symmetry, $W_{eg} = W_{ge}$ for just one ground and excited state. Without performing an

---

[20]For example, for YbOH, considering just $v_1' = 0 \rightsquigarrow v_1'' = 0, 1$, we have $\omega_{v''=1}^3/\omega_{v''=0}^3 \approx 0.92$.

orientation average, W_{eg} on resonance can be obtained from Fermi's Golden Rule [131] as:

$$W_{ji} = \frac{1}{\gamma_{\text{tot}}} \frac{|\langle g, i|T_p^1(d)|e, j\rangle|^2 E_0^2}{\hbar^2} = \frac{1}{\gamma_{\text{tot}}} r_{ij} \frac{D_{ge}^2 E_0^2}{\hbar^2} = \frac{\Omega_{ij}^2}{\gamma_{\text{tot}}} \tag{3.8}$$

where we have introduced the Rabi frequency, defined as $\Omega = E_0 d_{ij}/\hbar$, and $d_{ij} = r_{ij} D_{ge} = \langle i|T_p^1(d)|j\rangle$ is the matrix element connecting the state i to j. The matrix element is defined for a given polarization of the laser light that selects out the TDM component p. We note eq. 3.8 also agrees with the form given in Ref. [214] (there, W_{eg} is written as R).

The cross section on resonance, without orientation averaging, is then obtained by substituting 3.8 into 3.7. We obtain:

$$\sigma_{0,ij} = \frac{2}{\epsilon_0 \hbar c} \frac{\omega_0}{\gamma_{\text{tot}}} r_{ij} D_{ge}^2. \tag{3.9}$$

This form agrees with the Appendix of Ref. [218].

Meanwhile, the orientation averaged form of W_{ge}, denoted with a tilde, is given by [131]:

$$\tilde{W}_{J'J''} = \frac{1}{\gamma_{\text{tot}}} \frac{(2J'+1)}{3(2J''+1)} \tilde{r}_{J''J'} \frac{D_{ge}^2 E_0^2}{\hbar^2}. \tag{3.10}$$

The extra degeneracy factors arise from various averages over ground and excited state sublevels. We note that we still have $\tilde{W}_{eg} = \tilde{W}_{ge}$, shown in Ref. [131]. We substitute 3.10 into 3.7, and simplify with 3.5 to obtain:

$$\tilde{\sigma}_{0,J''J'} = \frac{\lambda^2}{2\pi} \frac{2J'+1}{2J''+1} \frac{\gamma_{J''J'}}{\gamma_{\text{tot}}} \tag{3.11}$$

which is the same form as Ref. [131].

We note that eqs. 3.9 and 3.11 hold for situations where γ_{tot} describes a total Lorentzian width that can receives contributions from multiple decay pathways, power broadening, or pressure broadening. The cross sections also hold for higher order transitions (M1, E2, etc.).

The cross sections here are derived for the resonant case. For off-resonant interactions, the cross section generalizes to have a frequency dependence, characterized by a lineshape function, $g(\omega - \omega_0) = g(\Delta)$, with units of inverse frequency. Here Δ is the detuning of the laser light from the resonance. We can normalize the lineshape such that $\int g(\omega - \omega_0) d\omega = 1$. We can derive the general form by noting the derivation in the resonant case from Ref. [131] involved multiplication by $g_L(0) = 2/(\pi \gamma_{\text{tot}})$, where $g_L(\Delta)$ is a Lorentzian lineshape. Therefore we can multiply by $g(\Delta)/g_L(0)$ to obtain the general lineshape.

Without orientation averaging, we obtain:

$$\sigma_{0,ij}(\Delta) = \frac{\pi \omega_0}{\epsilon_0 \hbar c} r_{ij} D_{ge}^2 \, g(\Delta). \tag{3.12}$$

For the orientation averaged cross section, we obtain:

$$\tilde{\sigma}_{0,J''J'}(\Delta) = \frac{\lambda^2}{4}\frac{2J'+1}{2J''+1}\gamma_{J''J'}\,g(\Delta).$$ (3.13)

Since $g(\Delta)$ is normalized, the integral of the cross section is always constant, which explains why the resonant value decreases with increasing width. When the natural linewidth dominates, $g(\Delta)$ is a normalized Lorentzian, and the resonant value reduces to eq. 3.11. We note that in some cases, it may be convenient to introduce the lineshape function, denoted $\hat{g}(\Delta)$, with a different normalization, such that $\hat{g}(0) = 1$. This allows everything to be expressed in terms of the resonant cross section, i.e., $\sigma(\Delta) = \sigma_0\,\hat{g}(\Delta)$.

Often we are interested in the scenario where we are dominated by Doppler broadening. In such a case, the distribution of resonance frequencies is given by a Gaussian function:

$$g_D(\omega - \omega_0) = \frac{1}{\Gamma_{\text{std},D}\sqrt{2\pi}}e^{-(\omega-\omega_0)^2/(2\Gamma_{\text{std},D}^2)}.$$ (3.14)

Here, we have written the Doppler "width" as a standard deviation. This can be converted to FWHM by $\Gamma_{\text{FWHM}} = 2\sqrt{2\ln 2}\,\Gamma_{\text{std}}$. The Doppler standard deviation is given by [131]:

$$\Gamma_{\text{std},D} = \frac{\omega_0}{c}\sqrt{\frac{k_B T}{M}}$$ (3.15)

where M is the mass of the species and T is its temperature. For YbOH at 4 K, the Doppler width is approximately $\Gamma_{\text{FWHM},D}/2\pi \approx 54$ MHz. However, we will find the lines are broader than this in the cell, partially a result of unresolved hyperfine structure.

We consider power broadening in a later section discussing fluorescence signals. In the case when multiple broadening mechanism are at an equivalent scale, we must represent the total lineshape as a convolution of the various lineshapes involved. In the case when the two mechanisms are Doppler and radiative broadening, the convolution of a Lorentzian with a Gaussian results in a Voigt distribution.

3.2.4.2 Absorption

Absorption spectroscopy measures the attenuation of laser radiation passing through a cloud of absorbing molecules (or atoms). The probability of a photon interacting with a molecule is encoded in the cross section $\sigma(\omega - \omega_0)$, where ω is the laser frequency and ω_0 is the separation of two energy levels interest. The cross section is maximized when the laser is on resonance with a transition, and the width of the cross-section is influenced by a combination of environmental and internal factors. Mechanisms that increase ("broaden") the cross-section width in CBGB

sources are usually Doppler broadening (~1 − 100 MHz), radiative linewidths (~ 10 MHz), and power broadening (0 − 100 MHz). Inhomogeneous electric and magnetic fields can also result in broadening, but we will not discuss that here. Details about cross sections are given in the previous section.

Interaction with a resonant photon can result in stimulated absorption or stimulated emission in the molecules. These two processes can be thought of as a time-reversal pair (a and $a^{\dagger}$ in a quantum picture), although we caution that this analogy is not technically exact due to differences in level degeneracies. Nonetheless, the two processes can be identified with the Einstein B coefficient. Indeed, in the absence of decoherence mechanisms, the cycle of emission and absorption is analogous to Rabi oscillations.

For stimulated absorption, a laser photon is incident on a molecule initially in a ground state. The energy and momentum of the photon is transferred to the molecule, promoting it to an excited state. This process can only occur if there are ground state molecules present. The cross section for such a process is given by eq. 3.11 for the case independent of M sublevels, and by eq. 3.9 for the case dependent on M sublevels.

If the laser propagates along the x-axis, absorption causes attenuation of the laser beam when measured at a location $I(x + dx)$ compared to $I(x)$. The absorption, dI, depends on the number density of absorbers in their ground state, n_g, their frequency dependent cross section $\sigma_{eg}(\omega)$, and the flux of incident photons, I. Explicitly, we have:

$$\mathrm{d}I = -n_g \sigma_{eg}(\omega) I \mathrm{d}x \tag{3.16}$$

where the sign indicates the intensity is attenuating as it passes through the sample. If we make the assumption that the absorber density is uniform, we can integrate the above equation over some length l, and then exponentiate, to obtain

$$I = I_0 e^{-n_g \sigma_{eg} l}. \tag{3.17}$$

This equation is sometimes referred to as the Beer-Lambert law. Here, I is the intensity transmitted through the absorbing sample, and I_0 is a reference intensity before encountering the sample. The quantity $OD = n\sigma l$ is often known as the optical depth (OD). Note that the optical depth is a logarithmic quantity, and can be related to the "linear" absorption fraction I/I_0 by $OD = \log(I_0/I)$. In the limit of small absorption, this can be expanded as $OD \approx 1 − I/I_0$, and the absorption fraction is linear in the number density of absorbers. We note all of these relationships hold for power of a transmitted laser beam as well.

On the other hand, if OD approaches 1, a majority of the light will be attenuated, and the sample is said to be "optically thick." In this regime, the transmitted intensity is exponentially

small, making it critical to calibrate any zero offsets of the detector used to measure the transmitted light. Furthermore, the sensitivity $dI/d(OD)$ is exponentially small, running into the limits of detector sensitivity. Therefore, absorption measurements are not very useful with optically thick samples. Often this is not an issue in practice if your goal is to make large quantities of a species of interest.

For stimulated emission, a laser photon is incident on a molecule initially in the excited state. The interaction with the light causes the molecule to emit an identical photon in energy and momentum, and the molecule transitions to a ground state. This process can only occur if there are excited molecules present. Using similar arguments to those for absorption, the effect of stimulated emission can be encapsulated as

$$I = I_0 e^{n_e \sigma_{ge} l}. \tag{3.18}$$

Here, the intensity increases proportional to the number of excited state molecules n_e. This is the same mechanism responsible for lasers, which leverage non-equilibrium n_e ("pumped gain media") to amplify light.

Two crucial factors remain: there are a finite number of absorbers present in a sample, and the excited state has a finite lifetime. The finite number of absorbers means a sample can be "saturated," and we shall run into this in the discussion of fluorescence as well. Consider a case where we perform absorption with what is initially a low light intensity. Most of the absorbers remain in the ground state, and their occasional excitation causes attentuation of the transmitted light according to eq. 3.17. As we increase the flux of the incident light, we increase the number of absorbers promoted to the excited state. Now, the transmission of the light is described by both stimulated absorption *and* emission:

$$I = I_0 e^{(n_e \sigma_{ge} - n_g \sigma_{eg})l}. \tag{3.19}$$

When $n_g \sigma_{eg} \approx n_e \sigma_{ge}$, then an incident photon is just as likely to encounter an excited state molecule compared to a ground state molecule. This will result in stimulated emission occuring at the same rate as absorption, increasing the transmitted light and counter-acting the attenuation. In the limit of very high photon flux, the two rates are balanced, and the absorption signal can disappear. We note that, from the previous section, $\sigma_{eg} = \sigma_{ge}$.

In practice, because the excited state can decay, population will naturally return from excited states to ground states. If the transition under consideration is "open," the excited state can decay to other ground states unaddressed by the laser. This population is lost, having been optically pumped to a dark state with large detuning to the excitation laser[21]. On the other hand, if the

---

[21]This is in contrast to coherent dark states, where the detuning can be small, but the state is dark as a result of interference.

transition is "closed" and all decays are addressed, then in steady state the molecules are distributed equally amoung the the ground and excited states. This has important consequences for molecule laser cooling, when we almost always have more ground states than excited states–even population distribution results in a smaller overall excited state fraction [115]. In the limit of high incident light flux, where the stimulated absorption/emission rate is much faster than the excited decay rate, the molecules are just as likely to be in the ground or excited state. Just as in the case of high photon intensity without decay, the transmitted light is unattenuated. In this case, the addition of excited state decay scrambles the phase of the excitation/de-excitation cycle throughout the sample.

We typically use absorption spectroscopy to monitor production of atoms and molecules in our CBGB sources. We measure absorption both inside the buffer gas cell and just in front of the buffer gas cell. For atomic species, densities can be high enough in the beam to perform absorption measurements downstream as well. We operate in the low saturation intensity ($s \ll 1$) limit to ensure the OD is linear in the ground state number density.

The absorption signals we obtain are time-dependent, and vary as the molecular cloud moves across the probe beam. Often we wish to integrate the signal to obtain a total number of molecules. If we assume the number density n is uniform across the length of the probe beam, then at a time t, the number of absorbers seen by the laser in a time increment dt is given by d$N = A_{abs}vn(t)$dt, where A_{abs} is the total area of the absorber cloud, for example the cross sectional area of the cell, and v is the speed of the absorbers moving through the laser. We can integrate this over the duration of the molecule pulse, from t_i to t_f, to obtain the total number of absorbers interrogated:

$$N_{tot} = \frac{A_{abs}v}{\sigma_{eg}l} \int_{t_i}^{t_f} \mathrm{d}t\, OD(t). \tag{3.20}$$

We will often refer to the quantity $\int \mathrm{d}t\, OD(t)$ as the *integrated OD*.

Since absorption is a fractional effect, it is robust to losses incurred along the beam path, such as from finite reflections or beam divergence/clipping. However, the sensitivity of absorption for measuring small signals is limited by the intensity noise of the transmitted background intensity.

To give some perspective on signal sizes, consider absorption of a 1 cm path length, with the Doppler broadened cross section for a strong transition on the order of $\sim 10^{-14}$ m^2 for atoms and $\sim 10^{-15}$ m^2 for molecules. Consider a photodetector with a dynamic range of 3 orders of magnitude, in other words a detector that can measure signals up to 5 V with 5 mV resolution. This is roughly the situation we have with standard photodiodes in lab. Such a detector is limited to measuring 0.1% fractional absorption, which corresponds to a number density of $10^7 - 10^8$ cm^{-3}. Achieving even this limit requires reducing both electronics noise and laser intensity noise to $< 0.1\%$. Furthermore, since our beam sources produce pulses of molecules, the absorption signal is pulsed with typical

timescales in the $\sim 1 - 10$ ms range. This means we are most sensitive to intensity noise $\lesssim 1$ kHz, which can be caused by mechanical vibrations, polarization noise (converted to amplitude noise by birefringent optics), or electronics noise in the signal chain.

A simple solution to improving the sensitivity of an absorption measurement is to perform multipass absorption, reflecting the laser beam many times through the sample before measuring attenuation. In the spectroscopy community, Herriott cells are used for such a purpose. Another approach is saturated absorption spectroscopy, which can be combined with lock-in techniques. This forms the basis of a setup used in our lab to calibrate absolute laser wavelength by comparing to co-recorded iodine spectra [219]. In general, lock-in techniques are powerful, as they encode the signal at a carrier frequency $f_c \gg$ kHz. This often moves the signal out of the bandwidth of significant $1/f$ noise, allowing for improved SNR. This is the basis of the frequency-modulated (FM) absorption technique, which was led by Nick Pilgram in our lab to perform sensitive absorption spectroscopy on vibrational excited states in a buffer gas cell [220]. The details of FM absorption are provided in his thesis [161] and in Refs. [221–225].

3.2.4.3 Fluorescence

As we discussed in the previous section, DC absorption spectroscopy is limited in sensitivity, and works best with a strong line and/or high number density. When the molecules enter the beam extension, the densities are reduced by nearly three orders of magnitude from the beam divergence, and therefore absorption spectroscopy no longer has adequate SNR. It is possible that sensitive absorption spectroscopy [220] could still observe the molecules downstream, but instead we turn to fluorescence spectroscopy, which has certain advantages over FM absorption, such as reduced complexity and easier interpretation.

Fluorescence spectroscopy is the process of using a laser to excite the molecules, and subsequently collecting the fluorescence decays, also known as laser-induced fluorescence (LIF). LIF detection can be very sensitive, a result of both the $\sim 10\%$ quantum efficiency of photon multiplier tubes (PMTs), as well as the ability to eliminate backgrounds by measuring LIF at a different wavelength than the excitation light. Such a scheme is referred to as off-diagonal detection, and is commonplace in molecules, as excited states can decay to other vibrational levels separated by $\gtrsim 10$ nm or more. Typically the excitation and signal light is separated by a series of filters[22]. Usually, fluorescence collection efficiencies are on the order of a few percent in our setups, with the possibility of reaching order $\sim 10\%$ when using large in vacuum collection optics.

We can estimate the SNR capability of fluorescence detection as follows. Assume we have effectively filtered out the excitation light and our SNR is detector limited. A typical PMT model

---

[22]It is best to use a combination of both interference and colored glass filters.

we utilize is a Hamamatsu H13543-300, with a spec of ~0.2 nA of RMS current noise when operated with a cathode to anode gain of 2×10^6. The PMT has a radiant cathode sensitivity of ~40 mA/W at the 577 nm, a wavelength of interest for YbOH. Therefore the PMT current noise can be translated to an RMS photon intensity noise of ~2.5 fW, or equivalently a noise of ~10 photons at this wavelength for a ~1 ms temporal pulse of molecules with constant scattering rate. Typical fluorescence collection efficiencies are on the order of ~1% of all emitted photons, and assuming each molecule only emits one detected photon, we obtain a molecule number noise floor of ≈1,000 molecules. Of course, there will be other non-idealities in the system, such as added noise from electronics, or non-ideal filtering resulting in the appearance of laser intensity noise, but this rough estimate shows the power of fluorescence detection.

Fluorescence from a closed optical cycle has two characteristic regimes, characterized by the balance between the excitation rate, which depends on light intensity, and the decay rate, which is constant[23]. When illuminating a species with resonant light, if the intensity is "low enough," the LIF signal will increase linearly with increasing intensity. This is the regime when the decay rate is much faster than the excitation rate. However, as we increase the intensity further, at some point response of the system becomes non-linear or *saturated*, and the LIF signal no longer increases. In this case the excitation rate matches or exceeds the decay rate, and the population is balanced between ground and excited states. As was mentioned in the absorption section, an incident photon is just as likely to stimulate emission than to be absorbed.

Actually, there are *two* mechanisms for saturation of fluorescence. All of the preceding discussion is relevant to atoms or molecules with closed optical cycles. However, as we often encounter with molecules, the excited state can decay to ground states unaddressed by the laser. In such a case, if the ground states are long-lived, they represent loss, the fluorescence will saturate as a result of the molecules being optically pumped away. Ref. [214] investigated the interplay of these two fluorescence mechanisms in the saturation of CaF fluorescence.

For quantitative analysis, we first consider the case of a closed optical cycle. It is convenient to define the saturation parameter on resonance, s_0, that allows us to characterize the cross over from linear to non-linear behavior of the atoms or molecules. The saturation parameter is defined by the relation $s_0 = I/I_s = 2\Omega^2/\gamma^2$. Here, I_s is the saturation intensity, and $\Omega = \Omega_{ij} = E_0 d_{ij}/\hbar$, and $d_{ij} = \langle i|T_p^1(d)|j\rangle$ is the matrix element connecting the state i to j for a given polarization of the laser light that selects out the TDM component p. We may write $\hbar^2\Omega^2 = r_{ij}D_{eg}^2E_0^2$, where r_{ij} can generically include vibrational branching. Further, by writing $E_0^2 = 2I/(c\epsilon_0)$, we can use eq. 3.6

---

[23]Unless the density of states is engineered. See the Purcell effect for details.

to solve for I_s, obtaining:

$$I_{s,ij} = \frac{\pi hc}{3\lambda^3 \tau} \frac{1}{r_{ij}}.$$ (3.21)

Here, r_{ij} is the branching ratio for the $j \to i$ transition, including both rotational and vibrational branching. As a sanity check, it makes sense that r_{ij} is in the denominator, as it means we must drive with more intensity before we saturate a transition with weak branching. The orientation averaged (i.e., summed over M sublevels) form of eq. 3.21 is obtained by substituting $r_{ij} \to \tilde{r}_{J''J'}(2J'+1)/(2J''+1)$. We note the factor of 3 in the denominator of eq. 3.21 can be confusing–it arises from the fact that the total decay rate is averaged over orientations, but the excitation rate is not. Finally, we can connect eq. 3.21 to the saturation intensity for an ideal two level system with excited lifetime τ as follows: $I_s = I_{s,ij} r_{ij}$.

The scattering rate of the molecules (or atoms), R, is directly proportional to the excited state population, $R = \gamma \rho_{ee}$. Here, $\gamma = 1/\tau$ is the decay rate of the excited state summed over all ground levels. Since we are interested in timescales longer than $\tau \sim 20$ ns, we employ a steady state approximation. If we were interested in the coherences of the system, we would need to use optical Bloch equations, see Ch. 5. In steady state, we can write ρ_{ee} in terms of the detuning $\Delta = \omega - \omega_0$ as follows:

$$\rho_{ee} = \frac{s_0/2}{1 + s_0 + 4\Delta^2/\gamma^2}$$ (3.22)

$$= \frac{s(\Delta)/2}{1 + s(\Delta)}$$ (3.23)

$$= \frac{s_0/2}{1 + s_0} \frac{1}{1 + 4\Delta^2/\gamma_p^2}.$$ (3.24)

We have written ρ_{ee} in three equivalent forms to highlight different aspects. In eq. 3.23, we have defined the frequency dependent saturation parameter, $s(\Delta) = s_0/(1 + 4\Delta^2/\gamma^2)$. Meanwhile in eq. 3.24, we have defined $\gamma_p = \gamma\sqrt{1 + s_0}$, which is known as the *power broadened* width. We note the equations provided here must be modified in the case of multiple ground states coupled to multiple excited states, as is the case with molecular laser cooling, see Refs. [115, 226] for details.

We now consider some limits of interest. We see that on resonance, $\Delta = 0$, for $s_0 \ll 1$, we have $\rho_{ee} \propto s_0$, and the excited state fraction (and therefore the scattering rate) is linear with intensity. The intermediate value of $s_0 = 1$ characterizes the cross over to saturation, and corresponds to $R = \gamma/4$. At the other limit, with $s_0 \to \infty$, we have $\rho_{ee} = 1/2$, and the excited state fraction is independent of intensity. The value of 1/2 can be understood intuitively as the atom or molecule being driven so rapidly that it spends equal amounts of time in the ground and excited states. As a result, the scattering rate on resonance will also saturate to $R = \gamma/2$. Off-resonance, however, the width will increase as $\gamma_p \propto \sqrt{s_0}$. The population off-resonance can still saturate at $R \approx \gamma/2$, provided we have $\Delta^2 \ll \gamma^2 s_0$.

Now we consider the mechanism of saturation resulting from loss to "dark states" not addressed by the excitation laser, referred to as *loss-induced saturation*. If dark state decays occur with probability p, and the molecules interact with the laser for total time T, then we are dominated by loss-induced saturation when $RT \gg 1/p$. For a molecule with $\approx 10\%$ decays out of the cycling manifold and a lifetime of $\tau = 20$ ns, we will encounter saturation for $T \gg 400$ ns, which is quite a short period of time, equivalent to 80 µm of travel for a 200 m/s fast molecular beam. Loss-induced saturation has the effect of increasing the width of a fluorescence lineshape, as even off-resonance molecules potentially do not require many scatters before they are pumped out. For a beam, loss-induced fluorescence can be modeled by a rate equation model that incorporates information about molecule travel time and laser intensity distributions, as was done in Ref. [214].

Finally, we note fluorescence measurements can be used to characterize atomic or molecular velocities using the Doppler shift. Consider a molecule, traveling with velocity $\vec{v}$, that encounters laser light at frequency ω_0 and described by a wavevector $\vec{k}$. In the frame moving with the molecule, the laser radiation appears shifted in frequency according to according to:

$$\omega = \omega_0 - \vec{k} \cdot \vec{v}. \tag{3.25}$$

Here, if ω is given in angular frequency, we have $k = 2\pi/\lambda$, and if we work instead with linear frequency, then $k = 1/\lambda$. For a molecule moving at 200 m/s with $\lambda = 577$ nm, we see the maximum scale of the Doppler shift is ~350 MHz. The Doppler shift is used in atoms and molecules to perform cooling, by red-detuning the excitation laser such that photons with counter-propagating momentum are preferentially absorbed. For a detailed review of molecular laser cooling, see Ref. [115].

The Doppler shift of a resonance can be used to determine the velocity of a CBGB. Naively, one might send the laser beam counter-propagating to the molecular beam to achieve the maximum Doppler shift scaling with velocity. However, this is not practical for a molecule beam, as the light will interact with the molecules usptream and optically pump them into dark states, long before the molecules reach the photon detector. Pusling the laser beam is difficult given for large spatial extent (~1 m) of the molecualr beam. Even for atoms with closed cycles, longitudinal Doppler probes are also not ideal, as the laser beam can cause slowing, interferring with the interpretation of velocity. Therefore, we use probes with $\vec{k}$ at $45°$ relative to the CBGB in order to characterize velocities. While this reduces the Doppler shift by $1/\sqrt{2}$, it has the benefit of having a well defined interaction region.

3.3 Order of Magnitude Improvement in Molecule Production

The work in this section was previously published in Ref. [227].

Molecular experiments with CBGB sources are limited by the achievable molecular flux, and stand to benefit from generic methods to make more cold molecules. In this section, we discuss a method for achieving an order of magnitude increase in the molecular yield from a CBGB source by using laser light to excite a metal atom precursor. Specifically, we greatly increase the yield of polyatomic YbOH from our CBGB source by resonantly driving the $^1S_0 \rightarrow ^3P_1$ atomic Yb transition inside the buffer gas cell. The metastable $^3P_1$ state has a lifetime of $\tau \approx 871$ ns [228], long enough for the atoms to engage in reactive collisions before radiatively decaying, while also short enough to allow for rapid laser excitation. Our results establish laser-induced chemical enhancement via metastable excited states as a promising tool for significantly improving the production of cold molecules in CBGB sources, with significant implications for a broad range of precision measurement experiments.

3.3.1 Excited State Chemistry

The study of reactive collisions involving excited species is a very active area within the chemical physics community. Depending on the species, promoting reactants to excited states can considerably modify the reaction dynamics and the product state distributions [229–231], with consequences for a wide range of fields, from astrophysics [232–234] to atmospheric chemistry [235–237]. In many cases, the additional energy made available by electronic excitation of reactants can convert an endothermic reaction to an exothermic one. Additionally, the reaction mechanism on the excited potential energy surface can differ considerably from the mechanism for ground state reactants. As a result, excited states can access more pathways and transition states that yield the product of interest, as was seen in a recent study of Be^+ reactions [238].

In addition to modifying chemical yield, excited state chemistry has been used to study the collisional physics of atoms and molecules. In the case of atoms isoelectronic to Yb, such as Ca, Sr, Ba, and Hg, excitation of reactants to metastable states was used for molecular spectroscopy [239, 240] and investigations of reactions in ovens or beams with gases such as SF_6 [230, 241], H_2 [241, 242], H_2O [243–245], H_2O_2 [246, 247], alcohols [230, 243, 245], halogens [230, 241], halogenated alkanes [230, 242, 248–250], and hydrogen halides [230, 241, 248, 251, 252]. More recently, the ability to trap and cool species to ultracold temperatures has enabled research of reaction dynamics between excited ions, atoms, and molecules [238, 253–255].

Here, we considered the the chemistry between Yb, in both the ground and metastable ^3P state, reacting with H_2O and H_2O_2, two reactants likely produced during laser ablation of solid targets containing $Yb(OH)_3$ [256–258]. These reactants are also of interest as they can be flowed into the cell via a capillary [108, 259]. Finally, previous studies with analogous metallic atoms, such as Ca, Sr, and Ba, reacting with H_2O and H_2O_2 [244–247] have shown that the reaction of the ground

state alkaline-earth atoms leads mostly to formation of the metal oxides, whereas the metastable atoms produce the metal hydroxides.

We first provide a simple thermochemistry estimate of the importance of excited state chemistry. Consider the reaction ΔE + Yb(^{1}S$_0$) + H$_2$O $\rightarrow$ YbOH($^2\Sigma$) +H, motivated by the use of water as CBGB reagent introduced via a heated fill line. Here, ΔE is the energy difference of the reaction, with $\Delta E > 0$ indicating an endothermic reaction, and $\Delta E < 0$ an exothermic reaction. In Ref. [260], the dissociation energy of the Yb-OH bond was experimentally determined to be 322 ± 12 kJ/mol 3.3 eV, and the atomic heat of formation for YbOH was determined to be 746 ± 12 kJ/mol = 7.7 eV. We can compute ΔE either by taking the difference between initial and final heats of formation, or by considering the energy required to break and form bonds. We take the latter approach, though the two approaches typically agree, as they should.

Bond dissociation energies can be found in the Argonne Active Thermochemical Tables online database[24], and also in an old NIST reference [261]. The H$_2$O $\rightarrow$ H + OH process has $\Delta E = 5.1$ eV. The net energy required to break the H$_2$O bond and form YbOH is then endothermic, $\Delta = 1.8$ eV = 14500 cm^{-1}. This motivates the use to promote Yb to the ^{3}P$_1$ excited state, which has $\approx$18000 cm^{-1} of energy, enough to make the reaction exothermic. We note the ^{1}P$_1$ state also provides enough energy in theory, however we suspect the short lifetime of the excited state is too fast compared to the mean time between collisions in the buffer gas cell. We were not able to observe enhancement when using ~5 mW of ^{1}P$_1$ laser power.

Performing a similar analysis for H$_2$O$_2$ + Yb(^{1}S$_0$) $\rightarrow$ YbOH($^2\Sigma$)+OH, we find $\Delta E = -1.2$ eV, and the reaction is exothermic. Clearly the choice of reagent matters considerably. However hydrogen peroxide is somewhat impractical–it has 5 times lower vapor pressure than water at 25°C, it thermally decomposes when heated, and it is difficult to work with at high concentrations.

To investigate more quantitatively, our chemistry collaborators, Svetlana Kotochigova and Jacek Kłos, performed quantum chemistry calculations of electronic structure and molecular dynamics. Their calculations show the back of the envelope estimates hold some merit. We direct the reader to our paper for the full details [227]. Here we provide an overview of the results.

Critical points on the high-dimensional potential energy surface of the reacting states are shown in correlation diagrams given in Fig. 3.6 and Fig. 3.7, obtained with Density Functional Theory (DFT) techniques. The intermediate complexes formed along the reaction paths of Yb(^{1}S)+H$_2$O/H$_2$O$_2$ and Yb(^{3}P)+H$_2$O/H$_2$O$_2$ correspond to minima or saddle points, and are referred to as transition states.

---

[24] https://atct.anl.gov/
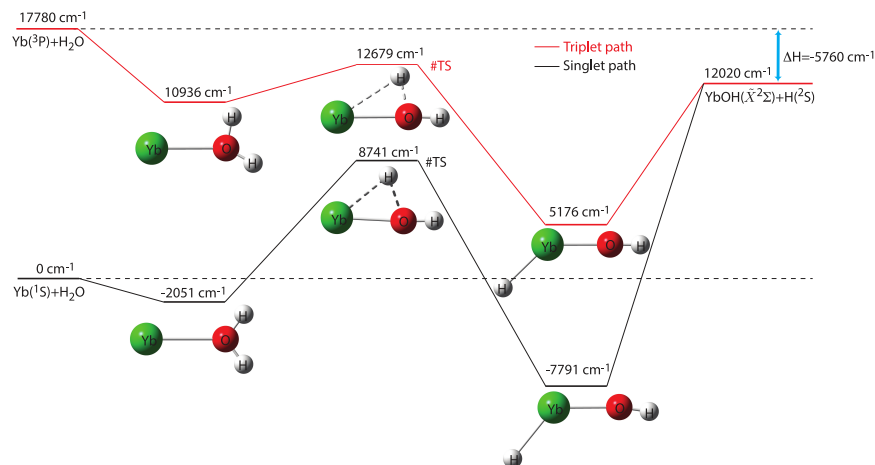
Figure 3.6: Energy profile for the Yb(^{1}S)+H$_2$O and Yb(^{3}P)+H$_2$O reactions leading to YbOH($\tilde{X}^2\Sigma^+$)+H(^{2}S) products calculated calculated with DFT and drawn with Gauss View 5. The molecular models represent the system geometries at critical points, and were drawn in the Gauss View 5 program. The Yb, O, and H atoms are represented by green, red and white spheres, respectively. Solid and dashed lines connecting the atoms correspond to σ bonds and temporary connections the transition states, respectively. These calculations are performed by Svetlana Kotochigova and Jacek Kłos, and are published in Ref. [227].
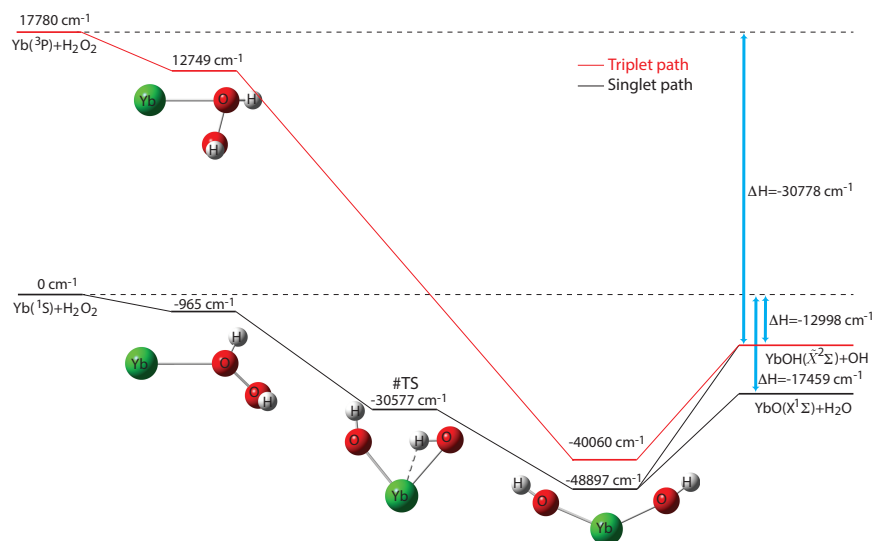
Figure 3.7: Energies and molecular geometries at critical points for the Yb(^{1}S)+H$_2$O$_2$ collision and Yb(^{3}P)+H$_2$O$_2$ reaction leading to either YbO($X^1\Sigma^+$)+OH($X^2\Pi$) and YbOH($\tilde{X}^2\Sigma^+$)+H calculated with DFT and drawn with Gauss View 5. The Yb, O, and H atoms are represented by green, red and white spheres, respectively. Solid and dashed lines connecting the atoms correspond to σ bonds and temporary connections the transition states, respectively. These calculations are performed by Svetlana Kotochigova and Jacek Kłos, and are published in Ref. [227].

The calculations demonstrate that the reaction between a ground state Yb(^{1}S) atom and an H$_2$O molecule is endothermic, requiring $E/hc = 12020$ cm^{-1} of relative kinetic energy to proceed and form the product YbOH($\tilde{X}^2\Sigma^+$)+H(^{2}S). Secondly, this singlet potential energy surface has a transition state, or saddle point, that lies at 8741 cm^{-1} above the entrance channel. It separates a local minimum corresponding to a symmetric-top molecule, where none of the bonds within H$_2$O are significantly affected by Yb, and the global minimum, where one of the hydrogen atoms has broken from the water molecule and the Yb atom is inserted.

In contrast, the collision between the excited Yb(^{3}P) state and H$_2$O is exothermic by 5760 cm^{-1}. Moreover, the corresponding triplet potential energy surface has a transition state that lies below its asymptotic channel energies. Such a submerged reaction barrier is indicative of large reaction rates. For both singlet and triplet channels, the product YbO+H$_2$ is energetically inaccessible, lying 27233 cm^{-1} above the Yb(^{1}S)+H$_2$O reaction channel.

We now consider the relevant spin singlet and triplet Yb+H$_2$O$_2$ reactions. For both Yb(^{1}S)+H$_2$O$_2$ and Yb(^{3}P)+H$_2$O$_2$ collisions, the product molecules have a lower electronic energy than the initial reactants. In fact, both YbO($X^1\Sigma^+$) + H$_2$O and YbOH($\tilde{X}^2\Sigma^+$) + OH($X^2\Pi$) products are energetically accessible, in contrast to the reaction with H$_2$O.

The relative kinetic energy of the product molecules is significantly larger than that for the product in the Yb(^{3}P)+H$_2$O reaction. The transition state on the spin singlet potential surface is submerged, and its global minimum corresponds to a deeply-bound (OH)-Yb-(OH) molecule. We thus expect strong reactivity along this pathway. Finally, the calculations did not find a transition state on the spin triplet surface, and spin conservation implies that only YbOH($\tilde{X}^2\Sigma^+$) + OH($X^2\Pi$) can be formed. However, we note that strong spin-orbit coupling is expected due to the large proton number of the Yb nucleus, and this will break spin conservation.

Our collaborators additionally performed classical Born-Oppenheimer Molecular Dynamics (BOMD) [262] calculations to investigate reaction kinetics. The simulations show that the Yb(^{1}S)+H$_2$O system forms a YbH$_2$O complex, without reacting and producing YbOH product molecules. For the Yb(^{3}P)+H$_2$O collision, the HYbOH intermediate forms immediately, after which the hydrogen atom attached to the Yb quickly flies away, leaving the YbOH product. The simulations are in agreement with previous studies of Ca(^{3}P), Sr(^{3}P), and Ba(^{1}D) reacting with H$_2$O and preferentially forming metal hydroxides [244, 245].

Meanwhile, for the Yb(^{1}S)+H$_2$O$_2$ simulations, we observe YbO and H$_2$O products, which have the lowest internal energy. The Yb(^{1}S)+H$_2$O$_2$ reaction occurs 4 times more slowly than Yb(^{3}P) reacting with H$_2$O$_2$. This contrast may indicate a difference in reaction mechanism between the two atomic states, which was previously suggested in prior work studying reactions of Ca and Sr with
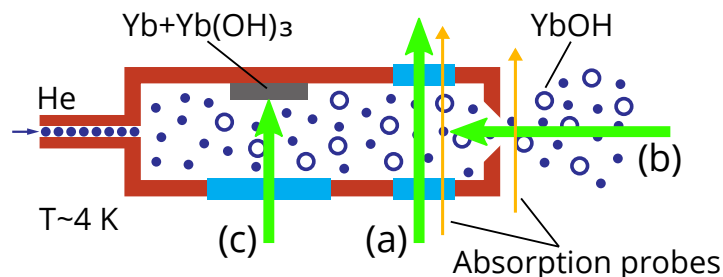
Figure 3.8: Depictions of the enhancement light geometries investigated. The enhancement light is depicted by the thick green arrows. The thin arrows indicate the absorption probes, which are fixed in position. (a) Transverse geometry: the enhancement light is introduced through a window ~ 25 mm away from the ablation target and ~ 12 mm away from the cell aperture. (b) Longitudinal geometry: the enhancement light is introduced through the cell aperture. (c) Collinear geometry: the enhancement light is sent through the ablation window, collinear with the YAG pulse.

H_2O_2 [246, 247]. Many more trajectories initialized with $Yb(^1S)+H_2O_2$ are needed to determine the branching ratio between the YbO and YbOH products, which were both found to form.

As a qualitative aside, we have experimentally looked for YbO and $YbOCH_3$ production in our source when ablating pressed $Yb+Yb(OH)_3$ targets and simultaneously exciting the Yb atoms to the $^3P_1$ state. From absorption measurements in cell, we estimate that our yields are $\gtrsim 100\times$ lower for YbO and $YbOCH_3$ compared to YbOH.

3.3.2 Enhancement Tests

We now discuss experimental tests of optically driven chemical enhancement to produce YbOH molecules. First, we describe the specific configuration of the 4 K source used for this work. Then we move on to describing the various parameters we varied and optimized. First, we discuss the tests of the properties of the enhancement laser: geometry, frequency, power, and timing. Then we examine properties of the cryogenic buffer gas cell environment: gas flow and YAG energy. We then move on to gauging the effect of the enhancement on rotation, vibration, and velocity. We then investigate the effect of varying the Yb isotope that is optically excited. We conclude with applications of the technique.

3.3.2.1 Apparatus

As discussed earlier, the source consists of a cryogenically cooled copper cell at ~4 K, depicted in Figure 3.8, which has an internal cylindrical bore with a diameter of 12.7 mm and a length of ~70 mm. The cell has windows that allow optical access for laser ablation and absorption spectroscopy. Helium buffer gas enters the cell through a fill line at one end of the cell, and exits at the other end through an aperture 5 mm in diameter. The source is typically operated with a helium flow rate of 3 SCCM, equivalent to a steady-state helium density in the cell of $\sim 2\times10^{15}$ cm^{-3} [178].

YbOH molecules are produced by laser ablation of a solid target with a pulsed nanosecond Nd:YAG laser at 532 nm. Unless stated otherwise, the data in this section were taken with $\sim$ 15 mJ of energy at a repetition rate of 1-3 Hz. The enhancement persists at repetition rates up to 10 Hz, though above this repetition rate the cell temperature begins to increase. The data were obtained from targets of pressed $Yb(OH)_3$ powder in a stoichiometric mixture with Yb powder, described in Section 3.2. The behavior of the laser-induced enhancement was found to be similar for variety of other targets with slightly different compositions. From such targets, a single ablation shot typically produces $\sim 10^{14}$ thermalized Yb atoms[25], orders of magnitude more than typical yields of molecular YbOH.

We can provide a basic picture of the in-cell dynamic based on previous work [179, 190]. At the helium densities considered here, the ablated material (atoms molecules, and reactants) ballistically expands to fill the cell in the first $\sim \mu$s after ablation. Buffer gas collisions then thermalize the molecules in $\lesssim$ 1 ms, and carry them out of the cell, through the aperture. At the flow rates considered here, roughly $\sim 10\%$ of the molecules are extracted, with the rest lost to the cell walls.

To study molecular production, we use a 577 nm laser to perform absorption spectroscopy on the $^Q Q_{11}(2)$ line of the $\tilde{X}^2\Sigma^+(000) \rightarrow \tilde{A}^2\Pi_{1/2}(000)$ transition in ^{174}YbOH. Here, $(v_1 v_2 v_3)$ denote the vibrational quanta in the Yb-O stretch, O bend, and O-H stretch, respectively. For ^{174}YbOH transitions, we use the labeling scheme described in Refs. [263, 264], as well as in Sec 4.1.3. The laser light is produced by doubling a 1154 nm ECDL using a PPLN waveguide. Absorption of the probe was used to determine the number density of molecules both inside the cell and immediately in front of the cell aperture. Unless stated otherwise, Yb refers to ^{174}Yb for both atomic Yb and YbOH.

To enhance the production of molecules, we excite the 556 nm $^1S_0 \rightarrow {}^3P_1$ transition in atomic Yb. The light is derived by sum-frequency generation of a CW Ti:Saph with a 1550 nm fiber laser, and has a linewidth of $<$ 50 kHz [26]. The light is pulsed on and off with a combination of an acousto-optical modulator (AOM) and mechanical shutter, allowing us to study the effect of the excitation timing relative to the ablation pulse. The mechanical shutter passes the light into the cell $\sim$4 ms before the ablation pulse, and blocks the light again $\sim$8 ms after the ablation, in order to keep the cell from being heated unnecessarily. The AOM is used in conjunction with the shutter to perform more precise measurements of the effects of pulse timing, to be discussed later. The shutter stays closed for every other molecule pulse, in order to normalize against drifts in molecular yield as the ablation spot degrades. Specifically, when ablating the same spot over time, we observe a decay in molecular yield, which has been previously observed in other CBGB sources [178, 191,

---

[25]We produce so many atoms this is a difficult number to gauge, as the absorption is optically thick. This estimate was based on looking at less abundant isotopologues of Yb.

[26]Sirah Mattise Ti:Saph and NKT ADJUSTIK+BOOSTIK combined in a Sirah MixTrain.
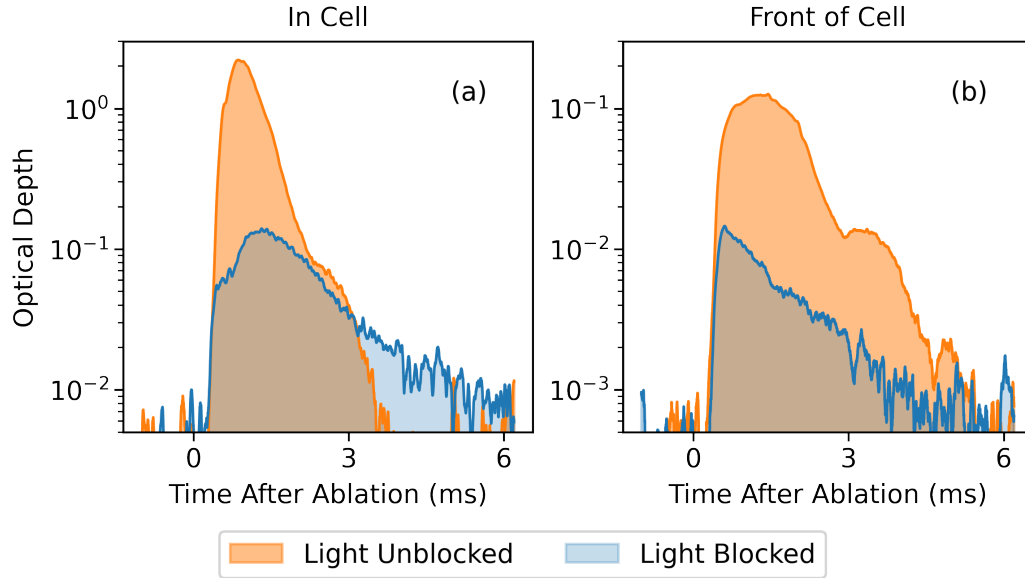
Figure 3.9: Log scale absorption spectroscopy of YbOH density in the $N = 2$, $\tilde{X}^2\Sigma^+(000)$ state, both in-cell and front-of-cell. This data was taken with the enhancement light in the transverse geometry. (a): In-cell un-enhanced yield of 4×10^{10} molecules, enhanced yield of 3×10^{11} molecules. (b): Front-of-cell un-enhanced yield of 7×10^9 molecules, enhanced yield of 8×10^{10} molecules. The difference in noise floors can be attributed to different photodiodes operating with different gains.

265], particularly when ablating pressed targets made from mixed powders [180]. This decay is present for both enhanced and unenhanced molecular pulses.

To determine the molecular yield inside the cell and the molecular flux leaving the cell, we integrate the optical depth (OD) over the duration of the resulting $\sim$ ms long molecule pulse. We compute the enhancement factor, or fractional increase in the number of molecules, by taking the ratio of the integrated OD with and without the enhancement light. Since the probe light is always fixed at the same molecule transition, common factors such as cross section divide out, making the OD ratio directly sensitive to changes in molecule number density induced by the enhancement light. When ablating a single spot over time, the enhancement factor does not exhibit the same decay present in the absolute molecular yield.

Typically, in-cell YbOH population in the $N = 2$, $\tilde{X}^2\Sigma^+(000)$ state was enhanced from $\sim 10^{10}$ to $\sim 10^{11}$, with front-of-cell numbers similarly enhanced, from $\sim 10^9$ to $\sim 10^{10}$ molecules. Figure 3.9 shows a representative absorption signal from a single ablation shot, both with and without the enhancement light present. The enhancement factor depends on a number of parameters, such as laser power, detuning, timing, and geometry, which we will now discuss.

3.3.2.2 Geometry

We investigated three geometries for introducing the enhancement light into the cell, indicated in Figure 3.8. The 556 nm light was typically collimated to a beam diameter of ~ 2.5 mm.

The largest enhancement signals were observed when the light was sent through the window in the cell used for absorption spectroscopy, shown in Figure 3.8(a). For a given target, the enhancement effect was repeatable for different ablation sites. For the second geometry, shown in Figure 3.8(b), the light entered the cell longitudinally through the circular, 5 mm diameter cell aperture. The resulting enhancement magnitude was reduced by a factor of ~2, with the effect somewhat independent of the ablation site. In the final geometry involved the enhancement light overlapped with the path of the ablation laser, shown in Figure 3.8(c). When compared to the aforementioned geometries, this collinear geometry resulted in smaller and less consistent enhancement.

Unless stated otherwise, the data in the rest of this section, and in fact this entire thesis, are from the first geometry, with the enhancement light sent through the spectroscopy window. Note that in this configuration, excited state atoms and reactions should be present only in the region where the laser is propagating, due to their short radiative lifetimes relative to the timescales associated with the buffer gas flow.

3.3.2.3 Frequency

To characterize the frequency dependence of the enhancement, we scanned the enhancement laser frequency across the atomic Yb line while monitoring the YbOH yield with a resonant absorption probe. The resulting enhancement magnitude for such scans at varied powers is shown in Figure 3.10, demonstrating the resonant nature of the enhancement. Since we apply sufficient laser power to power broaden the transition by an amount comparable to the Doppler broadening, we successfully fit the shape to a Voigt distribution. The extracted full-widths-at-half-maximum (FWHM), obtained from frequency scans in the longitudinal geometry, are plotted against enhancement power in the inset of Figure 3.10.

The observed enhancement widths indicate a broader reactant Yb frequency distribution than that expected from Doppler broadening at ~4 K and power broadening from ~200 mW of resonant light. A similarly broad distribution is observed from low intensity scans of the atomic line shape alone, shown for example in Fig. 3.11. At ablation energies of ~15 mJ, the first < 1 ms of the Yb absorption trace contribute to significant broadening, indicating the presence of an early, athermal Yb population [190]. The remaining population present after 1 ms are consistent with a Doppler broadening at $T \sim 4$ K. Because the enhancement light can excite this early athermal Yb population,

Longitudinal Enhancement Scans
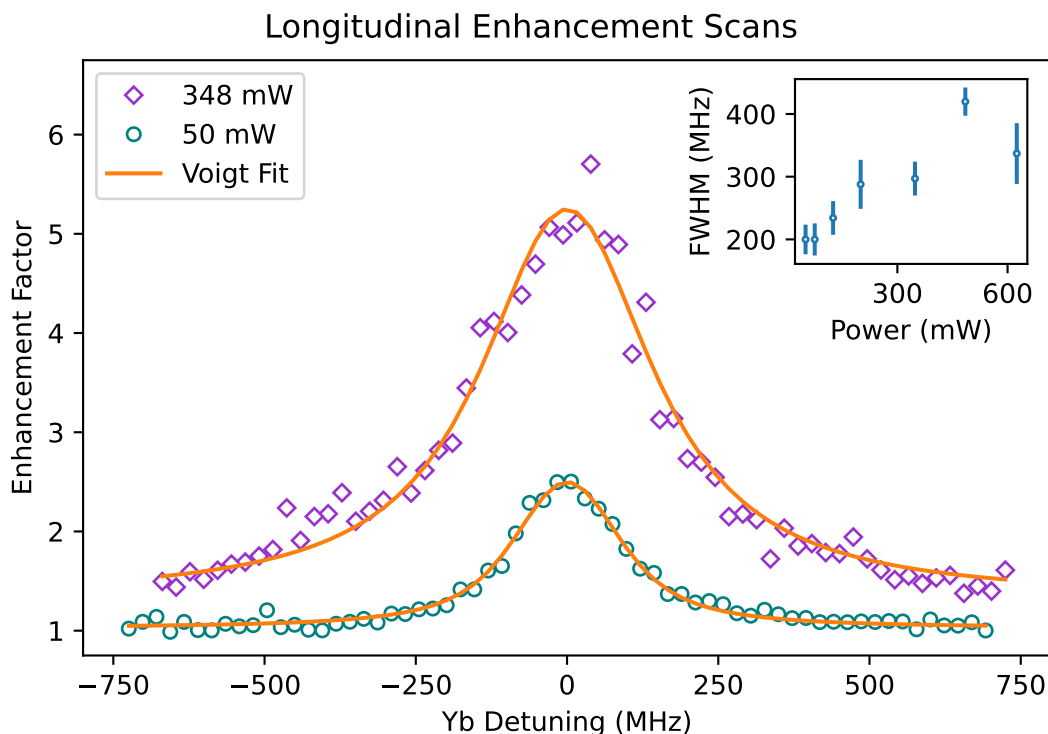
Figure 3.10: Enhancement line shapes, data taken with the longitudinal geometry. Left: Frequency scans and Voigt fits, demonstrating the variation of YbOH enhancement with detuning of the Yb laser at different powers. Right: Full widths at half maximum for the enhancement line shape as a function of the power sent into the cell. The Doppler width for the Yb atomic transition averaged over the entire ablation pulse is ~150 MHz.

Athermal Yb Signals
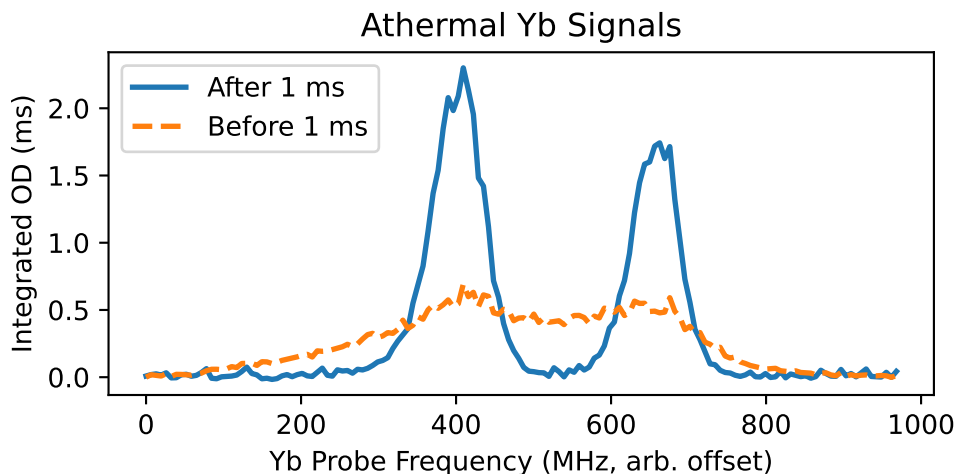
Figure 3.11: Absorption scans of the $^3P_1$ line, over the ^{173}Yb($\frac{5}{2} \rightarrow \frac{5}{2}$) transition (left peak) and the combined ^{171}Yb($\frac{1}{2} \rightarrow \frac{3}{2}$) + ^{173}Yb($\frac{5}{2} \rightarrow \frac{3}{2}$) transitions (right feature). The solid blue line is the integrated OD obtained by integrating signals > 1 ms after ablation. The dashed orange line is the integrated OD obtained by integrating from 0 to 1 ms. The athermal nature of the early Yb population is immediately apparent in the large linewidths. The YAG energy here was approximately 15 mJ/pulse.

we expect the atoms to react, providing the additional broadening we observe in the enhancement line shape. A typical value for the FWHM of a Doppler-broadened Yb atomic absorption line (in the limit of low saturation parameter) is ~ 70 MHz if the athermal component is excluded. Meanwhile the athermal features have ~250 MHz FWHM, corresponding to a Doppler temperature of ~60 K.

3.3.2.4 Power

The enhancement factor has a nonlinear dependence on the power of the enhancement light. This relationship is illustrated in Figure 3.12, showing the transition of the enhancement magnitude from linear behavior at low powers to saturation at high power. The crossover typically occurs between 100 and 300 mW for a ~ 2.5 mm beam, corresponding to an intensity range of ~ 10 W/cm^2. Such behavior is indicative of driving an optical resonance, and supports a simple model where the enhancement magnitude is proportional to the steady state excited Yb population. Notice that this cross-over intensity is considerably higher than the saturation intensity of the transition (0.14 mW/cm^2), which is due to the fact that the transition is Doppler broadened [131]. We expect the effect to saturate when the power broadening is comparable to the Doppler broadening [131]. The power broadened radiative width is $\gamma_{tot} \approx \gamma_{rad}\sqrt{s}$, where $\gamma_{rad} \approx 180$ kHz is the natural width and s is the saturation parameter. The broadened width becomes comparable to the Doppler width $\delta_D \approx 70$ MHz when $s \approx (\delta_D/\gamma_{rad})^2 \approx 10^5$, or $I \approx 10$ W/cm^2, consistent with our measurements.

3.3.2.5 Timing

By using an AOM switch to pulse the atomic transition light for sub-ms duration, we determined the majority of the enhancement occurs in the first few ms after ablation, corresponding to the duration when the cell is filled with atomic Yb. Data from timing tests is shown in Fig. 3.13. The pulses have 0.5 ms width, and are switched on at a variable time relative to ablation.

Notably, the enhancement is largest ~1 ms after the ablation, after the hot atoms have thermalized with the buffer gas. This observation, combined with the effect of geometry on enhancement, provides evidence that the enhancement occurs throughout the cell, rather than immediately in the region of the ablation plume. Furthermore, we observe a small revival in enhancement at late times, possibly indicative of pressure waves propagating through the cell.

3.3.2.6 Gas Flow

The enhancement magnitude was not found to have any significant dependence on He flow into cell, which was varied from 1 to 10 SCCM, equivalent to varying the stagnation He density in the cell from 6×10^{14} to 6×10^{15}cm^{-3} [178]. The enhancement magnitude was unaffected by the ablation
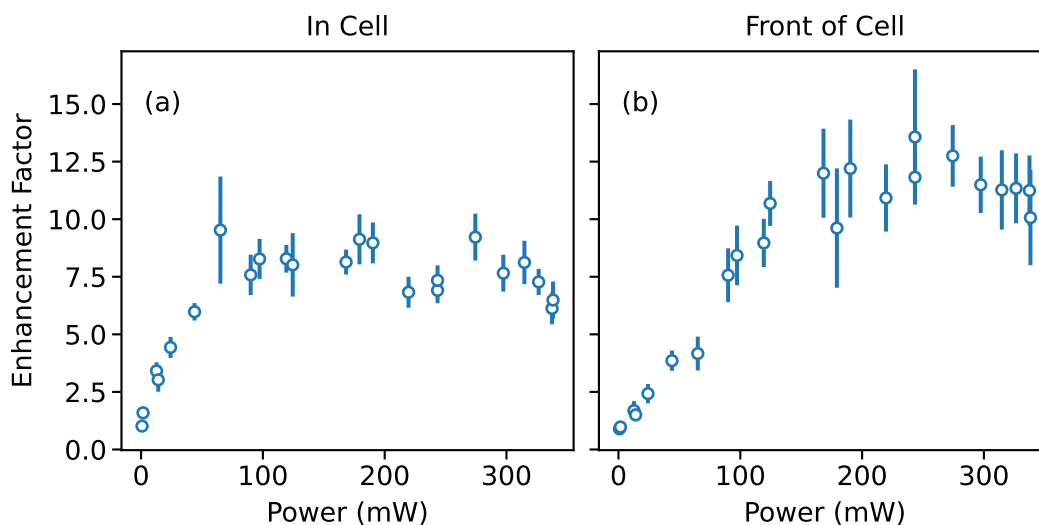
Figure 3.12: Enhancement magnitude, calculated as a ratio of optical depths, plotted against the laser power sent into the cell. The laser beam was collimated to a ~ 2.5 mm diameter. Error bars represent standard deviations of results, as opposed to standard error, in order to show the typical fluctuations over different shots and ablation spots. (a): In cell enhancement, (b): Front of cell enhancement.
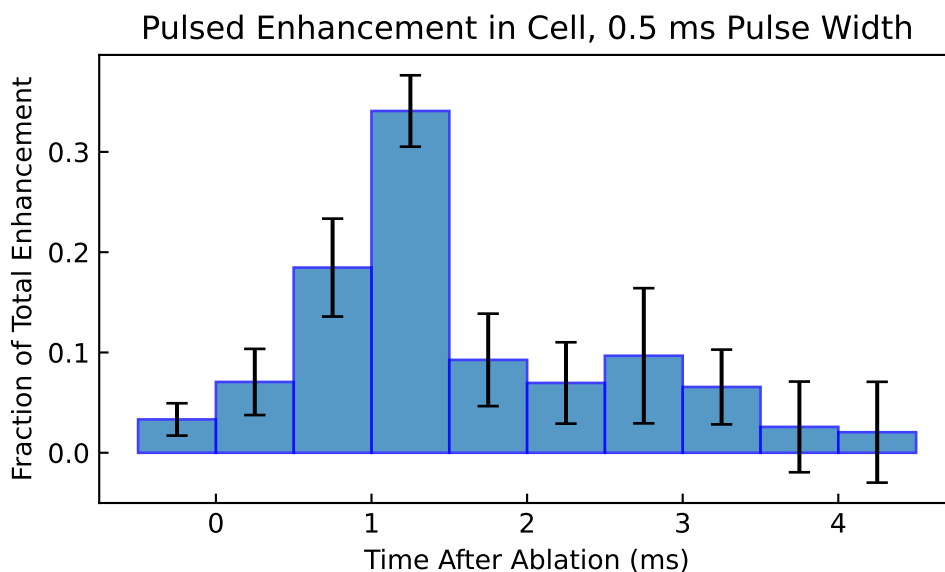
Figure 3.13: Pulsed enhancement in cell for fixed pulse width of 0.5 ms, beginning at different times relative to ablation. The y-axis is the fraction of enhancement that occurs in during a specific pulse, compared to the combined enhancement over all the different pulse times. Error bars are standard deviations.
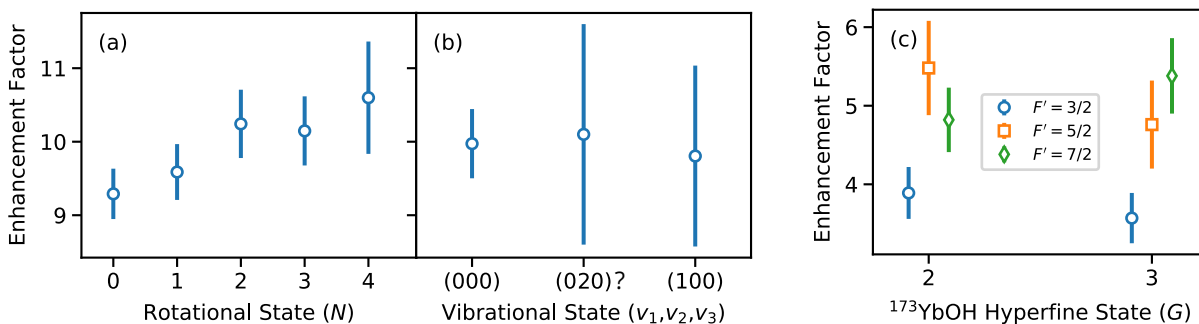
Figure 3.14: Enhancement of rotational and vibrational states in ^{174}YbOH, and hypefine states of ^{173}YbOH. Error bars represent the standard deviation of measured enhancement factors. (a), (b): Enhancement of ^{174}YbOH as a function of ground state rotational level (a) and ground state vibrational level (b). The rotational population was probed using $^Q Q_{11}(N)$ lines. ($v_1 v_2 v_3$) denote the vibrational quanta in the Yb-O stretch, O bend, and O-H stretch, respectively. The (000) data point is an average of the $N = 0$ through $N = 4$ rotational enhancements. The excited vibrational population was probed with diagonal transitions to the $\tilde{A}$ state with $\Delta v_{1,2} = 0$. We note the (020) transition assignment is not definitive, hence the question mark. (c): Enhancement of the molecular hyperfine levels in the odd ^{173}YbOH isotopologue, resulting from driving $F = 5/2 \rightarrow F'$ hyperfine transitions in atomic ^{173}Yb. The molecular quantum number G results from coupling of S to I_{Yb}, $G = S + I_{Yb}$.

energy used in the ablation pulse, which was varied from 5 to 25 mJ/pulse. In fact, for low ablation energies, YbOH was observed only with the aid of enhancement, as long as the ablation energy was above the threshold necessary to produce atomic Yb. This is encouraging for laser-cooling experiments, where lower energy ablation is useful for producing slow beams of molecules [182].

3.3.2.7 Rotational Distribution

We also investigated the effect of the enhancement light on the population of YbOH in different internal states. Since the energy scales of the chemical reactions involved are on the order of $\sim$10,000 cm^{-1}, much larger than those of molecular vibration ($\sim$100 $-$ 1000 cm^{-1}) or rotation ($\sim$0.1 $-$ 1 cm^{-1}), we expect that the molecules created by chemical reactions will populate many rotational and vibrational states after decaying to the ground electronic state. These distributions have been studied in excited state reactions producing molecules containing Ca and Sr, and they support the expectation that the released energy is distributed among the internal modes [245, 247].

Because rotational state-changing cross sections between molecules and helium are comparable to elastic collision cross sections [178], we expect this broad rotational distribution to rapidly thermalize in the buffer gas cell. By measuring the enhancement on $^Q Q_{11}(N)$ transitions that address different rotational levels in the ground vibronic state, we indeed observe such rotational

thermalization, as shown in Figure 3.14(a). Each rotational transition demonstrates approximately the same enhancement, indicating that the rotational distribution is essentially unchanged by the increased chemical production.

3.3.2.8 Velocity Properties

Since buffer gas collisions are also effective at thermalizing translational degrees of freedom, we expect the enhanced and un-enhanced molecule beams to have similar velocity properties. We verified this by monitoring the transverse velocity distribution of YbOH exiting the cell using an absorption probe in front of the cell aperture. The width of the resulting line shapes did not exhibit a measurable difference with and without the enhancement. Similarly, we monitored Doppler shifted fluorescence of the molecular beam $\sim$ 60 cm downstream, after a series of collimating apertures, and found the both the mean and width of the forward velocity distribution were unaffected by the enhanced molecular yield.

Intriguingly, we have noticed that the enhanced YbOH pulse usually arrives at the PMT *later* than the atomic Yb pulse produced from the ablation. We attribute this to the fact that a majority of the enhancement occurs ~1 ms after ablation, which means the enhanced molecules leave the cell later than the Yb atoms produced immediately upon ablation.

3.3.2.9 Vibrational Distribution

Conversely, vibration-quenching cross sections are typically smaller than those for other degrees of freedom, resulting in observations of non-thermal vibrational distributions in CBGB sources [178, 192, 266]. The efficiency of vibrational thermalization can vary for different molecular species, as well as for different modes of the same molecule [192]. In our source, we observe non-thermal vibrational distributions, probed by absorption of diagonal transitions ($\Delta v = 0$) from excited vibrational states in $\tilde{X}$ to the same vibrational state in $\tilde{A}$. We used the $\tilde{X}(100) \rightarrow \tilde{A}(100)$ line at 17378.58 cm^{-1} to probe the Yb-O stretch mode. Without enhancement, the population we observe in the $\tilde{X}(100)$ state $\sim$ 1 ms after ablation corresponds to a temperature of $T_{v_1} \approx 280$ K, in agreement with observations of athermal vibration in a recent study of SrOH in a closed cell [192].

Additionally, we used a line at 17345.09 cm^{-1} to attempt to probe the population in the excited bending mode. In Ref. [227], we tentatively assigned this line as $\tilde{X}(010) \rightarrow \tilde{A}(010)$, which we now know is an *incorrect* assignment (see Ch. 4, Sec. 4.3.1). This line is currently unknown, though we can possibly re-assign it to a transition originating from $\tilde{X}(020)$, see Ch. 4, Sec. 4.4 for details.

The vibrationally excited molecule population in the cell was also significantly enhanced by laser excitation of Yb. In Figure 3.14(b) we compare the enhancement for the (000), (100), and

(020)? vibrational levels of the $\tilde{X}$ ground electronic state. We find the enhancement factor to be consistent across these vibrational states, indicating buffer gas collisions do not efficiently quench the vibrational states populated by the excited state chemistry. Enhanced yield in vibrational states can be desirable, as excited vibrational levels may have little population in a typical beam source, but are required for laser cooling, spectroscopy, and precision measurements [17]. Furthermore, these vibrational populations can be easily "re-pumped" back into the ground state, e.g., using the same lasers that would already be available for laser cooling, resulting in further increases to beam brightness.

Indeed, we utilize the enhanced vibrational population to characterize the bending mode in Ch. 4. The enhanced vibrational population was also used for FM absorption spectroscopy of repumping transitions performed in our lab [220].

3.3.2.10 Studies with Different Isotopologues

Finally, we characterize the enhancement in the ^{173}YbOH isotopologue, which has high sensitivity to the symmetry-violating nuclear Magnetic Quadrupole Moment (NMQM)[17, 267], by investigating the enhancement of different ^{173}YbOH hyperfine states when driving hyperfine transitions in atomic ^{173}Yb ($I = 5/2$). The results are shown in Figure 3.14(c). We separately drive each of the three $^1S_0 \rightarrow {}^3P_1$ hyperfine transitions in ^{173}Yb ($F = 5/2 \rightarrow F' = 3/2, 5/2, 7/2$) and monitor the enhancement in either the $G = 2$ or $G = 3$ hyperfine state of ^{173}YbOH. Here, analogous to the case of ^{173}YbF [268], the coupled angular momentum $G = S + I_{Yb}$ results from the strong electric quadrupole interaction between the Yb-centered electron, with spin $S = 1/2$, and the non-spherical Yb nucleus, with spin $I_{Yb} = 5/2$. The molecule population was probed via absorption spectroscopy on the $^OP_{12}(2)$ and $^OP_{13}(2)$ lines of the $\tilde{X} \rightarrow \tilde{A}$ transition, where we label the odd isotopologue transitions using the convention from Ref. [268].

The enhancement in the $G = 2$ and $G = 3$ states is equivalent for each driven ^{173}Yb hyperfine transition, which is expected in a thermalized ensemble. While thermalization should also result in enhancement independent of the excited hyperfine F' state driven in ^{173}Yb, we find smaller enhancement for $F' = 3/2$ compared to $F' = 5/2$ and $F' = 7/2$. We attribute this to overlap of the ^{173}Yb($F = 5/2 \rightarrow F' = 3/2$) transition with the ^{171}Yb($F = 1/2 \rightarrow F' = 3/2$) transition, which differ by ~ 3 MHz [269], much less than the Doppler broadening in the cell. This overlap can explain lower enhancement rates, as the production of ^{171}YbOH will deplete the available population of other reactants.

We used the isotope selectivity of the enhancement to perform spectroscopy on the odd iso-topologues of YbOH, presented in Refs. [124, 157]. While driving the $^3P_1$ line in various isotopes, we noticed that we observe cross-isotope enhancement as well. That is, when we drive the $^3P_1$

transition in one isotope, we observe a resonant enhancement of YbOH population in not just the corresponding isotopologue, but also other isotopologues as well. The enhancement factor of other isotopologues is less by approximately ~2-3×. We attribute this cross-isotope enhancement to excitation transfer via collisions between different Yb isotopes, though this warrants further study.

3.3.3 Applications

By driving an electronic transition from Yb($^1S_0$) to Yb($^3P_1$), we have demonstrated significantly improved yield of molecular YbOH from a CBGB source. The resonant nature of the effect, as well as saturation at high power, confirms that the excited atomic population is responsible for the observed enhancement. Furthermore, we found that the cryogenic buffer gas environment is well suited to cooling the products from the resulting exothermic reactions. Buffer gas collisions effectively thermalized the translational and rotational energies of the resulting product molecules, while still maintaining an athermal vibrational population, which is useful for many applications.

By performing computational studies, we are able to provide insight into the reaction channels made possible by excited Yb(^3P) atoms. From our DFT simulations, we conclude that when Yb is in its ground state, only collisions with H_2O_2 produce ground state YbOH molecules. When Yb is excited to its triplet metastable state, collisions with both H_2O and H_2O_2 react to form ground state YbOH.

Our approach suggests a number of new directions for both improvements to molecular yield in future experiments and continued studies of cold chemical reactions. From our studies of geometry and timing, the enhancement can occur throughout the cell and over the entire duration of the molecular pulse, suggesting an optimal arrangement where the cell is evenly illuminated with resonant light. This could for example be achieved by shining the light onto a high scatter surface, or introducing the light into the cell using a fiber with large NA.

Although we used only a solid precursor in the studies presented here, another approach is to use reactant gases flowed into the buffer gas cell via a capillary [108, 180, 182, 259]. These molecular precursors react with ablated metal, providing a way to tune the reactant species. While the enhancement we report here is a compound effect, possibly involving several different reactants formed in ablation, our calculations suggest the possibility of finding the optimal reactant and optimal excited states for both the atom and molecule. Additionally, compared to using mixed targets, metal ablation can provide more consistent signals with slower decay [180]. Finally, enhancing reaction rates would allow for reduction of ablation energy without also compromising molecular flux.

While we have restricted our measurements to YbOH, it is likely that this method can be used to enhance CBGB production of many interesting species, both diatomic and polyatomic.

The chemical similarity of Yb with alkaline earth atoms, and the success of excited state chemical reactions producing a variety of Ca-, Sr-, and Ba- molecules with numerous ligands [240, 244, 245], suggests that CBGBs of alkaline-earth atoms with monovalent and ionic bonds (conveniently, those which can be generically laser cooled [113]) could benefit from this approach. Note, however, that the power requirements become higher for lighter species, since the radiative width of the metastable states arises from spin-orbit coupling, which is larger in heavier species [270]. Nonetheless, resonant excitation of the metal precursor could be especially helpful for experiments with rare isotopes where efficiency is critical, such as radioactive ^{225}Ra, which is a component of molecules with extremely high sensitivity to physics BSM [271, 272], or ^{26}Al, which is of astrophysical relevance [273]. While we have mostly focused on alkaline-earth or similar metals, CBGBs of other molecules of experimental importance, such as ThO [11], may also benefit from this approach by exciting the metal [274] or oxygen [241] produced in the ablation to a reactive, metastable state.

In addition to increasing CBGB yield, chemical enhancement can also serve as a resource for spectroscopy of dynamics inside the buffer gas cell. The dependence of the molecular yield on the application of enhancement light at a specific time and place can help study the distribution of the reactive dynamics in the cell. When compounded with probes monitoring the flux exiting the cell, or monitoring fluorescence downstream, this allows for study of beam properties, conditioned on where or when the molecules were produced. The ability to perform such spectroscopy could aid in understanding and optimizing buffer gas cell geometries.

Our enhancement method can also be used to disentangle complex spectroscopic data by comparing enhanced and normal spectral features, taking into account the enhancement dependence on the excited atomic state, as well as the molecular vibrational, rotational, and hyperfine state. Indeed, we have used this very technique to perform odd isotopologue YbOH spectroscopy in our lab [124, 157]. As another example, the spectra of hypermetallic species [275] could be uniquely distinguished from other molecules by their dependence on the chemical enhancement of the individual metal centers. Additionally, because the molecules resulting from enhancement can possibly populate vibrational states non-thermally, yet still yield translationally cold beams, enhancement is be useful for studying transitions out of excited vibrational modes, as we do in Chapter 4. The increased vibrational population is favorable for studies of vibration-quenching collisions in cryogenic environments [192].

Finally, for precision measurements relying on CBGBs, increased molecular flux directly translates to increased sensitivity to new, symmetry-violating physics beyond the Standard Model. Specifically, the enhancement we demonstrate for both the ^{174}YbOH and ^{173}YbOH isotopologues are directly applicable to experiments sensitive to new physics in both the leptonic and hadronic sectors [17, 267, 276–278].

C H A P T E R

4

Y<small>B</small>OH S<small>PECTROSCOPY</small>

In my experience, there's no such
thing as luck.

–Obi-Wan Kenobi

This chapter covers work done on the molecular spectroscopy of YbOH, in the service of precision measurements. In order to perform precision measurements on a molecule, we need to understand the molecule's energy levels and their behavior in electric and magnetic fields. This allows us to implement and calibrate our measurement, essentially testing for new physics by comparing to the physics we can model, e.g. electromagnetism. Though first principles theoretical treatments have increasingly impressive accuracy, they still fall short of the 10^{-8} precision needed to transitions at optical linewidths, let alone for precision measurements, which have ≲mHz sensitivity. Therefore, we turn to experimental molecular spectroscopy techniques to understand and model the behavior of the molecule, both in free field as a prerequisite, and in electromagnetic fields.

Additionally, high resolution spectroscopy is also a prerequisite to laser cooling and slowing molecules, which can aid future measurements. In order to establish a nearly closed optical cycle, we must understand the branching of spontaneous decays from the excited cycling state(s) to the various metastable and ground states present. This can involve identifying decays at anywhere from the 10^{-1} to 10^{-5} level, with higher precision required for applications requiring more photon scatters, such as optical slowing or magneto-optical trapping. To repump the decays, we must first spectroscopically identify, at 10^{-8} or better frequency precision, all the relevant rotational and hyperfine transitions involved. The states are then repumped with either laser radiation, as is the

case for unwanted vibrational decays, or microwave radiation, as is the case for unwanted parity decays (i.e., two photon decays, see YO [279] for details).

In this chapter, we present spectroscopy efforts to enable precision measurements with YbOH molecules. In particular, we focus on the "science state"—the doubly-degenerate bending mode, denoted $\tilde{X}^2\Sigma^+(010)$. We often abbreviate $\tilde{X}^2\Sigma^+(010)$ as $\tilde{X}(010)$. We present a complete characterization of the science state at high-resolution, including its behavior in electromagnetic fields. Additionally, we characterize the bending mode in the electronic excited state, denoted $\tilde{A}^2\Pi_{1/2}(010)$, which we will often abbreviate to $\tilde{A}(010)$. We identify a case of a spectroscopic K-resonance in $\tilde{A}(010)$ state, use the excited state to optically pump into $\tilde{X}(010)$, and determine $\tilde{X}(010) \rightarrow \tilde{A}(010)$ transitions useful for manipulating and probing the science state. The work in this chapter enables us to perform prototype Ramsey interferometry measurements in YbOH in the next chapter, Ch. 5.

The $\tilde{X}(010)$ work presented in this section was published in Ref. [280]. The $\tilde{A}(010)$ work is not currently published.

4.1 YbOH Overview

In this section we give a brief summary of the spectroscopic characterization of YbOH performed by others. We present the structure of the ground electronic, ground vibrational state, denoted $\tilde{X}(000)$. We also present the Stark and Zeeman parameters for $\tilde{X}(000)$. We then present a brief overview of the excited state structure of YbOH. We then summarize the prospects for photon cycling in YbOH.

4.1.1 Ground States

The $\tilde{X}$ state was studied at microwave resolution using the PPMODR technique in Ref. [281], and at optical resolution with laser induced fluorescence [264]. The optical study also determined Stark and Zeeman tuning parameters. We show the low-N structure of $\tilde{X}(000)$ in Figure 4.1. The ground state of YbOH is best described by a Hund's case (b) basis, owing to the absence of spin-orbit coupling ($\Lambda = 0$). The structure is similar to that of isoelectric diatomic fluorides, such as YbF or SrF, with the exception of the ligand hyperfine structure, which is much smaller in the hydroxides. Similar to YbF, YbOH exhibits a negative spin-rotation constant in the ground state, owing to perturbations from low-lying levels, discussed in Sec. 4.4.

The vibrational structure of the $\tilde{X}$ electronic manifold has been characterized in dispersed laser induced fluorescence (DLIF) measurements [144] at ~5 cm^{-1} accuracy. The location of the optical cycling states (i.e., $N'' = 1$) has been determined at high-resolution (~10 MHz) in the following ground states [106, 139, 220, 280]: $\tilde{X}(000)$, $\tilde{X}(100)$, $\tilde{X}(200)$, $\tilde{X}(02^00)$, $\tilde{X}(010)$, and $\tilde{X}(300)$.

We are most interested in the bending mode, the $\tilde{X}^2\Sigma^+(010)$ state, abbreviated as $\tilde{X}(010)$. A
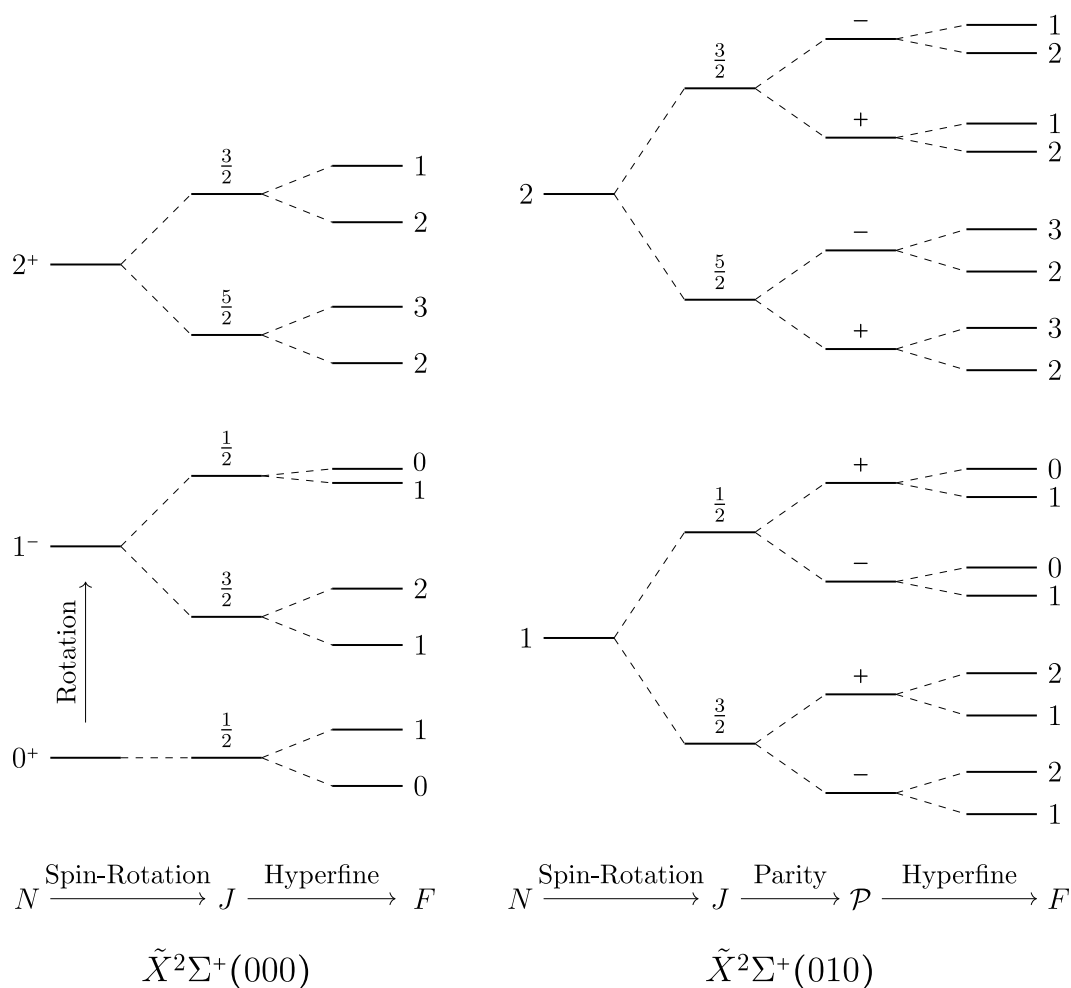
Figure 4.1: Diagram of the rotational structure in the $\tilde{X}^2\Sigma^+(000)$ (left) and $\tilde{X}^2\Sigma^+(010)$ (right) states of YbOH. The different values of N are first split by the rotational energy, $B \sim 7.5$ GHz. For $\tilde{X}(000)$, the value of N uniquely determines the state parity. Then, on a smaller scale, the spin-rotation interaction, parameterized by $\gamma \sim -100$ MHz, causes splittings of different J levels. In the $\tilde{X}(010)$ state, we have an additional fine structure, given by parity-doubling Coriolis interactions on the 20 MHz scale. For brevity, we have not included asymmetries that occur in the parity splittings. Finally, hyperfine couplings between I and S cause $\sim$4 MHz splittings for different values of F. We note that $\tilde{X}(000)$ goes through a hyperfine "resonance", such that the ordering of hyperfine states reverses between $N = 1$ and $N = 2$. Such a reversal does not occur in $\tilde{X}(010)$, owing to the different internuclear orientations of the spins in the symmetric top like bending mode compared to the linear rotor-like absolute ground state.

schematic level structure of this state is given in Fig. 4.1. We note the major difference between $\tilde{X}(000)$ and $\tilde{X}(010)$ is the parity doubling structure in the bending mode. In the bending mode, we now have two opposite parities for identical values of N and J. This additional degree of freedom associated with the molecular orientation will prove very useful in Ch. 5, Sec. 5.4, when we use applied fields to engineer useful quantum states for EDM measurements.

4.1.2 Excited States

The $^2\Pi$ electronic excited state is split by spin-orbit into an $\Omega = 1/2$ and $\Omega = 3/2$ manifold. Only the $\Omega = 1/2$ component has been definitively assigned, having being identified at 17323.5 cm^{-1} (577.2 nm) above the ground state. Characterization of the $\tilde{A}^2\Pi_{1/2}(000)$ state, including Stark and Zeeman tuning, was performed in an optical study of a supersonic molecular beam [264]. The Zeeman constants of the excited state were further refined in a subsequent work [282]. In Ref. [217], the lifetime of the $\tilde{A}$ state was found to be $\tau = 20(2)$ ns. The $\tilde{X}(000) \to \tilde{A}^2\Pi_{1/2}(000)$ transition is often referred to as the "origin" band.

In addition to the $\tilde{A}^2\Pi_{1/2}(000)$ excited state, survey DLIF spectroscopy of YbOH identified numerous other transitions [217]. Many of these transitions were either tentatively assigned or not assigned at all, owing to the complicated and congested spectrum. Later work showed the YbOH bands near 17640 cm^{-1} and 17680 cm^{-1} may have be overlapped with features from YbOCH$_3$. In this chapter we have investigated and determined the nature of the [17.33] band[1], assigning it to the $\tilde{X}^2\Sigma^+(010) \to \tilde{A}^2\Pi_{1/2}(010)$ transition. We also conducted high-resolution spectroscopy of the [17.68] and [17.64][2] bands, but we were not able to perform a conclusive assignment. Our investigations cast doubt on the ground state of these bands being $\tilde{X}(000)$, and are detailed further in Ref. [161]. Some of the many unassigned YbOH bands are thought to arise from excited states with holes in the inner $4f$ shell. Further discussion of unassigned bands and the general state of YbOH spectroscopy, including $4f$ states, is provided at the end of this chapter.

4.1.3 Transition Notation

We denote rotational lines with notation similar to Ref. [264]. Ground state quantum numbers are denoted with a double prime, e.g. N'', and excited states with a single prime, e.g. J'. We define $\Delta J = J' - J''$ and similarly for ΔN. The most general notation is to label transitions according to their value of ΔJ, such that $\Delta J = -1, 0, 1$ maps on to $\Delta J = P, Q, R$. This can be extended to $|\Delta J| > 1$ by continuing along the alphabet (i.e., $\Delta J = 2/-2 \to S/O$). The ΔJ label, combined with information about either J'' or J', provides us information about the excited state as well.

---

[1]The bands are labeled with a notation corresponding to their energy in cm^{-1}/1000, i.e., the origin band at 17323 cm^{-1} would be called the [17.32] band.

[2]This band was assigned as two separate features ([17.637] and [17.643]) in Ref. [217], but it is possible one band was YbOCH$_3$ contaminant.

Furthermore, molecules that have non-zero electron spin, such as YbOH, will have multiple J states for a given rotational manifold. These J levels group themselves differently depending on if we are in Hund's case (a) or Hund's case (b). Restricting our attention to doublet molecules ($S=1/2$), we can introduce the pattern forming label $F_i = 1, 2$, applicable in both case (a) and case (b). The notation F_i is used for historical reasons, and is not to be confused with the grand total angular momentum F. In Hund's case (b), the value F_i labels the spin rotation component of a state—$F_i = 1$ corresponds to the state with $J = N + S$, while $F_i = 2$ corresponds to the state with $J = N - S$. Meanwhile, in Hund's case (a), the value of F_i denotes the spin-orbit component of a state, with $F_i = 1$ corresponding to $|\Omega| = |\Lambda| - |\Sigma|$, e.g. $\Omega = 1/2$ for the YbOH $\tilde{A}$ state, and $F_i = 2$ corresponding to $|\Omega| = |\Lambda| + |\Sigma|$. The values of F_i can be generalized to label higher spin states.

In molecules such as YbOH, we often deal with transitions from a Hund's case (b) ground state to a Hund's case (a) excited state. These transitions are labeled with the following notation:

$$^{\Delta N}\Delta J_{F_i', F_i''}(N'') \tag{4.1}$$

where we have introduced the relevant quantities previously. Even though N' is not a good number, we obtain ΔN by associating $N' = 0$ with $J' = 1/2$ (which only exists in $F_i = 1$), $N' = 1$ with $J' = 3/2$, etc. Example lines and their quantum numbers can be found in Ref. [264].

In the above notation, the parity of the lines is determined by the rotational level of the ground state, N''. This works for ground states without parity doubling, where the state parity is given by $(-1)^N$ for a Σ^+ state. However, we also encounter ground states with parity doubling, such as the bending mode, in which case N'' alone is insufficient for determining the parity of the involved states. Therefore, for labeling transitions out of $\tilde{X}(010)$, we adopt a modified labeling scheme, given by:

$$^{\Delta N}\Delta J_{F_i', F_i''}^{\mathcal{P}''}(N''). \tag{4.2}$$

Here, we have added the subscript $\mathcal{P}'' = \pm$, which denotes the ground state parity explicitly.

4.2 The Science State

After the YbOH vibrational structure was analyzed in medium-resolution dispersed laser induced flourescence (DLIF) [144], we were able to use the reported location of $\tilde{X}(010)$, 319(5) cm^{-1}, as a starting point for high-resolution optical studies. We realized that we can directly probe the $\tilde{X}(010)$ state by driving the reverse of the laser cooling leakage transition back to the $\tilde{A}$ state. This transition has the added benefit of giving mostly off-diagonal decays to the blue of the excitation light, which is very easy to separate with interference filters. The transition is nominally "forbidden", but can still be driven with enough laser power.

In YbOH, the $\tilde{A}(000) \rightsquigarrow \tilde{X}(010)$ decay has a vibrational branching ratio of $r_{010} = 0.054(4)\%$ [144], and the lifetime of the $\tilde{A}^2\Pi_{1/2}$ state is $\tau = 20(2)$ ns [217]. The excited state population primarily decays to the vibrational ground state, $\tilde{X}(000)$, with $r_{000} = 89.44\%$ branching. Therefore, in our experiment, the fluorescence signal will saturate after roughly one photon scatter as the molecules are optically pumped out of the bending mode and mostly into the ground state. With a ~1 mm Gaussian laser beam intersecting a ~200 m/s molecular beam, we can estimate the saturation parameter required for a single photon scatter as $s \approx 1 \times 10^{-2}$. Using eq. 3.21 for the saturation intensity, and estimating the rotational branching at 1/3, we compute an intensity of $I \approx 300$ mW/cm^2 required to optically pump the forbidden transition $\tilde{X}(010) \rightarrow \tilde{A}(000)$. For a 1 mm diameter Gaussian laser beam, this requires $\gtrsim 1$ mW of optical power. While this simple estimate neglects experimental imperfections, it shows that the power requirements needed to produce fluorescence on such a forbidden line are feasible.

4.2.1 Apparatus

The cryogenic buffer gas beam (CBGB) apparatus is shown in Fig. 4.2a, and is described in Ch. 3, Sec. 3.2. We emphasize that we increase YbOH yield by around an order of magnitude by exciting atomic Yb to the excited $^3P_1$ state, as described in Ch. 3, Sec. 3.3. Specifically, this technique significantly increases the quantity of YbOH in excited vibrational states, including the $\tilde{X}(010)$ state, whose population is increased by a factor of ~10.

A few milliseconds after ablation, the He gas flow extracts the molecules out of the cell through the aperture. Molecule density is monitored both in the cell and outside the cell aperture with 577 nm absorption probes resonant with the $^RR_{11}(0)$ line of the $\tilde{X}(000) \rightarrow \tilde{A}(000)$ transition at 17325.0365 cm^{-1} [264]. The extracted beam is rotationally and translationally cold, but can have significant excited vibrational population, a result of inefficient vibrational thermalization from buffer gas collisions [192]. This provides a significant advantage, as we obtain ~10^9 molecules exiting the cell in the excited bending mode as a result. The molecular beam is collimated by a 6.4 mm diameter skimmer 4.8 cm downstream from the cell aperture, a 9.5 mm diameter hole 11.4 cm downstream from the cell aperture, and a 5 mm diameter hole 23.7 cm downstream from the cell aperture. The beam travels at $150 - 200$ m/s toward the laser-induced fluorescence (LIF) measurement region located ~60 cm downstream from the cell. The region is pumped by multiple turbomolecular pumps, and typical pressures when flowing He gas are $1 - 5 \times 10^{-7}$ Torr.

Downstream in the LIF region, molecules in the $\tilde{X}(010)$ bending mode are excited by a 588 nm laser resonant with the nominally forbidden $\tilde{X}(010) \rightarrow \tilde{A}(000)$ transition. The laser beam, with a ~1 mm diameter and ~40 mW of power, is sent perpendicular to the molecular beam (see Fig 4.2a) through windows at Brewster's angle. The resulting 577 nm fluorescence from decays to the $\tilde{X}(000)$

state is collected with a 19.4 mm diameter fused-quartz light pipe. A 25.4 mm diameter, 19 mm focal length retroreflecting concave mirror opposite the light pipe improves collection efficiency. We filter out the 588 nm scattered background light using a combination of interference and colored glass filters on the exit of the light pipe, obtaining a signal-to-noise ratio of >10. The fluorescence signal is incident on a photomultiplier tube (PMT) module (Hamamatsu H13543-300), and the resulting photocurrent is amplified with a 10^{-8} A/V trans-impedance amplifier with a 1.5 kHz low pass filter.

To obtain the field-free spectrum, we scan the 588 nm probe laser and record its frequency using a wavelength meter (HighFinesse WS7-30) with an absolute accuracy of 30 MHz and a measurement resolution of 1 MHz. To improve the absolute accuracy, we use the probe light to co-record sub-Doppler I_2 spectra, obtained with amplitude modulated saturated absorption spectroscopy [219]. Calibration of the laser frequency using the I_2 spectra results in one standard deviation error of 2.35 MHz in absolute frequency accuracy.

Figure 4.2b shows typical absorption and LIF signals obtained in a single shot. The LIF signal size typically varies from shot to shot due to ablation yield fluctuations. To construct the field-free spectrum, we scan the laser at approximately 1-2 MHz per shot, average the LIF signal for 4 shots, integrate over the molecule pulse duration, and plot the data against the calibrated probe frequency. The observed peaks are fit well by a Lorentzian function, with fitting errors < 3 MHz. For the Stark and Zeeman spectra, we step the laser in 3 MHz increments, and average the LIF signal for 10 shots at each step.

For Stark spectroscopy, we use two indium tin oxide (ITO) coated glass plates separated by a 4.99(3) mm gap to apply fields up to 265 V/cm in the LIF region. Before entering the field region, the molecular beam is further collimated with a 3 mm hole in a grounded aluminum plate. The molecules traveling through the ITO plates are then excited by the 588 nm laser (see Fig. 4.2a). The resulting fluorescence is collected through the glass plates with the setup described earlier. For Zeeman spectroscopy, we generate magnetic fields of $0 - 70$ Gauss using two pairs of wire coils outside the vacuum chamber (see Fig. 4.2a). The two coil pairs have a diameter of 21.4 cm with 500 windings each, and are each symmetrically spaced from the LIF region with distances of 7.5(1) cm and 11.3(1) cm to the molecules.

4.2.2 Modeling and Theory

We model the ground $\tilde{X}(010)$ state using a Hund's case (b) effective Hamiltonian describing a $^2\Pi$ vibronic state. This approach has provided an accurate description of the vibrational bending modes in other metal hydroxide molecules, such as CaOH and SrOH in optical [147] and millimeter wave [283] studies. The lack of first-order spin-orbit interaction means the electron spin S is largely
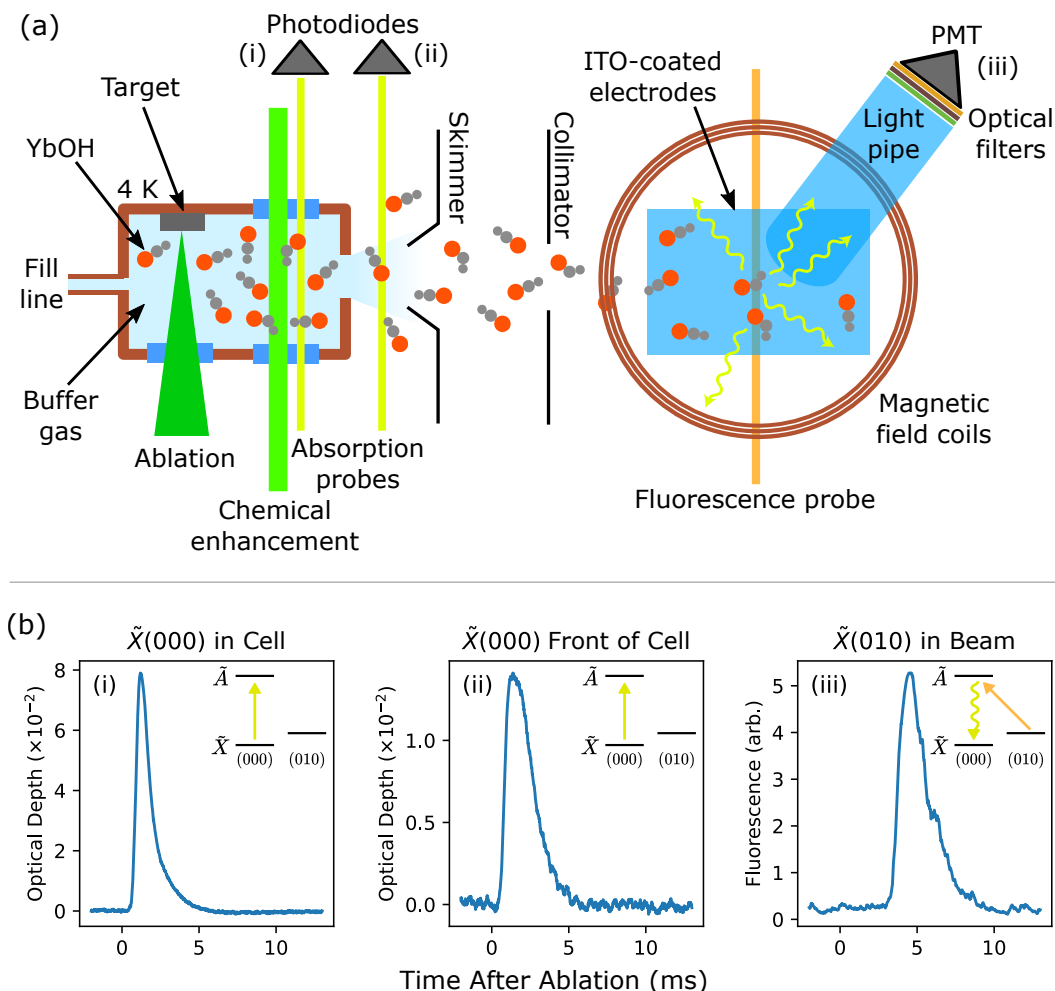
Figure 4.2: Experimental schematic of the $\tilde{X}(010) \rightarrow \tilde{A}(000)$ spectroscopy. (a) YbOH molecules are produced in the 4 K cryogenic buffer gas cell (brown box) by laser ablation (dark green triangle) of a solid pressed target. The molecules are thermalized by collisions with He buffer gas continuously flowed into the cell. The production of YbOH is enhanced by exciting Yb atoms using a laser (light green line) resonant with the $^1S_0 \rightarrow ^3P_1$ atomic Yb transition. Some of the molecules are produced in the $\tilde{X}(010)$ bending mode. The molecules are entrained in the He gas flow and extracted out of the cell. We detect the molecule number density in the $\tilde{X}$ state via absorption spectroscopy (yellow lines) both in the cell (i) and in front of the cell (ii). The molecular beam is collimated by a skimmer and collimators before entering the probe region with electric and magnetic fields. We apply magnetic fields using coils outside the vacuum chamber, and apply electric fields using ITO coated glass electrodes inside the vacuum chamber. In the center of the fields, molecules in the $\tilde{X}(010)$ state are excited by a laser (orange line) and their fluorescence is collected through a light pipe to a PMT (iii). (b) Sample signals from the CBGB. (i) In-cell absorption on the $^R R_{11}(0)$ line of YbOH $\tilde{X}(000) \rightarrow \tilde{A}(000)$. The peak optical depth corresponds to a molecule density of $\sim5\times10^9$ cm^{-3} in the $\tilde{X}(000)$, $N = 0$ state. (ii) Front of cell absorption on the same $^R R_{11}(0)$ line. The peak optical depth corresponds to a molecule density of $\sim2\times10^9$ cm^{-3}. (iii) Fluorescence after excitation of the bending mode on a strong $\tilde{X}(010) \rightarrow \tilde{A}(000)$ line. The integrated signal corresponds to ~8300 photons detected on the PMT.

independent of the internuclear axis, and therefore both Σ and P are undefined. Hund's case (b) is the natural basis, with N and its projection ℓ as good quantum numbers. The spin-rotation interaction then couples N with S to form well-defined J. Higher-order perturbations give rise to the ℓ-doubling interaction, and the $\tilde{X}$ eigenstates of good parity are written as:

$$|\ell; N, S, J, M, \mathcal{P} = \pm\rangle = \frac{1}{\sqrt{2}}(|\ell; N, S, J, M\rangle \pm (-1)^{p_b}| - \ell; N, S, J, M\rangle). \qquad (4.3)$$

The phase factor in Hund's case (b) is defined as $p_b = (-1)^{N-\ell}$. The additional factor of $\ell = 1$ means the action of the parity operator on a singly excited bending mode is similar to that of a Σ^- electronic state. We discuss this phase convention in detail in Ch. 2, Sec. A.2. Here, we note this convention has been used in the literature [129, 151, 167–169], though the choice is not universal. The parity phase and the sign of the ℓ-doubling Hamiltonian (which we take to match the Λ-doubling Hamiltonian) together determine if the lowest energy eigenstate of the effective Hamiltonian has positive or negative parity.

We use an effective Hamiltonian for the $\tilde{X}(010)$ state given by

$$\begin{aligned} H_{\tilde{X}(010)} = {} & B(\vec{N}^2 - \ell^2) + \gamma(\vec{N} \cdot \vec{S} - N_z S_z) + \gamma_G N_z S_z \\ & + \frac{p_G}{2}\left(N_+ S_+ e^{-i2\phi} + N_- S_- e^{i2\phi}\right) - \frac{q_G}{2}\left(N_+^2 e^{-i2\phi} + N_-^2 e^{i2\phi}\right). \end{aligned} \qquad (4.4)$$

This form was first derived in Ref. [162] and is presented in detail in Refs. [159, 168, 169]. Here, all subscripts on angular momenta $(z, \pm)$ denote molecule-frame quantities. The azimuthal angle of the bending nuclear framework is given by ϕ. The first term gives the rotational energy of a symmetric top. The next two terms describe the spin-rotation interaction coupling N and S to form J. The last two terms describe ℓ-type parity doubling caused by terms off-diagonal in the vibrational angular momentum G, and cause splittings of opposite parity states. For convenience, the spherical tensor [39] form of the Hamiltonian is provided below. Note the p and q subscripts denote lab frame and molecule frame components, respectively.

$$\begin{aligned} H_{\tilde{X}} = {} & T_0 + B(N^2 - \ell^2) + \gamma\left(N \cdot S - T_{q=0}^1(N)T_{q=0}^1(S)\right) \\ & + \gamma_G T_{q=0}^1(N)T_{q=0}^1(S) + \sum_{q=\pm 1} e^{-2iq\phi}\left(p_G T_{2q}^2(N, S) - q_G T_{2q}^2(N, N)\right). \end{aligned} \qquad (4.5)$$

For the spin-rotation interaction we have modified the usual expression, $\gamma N \cdot S$, by subtracting $\gamma N_z S_z$ to account for the bending motion. This modification is crucial for accurate description of low-N spectra. For linear molecules with $N_z = 0$, the spin-rotation term $N \cdot S$ implicitly only contains contributions from $N_x S_x$ and $N_y S_y$. However for a bending molecule, since $N_z \neq 0$, we explicitly subtract away $N_z S_z$. The effect of this modification is only noticeable at low N, and further information is provided in Appendix A.6 of Ref. [139].

Other perturbations can reintroduce the $N_z S_z$ term, referred to as axial spin-rotation, into the Hamiltonian. The term is labeled in the literature with the coefficient γ' [162] or γ_G [159, 169], in this work we use the latter label. The first order contribution to γ_G arises from magnetic dipole interactions [163] and is negligible for the Yb-centered electron in YbOH. At higher order, a combination of vibronic coupling and spin-orbit interactions can contribute to γ_G by mixing states with Π electronic character, as observed in NCO [284], CCH [285], and FeCO [286].

In Eq. 4.4, the q_G parity-doubling term is standard for a bending molecule in a $^2\Sigma$ electronic state. This term arises from Coriolis effects at second order, similar to the q term in Λ-doubling. The p_G term, also in analogy with Λ-doubling, is equivalent to a parity-dependent spin-rotation interaction. Owing to the weak coupling of the spin to the internuclear axis in Σ electronic states, this term is small and has only been observed in submillimeter spectroscopy of metal hydroxides [283, 287], ZnCN [288], and CrCN [289]. As with γ_G, this term receives higher-order contributions from vibronic mixing with electronic Π states.

We are using a sign convention for the ℓ-type doubling Hamiltonian outlined by Brown [159, 167], where the ℓ-type doubling Hamiltonian mirrors that used for Λ-doubling. However matrix elements of ℓ involve different phases than Λ. As a result of the $(-1)^\ell$ factor in our parity phase, we have the matrix elements $\langle \ell = \pm 1 | e^{\pm 2i\phi} | \ell' = \mp 1 \rangle = 1$, differing from the azimuthal matrix elements for Λ-doubling. Matrix elements and complete details of the effective Hamiltonian and conventions used are provided in Appendix A.

We construct the predicted spectrum by first separately diagonalizing the effective Hamiltonians for the ground and excited states. The Hamiltonian basis is truncated at $N'' = 6$ for the $\tilde{X}(010)$ state and $J' = 15/2$ for the $\tilde{A}$ state. Following Ref. [264], we include the $P = 3/2$ manifold when diagonalizing $\tilde{A}$. After obtaining eigenvectors and eigenvalues, we convert all eigenvectors to Hund's case (a) and compute matrix elements of the transition dipole moment (TDM) operator. Details of the TDM operator are given in section 4.2.3.3 and in Appendix A. For transitions with non-zero TDM, we compute the line position by taking the difference of excited and ground eigenvalues.

4.2.3 Results

4.2.3.1 Field-Free Spectrum

The observed spectrum (Fig 4.3) exhibits large splittings that match the excited state Λ-doubling and rotational separation. We perform combination-difference tests [39] with these splittings to obtain initial quantum number assignments of transitions. With these assignments, we compute initial guesses for the B, γ, and q_G Hamiltonian parameters for the $\tilde{X}(010)$ state. Using these values and fixing the excited state parameters, we construct a predicted spectrum and perform further line
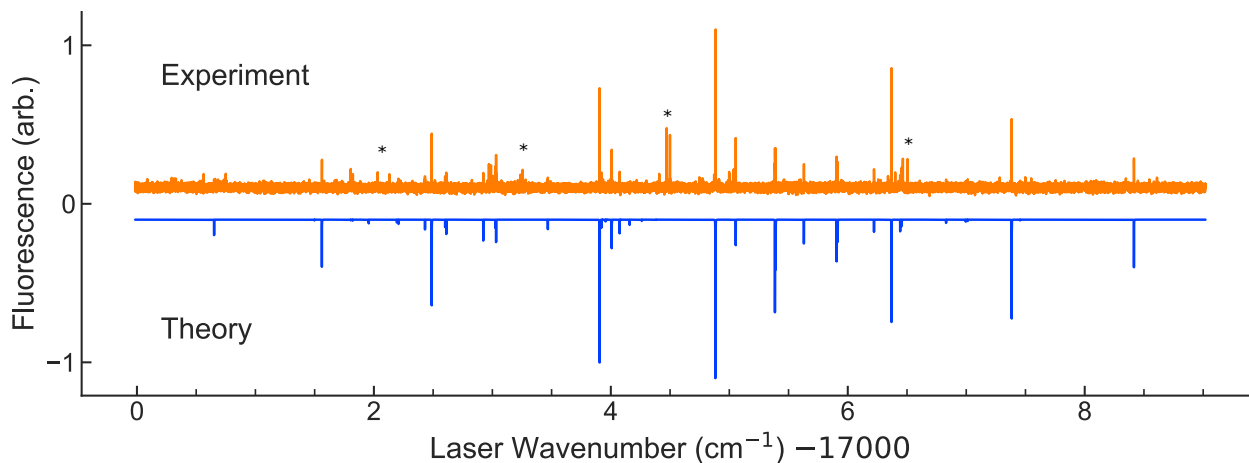
Figure 4.3: Field-free spectrum over a ~9 cm^{-1} range. Orange upper part is experimental observation and blue lower part is theory prediction. Prediction is using effective model detailed in section 4.2.3.3 with coefficients ($c_\mu = 0.28, c_\kappa = -0.49, c_B = 0.83$) and a temperature of $T = 2$ K. Lines marked with * are unassigned and could arise from other isotopologues or bands.

assignments. With this analysis, we determined the need for additional parameters p_G and γ_G to accurately describe the full spectrum.

Without the p_G term, various R and P branch features deviate from the prediction by a magnitude >20 MHz, much larger than our frequency error. Specifically, in the region scanned in Fig. 4.3, without p_G, lines with significant residuals are: $^R R_{11}^+(2)$, $^R R_{11}^-(3)$, $^O P_{12}^+(4)$, $^P Q_{12}^+(5)$, and $^P P_{11}^+(5)$. The magnitude and parity behavior of these residuals cannot be explained by centrifugal distortion, but can be explained by a parity-dependent spin-rotation interaction, namely p_G. By introducing p_G into the prediction, all of these residuals are reduced to values commensurate with the experimental error. Furthermore, using the fit value of p_G, we predicted and found the $^R R_{11}^+(4)$ and $^R R_{11}^-(5)$ lines (not visible in Fig. 4.3). These additional lines are added to the final fit and confirm the need for a p_G term to accurately model the full spectrum.

Unlike p_G, the γ_G term does not scale with N''. However, we find this term necessary to describe the $N'' = 1$ structure, which was crucial for accurate Stark and Zeeman analysis in section 4.2.3.2. In particular, we recorded multiple field-free calibration scans of the $^Q Q_{11}^+(1)$ and $^Q R_{12}^+(1)$ lines. Since these lines share the same excited state, their separation is insensitive to error in the $\tilde{A}$ state parameters. We use the separation of these lines to determine the $N'' = 1^+$ spin-rotation splitting to be 61.8(20) MHz, and we add this value as an additional data point for our analysis. By including the γ_G term in the spectral prediction, were we obtain an accurate prediction of the $N'' = 1^+$ splitting commensurate with our measurement error.

In total, we assigned 38 of the observed lines to 39 transitions originating from the $N'' = 1$ through $N'' = 5$ levels of the $\tilde{X}(010)$ state. Note the $^Q R_{12}^-(1)$ and $^P Q_{12}^-(5)$ lines are overlapped.

Table 4.1: Spectroscopic parameters for the low-lying vibrational states of the $\tilde{X}^2\Sigma^+$ manifold. The $\tilde{X}(010)$ parameters are obtained from the current work.

Parameter	$\tilde{X}(000)$ [290]	$\tilde{X}(010)$	$\tilde{X}(100)$ [264]
T_0/cm^{-1}	0	319.90901(6)	529.3269(3)
B/MHz	7348.4005(3)	7328.64(15)	7305.37(24)
γ/MHz	−81.15(6)	−88.7(9)	−110.6(21)
γ_G/MHz	–	16(2)	–
q_G/MHz	–	−12.0(2)	–
p_G/MHz	–	−11(1)	–

To obtain optimal effective Hamiltonian parameters, we vary the $\tilde{X}(010)$ state parameters and hold fixed the $\tilde{A}$ state parameters to the values given in Ref. [264]. We construct predicted spectra and perform nonlinear least-squares minimization of the residuals between the observed and predicted positions of all 39 assigned lines and the $N'' = 1^+$ spin-rotation splitting. A full list of lines and assignments is provided in Appendix D.

The best fit parameters are presented in Table 4.1. The fit residuals have a standard deviation of 6.1 MHz, consistent to order unity with the error reported in the previous optical study of the $\tilde{A}$ state [264]. The rotational and spin rotational $\tilde{X}(010)$ parameters are in good agreement with those for $\tilde{X}(000)$ and $\tilde{X}(100)$, also collected in Table 4.1. The location of the origin T_0 is in excellent agreement with previous dispersed fluorescence studies [144, 217]. The rotational constant B decreases in $\tilde{X}(010)$ as a result of vibrational corrections. The increasingly negative spin-rotation parameter γ between the three vibrational states is a result of second order spin-orbit perturbations from low-lying electronic states with $4f^{13}6s^2$ electronic configuration for the Yb centered electron, known as "4f hole" states [290, 291].

Vibronic mixing with electronic $^2\Pi$ states can also explain the observed γ_G and p_G parameters, which are not typical for the bending mode of an isolated electronic $^2\Sigma$ state. Vibronic mixing exchanges ℓ and Λ while preserving K. As a result, the $\tilde{X}(010)$ state can acquire some $\Lambda > 0$ electronic character, inheriting spin-orbit and Λ-doubling interactions from neighboring $^2\Pi$ states. Specifically, in the effective Hamiltonian, these interactions can arise at third-order via a combination of linear vibronic coupling and spin-orbit effects. This term was first described by Brown in the context of spin-orbit corrections to electronic $^2\Pi$ states as a result of mixing with other $^2\Sigma$ or $^2\Delta$ states [156]. Neighboring states that can contribute to γ_G and p_G include both the $\tilde{A}$ manifold and the $4f$ hole states. The exact nature of the $4f$ hole states and their vibronic mixing in YbOH is currently unknown and merits further study. However, their proximity to the ground state and their large spin-orbit interactions could explain the significant magnitude of p_G and γ_G

120
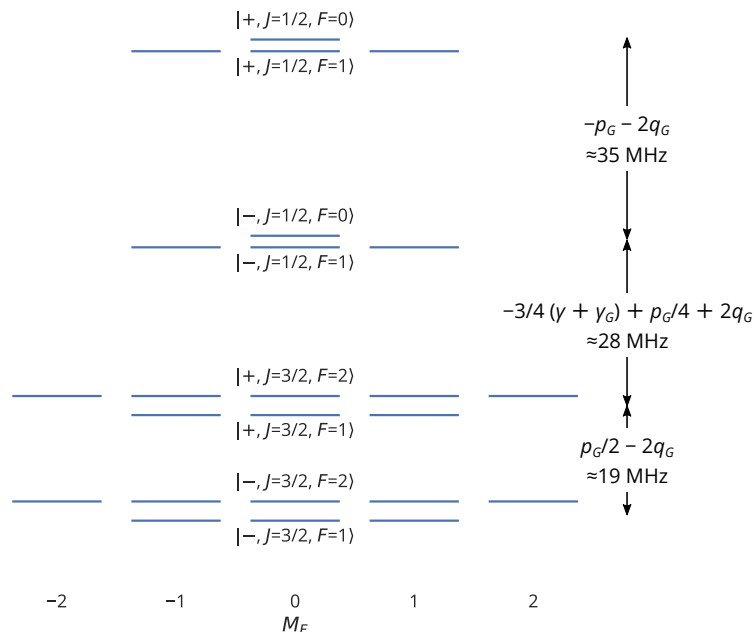
Figure 4.4: Field-free level structure of the $N = 1$ manifold in the $\tilde{X}(010)$ state. States are arranged vertically by energy and horizontally by their M_F angular momentum projection. States are labeled in the parity basis. The hyperfine structure was not resolved in our work, and is instead approximated using parameters from a study of the $\tilde{X}$ state [290].

in YbOH compared to other metal hydroxides [283].

The ℓ-type doubling parameter q_G is a similar magnitude to that of other metal-hydroxide $\tilde{X}(010)$ states [147, 283], and is in agreement with a recent theoretical calculation [292]. The parameter q_G can be interpreted in terms of the Coriolis coupling constants of a triatomic molecule [147, 154]:

$$q_G = -(v_2 + 1)\frac{B^2}{\omega_2}\left(1 + \sum_{n=1,3} \zeta_{2n}^2 \frac{4\omega_2^2}{\omega_n^2 - \omega_2^2}\right). \tag{4.6}$$

Here, v_2 is the number of quanta in the bending vibration ω_2, and ζ_{2n} is the Coriolis coupling constant between the bending mode and the v_n stretch modes. To estimate ζ_{21}, we can estimate the value of ω_3 (O-H stretch) using the CaOH value of 3778 cm^{-1} [293], and we set $v_2 = 1$, $\omega_2 \approx T_0$, and $\omega_1 \approx 529.3$ cm^{-1} [264]. Furthermore, we can use the relationship $\zeta_{21}^2 + \zeta_{23}^2 = 1$ [154] to eliminate ζ_{23}^2. Using our values of B and q_G, we then obtain a value of $\zeta_{21} \approx 0.137$, slightly smaller than in CaOH (0.1969) [147] and SrOH (0.179) [294]. This is likely due to the break down of the harmonic approximation $\omega_2 \approx T_0$ and the approximation of $B_e \approx B$. Further work is needed for a complete vibrational characterization.

Using the parameters obtained from our analysis, we construct a field-free level diagram for the

$N = 1$ manifold of the $\tilde{X}(010)$ state, shown in Figure 4.4. As stated previously, $N = 1$ is the lowest rotational manifold in the $\tilde{X}(010)$ state, as we always have $|\vec{N} \cdot \hat{n}| = 1$. Due to their small parity splittings, $N = 1$ states are easily polarized, making them useful for precision measurements [17]. The effect of the parity-dependent spin-rotation term, p_G, is apparent in the asymmetric parity-doubling of the $J = 1/2$ and $J = 3/2$ manifolds. Though we are not sensitive to hyperfine splittings, for completeness we have included the H hyperfine structure using the parameters obtained for the $\tilde{X}$ state in a previous study [290]. The hyperfine structure is not expected to change significantly in the bending mode.

The recorded spectrum has lines present that could not be assigned with combination-differences using the $\tilde{A}(000)$ structure, and are not observed in the prediction using the best-fit parameters. The lines are marked with * in Fig. 4.3. We conclude that some of these lines are indeed from ^{174}YbOH by comparing their chemical enhancement [227] when using $^1S_0 \rightarrow {}^3P_1$ transitions for different Yb isotopes. These lines could be unthermalized rotational states, or possibly another overlapping $\Delta\ell = \pm 1$ band, such as the $\tilde{X}^2\Sigma^+(02^{0,2}0) \rightarrow \tilde{A}^2\Pi_{1/2}(010)$ bands.

The additional γ_G and p_G terms mean that we can draw an analogy between picturing $\tilde{X}(010)$ as a dynamically bending linear molecule and a bent asymmetric molecule. We detail this correspondence further in Appendix C, and use it to make estimates of the bending angle θ indicating the displacement of the H atom from the internuclear axis³. Our rough estimates indicate $\theta \approx 20° - 30°$. We caution that these Cartesian estimates do not correspond to large deviations of the normal coordinate q_2, which is expected to remain harmonic.

4.2.3.2   Stark and Zeeman Spectra

After fitting the molecular structure with the field-free spectrum, we study the Stark and Zeeman spectra of the molecule in the presence of static (DC) electric and magnetic fields, using the experimental setup described in 4.2.1. We obtain the spectra by scanning the 588 nm probe laser across two lines corresponding to the field-free $N'' = 1^+ \rightarrow J' = \frac{3}{2}^-$ transition, ${}^QQ_{11}^+(1)$ and ${}^QR_{12}^+(1)$. The applied DC fields point along z, while the laser polarization is along x. Spectra are taken with the E-field varied from $0 - 264$ V/cm and with the applied B-field varied from $0 - 70$ G. Calibration spectra are taken with $E_Z = 0$ V/cm and $B_Z < 0.5$ G, and the observed line positions are compared to the I$_2$-corrected field-free positions to calibrate for frequency offsets.

The lines of interest are relatively well-isolated from other features, and the small $N'' = 1$ parity doubling allows us to enter the linear stark regime with modest laboratory fields $\gtrsim 100$ V/cm. Since the parity splittings of the excited $\tilde{A}^2\Pi_{1/2}$ state are >13 GHz, and its molecule frame dipole

---

³We define θ as the deviation from linearity, i.e., $\theta = 0$ is the nominally linear YbOH configuration.
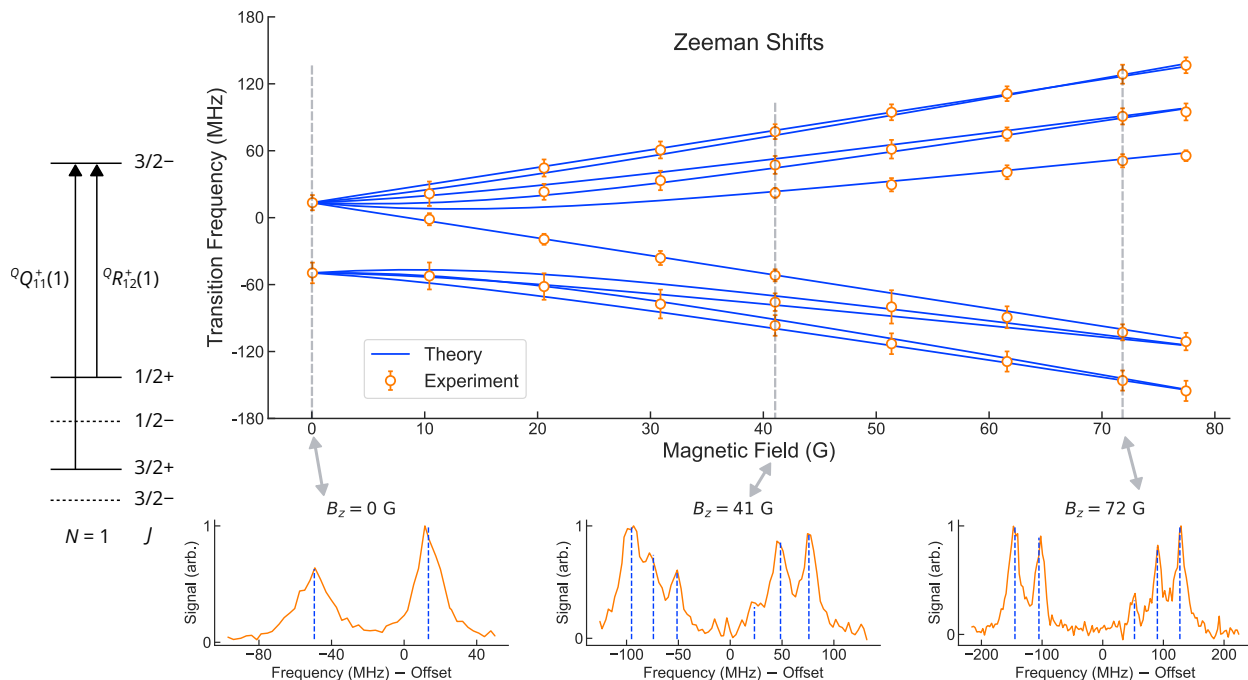
Figure 4.5: Zeeman spectroscopy of the $\tilde{X}(010)$ state. The main plot shows the transition frequency shift (with subtracted offset) in a magnetic field, the blue lines are optimized model predictions, and the orange circles are experimental measurements. Error bars are 1-σ measured peak widths, set by a combination of radiative broadening and unresolved hyperfine structure, limiting the ability to resolve closely-spaced lines. Lower subplots are slices of the spectra at various magnetic field values, with experimental data in orange and predicted line locations indicated with vertical dashed blue lines. On the left, we show the field-free level structure of the transitions studied.

moment is $D_{\tilde{A}} = 0.43(10)$ D [264], at the fields we consider the excited state Stark shifts are negligible. Furthermore, given our frequency resolution and the natural linewidth, we are only sensitive to the isotropic interaction of B_Z with the electron spin magnetic moment. Curl-type relationships [168] estimate anisotropic spin interactions at $6 \times 10^{-3}\mu_B$, and the nuclear magnetic moment is also suppressed at a similar level, with both effects giving shifts below our resolution.

To obtain energy levels and predicted lines, we fix the field-free parameters and diagonalize the combined Stark, Zeeman, and field-free Hamiltonian. We obtain optimal estimates for free Stark and Zeeman parameters by least-squares minimization of the residuals between observed and predicted line positions.

Both ground and excited levels are magnetically sensitive. The Zeeman shifts of the $\tilde{A}^2\Pi_{1/2}(000)$ and $\tilde{X}^2\Sigma^+(000)$ states were previously studied at similar magnetic field strengths in Ref. [264], and recently at high fields (~1 T) in Ref. [282]. Following these references, we use the following
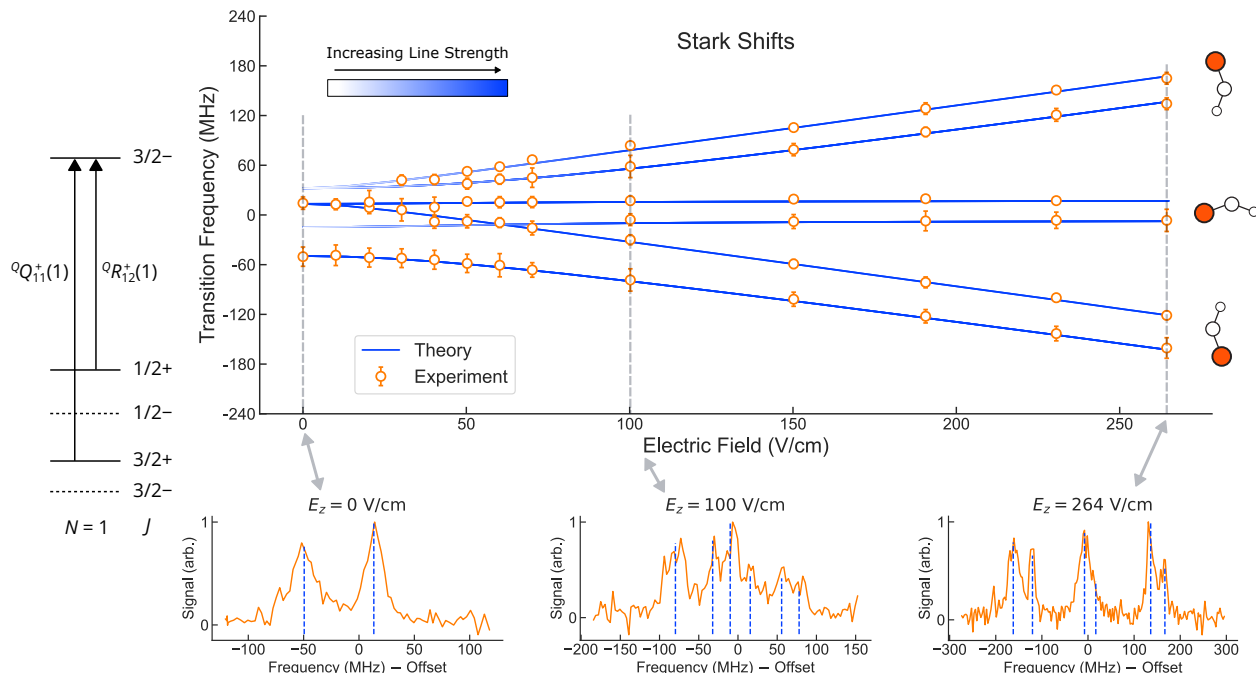
Figure 4.6: Stark spectroscopy of the $\tilde{X}(010)$ state. The main plot shows the transition frequency shift (with subtracted offset) in an electric field, the blue lines are optimized model predictions, and the orange circles are experimental measurements. The blue color gradient represents parity forbidden transitions that gain strength at finite electric field. Error bars are 1-σ peak widths, set by a combination of radiative broadening and unresolved hyperfine structure, limiting the ability to resolve closely-spaced lines. Lower subplots are slices of the spectra at various electric field values, with experimental data in orange and predicted line locations indicated with vertical dashed blue lines. On the left, we show the field-free level structure of the transitions studied.

effective Zeeman Hamiltonians for the ground and excited states:

$$H_X^{Zee} = g_S \mu_B S_Z B_Z \tag{4.7a}$$

$$H_A^{Zee} = g_S' \mu_B S_Z B_Z + g_L L_Z B_Z + g_l' \mu_B \left(e^{-2i\theta} S_+ B_+ + e^{2i\theta} S_- B_- \right). \tag{4.7b}$$

Here, Z refers to the lab-frame projection, $\pm$ refer to the molecule frame projections, and θ is the electronic azimuthal coordinate. For the excited state, we use the values from Ref. [282], fixing $g_S' = 1.860$, $g_L = 1.0$, and $g_l' = -0.724$. For the ground state, we allow g_S to vary in the fits to find an effective value that accurately describes the Zeeman shifts. While we do not include them here, at higher resolution or at higher field values, additional terms are expected to contribute in the effective Zeeman Hamiltonian, including terms associated with the bending angular momentum [168].

The Zeeman fits prefer a value of $g_S = 2.07(2)$, deviating from the free electron g-factor of 2.0023. The experimental Zeeman shifts and the prediction from the optimized model are shown in Fig. 4.5. Corrections to g_S can arise from mixing involving other states with different Zeeman

tuning. For example, the Zeeman shifts of the $\tilde{A}$ state were fit to $g'_S = 1.860$ in a recent high-field study [282], owing to perturbing $4f^{13}6s^2$ states. Since we observe perturbations from these $4f$ states in the field-free structure of the $\tilde{X}(010)$ state, it is natural to also find their effects in the Zeeman shifts. Furthermore, the $4f$ states are split into a higher energy spin-orbit anti-aligned manifold and a lower energy spin-orbit aligned manifold [291]. Due to energy proximity, while $\tilde{A}$ predominantly interacts with the $4f$ hole anti-aligned manifold, $\tilde{X}(010)$ will be perturbed more strongly by the aligned manifold. The difference in electron orientation of the two spin-orbit $4f$ manifolds can explain the difference between $\tilde{X}(010)$ and $\tilde{A}$ in the sign of the deviation of g_S from its nominal value.

To describe the Stark shifts, for the both ground and excited states we use the Hamiltonian $H_E = -\vec{D}_{\text{mol}} \cdot \vec{E}$. The molecule frame dipole moment D_{mol} is kept as a free parameter, and obtained from spectra where E_Z is scanned with $B_Z < 0.5$ G. The optimal fit value is $D_{\text{mol}} = 2.16(1)$ D = 1.09 h MHz/(V/cm). This value is in good agreement with the measured $\tilde{X}(000)$ dipole moment of 1.9(2) D. In Figure 4.6, we plot the theoretical prediction based on the optimal fit against the observed line positions.

The Stark shifts confirm the assignment of the $\tilde{X}(010)$ state and demonstrate the orientation control afforded by parity doublets. In the bending mode, the projection of the molecular axis on the lab-frame[4] $\hat{Z}$-axis is given by $\hat{n} \cdot \hat{Z} = \frac{(\vec{N} \cdot \vec{Z})(\vec{N} \cdot \hat{n})}{N(N+1)} \propto M_N \ell$. For field-free states, $\langle M_N \ell \rangle = 0$, and the molecule is unpolarized. In the presence of an electric field fully mixing parity doublets, the Stark shifts are linear, and the eigenstates are diagonal in the the decoupled basis $|\ell; M_N, M_S\rangle$. In this regime, the levels split into $2N + 1$ dipole moment orientations pointing along $\frac{M_N \ell}{N(N+1)}$, and splittings within each orientation manifold are due to the spin-rotation interaction.

4.2.3.3 Perturbations and Quantum Interference

Since the $\tilde{A}$ state has been previously fully characterized [264], the assignment of energy levels in $\tilde{X}(010)$ is fairly straightforward using the effective Hamiltonian approach. However, because this transition is nominally forbidden, interpreting the line intensities is a challenge. Electric dipole (E1) transitions involving $\Delta \ell \neq 0$ are forbidden in the Condon approximation, which separates electronic and vibrational degrees of freedom [135, 295]. These nominally forbidden vibronic transitions have been observed spectroscopically in many species of linear triatomic molecules, including NCO [296], NCS [297], MgNC [298], CaOH [147, 299, 300], SrOH [294, 301, 302], and YbOH [217], though modeling of the intensities is less common.

---

[4]As always, we use $\hat{X}, \hat{Y}, \hat{Z}$ to denote lab-frame axes and $\hat{x}, \hat{y}, \hat{z}$ to denote the molecule-frame. The molecule $\hat{z}$ axis and dipole moment D_{mol} both point from O to Yb.

These transitions borrow intensity from E1-allowed bands through a combination of vibronic and spin-orbit perturbations [143, 144]. Branching ratios involving forbidden vibronic transitions in YbOH were measured in a previous study [144] examining dispersed fluorescence from the $\tilde{A}(000)$ state, with resolution at the 10^{-5} level. The experimentally observed vibrational branching was in good agreement with a theoretical study published in the same work [144]. While these transitions are of interest as leakage channels for photon cycling, they can also be a resource for spectroscopy, as we show in the current work.

The observed spectrum exhibits anomalous rotational line intensities, with certain transitions completely missing at our level of sensitivity. For example, despite their expected thermal occupation ($N'' \leq 3$), the ${}^{P}Q_{12}^{+}(1)$, ${}^{P}P_{11}^{+}(2)$, ${}^{Q}Q_{11}^{+}(2)$, ${}^{P}P_{11}^{-}(3)$, ${}^{Q}P_{11}^{-}(3)$, and ${}^{Q}R_{12}^{-}(3)$ lines are missing (see Appendix C for a full list of lines). Anomalous line intensities for forbidden transitions have been previously observed in other molecules with vibronic mixing [147, 294, 298, 300, 301]. By considering the intensity-borrowing that gives transition strength to these forbidden transitions, we develop a model that qualitatively explains the observed line strengths.

In an E1 transition, the transition strength is proportional to the square of the transition dipole moment between the ground and excited state, $|\langle \tilde{A} | T_p^1(d) | \tilde{X} \rangle|^2$. We are using spherical tensor notation, where p denotes the component of the spherical tensor in the lab-frame and q in the molecule-frame. Using a Wigner $\mathcal{D}$ matrix, we can write the lab frame dipole moment in terms of its molecule frame projections: $T_p^1(d) = \sum_q \mathcal{D}_{p,q}^{(1)}(\omega)^* T_q^1(d)$. In the E1 approximation, $\Delta\Sigma = 0$, and the molecule-frame projection q of the transition dipole moment determines the selection rule for Λ. The perpendicular $q = \pm 1$ components drive $\Delta\Lambda = \pm 1$ transitions, for example the allowed $\tilde{A} - \tilde{X}$ band, while parallel $q = 0$ component drives $\Delta\Lambda = 0$, for example the allowed $\tilde{B} - \tilde{X}$ band.

In the limit of very large vibronic interaction, Λ and ℓ are fully mixed, and one might consider the $\tilde{X}(010) \rightarrow \tilde{A}(000)$ transition as a vibronic $^2\Pi - {}^2\Pi$ parallel band, with $\Delta K = 0$. In reality, the vibronic mixing is perturbative in the ground and excited states, and Λ and ℓ are well-defined. As a result, the observed line intensities are completely inconsistent with a solely parallel transition model.

Instead, we model the $\tilde{X}(010) \rightarrow \tilde{A}(000)$ transition as a mixture of perpendicular and parallel bands. We consider the effects of vibronic perturbations with the selection rule $\Delta\ell = \pm 1$, which can result in intensity borrowing. At first order, we have the dipolar Renner-Teller (RT) Hamiltonian, also referred to as Herzberg-Teller coupling [129, 151, 296],

$$H_{RT} = \frac{V_{11}}{2} \left(L_+ q_- e^{i(\theta - \phi)} + L_- q_+ e^{-i(\theta - \phi)} \right). \tag{4.8}$$

This interaction is a form of linear vibronic coupling [303]. Here, V_{11} parameterizes the interaction strength, θ is the electronic azimuthal coordinate, ϕ is the bending azimuthal coordinate as before,
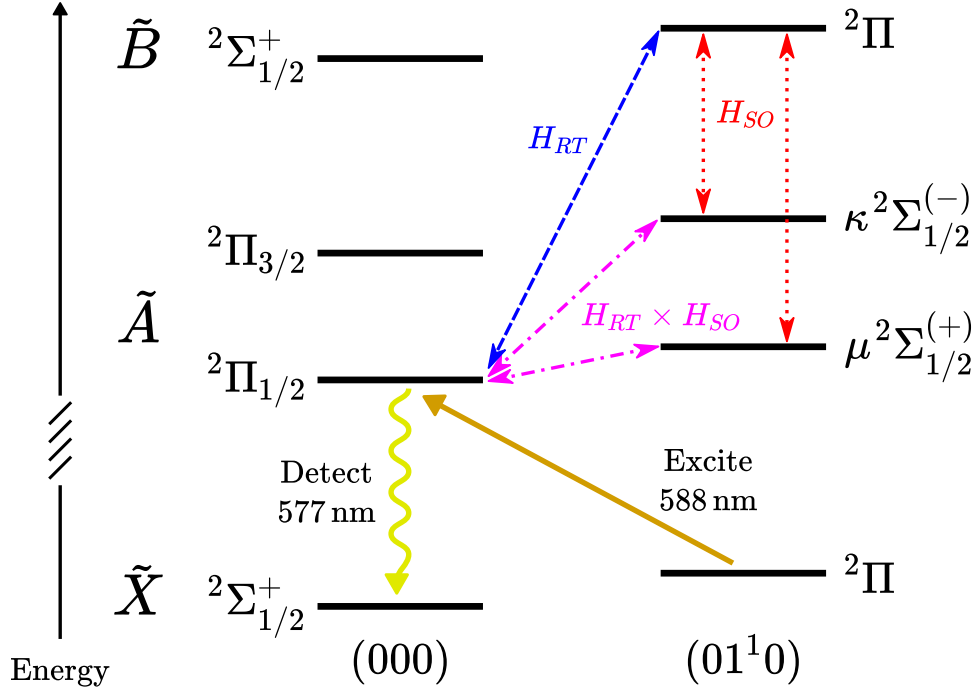
Figure 4.7: Level schematic for relevant states and perturbations in YbOH. Levels are labeled by their vibronic term symbol. We detect the $\tilde{X}(010)$ bending state (which is a vibronic $^2\Pi$ state) by laser excitation (orange line) up to the $\tilde{A}^2\Pi_{1/2}(000)$ state and observe the fluorescence from decays to the ground $\tilde{X}(000)$ state (yellow wavy line). This excitation is a forbidden E1 transition, however, it acquires intensity by mixing of the excited $\tilde{A}^2\Pi_{1/2}(000)$ state with other $|\ell| = 1$ states. Mixing with $\tilde{B}(010)$ occurs via first-order (blue) Renner-Teller (RT) interactions, and mixing with the $\mu, \kappa(010)$ states occurs via second-order (purple) cross terms between RT and spin-orbit (SO) (red) interactions. Not shown for simplicity are similar SO interactions between $\tilde{A}^2\Pi_{1/2}(000)$ and $\tilde{B}(000)$ and similar RT interactions between $\mu, \kappa(010)$ and $\tilde{B}(000)$, which also contribute to state mixing.

$L_\pm$ is a raising/lowering operator with $\Delta\Lambda = \pm 1$, and $q_\pm$ is a dimensionless raising/lowering operator with $\Delta\ell = \pm 1$. Physically, this interaction can be interpreted as the electrostatic interaction between the displaced bending dipole moment and the electron cloud. The interaction preserves the composite projection number $K = \Lambda + \ell$.

At second order, the dipolar RT Hamiltonian can combine with the perpendicular spin-orbit Hamiltonian,

$$H_{SO} = \frac{A_\perp}{2} \left(L_+ S_- + L_- S_+ \right) \tag{4.9}$$

where $L_\pm$ is defined as before, $A_\perp$ is the off-diagonal spin-orbit coupling, and $S_\pm$ is the raising/lowering operator with $\Delta\Sigma = \pm 1$. The combination of $H_{RT}^{(1)} \times H_{SO}^\perp$ is an effective interaction with terms $q_\pm S_\mp$. This interaction has $\Delta K = -\Delta\Sigma = \pm 1$, but preserves the total angular momentum projection number $P = \Lambda + \Sigma + \ell$.

Denote the unperturbed excited state as $|\tilde{A}^2\Pi_{1/2}(000)\rangle_0$ and the true, perturbed eigenstate as $|\tilde{A}^2\Pi_{1/2}(000)\rangle$. We can then expand the perturbed eigenstate in terms of dominant $\ell = 1$ vibronic contributions [143, 144]:

$$
\begin{aligned}
|\tilde{A}^2\Pi_{1/2}(000)\rangle \propto & \\
|\tilde{A}^2\Pi_{1/2}(000)\rangle_0 &+ c_\mu|\mu^2\Sigma^{(+)}_{1/2}(010)\rangle_0 + c_\kappa|\kappa^2\Sigma^{(-)}_{1/2}(010)\rangle_0 + c_B|\tilde{B}^2\Pi(010)\rangle_0.
\end{aligned}
\tag{4.10}
$$

The perturbative coefficients c_μ, c_κ, c_B represent the relative admixture of the intensity-borrowing states. The relevant states and perturbations are shown schematically in Fig. 4.7. The $\mu^2\Sigma^{(+)}_{1/2}$ state is the $P = 1/2$ component of the $\Omega = 1/2$, $v_2 = 1$, $\tilde{A}$ manifold, and the $\kappa^2\Sigma^{(-)}_{1/2}$ state is the $P = 1/2$ component in the $\Omega = 3/2$, $v_2 = 1$, $\tilde{A}$ manifold. These two states are connected to $\tilde{A}^2\Pi_{1/2}(000)$ by the second-order perturbation $H_{RT} \times H_{SO}$. The $\tilde{B}^2\Pi$ vibronic state is the $v_2 = 1$ component of the $\tilde{B}^2\Sigma^+_{1/2}$ electronic state, and is connected to $\tilde{A}^2\Pi_{1/2}(000)$ state via the first-order perturbation H_{RT}.

Each of these perturbing states contribute to different molecule-frame components of the transition dipole moment (TDM). For example, the transition $\tilde{X}^2\Pi \rightarrow \tilde{B}^2\Pi$ is generated by the $q = 0$, z component of the TDM, with $\Delta K = \Delta P = 0$. The other transitions to μ and κ have $\Pi \rightarrow \Sigma$ vibronic character, and couple via the $q = \pm 1$, x, y TDM components. The perturbing μ and κ states have opposite spin orientation compared to the original $\tilde{A}^2\Pi_{1/2}$ state. This means the intensity-borrowing states have mixed spin projection Σ, and the $\Delta\Sigma = 0$ selection rule is not well-defined.

The transition was modeled by first diagonalizing the $\tilde{A}^2\Pi_{1/2}(000)$ and $\tilde{X}^2\Sigma(010)$ states separately to obtain the level positions of both states. The eigenstates of $\tilde{X}(010)$ are best described by Hund's case (b) wavefunctions, while the eigenstates of $\tilde{A}$ are described by Hund's case (a) wavefunctions. To calculate transitions, we convert between the two cases using the following formula from Brown [160]:

$$
|N, K, S, J, M\rangle = \sum_{\Sigma, P} (-1)^{N-S+P}\sqrt{2N+1}
\begin{pmatrix} J & S & N \\ P & -\Sigma & -K \end{pmatrix}
|S, \Sigma; J, P, M\rangle.
\tag{4.11}
$$

Here, $P = \Lambda + \Sigma + \ell$, and $K = \Lambda + \ell$. Note this form is equivalent to that given by Hirota in Ref. [129].

Next, to evaluate the TDM, we perform a change of basis to transform the $\tilde{A}^2\Pi_{1/2}(000)$ effective Hamiltonian eigenvectors into eigenvectors of the admixed states with $|\ell| = 1$. The change of basis from must use appropriate selection rules for vibronic mixing and preserve parity. The states of

interest with $|\ell| = 1$ are $\tilde{A}\mu^2\Sigma^{(+)}_{1/2}(010)$, $\tilde{A}\kappa^2\Sigma^{(-)}_{1/2}(010)$, and $\tilde{B}^2\Pi(010)$, where we are using vibronic term symbols $^{2S+1}K_P$. Each eigenvector of $\tilde{A}(000)$ is transformed into a linear combination of eigenvectors from the admixed states, with amplitudes c_μ, c_κ, c_B.

The mixing between $\tilde{A}^2\Pi_{1/2}(000)$ and $\tilde{B}^2\Pi(010)$ occurs at first order due to H_{RT}. Since this interaction preserves K and P, it simply exchanges one quanta between ℓ and Λ. Since $\tilde{A}^2\Pi_{1/2}(000)$ has $P = 1/2$, we only consider mixing other $P = 1/2$ states. We perform the following change of basis:

$$\langle\tilde{B}(010), \Lambda = 0, \ell, \Sigma, P \mid \tilde{A}(000), \Lambda', \ell' = 0, \Sigma', P' = \pm 1/2\rangle$$
$$= \delta_{\ell,\Lambda'}\delta_{P,P'}\delta_{\Sigma,\Sigma'}(-1)^{P-1/2} \tag{4.12}$$

Note the phase factor $(-1)^{P-1/2}$ is explicitly included to preserve parity[5]. This factor accounts for the extra $(-1)^\ell$ phase factor in the parity of an $\ell \neq 0$ state compared to an $\ell = 0$ state. This basis transformation can be succinctly represented in the space of a single J state and $\pm P$ states as being proportional to the Pauli matrix σ_z.

The admixture of the μ and κ states occurs via a second-order combination of H_{RT} and H_{SO}. These interactions preserve P but can change K. For $\mu(010)$ we obtain the following change of basis:

$$\langle\mu(010), \Lambda, \ell, \Sigma, P \mid \tilde{A}(000), \Lambda', \ell' = 0, \Sigma', P' = \pm 1/2\rangle$$
$$= \delta_{\Lambda,-\Lambda'}\delta_{\ell,\Lambda'}\delta_{\Sigma,-\Sigma'}(-1)^{P-1/2} \tag{4.13}$$

And for $\kappa(010)$:

$$\langle\kappa(010), \Lambda, \ell, \Sigma, P | \tilde{A}(000), \Lambda', \ell' = 0, \Sigma', P' = \pm 1/2\rangle$$
$$= \delta_{\Lambda,\Lambda'}\delta_{\ell,-\Lambda'}\delta_{\Sigma,-\Sigma'}(-1)^{P-1/2}. \tag{4.14}$$

We note that all of these change of basis formulae can be derived from the Hamiltonian if we write the Herztberg-Teller interaction as $\propto \sin(\theta - \phi)$. Instead of using imaginary numbers, we have instead opted to encode the hermitian conjugate's sign flip by hand to preserve the state parity.

The total TDM is the sum over the individual TDMs evaluated between $\tilde{X}(010)$ and the intensity-borrowing states. The transition dipole moment (TDM) matrix element is evaluated in

---

[5]This factor is only valid for $P = 1/2$.

Hund's case (a):

$$
\begin{aligned}
\langle \ell; \Lambda; S, \Sigma; J, P, M | T_p^1(d) | \ell'; \Lambda'; S, \Sigma'; J', P', M' \rangle \\
= \delta_{\Sigma,\Sigma'} \delta_{\ell,\ell'} \\
\times (-1)^{J-M} \begin{pmatrix} J & 1 & J' \\ -M & p & M' \end{pmatrix} \\
\times \sqrt{(2J+1)(2J'+1)} (-1)^{J-M} \\
\times \sum_q \begin{pmatrix} J & 1 & J' \\ -P & q & P' \end{pmatrix} \delta_{\Lambda,\Lambda'+q} \\
\times \langle \Lambda || T_q^1(d) || \Lambda' \rangle.
\end{aligned}
\tag{4.15}
$$

The last term is the reduced matrix element encoding the transition dipole integral between two electronic states. The $\Delta\ell = 0$ selection rule is explicit in the above matrix element. This means we can only drive $\tilde{X}(010)$ to admixtures in $\tilde{A}(000)$ with $|\ell| = 1$. These admixed states provide the transition intensity and non-zero transition dipole moment. To obtain the transition intensity, the TDM is squared after the sum, allowing TDMs from different states to interfere with each other. This interference is the source of the anomalous line intensities.

After changing basis to states with $|\ell| = 1$, we compute the transition dipole matrix element using equation 4.15. The transition amplitudes for the different state admixtures are added together, and the resulting interference depends on the mixing coefficients c_μ, c_κ, c_B. Finally, to obtain relative intensities, we square the total transition amplitude.

The mixing coefficients, c_μ, c_κ, c_B could not be modeled with a deperturbation Hamiltonian, since neither the μ, κ, or $\tilde{B}$ state have been extensively studied or modeled, and both states are expected to be affected by perturbations from nearby states with $4f^{13}6s^2$ Yb character [291]. Instead, the mixing coefficients are kept as free parameters and their ratios were fit to the experimentally observed, relative field-free intensities. For the intensity fits, the rotational temperature is fixed at $T = 2$ K (the molecule beam is cooled by expansion out of the cell aperture), and since only relative intensities were fit, the c_B parameter is held fixed. The normalized best fit mixing coefficients are found to be $(c_\mu, c_\kappa, c_B) = (0.28, -0.49, 0.83)$. This implies ~69% of the $\ell = 1$ character in $\tilde{A}^2\Pi_{1/2}(000)$ arises from mixing with $\tilde{B}(010)$, ~24% from $\kappa(010)$, and ~7% from $\mu(010)$. This is in good agreement with recent theory work on intensity borrowing in YbOH, which attributed 70% of the intensity borrowing to mixing with $\tilde{B}(010)$ [144]. However, it is important to note that due to interference effects, relative amplitudes of the coefficients, not their squares, are important for determining rotational line intensities.

We find that using these parameters to model the transition provides good qualitative understanding of the observed spectrum, as evidenced by the theory and experiment comparison in Figure

4.3. Further studies of the excited state perturbations would be required to improve the fit; however, as the exact intensities are not critical for future experiments with this molecule, this model is sufficient to provide physical understanding of the intensities and behavior of this transition.

4.2.4 Summary

In this work, we performed high-resolution optical spectroscopy on the rovibrationally forbidden $\tilde{X}^2\Sigma^+(010) \rightarrow \tilde{A}^2\Pi_{1/2}(000)$ transition of ^{174}YbOH. In total, we observed 39 transitions out of low rotational states with $N'' \leq 5$. The $\tilde{X}(010)$ structure is well-described by a Hund's case (b) $^2\Pi$ effective Hamiltonian, and the ℓ-type parity doubling is described by two constants, $q_\ell = -12.0(2)$ MHz and $p_\ell = -11(1)$ MHz. We modeled the anomalous line intensities of the forbidden band with mixing coefficients representing vibronic perturbations in the excited state. The anomalous intensities arise from quantum interference between TDMs from the perturbing $\tilde{B}(010)$, $\mu(010)$, and $\kappa(010)$ states. From the Zeeman spectra, we found the magnetic tuning of $\tilde{X}(010)$ is consistent with an effective isotropic electron spin g-factor, $g_S = 2.07(2)$. From the Stark spectra, we extracted the molecule-frame dipole moment of 2.16(1) D. These values are in good agreement with the parameters of the $\tilde{X}$ state.

In our study, the hyperfine structure and higher-order Zeeman g-factors were unresolved. Our work provides a basis for future studies with narrow-linewidth methods, such as RF, microwave, and two-photon spectroscopy, to precisely determine these properties.

This work is an essential step towards measurements of CP-violating physics in YbOH [17], as well as other metal hydroxide molecules proposed for CP violation and parity violation searches that utilize the parity doublets in the bending mode. We showed the $\tilde{X}(010)$ state ℓ-doubling offers spectroscopically resolvable states of molecule polarization pointing along, against, and perpendicular to the applied electric field, over a wide range of field values. This orientation control over the dipole moment offers robust systematic error rejection without compromising laser cooling. The combination of these features make linear polyatomics a promising platform for new physics searches. With our measured data, we can compute the EDM sensitivity, which is proportional to the electron spin projection on the internuclear axis, Σ. We find a local maximum value of $\langle \Sigma \rangle = 0.40$ in the $N = 1, J = \frac{1}{2}^+$ state at $E = 101$ V/cm, similar to what was predicted in prior theoretical work [117, 139]. Furthermore, understanding the structure of ^{174}YbOH is a step toward characterizing the more complicated structure of the odd isotopologues ^{171}YbOH and ^{173}YbOH, which have sensitivity to parity violation [304] and hadronic CP violation [57], respectively.

Lastly, our determination of the $\tilde{X}(010)$ location and structure is crucial for understanding the complicated excited state structure in YbOH. For example, with our knowledge of the bending

frequency, we can tentatively assign the unknown [17.33] band in Ref. [217] to the $\tilde{X}^2\Sigma^+(010) \rightarrow \tilde{A}^2\Pi_{1/2}(010)$ band. This would put the excited $\tilde{A}^2\Pi_{1/2}(010)$ manifold at approximately $17652\,\mathrm{cm}^{-1}$. This state is an excellent candidate for optically pumping population from $\tilde{X}$ into $\tilde{X}(010)$, an important step for signal-to-noise-ratio improvements in precision measurements using the bending mode. Furthermore, the location of $\tilde{X}(010)$ is necessary for the determination of repumping pathways for laser cooling, slowing, and trapping of YbOH, toward next-generation CP violation searches.

4.3 The Bending Excited State

4.3.1 Introduction

With the ground state bending mode characterized, we moved on to finding optical pumping pathways to further populate the state and perform coherent manipulations. Since YbOH has fairly diagonal FCFs, the majority of spontaneous decays conserve the vibrational state, i.e., ∼90% of decays satisfy $\Delta v_{1,2,3} = 0$. This makes the bending states of the $\tilde{A}^2\Pi_{1/2}$ manifold ideal for optical pumping from $\tilde{X}(000)$ into the ground bending state, $\tilde{X}(010)$. In related fashion, the bend-to-bend transitions will have strong optical TDMs, greatly aiding our $\tilde{X}(010)$ state preparation and readout efforts in Ch. 5 Sec. 5.3. In particular, we are interested in the $\Omega = 1/2$ excited states with $v_2 = 1, |\ell| = 1$. We will often abbreviate the label $\tilde{A}^2\Pi_{1/2}(010)$ to just $\tilde{A}(010)$, with the understanding that we are not discussing the $|\Omega| = 3/2$ states.

The interactions of orbital electronic angular momentum L with vibrational angular momentum ℓ, known as Renner-Teller [170] (RT) or vibronic interactions, are the subject of many experimental and theoretical works. As the molecule bends, Λ can deviate from integer values, though in practice we set $|\Lambda| = 1$ and consider RT effects as perturbative corrections. RT interactions are discussed in various molecular physics textbooks, including: Herzberg [295, 305], Hirota [129], Bunker and Jensen [140], Demotroder [135], and Duxbury [306], to name a few. Additionally, Ref. [307] provides an excellent historical review on the Renner-Teller effect.

For experimentalists working with effective Hamiltonians, we will provide an overview of useful references here. First, Ref. [151] by Brown provides both a pedagogical overview and a concise summary of the relevant information. Brown originally derived the effective Hamiltonian for RT effects in Ref. [156], and added centrifugal effects in Ref [159]. Brown and Jørgenson provide a detailed discussion of the RT effect in Ref. [173], including a comparison of multiple approaches to the problem. Jungen and Merer also provide extensive discussion in Ref. [308], where they model RT effects with both linear and bent molecule limits. Anharmonic effects are considered in Refs. [309] and [172].

For theorists performing first principles calculations, vibronic coupling refers to derivative

couplings in the Hamiltonian, $\partial H_e / \partial q$, where q is a normal vibrational coordinate, and H_e is the electronic Hamiltonian [135]. This interaction is non-adiabatic, i.e., couples the electronic and nuclear degrees of freedom, and is neglected under the Born-Oppenheimer approximation. For calculations with vibronic coupling, theorists use quasi-adiabatic states and the KDC Hamiltonian, first presented in Ref. [303]. This formalism was used in Ref. [144] to perform first principles vibronic calculations for M-OH molecules and obtain predictions for vibrational branching ratios. Furthermore, we also note the theory work of Refs. [310, 311], where the authors derive a vibronic spin-orbit term that can couple ℓ and Σ, in other words mixing $\Omega = 1/2$ and $\Omega = 3/2$. They argue this effect is most prominent in when spin-orbit and vibrational splittings are approximately equal, such as in the GeCH molecule [312]. In the effective Hamiltonian picture, this interaction is referred to as a Sears resonance [312]. Since our $|\Omega|$ states are well separated in YbOH, we do not concern ourselves with this interaction, but we mention it for completeness.

Often it is useful to consult papers where effective Hamiltonians were used to model experimental molecular spectra. RT effects have been studied in many molecules, and here we provide a brief list of possibly useful references: $CuCl_2$ [313], BS_2 [314], BO_2 [315], CO_2 [316], CaOH [147, 317], SrOH [301, 318], GeCH [312], SiCH [319], NCS [320], NCO [171, 321], NCN [169], CCN [168], CaCCH [322], and HCCS [323]. Many of these papers provide effective Hamiltonians. In particular, while we focus on $v_2 = 1$, we note Ref. [321] has effective Hamiltonians (written with analytic matrix elements) for arbitrary v_2. Meanwhile Ref. [312] "shows their work" when constructing the effective Hamiltonian, which can be instructive.

In the $v_2 = 1$ manifold, RT interactions couple Λ and ℓ together to form the composite projection $K = \Lambda + \ell = \vec{N} \cdot \hat{n}$. If we add spin-orbit coupling, then it is useful to consider the total projection $P = \Lambda + \ell + \Sigma = \vec{J} \cdot \hat{n}$. If we just consider interactions within the $v_2 = 1$ manifold, then P is a good quantum number. However, we shall see that parity doubling interactions can mix both K and P values. This makes sense, as parity doubling in the effective Hamiltonian actually encodes off-diagonal interactions with other vibrational or electronic manifolds, which generally have different projection quantum numbers.

In Figure 4.8, we provide a schematic diagram of the energy levels of a $S = 1/2$, $|\Lambda| = 1$ electronic state in both $v_2 = 0$ and $v_2 = 1$ vibrational states. We label states with vibronic term symbol notation, $^{2S+1}K_P$, with $K = \Sigma, \Pi, \Delta, \Phi, \ldots$. The spin-orbit interaction strength is given by A, and the RT interaction is parameterized by the constant ϵ. The behavior of the $v_2 = 0$ manifold is familiar to us from the $\tilde{A}(000)$ state. Meanwhile, in the $v_2 = 1$ manifold, with just Renner-Teller coupling active, we obtain three vibronic states: $^2\Sigma^+$, $^2\Sigma^-$, and $^2\Delta$. Here, the $\Sigma^\pm$ label distinguishes $K = 0$ states obtained by a symmetric (+) or anti-symmetric (−) combination of states with $\Lambda = -\ell$. Adding spin-orbit causes the $^2\Delta$ state to split into $\Omega = 1/2, P = 3/2$ and
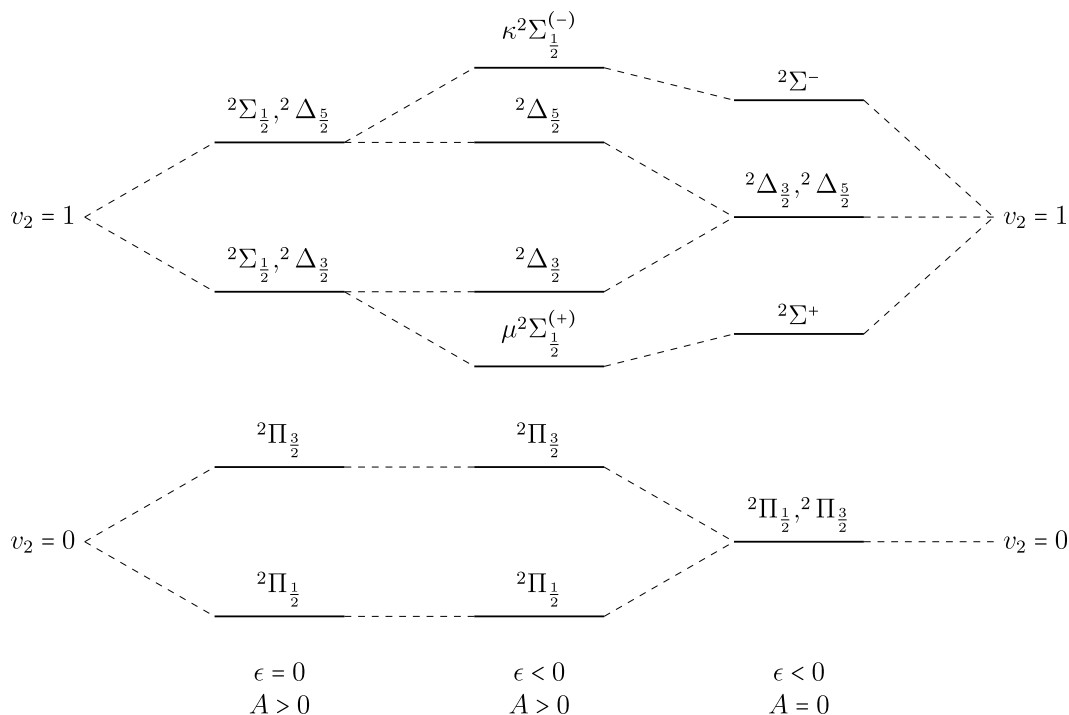
Figure 4.8: Level diagram showing the splittings of a $^2\Pi$ electronic state in $v_2 = 0, 1$ vibrational states. We label states with vibronic term symbol notation, $^{2S+1}K_P$. The spin-orbit strength is A, and the Renner-Teller (RT) interaction is given by ϵ. Dotted lines show the correlation of states as spin-orbit and RT interactions are turned on and off. We choose to show $\epsilon < 0$ and $A > 0$ to match the sign of these parameters in the M-OH molecules we consider. Diagram adapted from Ref. [295]. Thanks to Jane Panangaden for helping make the diagram.

$\Omega = 3/2, P = 5/2$ components. Spin-orbit also mixes the $\Sigma^\pm$ states, causing them to transition from case (b) to case (a) such that the $\pm$ label is no longer appropriate. Instead, these states are denoted as $\mu^2\Sigma_{1/2}^{(+)}$ and $\kappa^2\Sigma_{1/2}^{(-)}$, though often we will drop the $(\pm)$ superscript. We note Fig. 4.8 is drawn for $\epsilon < 0$, which is the case for M-OH molecules. This sign causes the $^2\Sigma^+$ state to be lower in energy than $^2\Sigma^-$. For $\epsilon > 0$, the energy ordering of the $^2\Sigma^\pm$ states is reversed.

4.3.2 Modeling Renner-Teller Effects

We will model the states using the Hund's case (a), parity-symmetrized basis:

$$
\left|\Lambda; v_2, \ell; S, \Sigma; J, P, M, \mathcal{P} = \pm\right\rangle
$$
$$
= \frac{1}{\sqrt{2}}\left(\left|\Lambda; \ell; \Sigma; J, P, M\right\rangle \pm (-1)^{p_a}\left|-\Lambda; -\ell; -\Sigma; J, -P, M\right\rangle\right). \tag{4.16}
$$

Here, $\mathcal{P} = \pm$ refers to positive/negative parity, and the Hund's case (a) parity phase factor is given by $p_a = J - S - \ell$, in accordance with the phase conventions of Hirota [129] and Brown [151, 159]. This phase factor has consequences the matrix elements that raise or lower ℓ, and therefore parity doubling parameters.

Since we have three projections ($\Lambda\ell\Sigma$) and each projection can take on two oppositely signed values, we will have to deal with 8 levels. To stay consistent, we will write states using a rule where the first state in superposition of eq. 4.16 has $\Lambda = 1$. Then we can write all the other quantum numbers if we know the K value of the state. For example, the $|\Omega| = 1/2$ states are written as:

$$\left|^2\Delta_{3/2}, \mathcal{P} = \pm\right\rangle =$$
$$\frac{1}{\sqrt{2}}\left(\left|\Lambda = 1; \ell = 1; \Sigma = -\frac{1}{2}; P = \frac{3}{2}\right\rangle \pm (-1)^{p_a}\left|\Lambda = -1; \ell = -1; \Sigma = \frac{1}{2}; P = -\frac{3}{2}\right\rangle\right) \tag{4.17}$$

$$\left|\mu^2\Sigma_{-1/2}, \mathcal{P} = \pm\right\rangle =$$
$$\frac{1}{\sqrt{2}}\left(\left|\Lambda = 1; \ell = -1; \Sigma = -\frac{1}{2}; P = -\frac{1}{2}\right\rangle \pm (-1)^{p_a}\left|\Lambda = -1; \ell = 1; \Sigma = \frac{1}{2}; P = \frac{1}{2}\right\rangle\right). \tag{4.18}$$

Here, we have explicitly written the μ state as $^2\Sigma_{-1/2}$. This notation makes it clear the $(-1)^{p_a}$ phase factor is on the $P > 0$ ket, unlike the case in $^2\Delta$ when $(-1)^{p_a}$ multiplies the $P < 0$ ket.

For completeness, we mention that our method of writing states needs modification if we consider other v_2 states. For $v_2 = 1$, the $|K| > 0$ states all have $|K| = |\ell| + |\Lambda|$. In the literature, these states are referred to as "unique" states [151]. However, if we were to consider higher v_2, for example $v_2 = 3$, we could have states with $|K| > 0$ that are written $|K| = |\ell| - |\Lambda|$. In such a case, thinking again in the example of $v_2 = 3$, we have two ways of writing $|K| = 2$, one as $|\ell_2| - |\Lambda|$ with $|\ell_2| = 3$, and the other as $|\ell_1| + |\Lambda|$ with $|\ell_1| = 1$. To distinguish these two states in general, we can modify our rule to write ℓ_1 states with $\Lambda = 1$ in the first ket of the superposition (the one not multiplied by the parity phase), and write the ℓ_2 states with $\Lambda = -1$ as the first ket in the superposition.

As stated earlier, the effective Hamiltonian for the Renner-Teller effect was first derived by Brown in 1977 [156], and subsequently refined upon in later contemporary works [151, 159] that provide comprehensive summaries. The Renner-Teller interaction contributes the following terms to the effective Hamiltonian:

$$H_{RT} = \frac{1}{2}\epsilon\omega_2\left(q_+^2 e^{-2i\theta} + q_-^2 e^{2i\theta}\right) + g_K(G_z + L_z)L_z + \frac{1}{2}\epsilon\omega_{2,D}\left(q_+^2 e^{-2i\theta} + q_-^2 e^{2i\theta}\right)\vec{N}^2 \tag{4.19}$$

Here, θ is the electronic azimuthal coordinate, and $q_\pm$ are dimensionless raising and lowering operators for the vibrational angular momentum G, with matrix elements available in the literature [129, 143, 151, 173]. The term $\epsilon\omega_2$ is the Renner-Teller coupling term derived originally by Renner [170], g_K is a correction derived by Brown [156] that encodes the change in Λ caused by bending-induced mixing with other electronic states, and $\epsilon\omega_{2,D}$ is the centrifugal correction to the Renner-Teller interaction [159], which we do not consider further but have included for completeness.

The $\epsilon\omega_2$ term in H_{RT} has the following selection rules: $\Delta\Lambda = -\Delta\ell = \pm 2, \Delta v_2 = 0, \pm 2, \Delta K = 0, \Delta\Sigma = 0, \Delta P = 0$. From these selection rules, it is clear that for a $^2\Pi(010)$ state, the RT interaction within a v_2 manifold only has non-zero off-diagonal matrix elements among the $K = 0$ states. There will be matrix elements connecting to other vibrational states, and these can be taken into account using perturbation theory for $|\epsilon| \ll 1$ (i.e., in the harmonic approximation, anharmonic correcitons are discussed elsewhere [309]). Refs. [151, 156, 312] discuss effective Hamiltonian perturbation theory for RT effects in detail.

The main parameters that define our vibronic state are the spin-orbit splitting A, harmonic bending energy ω_2, and Renner-Teller parameter ϵ. For YbOH, we are interested in the regime when $A \gg |\epsilon\omega_2|$. This is the case for certain triatomic molecules studied in the literature–CaOH [147], SrOH [301], GeCH [312], $CuCl_2$ [313], OCS^+ [324], $BrCN^+$ [325–329], and ICN^+ [330, 331]. In these molecules, the vibronic states are split by the Renner-Teller interaction and grouped by common values of $|\Omega|$. In particular, both $BrCN^+$ and ICN^+ additionally satisfy $A > \omega_2$, which means spin-orbit effects must be considered at zeroth order in the derivation of the effective Hamiltonian, when considering off-diagonal vibrational perturbations. The two $|\Omega|$ groups essentially become separate electronic states, and the vibronic states are pushed together and heavily mixed by the parity-doubling interactions, with K no longer a good quantum number.

We can gain further insight by considering an effective Hamiltonian matrix derived by Brown and coworkers considering spin-orbit at zeroth order, explicitly presented in analytic form Refs. [313] and [151]. The same effective Hamiltonian is presented in operator form in Refs. [168, 169]. We note that Ref. [313], $\pm$ refers to e/f parity [332], while in Ref. [151], $\pm$ refers to overall parity. As an aside, for perturbative spin-orbit, analytic formulae are given in Ref. [315]. We reproduce the effective Hamiltonian matrix for strong spin-orbit below in Table 4.2, correcting for minor typos, but dropping all centrifugal distortion terms for convenience. For the origin, we replace 2ω with $T_0 + \omega$, where T_0 is the origin of the $\tilde{A}(000)$ manifold, including zero-point harmonic energy. The Hamiltonian is block diagonal in J in the absence of hyperfine effects. Because no state can exist with $|P| > J$, the Hamiltonian is 2x2 for $J = 1/2$, 3x3 for $J = 3/2$, and 4x4 for $J \geq 5/2$.

We now discuss the matrix elements. As expected, the diagonal energies receive dominant contributions from spin-orbit A, and the g_K term offsets the origin of the $^2\Delta$ states. The terms with $2\omega \pm A$ in the denominator contribute to the Δ and Σ splittings within each $|\Omega|$ manifold. To estimate this splitting, we first note that we expect YbOH to have similar vibronic coupling strength to CaOH [144], providing an estimate of $\epsilon \sim -0.1$. The value of g_K is harder to approximate, as it encodes mixings with distant Δ and Σ electronic states that occur as the molecule bends. In CaOH, $g_K \approx 0.5$ cm^{-1} [147], but in other molecules with nearby perturbers, it has been observed to be larger, $g_K \sim 10$ cm^{-1} [312, 319]. It is likely the g_K value of YbOH is influenced by mixing with

136

$^{(2S+1)}K_P$ $\Lambda,\ell,\Sigma,\pm$	$^2\Delta_{5/2}$ $1,1,1/2$	$^2\Delta_{3/2}$ $1,1,-1/2$	$\kappa^2\Sigma_{1/2}$ $1,-1,1/2$	$\mu^2\Sigma_{-1/2}$ $1,-1,-1/2$
$^2\Delta_{5/2}$ $1,1,1/2$	$T_0+\omega+2g_K$ $-\dfrac{3(\epsilon\omega)^2}{2(2\omega-A)}$ $+\dfrac{A}{2}$ $+B(z-4)$	$-(z-3)^{\frac12}B^*$	$-\dfrac{q_G}{2}(z^2-z)^{\frac12}$	$\pm(-1)^{p_a}\dfrac{q_e}{2}$ $\times(z^2-3z)^{\frac12}$
$^2\Delta_{3/2}$ $1,1,-1/2$		$T_0+\omega+2g_K$ $-\dfrac{3(\epsilon\omega)^2}{2(2\omega+A)}$ $-\dfrac{A}{2}-\gamma+Bz$	$\pm(-1)^p\dfrac{q_e}{2}$ $\times(z^2+z)^{\frac12}$ $+\dfrac{p_G+2q_G}{2}z^{\frac12}$	$\mp(-1)^p$ $\times\dfrac{p_e+2q_e}{2}z^{\frac12}$ $-\dfrac{q_G}{2}(z^2+z)^{\frac12}$
$\kappa^2\Sigma_{1/2}$ $1,-1,1/2$			$T_0+\omega$ $-\dfrac{(\epsilon\omega)^2}{2(2\omega-A)}$ $+\dfrac{A}{2}$ $+B(z+2)$	$-(z+1)^{1/2}B^*$ $\mp(-1)^p\epsilon_{\text{corr}}\omega$
$\mu^2\Sigma_{-1/2}$ $1,-1,-1/2$				$T_0+\omega$ $-\dfrac{(\epsilon\omega)^2}{2(2\omega+A)}$ $-\dfrac{A}{2}-\gamma$ $+B(z+2)$

Table 4.2: The effective Hamiltonian within the $\tilde{A}(010)$ manifold. The matrix is symmetric about the diagonal. For $J=1/2$, the matrix is only the bottom right 2x2 block and for $J=3/2$, only the bottom right 3x3 block. The upper/lower signs refer to $\pm$ overall parity. The parity phase is $p=J-S-\ell$. For brevity we write: $z=(J+1/2)^2-1=J(J+1)-3/4$; $B^*=B-\gamma/2$; $\omega=\omega_2$; and $\epsilon_{\text{corr}}=\epsilon\left(1+\frac{(\epsilon\omega)^2}{4}\frac{8\omega^2-6A^2}{(4\omega^2-A^2)^2}\right)$.

$4f$ states as well as the $\tilde{B}\Sigma^+_{1/2}$ state. Nonetheless, by taking $g_K\sim0.5$ cm^{-1} and $A\sim1350$ cm^{-1}, we find that the splitting of vibronic states is approximated as $E_{\Delta\Sigma}\sim-10^{-2}\epsilon\omega_2+2g_K\lesssim1$ cm^{-1} for large spin-orbit coupling. However, when the Δ and Σ vibronic states are pushed so close together, they will be mixed by any interaction that can couple them at the $\sim0.01-1$ cm^{-1} level, namely rotation and parity-doubling/coriolis effects. We must therefore investigate the off diagonal entries of 4.2.

The off-diagonal elements of the matrix encode interactions that can flip molecule frame angular momentum projections, as discussed in Ch. 2, Sec. 2.2.3. When these interactions couple

the two reversed projections (i.e., $+\Lambda$ and $-\Lambda$) of a parity state, we obtain parity factors of $(-1)^p$ and factors of $\mp$ arising from the phase convention for matrix elements of the electronic angle $e^{2i\theta}$. The term $B^* = B - \gamma/2$ arises from the $\vec{J} \cdot \vec{S}$ spin-uncoupling terms from both the rotational and spin-rotational Hamiltonians. The remaining terms of interest are all the p and q parity-doubling terms, as well as the off-diagonal Renner-Teller coupling $\epsilon_{corr}\omega_2$, which also has parity dependence. Note, both references [151, 313] have minor typos in the expression for ϵ_{corr}, which is a sort of spin-orbit correction the Renner-Teller parameter (analogous to the Renner-Teller correction to spin-orbit in the perturbative spin-orbit treatment). The effect of this correction is minor, as for large A, we have $\epsilon_{corr} \approx 1$.

The parity-doubling effects are grouped into purely rotational effects, represented by q_G and q_e, and spin-orbit-rotational effects, represented by p_G and p_e in case (b) and the combination $p + 2q$ in case (a). All of these terms arise at second order in the effective Hamiltonian and involve couplings to a different electronic state and back. In the limit of mixing with a unique perturber, the Curl relations relate the scale of the two effects by $q \sim pB/A$ [167], noting that the p effects are dominant with large spin-orbit. For this reason, and because we focus on the $|\Omega| = 1/2$ manifold, we can neglect the $^2\Delta_{5/2}$ state, which is only coupled off-diagonally by q terms.

All parity doubling Hamiltonians have $\Delta J = 0$ selection rules. We are most interested in the electronic doubling H_Λ, given by:

$$
\begin{aligned}
H_\Lambda &= \frac{1}{2}(p_e + 2q_e)\left(J_+S_+e^{-2i\theta} + J_-S_-e^{2i\theta}\right) - \frac{q_e}{2}\left(J_+^2 e^{-2i\theta} + J_-^2 e^{2i\theta}\right) \\
&= (p_e + 2q_e)\sum_{q=\pm 1} e^{-2iq\theta}T_{2q}^2(J,S) - q_e\sum_{q=\pm 1} e^{-2iq\theta}T_{2q}^2(J,J)
\end{aligned}
\tag{4.20}
$$

where $q = \pm 1$ subscripts are in the moelcule frame, θ is the azimuthal electronical angle, and the second line is written with spherical tensor notation. Recall terms such as $e^{\pm 2i\theta}$ are raising/lowering operators for the angular momentum $L_z = -i\frac{\partial}{\partial \theta}$. Further, H_Λ has the following selection rules [147]: $\Delta\ell = 0, \Delta\Lambda = \pm 2, \Delta\Sigma = 0, \mp 1$, and $\Delta P = \pm 2, \pm 1$. We note the pairs of selection rules correspond to the two different Λ-doubling interactions, purely rotational (J_+^2) and spin-orbit-rotational (J_+S_+).

The vibrational doubling Hamiltonian, H_ℓ, can be obtained eq. 4.20 by making the following replacements: $p_e \rightarrow p_G, q_e \rightarrow q_G, \theta \rightarrow \theta$. As a result, H_ℓ has similar selection rules [147]: $\Delta\ell = \pm 2, \Delta\Lambda = 0, \Delta\Sigma = 0, \mp 1$, and $\Delta P = \pm 2, \pm 1$. Once again, the pairs of selection rules refer to the two different doubling interactions, q_G and $p_G + 2q_G$ type[6].

To be explicit, in this section, we use the phase conventions from Refs. [39, 151, 159, 168,

---

[6]We use the G subscript to maintain consistency with Sec. 4.2, and with Refs. [151, 169, 333]. In Ref. [147], the subscript v is used instead.

169]:

$$\langle \Lambda = \pm 1 | e^{\pm 2i\theta} | \Lambda = \mp 1 \rangle = -1 \tag{4.21}$$

$$\langle \ell = \pm 1 | e^{\pm 2i\phi} | \ell = \mp 1 \rangle = 1. \tag{4.22}$$

By examining the selection rules and Table 4.2, we see both Λ-type and ℓ-type doubling can mix the $^2\Sigma$ and $^2\Delta$ states, in what is called a "K-resonance" in the literature. K-resonances have been observed previously in many of the molecules mentioned earlier in this section. These resonances can manifest as level repulsion or even avoided-level crossings. The full K-resonance Hamiltonian, $H_K = H_\Lambda + H_\ell$, has many off-diagonal couplings, requiring full diagonalization of the effective Hamiltonian.

We consider the scale of the parity splittings of levels in $\tilde{A}(010)$, which can provide information on the degree of K-resonance present. An isolated $|P| > 1$ state, such as the $^2\Delta_{3/2}$ state, is expected to have small parity splitting, as the doubling interactions we consider have $\Delta P = \pm 2, \pm 1$ selection rules. Therefore, any parity interaction with $|\Delta P| > 2$, which is required to connect P and $-P$ levels with $|P| > 1$, must occur at second order in the effective Hamiltonian[7] or higher. Incidentally, this provides an intuitive understanding of why parity splittings are small in a spin-orbit split, electronic $^2\Pi_{3/2}$ state ($E_{3/2\pm} \lesssim$ MHz). In such a case, the $P = 3/2$ state must be connected to $P = -3/2$ via the $^2\Pi_{1/2}$ state, and the coupling is mediated by q_e and B. This provides an overall parity splitting of $\Delta E_{3/2\pm} \sim q_e B / A$. We can compare this to the p_e dominated parity splitting of the $P = 1/2$ state by recalling the approximate relation $q_e \propto p_e B / A$ [39]. Therefore, the $\Delta E_{3/2\pm}$ splitting is smaller than the $\Delta E_{1/2\pm}$ splitting by a factor of $B^2 / A^2 \lesssim 10^{-7}$. By the same logic, if the vibronic $^2\Delta_{3/2}$ state is isolated, its parity splitting is expected to be quite small, with relevant contributions to become parity-dependence in other off-diagonal couplings, or in neglected higher order terms, such as the centrifugal Renner-Teller correction [159].

The parity splitting of the μ and κ $^2\Sigma_{1/2}$ states also arises from off-diagonal terms, but is expected to be larger than for the $^2\Delta$ states. Consider the case of $J = 1/2$, when we only have the $^2\Sigma - 1/2$ states active in the model. The primary[8] parity-dependent contribution arises from the $\mp(-1)^P \epsilon_{\text{corr}} \omega_2$ term mixing the two Σ states. Depending on the sign, $B^* \approx B$ adds constructively or destructively. This provides a rough scale for the parity splitting:

$$\begin{aligned} \Delta E_\pm &\approx \frac{(B + \epsilon\omega_2)^2}{A} - \frac{(B - \epsilon\omega_2)^2}{A} \\ &= 4\frac{B\epsilon\omega_2}{A}. \end{aligned} \tag{4.23}$$

---

[7] Note that effective Hamiltonian terms like H_Λ or H_ℓ are already themselves actually higher-order combinations of other interactions in the full molecular Hamiltonian.

[8] There is explicit diagonal parity-dependence in the centrifugal distortion term $\epsilon\omega_{2D}$. This term is $\sim 10^{-3}$ cm^{-1} in CaOH, so we do not consider it further.

For YbOH, this splitting is expected to be ~ 700 MHz, which is spectrally resolvable, and results in very different dc polarizability when compared to the case of <MHz splitting. Therefore the parity splitting of the levels we observe can give us insight into the degree of mixing present between different vibronic levels. Crucially, the $J = 1/2$ Σ states cannot be mixed with Δ states, as the parity couplings satisfy $\Delta J = 0$ and the states must satisfy $J \geq |J \cdot \hat{n}| = |P|$.

Since we are spin-orbit dominated, the $p_e + 2q_e$ electronic Λ doubling term is primarily responsible for the K mixing of the $|\Omega| = 1/2$ manifold. This was the case in CaOH [147] and SrOH [301], where the vibronic states are initially separated by ~ 10 cm^{-1}, and have an avoided level crossing at higher J. However, in YbOH, the vibronic levels are expected to be much closer. In the $v_2 = 0$ state of YbOH, we have $p_e + 2q_e \approx -0.44$ cm^{-1} (-13 GHz), which is of the same order of the Δ and Σ state splitting we estimated earlier. If the vibronic levels are right on top of each other, they will be fully mixed for all J. Intuitively, we can think of this new state configuration as having $\langle |K| \rangle \approx 1$. In such a case the energies look like that of a case (b) $^2\Pi$ state, with both $P = 3/2$ and $P = 1/2$ components present. We can think of the combination of spin-orbit and rotational effects, encapsulated in H_Λ, as "quenching" the electronic angular momentum, resulting in only the bending degree of freedom. This is similar in spirit to the case of asymmetric molecules, where the electronic angular momentum can be smaller than its maximum possible projection due to anisotropic spin-rotation and spin-orbit effects [123]. We will discuss K-resonances further when we examine the energy level structure observed in the experiment.

4.3.3 Apparatus

The setup is similar to that described in Sec. 4.2.1, with an identical CBGB source. However, the beamline now has two interaction regions, an upstream "pump" region, to deplete the ground state, and a donwstream "probe" region, to probe the depletion. After the collimated molecule beam exits the source, it enters the pump region: a 6-way KF50 cross, ~40 cm downstream from the cell aperture. There, the molecules encounter the pump beam, which travels transverse to the molecule beam, is cylindrically shaped (~1 × 3 mm), and is retroreflected with orthogonal polarization. The fluorescence is monitored using a stack of collection optics mounted 125 mm away from the molecules, outside the vacuum chamber.

After being pumped, molecules then travel further downstream to the probe region ~60 cm away from the cell. The region is a KF50 octagon, the same from Sec. 4.2.1. As described there, the molecules first travel through a metal collimator plate before entering an interaction region between two ITO-coated glass electrodes. We can also apply magnetic fields to this region using coils mounted outside the vacuum chamber. The molecules in the interaction region encounter a probe laser (~1 mm diameter, single pass), and their fluorescence is collected with an in-vacuum
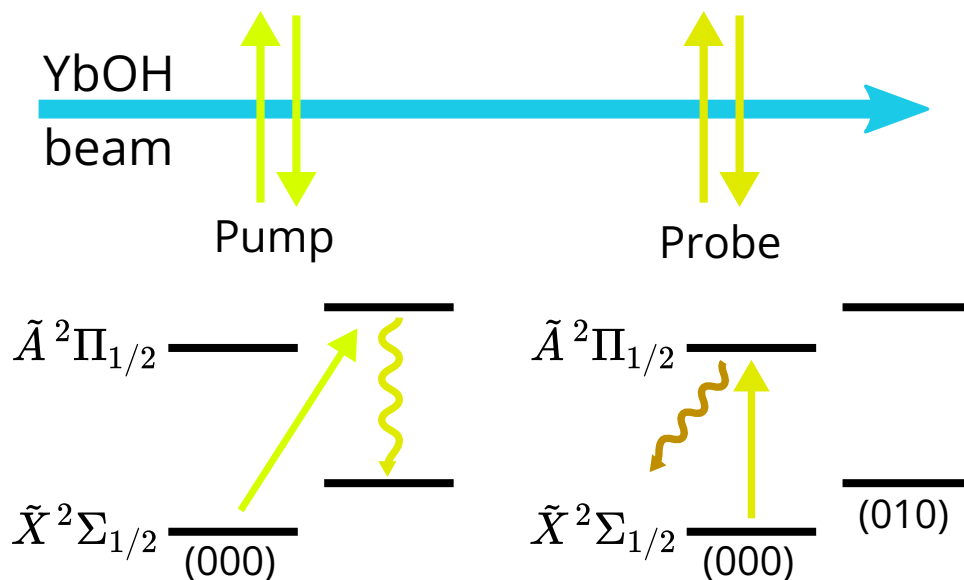
Figure 4.9: Schematic diagram of the beamline used for pump probe experiments to study the $\tilde{X}(000) \rightarrow \tilde{A}(010)$ transition. Upstream, the pump light is scanned. Downstream, the probe light monitors a single rotational level in $\tilde{X}(000)$. If the pump laser hits a resonance, we will see fluorescence in the pump region. Furthermore, if the pump addresses the same ground state as the probe, then we will observe correlated loss of the probe fluorescence.

light pipe and an in-vacuum retroreflecting mirror.

In both regions, the collected fluorescence passes through optical filter stacks consisting of both interference and colored glass filters, before arriving at a Hamamatsu H13543 PMT module. The filters are setup to detect light off-diagonally, as there is too much on-diagonal light scatter. In the pump region, the PMT photocurrent is amplified and low pass filtered with an SRS SR570 current preamplifier, while in the probe region, the photocurrent is amplified and low pass filtered with a Pluto Instruments PCG-380F current preamplifier.

The setup was designed to look for correlated fluorescence. Typically, the upstream pump beam is scanned, while the downstream probe is held fixed on a line of interest. Correlation of increased upstream fluorescence with loss of downstream fluorescence indicates both transitions share a common ground state.

4.3.4 Observations

We began by searching for the $\tilde{X}^2\Sigma^+ \rightarrow \tilde{A}^2\Pi_{1/2}(010)$ transition in the upstream pump region. Depletion caused by the pump was probed downstream using the $\tilde{X}^2\Sigma^+ - \tilde{A}^2\Pi_{1/2}(000)$ transition at 577 nm and detecting the off diagonal fluorescence to (100) at 595 nm. The schematic setup is shown in Figure 4.9.

Though the excited $\tilde{A}^2\Pi_{1/2}(010)$ state had not yet been assigned, we were able to estimate its

location. Motivated by the similarity of the spectra for the [17.33] band and the origin band, we assigned the [17.33] transition to $\tilde{X}^2\Sigma^+(010) \rightarrow \tilde{A}^2\Pi_{1/2}(010)$. This was previously assigned as a transition out of $\tilde{X}^2\Sigma^+$ [217]. With our reassignemnt, and using the origin of the $\tilde{X}^2\Sigma^+(010)$ state determined in this work, we were able to estimate the location of the excited $\tilde{A}^2\Pi_{1/2}(010)$ state to be ~17652 cm^{-1}. We used a Sirah MixTrain to generate the required 567 nm light, and the fluorescence collection filters were chosen to detect off diagonal fluorescence at 577 nm, corresponding to $\tilde{A}^2\Pi_{1/2}(010) \rightsquigarrow \tilde{X}^2\Sigma^+(010)$ decays.

The first scan immediately found two strong lines near 17652.14 cm^{-1}, shown in Figure 4.10. These lines were split by $\sim$ 122 MHz, matching the $N'' = 1$ spin-rotation splitting in $\tilde{X}(000)$. This splitting provided strong evidence that we had observed transitions originating from the ground state. This assignment was verified by observing depletion of the $N'' = 1$ states of $\tilde{X}(000)$, downstream in the probe region, only when the pump was on resonance. Note that depletion was only observed after increasing power in the pump beam from $\sim$ 10 mW to $\sim$ 100 mW, indicative of the forbidden nature of the non-bend to bend transition. A similar set of lines, split again by the $N'' = 1$ spin-rotation splitting, were also found near 17651.37 cm^{-1}, shown in Figure 4.10. Further depletion tests confirmed these lines *also* originated from $N'' = 1$ in $\tilde{X}$.

Since the observed lines originate from $N'' = 1^-$, consisting of both a $J'' = 1/2^-$ and $J'' = 3/2^-$ state, the excited state must be either $J' = 1/2^+$ or $J' = 3/2^+$, in accordance to the parity selection rule and the $\Delta J = \pm 1, 0$ selection rule[9]. To identify the excited state J quantum number, we searched for a P line that could only arise from a $J'' = 5/2^- \rightarrow J' = 3/2^+$ transition. Since the levels of the $\tilde{X}$ state are well known, searching for this P line is simply a matter of detuning the pump laser by the energy difference between $N'' = 3, J'' = 5/2^-$ state and the $N'' = 1, J'' = 3/2^-$ state.

To our surprise, we observed P lines corresponding to *both* the excited state of the 17652.14 cm^{-1} lines and the excited state of the 17651.37 cm^{-1} lines. The ground state assignment of these P lines was confirmed by observing depletion of an $N'' = 3, J'' = 5/2^-$ probe downstream. This meant we had observed *two* $J' = 3/2^+$ excited states, separated by ~23 GHz. The large energy separation rules out the possibility that these two states arise from hyperfine mixing of J. Since each vibronic state should only have one state with a given J and parity, we arrived at the conclusion that we had observed the $J' = 3/2^+$ components of two separate vibronic states, namely the $\mu^2\Sigma_{1/2}^{(+)}$ and $^2\Delta_{3/2}$ states in the $\tilde{A}^2\Pi_{1/2}(010)$ manifold. Such an arrangement of $^2\Sigma$ and $^2\Delta$ vibronic states, separated by $\lesssim$ 1 cm^{-1}, may arise in the context of large spin-orbit coupling and relatively weak Renner-Teller coupling.

---

[9]We do not consider $\Delta J = \pm 2$ transitions in the even isotopologues, as they would only receive strength from weak mixing from the distant hydrogen hyperfine interaction. In the odd isotopologues, large hyperfine mixing from the Yb nuclear spin makes the appropriate selection rule $\Delta F = \pm 1, 0$.
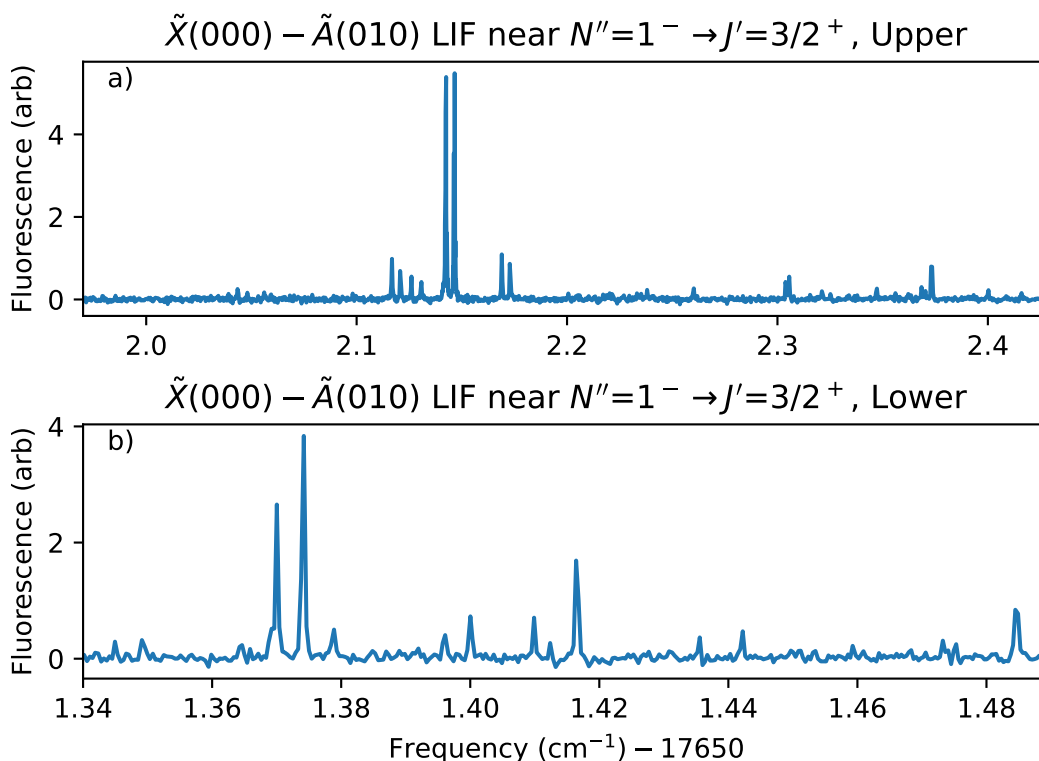
Figure 4.10: Sample LIF spectra obtained from excitation of the $\tilde{X}(000) \rightarrow \tilde{A}(010)$ transition. a) The two largest features correspond to $Q_{11}(1)$ and $R_{12}(1)$ lines addressing the upper $J' = 3/2^+$ state. b) The two largest features correspond to a second pair of $Q_{11}(1)$ and $R_{12}(1)$ lines addressing the lower $J' = 3/2^+$ state.
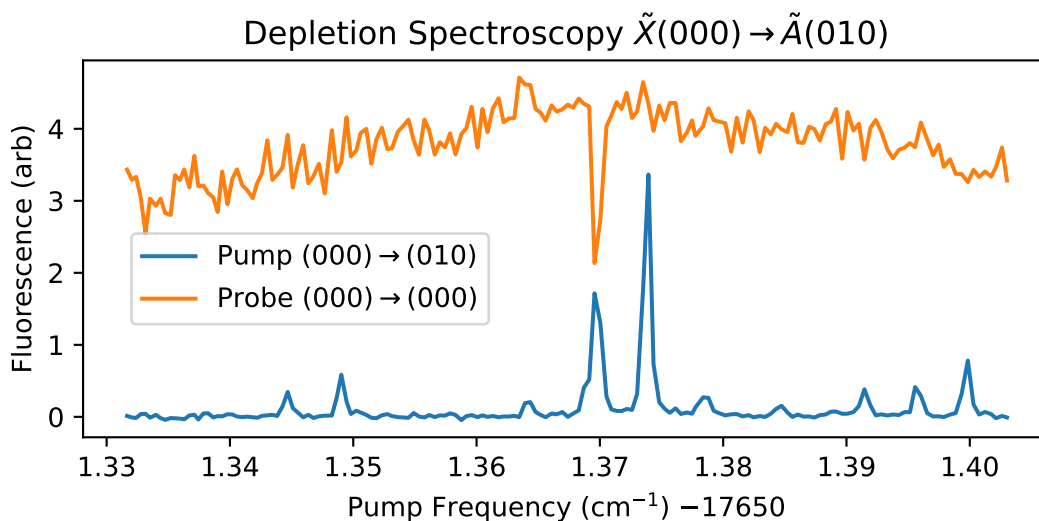
Figure 4.11: Sample depletion spectra obtained from pump-probe spectroscopy. The upstream pump laser is scanned over the $\tilde{X}(000) \rightarrow \tilde{A}(010)$ features shown in Fig. 4.10b, with LIF plotted in blue. Meanwhile, the downstream probe is fixed on a $\tilde{X}(000) \rightarrow A(000)$ line probing $N'' = 1, J'' = 1/2^-$, with LIF plotted in orange. The depletion signal at 17651.37 cm^{-1} shows both pump and probe share a common ground state.

The pump-probe technique that we used to identify the $\tilde{A}^2\Pi_{1/2}(010)$, $J' = 3/2^+$ states was readily applicable to the rest of the $\tilde{X}^2\Sigma^+ \to \tilde{A}^2\Pi_{1/2}(010)$ band. A benefit of this approach is that it is agnostic to the vibronic character of the excited states. The downstream probe was parked on a known $\tilde{X}^2\Sigma^+ \to \tilde{A}^2\Pi_{1/2}(000)$ transition, usually in the Q branch for technical convenience. Meanwhile, the upstream $\tilde{X}^2\Sigma^+ \to \tilde{A}^2\Pi_{1/2}(010)$ pump was scanned across lines of interest. LIF was monitored from both the upstream pump and downstream probe regions. Downstream depletion correlated with upstream signal provides a definitive assignment of the ground state. An example of a depletion spectrum is shown in Fig. 4.11.

The observed lines and their assignments are presented in Table 4.3. Definitive excited assignments were made for excited states where all three P, Q, and R lines were observed. However, the lack of observation of one of these lines cannot be interpreted as an indication that such a line does not exist. The TDM for the unobserved line could simply be weak due to transition interference from intensity borrowing, as was seen in the $\tilde{X}^2\Sigma^+(010) \to \tilde{A}^2\Pi_{1/2}(000)$ spectrum. Nonetheless, many lines could be definitively assigned. In Table 4.3, we also show the $\tilde{A}(010)$ state energy obtained by subtracting the energy of the $\tilde{X}(000)$ from the observed transition energy.

When the $\tilde{A}^2\Pi_{1/2}(010)$ energies are plotted (Fig. 4.13, a clear rotational structure is present. By comparing the expected rotational constant ($B \sim 0.25$ cm^{-1} ~ 7.5 GHz) to the observed energies, we can refine our initial J assignments for ambiguous lines. State assignments in Tab. 4.3 marked with an asterisk ($*$) represent assignments made based on rotational pattern matching, as opposed to definitive assignment based on observation of all three P, Q, R features. Our dataset therefore consists of 10 levels, 5 of each parity, with 2x degeneracy of a given parity for $J > 1/2$.

The parity doublet structure of the excited state is on the scale of ~ 500 MHz (0.017 cm-1) for all observed states. While this is in contrast to what would naively be expected for an isolated $P = 3/2$ state, it is in good agreement with the ~ 700 MHz parity doubling scale estimated earlier in Sec. 4.3.2. The fact that all observed levels indicate similar parity splitting is further indication of the strong mixing between Δ and Σ vibronic states.

4.3.5 Hamiltonian Fit and Discussion

With the location of 10 levels in $\tilde{A}^2\Pi_{1/2}(010)$ known to $\sim$0.001 cm^{-1} (30 MHz) precision, we move on to modeling the state by fitting to the effective Hamiltonian in Table 4.2. First, we reduce the number of fit parameters, using approximations and constraints informed by trends in other similar molecules. We fix p_e to the value obtained for the $\tilde{A}^2\Pi_{1/2}(000)$ state, $p_e = -0.4378$ cm^{-1}. This approximation holds well in both CaOH [147] and SrOH [301]. However, while most references fix $p_G = 0$, we do not, as we generically expect $p_G \neq 0$ in $\tilde{A}(010)$, considering we found $p_G \neq 0$ in $\tilde{X}(010)$. Further, by inspection of the effective Hamiltonian, we see the q_G and

Table 4.3: Characterized $\tilde{X}^2\Sigma^+(000) - \tilde{A}^2\Pi_{1/2}(010)$ lines. Wavenumber readings are taken obtained from a HighFinesse WS7-30 wavemeter, which has an absolute frequency error of 0.001 cm^{-1}. Lines are grouped by common excited state. The excited state energy is obtained by adding the observed transition wavenumber with the energy of the $\tilde{X}^2\Sigma^+$ ground state, which obtained from exact diagonalization without hyperfine. The final excited state energy is reported as an average of the excited state energies obtained from all common lines. The variation of the energy obtained from each line is on the order of ~0.0005 cm^{-1} or less. The "Evidence" column reports the basis behind the ground state assignment. "Depletion" means the ground state was observed to be depleted by the transition of interest. "Splitting" means the splitting of the transition from other lines matches the energy splitting expected in the ground state.

Observed Line (cm^{-1})	$N'', J'', \mathcal{P}''$	$J', \mathcal{P}'$	Excited State (cm^{-1})	Evidence
17 650.9630	$1, 3/2, -$	$1/2^*, +$	17651.4518	Splitting
17 650.9588	$1, 1/2, -$	$1/2^*, +$		Splitting
17 649.9938	$1, 1/2, -$	$1/2^*, -$	17 651.4685	Depletion
17 651.8464	$0, 1/2, +$			Depletion
17 650.3787	$2, 5/2, +$	$3/2, -$	17651.8466	Depletion
17 650.3719	$2, 3/2, +$			Splitting
17 651.3741	$1, 3/2, -$			Depletion
17 651.3700	$1, 1/2, -$	$3/2, +$	17651.8628	Depletion
17 648.9158	$3, 5/2, -$			Depletion
17 652.6182	$0, 1/2, +$	$3/2^*, -$	17 652.6182	Depletion
17 652.1465	$1, 3/2, -$			Depletion
17 652.1424	$1, 1/2, -$	$3/2, +$	17652.6353	Depletion
17 649.6884	$3, 5/2, -$			Depletion
17 649.9157	$3, 5/2, -$			Depletion
17 649.9251	$3, 7/2, -$	$5/2, +$	17652.8624	Splitting
17 652.3733	$1, 3/2, -$			Splitting
17 651.4165	$2, 5/2, +$			Depletion
17 651.4096	$2, 3/2, +$	$5/2, -$	17652.8845	Depletion
17 647.9756	$4, 7/2, +$			Depletion
17 653.6298	$1, 3/2, -$			Depletion
17 649.9251	$3, 5/2, -$	$5/2, +$	17654.1210	Splitting
17 652.3733	$3, 7/2, -$			Splitting
17 651.6782	$2, 5/2, +$	$5/2^*, -$	17654.1462	Splitting
17 650.6716	$2, 3/2, +$			Splitting

* The excited state assignment is more tentative in the case when multiple lines are not observed, in which case the assignment is marked with an asterisk $*$.

Table 4.4: Effective Hamiltonian parameters used to model the $\tilde{A}(010)$ state of YbOH. See main text for details.

Parameter*	YbOH $\tilde{A}(010)$
ω_2	327.83(1)
A	1350[†]
B	0.2527(5)
g_K	0.22(1)
ϵ	−0.066(7)
$\epsilon\omega_2$	−21.6(11)
p_e	−0.4378[†]
q_e	0[†]
p_G	−0.46(8)
q_G	0[†]
γ	0[†]

* All parameters are given in cm^{-1}, except for ϵ, which is unitless. Parentheses represent 2σ errors (68% confidence interval). $\epsilon\omega_2$ is obtained by multiplication and propagation of errors.

[†] These values were fixed, see main text for details.

q_e terms have independent contributions only between the $\Omega = 3/2$ and $\Omega = 1/2$ manifolds. Since our measurements are only of the $\Omega = 1/2$ manifold, the effects of q_e and q_G are drowned out by p_e and p_G terms, and therefore we set $q_e = q_G = 0$. For q_e, this approximation is justified by the unique perturber relation [39, 167], $q_e \approx p_e B/A \approx 2 \times 10^{-4} p_e$, which is beyond our level of sensitivity. For q_G, the approximation is justified by the small value of $q_G = -0.0004$ cm^{-1} obtained for the $\tilde{X}(010)$ state. In general we expect q_G to be similarly small in $\tilde{A}(010)$ as it arises predominantly from Coriolis effects that only depend on the vibrational state [147, 167, 301]. As is usual for YbOH, we fix $A = 1350$ cm^{-1}, and we also fix $T_0 = 17998.5875$ cm^{-1}, corresponding to the $\tilde{A}^2\Pi_{1/2}(000)$ origin[10] [264]. Finally, we fix $\gamma = 0$, which is justified by the form of the Hamiltonian in Table 4.2, where the effects of γ are largely indistinguishable from B and origin offsets. Empirically, the predictions were not very sensitive to γ, justifying our approximation.

The remaining fit parameters are then $\omega_2, \epsilon, B, g_K$, and p_G. For initial values of the parameters, we used $\omega_2 = 330$, we approximate $p_G = p_E$, and the rest of the initial values were taken either from CaOH $\tilde{A}(010)$ (ϵ, g_K) or YbOH $\tilde{A}(000)$ (B, γ). With these initial values, we use Nelder-Mead optimization to determine a first set of fit parameters, and then use those parameters as initial values for Levenberg-Marquardt non-linear least-squares fitting to obtain final parameters.

The fits are able to accurately model the observed energy levels with a residual standard deviation of ≈ 0.0012 cm^{-1} (36 MHz), in good agreement with the experimental errors. However,

---

[10]This is in the R^2 formalism, see Ref. [39] 7.5.3 for details.

due to our limited dataset and many fit parameters, there are strong correlations ($> 90\%$) between ω_2, ϵ, and g_K, moderate correlation ($\sim 60\%$) of those parameters with p_G, and little correlation ($\sim 15\%$) with B. While the strong correlations could be removed by fixing ω_2, we decided not to, as this results in parameter uncertainties that were unreasonably small. Instead, in Fig. 4.12, we provide a plot of parameter confidence intervals, obtained from F-tests. The confidence intervals show the correlated nature of the parameters and provide a sense of our true uncertainties. As we will discuss, all of the parameter intervals correspond to physically reasonable values.

From the final fits, we obtain the parameter values shown in Table 4.4. A comparison of the model energy levels and the observed experimental energy levels is shown in Figure 4.13. Our value of $\epsilon\omega_2 \approx -22$ cm^{-1} is in good agreement with the CaOH value of -36 cm^{-1} [147] and the SrOH value of -31 cm^{-1} [301]. The Renner-Teller coupling is expected to decrease with increasing mass [147, 151]. According to the supplemental information of Ref. [144], the vibronic couplings ($\langle\frac{\partial H_e}{\partial q}\rangle$) are of similar size when comparing CaOH to YbOH. However, the separation of vibronic states increases with larger spin-orbit, and therefore we receive weaker contributions to the effective Hamiltonian parameters from mixing with other vibronic states.

The value of $\omega_2 \approx 328$ cm^{-1} is in good agreement with the frequency in the $\tilde{X}(010)$ state, where we found $\omega_2 \approx 320$ cm^{-1}. We note in our approximate treatment, we have not distinguished between harmonic and overall bending frequencies. In general, the bending frequency will receive anharmonic contributions, neglected here. A good discussion can be found in Ref. [309], and further Ch. 7 of Ref. [317] discusses various calculations of harmonic and anharmonic frequencies for CaOH.

Using $\epsilon\omega_2 \approx -22$ cm^{-1}, we can estimate the scale of mixings between the $\tilde{X}(010)$ and $\tilde{A}(000)$ states. These mixings were relevant for the earlier discussion (Sec. 4.2) of perturbations to $\tilde{X}(010)$. For example, contributions to axial spin-rotation, γ_G, can occur at third order: $\gamma_G \sim (\epsilon\omega_2)^2 A/(\Delta E_{\Pi\Sigma})^2 \sim 0.002$ cm^{-1} (65 MHz). This is slightly too large to explain the observed value, but we note the Renner-Teller parameter ϵ actually receives two contributions in the effective Hamiltonian [143, 173, 200, 312, 319, 334]: $\epsilon \approx \epsilon_1 + \epsilon_2$. These are the dipolar (ϵ_1) and quadrupolar (ϵ_2) contributions[11]. In CaOH, both of these terms were found to both be negative [200], and we expect a similar situation here. Only the dipolar ϵ_1 term is responsible for $\Sigma - \Pi$ mixing. This means we expect our earlier estimate using $\epsilon\omega$ to be too high. Further, its very possible there are multiple states contributing to the the axial spin-rotation effect, for example the $4f$ states. On the other hand, application of a similar estimate to obtain p_G from third order contributions of p_e is

---

[11]There can be some confusion, as some references instead use $\epsilon^{(2)}$ to instead refer to the dipolar contribution, since this term contributes to the effective Hamiltonian at 2nd order, and vice versa for $\epsilon^{(1)}$. Also, Ref. [172] has an extra factor of $(1 + \epsilon_1)^{-1}$, as mentioned at the end of Ch. 2.
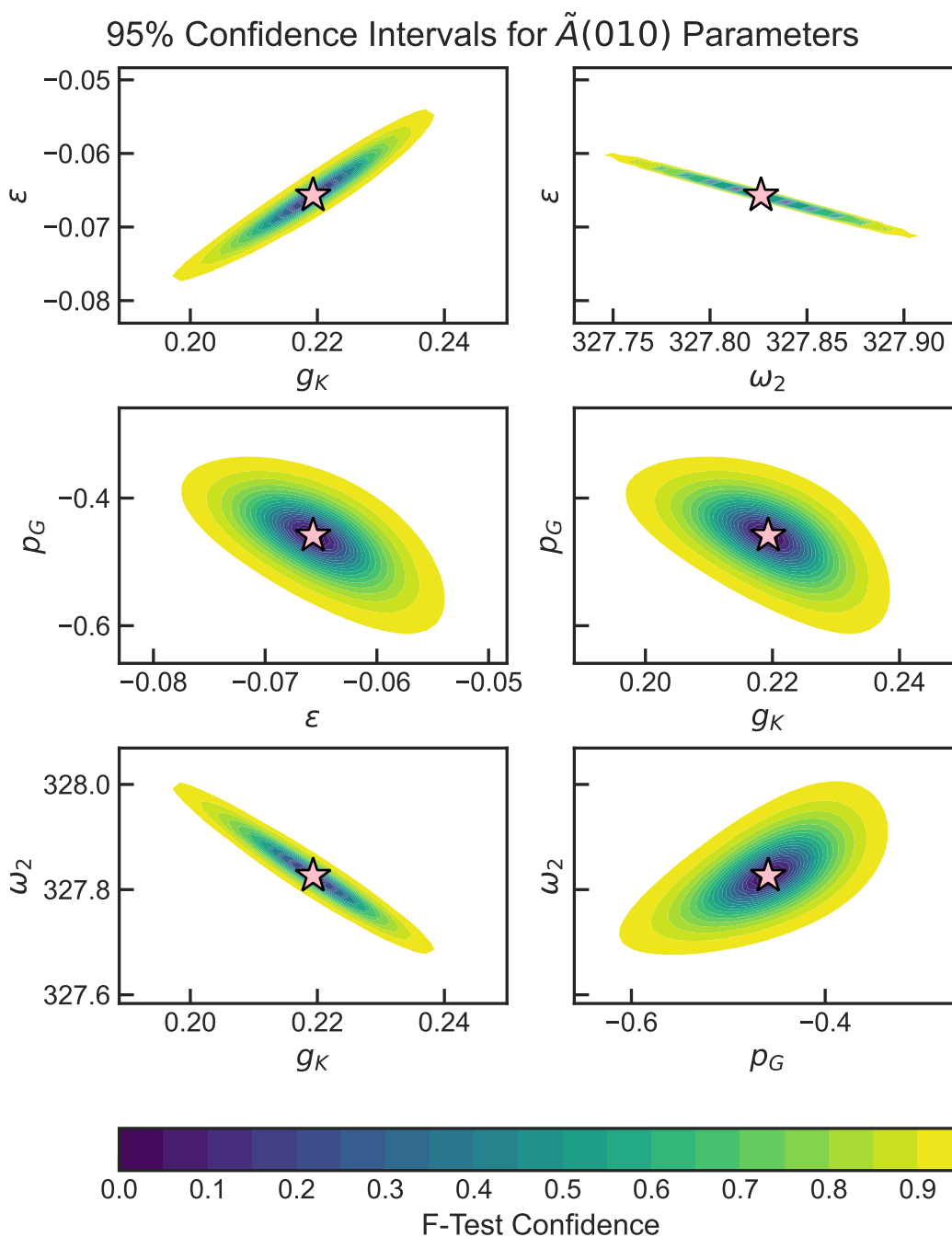
Figure 4.12: 2-D confidence interval plots of correlated parameters from the $\tilde{A}(010)$ effective Hamiltonian fits. See main text for details on parameters. Confidence intervals calculated using F-tests. The star indicates the best-fit parameter values. Though we observe strong correlations, overall the range of fit parameters have physically reasonable values, see main text for discussion.

Figure 4.13: Energy level diagram for the $\tilde{A}^2\Pi_{1/2}(010)$ manifold of YbOH. Assignemnts are given in terms of J and parity $\mathcal{P}$ quantum numbers. $\mathcal{P} = \pm 1$ levels are separated horizontally for clarity. The center of the diagram shows the levels observed in the experiment, while the dashed lines on the side shows the levels obtained from diagonalizing the Hamiltonian from Table 4.2 with the parameters provided in Table 4.4.

wildly inaccurate, as $A \gg p_e$. However, it is possible p_G receives contributions from $4f$ mixing as well, which can have very different matrix elements than what we estimate with $\epsilon\omega_2$.

Finally, we can set $H_K = 0$ in the model, essentially turning off the K resonance. This allows us to visualize the effects of the K-resonance. In Figure 4.14, compare the actual and deperturbed eigenvalues of the effective Hamiltonian. As we can see, the deperturbed Σ and Δ states are near degenrate. Turning on H_K mixes and splits the levels, with separation roughly given by $\Delta E \approx (p_e + 2q_e)(J(J+1) - 3/4)^{1/2}$.

To very good approximation, the resulting eigenstates are full mixtures of $^2\Delta$ and $^2\Sigma$, and as alluded to earlier, the mixed eigenstates have $\langle|K|\rangle = 1$. The resulting level pattern is similar to that of a case (b) $^2\Pi$ state, with large scale rotational structure characterized by N, and smaller scale spin-rotational splittings characterized by J. The "emergent" spin rotation splitting, on the order of $\gamma \sim 0.3$ cm^{-1} for the states we observe, is set by the combination of Λ-type doubling and overall rotation, very reminiscent of quenching of electronic angular momentum in non-linear polyatomic molecules [123]. We can compare this emergent γ value to an estimate of the contribution to the spin-rotation parameter in the $\tilde{A}^2\Pi_{1/2}$ state from second order mixing with the $\tilde{B}^2\Sigma^+$ state, given in [39], eq. 7.122. Using 602 cm^{-1} for the spin-orbit matrix element [144], 3152 cm^{-1} for the splitting between $\tilde{A}^2\Pi_{1/2}$ and $\tilde{B}$ [335], and using the pure precession hypothesis to evaluate $L_\perp^2 \sim \lambda(\lambda+1) = 2$, we obtain $\gamma \sim 0.38$ cm^{-1}. This is reasonable agreement, especially if we recall the spin-rotation splitting is $\frac{3}{4}\gamma$ for a bending $N = 1$ state.

To make the energy structure manifest for mixed vibronic character, we consider just the $|\Omega| = 1/2$ matrix elements in 4.2, obtaining a 2x2 matrix for all $J > 1/2$. We neglect the contributions at second order and higher from mixing with the distant $|\Omega| = 3/2$ states; these contributions can be taken into account via perturbation theory, if necessary. Then, we rewrite the 2x2 matrix in terms of a new basis, $|^2\Delta_{3/2}\rangle \pm (-1)^p|\mu^2\Sigma_{1/2}\rangle$, implemented with the unitary matrix $U = \frac{1}{\sqrt{2}}\begin{pmatrix} 1 & 1 \\ (-1)^p & -(-1)^p \end{pmatrix}$. Finally, we drop q_G, owing to its smaller magnitude compared to $p_e + 2q_e$. We then have:

$$H_{\text{eff}} = E_0 + BJ(J+1)$$
$$+ \begin{pmatrix} \mp\dfrac{p_e + 2q_e}{2}\left(J(J+1) - \dfrac{3}{4}\right)^{\frac{1}{2}} & g_K - B - \dfrac{(\epsilon\omega)^2}{2(2\omega + A)} \\ g_K - B - \dfrac{(\epsilon\omega)^2}{2(2\omega + A)} & \pm\dfrac{p_e + 2q_e}{2}\left(J(J+1) - \dfrac{3}{4}\right)^{\frac{1}{2}} \end{pmatrix} \quad (4.24)$$

where $E_0 = T_0 + \omega - \frac{A}{2} + g_K + \frac{B}{4} - \gamma - \frac{(\epsilon\omega)^2}{2\omega + A}$, and the upper/lower signs refer to overall parity. Now the Λ doubling terms contribute to the splitting of the two states, while the Renner-Teller effects

Figure 4.14: Deperturbation diagram of the $\tilde{A}^2\Pi_{1/2}(010)$ state of YbOH. The levels are obtained by diagonalizing Tab. 4.2 using the parameters in Tab. 4.4. We have grouped the levels on the right/left sides according to their rotationless e/f parity [332], where e levels have $\mathcal{P} = (-1)^{J-S-l}$ and f levels have $\mathcal{P} = -(-1)^{J-S-l}$.

cause mixing that attempts to restore the original vibronic basis. Using our fit parameters, we see the off-diagonal elements are fixed at ~ -0.3 cm^{-1} magnitude, while the on-diagonal elements scale like $(p_e + 2q_e)\sqrt{J^2 + J - 3/4}$, which becomes $\sim (p_e + 2q_e)(J + 1/2)$ for large J.

In conclusion, the $\tilde{A}(010)$ level of YbOH exhibits a rich and unique structure. To our knowledge, this is the first observation of a K-resonance severe enough that it changes the energy level pattern from case (a) to case (b). Using an effective Hamiltonian model, we have been able to provide an approximate, physical picture of the $\tilde{A}(010)$ state behavior, though further investigation is need to confirm our spectroscopic interpretation. In particular, it would help to identify higher J lines, and to determine the location of the $\Omega = 3/2$ manifold.

4.3.6 Bend to Bend Transitions

With the excited state energies characterized to reasonable accuracy, we moved on to identifying diagonal $\Delta v_2 = 0$ transitions out of $\tilde{X}(010)$. This band, designated $\tilde{X}^2\Sigma^+(010) \rightarrow \tilde{A}^2\Pi_{1/2}(010)$, is useful for bending mode manipulation. Due to the quasi-diagonal FCFs, the vibrational potential energy surface is similar between $\tilde{X}$ and $\tilde{A}^2\Pi_{1/2}$. Therefore the diagonal $\tilde{X}(010) \rightarrow \tilde{A}(010)$ band shares many characteristics in common with its $\tilde{X}(000) \rightarrow \tilde{A}(000)$ counterpart. The wavelength of the $\tilde{X}(010)$ transition is only 0.3 nm away from the $\tilde{X}(000)$ transition, allowing us to use the same lasers to generate diagonal $\delta v_2 = 0$ light. Furthermore, fluorescence decays are expected to be roughly similar: $\sim 90\%$ of decays should have $\Delta v_2 = 0$ and$\sim 9\%$ should have $\Delta v_2 = 1$, with the remaining 1% emitted to many possible states [144, 217].

We obtained $\tilde{X}(010) \rightarrow \tilde{A}(010)$ line predictions by subtracting the $\tilde{X}(010)$ energies (obtained via diagonalization) from the $\tilde{A}(010)$ energies listed in Table 4.3. The resulting lines for the lowest N'' states are around $17331 - 17332$ cm^{-1}. This is right where the so-called [17.33] band was observed in Ref. [217]—however, it had previously been assigned as a transition from $\tilde{X}(000)$ to an unknown excited state. Our work definitively re-assigns this band as originating from $\tilde{X}(010)$. Both Refs. [217, 335] have also observed features further blue around 17338 cm^{-1} and 17345 cm^{-1}. These could possibly be diagonal transitions involving $v_2'' = 2$ or higher states.

The apparatus is the same as that described in Sec. 4.3.3. In Figure 4.15, we provide a schematic diagram of the beamline. We now tune the upstream pump laser to the $\tilde{X} \rightarrow \tilde{A}(010)$ transition at 567 nm, detecting off diagonal decays to $\tilde{X}(010)$ at 577 nm. This optically pumps molecules from the ground state into the bending mode. Then in downstream region, we tune the probe laser to the $\tilde{X}(010) \rightarrow \tilde{A}(010)$ transition at 577 nm, detecting off diagonal 595 nm decays to the $\tilde{X}(110)$ state (see Ref. [144] for vibrational energies). Because we know the energies of all states involved—$\tilde{X}(000)$, $\tilde{X}(010)$, and $\tilde{A}(010)$—we did not need to take extensive spectra, and simply performed 100 MHz scale scans to confirm the line positions at high resolution.
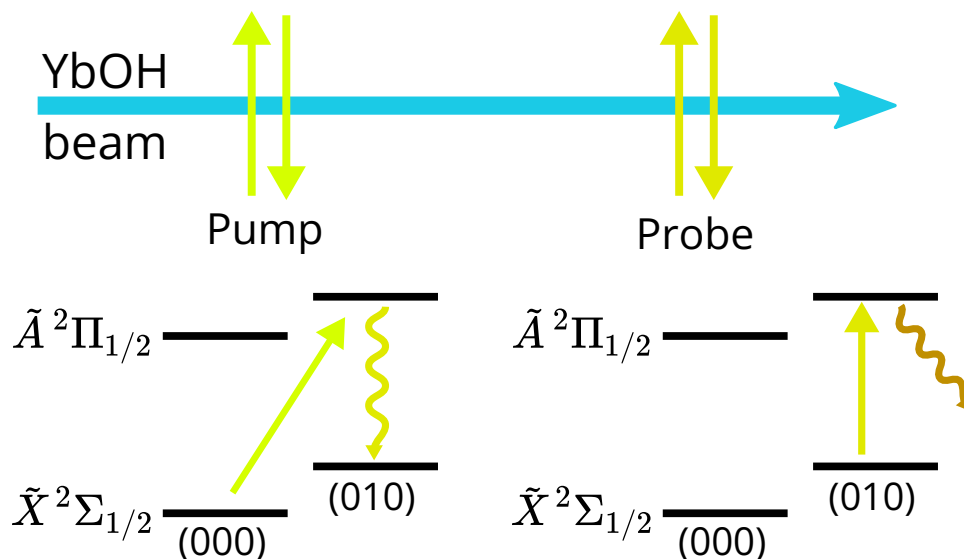
Figure 4.15: Schematic of the beamline used for tests of optical pumping into the $\tilde{X}(010)$ state and characterization of $\tilde{X}(010) \to \tilde{A}(010)$ lines. Upstream, the molecules are pumped out of $\tilde{X}(000)$ through the excited $\tilde{A}(010)$ state, decaying into $\tilde{X}(010)$. Downstream, we probe the increased fluorescence in the $\tilde{X}(010)$ state using the diagonal transition to $\tilde{A}(010)$.

We were able to identify multiple transitions from $N'' = 1, 2$ in $\tilde{X}(010)$ up to $J' = 1/2, 3/2$ in $\tilde{A}(010)$. The lines exhibit anomalous intensities that can be attributed to TDM interference caused by the K resonance. All transitions visible above the noise floor were found close to their predictions, giving faith in the excited state energies and assignments. In this pump-probe configuration, we can alternate pump on/off to characterize the optical pumping into $\tilde{X}(010)$.

In Fig. 4.16(a), we show an example of a scan over the $N'' = 1^-$ spin-rotation features when exciting up to the $J' = 3/2^+$ in the "$N' = 1$" manifold. We compare signals with and without 265 mW (before retro-reflection) of optical pumping light upstream. The optical pumping on $\tilde{X}(000) \to \tilde{A}(010)$ causes an increase of ~8x in the $\tilde{X}(010)$ population. The two spin-rotation features are blended, in part due to the small parity doubling, and in part due to power broadening by the 465 µW downstream probe ($I_0 \approx 98$ mW/cm^2, $s \sim 20$ for $I_s \approx 5$ mW/cm^2). On the other hand, the spectrum in Fig. 4.16(b) is taken with a 70 µW beam ($I_0 \approx 14$ mW/cm^2, $s \sim 3$), and the spin-rotation splitting is resolved to be 44.7 ± 3 MHz, another confirmation of the bending mode spectroscopy. The apparently low (~10 mW/cm^2) saturation intensity matches that for the diagonal $\tilde{X}(000) \to \tilde{A}(000)$ transition, which is another confirmation of the transition assignment. The low power requirements for saturation are a demonstration of the strong optical TDMs afforded by quasi-diagonal FCFs.

To further study the saturation intensity, we can fix the pump and probe frequencies at resonant values, and scan the pump power. The resulting data is shown in Fig. 4.17(a). The probe line
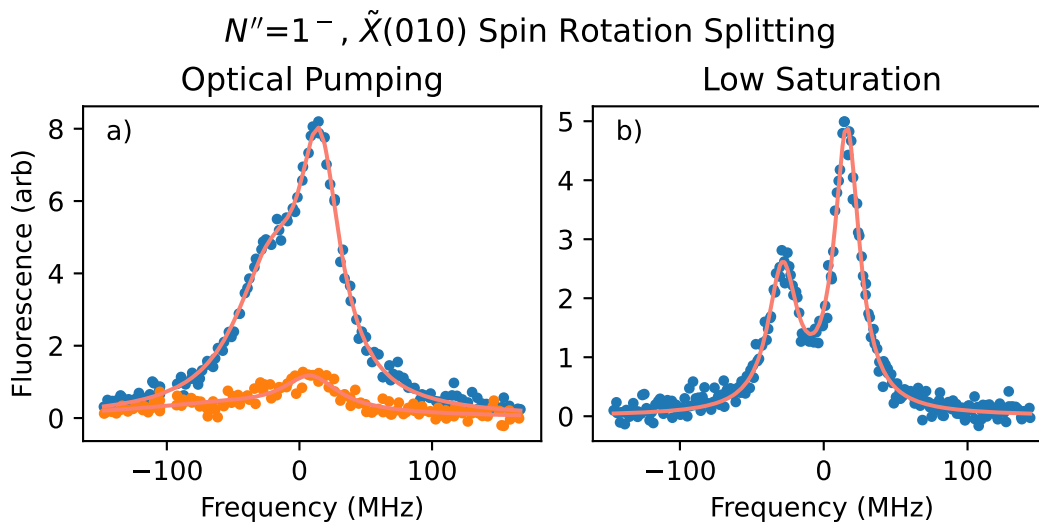
Figure 4.16: Sample LIF spectrum obtained from excitation of the $\tilde{X}(010) \rightarrow \tilde{A}(010)$ transition, driving the $J = 1/2, 3/2$ components of $N'' = 1^-$ to the lower $J' = 3/2^+$ state. The zero frequency offset is 17331.7093 cm^{-1}, and the line centers are fit to be 17331.7083 cm^{-1} and 17331.7098 cm^{-1}. a) Optical pumping into the bending mode is visible by comparing the blue (pump on) and orange (pump off) signals. The salmon lines are two Lorentzian fits. The optical pumping is performed with 265 mW of power, retroreflected, on the $\tilde{X}(000) \rightarrow \tilde{A}(010)$ line at 17651.3740 cm^{-1}, addressing the lower ($N' = 1$) $J' = 3/2^+$ state. As mentioned in the main text, the probe power of 465 µW in 1.1 mm diameter beam results in power broadening. b) The same spectrum taken with smaller frequency steps and 70 µW power. The optical pumping light is always on, and the salmon line is once again a two Lorentzian fit.

here is fixed 17331.4810 cm^{-1}, corresponding to the $N'' = 1, J'' = 1/2^- \rightarrow J' = 3/2+$ transition for the "$N' = 2$" manifold. We compare optical pumping results when addressing both the upper $N' = 2, J = 3/2^+$ state, and the lower $N' = 1, J' = 3/2^+$ state. Optical pumping into the bending mode is clearly visible, with the effect saturating around $\sim$100 mW, corresponding to $I \sim 4$ W/cm^2. We note the pumping efficiency varies with the J' state used. Furthermore, the transitions with larger bending mode pumping efficiency can actually demonstrate less overall LIF from the pump beam, shown in Fig 4.17(b). This can be understood due to different branching ratios and TDMs of the excited states.

The optical pumping we demonstrate will be an invaluable tool for experiments using YbOH. We note that the pumping efficiency can be further optimized with technical modifications. Increasing the number of laser passes will increase the interaction time and aid pumping efficiencies. Furthermore, applying microwaves in the pumping region can mix rotational states and increase the quantity of pumped molecules, a technique that was applied in ThO [67].

We also briefly performed Stark spectroscopy on the $\tilde{X}(010) \rightarrow A(010)$ transition, using the same apparatus outlined in Sec. 4.2.1. We specifically examined the lines shown in Fig. 4.16 at
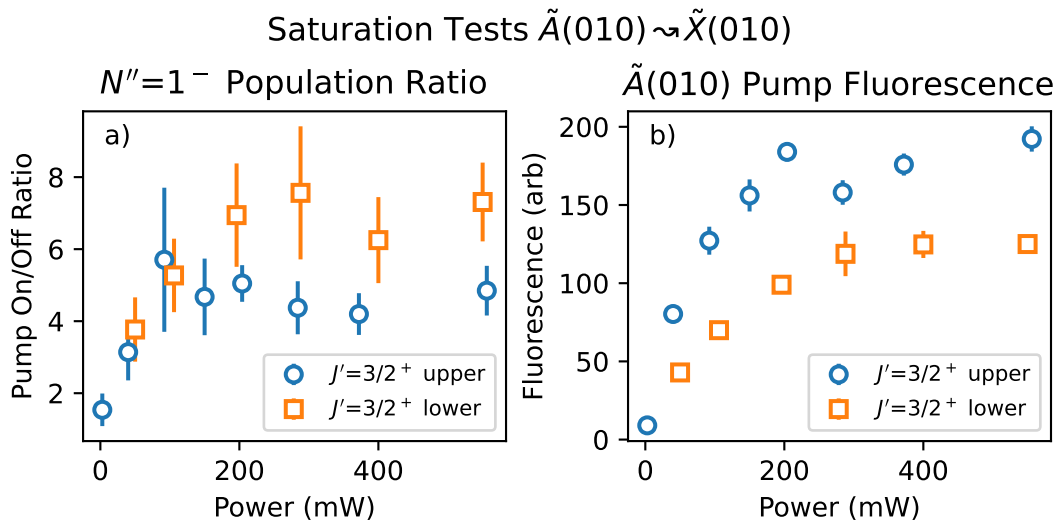
Figure 4.17: Saturation signals obtained by fixing the laser frequencies on a pump-probe pair of lines and scanning the pump power. In both plots, the probe was fixed on the $N'' = 1, J'' = 1/2^- \rightarrow J' = 3/2^+, N' = 2$ transition of the $\tilde{X}(010) \rightarrow \tilde{A}(010)$ band, while the pump was varied. In both plots, orange squares (blue circles) indicate the pump addresses the upper, $N' = 2$ (lower, $N' = 1$) $J' = 3/2^+$ state in $\tilde{A}(010)$. a) The ratio of pump on vs pump off population probed in the bending mode. The different excited states for pumping have different pumping efficiencies and saturate to different values. b) The fluorescence detected in the pump region when driving the $\tilde{X}(000) \rightarrow \tilde{A}(010)$ transitions at 17651.3740 cm^{-1} (lower) and 17652.1465 cm^{-1} (upper). The traces indicate both a difference in saturation intensity and saturation fluorescence.

different DC electric field values, up to 244 V/cm. The Stark behavior matched the spectra taken on the $\tilde{X}(010) \rightarrow \tilde{A}(000)$ band in Sec. 4.2.3.2. This is a confirmation that the excited state parity splittings are somewhat large. For example, using the 0.43 D dipole moment of $\tilde{A}(000)$, and estimating the parity splitting of $\tilde{A}(010)$ at $\Delta E \approx 500$ MHz, we find the second order energy shift from the $E = 244$ V/cm applied field to be $(D_\text{mol}E/2)^2/\Delta E \sim 1$ MHz, too small for us to resolve.

4.3.7 Transition Dipole Moments

While studying the optical pumping, we observed significant variation of the rotational branching ratios describing $\tilde{A}(010)$ decays to $\tilde{X}(010)$. For example, some excited states resulted in little to no pumping into $N'' = 1$, while others exhibited no pumping into $N'' = 2$. This is a result of transition dipole moment (TDM) interference from the K mixing of the excited vibronic states. Determination of TDMs on the $\tilde{X}(010) \rightarrow A(010)$ transition is of importance to science state preparation and readout schemes. Therefore we performed an investigation of the optical pumping efficiency of various $\tilde{A}(010)$ levels. Our characterization is not exhaustive, as the goal of our work is not a detailed determination of exact TDMs, but rather a heuristic understanding of useful transitions for optical pumping and science state control.

The lines we investigated are shown in Table 4.5. Typically, the pump was parked on a given excited state, driving $\tilde{X}(000) \rightarrow \tilde{A}(010)$, and the probe scanned across the $\tilde{X}(010) \rightarrow \tilde{A}(010)$ line. By sitting on the same probe and comparing different excited states, we can qualitatively assess which excited state has stronger TDMs with the ground state in question. In this way, we use the decay strength from $\tilde{A}(010)$ obtain TDM estimates for transitions that we have not explicitly observed in excitation on the probe spectrum (those marked with $*$ in the table).

Some interesting patterns emerge in the TDMs. First, we observe that the $\Delta J = 0$ lines addressing $J' = 1/2^{\pm}$ are completely missing. These lines were not observed in either probe fluorescence or optical pumping. Actually, the explanation for these missing lines is somewhat straightforward, given the $J' = 1/2$ states are *pure* $^2\Sigma_{1/2}$ vibronic states, as the $^2\Delta_{3/2}$ and $^2\Delta_{5/2}$ states cannot support $J = 1/2$. Therefore, we can consider the matrix elements for the transition in a straightforward manner. The ground state can be parameterized in Hund's case a) as symmetric and anti-symmetric combinations of case a) states:

$$\left| \tilde{X}(010), N'' = 1, J'' = \frac{1}{2}, \mathcal{P} = \pm \right\rangle =$$
$$\frac{1}{\sqrt{2}} \left(\left| \ell = 1, \Sigma = -\frac{1}{2}, P = \frac{1}{2} \right\rangle \pm (-1)^p \left| \ell = -1, \Sigma = \frac{1}{2}, P = -\frac{1}{2} \right\rangle \right). \tag{4.25}$$

Here, we use $\pm$ to denote the state parity, with the parity phase given by p. We have also suppressed $\Lambda = 0$ in the kets for brevity. The excited state can be written in a similar fashion:

$$\left| \mu^2 \Sigma_{1/2}(010), J' = \frac{1}{2}, \mathcal{P} = \pm \right\rangle =$$
$$\frac{1}{\sqrt{2}} \left(\left| \Lambda = 1, \ell = -1, \Sigma = -\frac{1}{2}, P = -\frac{1}{2} \right\rangle \pm (-1)^p \left| \Lambda = -1, \ell = 1, \Sigma = \frac{1}{2}, P = \frac{1}{2} \right\rangle \right). \tag{4.26}$$

Note we always must have $|\Omega| = 1/2$, as we are dealing with a strongly spin-orbit coupled molecule. Finally, because we are considering a $\Delta J = 0$ transition, the two p phase factors are identical, and we can drop the $(-1)^p$ factor.

Now we consider the selection rules for E1 transitions. The parity selection rule couples $+ \leftrightarrow -$ parity states. We will also have $\delta_{\Sigma'\Sigma''} = \delta_{\ell'\ell''} = 0$, owing to the properties of the TDM operator in the approximation of separated electronic, vibrational, and spin degrees of freedom. To evaluate the selection rules on Λ, recall the matrix element in the molecule frame, $\langle \Lambda' | T_q^1(d) | \Lambda'' \rangle$, is nonzero only if $\Lambda' - \Lambda'' = q$. In other words, the transverse TDM components (d_x, d_y) generate perpendicular bands with $\Delta\Lambda = \pm 1$, and d_z generates parallel bands with $\Delta\Lambda = 0$. Since we are considering a transition from $\Lambda'' = 0 \rightarrow \Lambda' = \pm 1$, we are coupling to the *perpendicular* components of the molecule frame TDM. Finally, from the rotation of $T^1(d)$ from the lab frame into the molecule frame, we obtain a 3j-symbol that constrains $\Delta P = \Delta\Lambda$ (we could have also derived this by noting Σ and ℓ do not change).

Table 4.5: Characterized $\tilde{X}^2\Sigma^+(010) - \tilde{A}^2\Pi_{1/2}(010)$ lines. Wavenumber readings are taken obtained from a HighFinesse WS7-30 wavemeter, which has an absolute frequency error of 0.001 cm^{-1}. Lines are grouped by ground N'' manifold and excited J' manifold. The excited states are also labeled by their emergent N' value (see main text). The qualitative TDM characterization has the following meanings: "Strong" means the ground state population downstream was increased by optical pumping upstream on a $\tilde{X}(000) \rightarrow \tilde{A}(010)$ transition addressing J'; "Weak" means the ground state population was not significantly increased by pumping; "Moderate" characterizes an intermediate pumping efficiency regime; "Unclear" means the data was inconclusive or not taken in our study; "Missing" means the probe line was looked for but not observed. Missing line frequencies are explicitly denoted with −.

Observed Line* (cm^{-1})	$N'', J'', \mathcal{P}''$	$N', J', \mathcal{P}'$	TDM Strength
17 331.2998	$1, 3/2, -$	$1, 1/2, +$	Strong
−	$1, 1/2, -$	$1, 1/2, +$	Missing
17 331.3145	$1, 3/2, +$	$1, 1/2, -$	Unclear
−	$1, 1/2, +$	$1, 1/2, -$	Missing
17 331.7098	$1, 3/2, -$	$1, 3/2, +$	Strong
17 331.7083	$1, 1/2, -$	$1, 3/2, +$	Strong
17 331.6929	$1, 3/2, +$	$1, 3/2, -$	Strong
17 331.6908	$1, 1/2, +$	$1, 3/2, -$	Strong
−	$1, 3/2, -$	$2, 3/2, +$	Missing
17 332.4810	$1, 1/2, -$	$2, 3/2, +$	Moderate
17332.4650*	$1, 3/2, +$	$2, 3/2, -$	Weak
17332.4630*	$1, 1/2, +$	$2, 3/2, -$	Weak
17330.7187*	$2, 5/2, +$	$1, 3/2, -$	Unclear
17330.7130*	$2, 3/2, +$	$1, 3/2, -$	Unclear
17330.7329*	$2, 5/2, -$	$1, 3/2, +$	Weak
17330.7265*	$2, 3/2, -$	$1, 3/2, +$	Weak
17 331.4900	$2, 5/2, +$	$2, 3/2, -$	Strong
17 331.4845	$2, 3/2, +$	$2, 3/2, -$	Strong
17 331.5048	$2, 5/2, -$	$2, 3/2, +$	Strong
17 331.4984	$2, 3/2, -$	$2, 3/2, +$	Strong

* Lines marked with ∗ are theory values. The lines are not necessarily missing, but simply were not searched for.

Now we consider the possible transitions. We could try, for example, to couple $P'' = \pm 1/2 \rightarrow P' = \mp 1/2$ states. However, we observe that this would involve coupling $\ell'' = \pm 1 \rightarrow \ell' = \mp 1$ states, which is explicitly forbidden for an E1 transition. Therefore, within the E1 selection rule, the transition $J'' = 1/2 \rightarrow J' = 1/2$ for the $\tilde{X}(010) \rightarrow \mu^2\Sigma_{1/2}(010)$ band is forbidden. We can see this clearly by considering a quantum number $\Omega_\ell = \ell + \Sigma$, which is invariant under E1 transitions, and captures the spin-bending alignment of a state. The excited state has $|\Omega'_\ell| = 3/2$, while the ground state has $|\Omega''_\ell| = 1/2$. Because the two states have opposite spin-bending alignment, they cannot be connected by an E1 transition. Further, we can surmise the $J'' = 1/2 \rightarrow J' = 1/2$ transition should be *allowed* when addressing the $\kappa^2\Sigma_{1/2}(010)$ excited state, which has ℓ and Λ flipped, and therefore has $|\Omega_\ell| = 1/2$.

The remaining TDMs for $J' > 1/2$ are more complicated, as we must now consider K-mixing between the Σ and Δ vibronic states, which will also mix $|\Omega_\ell|$. We consider the excited state as admixtures of $^2\Sigma_{-1/2}$ and $^2\Delta_{3/2}$, which can be treated as a coupled two level system, with superposition eigenstates characterized by a mixing angle θ [213]. For resonant K-mixing, $\cos\theta \approx 1/\sqrt{2}$, and we have:

$$\left|\tilde{A}^2\Pi_{1/2}(010), J, (\pm), \pm\right\rangle = \frac{1}{\sqrt{2}}\left(\left|^2\Sigma_{-1/2}, \pm\right\rangle (\pm)\left|^2\Delta_{3/2}\right\rangle\right)$$

$$= \frac{1}{2}\left(\left|\Lambda = 1, \ell = -1, \Sigma = -\frac{1}{2}\right\rangle \pm \left|\Lambda = -1, \ell = 1, \Sigma = \frac{1}{2}\right\rangle\right) \quad (4.27)$$

$$(\pm)\frac{1}{2}\left(\left|\Lambda = 1, \ell = 1, \Sigma = -\frac{1}{2}\right\rangle \pm \left|\Lambda = -1, \ell = -1, \Sigma = \frac{1}{2}\right\rangle\right).$$

Here, we use $(\pm)$ to denote the phase of the K mixture, which is determined by the Λ-doubling interaction. Meanwhile $\pm$ without parentheses denotes the rotationless e/f parity of the state [332], where e states are $+$ combinations and f states are $-$ combinations. We have used the convention where all states are written with $\Lambda = 1$ as the first element of the superposition [151]. We note these states are reminiscent of the states of a Hund's case (b) ket, $|NSJK\rangle$, written in terms of Hund's case (a). We can make this more manifest by rewriting the states using $\Omega = \Lambda + \Sigma$.

$$\left|\tilde{A}^2\Pi_{1/2}(010), J, (\pm), \pm\right\rangle$$

$$= \frac{1}{2}\left(\left|\ell = -1, \Omega = \frac{1}{2}\right\rangle \pm (\pm)\left|\ell = -1, \Omega = -\frac{1}{2}\right\rangle\right) \quad (4.28)$$

$$\pm \frac{1}{2}\left(\left|\ell = 1, \Omega = -\frac{1}{2}\right\rangle \pm (\pm)\left|\ell = 1, \Omega = \frac{1}{2}\right\rangle\right).$$

The spin-orbit coupling is so strong that the vibronic $P = 1/2, 3/2$ states are mixed and the state actually resembles a case (b) $^2\Pi$ state, which has both orientations Ω relative to ℓ. Indeed, if we

write out the bending ground state, we see it has a similar form:

$$\left|\tilde{X}^2\Sigma^+(010), N, J, \pm\right\rangle$$

$$= \frac{1}{2}\left(\alpha\left|\ell = 1, \Sigma = \frac{1}{2}\right\rangle + \beta\left|\ell = 1, \Sigma = -\frac{1}{2}\right\rangle\right) \tag{4.29}$$

$$\pm \frac{1}{2}\left(\alpha\left|\ell = -1, \Sigma = -\frac{1}{2}\right\rangle + \beta\left|\ell = -1, \Sigma = \frac{1}{2}\right\rangle\right)$$

Here, α and β are the real, normalized coefficients obtained form the Hund's case (a) to (b) unitary basis change, and generically depend on $N, J, \ell, \Sigma, \Lambda$ [129, 156]. The relative phase of α and β, along with their magnitudes, encodes the difference between the $N = J - S$ and $N = J + S$ components of a given J state. We can see the ($\pm$) mixing phase mimics the effect of the relative sign between α and β, and maps on to the extra quantum number N in the case (b) limit.

While our resonant mixing assumption results in equal admixtures of the two vibronic states, the coefficients α and β are generically not of the same magnitude for a given case (b) state. For example, a $N = 1, J = 3/2$ state contains more $P = 3/2$ admixture than the $N = 2, J = 3/2$ state, which can be intuitively understood as a consequence of spin-rotation alignment or anti-alignment. If the eigenstates are equal vibronic mixtures, then the transition will not exactly follow Hund's case (b) patterns. For example, for a $^2\Pi(b) - ^2\Pi(b)$ transition, Herzberg [336] mentions an approximate selection rule, $\Delta N = \Delta J$. This selection rule results from the fact that an E1 transition cannot flip a spin, so the spin-rotation state is preserved, and J only changes when N does. However, we are dealing with a perpendicular transition that nonetheless approaches a case (b) limit, and therefore we do not expect such a selection rule to hold. In particular, if spin-orbit is large, we cannot distinguish L from S, and we do not have the same notion of a "spin-flip."

Empirically, we find there is a $\Delta N = 0$ selection rule. This can be rationalized in the following way—in a transition, the photon angular momentum is transmitted to the electron orbit, while the bending rotation remains decoupled. Unfortunately, we did not take sufficient data to make further inferences. In particular data on whether or not such a selection rule holds for higher N states would be interesting. We are confident that with further investigation, the transition interference in the excited bending mode can be accurately modeled.

4.4 The State of YbOH

The YbOH spectroscopy necessary to perform a precision measurement of P, T violation in a beam has been completed. Nonethless, there still remain several outstanding spectroscopic questions regarding YbOH. Further investigation of these questions will be necessary to enable efficient laser cooling and magneto-optical trapping of YbOH for the next-generation of new physics searches. In this section, we outline the outstanding spectroscopic questions in YbOH.

4.4.1   4f States and Laser Cooling Prospects

YbF and YbOH are both affected by the existence of states corresponding to an electron being excited out of the inner-shell $4f$ orbital localized on the Yb atom. The study of these so-called $4f$ hole states is underway in YbF [291, 337]. These states both perturb the excited states and provide leakage pathways for optical cycling. In YbOH, evidence for perturbation from $4f$ states is present in many aspects of the spectroscopy already summarized, such as negative ground state spin-rotation constants [281], congested excited state spectra, with some states having ~100 ns lifetimes [217], and the value of $g_S = 1.86$ for the effective electron g-factor in the $\tilde{A}^2\Pi_{1/2}(000)$ state [282].

The existence of $4f$ hole states can be intuitively connected to the electronic configurations of the Yb$^+$ ion. In ligand field theory [137, 138], Yb containing molecules can be modeled as Yb$^+$ X$^-$ (X=F, OH, etc.), with the atomic $6s$ valence electron remaining localized on Yb. The ground state configuration of the Yb$^+$ ion is $^2S_{1/2}$, and there is an excited state $^2P_{1/2}$ with opposite parity, analogous to the $\tilde{X}$ and $\tilde{A}$ states. However, the Yb$^+$ ion also has metastable states that arise from the $4f^{13}6s^2$ configuration, with term symbols $^2F_{J_e}$, with two spin-orbit states with electronic angular momentum $J_e = 5/2, 7/2$, split by ~10000 cm^{-1}. These are the ionic counterpart to the $4f$ states in YbF and YbOH. We also note there are more $4f$ states in the Yb$^+$ ion, corresponding to $4f^{13}6s5d$ excitations (as well as $6s6p, 5d^2$, etc.). It is not currently known where such configurations are located in the molecule.

The ligand electric field splits the $J_e = 5/2$ manifold into $|\Omega| = 1/2, 3/2$, and $5/2$ states, each separated by ~1000 cm^{-1}. Because we are now discussing a valence hole, the spin-orbit interaction has opposite sign compared to the $\tilde{A}$ states, and therefore the anti-aligned $J_e = 5/2$ is higher in energy. These $J_e = 5/2$ states are expected to overlap with the "normal" (i.e., E1 allowed) excited states in the region ranging from $17600 - 20000$ cm^{-1}. One such perturbing state has already been identified in YbOH at 17731 cm^{-1}, denoted as [17.73] [217]. The $J_e = 5/2$ states in YbF have been characterized more thoroughly, summarized in a recent deperturbation analysis [291]. We expect their findings to generalize to YbOH, which would mean the $\tilde{A}$ and $\tilde{B}$ states are mixed with $4f$ states by a two-electron interaction with magnitude of roughly $50 - 100$ cm^{-1}. Further, there is the added extra complexity of the bending modes in YbOH, which result in a higher density of states, and in the possibility of vibronic mixing with the $4f$ states, which can mix Ω.

The lower $J_e = 7/2$ manifold is also split by the ligand field into $|\Omega| = 1/2, 3/2, 5/2$, and $7/2$ states. These states are expected to lie in the ~$7500 - 10000$ cm^{-1} range, which means they can be directly populated by decays from $\tilde{A}^2\Pi_{1/2}(000)$. The intensity borrowing for this decay is primarily caused by mixing of the $J_e = 7/2$ states with the $\tilde{X}$ manifold [291]. These low-lying leakage states have lifetimes in the ~$1 - 10$ ms range, too slow to wait for population to decay back

down to $\tilde{X}(000)$. However optically pumping these states is also a challenge, as transitions back to the manifold of $\tilde{A}$ and $\tilde{B}$ states are two-electron transitions with weak transition dipole moments.

Currently, decays to the $4f$ manifold are expected to arise at the ~0.05% level, limiting photon cycling of YbF and YbOH molecules to $1 - 2 \times 10^3$ photon scatters. While this is insufficient for laser cooling, slowing, and magneto-optical trapping, it is still adequate for 2D cooling [106], as well as for cycling in state preparation and readout. Therefore, in the medium term, beam experiments utilizing YbOH will be able to leverage optical cycling techniques to increase beam density, reduce divergence, and perform efficient state preparation/readout. However, in the long term, characterization of repumping schemes for the $4f$ states is necessary to realize precision measurements on laser-cooled and trapped YbOH molecules. Depending on the strength of the repumping transition, significant laser power may be necessary, although we note that weaker decay branches in the optical cycle do not need to be saturated in order to achieve adequate repumping.

Methods that can be used to identify the low-lying, $J_e = 7/2$ manifold of $4f$ states include:

1) Detection of DLIF from decays that populate the $4f$ states. For example, decays from the $\tilde{A}^2\Pi_{1/2}(000)$ manifold are expected to populate $4f$ states with $\sim 0.05\%$ branching. Detecting this scale of DLIF is additionally challenging as quantum efficiencies for cameras are typically worse in the infrared. Nonetheless, the Doyle group at Harvard has observed[12] a weak $\tilde{A}^2\Pi_{1/2}(000)$ DLIF feature at 1033 nm, corresponding to decays populating a low-lying $4f$ state. Based on comparisons with theory, this decay is thought to be down to the $\Omega = 1/2$ state, but the vibrational level is unclear. For YbF, the DLIF method was used to observe $4f$ states in Ref. [337]. They proceeded by first exciting to high-lying, $4f$ character electronic states around $31000 - 33000 \, \mathrm{cm}^{-1}$, and then detecting subsequent visible wavelength fluorescence, which has higher camera efficiency. While the ionization energy in YbOH is lower, a similar approach could still work by monitoring fluorescence from a high-lying excited state with $4f$ character, pushing the decays of interest into visible wavelengths.

2) Direct detection of transitions involving $4f$ states using FM absorption spectroscopy. FM absorption techniques can significantly increase the absorption detection threshold [220, 222] with standard experiments reaching sensitivities on the order of 10^{-4}, and advanced techniques pushing sensitivities to 10^{-6} [225, 338]. Infrared laser generation and detection technology is well developed, large molecular densities are present in the cell, and multi-pass absorption can help boost signal sizes. The standard approach would be to look for transitions from $\tilde{X}(000) \rightarrow 4f$. Alternatively, it is possible there is enough natural $4f$ population in the cell, after laser ablation and enhancement, to search for transitions from $4f$ states up to a known excited state, such as $\tilde{A}$ or $\tilde{B}$.

---

[12]This information was obtained in a private communication with Alex Frenett.

3) Optical cycling to populate $4f$ states, and then performing direct LIF detection of $4f$ repumping transitions. This typically would occur in a beam. First the molecules undergo optical cycling upstream. After sufficient interaction time, they will decay to the unaddressed $4f$ states. Then, downstream, a repump laser is scanned across a possible transition from $4f$ states to some excited state. Upon successful repumping, the $4f$ population returns to the ground state, and cycling can be performed again further downstream. This technique has been used to determine repumpers in YbOH [139] and CaOH [200], and is most effective when the rough location of the line is already known (to < 10 cm^{-1}). Direct detection of absorption has advantages is in contrast with optical cycling techniques; for example, in YbOH, pumping into the $4f$ states would require ~ 7 lasers.

4.4.2   Unassigned Bands

In this section, we overview the many transitions that have been observed in YbOH in the range from $17300 - 19000$ cm^{-1}. Ref. [217] performed initial survey spectroscopy with DLIF and excited state lifetime measurements. Meanwhile, in Ref. [335], REMPI spectroscopy was used to distinguish YbOH features from overlapped YbOCH$_3$ lines, and to perform spectroscopy on YbOD. In both references, the transitions are labeled according to their wavenumber in cm^{-1}, divided by 1000. For example, the $\tilde{X} - \tilde{A}$ band at 17323 cm^{-1} would be labeled as [17.32].

Transitions between the $\tilde{X}$ and $\tilde{A}$ vibrational manifolds can be grouped into various frequency ranges according to the change in vibrational quantum numbers. In an approximately harmonic approximation, $\Delta v_1 = \Delta v_2 = 0$ transitions are found in the $\sim 17300 - 17400$ cm^{-1} range. Meanwhile, $\Delta v_1 = 1$ transitions are found around 17900 cm^{-1}, and $\Delta v_2 = 1$ transitions around $\sim 17600 - 17700$ cm^{-1}, and so on. The proximity of different transitions with the same Δv indicates roughly similar ground and excited state vibrational energies, which is related to the diagonal nature of the FCFs.

We begin discussion of the states of YbOH with the [17.73] state. This is an $\Omega = 1/2$ excited state at 17731 cm^{-1} that has been identified to have significant $4f$ character [217]. The assignment is made both due to its ~ 5 times longer lifetime compared to the $\tilde{A}^2\Pi_{1/2}(000)$ state, and due to its rotational splittings in high-resolution spectra[13]. This state has also been successfully used for repumping population during laser cooling [106], confirming its assignment. Finally, this state was observed in a recent REMPI study [335], which studied the spectra of YbOD. The replacement of H with D, known as deuteration, can help better understand vibrational structure, with prior application in CaOH/CaOD [147] and GeCH/GeCD [312]. Continuing, the YbOD spectra in Ref. [335] exhibited a feature shifted to the blue by 6 cm^{-1}. This shift was taken as an indication that the state does not have significant bending content. For comparison, the origin band is also

---

[13]Private communication with Tim Steimle.

shifted by a small amount upon deuteration, roughly 5 cm^{-1} to the red [335].

At Caltech, we have performed high-resolution FM spectroscopy on two unassigned bands, denoted [17.64] and [17.68]. These bands were observed in both Ref. [217] and Ref. [335]. Our characterization of these bands, including observed transition frequencies, is provided in Ref. [161]. We were unable to correlate these bands to the ground $\tilde{X}(000)$ state using depletion tests. However, we mention a few relevant observations. First, the [17.68] spectra exhibits a significant gap in the center of the spectra, $\sim$1 cm^{-1} wide. This could correspond to a $\Sigma - \Sigma$ transition, which is expected to have a "Q gap" with size given by $4B'$, where B' is the excited state rotational constant. Furthermore, Ref. [335] found the [17.68] transition was blue-shifted by 19 cm^{-1}, and concluded the state does not have significant bending content.

In Ref. [335], the deuterated counterpart to the [17.64] transition could not be observed at all. The authors of Ref. [335] postulate this could mean the [17.64] excited state has bending character. As they explain, it is possible the band borrows intensity in YbOH via an accidental near-degeneracy that is not present in YbOD. Here, we expand on their explanation. The bending frequency shift upon deuteration for an XY-H molecule is given in Ref [312], which is in turn taken from Herzberg [305]. The ratio is:

$$\frac{\omega_{2,\mathrm{D}}}{\omega_{2,\mathrm{H}}} = \sqrt{\frac{\frac{r_{\mathrm{YbO}}^2}{m_D} + \xi}{\frac{r_{\mathrm{YbO}}^2}{m_{\mathrm{H}}} + \xi}} \tag{4.30}$$

$$\xi = \frac{r_{\mathrm{OH}}^2}{m_{\mathrm{Yb}}} + \frac{(r_{\mathrm{YbO}} + r_{\mathrm{OH}})^2}{m_{\mathrm{O}}}. \tag{4.31}$$

Using the parameters for the YbOH ground state [290], we obtain $\omega_D/\omega_H = 0.748$. Note this is similar to the naive scaling of the reduced mass as $1/\sqrt{2}$. We can therefore use the ω_2 value of YbOH to estimate the YbOD value as $\omega_{2,\mathrm{D}} \approx 240$ cm^{-1}. In addition to changing the vibrational ladder spacings, deuteration also affects zero point energies. For diagonal $\delta v_2 = 0$ transitions, the effect of deuteration is largely common mode between the ground and excited states, which is why the origin shift is only $\sim$5 cm^{-1}. However, if the transition in question is off-diagonal, with $\Delta v_2 = \pm 1$, then we expect deuteration to have a significant effect. If the ground state has larger v_2 than the excited state, then the transition should shift to the blue by $\sim$80 cm^{-1}. On the other hand, if the excited state has larger v_2, then the transition will shift to the red by roughly the same amount. In the spectra of Ref. [335], the region 80 cm^{-1} to the blue is explicitly shown as having no features. However, the region to the red is not shown. If the deuterated shift were to pull the transition 80 cm^{-1} to the red, this would mean the [17.68] is a $\delta v_2 = +1$ line that connects to an excited state with 1 more bending quanta than the ground state. These arguments also give us

reason to believe that the transitions in Ref. [335] observed with relatively small deuterated shifts are likely $\Delta v_2 = 0$.

We briefly mention two other bands here that have observed in our source at Caltech. We have observed lines in high-resolution in the following ranges: $17345 - 17346$ cm^{-1}, denoted [17.34] and $17394 - 17395$ cm^{-1}, denoted [17.39]. Originally, the [17.34] was thought to be the $\tilde{X}(010) \rightarrow \tilde{A}(010)$ line, though now we know that is definitely not the case. This could instead by another diagonal transition involving other bending ground and excited states. Meanwhile, the [17.39] band was originally thought to be the $\tilde{X}(010) \rightarrow [17.73]$ transition. However, with our determination of the bending mode frequency, such a band should instead be at 17411 cm^{-1}, which makes the [17.39] assignment a mystery. We note the [17.39] band has a Q-branch like structure, and the absorption signal was experimentally found to saturate with a saturation intensity of ≈ 88 mW/cm^2. This is $\sim 10\times$ is weaker than the origin band, indicating this excited state could have mixed $4f$ character.

We also mention two more un-assigned transitions from Ref. [217]: the weak [17.71] band, and a reasonably strong transition at 17900 cm^{-1}, labeled [17.90]. The only information we have about [17.71] is that it is weak and has a long vibrational progression in the DLIF. On the other hand, the [17.90] transition is very close to the $\tilde{X}(000) \rightarrow \tilde{A}(100)$ band at 17908 cm^{-1}, and was observed to have similar lifetimes and DLIF as the $\tilde{A}(100)$ state. This transition was not observed in the deuterated spectra of Ref. [335], attributed to the signal being below the noise floor. Nonetheless, the observation of the [17.90] band so close to the $\Delta v_1 = 1$ line out of $\tilde{X}(000)$ could indicate [17.90] is also a $\Delta v_1 = 1$ transition, but originating instead out of $X(100)$.

Additionally, another excited state has been observed in fluorescence at ~ 18577 cm^{-1} [339]. This state has been attributed to have $\Omega = 3/2$ character, suggesting assignment as the $^2\Pi_{3/2}$ component of the $\tilde{A}$ state. This would put the spin-orbit splitting at ~ 1254 cm^{-1}. However, Zeeman tuning indicates a reduced g-factor from expectation [339], indicating the possibility of mixing with another state, possibly a $\Delta_{3/2}$ state with $4f$ character. This band is overlapped with excitation of the [557] band in YbF (labeled according to different convention) [291, 340].

Recently, the $\tilde{B}^2\Sigma^+_{1/2}(000)$ state was observed in REMPI spectroscopy [337]. The origin of the state was found to be 20473 cm^{-1}, and the lifetime was $31(5)$ ns. The state was perturbed, limiting the accuracy of the medium-resolution spectral fit.

4.4.3 Reassignment

Here, we suggest an avenue for re-assignment of the YbOH excited state spectrum. We focus on the interpretation of the [17.34], [17.39], [17.64], [17.68], and [17.71] features. We propose these transitions arise out of the excited bending modes of $\tilde{X}^2\Sigma^+$. Indeed, this was the case with
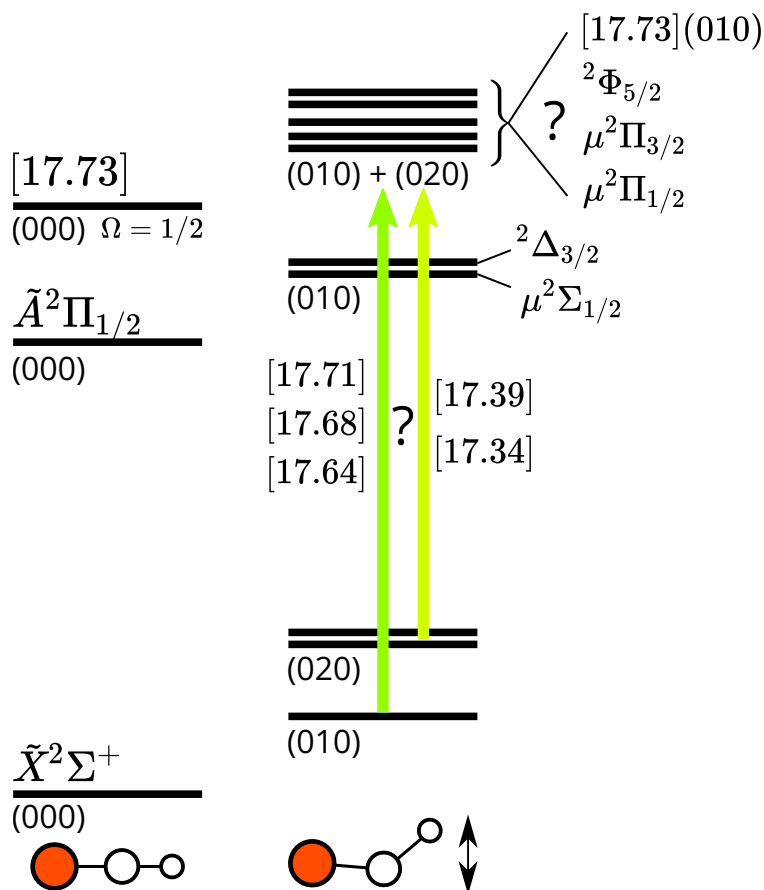
Figure 4.18: An energy level diagram of the lowest lying bending levels of the $\tilde{X}$, $\tilde{A}$, and [17.73]($\Omega = 1/2$) manifolds. Diagram not to scale. The splitting of $\tilde{X}(020)$ indicates the anharmonic splitting of the $\ell = 0, 2$ levels. Lines marked with "?" are potential re-assignments. See main text for details.

the previously unknown [17.33] band. Further, we propose the excited state they connect to is a mixture of bending states with combined $\tilde{A}^2\Pi_{1/2}(020)$ and [17.73](010) character.

The situation is illustrated schematically in Fig. 4.18. For now, we only consider bending modes, so we abbreviate $(0v_20)$ as simply v_2. The $v_2 = 0$ origin of $\tilde{A}^2\Pi_{1/2}$ is located at 17323 cm^{-1}. In this chapter, we identified the $v_2 = 1$ state of $\tilde{A}^2\Pi_{1/2}$ at 17651 cm^{-1}. Naturally, the $v_2 = 2$ state should be located higher by approximately one quanta, at approximately ~17980 cm^{-1}. This state will be split into three $\Omega = 1/2$ vibronic components [295], designated $\mu^2\Pi_{1/2}$, $\mu^2\Pi_{3/2}$, and $^2\Phi_{5/2}$. The origins of the states can be understood as follows: the Φ state is the "stretched" configuration corresponding to $\ell = 2$ and $\Lambda = 1$ fully aligned. We can also imagine an anti-aligned state with with $\ell = 2$ and $\Lambda = -1$, giving us $^2\Pi_{3/2}$ by virtue of our $\Omega = 3/2$ restriction. To obtain the $^2\Pi_{1/2}$ state, recall that the two bending quanta in $v_2 = 2$ can be anti-aligned as well[14], which gives us

---

[14]"Projection quanta" must always be aligned or anti-aligned with the internuclear axis, unlike an ordinary $J = 1$

$\ell = 0$. In such a case, our vibronic state just looks like the $^2\Pi_{1/2}$ origin, except shifted up by the vibrational energy $2\omega_2$.

We expect all of the $\tilde{A}^2\Pi_{1/2}(020)$ states to be scattered around $\sim 17960 - 18000$ cm^{-1}. Incidentally, this range is overlapped with the very strong $^3P_1$ atomic Yb feature at 17992 cm^{-1}. Atomic Yb emission was a contaminant in the DLIF taken in Ref. [217]. As a result, it is very possible that any blue YbOH decays near the Yb line would have been drowned out and missed. Therefore we suggest retaking the YbOH excited state spectrum in the $17960 - 18000$ cm^{-1} region, making sure to account for Yb emission.

Now we consider the [17.73], $\Omega = 1/2$ perturbing state with a hole in the $4f$ orbital. Though Λ is not a good quantum number in Hund's case (c), this state can be thought of as deriving from the $2^\Pi_{1/2}$ configuration. The origin of this state is at 17731 cm^{-1}. The first excited bending state, very naively, would be at $\sim 17731 + 330 = 18061$. Recall in YbF, the interaction that mixes $4f$ states with the $\tilde{A}$ manifold has ~ 100 cm^{-1} strength. Since YbOH is isoelectronic to YbF, we expect a similar coupling strength. Therefore the $\tilde{A}^2\Pi_{1/2}(020)$ manifold will be perturbed by the $v_2 = 1$ states of [17.73]. Further, we note if we think of [17.73] as a $^2\Pi_{1/2}$ state, then in $v_2 = 1$ we obtain two states, $^2\Sigma_{1/2}$ and $^2\Delta_{3/2}$. Of course, since Λ is strongly mixed in $4f$ states, we will also have some mixture of $\Lambda = \Delta$ and Φ as well.

We therefore expect a total of 5 vibronic states in the approximate region given by $\sim 17950 - 18050$ cm^{-1}. Three states derive from $\tilde{A}, v_2 = 2$, while two derive form [17.73], $v_2 = 1$. The mixing between these vibrational manifolds means v_2 is no longer well-defined. As a result, if we consider driving transitions to these vibronic states from the ground $v_2'' = 1, 2$ states, we expect transition strength for both $\Delta v_2 = 0$ and $\Delta v_2 = 1$. This would explain why the transitions from $v_2'' = 0$ would be weak in comparison.

Earlier in Sec. 4.3.1, we mentioned Refs. [310, 311] had developed a theoretical treatment of the Renner-Teller effect that includes a linear relativistic coupling term. They connected their term to the mixing interaction causing Sears resonances in experimental studies of GeCH [312]. A Sears resonance refers to an effective operator of the form $q_\pm S_\mp$, where $\pm$ denote the usual ladder operators in the molecule frame, q is the normal coordinate of the bending mode, and S is the electron spin. Effectively, the form of this interaction mimics the $L_\pm S_\pm$ form of the transverse spin-orbit interaction, but with the bending angular momentum instead. This makes sense in the relativistic limit, as we can no longer distinguish Λ from Σ, and we are already familiar with $L_\pm q_\mp$ terms from the dipolar Renner-Teller Hamiltonian. The coupling of Σ and ℓ preserves P, so the interaction will occur when states with the same P come near degeneracy. In GeCH, this happens when the manifolds separated by $\Delta v_2 = \pm 1$ are pushed together by the spin-orbit interaction.

that has an $M = 0$ projection.

However, in YbOH, this can occur due to the overlap of two different vibrational manifolds in two separate electronic states, $\tilde{A}^2\Pi_{1/2}$ and [17.73]. Therefore we expect relativistic vibronic mixing between $[17.73]^2\Delta_{3/2} \leftrightarrow \tilde{A}\mu^2\Pi_{3/2}$ and $[17.73]^2\Sigma_{1/2} \leftrightarrow \tilde{A}\mu^2\Pi_{1/2}$. This is on top of whatever resonances and mixings may occur within the vibronic manifolds of a given electronic state, such as the K-resonance we observed in $\tilde{A}^2\Pi_{1/2}(010)$.

We now consider the lowest ground states with excited bending vibration, $\tilde{X}(010)$ ($E = 320$ cm^{-1}, experiment), $\tilde{X}(02^00)$ ($E = 627$ cm^{-1}, experiment), and $\tilde{X}(02^20)$ ($E = 654$ cm^{-1}, theory). If we perform combination differences of these vibrational levels with the transition frequencies of the [17.64], [17.68], [17.71], [17.34], and [17.39] bands, we notice a pattern. If the [17.64], [17.68], and [17.71] bands originate from $\tilde{X}(010)$, their true excited state origins (compared to the absolute ground state) are at 17960 cm^{-1}, 18000 cm^{-1}, and 18030 cm^{-1}. This is right in the region where the $\tilde{A}^2\Pi_{1/2}(020)$ manifold and [17.73](010) manifolds are expected to lie. Additionally, if the [17.34] and [17.39] bands are taken to originate from $\tilde{X}(02^00)$, their origins are then at 17972 cm^{-1} and 18021 cm^{-1}. Once again this is the region of interest with the $v_2 = 2$ and $v_2 = 1$ overlap. It is very possible that all of these bands are addressing a cluster of states near $\sim$18000 cm^{-1}, which was not observed in the original DLIF studies due to Yb atom contaminant.

We caution that this discussion is speculative. Nonetheless, if we can better determine the location of the $\tilde{A}^2\Pi_{1/2}(020)$ manifold, we can begin the task of deperturbing the $4f$ state mixing in YbOH, similar to that which has been done in YbF [291]. The spectra of YbOH is interesting in its own right from a spectroscopy perspective, owing to strong mixings and the emergence of new patterns and degrees of freedom, much as we saw with orbital angular momenutm quenching in the $\tilde{A}^2\Pi_{1/2}(010)$ K-resonance. Addittionally, the deperturbation of YbOH is an important step toward repumping the $4f$ state decays, and eventually trapping YbOH molecules for EDM measurements with orders-of-magnitude improved sensitivity to BSM physics.

C H A P T E R

5

State Preparation and Measurement

Now *this* is podracing!

> *–Anakin Skywalker*

5.1 Introduction

In this chapter, we discuss the development of state preparation and readout schemes for precision measurements on linear polyatomic molecules. Any quantum precision measurement experiment requires such protocols. As usual, molecules present unique challenges for coherent control, but also they provide numerous additional handles for control that are lacking in atoms. In particular, arguably the most important handle afforded by molecules is control over the orientation of the body-fixed rotation of the molecule. Indeed, this is the primary draw of working with polyatomics—the projection of angular momentum on the internuclear axis provides natural opposite parity states. As a result of angular momentum coupling, the internuclear axis can be coupled to external fields, allowing for manipulation, control, and state engineering.

We begin with an introduction of relevant concepts for precision measurements with molecules. In Section 5.1.1, we first overview of two essential techniques for performing quantum measurements, namely Rabi and Ramsey interferometry. We then briefly review the schemes used by existing molecule experiments, namely ACME [11] and JILA [10], to perform state preparation and readout.

In Section 5.2 we move on to describing initial state preparation tests in YbOH using coherent population trapping (CPT). We first overview the connection of CPT to dark states. We discuss

difficulties with CPT that arise when working with species with unresolved hyperfine structure in the ground and excited states. We demonstrate a method for circumventing this issue by using circularly polarized light to perform spin precession in the $\tilde{X}(000)$ ground state of YbOH.

Then, in Section 5.3, we present state preparation and readout tests performed on the $\tilde{X}(010)$ state in YbOH. For these tests, we use two-photon resonances, which encompass both resonant CPT and detuned Raman transitions. We demonstrate the power of two-photon transitions by performing hyperfine resolved spectroscopy on the $N = 1$ manifold of the $\tilde{X}(010)$ state. Finally, we conclude by using two-photon transitions to perform Ramsey interferometry in the $\tilde{X}(010)$ state in the presence of a magnetic field. The results of this section can be immediately generalized to precision measurements of P, T violating physics in YbOH.

Finally, in Section 5.4, we present prototype electron EDM (eEDM) sensitive measurements in optically trapped CaOH. For these results, we collaborate with the Doyle group at Harvard. Trapped polyatomic molecules are particularly promising avenue for next-generation searches for P, T violation. We prepare ultracold CaOH molecules in a single quantum state, polarize them in an electric field, and use microwaves to perform Ramsey interferometry in an eEDM sensitive state. To extend the coherence time of the measurement, we utilize eEDM sensitive states with tunable, near-zero magnetic field sensitivity. Such "zero g-factor" states are generic in polyatomic molecules with parity doubling. Our results demonstrate the power of quantum state engineering for EDM searches, and provide a clear pathway towards orders-of-magnitude improved experimental sensitivity to P, T violating physics.

5.1.1 Rabi and Ramsey Interferometry

There are two techniques primary techniques for perfomring measurements of the frequency difference between two quantum mechanical levels: Rabi and Ramsey measurements. We breifly review these techniques, with a focus on Ramsey measurements.

We consider a two-level system. We note in advance that some of the factors of 2 in our discussion will need to be modified to deal with an arbitrary multi-level system, see Ref. [67] for details. Proceeding, we denote the states $|0\rangle$ and $|1\rangle$, with the bare Hamiltonian $H_0 = -\frac{1}{2}\omega_{01}\sigma_z$. We wish to measure the frequency splitting ω_{01}. In both Ramsey and Rabi schemes, we have two tools available: the action of unitary operators that couple $|0\rangle \leftrightarrow |1\rangle$, and the ability to perform projective measurements in the $\{|0\rangle, |1\rangle\}$ basis. As a result of our ability to perform projective measurements, we can generically take the initial state to be $|0\rangle$. The special case of $\omega_{01} \sim \tau^{-1}$ is that of *spin precession* measurements. In general, when $\omega_{01} \gg \tau^{-1}$, we have a situation analogous to that in atomic clocks. The difference is simply whether the spin precession occurs in the lab frame (precession) or rotating frame (clocks). In practice this distinction is not consequential, and

we may refer to time evolution in either case as "precession."

In the Rabi scheme, we apply a near-resonant AC coupling at a frequency $\omega = \omega_{01} + \Delta$, where we have defined the detuning Δ. The Hamiltonian is now given by

$$H = H_0 + H_{int} = -\frac{1}{2}\omega_{01}\sigma_z + \frac{1}{2}e^{-i\omega t}\Omega\sigma_y \tag{5.1}$$

with Ω the Rabi frequency for the drive oscillating at frequency ω. We have chosen the phase of Ω such that it aligns along σ_y for convenience. In the frame rotating at ω, the Hamiltonian becomes

$$H_R = -\frac{1}{2}\Delta\sigma_z + \frac{1}{2}\Omega\sigma_y. \tag{5.2}$$

We can either solve the time-dependent Schrodinger equation for $|\psi(t = 0)\rangle$, or we can diagonalize H_R and expand $|\psi(t = 0)\rangle$ in terms of eigenstates with time evolution given by an energy dependent phase factor. Either way, we find that the population undergoes Rabi oscillations between the two states, $|0\rangle \leftrightarrow |1\rangle$. In the Bloch sphere, we can think of the state vector as undergoing rotations about some vector with polar angle $\theta = \arctan(\Omega/\Delta)$. This reduces to $\theta = \pi/2$ in the resonant limit, indicating rotations about the y axis of the Bloch sphere (the choice of rotation axis is arbitrary and determined by the drive phase).

We stop applying the coupling after an interaction time τ, and then perform a projective measurement of $|\psi(t = \tau)\rangle$ in the $|0\rangle, |1\rangle$ basis. The probability of measuring the population in state $|1\rangle$ is given by [213]:

$$P_1(\Delta, \tau) = \frac{\Omega^2}{\tilde{\Omega}^2}\sin^2\left(\frac{\tilde{\Omega}\tau}{2}\right) \tag{5.3}$$

where we have defined the generalized Rabi frequency $\tilde{\Omega} = \sqrt{\Omega^2 + \Delta^2}$. The function defined by eq. 5.3 is plotted in Fig. 5.1 as a function of Δ. The width of the lineshape is given by $\sim \Omega$, and the oscillations of P_1 that occur with varying Δ are known as Rabi fringes. Various inhomogeneities and imperfections will result in broadening of this Rabi lineshape. For an EDM measurement, we perform a differential measurement, and so we care about the *slope* of the lineshape.

To elaborate further, we write $\omega_{01} \to \omega_{01} \pm \epsilon$, where $\epsilon \ll \omega_{01}$ represents a small energy shift we would like to measure, such as an EDM shift. The $\pm$ sign represents our ability to reverse the EDM interaction. If we keep the frequency of the coupling interaction fixed at ω, then the EDM shift shows up as modifications to the detuning, which we parameterize as $\Delta \mp \epsilon$. We are therefore interested in the population difference represented by $\delta P_1 = P_1(\Delta + \epsilon, \tau) - P_1(\Delta - \epsilon, \tau)$. For small ϵ, this is essentially the derivative, scaled by ϵ, and we can write the measurement sensitivity as $\epsilon|\partial P_1/\partial\Delta|$. We have written the absolute value to indicate we are agnostic about the sign of the $\pm\epsilon$ shift.

To maximize measurement sensitivity, we want to choose the drive detuning such that we are sitting on one of the Rabi fringes where the slope is large. We choose $\Omega\tau = \pi$, which corresponds to a single "Rabi flop" on resonance. This turns out to maximize the slope, and is technically convenient as we do not have to deal with dispersion from many Rabi flops. The sensitivity is then maximized by detuning the drive by $\Delta \sim \Omega$.

There are some drawbacks to the Rabi measurement scheme, however. The applied fields are always on during the interaction time, and so the measurement is sensitive to fluctuations of Ω and Δ in the bandwidth given by $1/\tau$. For long τ, we become more and more sensitive to $1/f$ noise. Maintaining homogeneity in Δ is a matter of controlling ambient fields and field sensitivities, and we will have to deal with this in the Ramsey scheme as well. However, maintaining Ω, which is often the coupling of an oscillating field, can be challenging, as it requires control over the amplitude and polarization of an oscillating field. Further, near resonant fields such as Ω can cause light-shifts of the transition we wish to measure, compounding the results. Finally, when $\omega_{01} \approx \tau^{-1}$ as in the case of spin precession measurements, we may be hard pressed to find amplitude stable sources of oscillating fields at frequencies of ~ 1 kHz for a beam and $\lesssim 1$ Hz for a trap.

In the scheme of Ramsey interferometry, we no longer apply the resonant coupling during the interaction time τ, and the measurement is said to "happen in the dark." Instead, we split the application of the resonant field to two short "Ramsey" pulses, with pulse time $t_p \ll \tau$. One pulse begins the measurement at $t = 0$, and one pulse ends the measurement at $t = \tau$.

As with before, the molecules begin in state $|0\rangle$. At $t = 0$, we apply the first Ramsey pulse, turning on the same resonant coupling $H_{int} \propto \sigma_y$ as before, and performing the same transformation into the rotating frame. Unlike the Rabi case, we choose the drive frequency ω to be close to resonance, $\Delta/\omega_{01} \ll 1$, and we optimize the pulse strength, Ω, such that $\Omega t_p = \pi/2$. This implements a $\pi/2$-pulse, a rotation of the state from $|0\rangle$ to the superposition $|\psi\rangle = \frac{1}{\sqrt{2}}(|0\rangle + |1\rangle)$. In the Bloch sphere, the rotation occurs about the y axis. We note we can choose the phase of the initial superposition with the appropriate choice of the Ω drive phase.

As an aside, we note that the intial preparation Ramsey pulse need not be a dynamic $\pi/2$-pulse. In the case of the ACME experiment, for example, the preparation pulse is instead a projection of the state onto a basis of optical bright and dark states. After a few photon scatters, the bright state is pumped out, and the remaining dark state can be used for Ramsey measurements. We will further discuss such a scheme later in this chapter.

With the initial Ramsey pulse over, the molecules now evolve according to H_0 alone. In the lab frame, the superposition $|\psi\rangle$ undergoes oscillations at the ω_{01} frequency, with time evolution

given by:

$$|\psi(t)\rangle = \frac{|0\rangle + e^{-i\omega_{01}t}|1\rangle}{\sqrt{2}}. \tag{5.4}$$

Here we have used the global phase invariance of quantum mechanics to rewrite the phase evolution all on the $|1\rangle$ for convenience. This is where a spin precession measurement diverges from a clock measurement. For spin precession, we recall $\omega_{01} \approx \tau^{-1}$, and we seek to measure the phase accrued in the lab frame. In the case of a clock, however, $\omega_{01} \gg \tau^{-1}$, and the state $|\psi(t)\rangle$ evolves rapidly in the lab frame. In such a case, the drive phase, which is initially coincident with $|\psi(0)\rangle$, is also rotating, but at a frequency ω.

Therefore, by transforming into in the frame rotating at ω, the time evolution is determined by the detuning instead:

$$|\psi(t)\rangle_R = \frac{|0\rangle + e^{-i\Delta t}|1\rangle}{\sqrt{2}} \tag{5.5}$$

where we use the subscript R to explicitly denote the rotating frame. We see that the rotating frame allows us to simplify the picture of the dynamics. In general, the evolution of the state is governed by the detuning Δ, which can be controlled in the experiment to good degree. If we somehow have $\Delta = 0$, then the state actually does not undergo phase evolution in the rotating frame at all!

Now, after $t = \tau$, we re-apply the same $\pi/2$-pulse as we did in the prep Ramsey beam, denoted as the readout Ramsey pulse. We then perform a projective measurement in the $|0\rangle, |1\rangle$ basis. For zero detuning, the prep $\pi/2$ and readout $\pi/2$ pulses combine to transfer all population to the $|1\rangle$ state.

For small non-zero detuning, such that the Ramsey pulses are still approximately good $\pi/2$ pulses, $|\psi(\tau)\rangle_R$ is rotated in the Bloch sphere by an angle $\phi = \Delta \tau$ relative to its starting point along x. If the drive is taken to be along the y axis of the rotating frame Bloch sphere, then we see it can only rotate the component of $|\psi(\tau)\rangle_R$ that remains along the on the x axis. For example, when $\Delta t = \pm \pi/2$, the readout pulse does not rotate the state at all. Generalizing, we see the readout Ramsey pulse therefore maps the projection remaining along $|\psi(0)\rangle$ onto the $|0\rangle, |1\rangle$. We can compute the probability of measuring $|1\rangle$ by considering the projection $|\langle\psi(0)|\psi(\tau)\rangle|^2 = \cos^2 \Delta t/2$.

For the case of arbitrary detuning Δ, we can generalize these arguments to obtain:

$$P_1(\Delta, t_p, \tau) = 4\frac{\Omega^2}{\tilde{\Omega}^2} \sin^2\left(\frac{\tilde{\Omega}t_p}{2}\right)\left[\cos\left(\frac{\Delta\tau}{2}\right)\cos\left(\frac{\tilde{\Omega}t_p}{2}\right) - \frac{\Delta}{\tilde{\Omega}}\sin\left(\frac{\Delta\tau}{2}\right)\sin\left(\frac{\tilde{\Omega}t_p}{2}\right)\right]^2 \tag{5.6}$$

where we have defined $\tilde{\Omega} = \sqrt{\Delta^2 + \Omega^2}$ as before, t_p are the Ramsey pulse times, and τ is the interaction time. We will find it convenient to parameterize the ratio of pulse time to interaction
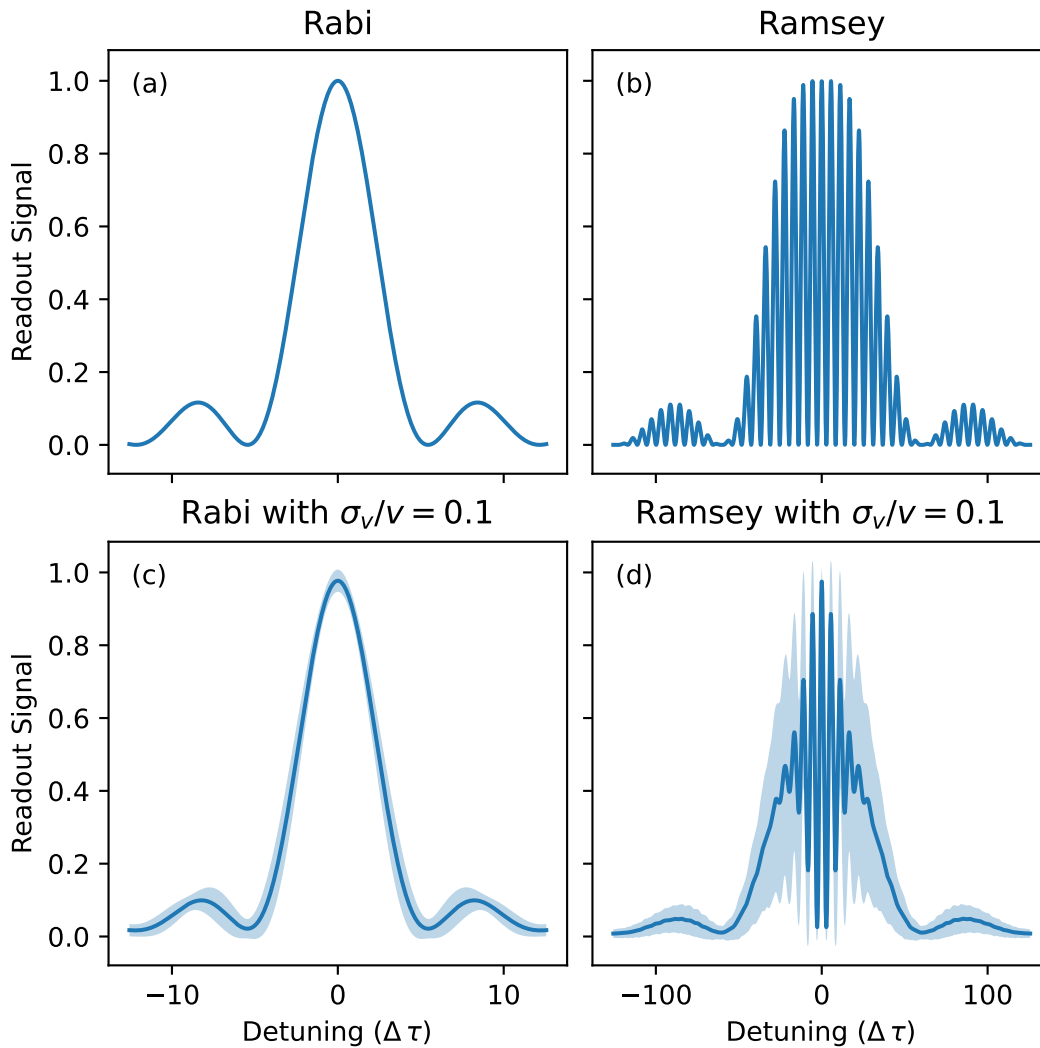
Figure 5.1: Rabi and Ramsey lineshapes, plotted as a function of unitless detuning $\Delta\tau$, where τ is the interaction time. For the Rabi lineshape, we fix the condition $\Omega_{Rab}\tau = \pi$. For the Ramsey case, we fix $\Omega_{Ram}t_p = \pi/2$, and set $\tau = \eta t_p$, with $\eta = 0.1$. Plots (a) and (b) are with no velocity dispersion. For plots (c) and (d), we add velocity dispersion given by $\sigma_v/v = 0.1$, which is a conservative estimate. Dispersion is modeled by random sampling from a Gaussian distribution. We use light shading to indicate 1-σ variation of the readout signal.

time, $t_p = \eta\tau$. For a 200 m/s molecule beam with $\tau = 1$ ms and a 1 cm pulse region, we have $\eta \approx 0.05$.

We compare the Ramsey and Rabi lineshapes, plotted in Fig. 5.1 as a function of $\Delta\tau$. The Ramsey lineshape $\eta = 0.1$, a conservative estimate. We note both measurements have zero slope at zero detuning, requiring us to move off resonance to obtain differential sensitivity. This can be achieved either by purposefully applying a detuning to ω, or, unique to the Ramsey case, by applying a $\pi/2$ phase shift to the readout Ramsey pulse compared to the prep Ramsey pulse. Additionally, we can see the Ramsey lineshape has many more fringes available for measurement compared to the Rabi lineshape. The Ramsey lineshape is noticeably plotted on a different detuning scale than the Rabi lineshape–the Δ scaling, and therefore the width of the overall Ramsey feature, is set by the size of η, the ratio of the pulse time to the interaction time. At very large Δ, the contrast decreases, as now the Ramsey pulses barely rotate the state. However, we caution that the picture changes if we incorporate velocity dispersion, which impacts Ramsey measurements more significantly than Rabi measurements.

So far, our discussion has been generic to a beam or a trap, and now we discuss differences in the two approaches. In a beam, we must contend with spatial field inhomogeneities, velocity dispersion, and finite molecule pulse width. Our beams are characterized by mean velocity $v \sim 200$ m/s and dispersion $\sigma_v \sim 10$ m/s, with interaction times of order $\tau \sim 1$ ms. Further, the molecular beam itself is $\gtrsim 20$ cm long, making it challenging to pulse on/off state preparation and readout–instead, we must apply our operations in a continuous-wave fashion, manipulating the molecules as they fly through radiation fields. The case of a trap is more straightforward, as we can simply pulse on and off state manipulations. Also, it is easier to control ambient fields in a trap than a beam, owing to the much smaller spatial extent of the trap ($\lesssim$ mm^3).

We focus on velocity dispersion, which causes a variation of the interaction time $\delta\tau = -\tau\delta v/v$ in both Rabi and Ramsey cases. In the Ramsey case, velocity dispersion will also result in similar variation of t_p, though this effect will be minor in comparison. We model this dispersion by sampling values for $\delta\tau$ taken from a Gaussian distribution with variance $\sigma_v/v = 0.1$, which we note is a conservative estimate for a CBGB[1]. The effects of velocity dispersion are shown in Fig. 5.1. The Rabi shape is only slightly broadened, while the Ramsey shape changes significantly. For large detunings, the measurement results have large spread, and upon averaging the fringes are reduced in size. We can understand the loss of fringe contrast as resulting from dephasing, which will be significant when $\Delta\delta\tau \gtrsim \pi$.

Finally, in Fig. 5.2, we directly compare the two methods on the same detuning scale using equal

---

[1]Our velocity dispersion is closer to $\sigma_v/v \approx 0.05$.
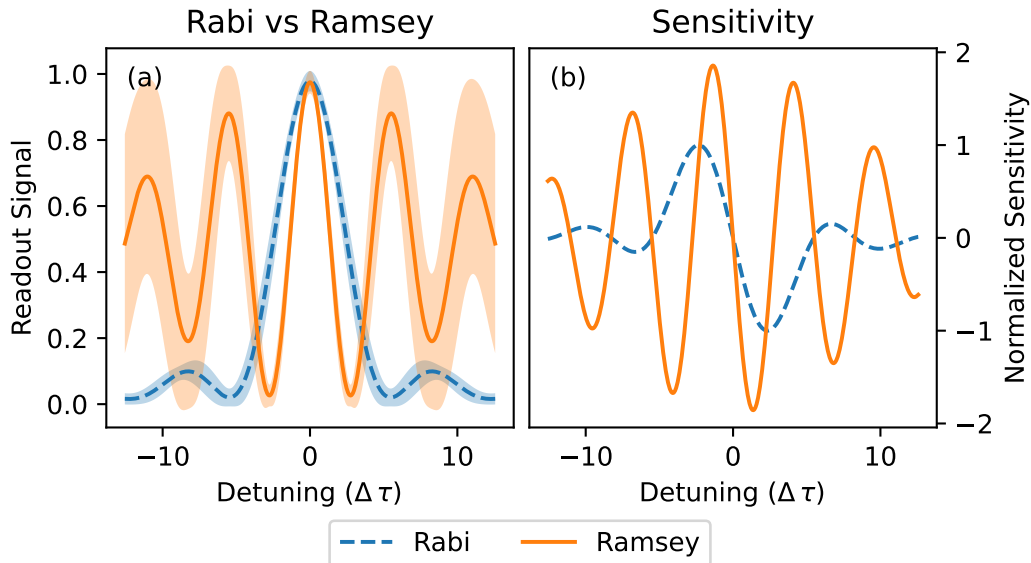
Figure 5.2: A comparison of Rabi and Ramsey lineshapes Rabi and Ramsey lineshapes, plotted as a function of unitless detuning $\Delta\tau$. We use the same parameters as Fig. 5.1 and explicitly set the interaction times equal. (a) Rabi and Ramsey lineshapes with velocity dispersion $\sigma_v/v = 0.1$, which is a conservative estimate. The line widths indicating 1-σ variation. (b) Derivatives of the lineshapes, representing differential sensitivities, normalized by the maximum value of the Rabi sensitivity. With dispersion, the maximum Ramsey sensitivity is ≈ 0.54 and the maximum Rabi sensitivity is ≈ 0.29.

interaction times[2]. Even with the velocity dispersion, the lineshapes are not affected significantly near the resonance. Furthermore, the Ramsey slope is clearly larger than the Rabi slope, resulting in improved measurement sensitivity. In passing, we mention the *spin-echo* technique [213, 341], which can be used to improve sensitivity to dispersion in a Ramsey measurement.

The choice of Rabi or Ramsey is unique to each experiment. In the discussion presented in this section, we see that Ramsey is more sensitive, but only by a factor of order unity. Finally, in our analysis, we have neglected another, intrinsic source of noise–*quantum projection noise* (QPN), which is discussed in Ch. 1. Unless we use entangled states [342], the precision of a phase measurement with either Ramsey or Rabi will scale like $N^{-1/2}$, where N is the number of independent measurements.

5.1.2 Molecular EDM Experiments

To measure an EDM in any system, experiments proceed by first applying an electric field to the system in question, breaking parity symmetry. As discussed in Ch. 1, this is necessary to make the P violating EDM shifts observable. The free-field Hamiltonian H commutes with the

---

[2]For equal τ, we obtain the relationship between the optimal Rabi rates as $\Omega_{Ramsey} = \Omega_{Rabi}/(2\eta)$.

parity operator $\mathcal{P}$, and therefore EDM shifts, which are parity-odd, vanish in free-field. This can be seen, for example, by explicitly writing a given parity state in Hund's case (a), where it forms superposition of $\pm\Sigma$ states ($\Sigma = S \cdot \hat{n}$), which have opposite EDM shifts and cancel. By mixing these projection states, we break parity symmetry and create states of the molecule with well defined orientation in the lab frame. In solid state systems [343], this polarization occurs via the crystal lattice, while in molecular gas measurements, we typically apply an external electric field.

The choice of "science state" in a molecule is motivated by the desire for good EDM sensitivity as well as favorable molecular structure. The $^3\Delta_1$ states in ThO and HfF$^+$, for example, both provide two important features: 1) the states have g-factor cancellation arising from the anti-alignment of Λ and Σ, resulting in $g \sim \mu_B/50$. 2) The states have small parity-doublets from the Ω-doubling, with the parity splitting measured to be $\approx$400 kHz in the lowest $J = 1$ state of ThO [344]. The parity doublets allows for full polarization in low fields, as well as control over the sign of the EDM interaction (Σ) without changing external fields. Both of these features have proven crucial for state-of-the-art EDM measurements [10, 11, 17].

In the Advanced Cold Molecule Experiment (ACME), an eEDM measurement is performed via Ramsey interferometry on opposite electron spin states in a beam of polarized ThO molecules in the metastable $H^3\Delta_1$ state. Details can be found elsewhere [11, 41, 67, 100]. Here, we focus on the state preparation and measurement scheme to motivate our work with YbOH.

The molecule beam flies downstream, passing through various laser beams and electromagnetic fields, implementing a sequence of preparation, measurement, and readout. The molecules begin in the $X^1\Sigma$ ground state and are first optically pumped into the $H^3\Delta_1$ state, similar to how we have to populate the science state in metal hydroxides with optical pumping. Then, the molecule beam enters an interaction region with magnetic and electric fields pointing along $\hat{Z}$, and lasers beams in two regions, one for preparation usptream, and the other downstream for readout.

The EDM measurement state in the ACME experiment is a superposition of $M = \pm 1$ levels in a $J = 1$ state with well-defined molecule dipole orientation. This superposition is sensitive to T violating effects, which shift $\pm M$ levels oppositely. We may write the state as

$$|\psi(\phi)\rangle = \frac{1}{\sqrt{2}} \left(|M = 1\rangle + e^{i\phi}|M = -1\rangle \right). \tag{5.7}$$

The quantization axis here is taken to lie along $\hat{Z}$, in the direction of the applied polarizing electric field. The ACME experiment works in the basis [67] given by $|X\rangle := |\psi(0)\rangle$ and $|Y\rangle := |\psi(\pi)\rangle$. In the language of angular momentum polarization, $|X/Y\rangle$ is an aligned state, lying in a plane containing $\hat{Z}$ and one of $\hat{X}$ or $\hat{Y}$, depending on the $\pm$ sign. In Figure 5.3, we visualize these states using the angular momentum probability surfaces, discussed in Appendix E. These visualizations

$$|X\rangle = \frac{|M=1\rangle + |M=-1\rangle}{\sqrt{2}} \qquad\qquad |Y\rangle = \frac{|M=1\rangle - |M=-1\rangle}{\sqrt{2}}$$
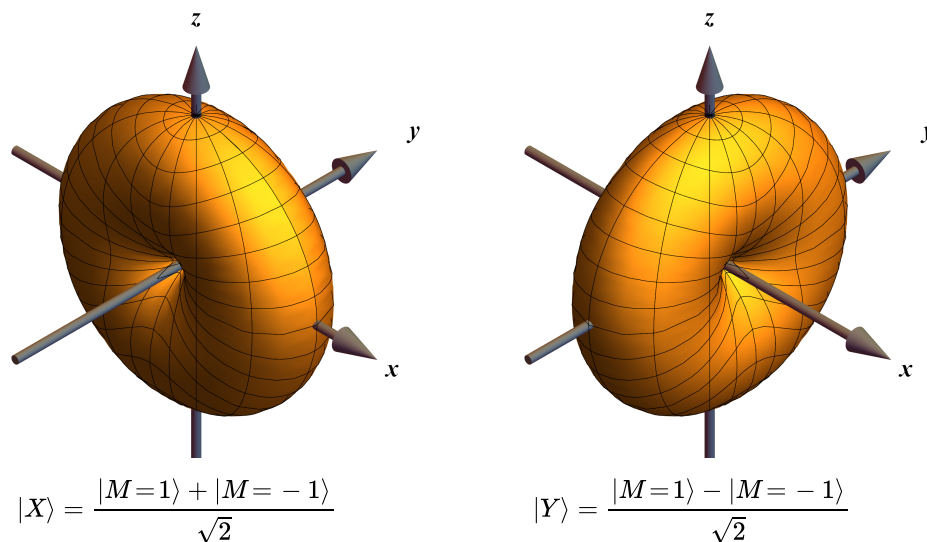
Figure 5.3: The angular momentum probability distribution for the $|X\rangle$ and $|Y\rangle$ states used for the ACME measurement, see main text for details. The distributions are plots of $\langle J, J(\theta, \phi)|\rho|J, J(\theta, \phi) = J\rangle$, where $M(\theta, \phi) = J$ describes the state with maximum projection in an arbitrary direction. Figures are made using the AtomicDensityMatrix package in Mathematica.

plot the probability distribution for measuring the maximum angular momentum projection along a given quantization axis.

The effect of the EDM is to create a differential phase in the superposition, proportional to the splitting of the T-reversed $\pm M$ states. In terms of the angular momentum distribution, an EDM means the electric field of the molecule, pointing along $\hat{Z}$, causes rotation of the probability distribution about $\hat{Z}$. The T-violating nature of the EDM is immediately apparent, as a magnetic field applied along $\hat{Z}$ will also cause the same rotation of the superposition state. We see the superposition of time-reverse states offers insensitivity to electric field shifts, at the cost of "maximal" magnetic field sensitivity. Of course, the suppression of the g-factor in the $H^3\Delta_1$ state aids in this aspect [345].

With the spin precession scheme occuring in the space of $\pm M$ states, the only thing remaining is to prepare and readout such an aligned state in a Ramsey style measurement. The ACME experiment prepares the superposition state implementing Coherent Population Trapping (CPT) with linearly polarized light. We discuss CPT in detail later in Sec. 5.1.3. Here, we will intuitively explain the connection of linear polarization to the distributions in Fig. 5.3.

Consider the application of $\hat{Z}$ polarized light on a $J'' = 1 \rightarrow J' = 1$ transition. Due to the selection rules from the Wigner-Eckart theorem, the $M'' = 0$ ground state is not coupled to the excited state and is a dark state (the photon's momentum must go somewhere!). On the other hand, the $M = \pm 1$ are coupled to the excited state and are optically pumped away. If we visualize the

angular momentum probability surface of just the $M = 0$ state that remains, we see it looks exactly like the surfaces in Fig. 5.3, except rotated such that the torus lies in the $\hat{X}\hat{Y}$ plane. This makes sense, as $M = 0$ should have no probability density along $\hat{Z}$. Due to rotational invariance, this means the $|X\rangle$ and $|Y\rangle$ states are also dark states generated by the application of linearly polarized light, but this time light polarized perpendicular to the quantization axis. The linear polarization axis runs through the center of the torii, determining the angle of the dark state superposition. We can think of the light polarization as coupling to all co-aligned transition dipoles, pumping them away and leaving behind dark states that lie perpendicular to the polarization axis.

The ACME experiment begins with the $|X\rangle$ state, prepared by the application of $\hat{Y}$ polarized light[3] As spin precession occurs, the applied bias magnetic field rotates the angular momentum distribution along $\hat{Z}$, and the state $|X\rangle$ goes from being aligned in the $\hat{X}\hat{Z}$ plane to aligned the $\hat{Y}\hat{Z}$ plane, transforming into $|Y\rangle$. Now, application of the same linearly polarized $\hat{Y}$ light will project the formerly dark superposition partially onto the bright state, causing the emission of fluorescence containing information about the precession phase. As a technical detail, the ACME experiment rapidly switches the polarization of the readout beam, ensuring each molecule is illuminated by both polarization and allowing for normalized readout in each shot.

In summary, the ACME experiment implements a Ramsey measurement using CPT for state preparation and readout. The JILA experiment performs state preparation in an entirely different way, essentially using a rotating electric field to implement $\pi/2$-pulses that prepare an EDM sensitive superposition [346]. The Ramsey measurement then proceeds as usual. We do not discuss their scheme further, as it leverages aspects unique to their experiment. We do however note there is an equivalent scheme in a non-rotating frame, using transverse DC magnetic fields to engineer higher order couplings that implement $\pi/2$ pulses between states of interest, discussed further in Ref [70].

Naturally, we first attempted to perform state preparation using CPT in YbOH. However, we soon ran into difficulties from that are absent in ThO and other similar diatomics. The issues in particular stem from the unresolved hyperfine structure in M-OH molecules. Before we can discuss our results, we first overview CPT in detail.

5.1.3 CPT and Dark States

First, we present a more detailed quantum mechanical treatment of CPT. We consider a system with multiple ground and/or excited states. The concept of a rotating frame for a two level system can be generalized to a multi-level system by appropriate choice of the rotation matrix [347]. In general, each state in the Hamiltonian can be transformed into a state rotating at some arbitrary

---

[3]$\hat{Y}$ light generating $|X\rangle$ makes sense if we remember $|X\rangle$ is dark to $\hat{Y}$.
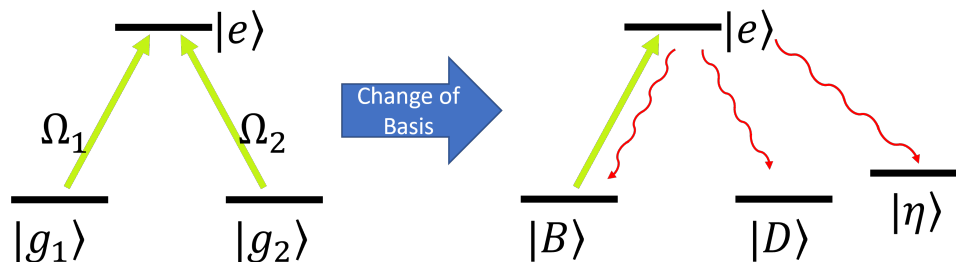
Figure 5.4: A schematic diagram describing coherent population trapping. On the left, we have two ground states $|g_1\rangle$, $|g_2\rangle$, connected to the excited state $|e\rangle$ by arbitrary TDMs. We can perform a change of ground state basis (detailed in the main text) to transform to the optically bright/dark basis, shown on the right. The bright state $|B\rangle$ is coupled to the excited state, while the dark state $|D\rangle$ is not. Excited state decays can either repopulate the bright/dark manifold, or they can decay to different level manifolds dark to the laser, represented by $|\eta\rangle$.

frequency ω_R, which does not necessarily have to be the same for the different states. It is often most convenient to chose the values of ω_R to coincide with the optical frequencies of the lasers in the problem, removing the time dependence associated with fast oscillations.

When laser light drives a resonant atomic or molecular transition, depending on the couplings and degeneracy of the ground $|g\rangle$ and excited $|e\rangle$ states, it is possible to obtain *dark states*, denoted $|D\rangle$. Remarkably, despite the presence of resonant radiation, such states are decoupled from the excited state: $\langle e|H|D\rangle = 0$. As we shall see, this decoupling occurs as a result of interference between transition amplitudes from different ground states to a common excited state. Because of the requirement of common couplings, dark states arise when the number of degenerate ground states is greater than the number of degenerate excited states, $n_g > n_e$. In some cases, depending on the couplings of ground and excited states, we can also have dark states when $n_g = n_e$. Finally, when $n_e > n_g$, all ground states are coupled to excited states, and all eigenstates are "bright states," denoted $|B\rangle$.

Dark states provide a resource[4] for quantum control via coherent population trapping (CPT) [350]. By projecting a mixed state onto a dark/bright basis, we can purify the mixed state by pumping out the bright states and retaining the dark states. In addition to its use in state preparation for the ACME experiment, CPT is used in many different atomic physics experiments [351–356]. CPT in multi-level atomic systems is discussed in detail in Refs. [357–364]. Further, Refs. [365–369] discuss/demonstrate CPT using elliptically polarized light, which could possibly be applied to advanced CPT schemes in molecules to deal with the issues we will encounter in this section. Dark states also form the foundation for certain adiabatic transfer techniques, such as Stimulated Adiabatic Rapid Passage (STIRAP) [370, 371].

---

[4]In contrast, dark states are an issue for optical cycling in molecules, see Refs. [348, 349].

We provide a heuristic derivation of dark states in a 3 level system. Consider a Λ system, with ground states $|g_1\rangle.|g_2\rangle$, and excited state $|e\rangle$, shown in Figure Ṡuppose we couple the ground and excited states with resonant radiation described by coupling matrix elements Ω_1 and Ω_2. If we write the dark state in terms of arbitrary coefficients, $|D\rangle = c_1|g_1\rangle + c_2|g_2\rangle$, we can then consider the condition $\langle e|H|D\rangle = 0$, where the Hamiltonian H includes the light couplings. In the rotating frame, we find that $|D\rangle$ is dark if the coefficients satisfy $c_1\Omega_1 + c_2\Omega_2 = 0$. We can now write the dark state as:

$$|D\rangle = \frac{\Omega_2|g_1\rangle - \Omega_1|g_2\rangle}{\sqrt{\Omega_1^2 + \Omega_2^2}}. \tag{5.8}$$

If the coupling strengths are taken to be equal in magnitude, then the dark state is an equal superposition of the ground states. In general, such a superposition dark state is referred to as a *coherent* dark state. By switching the relative sign of Ω_1 and Ω_2, we can change the phase of the coherent dark state, a useful trick employed by the ACME experiment. If we take $\Omega_1 \gg \Omega_2$, then we see the dark state is dominated by $|g_2\rangle$, and vice versa if $\Omega_1 \ll \Omega_2$. In any event, we can always perform a unitary change of basis from the g_1, g_2 basis into the D, B basis, where B is the bright superposition with opposite phase compared to D. In such a basis, the dark state is explicitly decoupled from the excited state.

We take a moment to examine in further detail the couplings Ω. Explicitly, these couplings are Rabi rates, written as $\hbar\Omega_{ij} = \langle i|\vec{d} \cdot \vec{E}|j\rangle$, where $\vec{E}$ is the oscillating electric field. Expanding the dot product in the spherical tensor basis and pulling out $\vec{E}$, we have $\hbar\Omega = \sum_p (-1)^p \langle i|T_p^1(d)|j\rangle T_{-p}^1(E)$. We therefore see that the phase of the coupling arises from two sources: the transition dipole moment (TDM) matrix element connecting the two states, *and* the phase of the applied AC laser field, which is connected to the polarization of the light. This will be an important distinction later, when we consider the formation of multiple simultaneous Λ-systems with the same light polarization but different TDMs.

We now expand our discussion from a 3 level system to a case with multiple ground states coupled to multiple excited states, with $n_g < n_e$. As an example, we consider a $J = 2 \rightarrow 1$ system driven by $\hat{X}$ polarized light, shown in Figure 5.5(b). We now have have two independent "linkages"—a Λ system between $M = \pm 1$ in the ground state, and an "M" system between $M = \pm 2, 0$ in the ground state. The Λ-system is the same linkage we encountered earlier. Meanwhile, the dark states in the M system are superpositions of all the involved ground states. We note we could have also reached these conclusions by rotating our basis to make our light $\hat{Z}$ polarized.

Earlier, we pointed out that the condition $n_g = n_e$ requires specific care. Consider a $J = 1 \rightarrow J = 1$ transition. Recall from Sec. 5.1.2, if we apply light linearly polarized along $\hat{Z}$, we now have a single $M = 0$ dark state as a result of selection rules. However, we now consider another $n_g = n_e$
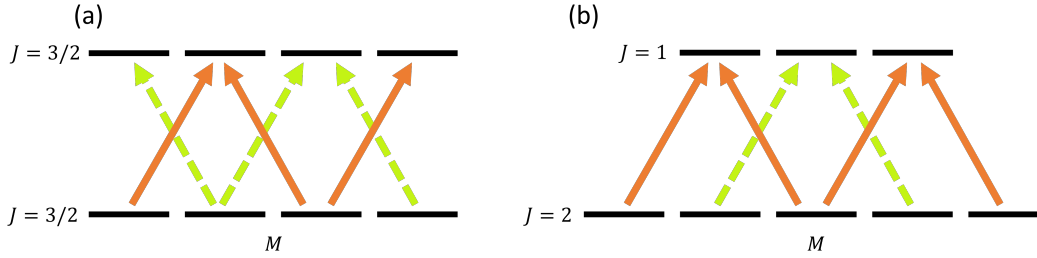
Figure 5.5: Schematic diagram describing CPT linkages in multi-level transitions. Laser couplings are indicated with full red and dashed green arrows to clearly indicate the various linkages. In both cases the light is transversely polarized. Rotating to $\hat{Z}$ polarization makes the dark states self-evident. (a) A $J = 3/2 \to 3/2$ transition. In this case we do not have any dark states. (b) A $J = 2 \to J = 1$ transition. Now we have two dark states. The first results from the "M" linkage, indicated with red arrows. The other dark state results from the Λ linkage, indicated with green dashed arrows.

system, this time a $J = 3/2 \to 3/2$ transition, indicated in Fig. 5.5(a). We can see that for either $\hat{Z}$ or $\hat{X}$ light, all ground states are coupled to multiple excited states, and therefore there will be no dark states with linearly polarized light. On the other hand, circularly polarized $\sigma^{\pm}$ light has trivial dark states, as we shall see later. In general, the existence of dark states with $n_g = n_e$ requires care in the analysis[5]. Finally, it is straightforward to show that when $n_e > n_g$, there are no dark states.

For multi-level systems, we see the linkages increase in complexity. For more complicated systems, we can always take the "brute force" approach to finding the dark states by directly diagonalizing the full Hamiltonian of our system, keeping track of all the various TDM phases. However, direct diagonalization has difficulty treating degenerate states, requiring us to add small detunings to enforce the M sublevel basis. An alternative approach is to use the Morris-Shore transformation, which is a generic method for converting a $n_g \to n_e$ excitation into a series of bright and dark states. This approach is discussed further in Refs. [349, 357, 373].

We conclude with a discussion of CPT when the ground state degeneracy is lifted. We consider the scenario from Fig. 5.4, but now we imagine the ground states degeneracy is lifted by a splitting $\Delta E_{g_1,g_2} = \Delta$. As with before, we couple the two ground states to e with a shared laser beam at a single frequency. If our laser is resonant with $g_1 \leftrightarrow e$, then it will be detuned from $g_2 \leftrightarrow e$ by the splitting Δ. If we rotate into the bright/dark basis, we find once again that the dark state with interfering transition amplitudes is not coupled to e by the laser interaction. However, in the frame rotating at the laser frequency, the detuning Δ couples the dark state to the bright state[6]. Essentially,

---

[5]In reality there is no such thing as a pure $J = 3/2$ system that interacts with a photon, as half integer angular momenta can always be traced back to electronic or nuclear spins that are decoupled from the light in the E1 approximation. This point is discussed further in Ref. [372], and we return to it later. Finally, we also note that the E1 approximation of a decoupled spin can break down with strong spin-orbit coupling.

[6]This is identical to the mechanism for magnetic remixing of dark states [348].

the dark state now contains some excited state admixture, proportional to Δ/Ω. We refer to such a dark state as a *gray state*. For the states we consider, Δ is often caused by hyperfine splittings. Finally, we note that in the above discussion, a single laser field was used to couple both ground states. If we have one laser field resonantly addressing just g_1 and another resonant laser field addressing just g_2, the dark state is stabilized, as there are no detunings from the rotating frames of the independently chosen frequencies. However, if cross-excitation is possible, we will need to consider the possibility of "off-resonant" scattering of one state by the laser resonant with the other state. Generalization of the Morris-Shore transformation to dark states with weak detunings is discussed in Ref. [374].

So far, all of our discussion has invovled individual, optically resolved levels. However, this is distinctly not the case in M-OH molecules.

5.1.4 Unresolved Hyperfine Structure

In alkaline-earth(-like) hydroxides, if the metal atom has no nuclear spin, the only hyperfine structure arises from the distant hydrogen nucleus. In YbOH, the Yb to H distance is $\sim$3 Å, and since the valence electron is Yb-centered, the resulting hyperfine effects are suppressed. In fact, spectroscopic confirmation of small hyperfine in hydroxides was initially used as a confirmation of the metal-localized nature of the valence electron orbital [375].

Note that in this section, we only consider the hyperfine interaction with the hydrogen in the -OH ligand. This means we consider even isotopologues, e.g., ^{174}YbOH. The Yb hyperfine structure of the odd isotopologues of YbOH is resolved and has been characterized in Ref. [157]. For weak hyperfine interactions in $^2\Sigma^+$ states, the hyperfine interaction is generically given by:

$$H_{\text{hyp}} = b_F \vec{I} \cdot \vec{S} + \frac{c}{3}\left(3I_z S_z - \vec{I} \cdot S\right).$$

(5.9)

The full hyperfine Hamiltonian includes additional terms not relevant here but discussed in Ch. 2. The Fermi contact interaction strength, b_F, is proportional to the magnitude of the electron wave function overlap at the hydrogen nucleus, $|\psi(r_H)|^2$. For YbOH, SrOH, and CaOH, b_F has been measured to be 4.80 MHz [290], 1.67 MHz [376], and 2.60 MHz [375], resulting in splittings smaller than the typical excited state linewidths ($\sim$8 MHz). Therefore the hyperfine structure is optically unresolved, and these constants are obtained by using a combination of optical-radio-frequency or optical-microwave double resonance techniques. The other relevant interaction is the dipolar hyperfine term, c, is measured in the same references to be 2.46/1.67/2.05 MHz. In general, the angular momentum matrix elements associated with c are smaller than those for b_F. By contrast, in a diatomic molecule such as YbF, the ^{19}F nucleus ($I = 1/2$) is closer to the metal-centered electron, and consequently the hyperfine structure is much larger. For example, in the

ground state of YbF, the hyperfine parameters are $b_F = 170$ MHz and $c = 85$ MHz [377], with similarly large values in CaF and SrF [378].

On the other hand, in both the hydroxides and fluorides considered, the excited state hyperfine structure is very small, and there are not many reliable measurements. The smaller interaction is a result of the electron being further polarized away from the bonding region (and therefore away from the other nuclei). This is also reflected in the smaller excited state molecular frame dipole moments. In the ionic picture, the molecule can be thought of as Yb$^+$ OH$^-$. Upon excitation, if the negatively charged valence electron is polarized further toward Yb$^+$, the dipole moment will be lowered, as is observed ($D_X = 1.9$ D $\rightarrow D_A = 0.43$ D). In CaF, the lowest lying excited states were found to have a hyperfine splitting of 4.8 ± 1.1 MHz [214], but there has not been a full characterization. In YbOH, the excited state hyperfine splitting is unknown and expected to be even smaller, owing to the larger Yb to H distance.

The unresolved hyperfine in hydroxides means the selection rules for transitions follows a $\Delta J = \pm 1, 0$ pattern, even though the states are technically characterized by F. The hyperfine interaction causes very weak J mixing, which results in very small intensity borrowing for $\Delta J = \pm 2$ transitions. Magnetic tuning beyond ~ 1 G uncouples the electron spin from the hyperfine interaction and the Zeeman shifts deviate from linear behavior, which has consequences for accurate modeling of magneto-optical trapping [120]. For photon cycling and calculations of effective scattering rates, the unresolved hyperfine is also important for state counting.

The inability to optically resolve the hyperfine structure is a challenge for coherent quantum control and precision measurement. Typically, coherent operations are performed after collecting population into one or two quantum states. This reduces entropy and increases SNR. For example, recent work with CaF in optical tweezers [379, 380] proceeds first by using lasers to optically pump into the $F = 0, N = 0$ state. Such a scheme is not possible in metal hydroxides as the ground state hyperfine is unresolved. Furthermore, because the excited state structure is unresolved, selective optical depletion of the ground state is not possible. In Sec. 5.4, we utilize microwaves to prepare a pure initial state.

Finally, the unresolved hyperfine structure has drastic consequences for CPT, causing destructive interference of dark states. This interference effect was first studied experimentally in Ref. [381]. There, the authors investigated CPT with linearly polarized light on the D_1 line ($J = 1/2 \rightarrow 1/2$) of ^{87}Rb in a room temperature buffer gas cell. The excited $^2P_{1/2}$ state has a ~800 MHz hyperfine splitting[7], and their experiment had 540 MHz Doppler broadening. When operating with a detuning approximately half way between the two excited states, the authors observed a 40 times

---

[7]Note there is a typo in the paper when describing the excited state hyperfine splitting. The correct values can be found at `https://steck.us/alkalidata/rubidium87numbers.1.6.pdf`.

weaker CPT resonance when using a lin $\parallel$ lin polarization configuration compared to a using a σ-σ configuration.

We too shall encounter the issue of destructive hyperfine interference when performing CPT on YbOH molecules. Later, we will also show that CPT can still be achieved if we make the correct choice of polarization and excited state. In these cases, just like Ref. [381], we will see the strength of the CPT resonance is polarization sensitive.

5.2 Initial State Preparation Tests

5.2.1 CPT Difficulties

We initially attempted to perform prototype spin precession in $\tilde{X}^2\Sigma^+(000)$ using the same scheme as ACME, described in Sec. 5.1.2. We used two linearly polarized laser beams, one for Ramsey prep, one for Ramsey read out, focused down to $\sim$300 µm spots separated by 3 mm. Both beams were resonant with the $\tilde{X}^2\Sigma^+(000) \rightarrow \tilde{A}^2\Pi_{1/2}(000)$ transition, specifically driving the $^QQ_{11}(0)$ transition. The prep beam was intended to project the states onto a bright dark basis, and the read out beam would project either on the same or different basis, depending on the relative angle between prep and readout polarizations.

The ambient magnetic field in the precession region was reduced to $\sim$ 10 mG using 3 axis square coil pairs and homemade magnetic shielding. The shielding consisted of mumetal plates cut with scissors and mounted on a mini-8020 frame around the vacuum chamber, which is a KF50 six way cross. Strips of metglas were taped and wrapped around the mumetal to cover up gaps and improve the shielding performance. A photo of the setup is shown in Fig. 5.6.

The magnetic field magnitude was calibrated with a magnetometer[8] when the vacuum chamber was vented. Additionally, when under vacuum, we were able to use atomic Yb atoms in our CBGB to zero the magnetic field. Specifically, we used the directional Hanle effect in the excited $^3P_1$ state [382]. Briefly, the Hanle effect [383, 384] uses the rotation of angular momentum polarization, either in the ground or excited state, to perform magnetometry [385, 386] or to measure lifetimes/decoherence rates. Incidentally, Hanle effect has actually been used to study the magnetic fields of the sun [387]. Semiclassically, the Hanle effect in the excited state understood as the magnetic rotation of the excited state angular momentum, manifested in spatial and polarization anisotropy of the decay fluorescence. We note that Ref. [388] compares the Hanle effect with other atomic magnetometry techniques, which may also find use in CBGBs. For further details on the magnetic calibration using the Hanle effect, see Appendix B. In summary, we were able to use Yb atoms to calibrate our residual fields down to $\lesssim$10 mG.

---

[8]AlphaLab Inc. MR3
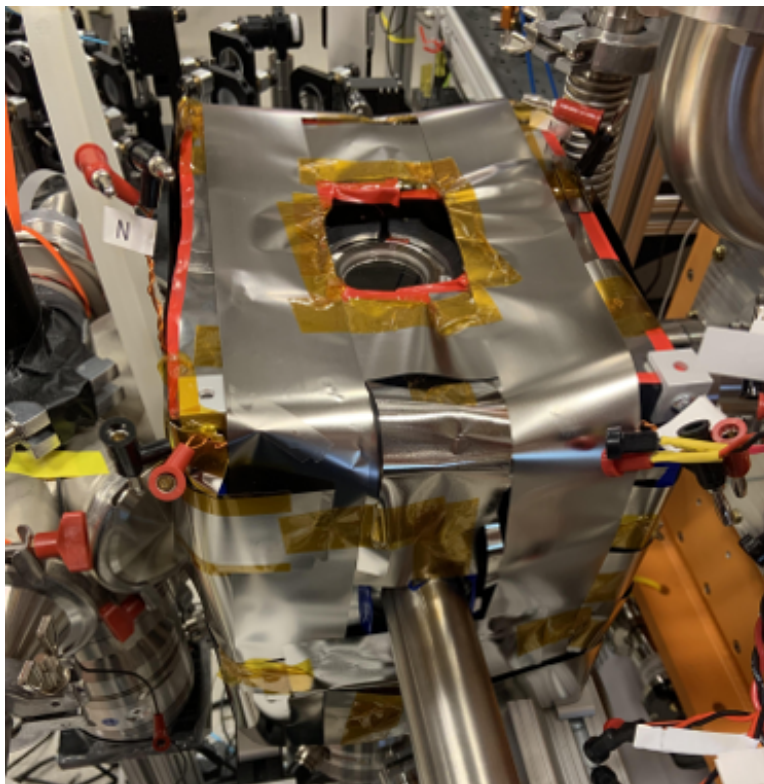
Figure 5.6: A photo of the home-made magnetic shielding around the six-way KF50 cross. See main text for details.

Nonetheless, we were unable to observe spin precession using linearly polarized light. In addition to controlling stray fields, we tried focusing the precession laser beams to increase intensity and reduce the effect of optical pumping in the beam intensity tails. We also designed an optical setup to selectively detect fluorescence from solely the readout beam. We used off-the-shelf lenses to focus the fluorescence light into a 400 μm multimode fiber, which was fed into a photomultiplier tube (PMT). Using this setup, we were able to observe ~60% depletion of the readout fluorescence when the prep beam was unblocked. This depletion was independent of the polarization angle between the readout and prep beams, which indicates a lack of coherent population trapping. Instead, the depletion is attributable to standard optical pumping of molecules out of the $J'' = 1/2$ state.

Upon further examination, we realized that the unresolved hyperfine structure of the excited state was interfering with the formation of dark states. To understand this effect, we consider the case of dark states formed by linearly polarized light exciting the $^{Q}Q_{11}(0)$ line. This is a $F'' = 0, 1 \rightarrow F' = 0, 1$ transition. The situation is shown schematically in Figure 5.7. Since the linewidth of optical excitation is larger than the hyperfine splitting, all allowed hyperfine transitions are excited.
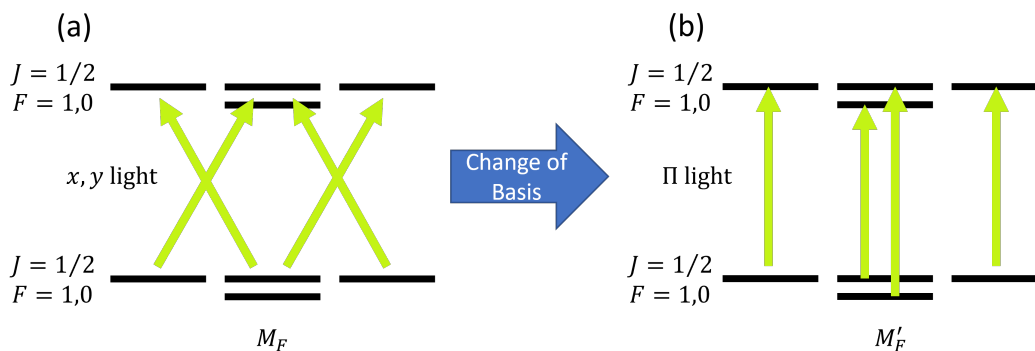
Figure 5.7: A schematic diagram of the ground and excited states in the $J'' = 1/2 \rightarrow J' = 1/2$ transition driven by linearly polarized light. We consider two bases that both describe equivalent physics. (a) Excitation by transversely polarized light in the quantization axis defining M_F. (b) Performing a basis rotation, we can consider a rotated quantization axis defining M_F'. Now the excitation light is parallel polarized, showing all ground states are coupled to a unique excited state.

First, consider the case where the light is $\hat{Z}$ polarized and we have excitation of Π-type transitions, shown in Fig. 5.7(b). The selection rules forbid $M'' = 0 \rightarrow M' = 0$ transitions unless $\Delta F \neq 0$. Therefore the $M = \pm 1$ states are excited and optically pumped away. Meanwhile the $F'' = 0$ state is excited only to $F' = 1, M' = 0$, and similarly the $F'' = 1, M'' = 0$ is excited only to $F' = 1, M' = 0$. Each ground state therefore is connected to an excited state that can decay elsewhere, causing optical pumping out of the $J = 1/2$ ground state. Even if the excited molecule decays back to the same manifold, it can be re-excited, and after a few scatters will almost certainly be pumped elsewhere. As long as the magnetic field splitting is small compared to optical linewidths, we are justified in the choice of quantization axis along the light polarization. However, it is instructive to consider the problem in a rotated quantization axis as well.

Consider now the case when the light is $\hat{X}$ polarized, and the excited transitions are a linear combination of σ^+ and σ^- transitions, shown in Fig. 5.7(a). The $M'' = 0$ ground state is excited to a linear superposition of $M' = \pm 1$ excited states. This superposition promptly decays in ~ 20 ns, resulting in optical pumping and loss. However, the $M'' = \pm 1$ states can connect to the same $M' = 0$ excited state. Because of the unresolved excited state hyperfine, *both* the $F' = 1$ and $F' = 0$ are coupled to the $M'' = \pm 1$ ground states, forming two distinct Λ-systems. For an isolated $F' = 1$ or $F' = 0$ excited state, this would result in coherent population trapping in a dark state, as there are more ground states.

However, when both excited states are simultaneously addressed, the two Λ systems have orthogonal dark states. This is a result of the Clebsch-Gordan coefficients used to couple J and I together to form F. We can see this by writing the states in the decoupled M_J, M_I basis, shown in Figure 5.8. The Clebsch-Gordan coefficients tell us the $M_F = 0$ components of the singlet $F = 0$

$$J = 1/2 \quad \underline{}_{|\downarrow\downarrow\rangle} \quad \underline{\underline{}}_{|\uparrow\downarrow\rangle + |\downarrow\uparrow\rangle} \quad \underline{}_{|\uparrow\uparrow\rangle} \quad \begin{array}{l} F = 1 \\ F = 0 \end{array}$$

$$|\uparrow\downarrow\rangle - |\downarrow\uparrow\rangle$$

$$J = 1/2 \quad \underline{}_{|\downarrow\downarrow\rangle} \quad \underline{\underline{}}_{|\uparrow\downarrow\rangle + |\downarrow\uparrow\rangle} \quad \underline{}_{|\uparrow\uparrow\rangle} \quad \begin{array}{l} F = 1 \\ F = 0 \end{array}$$

$$|\uparrow\downarrow\rangle - |\downarrow\uparrow\rangle$$
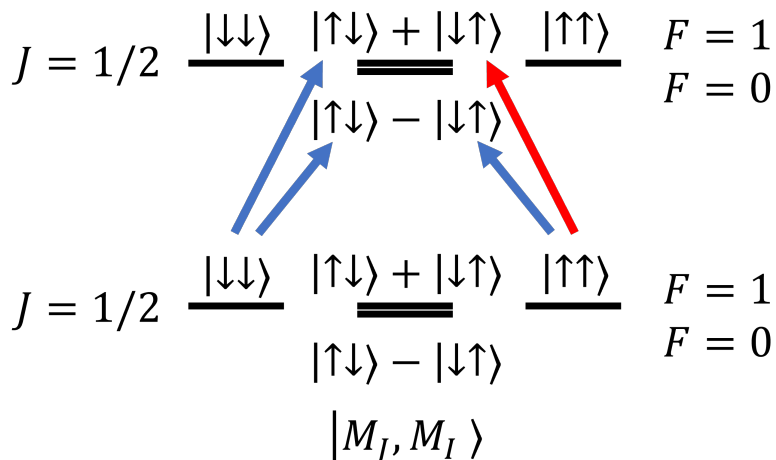
$$\left| M_J, M_I \right\rangle$$

Figure 5.8: A schematic diagram of the ground and excited states in the $J'' = 1/2 \rightarrow J' = 1/2$ transition driven by transverse polarized light. The hyperfine states are written in the decoupled $|M_J, M_I\rangle$ basis. In this basis, E1 selection rules enforce $\Delta M_I = 0$, and with transverse polarization we have $\Delta M_J = \pm 1$. The TDM phase for optical coupling depends on the excited state Clebsch-Gordan coefficients. We have colored the excitation laser according to the TDM phase, where red is positive and blue is negative. We see the two Λ systems have opposite relative phase on the two excitation arms, resulting in destructive interference of dark states.

and triplet $F = 1$ manifolds must be written with an opposite relative sign. This sign controls the relative phase of the TDMs in the two Λ-systems, which in turn controls the dark state phase, see Sec. 5.1.3 for details. In this case, the dark state of one Λ-system is the bright state of the other Λ-system, and the dark states are destabilized. As a result of destructive interference, all states are bright. This sign difference is generic to hyperfine $M_F = 0$ states, and persists even in the presence of an electric field.

Magnetic fields will mix and split the $M_F = 0$ states, but this is usually inconvenient for spin precession measurements. Still, we can consider the application of a magnetic field strong enough to decouple the hyperfine structure by mixing the excited $M_F' = 0$ states and increasing their separation. To avoid optical excitation, the splitting needs to be increased to > 20 MHz. This requires >15 G magnetic fields, causing rapid spin precession. While this is hard to measure with "DC" spin precession, we could in principle use clock methods. However, the transition dipole moments used to form coherent dark states also lose their T-symmetry, requiring finely tuned elliptical beam polarizations to achieve balanced superposition amplitudes.

One solution is to use optical dressing of an excited state with a separate ground state to split the excited states with light shifts. However, in YbOH and other metal hydroxides, the inability to optical address individual hyperfine ground states causes further complications with such a scheme. Any transition with $\Delta J = \pm 1$ will have at least two pairs of hyperfine states coupled by an optical

laser, resulting in level separations of the excited state given by differential light shifts. This requires large amounts of power to sufficiently split the levels, and if the beams are off resonant, the effect is even more difficult to achieve.

Another effect we have neglected is the existence of so-called gray states, introduced in Sec. 5.1.3. These are dark states created from superpositions of states with differing laser detunings. For example, a single power broadened laser can address multiple unresolved ground states, coupling them to a shared excited state. These unresolved hyperfine states nonetheless have some energy splitting, and this hyperfine splitting causes a rotation of the dark state into the bright state. The hyperfine interaction performs remixing, much as applied magnetic fields remix dark states for molecular laser cooling experiments. The instability of these dark states is why we refer to them as gray states.

We see that unresolved hyperfine structure limits the coherences that can be generated or observed using conventional techniques. In Ref. [372], this result was formalized using the theory of density matrix polarization moments. The authors considered single photon methods for producing atomic polarization, namely depopulation pumping (i.e., absorption removing population from certain ground states) and repopulation pumping (i.e., decay returning population to certain ground states). Unresolved hyperfine structure places limits on the atomic polarization that can be produced with lasers at "low power." Somewhat intuitively, polarization moments are limited by electronic angular momentum. In the case of molecules, this corresponds to J. We note there is a key distinction with molecules—while atoms can reach a steady state optical pumping configuration, in molecules if there is any excited state coupling for a ground state, it will eventually scatter into a dark vibrational state and be lost (unless we apply repumping light).

According to Ref. [372], the limit on ground state polarization moments depends on the method used. Depopulation pumping with unresolved excited state hyperfine structure is limited to produce moments with rank $\kappa \leq 2J''$ (i.e., limited by ground state J). Meanwhile repopulation pumping with unresolved ground state hyperfine structure is limited to produce moments with rank $\kappa \leq 2J'$ (i.e., limited by excited state J). Furthermore, because a photon is a spin-1 particle, a single photon process can change polarization moments by $|\Delta\kappa| \leq 2$. Additionally, fluorescence and absorption detection methods are limited by unresolved hyperfine structure. Absorption is limited by unresolved excited state hyperfine to only detect moments with $\kappa \leq 2J''$, while regardless of resolved hyperfine, fluorescence is limited to detecting moments with $\kappa \leq 2J'$ and $\kappa \leq 2$. Note the second restriction on fluorescence arises from the spin-1 nature of the photon and the single photon nature of spontaneous decay.

YbOH has unresolved hyperfine structure in the both ground and excited states, and both depopulation and repopulation pumping are thus limited. Note, CPT can be considered a form

of depopulation pumping (limited by unresolved excited hyperfine), as the initial mixed state is polarized by pumping out the bright state. For the ${}^{Q}Q_{11}(0)$ we tried for initial testing, both ground and excited states have $J = 1/2$, and therefore we can only produce rank 1 (orientation) moments with any type of pumping. The CPT scheme from ACME requires the creation of rank 2 (alignment) moments. For further information on orientation vs alignment, see Appendix E for details.

We can now consider states with higher J. For example, we can drive $J'' = 3/2 \rightarrow J' = 1/2, 3/2, 5/2$, corresponding to P, Q, and R lines. We note the arguments we make are actually generic to any J. For the R lines, the number of excited states outnumbers the number of ground states, and there are no dark states generically. Meanwhile, for a P line, with linearly polarized light there is optical pumping into the stretched states, which are manifestly dark to the laser. We now consider the Q line. Due to the selection rule preventing $M'' = 0 \nrightarrow M' = 0$ for $\Delta F = 0$, the $M'' = 0$ states are pumped out by the $|\Delta F| = 1$ transitions. Similarly, the stretched states are also pumped out. Meanwhile, the non-stretched states can be considered in a manifold of 4 states, two ground, two excited. Whether or not we obtain dark states now depends on the nature of the TDMs involved. It turns out such a transition actually does have dark states in the $|M| = 1$ states, as the excited state TDMs have the same relative phase. Due to the hyperfine splitting, these states are gray states, and the differential laser detuning will cause differential phase evolution that turns the dark state bright.

We can generalize this analysis by examining the matrix element for optical TDMs. We approximate the states as having J as a perfect quantum number. Such an approximation works well in our case when J mixing is weak and the hyperfine is unresolved. Since we only care about differential properties within a J manifold, we also ignore all quantum numbers comprising J. In this case, the treatment of atoms and molecules proceeds identically. We then write the TDM as follows:

$$
\langle JIFM|T_p^1(d)|J'IF'M'\rangle =
$$

$$
\times (-1)^{F-M} \begin{pmatrix} F & 1 & F' \\ -M & p & M' \end{pmatrix}
$$

$$
\times (-1)^{F'+J+I+1} \sqrt{(2F+1)(2F'+1)} \begin{Bmatrix} J' & F' & I \\ F & J & 1 \end{Bmatrix}
$$

$$
\times \langle J||T^1(d)||J\rangle.
$$

(5.10)

Here, the reduced matrix element $\langle J||T^1(d)||J\rangle$ encodes all TDM properties that are identical for all hyperfine states under consideration, including transformations into the molecule's rotating frame.

$$|M_Y = +1\rangle \qquad\qquad |M_Y = -1\rangle$$
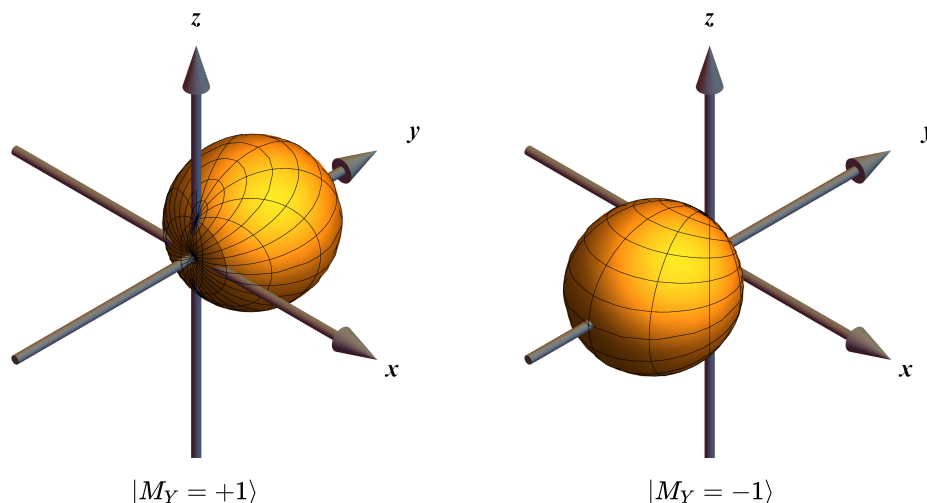
Figure 5.9: Oriented states used to implement spin precession using circularly polarized light. The notation $M_Y = F \cdot \hat{Y}$ indicates our quantization axis is along $\hat{Y}$. These states are dark states of $\sigma^{\pm}$ beams, and rotate into each other by the action of transverse magnetic fields along $\hat{X}$ or $\hat{Z}$.

5.2.2 Spin Precession with Circularly Polarized Light

We have seen that CPT schemes can encounter difficulties with unresolved hyperfine structure. Therefore, we next turned to measuring spin precession using angular momentum orientation instead of alignment (see Appendix E for details). We were inspired by Ref. [389], which used circular polarization to perform spin precession of a beam of Lithium atoms in a ficticious magnetic field generated by off-resonant laser light.

The application of circularly polarized light can optically pump molecules into a stretched state, which can be intuited as a transfer of angular momentum from the light to the molecules. Consider a σ^+ transition on a Q line. The $M'' = J$ stretched state is dark to the excitation laser, while all other ground states are addressed. For an atomic sample, the excited population can rain back down and continue to be pumped in a closed cycle until it is transferred to the stretched state. However, in a molecule most of the polarization occurs via depopulation, as excited molecules tend to decay elsewhere after one or two scatters. In any event, for the molecules remaining, the final state is a pure stretched state, which is dark on a Q line. We now show to this dark state can be used for spin precession.

We consider the following coordinate frame: the molecule beam propagates along the $+\hat{X}$ direction, the light is right hand circularly polarized along $+\hat{Y}$, and the magnetic field points along the $+\hat{Z}$ axis. Consider light resonant with the $^{Q}Q_{11}(0)$ line. To understand the optical pumping of the light, we consider a quantization axis aligned along $+\hat{Y}$. By conservation of angular momentum, this drives σ^+ transitions with $\Delta M_Y = 1$, and addresses both the $F = 0$ and $F = 1$ ground states. After a few light scatters, population is concentrated in the dark $M_Y = F \cdot \hat{Y} = +1$ stretched state.

The angular momentum probability surface for this stretched state is shown in Figure 5.9. As expected, the state exhibits orientation along $\hat{Y}$. Since magnetic fields cause rotation of angular momentum polarization, fields along $\hat{Y}$ have no effect due to distribution's $\hat{Y}$ symmetry. Another way to say this is the magnetic field interaction is diagonal in the M_Y basis and simply causes phase evolution. However, as we saw in the Hanle effect, transverse fields can rotate the polarization distribution. The situation here is analogous: the B_Z field rotates our stretched state. After half a Larmour period, the polarization will point along $-\hat{Y}$, and the state has been rotated to the $M_Y = -1$ stretched state, shown also in Fig. 5.9. In between, the state amplitude is distributed among the non-stretched states.

By using left or right hand circular light to drive σ^+ or σ^- transitions, the population can be effectively projected onto a bright/dark basis consisting of one of the stretched states as the dark state. In a sense, our measurement scheme is a form of magnetically sensitive optical dichroism. This scheme allows us to implement a precession similar to that of the ACME experiment described earlier. However, unlike the aligned ACME state, our oriented spin states precess at half the frequency. As we shall see, this is because we are measuring the energy difference relative to the $M = 0$ state.

We provide a more quantitative picture of the B_Z dynamics in Figure 5.10. First, we begin with the $M_Y = +1$ state, and rotate our quantization axis to point along $\hat{Z}$. We implement this using a Wigner D-matrix, $\mathcal{D}^{((F))}_{M,M'}(\omega)$, where $\omega = (0, \frac{\pi}{2}, \frac{\pi}{2})$. The $M_Y = 1$ state in the M_Z basis at time $t = 0$ is given by:

$$|\psi(t = 0)\rangle = |M_Y = 1\rangle = \frac{1}{2}|M_Z = -1\rangle - \frac{1}{\sqrt{2}}|M_Z = 0\rangle + \frac{1}{2}|M_Z = 1\rangle \tag{5.11}$$

Now, we consider the application of the magnetic field, which generates time evolution according to the operator $U = e^{-iHt}$. Since B_Z is diagonal in the M_Z basis, time evolution just consists of phase evolution at the Larmour frequency, $\omega_B = g\mu_B M_Z$, where g is the g-factor of the state. After half a period, $\tau = \pi/\omega_B$, has passed, the state is now given by:

$$|\psi(t = \tau)\rangle = -\frac{1}{2}|M_Z = -1\rangle - \frac{1}{\sqrt{2}}|M_Z = 0\rangle - \frac{1}{2}|M_Z = 1\rangle. \tag{5.12}$$

Crucially, the relative phase between the the $M_Z = \pm 1$ and $M_Z = 0$ states have reversed. We now rotate the time evolved state back to the M_Y basis using the inverse Wigner rotation, $\mathcal{D}^{((F))}_{M,M'}(-\omega)$. The time evolved state now maps on to the $M_Y = -1$ state, $|\psi(t = \tau)\rangle = |M_Y = -1\rangle$. If we had instead considered $\pi/2$ precession in the $\hat{Z}$ frame, we would have had an imaginary phase relative phase, which maps on to the state pointing along $\hat{X}$. We have now reached the same conclusion on the dynamics via two separate paths: one by using basis rotations of angular momentum states, and by considering dynamics of angular momentum probability distributions.
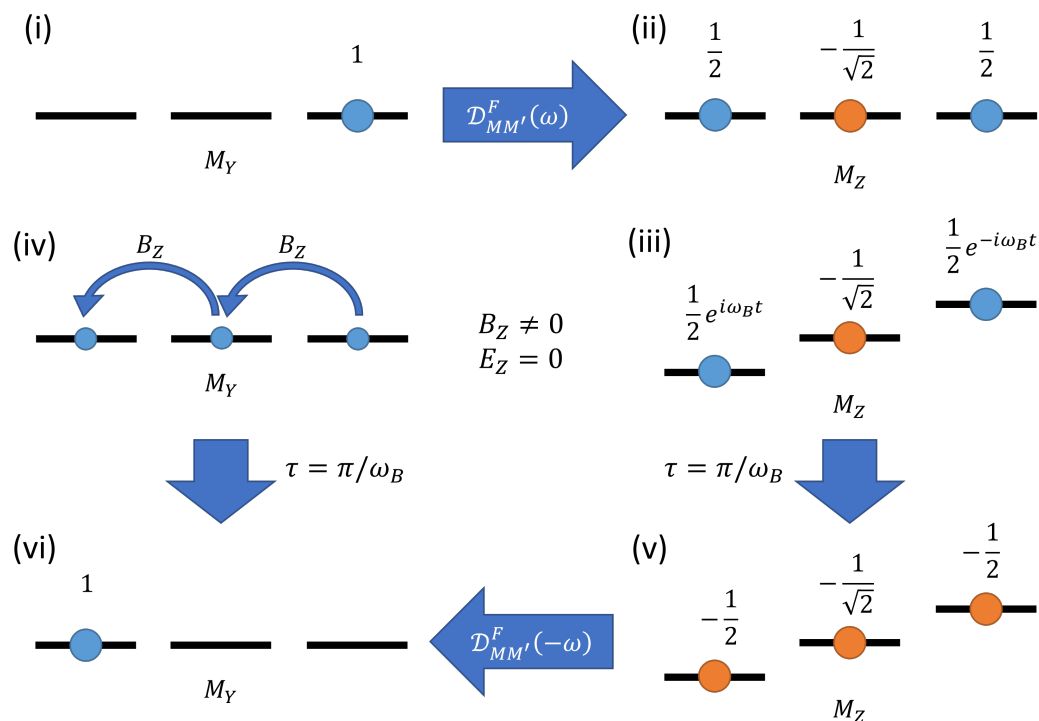
Figure 5.10: Schematic diagram of dynamics with the circularly polarized spin precession scheme. The left side of the diagram has $\hat{Y}$ as the quantization axis, while the right side has $\hat{Z}$ as the quantization axis. (i) The molecules are initially optically pumped into $|M_Y = 1\rangle$ using σ^+ light. We work with a Q line, and therefore $M_Y = 1$ is dark to σ^+. (ii) With a Wigner rotation, we can write $|M_Y = 1\rangle$ in a rotated basis as a superposition of $M_Z = -1, 0, +1$ states. (iii) In the $\hat{Z}$ frame, the application of a B_Z magnetic field causes the M_Z levels to split by the Larmour frequency $\omega_B = g\mu_B M_Z$, where g is the state g-factor. (iv) Alternatively, in the $\hat{Y}$ frame, the B_Z field is transverse and causes $\Delta M_Y = \pm 1$ couplings that move population between states. (v) After half a Larmour period, in the $\hat{Z}$ frame, the two $M_Z = \pm 1$ have reversed their sign relative to the $M_Z = 0$ state. (vi) In the $\hat{Y}$ frame, which can be obtained from (v) by an inverse Wigner rotation or directly time-evolved from (iv), we see the state has now evolved into the $|M_Y = -1\rangle$ configuration. The spin has now reversed direction, and this state can now be probed by σ^+ light.

5.2.3   Experimental Tests with Circularly Polarized Light

We now describe experimental tests. The experimental schematic is shown in Figure 5.11. The experiment takes place 40 cm downstream from the cryogenic buffer gas cell. The magnetic field is generated by 3-axis pairs of square coils able to generate fields up to ~1 G. The prep and readout beams are sent along the $+\hat{Y}$ axis, and they are separated in the $+\hat{X}$ direction by 1-5 mm. The two beams are split with a non-polarizing 50/50 beam splitter, separately focused with a 1000 mm focal length lenses, and recombined in another non-polarizing beam splitter. Adjustment of one beam path relative to the other allows for precise positioning of the two beams.

By setting up two circularly polarized laser beams along the molecule beam path, the upstream

laser beam acts as a preparation beam, while the downstream laser beam is the readout beam. Since the sample begins as unpolarized, the initial fluorescence of the prep beam is independent of polarization. After being polarized, the oriented molecules may or may not precess, depending on the B_z field magnitude. Upon encountering the readout beam, the molecules are projected onto the bright/dark stretched state basis. If the readout and prep handedness are the same, then the readout beam projects back on the initial stretched state. If the handedness is different, the readout beam probes the oppositely oriented stretched state. Therefore, the fluorescence of the readout beam has oscillatory dependence on the magnitude of B_z. Specifically, projection of the final population on the initial state is given by:

$$|\langle \psi(t)|M_Y = 1\rangle|^2 = \cos^4 \frac{\omega_B t}{2}. \tag{5.13}$$

The non-sinusoidal form is a result of the population dispersing throughout the non-stretched states, before rephasing at the stretched state. For states with $F \gg 1$, the population spends a large extent of time in other non-stretched states before rephasing.

The circularly polarized spin precession data is shown in Figure 5.12. To obtain the data, we switch the readout beam on and off for alternate shots, and plot the ratio of the fluorescence. This accounts for the constant prep beam fluorescence, which is relatively similar for adjacent shots (especially after averaging). If we use $g = 2$, which is accurate for a stretched state, we obtain a precession time of $\tau = 14.8$ µs. For a 200 m/s beam, this corresponds to a ≈ 3 mm precession length.

Thus far, all of the presented data was taken with the $\tilde{X}(000)$ ground state. This state behaves like a diatomic molecule, and in particular requires fields > 1 kV/cm to obtain appreciable Stark shifts. Therefore, we did not perform circularly polarized spin precession in the presence of an electric field on the $\tilde{X}(000)$ state. However, there are technical reasons that make such a spin precession scheme challenging.

Primarily, the Stark effect from the electric field will shift levels according to their value of $|M|$, causing rapid phase evolution of $M = \pm 1$ states with respect to $M = 0$. In the angular momentum probability picture, the E field results in rapid inversions of the stretched state through the origin, on top of the slow rotation from the magnetic field. If we average over these oscillations, the oriented state looks more like an aligned state that points in both directions. This rotating state still generates an oscillating fluorescence signal, but with reduced contrast. Finally, all of these discussion apply only to integer states: for half-integer states, the lack of an $M = 0$ state means the Stark oscillations do not fully wash out the state orientation. Nonetheless, a reduction in contrast still occurs. In theory, with a fast enough detection setup, one could use the Stark modulation of the fluorescence signal to perform a lock-in measurement. However, this is not practical for a beam, so we did not pursue it further.
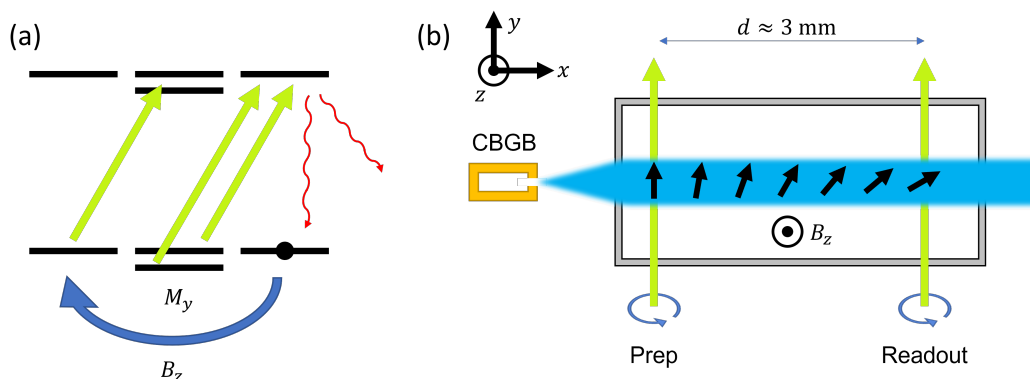
Figure 5.11: A diagram detailing the circular polarization spin precession scheme. (a) A level diagram of the Q line is shown schematically in the M_Y basis. The green arrows indicate optical pumping into the stretched state by σ^+ light propagating along $\hat{Y}$. (b) Schematic diagram of the beam line, with the $\hat{Z}$ axis coming out of the page. The molecules exit the CBGB, enter the magnetically shielded region, and encounter the prep beam. Then, they precess freely for ≈ 25 μs before being probed by the readout beam. We have shown the prep and readout beams with the same polarization, but they can in principle be made opposite to change the spin precession phase, similar to the ACME polarization switch.
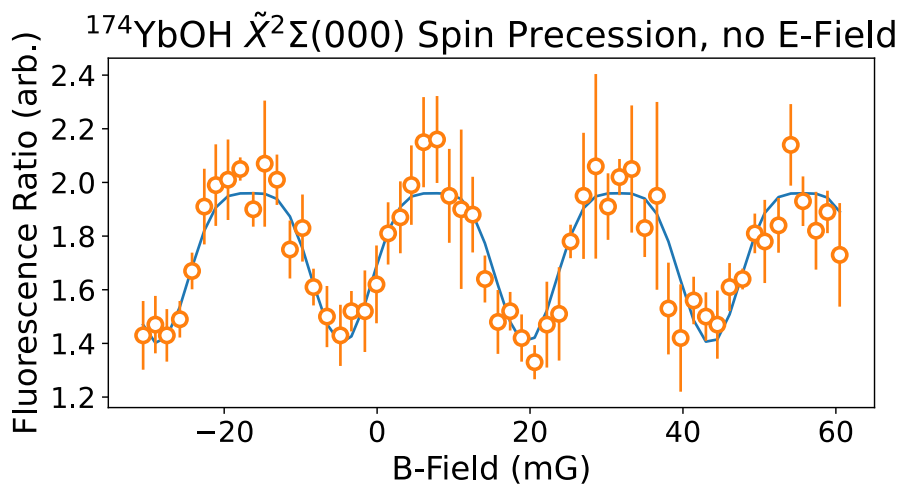
Figure 5.12: Spin precession data obtained using oriented stretched states. Here, the prep and readout beams both had the same circular polarization handedness. The y-axis plots the ratio of the fluorescence with and without the readout beam. When $B \approx 0$, the initial dark state does not precess and remains dark, and the fluorescence ratio is at a minimum. As we vary the magnetic field, the stretched state is rotated into bright states, which can fluoresce and give us signals.The functional form of the fit is $\cos^4 \omega B/2 + \phi$, where $\omega = g\mu_B \tau/2$. Using $g = 2$, we obtain $\tau = 14.8$ μs.

After taking the data shown in this section, we discovered and characterized the $\tilde{X}(010)$ bending mode in YbOH [280]. Therefore, all of the following data is from tests in the $\tilde{X}(010)$ state.

5.3 Ramsey Interferometry in a YbOH Beam

In this section, we discuss Ramsey tests performed using two-photon schemes. All of these measurements are performed in the $\tilde{X}(010)$ state of YbOH using population in the CBGB present after chemical enhancement [227].

An alternative to "projection-based" state preparation schemes, such as coherent population trapping (CPT), is to resonantly prepare superpositions using $\pi/2$ pulses between states of interest. This requires coupling between two states in the bending mode that can be switched on and off. Ideally, this coupling can select out single states, can be localized to specific regions in the beamline, and is continuous-wave in nature.

Coupling can be performed with radi-frequency radiation, microwave radiation, or two-photon optical radiation. Each technique has its associated advantages and disadvantages. Microwave radiation is primarily used in Section 5.4, which discusses prototype measurements in a trap. For a beam, microwaves can be challenging in terms of obtaining spatial and polarization homogeneity over the long molecule cloud, while also preventing leakage into the interaction region for Ramsey measurements. The CeNTreX experiment, a search for T-violation in ^{205}TlF molecules [390] uses microwaves for adiabatic state transfer pulses, but not for preparing the Ramsey states for measurement. For Ramsey state preparation, they use radio-frequency (RF) magnetic fields, which we discuss in Sec. 5.3.1.

Finally, we introduce optical two-photon methods, which include both resonant processes, like CPT, as well as detuned processes, such as Raman transitions. The benefit of optical two-photon approaches is that the light can be very well localized spatially, the polarization can be well controlled, and there are many technologies available for modulating light and applying sidebands. We performed extensive work with two-photon transitions in YbOH. In Sec. 5.3.3.2, we lay out the foundations for simulating two-photon physics using master equations. In Sec. 5.3.3.2 we present tests implementing two-photon CPT in a YbOH beam. In Sec. 5.3.5 we present tests driving two-photon detuned Raman transitions in a YbOH beam. We also use the resulting two-photon spectra to determine the hyperfine constants of the $\tilde{X}(010)$, $N = 1$ state. Finally, in Sec. 5.3.6, we use detuned Raman transitions to implement Ramsey interferometry on single quantum states in YbOH. We conclude with an outlook on performing EDM sensitive measurements in YbOH.

5.3.1 Radio-Frequency Electric Field Tests

When using radio-frequency (RF) techniques, the radiation is usually generated in the near-field regime. For example, RF radiation can be engineered by applying time-varying voltages or currents to antennae such as plates or coils, which can also source DC fields. This was the method used by the YbF beam experiment [391]. In both YbF and TlF, magnetic RF radiation is used to drive transitions between same parity states. In molecules with ~MHz parity doubling, such as bending modes of polyatomics, we can also use ~MHz RF electric fields to drive transitions between opposite parity states. We note the selection rules for electric dipole RF transitions varies for polarized molecules compared to non-polarized molecules. Specifically, polarized molecules with lab frame orientation $\langle M_N K \rangle = 1$ can only be strongly coupled to $M_N = 0$ states via transverse RF radiation, as parallel RF radiation coupling for oriented molecules is suppressed. Additionally, flipping the orientation to $\langle M_N \rangle = -1$ requires coupling via the intermediate $M_N = 0$ states. Such transitions can be driven by multiphoton RF techniques [392, 393].

We briefly looked for RF transitions among $\tilde{X}(010)$ levels our beam source. Using the same apparatus reported for the bending mode Stark spectroscopy in Ch. 4, Sec. 4.2.1, we applied an RF drive to the Stark electrodes, corresponding to $V_{rms} \approx 3.5$ V/cm. When the molecules passed through the RF field, they were simultaneously excited by a laser resonant with the $^Q Q_{11}(1)$ line of the $\tilde{X}(010) \rightarrow \tilde{A}(000)$ transition, and we collect the resulting LIF. Interpreting signals with simultaneous drives is challenging, as it depends on the ratio of the two drives. For very strong RF drive, we expect the molecule states to be dressed by the RF field, resulting in Autler-Townes splitting[9] of the optical line. We are not in this regime, however, and rather we expect the RF to mix parity states, which would have the effect of increasing LIF.

We observed a correlated increase in molecular fluorescence by ~18% when driving the RF drive at 25.53 MHz. At the time we did not have an assignment for this RF resonance, though now we believe this might have been the $J = 3/2^+, F = 2 \leftrightarrow J = 1/2^-, F = 1$ resonance, in agreement with the ground state of the optical transition.

We then tried amplifying the RF drive into the plates, generating an RF amplitude of ~15 V/cm. In this configuration, by contrast, we observed ~50% *depletion* of the molecule LIF, correlated with the RF drive being on. The depletion was broadly located around 30 MHz with at least ~1 MHz width, though our RF signal generator was limited to a maximum frequency of 30.2 MHz. At the time, we thought this might be strong Autler-Townes splitting causing the optical resonances to shift. The RF correlated LIF depletion was observed when probing both $J'' = 1/2^+$ and $J'' = 3/2^\pm$ ground states of the bending mode. However, after replacing the wire pair sourcing the RF with

---

[9]Incidentally first observed in bending modes of triatomic molecules! See Ref. [394].
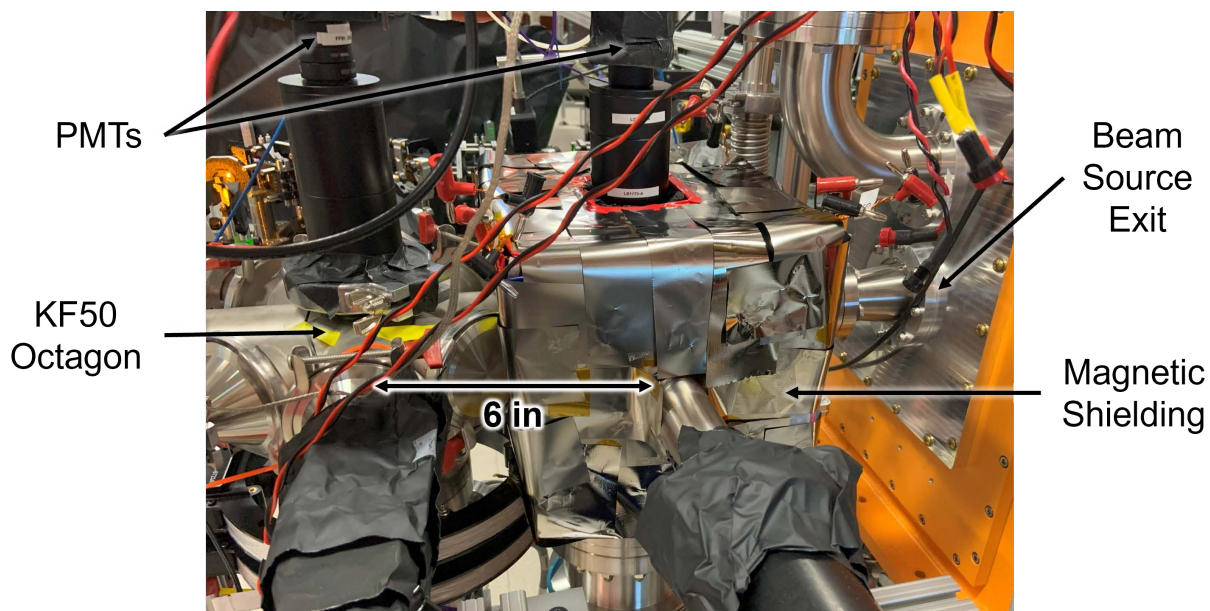
Figure 5.13: A photo of the beamline used for the two-photon tests. The molecule beam exits the beam source on the right and travels toward the left. The region wrapped in magnetic shielding contains the upstream KF50 cross and the 3-axis square magnetic field coils, and is where the two-photon tests occur. The downstream octagon is where we perform state readout and collect LIF. The 6 inch scale indicated is approximate.

coax cable, we were unable to recover the effect. We suspect stray inductances from the wire pair may have been causing resonant behavior, driving the fields with large amplitude rf.

Having encountered difficulty with the repeatability and interpretation of direct RF driving, we turned instead to two-photon Raman transitions. In a way, the optical two-photon scheme generates an effective RF field via the beat note of two optical frequencies. However the two techniques have very different selection rules, as we shall see.

5.3.2 Apparatus

5.3.2.1 Beamline

We performed two-photon transition tests on the 4 K source, performing both projective CPT tests and detuned Raman transition tests. YbOH beams were produced with the cell and source design described in Ch. 4, Sec. 4.2.1, as well as earlier in Ch. 3, Sec. 3.2. We describe now the setup for the beam extension for these tests.

After the 4 K CBGB source, we have two downstream interaction regions. Let X denote the distance from the cell aperture along the molecule beam axis. In the lab, this physically corresponds to the North/South axis. The cell aperture is at $X = 0$. The first, the "upstream" region of the beam extension is a six-way KF50 cross centered at $X \approx 42$ cm. The interior of the cross and all

arms are blackened with Alion MH2200 paint. The transverse arms of the cross run parallel to the ground (Y axis, East/West) and perpendicular to the ground ($\hat{Z}$ axis, Top/Bottom). The $-\hat{Z}$ arm of the cross adapts to CF 6-in, connecting to a 300 L/s turbo pump[10], and the $+\hat{Z}$ arm of the cross terminates in a KF50 window. Attached to this window is a collection optics stack that sends light through spectral filters into a PMT. The collection optics were optimized for 125 mm distance with an NA of $\approx$0.2. The $\pm\hat{Y}$ arms of the cross are adapted from KF50 to KF40 and connected to KF40 nipples terminated in AR-coated windows.

The upstream cross is surrounded by a cubic frame made from mini-8020 parts. The cube has 16.3 cm side length, making it roughly the same size as the six way cross. Each cube face is wound with square coils with 3 windings for each coil. The coil pairs allow for 3-axis control of the magnetic field inside the cross. To help with passive stability, the cubic frame is surrounded by mumetal plates, cut to size with shears, and attached to XE25 framing with clamps made from L-brackets. This mumetal functions as rudimentary magnetic shielding, particularly assisting with variations from lab activity and drift. To improve the shielding, we wrapped the mumetal with metglas strips, to help cover gaps and to provide magnetic continuity between the cube faces. With a magnetometer, we verified that the internal field was at the $\lesssim$ 20 mG level. Fig. 5.13 shows photo of the shielding on the beamline.

We performed field-free tests of both two-photon Raman transitions and CPT in a ^{174}YbOH molecular beam. Both schemes share similarities in setup and apparatus—the main difference is simply the one-photon detuning and the optimal powers involved. All tests were performed on the $\tilde{X}(010)$ state, using the athermal vibrational population present after laser enhancement. Absorption tests in front of cell on the $\tilde{X}(010) \rightarrow \tilde{A}(010)$ line at 17331.7130 cm^{-1} indicate that $\sim$4 $\times$ 10^9 bending mode molecules exit the cell each shot.

A schematic of the beamline is shown in Fig. 5.14. To summarize, we provide a brief overview before diving into details. First, the molecules encounter $\tilde{X}(010) \rightarrow \tilde{A}(000)$ light that depletes a specific hyperfine-spin-rotation level in $\tilde{X}(010)$ with parity $\mathcal{P}$, denoted $\psi_1 = |\mathcal{P}, NJF\rangle$. Then, we apply two-photon light on the $\tilde{X}(010) \rightarrow \tilde{A}(010)$ transition to couple $\psi_1 \leftrightarrow \psi_2$, where $\psi_2 = |\mathcal{P}, NJ'F'\rangle$ is a different hyperfine-spin-rotation level in $\tilde{X}(010)$. Either via diabatic projection (a.k.a CPT) or detuned Raman Rabi oscillations, population will be transferred from ψ_2 to ψ_1. Finally, at the end of the experiment, we measure the ψ_1 population via LIF, using a $\sim$10% pickoff of the upstream depletion light.

In detail, consider two spin-rotation manifolds, $J = N \pm 1/2$, in a given rotational state N, denoted ψ_1 and ψ_2. The two-photon resonances we wish to study are essentially couplings between ψ_1 and ψ_2, causing population transfer. If the coupling is unitary, which it is in the absence of

---

[10]Agilent TwisTorr 304 FS.
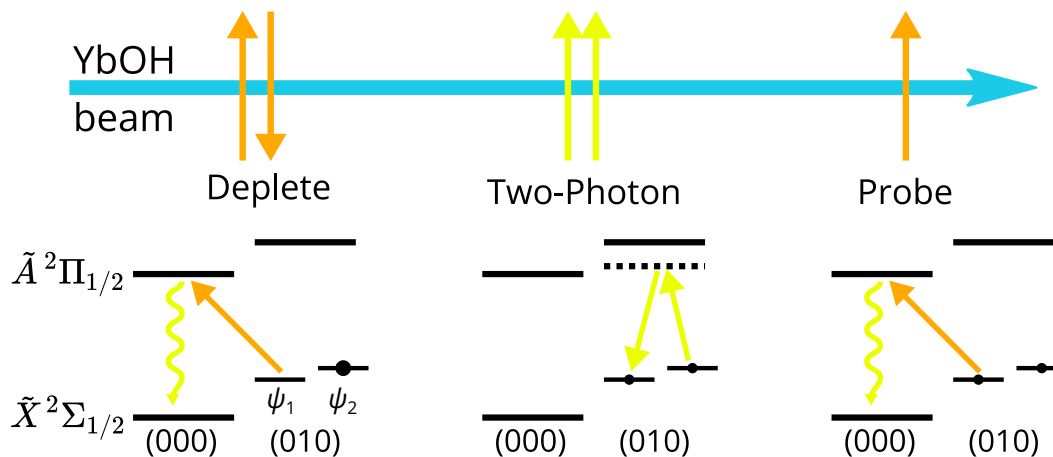
Figure 5.14: A schematic of the two-photon experiments performed in this section. In the first stage, the population in $\psi_1 = |N = 1, J = 1/2^+\rangle$ is depleted using $\tilde{X}(010) \to \tilde{A}(000)$ light. Then, the molecules encounter the two-photon light, in either CPT or detuned Raman configurations. When the two-photon resonance matches the spin-rotation splitting, there is population transfer from $\psi_2 = |N = 1, J = 3/2^+\rangle$ to ψ_1. In the final stage, the population revival in ψ_1 is readout with the same light that was used for depletion, and we collect the fluorescence.

spontaneous emission, the reverse process will also occur, and we have $\psi_1 \leftrightarrow \psi_2$. This means measurements of population contrast are limited by the population difference between ψ_1 and ψ_2. Since spin-rotation states are separated by ~ 100 MHz, they will have similar thermal occupation at the temperatures we consider (~ 1 K), and we must instead rely on optical pumping to first prepare an ensemble with large population imbalance between ψ_1 and ψ_2.

Since we can optically resolve the levels ψ_1 and ψ_2, we can selectively deplete just one level with a resonant laser beam. We consider depletion of ψ_1, achieved by driving the $\tilde{X}(010) \to \tilde{A}(000)$ transition using resonant light at 588 nm. To avoid optical dark states or gray states (see Sec. 5.1.3), we use an R line to perform pumping. We further ensure that the ψ_1 depletion line is not power broadened to the point where pumping of ψ_2 also occurs, though this was not a regime we could access with the laser power available, given the nominally forbidden nature of the transition. We use cylindrical lenses to expand the beam in the vertical direction transverse to the molecule beam, ensuring we address a majority of the molecules. The laser beam travels along Y, and has a diameter of ~ 3 mm in the vertical Z direction and ~ 1 mm in the X direction, which is the direction of the molecule beam forward velocity.

After achieving population imbalance between ψ_1 and ψ_2, we apply light downstream to drive the two-photon resonance. This couples $\psi_1 \leftrightarrow \psi_2$ and causes Rabi oscillations between the levels. After the molecules leave the two-photon light, they travel downstream to the detection region, where a pickoff of the 588 nm light is used to probe the initially depleted level, ψ_1. Rabi oscillations can cause a revival of population in ψ_1, which is detected in the LIF obtained in the detection region. If

the depletion is efficient and the Rabi oscillations are coherent, the variation of population in ψ_1 can be nearly 100% of the total population. In practice, experimental imperfections reduce contrast; for example, the depletion power is limited, there is velocity dispersion of the molecules, etc. For initial tests, decoherence is not a concern—even if the oscillations decohere quickly, there will still be an overall population transfer from $\psi_2 \to \psi_1$ as population is split between the two manifolds. Finally, by using a shutter to block and unblock the two-photon light in subsequent shots, even small population signals can be observed.

The two-photon light, either sourced by the EOM or AOMs, is fiber coupled over to the experiment with a PM fiber. After launching the beam, we use cylindrical beam shaping optics to expand the beam to roughly a 3 mm by 1 mm shape, and we use metal mirrors to ensure the polarization state of the light remains unperturbed. We also installed a mechanical shutter to turn the light on and off, which was useful for initial tests before optimizing SNR. The two-photon light intersects the molecules downstream of the depletion light, but still inside the six way cross. Since the two-photon light is at 577 nm, we wanted to separate it from the detection region in the octagon, where we look for 577 nm decays after probing the $\tilde{X}(010) \to \tilde{A}^2\Pi_{1/2}(000)$ transition.

5.3.2.2   Generating Two-Photon Light

We performed tests with two-photon light generated from both AOMs and EOMs. In both setups, we begin with a Raman fiber amplifier (RFA) that amplifies a seed laser operating at 1154 nm. When doubled with SHG, this turns into 577 nm light near relevant lines in $\tilde{X}^2\Sigma^+(010) \to \tilde{A}^2\Pi_{1/2}(010)$. For the EOM setup, we used in-fiber EOMs[11] inserted in the fiber path from the 1154 nm IR seed and the RFA. The modulation of the seed is directly mapped over to the RFA output. When the amplifier IR light is passed through an SHG crystal, the sideband frequencies do not change, but the modulation depth is doubled. This can be shown mathematically [395] but also understood intuitively—the SHG crystal is like a mixer, generating photons by multiplying any two sidebands (including the carrier). As a result, we optimize the EOM power by using a scanning cavity to examine a pickoff of the 577 nm light exiting the doubler.

For the AOM setup, we do not modulate the IR seed, and instead work directly with the 577 nm visible output of the SHG crystal, referred to as the VRFA output (visible RFA). This light is fiber coupled and sent to an optics breadboard with two AOMs, labeled 1 and 2. As the names suggest, AOM 1 generates laser beam $L1$ primarily addressing ψ_1, and AOM 2 generates $L2$ primarily addressing ψ_2.

The AOM optics setup is shown in Fig. 5.15. The light is split with a polarizing beam-splitter (PBS) and sent through two arms, one containing AOM 1 in a single pass configuration, resulting

---

[11] EOSPACE PM-0S5-10-PFA-PFA-1154-UL-SOP125mW.

Figure 5.15: The annotated acousto-optic modulator (AOM) setup used to generate two-photon light. White arrows label optical path directions for the double-pass setup. Parts are labeled as follows: VRFA, visible Raman fiber amplifier; HWP, half waveplate; QWP, quarter waveplate; PBS polarizing beam-splitter; BS, 50/50 beam-splitter; H/V, horizontal/vertical polarization; L/R, left/right handed circular polarization. See main text for details. We thank Yi Zeng for setting up the breadboard.

in a frequency shift f_1, the other containing AOM 2 in a double pass configuration, resulting in a frequency shift $2f_2$. The resulting beams are then recombined with a non-polarizing 50/50 beam-splitter (BS) and coupled into an optical fiber, to be sent over to the experiment. We use separate half waveplates (HWPs) on the A and B paths to independently adjust the polarization of each beam. A final HWP at the fiber couple, combined with separate quarter waveplates (QWPs) for each beam to remove ellipticity, allows us to perform effective polarization alignmnent to the fiber.

By tuning the diffraction order used, we can generate sidebands separated by $|f_1 + 2f_2|$ or $|f_1 - 2f_2|$, allowing us to overcome limitations on AOM dynamic range. Further, the double pass configuration of AOM B allows us to scan f_2 without significantly changing the beam pointing. Our AOMs have a 100 MHz center and 25 MHz bandwidth. To generate sidebands seprarated by

~ 60 MHz, the scale of $N = 1^+$ spin-rotation splittings, we use $f_1 = -120$ MHz, and $f_2 = -90$ MHz, resulting frequency splittings of $|f_1 - 2f_2| = 60$ MHz.

The double pass AOM 2 setup is implemented with standard techniques [396]. In brief, the light incident on AOM 2 is linearly polarized by a PBS. The first order diffracted beam exiting AOM 2 passes through a QWP, transforming linear polarization to circular. The beam is then focused with a 30 mm lens onto a retro-reflecting flat mirror, creating a cat-eye retro-reflector that is robust to variations in beam pointing. Another variation of this scheme is to center the AOM at the focus of a Keplerian telescope. In either setup, the retro-reflected beam has reversed circular polarization, which is converted to opposite linear polarization by the second pass through the QWP before re-entering AOM 2. Upon exiting and diffracting once again, this beam is now shifted by $2f_2$, and, because the polarization is opposite, is now reflected by the initial PBS and separated from the input beam.

The setup alignment is optimized at a central value $f_{2,0}$. We characterized the power variations about this central value by scanning f_2 and monitoring the power out of the fiber couple. We were able to fit the power efficiency to a Gaussian curve with a FWHM of ≈17.5 MHz. Since the two-photon frequency difference is proportional to $2f_2$, this results in a two-photon scan range with a FWHM of ≈35 MHz. This setup can be further improved by using a curved retro-reflecting mirror, and with other improvements detailed elsewhere [396]. We note for the $N = 1$ measurements detailed in Sec. 5.3.4, we had not yet implemented the lens for the double pass setup, and therefore our two-photon frequency efficiency range was limited to a FWHM of ≈5.8 MHz.

5.3.3 Two-Photon Physics

A two-photon transition essentially uses the beat note formed by two interfering lasers to drive a transition in an atom or molecule. In the E1 dipole approximation, single photon transitions are parity odd, and therefore two-photon transitions can only connect same parity states. Conveniently, the parity dependent spin-rotation term p_G in the $\tilde{X}(010)$ Hamiltonian ensures transitions correspond to the two parities are not overlapped. Additionally, two-photon transitions also have different F and M selection rules—transitions can now occur with $|\Delta F| = 2$ and $|\Delta M| = 2$. These selection rules can be derived by considering the selection rules of two back-to-back single-photon transitions.

Two-photon transitions are not limited by the excited state lifetime, making it possible to obtain very-high resolution spectra and address individual hyperfine states. The width of the two-photon resonance can depend on many factors, such as power-broadening, background field variation and inhomogeneity, and time-of-flight broadening. In practice, since fields in the region were limited to the ~10 mG level, at lower powers the resolution is limited primarily by time-of-flight broadening,

which is on the order of ~200 kHz for a 200 m/s molecule beam traversing a 1 mm wide laser beam. This is narrow enough to resolve the hydrogen hyperfine structure common to metal hydroxides, which is on the order of $1 - 10$ MHz for low-N states.

For the discussion to follow, we will find it useful to introduce a toy model consisting of a three level Λ-system, shown in Fig. 5.16a. The ground states, ψ_1 and ψ_2, will be typically taken to represent the two same parity spin-rotation states of $\tilde{X}(010)$ in a single N manifold. The excited state represents an excited state J' in $\tilde{A}(010)$ with opposite parity to the ground states. In our toy model, we have drawn two lasers, $L1$ and $L2$ addressing ψ_1 and ψ_2. While this is accurate for the AOM scheme, in the EOM scheme there will generically be more frequencies, shown in Fig. 5.16b, and discussed later. Continuing in the AOM picture, we define the one photon detuning Δ as $\Delta = \omega_{L2} - \omega_{e2}$, where ω_{e2} is the resonant transition energy to excite ψ_2. Meanwhile, the two-photon detuning is defined as $\delta = \omega_{L2} - \omega_{L1} - \omega_{12}$, where ω_{12} is the energy difference between ψ_1 and ψ_2. This definition of the two-photon detuning is convenient as the two-photon resonance occurs at $\delta = 0$. However, in the experiment we control the value $\delta' = \omega_{L1} - \omega_{L2}$, and so later we will switch to this definition of the two-photon detuning.

In Ref. [397], the authors show that in the limit of large Δ, the three level system in Fig. 5.16(a) can be reduced to a two level system described by the following effective Hamiltonian in frame rotating at ω_{12}:

$$\tilde{H}_{\text{eff}}/\hbar = \begin{pmatrix} -\delta/2 - \frac{|\Omega_1|^2}{4\Delta} & -\Omega_{\text{eff}}^* \\ -\Omega_{\text{eff}} & \delta/2 - \frac{|\Omega_2|^2}{4\Delta} \end{pmatrix}. \tag{5.14}$$

On the diagonals we have the AC Stark shifts, and on the off-diagonals we have coupling driven by Ω_{eff}, the effective Raman Rabi frequency, given by:

$$\Omega_{\text{eff}} = \frac{\Omega_1^* \Omega_2}{4\Delta}. \tag{5.15}$$

We can estimate the power needed to drive two-photon transitions. We assume $\Omega_1 = \Omega_2 = \Omega$, and write $\Omega = \gamma \sqrt{r_{ij} s/2}$, where r_{ij} is the branching ratio for the transition, defined in eq. 3.2. We approximate $r_{ij} \sim 1/2$ and use $I_s \approx 5$ mW/cm^2 as in YbOH. With $\Delta = 2\pi \times 1$ GHz, we obtain $\Omega_{\text{eff}} \approx s \times 2\pi \times 2.4$ kHz. We see we need to operate with $s \approx 80$ to obtain $\Omega_{\text{eff}} \approx 200$ kHz, on the order of the time of flight broadening. Luckily, we are working with quasi-diagonal FCFs on a strong transition, so we can achieve this saturation parameter with ~12 mW in each sideband for a 1 mm $\times$ 3 mm cylindrical beam.

To generate the two-photon light, we need to create coherent sidebands in the frequency spectrum of the laser. Two approaches were available to us: electro-optic modulators (EOMs) and acousto-optic modulators (AOMs). Though both have advantages and disadvantages, we ran
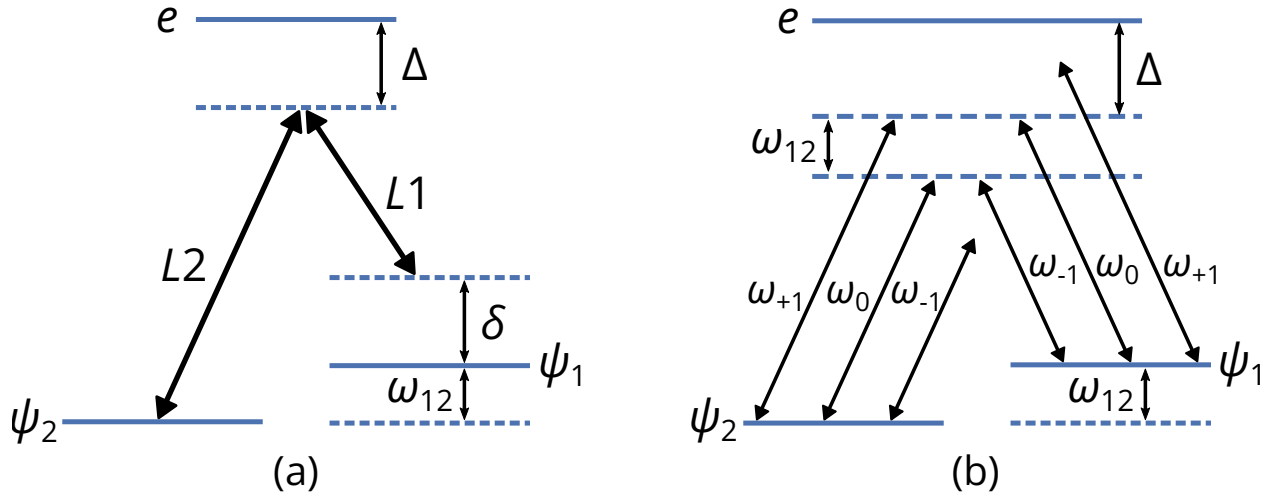
Figure 5.16: Three level toy models for AOM and EOM two-photon setups. The two ground states are ψ_1 and ψ_2, split by ω_{12}, and the excited state is e, separated from the ground states be ω_{e2} and ω_{e1}. (a) With an AOM, we generate two laser beams, $L1$ and $L2$, that can address either ground state. The one photon detuning is given by $\Delta = \omega_{L2} - \omega_{e_2}$, and the two-photon detuning is $\delta = \omega_{L2} - \omega_{L1} - \omega_{12}$. (b) With an EOM, we generate three frequencies: the carrier ω_0, and two sidebands ω_{+1} and ω_{-1}. The diagram shows the resonant two-photon case when $|\omega_0 - \omega_{\pm 1}| = \omega_{12}$. On resonance, we have two separate two-photon linkages, $\omega_0 \omega_{-1}$ and $\omega_{+1} \omega_0$. The relative phase of -1 between the sidebands results in destructive interference of the total $\psi_1 \leftrightarrow \psi_2$ transition amplitude, see main text for details. (b) is adapted from Ref. [398]

into two key distinctions that made AOMs more favorable to EOMs for generating two-photon light. First, the AOM produces a sideband that has a different k vector from the carrier, allowing independent control of the two polarizations, while the EOM produces two or more sidebands, all with the same k vector as the carrier, and same polarization properties. Second, the EOM produces positive and negative sidebands symmetric about the carrier, with a phase relationship of $(-1)^n$ between the nth and $-n$th sideband. This phase relationship results in destructive interference between the various carrier-sideband combinations that satisfy the two-photon resonance.

5.3.3.1 EOM Interference

Destructive interference when using an EOM to implement a two-photon transition is discussed in detail in Refs. [398, 399]. Consider an electric field oscillating at ω_0 subject to sinusoidal phase modulation with modulation index β:

$$E(t) = E_0 \cos(\omega_0 t + \beta \sin \omega t) = \frac{E_0}{2} e^{i(\omega_0 t + \beta \sin \omega t)} + \text{c.c.} \tag{5.16}$$

We now drop the ω_0 oscillation as well as the complex conjugate term, equivalent to performing a rotating frame transformation and rotating wave approximation. We can expand the remaining

exponetial using the Jacobi-Anger expansion as follows:

$$\frac{E_0}{2}e^{i\beta\sin(\omega t)} = \frac{E_0}{2}\sum_{n=-\infty}^{\infty}J_n(\beta)e^{in\omega t}. \tag{5.17}$$

The sum describes sidebands separated by ω, where each sideband amplitude is proportional to $J_n(\beta)$, which is a Bessel function of the first kind. We can then define a Rabi frequency for each sideband as $\hbar\Omega_n = D_{eg}E_0J_n(\beta)$. For now we ignore branching ratios and complex phases. In the case when sideband n and n' form a two-photon resonance at $(n - n')\omega$, we can then write the effective Rabi frequency as $\Omega_{n,n'} = \Omega_n\Omega_{n'}/(4\Delta)$.

First, we consider the case with low modulation depth, where the prominent signals are the carrier ($n = 0$) and first order sidebands ($n = \pm 1$). When the modulation frequency is resonant with the ground state splitting, we have the situation shown in Fig. 5.16b. We see there are two separate two-photon resonances that can occur, and we write the total transition amplitude as $\Omega_{tot} = \Omega_{0,-1} + \Omega_{0,+1}$. Now, we recall that $\Omega_n \propto J_n(\beta)$, and $J_n(\beta) = (-1)^n J_{-n}(\beta)$. Therefore the two terms contributing to Ω_{tot} are opposite in phase, causing destructive interference of the transition amplitude. To see how severe the cancellation is, we write $\Omega_{+1} = -\Omega_{-1} = \Omega_1$, and expand the transition amplitude:

$$\Omega_{tot} = \frac{\Omega_0\Omega_1}{4\Delta} - \frac{\Omega_0\Omega_1}{4(\Delta + \omega_{12})} \tag{5.18}$$

$$= \frac{\omega_{12}}{\Delta + \omega_{12}}\frac{\Omega_0\Omega_1}{4\Delta}. \tag{5.19}$$

We see that the effective Rabi frequency is supressed by the ratio ω_{12}/Δ for $\Delta \ll \omega_{12}$.

We now revisit our earlier power estimate. We take $\Delta = 2\pi \times 1$ GHz and $\omega_{12} \sim 2\pi \times 100$ MHz, which means our effective two-photon frequency is now at least $10\times$ weaker. Furthermore, if we increase the power, we have to contend with more off-resonant scattering. Normally, the scattering rate scales with intensity as $R_{sc} \propto I/\Delta^2$, while $\Omega_{eff} \propto I/\Delta$, and we can just move to larger detuning to improve the ratio Ω_{eff}/R_{sc}. However, with EOM interference, the extra factor of ω/Δ in eq. 5.18 now means $\Omega_{eff} \propto I/\Delta^2$ has the same detuning dependence as R_{sc}, and we no longer win by going to larger detuning.

This interference can motivate us to try driving two-photon transitions with larger frequency spacings, for example by modulating at $\omega_{mod}/2$, such that the $+1, -1$ sidebands form a resonance. However, we recall that the sideband intensities are given by Bessel functions $J_n(\beta)$. As we increase β to make the $|n| = 1$ sidebands larger, appreciable $|n| = 2$ sideband intensity will form. Therefore, we will also have resonances that form between the $0, \pm 2$ sidebands, and these resonances have opposite phase to the $+1, -1$ sideband resonance, resulting in further destructive interference.

Mathematically, one can show that no matter what sidebands we use, as long as the amplitudes are given by eq. 5.17, there will be destructive interference. The relatively straightforward proof is provided in Appendix F of Ref. [399]. The end result is the following statement:

$$\sum_{n=-\infty}^{\infty} J_n(\beta)J_{n'}(\beta) = \delta_{n,n'} \tag{5.20}$$

where $\delta_{n,n'}$ is the Kronecker-Delta function. The cross terms represent amplitude modulation at $(n - n')\omega$, and they vanish because we are performing pure phase modulation. As we showed earlier, the cancellation is not complete, as the sum we consider is also weighted in the denominator by the detuning Δ, which will have small variation for different sideband combinations. However, the cancellation is still severe, and we cannot improve the situation by using higher order sidebands.

In Ref. [398], the authors circumvent this issue by separating the ω_0 carrier with interferometric techniques, and deliberately applying an extra frequency shift to just ω_0 before recombining with the sidebands. Meanwhile, in Ref. [395], the authors present three methods: one uses a Mach-Zender interferometer to add differential phase shift, the second approach purposefully introduces sideband asymmetry by parking on the efficiency slope of a SHG gain curve, and the third approach uses a cavity to filter out unwanted sidebands. We note the second approach is very similar to our setup, where we perform phase modulation before a doubling crystal. Finally, in Ref. [399], the authors use a dispersive element to convert phase modulation to amplitude modulation.

As shown in the references above, we can circumvent the interference issue if we purposefully introduce amplitude modulation into the problem, equivalent to breaking the symmetry of the EOM sidebands. Asymmetric sidebands are actually somewhat common and usually unwanted, and can result from driving an EOM with harmonics of the modulation frequency. Therefore, we can purposefully drive the EOM with additional tones at harmonic frequencies, adjusting their amplitude and phase by optimizing for asymmetry in the sideband spectrum.

In the experiment, we tried performing detuned Raman transitions using two-photon light derived from an EOM. We were unable to see any effect at low powers, thought at sufficiently high power we did see some weak signals correlated with the EOM being on. Unfortunately the SNR was very poor and the power required was >100 mW, resulting in noticeable off-resonant scattering at a detuning of 1 GHz. Finally, we tried generating asymmetric sidebands by driving the EOM with a waveform at 2ω in addition to ω. By adjusting the amplitude and phase of the two waveforms, we were able to create a 1:4 asymmetry ratio of n and $-n$ sidebands. However, because we did not use a doubler but instead used two different output channels, we had relative frequency offsets between our ω and 2ω tones that caused sideband asymmetry drift over timescales of seconds.

Even if the destructive interference from opposite phase sidebands was not an issue, EOMs

are still limited to generate sidebands with identical polarization to the carrier[12]. This can result in interference issues when combined with unresolved hyperfine structure. We previously encountered this issue in Sec. 5.2, where for certain transitions, hyperfine doubling destabilized dark states.

In both AOM and EOM based approaches, hyperfine doubling results in two contributions to the two-photon transition amplitude, one from each excited F state for a given M_F. The specific TDM couplings depend on Wigner-6j and 3j symbols. The two hyperfine contributions generally have opposite sign, though not opposite magnitude, and this has different consequences for CPT compared to detuned Raman transitions. For CPT, the dark states are proportional to the transition amplitudes and their phases. The presence of two oppositely signed two-photon couplings means there is wavefunction overlap with the bright state of one coupling and the dark state of the other coupling, resulting in optical pumping and loss. This is the same mechanism that is detailed in Sec. 5.2. Meanwhile, in the case of detuned Raman transitions, the transition amplitudes for the different two-photon paths are added together. Because the matrix elements between $\Delta F = -1, 0, +1$ states are generically different, there is not an exact cancellation of transition amplitudes, and the total amplitude can retain a decent fraction of its nominal value.

Further, CPT can still be pursued if there is no hyperfine doubling in the excited state. This is the case whenever addressing transitions to stretched excited states, as they correspond to a unique $M_I = I \cdot \hat{Z}$ configuration in the decoupled nuclear spin basis. The existence of a single, unique excited state means only one dark state forms, and is orthogonal to any other bright states. Indeed, later we achieve a successful CPT resonance using an EOM to couple stretched states. Stretched states also do not have order unity reduction of the transition amplitude in detuned Raman transitions. In order to leverage stretched excited states for two-photon resonances, we must consider the level degeneracies of the ground and excited states, as well as the optical linkages formed by our polarizations of choice.

5.3.3.2 Master Equation Simulations

In addition to experimental tests, we model the two-photon dynamics using a Lindblad master equation (a.k.a. optical Bloch equations), implemented in QuTiP[13]. For specific details on modeling dynamics with master equations, see Ch. 4 of Ref. [349] as well as Refs. [120, 400, 401]. Master equations are powerful tools that allow us to combine unitary dynamics (entropy preserving) with dissipative dynamics (entropy increasing). In our case, unitary dynamics are implemented by optical couplings, while dissipation results from spontaneous emission. Therefore a master equation describes the evolution of a density matrix ρ, which can describe both coherent superpositions and

---

[12]There are clever and complicated techniques that can be leveraged to split a carrier and its sidebands, see Ref. [398] which used this to avoid EOM interference.

[13] https://qutip.org/

statistical mixtures. Though we do not pursue it here, the master equation approach can also be generalized to generate quantum state trajectories [402].

The Lindblad master equation describes the time evolution of the density matrix ρ subject to both coherent operations and dissipation. The master equation is given by [213, 402]:

$$\frac{d\rho}{dt} = -\frac{i}{\hbar}[H, \rho] + \sum_{ij} \gamma_{ij} \mathcal{D}[c_{ij}]\rho. \tag{5.21}$$

The master equation is the same in the rotating frame[14], so long as we substitute $\tilde{H}$ for H and $\tilde{\rho}$ for ρ. The commutator $[H, \rho]$ generates unitary dynamics, while the "superoperator" $\mathcal{D}$ generates dissipative dynamics. Meanwhile, the sum is taken over the ground states i and excited states j, with the partial width γ_{ij} given in eq. 3.1. The operator $c_{ij} = |i\rangle\langle j|$ represents the multi-level equivalent of σ_- that transfers population from $e \rightsquigarrow g$. Finally, the dissipation superoperator $\mathcal{D}$ is defined as $\mathcal{D}[c]\rho = c\rho c^\dagger - \frac{1}{2}\{c^\dagger c, \rho\}$, where $\{A, B\} = AB + BA$ is the anti-commutator.

To represent the ground state manifold, we use the eigenstates obtained by diagonalizing the $\tilde{X}(010)$ effective Hamiltonian obtained in Ch. 4. To model the excited state, we use the eigenstates obtained by diagonalization of the $\tilde{A}^2\Pi_{1/2}(000)$ state, and when calculating the E1 TDM, we substitute $\Lambda \to \ell$, i.e., we treat the state as a $^2\Pi_{1/2}$ *vibronic* state where Λ and ℓ are indistinguishable. In such an approximation, transitions are generated by the parallel $T^1_{q=0}(d)$ component of the molecule frame transition dipole. This is not strictly accurate, as we know from Ch. 4 that the E1 transition up to $\tilde{A}$ should couple via $T^1_{q=\pm1}(d)$ components. Nonetheless, accurate modeling of the bend-to-bend TDMs is significantly complicated by the K-resonance, and was beyond the scope of our work. Further, the approximation is not necessarily a bad one considering the K-resonance makes the $\tilde{A}(010)$ state *look* like a $^2\Pi(b)$ state. We will refer to our approximated state as $\tilde{A}(010)$ for convenience, though the reader should remember we are not treating the exact TDMs with detail.

For the coherent dynamics, we use a total Hamiltonian consisting of the eigenvalues of direct diagonalization on the diagonals, and the computed TDMs for the off diagonals. We setup the problem in a basis containing all $\tilde{X}(010)$ states of parity $\mathcal{P}$ in a single rotational manifold N, including all J, F, M states. For the excited states, we include in the basis all $\tilde{A}(010)$ states of opposite parity, $\mathcal{P}' = -\mathcal{P}$, in a single excited state J' manifold, including hyperfine parameters that are deliberately set to be $\sim100\times$ smaller than the $\tilde{X}(000)$ hyperfine.

We treat the two-photon light generated by the AOMs as consisting of two light fields, $\hat{\epsilon}_1 E_1 \cos(\omega_{L1}t)$ and $\hat{\epsilon}_2 E_2 \cos(\omega_{L2}t)$, where E_i is the electric field amplitude and $\hat{\epsilon}_i$ is the polarization. We take $L1$ to address ψ_1, the ground J manifold that is initially depleted. Then $L2$

---

[14]Diagonal values of ρ and $\tilde{\rho}$ are also the same, but the off-diagonal entries can be different.

addresses the undepleted ground manifold ψ_2. The two-photon detuning is given by $\delta = \omega_{L2} - \omega_{L1}$, and the one photon detuning is given by $\Delta = \omega_{L2} - \omega_{e\psi_1}$, where $\omega_{e\psi_1}$ is the transition energy from the excited state to the ψ_1 manifold. Fig. 5.17 shows a schematic of relevant transitions and levels when considering the $N = 1$ ground state manifold.

Transition dipole moments are written as $\Omega_{ge}^{(i)} = \langle g|T^1(d) \cdot T^1(\hat{\epsilon}_i)|e\rangle E_i/\hbar$, where i denotes $L1, L2$, and e, g denote arbitrary ground and excited states. We connect Ω to experiment via the saturation parameter, $s = I/I_s = 2\Omega^2/\gamma^2$, where $\gamma = 1/\tau$ and $I_s = \frac{\pi h c}{3\lambda^3 \tau}$. Rewriting in terms of branching ratios the line strength $m_{ij} = \langle i|T_p^1(d)|j\rangle/D_{eg}$, we have $\Omega_{eg} = \gamma m_{ij}\sqrt{s/2}$. We note that the saturation parameters should be interpreted very approximately, as we do not model the Gaussian extent of the laser beam, nor do we know the excited state TDMs accurately.

Suppressing M sublevels and hyperfine quantum numbers for convenience, we can write the Hamiltonian in a basis given by

$$\left\{\left|e, J'\right\rangle, \left|\psi_1, J_1\right\rangle, \left|\psi_2, J_2\right\rangle\right\}. \tag{5.22}$$

We transform into the rotating frame defined by $R = e^{i\xi t}$, with ξ a diagonal matrix with diagonal entries given by $\{\omega_{L2}, \delta, 0\}$. In this choice of rotating frame[15], the J_1 spin-rotation manifold energy is defined relative to frame rotating at the two-photon frequency δ. We also define the spin-rotation splitting as E_{SR} as the energy separation between J_1 and J_2. We can then write the rotating frame Hamiltonian as:

$$\tilde{H} = \begin{pmatrix} -\Delta & \frac{1}{2}\Omega_{J'J_1}^{(1)} + \frac{1}{2}e^{-i\delta t}\Omega_{J'J_2}^{(2)} & \frac{1}{2}e^{i\delta t}\Omega_{J'J_1}^{(1)} + \frac{1}{2}\Omega_{J'J_2}^{(2)} \\ \text{h.c.} & -\delta + E_{SR} & 0 \\ \text{h.c.} & \text{h.c.} & 0 \end{pmatrix}. \tag{5.23}$$

where h.c. denotes Hermitian conjugate of the upper half diagonal. For convenience, have taken the Rabi frequencies Ω to be real, as we only consider light linearly polarized along $\hat{Z}$ and $\hat{X}$. The form of the Hamiltonian sheds some light on how detuned Raman transitions work.

To generalize the above matrix to the full basis, one can add the hyperfine energies to the diagonal elements, and take into account the hyperfine state quantum numbers when computing the Rabi frequency matrix elements. Finally, we note with the $\tilde{X}(010)$ parameters from Ch. 4, there are two separate values of E_{SR} in $N = 1$, one for each parity, calculated to be $E_{SR}^{(-)} = 45.3$ MHz and $E_{SR}^{(+)} = 62.1$ MHz.

Finally, we implement a few phenomenological additions to the simulations. First, we add an extra ground state that is uncoupled by coherent manipulations, but can be populated by excited state decays. This "dump" state is meant to model leakage to other vibrational states dark to the

---

[15]An alternative parameterization is $\{\omega_{L2}, \delta, 0\}$, which is easier for comparison to the effective Hamiltonian eigenvalues, as the diagonal entries are just state energies.

laser, and its branching ratio is obtained by assuming the $\Delta v = 0$ decay from $\tilde{A}(010)$ has the same vibrational branching ratio (89.44%) as the equivalent decay from $\tilde{A}(000)$ [144, 217]. Secondly, to phenomenologically model Doppler broadening of the excited state, for CPT simulations only we add excited state dephasing using $\sum_J \gamma_D \mathcal{D}[d_j]\rho$, where γ_D is the Doppler width (~10 MHz) and $d_j = |j\rangle\langle j|$ is the excited state projector. This can be thought of as the multi-level equivalent of a σ_z dephasing operator, which eliminates off-diagonal coherences. This approximation is fine so long as we are not interested in coherent physics on time scales shorter than the excited state lifetime. Otherwise we must average the master equation solutions over one-photon detuning values (the sidebands are co-propagating and the two-photon detuning is Doppler free).

Simulations are performed with a 1.2 ns timestep. Such a short timestep is necessary because we are directly simulating the phase oscillation of the off-diagonal matrix elements, which have a period of $E_{SR}^{-1} \approx 17$ ns. On one hand, this allows us to use the same simulation for resonant CPT and detuned Raman processes, just changing the one photon detuning. If we were just interested in detuned Raman transitions, we could have instead developed an effective model that eliminates the excited state in favor of an effective two-photon Rabi rate. See Ref. [397] for a discussion of what "eliminating" the excited state means.

5.3.4 Two-Photon CPT Tests

First, we performed experiments on resonance, using transition interference between the two AOM sidebands to implement coherent population trapping (CPT). We label the two laser sidebands as $L1$, addressing the depleted state ψ_1, and $L2$, addressing the undepleted state ψ_2. The two-photon detuning is given by $\delta = \omega_{L2} - \omega_{L1}$, the one photon detuning is given by $\Delta = \omega_{L2} - \omega_{e\psi_2}$, and the spin-rotation splitting is given by E_{SR}. See the previous section for details on notation.

To understand how a dark state can result in population transfer, we imagine the bright and dark states are given by $|B/D\rangle \propto |\psi_1\rangle \pm |\psi_2\rangle$. Now we expand the initial state, ψ_2, in the bright/dark basis, as $|\psi_2\rangle \propto |B\rangle - |D\rangle$. As the molecule enters the light field, the coupling $|B\rangle \rightarrow |e\rangle$ increases, while $|D\rangle$ remains dark. After a few photon scatters, the bright state is pumped away, but the dark state remains, and the population is spread between ψ_1 and ψ_2. We can also think of the transitions between the two ground states as occurring via stimulated absorption followed by stimulated emission.

In the experiment, we fix ω_{L2} on resonance, $\Delta \approx 0$, and we scan ω_{L1} by varying the AOM drive. We can adjust the relative polarization angle between $L1$ and $L2$ using a half waveplate, as detailed in the apparatus section. Based on the issues with hyperfine interference discussed in Sec. 5.2, we expect that if $L1$ and $L2$ are both polarized along the same direction, we will have destabilized dark states. We can see this by choosing the polarization direction to be $\hat{Z}$, which makes the hyperfine
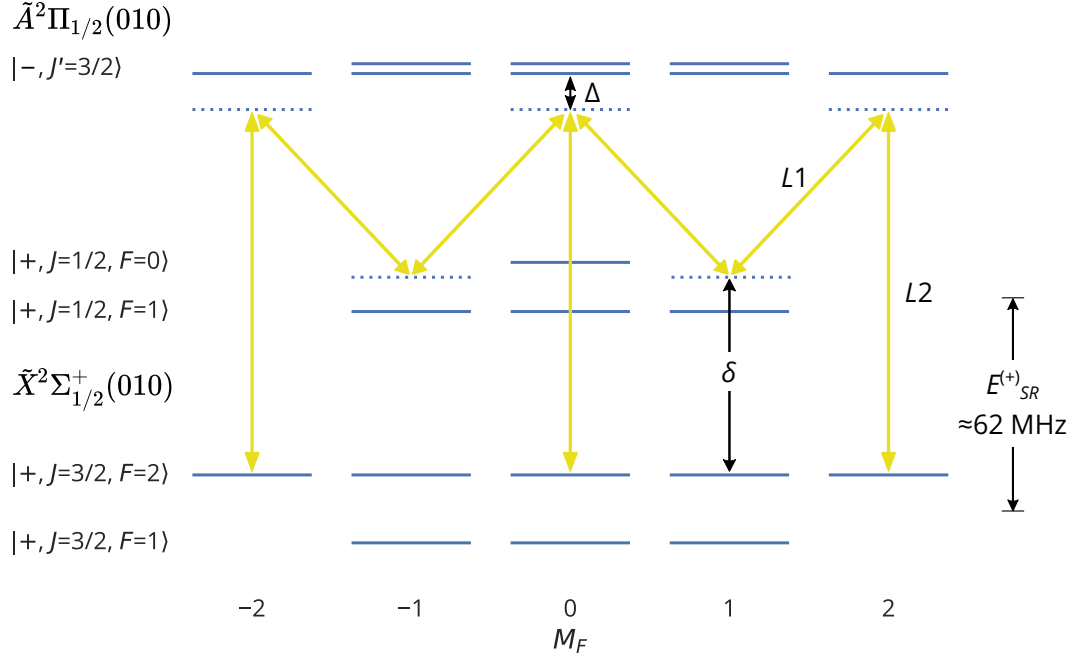
Figure 5.17: A schematic diagram of the $\tilde{X}(010)$ and $\tilde{A}(010)$ states involved in the two-photon experiments with orthogonal polarizations. The diagram is applicable to both CPT and detuned Raman transitions. Here, we show the case of $|\psi_1\rangle = |J = 1/2^+\rangle$ and $|\psi_2\rangle = |J = 3/2^+\rangle$. The two AOM sidebands are $L1$ and $L2$, and we indicate the one photon detuning Δ and the two-photon detuning δ (see main text for more details). Here, we have only shown one of the possible linkages between $F = 2$ and $F = 1$. In general there will also be linkages involving $F = 2, M_F = \pm 1$ states, not shown.

interference clear. On the other hand, we expect that with orthogonal polarizations, dark states will exist. We can obtain these conclusions by examining the linkages (two-photon resonances) formed by the two optical couplings, shown in Fig. 5.17. If a linkage has more ground states than excited states, then a dark state will exist. If the number of states is equal between ground and excited, then given the hyperfine doubling, we expect the dark states to be destabilized by resonant bright state scattering via the hyperfine doubled excited state.

We first investigated CPT resonance for the $N = 1, \mathcal{P} = +1$ manifold of the ground state, where we identify $|\psi_1\rangle = |J = 1/2\rangle$ and $|\psi_2\rangle = |J = 3/2\rangle$. We deplete the $J = 1/2$ manifold using the strong ${}^Q R_{12}^+(1)$ line of the $\tilde{X}(010) \rightarrow \tilde{A}(000)$ transition. The two-photon laser $L2$ is fixed on the transition from $\tilde{X}(010), J = 3/2$ up to $\tilde{A}(010)$, specifically the lower $J' = 3/2^+$ state ("$N' = 1$") of $\tilde{A}(010)$ at 17331.7010 cm^{-1}. We then scan the frequency of ω_{L1} via by changing the RF frequency driving our double-pass AOM detailed earlier in the apparatus section. Figure 5.18(a) shows both data and theory for the CPT resonance with perpendicular polarizations for $L1$ and $L2$. The lineshape is similar to that obtained in electromagnetically-induced transparency. We note the CPT data shown was taken with a limited AOM double-pass configuration, resulting in extinction

$\tilde{X}(010),\, N{=}1^{\,+} \leftrightarrow \tilde{A}(010),\, J'{=}3/2^{\,-}$ CPT
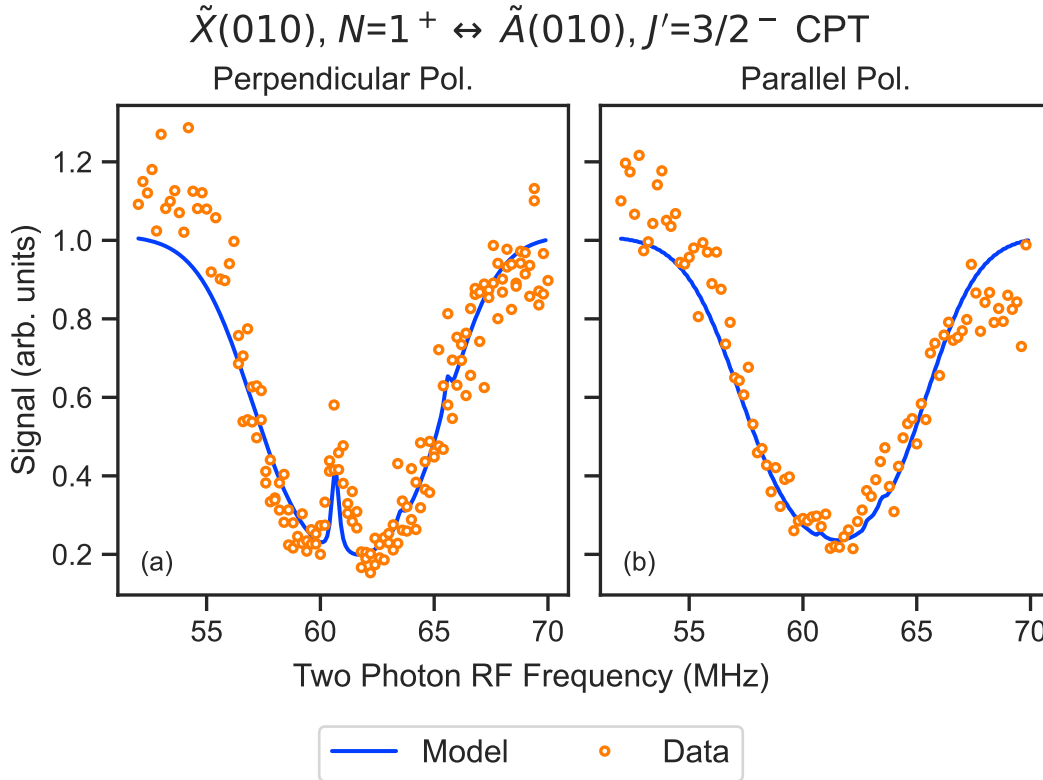
Figure 5.18: Coherent population trapping (CPT) features obtained with $\Delta = 0$ scanning the two-photon frequency δ across the $N = 1^{+}$ spin-rotation splitting. The signal is the population read out from the $J = 1/2$ level, denoted ψ_1 in the main text. All model curves are calculated with $s_1 = 0.5$, $s_2 = 10$, taking into account the AOM scanning efficiency with $\sigma = 2.5$ MHz, and using a 10 MHz excited state Doppler broadened width. Both data curves have slopes due to target decay and heating. (a) CPT signals obtained with perpendicular polarization on the two sidebands $L1$ and $L2$. The feature in the middle is a dark state formed by connecting $J = 3/2, F_2 = 2 \leftrightarrow J = 1/2, F = 1$. (b) The CPT feature is absent when using parallel polarization on $L1$ and $L2$, a result of hyperfine interference.

of $L1$ power when 55 MHz $< \delta <$ 65 MHz, see the apparatus Section 5.3.2.2 for details. The theory curves take into account this power variation. We now explain the general lineshape of the feature.

When ω_{L1} is far off resonance (or extinguished), there is no two-photon resonance. Instead, we will only have a "one-photon resonance" from ω_{L2}, which optically pumps population from ψ_2 to ψ_1 via the pathway $\psi_2 \rightarrow e \rightsquigarrow \psi_1$. In our downstream probe of ψ_1 shown in Fig. 5.18, this looks like an increase in population compared to when ω_{L2} is blocked. Now we consider the case when ω_{L1} is detuned from the ψ_1 resonance (and therefore from the two-photon resonance) by $\gtrsim 1$ MHz. The interference of $L1$ and $L2$ results in a dark state, but it is not stable. In the frame rotating at E_{SR}, the dark state phase is oscillating at a frequency $E_{SR} - \delta \gtrsim 1$ MHz, and

therefore within 1 µm or faster it transforms to a bright state that is pumped out by the lasers. Therefore, any population that decays into ψ_1 via optical pumping will inevitably be pumped back out, and we see the signal representing the ψ_1 population drops accordingly. This large dip should be as wide as the total width of the one photon fluorescence feature, but in the experiment we are limited by loss of $L1$ power as we scan δ. Finally, in the middle of the large depletion dip, we see a narrow feature, corresponding to the two-photon CPT resonance. The interference between $L1$ and $L2$ is on resonance with the spin-rotation splitting, $E_{SR} - \delta \approx 0$, and therefore the dark state phases remain stable in the frame rotating at δ. We note that we can also observe the population in the $J = 3/2, \psi_2$ state in the simulations, which indicates the exact opposite lineshape—a wide one photon pumping feature corresponding to increased ψ_2 population, and a series of narrow CPT resonant dips corresponding to dark state transfer to ψ_1.

The simulations agree with the data well, although they require us to modify the saturation parameters s_1 and s_2 from the naive expectation. This should not be a surprise, considering we do not know the exact excited state TDMs. The simulations indicate the other hyperfine components are buried under the noise floor of the depletion signal, combined with the loss of light from technical imperfections in the initial AOM setup.

We now discuss the width of the feature. Since magnetic fields in the region are controlled down to $\lesssim 30$ mG levels, this can give a Zeeman broadened width of at most 50 kHz. In the absence of power broadening, we expect the dominant contribution to the width to be time-of-flight broadening. The molecules are traveling at 200 m/s, and the laser beam is ∼1 mm wide, resulting in a $t_{TOF} = 5$ µs time-of-flight, and a broadening of $\sim t_{TOF}^{-1} = 200$ kHz. We can intuitively understand time-of-flight broadening as limiting the number oscillations, experienced by the molecules, of the RF beat note between the two sidebands. The width observed in the data is larger than expected, possibly due to uncompensated stray fields.

The data in Fig. 5.18(a) was taken with balanced power in both sidebands, approximately 500 µW split between both beams. Using $I_s = 5.4$ mW/cm^2, as is the case for the $\tilde{X}(000) - \tilde{A}(000)$ band in YbOH, this would nominally correspond to $s \approx 1.5$. However, the middle CPT feature is too strong to be explained by such a value in the simulations. We note this discrepancy could be due to s_1 being lower as a result of the AOM fiber couple issues mentoned earlier.

We also studied the effect of varying the power in the beams. Generically, the dark states that form are may be as $\Omega_2|\psi_1\rangle - \Omega_1|\psi_2\rangle$ assuming all positive Ω. We therefore see that we can increase the amount of population returned to ψ_1 (and therefore the contrast of the CPT lineshape) by increasing the intensity of the $L2$ laser addressing ψ_2. Finally, due to the fact that $E_{SR} \approx 6\gamma$, where γ is the radiative linewidth, if we increase the power of either beam such that $E_{SR} \sim \gamma\sqrt{1 + s}$, then the power broadened resonance results in off-resonant scattering of ψ_1 by $L2$ and vice-versa,

which can destroy the dark state via optical pumping. Indeed, if we increase the powers too high, we observe loss of the CPT resonance in the experiment.

We also investigated the configuration where both AOM sidebands have the same polarization orientation. The data and simulation results for parallel optical polarizations are shown in Fig. 5.18(b). While the depletion dip is still present, we see the CPT resonance has been reduced to below the noise floor. As discussed earlier, this is a result of hyperfine doubling in the excited state, which is easiest to see if we consider both beams as $\hat{Z}$ polarized, and thus the lasers only connect states with $\Delta M_F = 0$. Then there are two excited hyperfine states that each form a Λ-system for a given pair of ground M_F states. The dark state of one system is the bright state of the other, and resulting in optical pumping and depletion of the dark state. The only excited states sublevels without hyperfine doubling are the $M'_F = \pm 2$ stretched states, and these cannot connect via $\Delta M_F = 0$ transition to both spin-rotation manifolds in the ground state, as only $J = 3/2$ has $M_F = \pm 2$ stretched states.

Though we do not go into detail here, we additionally performed two-photon CPT on the $N = 2, \mathcal{P} = +1$ manifold of the $\tilde{X}(010)$ state. Now we identify $|\psi_1\rangle = |N = 2, J = 3/2^-\rangle$ and $|\psi_2\rangle = |N = 2, J = 5/2^-\rangle$. We performed upstream depletion and downstream probing with the ${}^{Q}R_{12}^-(2)$ line of the $\tilde{X}(010) \rightarrow \tilde{A}(010)$ transition. For the two-photon light, we couple to the upper $J' = 3/2^+$ state ($N = 2$) in $\tilde{A}(010)$. The resonant line corresponding to the $J'' = 5/2^- \rightarrow J' = 3/2^+$ transition is located at approximately 17331.5050 cm^{-1}. The spin rotation splitting in $N = 1^-$ is 192.5 MHz, which was too far for our AOMs.

For the $N = 2$ CPT tests, we generated the two-photon light using an EOM. Since we are on resonance ($\Delta = 0$), we do not have to worry about the destructive interference discussed earlier. Further, we now have stretched $M'_F = \pm 2$ states in the excited $J' = 3/2$ state. These levels can be connected via $\hat{Z}$ polarized light to the $M_F = \pm 2$ levels avialable in both ground states ψ_1 and ψ_2. Therefore, we expect to have have dark states in spite of the hyperfine doubling. Indeed, we successfully observed a CPT feature, similar to those seen for $N = 1$, when using an EOM with parallel polarizations.

A benefit of the CPT approach is that the resonance is not subject to light shifts. Unfortunately, CPT occurs in the presence of a one-photon background dip with a center value that depends on the one photon detuning Δ. Therefore frequency noise on the laser causes variation of the one photon depletion background, making small hyperfine features difficult to distinguish. We therefore moved on to try detuned two-photon Raman transitions, which are background free at the expense of light shifts.

5.3.5 Two-Photon Detuned Raman Spectroscopy

In the detuned Raman case, we operate with non-zero one-photon detuning $\Delta = 2\pi \times 1$ GHz. This should suppress the scattering rate by a factor of $\sim \gamma^2(1+s)/(4\Delta^2) \approx 10^{-5} \times (1+s)$ compared to the resonance. However, we will now have light shifts, also known as AC Stark shifts. These shifts originate from the off-resonant, "dispersive" interaction of the transition dipole with the oscillating field, and we discuss them in detail later in this section.

To perform the experiment, we fix ω_{L2} and scan ω_{L1} over the two-photon resonance by varying the AOM RF drive frequency[16]. The two-photon resonances will be split by hyperfine structure, and on resonance the coupling $\psi_1 \leftrightarrow \psi_2$ causes Rabi oscillations. As we vary the power in the two-photon beams, we vary the number of oscillations undergone for a single velocity class. In general, the population will be spread between ψ_1 and ψ_2, and we will observe revival of ψ_1 population downstream. Similar to the CPT case, we expect the resonances to be time of flight broadened.

In Fig. 5.19, we show both experimental and simulation results for detuned two-photon Raman resonances of the $N = 1, \mathcal{P} = +1$ manifold, using perpendicularly polarized sidebands to drive transitions between spin rotation states. We can clearly resolve the hyperfine structure of the $\tilde{X}(010)$ bending mode. We distinguish the two hyperfine $F = 1$ levels by writing $F = 1^+$ for the upper level in $J = 1/2$ and $F = 1^-$ for the lower level in $J = 3/2$. We assign the four peaks as corresponding to all possible $\psi_2, F \leftrightarrow \psi_1, F$ features: $2 \leftrightarrow 1^+$, $2 \leftrightarrow 0$, $1^- \leftrightarrow 1^+$, and $1^- \leftrightarrow 0$. To perform the assignment of the hyperfine levels, we use an initial guess based on the $\tilde{X}(000)$ hyperfine parameters. The observed transition frequencies and their assignments are given in Table 5.1.

We note $\Delta F = 2$ transitions are possible because we are performing a two-photon transition, and each photon can give us $\Delta F = 1$. However, we add that in the parallel polarization case, the $1^- \leftrightarrow 0$ transition has zero amplitude, owing to the $M = 0$ selection rule on $1 \rightarrow 1$ transitions. To perform the assignment of the hyperfine levels, we use an initial guess based on the $\tilde{X}(000)$ hyperfine parameters. This is a good initial guess, as constants of the weak hyperfine interaction from the H spin are expected to be similar for states in the same electronic manifold.

We also performed similar two-photon spectroscopy in the $N = 1, \mathcal{P} = -1$ manifold. Because E_{SR} is now smaller by ≈ 17 MHz, we had to slightly tweak our AOM setup to be centered at $E_{SR}^{(-)} \approx 43$ MHz. The fact that we saw the negative parity two-photon transitions here is another testament to the accuracy of the $\tilde{X}(010)$ spectroscopy in Ch. 4. We were able to identify the equivalent four hyperfine transitions in the negative parity level as well, shown in Table 5.1.

In general, the SNR was worse when operating with the negative parity $N = 1$ manifold

---

[16]By this point we improved the AOM scanning using the lens described in Sec. 5.3.2.2
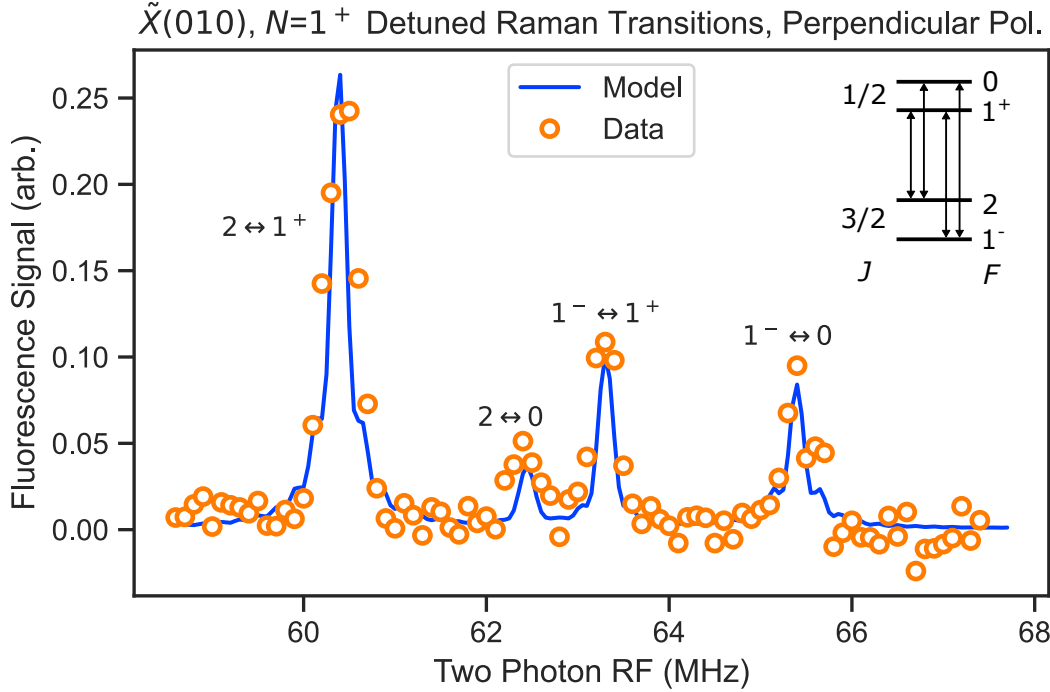
Figure 5.19: Detuned Raman transitions between $N = 1, J_2 = 3/2^+$ and $N = 1, J_1 = 1/2^+$ hyperfine states, driven by perpendicular two-photon beams. The hyperfine transitions are labeled as $F_2 \leftrightarrow F_1$. The inset in the top right shows a diagram of the levels involved, not to scale. The data correspond to the LIF signal characterizing population revival in ψ_1. The two-photon laser beam has 22.5 mW of total power split evenly between both sidebands. The beam is cylindrical with $d_X = 2$ mm along the molecule travel direction and $d_Z = 5.2$ mm along the transverse direction. Model curves are obtained using $s_1 = s_2 = 220$, and $b_F = 4.07$ MHz and $c = 3.49$ MHz, see main text for details. The model curve is offset by 700 kHz to account for unknown light shifts and inaccuracies in the optically determined spin-rotation parameters.

compared to the positive parity manifold. This is attributable to parity-dependent nature of the intensity borrowing that gives strength to the $\tilde{X}(010) \rightarrow \tilde{A}(000)$ transitions we use for depletion and signal readout. The $^Q R_{12}^-(1)$ line is too weak for depletion pumping, so instead we used the $^R R_{11}^-(1)$ transition, and depleted the $J = 3/2^-$ level, which becomes our equivalent of ψ_1. In that case, the ψ_2 level is $J = 1/2^-$, and because this has lower degeneracy and therefore less population, we had weaker readout signals.

As the intensity of the two-photon light is increased, the off-resonant dispersive interaction generates light shifts that modify the energies of the levels of interest. The light shift is given as:

$$\delta_{LS} = \frac{\Omega^2}{4\Delta} = r_{ij}s\frac{\gamma^2}{8\Delta} \approx r_{ij}s \times 8 \text{ kHz} \times 2\pi \tag{5.24}$$

where we have used the relationships for Ω that we discuss in the simulation discussion in Sec. 5.21. Further, the light shifts can be decomposed into shifts that are common for all levels of a given N

Table 5.1: Observed $\tilde{X}(010) - \tilde{X}(010)$, $N = 1$ spin-rotation-hyperfine lines obtained from detuned Raman spectroscopy. Radiofrequency (RF) values correspond to two-photon resonances, and are obtained from Lorentzian peak fits of data. We use $F = 1^{\pm}$ to denote the upper/lower $F = 1$ state in the $N = 1$ manifold. Parentheses are 2-σ errors.

Observed Line (MHz)	$J'', F'', \mathcal{P}''$	$J', F', \mathcal{P}'$
60.42(14)	$3/2, 2, +$	$1/2, 1^+, +$
62.40(10)	$3/2, 2, +$	$1/2, 0, +$
63.29(13)	$3/2, 1^-, +$	$1/2, 1^+, +$
65.40(10)	$3/2, 1^-, +$	$1/2, 0, +$
43.48(12)	$3/2, 2, -$	$1/2, 1^+, -$
45.50(23)	$3/2, 2, -$	$1/2, 0, -$
46.30(15)	$3/2, 1^-, -$	$1/2, 1^+, -$
48.50(17)	$3/2, 1^-, -$	$1/2, 0, -$

and shifts that are differential among levels with different J. We are insensitive to shifts common to all states, and the shifts differential in J simply change the δ location of the center of mass of the lines. The hyperfine splittings we measure will however be sensitive to shifts that are differential among the hyperfine levels. In analogy to differential AC Stark shifts in a trap, the differential light shifts will be smaller by a factor of differences in branching ratios r_{ij}, which are determined by subtracting various Clebsch-Gordan coefficients.

Experimentally, we can measure AC Stark shifts by monitoring the frequency of a two-photon resonance as a function of light intensity. Specifically, we studied absolute frequency shifts of the $F = 2 \leftrightarrow 1^+$ transition as a function of total two-photon light power balanced between $L1$ and $L2$. This transition is sensitive to J-dependent and F-dependent shifts. The AC Stark shifts were found to depend linearly on the total laser beam power, as expected from eq. 5.24. The shifts for the $\mathcal{P} = +1$ level are $-2.6(7)$ kHz/mW, while the shifts for the $\mathcal{P} = -1$ level are $-2.0(8)$ kHz/mW, and in both cases parentheses denote 2-σ error bars. The laser beam is cylindrical, with diameters $d_X \approx 2$ mm and $d_Z \approx 5.2$ mm. The data in Fig. 5.19 was taken with 22.5 mW in both sidebands, resulting in ∼50 kHz shifts. So long as we do not operate in the significantly power broadened regime, we see that our line uncertainties are dominated by the time-of-flight broadening and target decay, compared to differential AC Stark shifts.

Finally, we can use the measured hyperfine splittings and uncertainties ($\sigma \sim 100$ kHz) to determine the hyperfine parameters of the $\tilde{X}(010)$ state. We only fit the line splittings[17], not the line locations, and therefore we are insensitive to J-differential AC Stark shifts. At our level of

[17]Even if we fit J splittings, we find the p_G and γ_G parameters from Ch. 4 are optimized to values within their reported error bars.

resolution, we do not find evidence for parity-dependent hyperfine effects, i.e., the Frosch and Foley d term[39]. The least-squares fit obtains the following optimal hyperfine parameters for $\tilde{X}(010)$: $b_F = 4.07(18)$ MHz and $c = 3.49(38)$ MHz, where 2-σ uncertainties are given in parentheses. The fit residuals are $\sigma_{STD} = 86$ kHz, and the reduced chi-squared is $\chi_r^2 = 1.07$. The residuals are in good agreement with our uncertainty from time-of-flight broadening.

We can compare the $\tilde{X}(010)$ parameters to the parameters of the $\tilde{X}(000)$ state, which will allow us to estimate the bend angle of the H atom. Hyperfine parameters for $\tilde{X}(000)$ were obtained in Ref. [290], with $b_F = 4.80(18)$ MHz and $c = 2.46(48)$ MHz. Upon excitation of the bending mode, b_F decreases by 15%, while c increases by 42%. A similar pattern was observed in the hyperfine parameters of $\tilde{X}(010)$ in CaOH in Ref. [403].

The reduction of b_F implies the valence electron has proportionally less probability density at the distant H nucleus in the bending mode. This could be due to the displacement of the H nucleus away from the internuclear axis. On the other hand, the c value is somewhat significantly larger in the bending mode. This term encodes the isotropic dipole-dipole interaction, and in the molecule frame, we can write it as [39, 157]:

$$c \propto \left\langle \frac{3\cos\theta^2 - 1}{r^3} \right\rangle \tag{5.25}$$

Here, r is the magnitude of the separation between the electron and nuclear spin, and θ is the angle[18] between the separation $\vec{r}$ and the internuclear axis. For the bending mode, we expect θ to increase slightly, but we note this will be accompanied by a decrease in r as the H nucleus is closer to the Yb nucleus in the bent molecule. In Appendix C, we estimate the effect of bending angle on the variation of the c parameter with a simple model, and find the results inconclusive. Nonetheless, the observation of an increase of the bending c value in both CaOH and YbOH $\tilde{X}(010)$ indicates the bending atom is displaced from the internuclear axis.

With a solid understanding of both resonant and detuned two-photon processes in the bending mode, we moved on to perform tests of Ramsey interference, described in the next section.

5.3.6 Ramsey Tests

With field-free tests of two-photon transitions complete, we next performed proof-of-principle Ramsey interferometry between two specific levels in $\tilde{X}(010)$. For this test, the specific states we targeted were $|\psi_1\rangle = |N = 1, J = 1/2^+, F = 1, M_F = 1\rangle$ and $|\psi_2\rangle = |N = 1, J = 3/2^+, F = 2, M_F = 2\rangle$. Application of a bias field of $B_Z \approx 320$ mG lifts the Zeeman degeneracy of the M_F states by the shift $\Delta E = g_F M_F \mu_B B_Z := g\mu_B B_Z$, while still remaining in the coupled basis with linear Zeeman shifts. A level diagram showing the states of interest is provided in Figure 5.20.

---

[18]Caution, this is not the bending H angle!
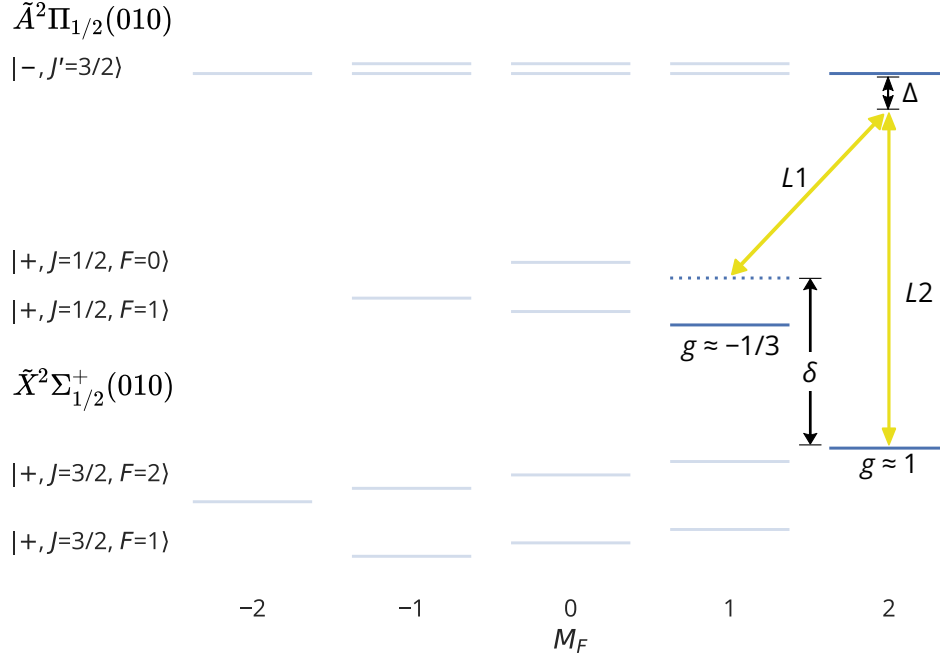
Figure 5.20: A schematic diagram of the $\tilde{X}(010)$ and $\tilde{A}(010)$ states involved in the Ramsey interferometry tests with $B_Z = 320$ mG. Level positions are representative only and not to scale. The states of interest, $M_F = 2$ and $M_F = 1$, are detailed in the main text, and their total g-factors (in terms of μ_B) are also indicated. The other states are off-resonant and/or depleted. The two AOM sidebands are $L1$ and $L2$, and with polarizations $\hat{X}$ and $\hat{Z}$, respectively. Levels are labeled according to their free-field quantum numbers.

The g_F-factor of the ψ_2 state is given by $g_F \approx 1/2$, while the ψ_1 state has $g_F \approx -1/3$, resulting in a total differential g-factor of $g_{\text{total}} \approx -4/3$, where we have absorbed the factors of M_F. We note the exact values obtained from diagonalization[19] differ slightly, a result of hyperfine mixing, B_Z mixing, and the value $g_S = 2.07$. Due to the opposite g-factor sign, the two-photon resonance between ψ_1 and ψ_2 is always the lowest frequency resonance, and can be isolated from other resonances with magnetic tuning. Interference with overlapping resonances is an issue if looking at the opposite $F = 2$, $M_F = -2$ and $F = 1$, $M_F = -1$ resonance. In such a case, since the magnetic shifts are on the same order as the ground state hyperfine splittings, multiple transitions to other M_F states can cause transition interference, causing Fano lineshapes.

Another advantage of using the $M_F = 2$ stretched state in $F = 2$ is our ability to increase this state's population using optical pumping. By applying light linearly polarized along $\hat{Z}$ and resonant with a P line ($\Delta J = -1$) of the $\tilde{X}(010) \rightarrow \tilde{A}(010)$ transition, we can optically pump population into a mixed state of the stretched $F = 2$, $M = \pm 2$ states. Essentially, we are using light to produce angular momentum polarization alignment, so we will refer to this as "polarization pumping." Since the excited state branching is not fully understood, there is likely a combination of increased

---

[19]At 320 mG (0 mG), we obtain $g_F = 0.517$ ($g_F = 0.517$) for ψ_2, and $g_F = -0.302$ ($g_F = -0.317$) for ψ_1.

stretched state population from decays, as well as depletion of population from the middle M states. The polarization pumping not only provides increased SNR, but also reduces congestion of the two-photon spectra obtained in the presence of Zeeman shifts.

We implemented polarization pumping using an infrared external cavity diode laser that is frequency doubled to 577 nm in a waveguide SHG module. The light is resonant with the $\tilde{X}(010) \rightarrow \tilde{A}(010)$ band, and the excited state can decay back to the bending mode—therefore, we perform this pumping step before depleting ψ_1. The pumping light addresses the $J'' = 3/2^+ \rightarrow J' = 1/2^-$ transition located at 17331.3143 cm^{-1}. The line location was optimized by looking for $J'' = 3/2^+$ depletion downstream. The polarization of the pumping light was optimized by rotating the linear light polarization and maximizing the magnitude of the two-photon resonance corresponding to transitions out of the stretched $M_F = 2$ state.

A full schematic of the Ramsey beamline is shown in Figure 5.21. The molecules first encounter optical pumping light, followed by depletion light, a prep Ramsey pulse, a variable distance for time evolution, a readout Ramsey pulse, and finally a probe laser. To perform Ramsey interferometry, we use a 90 degree prism to retroreflect the two-photon light back through the molecule beam, displaced by some distance in the $\hat{X}$ axis (the axis collinear with the molecular beam). This means our two Ramsey beams naturally have relatively balanced powers. By mounting the prism on a micrometer stage, we can adjust the distance between the initial and retroreflected beams, which implement the prep and readout Ramsey pulses, respectively. The molecule beam velocity converts this distance to an interaction time, τ. Figure 5.22 shows a photograph of the laser beams exiting the window on the vacuum chamber. All experimental stages are visible except for the final population readout, which is performed downstream.

The Ramsey sequence follows the general outline discussed in Section 5.1.1. The first Ramsey beam the molecules encounter implements a $\pi/2$ pulse, mapping the initial $|F = 2, M = 2\rangle$ population onto the supersuperposition state $\propto |F = 2, M = 2\rangle + |F = 1, M = 1\rangle$. As the molecules cross the distance from the first beam to the second beam, the superposition phase evolves under the influence of the applied magnetic field. The detuning between the magnetically tuned molecular energy splitting ω_{12} and the two-photon frequency δ causes spin precession in the rotating frame, given by $\omega = \delta - \omega_{12}$. If we parameterize $\omega_{12} = \omega_{12}^{(0)} + g_{\text{tot}}\mu_B B_Z$, where $\omega_{12}^{(0)}$ is the free-field frequency, we may write $\omega = \delta' - g_{\text{tot}}\mu_B B_Z$, where $\delta' = \delta - \omega_{12}^{(0)}$. The precession time is ~50 µs for molecules traveling a distance of distance of ~1 cm with ~200 m/s velocity. Note that the velocity dispersion in the molecular beam will cause variation in precession time, as discussed in Section 5.1.1.

Upon re-encountering the retro-reflected two-photon beam, the molecules undergo another $\pi/2$ pulse, and the superposition phase is mapped back onto populations in the M_F sublevels. Due to
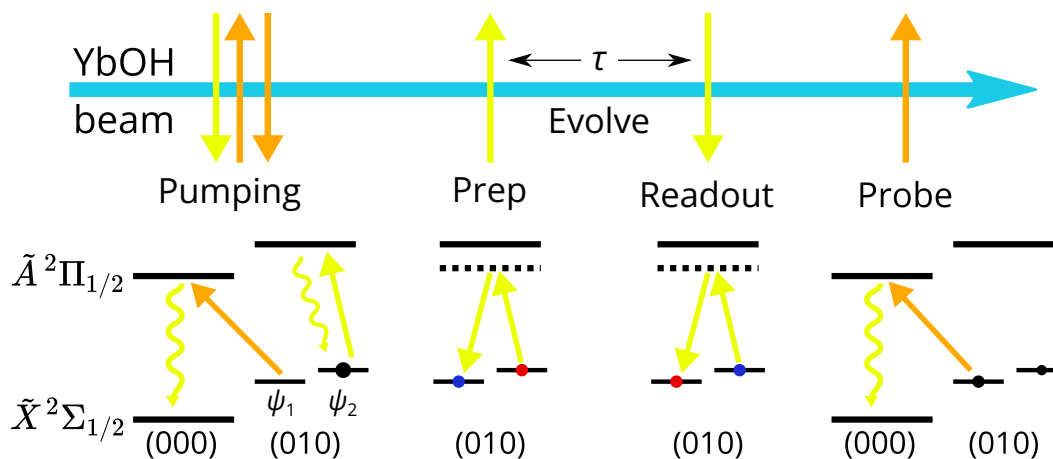
Figure 5.21: A schematic of the two-photon experiments performed in this section. In the Depletion stage, we first apply polarization pumping to collect population in $|\psi_2\rangle = |J = 3/2^+, F = 2, M = 2\rangle$. Then, we apply depletion pumping to deplete $|\psi_1\rangle = |J = 1/2^+, F = 1, M = 1\rangle$. Next, in the Prep stage, we apply a $\pi/2$ pulse between ψ_1 and ψ_2 using a detuned two-photon transition. After a free evolution time τ, we then apply another $\pi/2$ pulse in the Readout stage, mapping the superposition phase evolution onto ψ_1 and ψ_2 populations. Finally, in the Probe stage we use resonant light to probe the ψ_1 population.
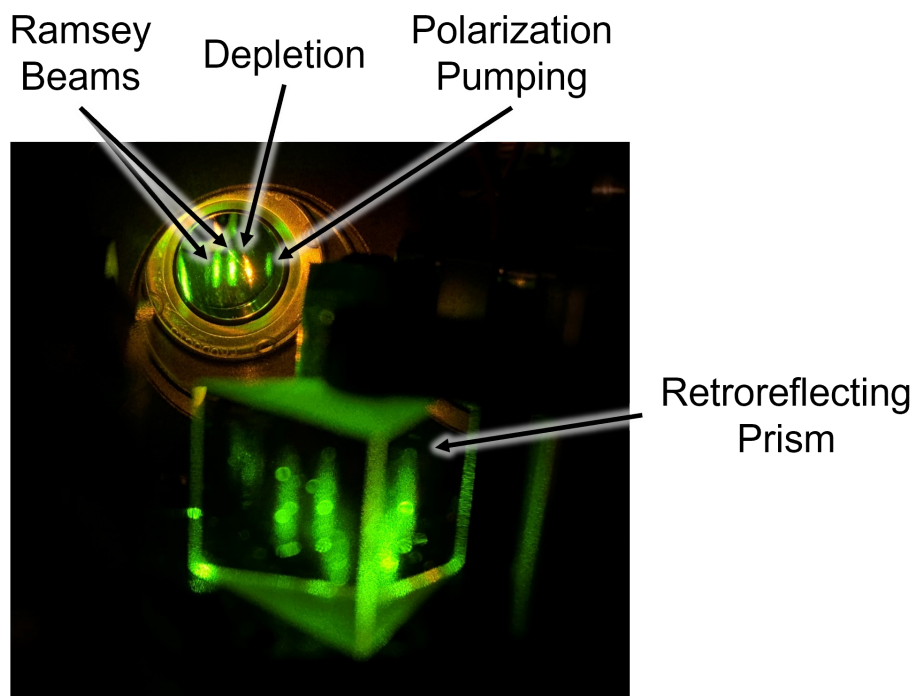
Figure 5.22: A photo of the laser beams used to perform Ramsey interferometry. The beams are cylindrically shaped to cover the entire molecular beam. The molecules first encounter polarization pumping, followed by depletion, and then Ramsey beams. See main text for details. Readout is not pictured. The retroreflecting prism used to generate the second Ramsey beam is visible.

the cyclical nature of phase evolution, the populations of $M_F = 1$ and $M_F = 2$ will oscillate as the precession time or frequency are varied, as given in eq. 5.6. By using the micrometer stage to adjust the distance between the two Ramsey beams, we effectively change the spin precession time for each velocity class. We can also scan the RF frequency driving the two-photon AOM, effectively varying the detuning in the rotating frame.

After the molecules exit the second Ramsey beam, they travel downstream to the detection region in the KF50 octagon. The detection here is similar to what has been detailed in previous sections. The molecules encounter a pick-off of the 588 nm depletion light, this time acting as a fluorescence probe of the population in $|\psi_1\rangle = J'' = 1/2^+$, including the oscillating population in $|F = 1, M_F = 1\rangle$. We collect LIF emitted at 577 nm using the same setup described previously.

To optimize the Ramsey pulses, we first block the return Ramsey beam. In this configuration, the readout fluorescence is proportional to the population transfer from $M_F = 1$ to $M_F = 2$. The overall total power of the Ramsey light was varied while monitoring the detection fluorescence, and the final Ramsey power fixed at the halfway point between the fluorescence minimum and maximum. This value was 13.5 mW in both sidbenads, and the laser beam was cylindrical with with diameters $d_X \approx 2$ mm and $d_Z \approx 5.2$ mm.

The optimization of $\pi/2$-pulses is complicated by AC Stark shifts characterized in the previous section. If the two-photon frequency is fixed and the power scanned, these shifts cause an effective detuning that modifies the Rabi frequency of the $\pi/2$-pulse. However, due to velocity dispersion, there will always be a variation of the $\pi/2$-pulse interaction time, limiting the utility of pulse optimization in the prototype apparatus.

We observed a clear spin precession signal by varying the distance between the two Ramsey beams. Figure 5.23 shows the spin precession signals for different time-of-flight velocity groups, with Ramsey oscillations clearly visible. We use time-of-flight to select different velocity classes. In detail, the molecule pulse has extended temporal width, in our case a total of 6 ms. By restricting our analysis region to 1 ms wide time windows, we only analyze signals from molecules that arrived in that window, acting as a velocity filter. Unfortunately, because molecules exit the cell at different times, multiple velocity classes can have the same arrival time. However, we can also estimate the exit time of the molecular pulse by examining the absorption data taken in front of the cell. Both the absorption upstream and fluorescence downstream have similar temporal profiles; by matching their pulse shapes, we can assign each class of arrival times a corresponding exit time from the cell. By taking the difference between arrival time and exit time, we obtain the total time of flight, which is converted to velocity using the 60 cm distance from the cell to the detection region.

We then use the velocity class values to convert the ~1 cm Ramsey distance to a variable
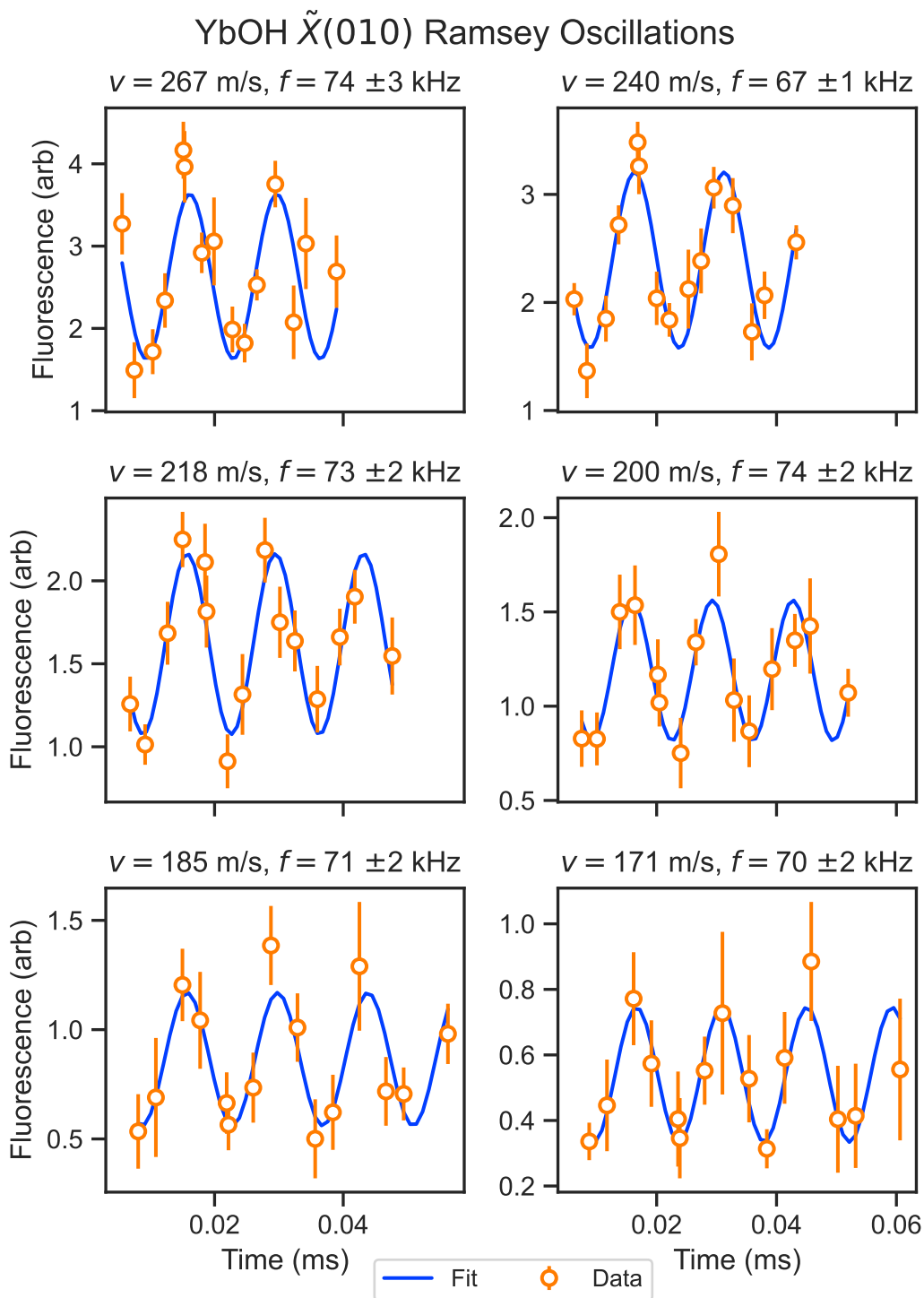
Figure 5.23: Ramsey oscillations for various velocity classes in the molecular beam, denoted v. The time axis is obtained from d/v, where d is the spacing between Ramsey beams. Error bars are 1-σ standard deviations of the data. The data are fit to a sinusoid with frequency f, representing the detuning, included above each plot, along with standard fit errors.

Ramsey evolution time, obtaining the plots shown in Fig. 5.23. The slowest molecules undergo more oscillations than the fastest molecules, as expected. Further, we see the detuning is independent of velocity, as expected. The best fit precession frequencies, $f = \omega/2\pi$, agree among all the velocity classes, with a mean value of $f = 71.5 \pm 1.1$ kHz. Additionally, we see the phases of the sinusoid fits vary with velocity. This is expected, as different velocity classes are rotated by different angles during the initial and final Ramsey pulses.

In addition to scanning the spin precession time, we can also fix the interaction distance and scan the two-photon RF frequency. Since we are changing the detuning, this is equivalent to scanning the magnetic field. The resulting interference lineshapes are plotted in Figure 5.24. The signals clearly show multiple Ramsey fringes, and are very similar to the two level system model results in Sec. 5.1.1, Fig. 5.1. Over the whole 4 ms wide molecular pulse, shown in inset 5.24(ii), velocity dispersion washes out the fringes after a few oscillations. On the other hand, if we select a 1 ms wide arrival window of molecules centered at 200 m/s, we observe coherent oscillations even at larger detunings, shown in the main plot of Fig. 5.24(ii). If we compare different velocity classes, the middle peak at $f_0 = 59.536$ MHz does not shift, indicating it corresponds to the true resonance. Finally, the inset 5.24(i) zooms in on the region near the resonance, where we fit the data to eq. 5.6, with velocity dispersion included by random sampling from a Gaussian distribution. The fit parameters are provided in the figure caption, and their values barely deviate from our expectations. For example, the micrometer position corresponds to a 9.1 mm evolution distance, giving us a 46 µs precession time for 200 m/s molecules. The fit indicates values closer to 42 µs are more accurate, which is nonetheless excellent agreement. Similarly, the fit favors a velocity dispersion of $\sigma_v = 13.2$ m/s, in line with our expectation of CBGBs [178], and a pulse interaction time of 4.2 µs, in excellent agreement with our estimates of ≈ 1 mm FWHM Ramsey beams.

Finally, we were unable to observe CPT on the $F = 2, M_F = 2 \leftrightarrow F = 1, M_F = 1$ two-photon resonance with this setup. In general, the SNR was worse for CPT tests, as we must deal with the background from "one photon" depletion. Furthermore, there are technical issues that may have prevented CPT. For example, the bias magnetic field may have not been exactly aligned to the light polarization axis. In such a case, the dark state fidelity can be compromised by scattering from unwanted polarization components. An equivalent model for transverse fields is that they can couple nearby levels, causing the dark state to mix with bright levels. In principle, such a problem could be solved with elliptically polarized beams, but that was beyond the scope of our work.

These experiments demonstrated the power of two-photon transitions for high-resolution Ramsey interferometry and precision spectroscopy in a molecular beam. We showed that the velocity dispersion in the beam does not wash out contrast, and with time of flight selection we can observe the differences in precession time. Further, the local nature of two-photon manipulation allows
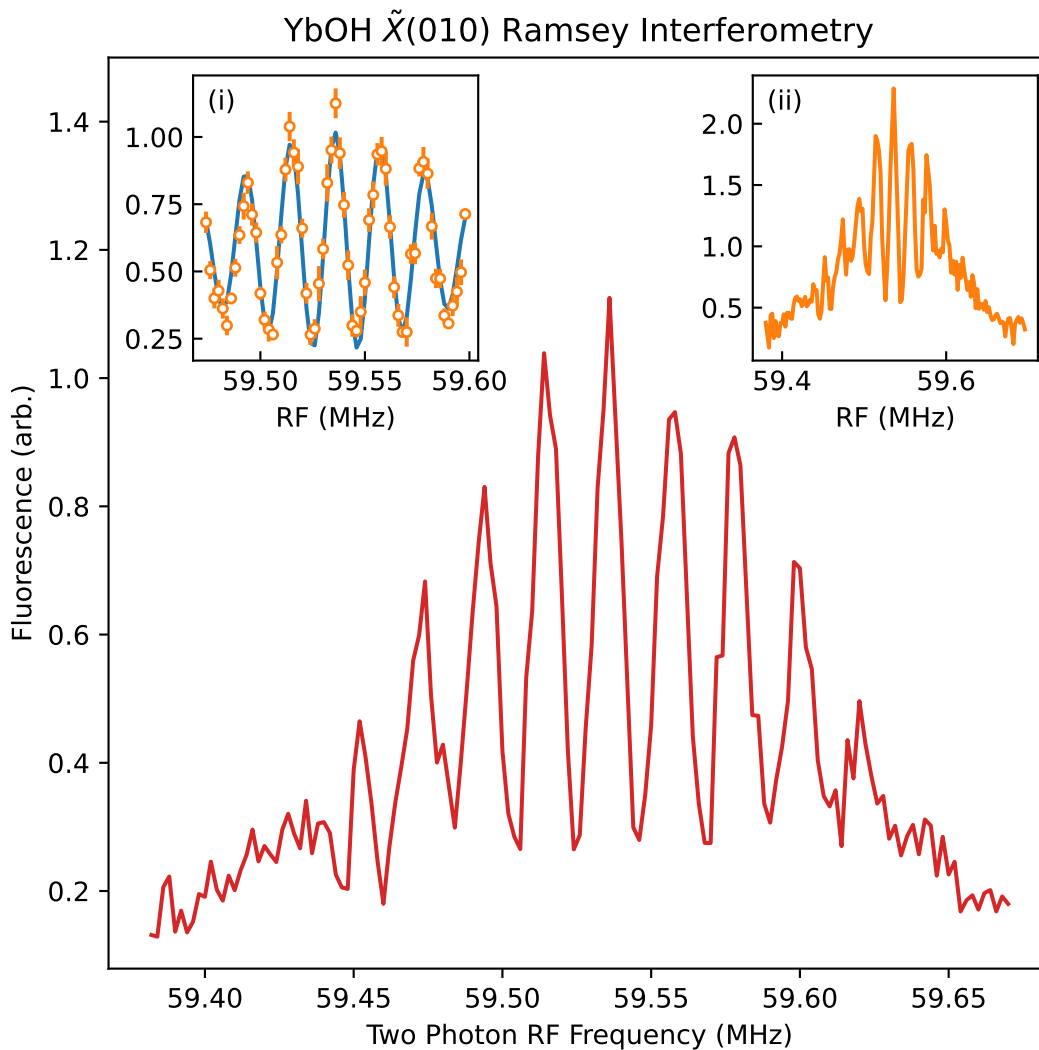
Figure 5.24: Ramsey interferometry on the $F = 2, M_F = 2 \leftrightarrow F = 1, M_F = 1$ transition. The main plot shows data from a 1 ms wide arrival window of molecules with 200 m/s mean velocity. (i) A zoom in on the region near zero detuning. Data given by orange markers with error bars representing standard error. The blue line is a fit using eq. 5.6 with velocity averaging. Parameters are center frequency $f_0 = 59.536$ MHz, interaction time $\tau = 41.7$ µs, $\Omega t_p = \pi/2$, $t_p = \tau/10$, and $\sigma_v = 13.2$ m/s. (ii) The interference lineshape obtained by integrating all arrival times over the 4 ms wide pulse. Fewer fringes are visible due to larger velocity dispersion.

for well-defined preparation and readout regions, and by using a bending excited state, our power requirements (~10-20 mW) are reasonable.

5.3.7 Outlook

We have achieved coherent control of polyatomic molecules using two-photon resonances. We demonstrate both resonant CPT effects and detuned Raman transitions, and we use the latter to perform Ramsey interferometry on spin-rotation-hyperfine states. Our results have excellent agreement with simulations and modeling. We note that throughout our tests, quasi-diagonal FCFs were useful for performing state manipulation and readout. Our results are immediately applicable to searches for P, T violating moments in YbOH, such as the electron EDM search in ^{174}YbOH [17], nuclear Schiff moment or parity violation searches [404] in ^{171}YbOH, and the nuclear magnetic quadrupole moment (MQM) search in ^{173}YbOH [57, 405–407]. Further, our results are generally useful to the broad class of polyatomic molecules that follow the M-OH motif, including SrOH [302] and RaOH [272, 408].

The next step from this work is to perform Ramsey interferometry in an electric field E_Z, which would constitute a P, T-violation-sensitive signal. There are a few choices for Ramsey states ψ_1 and ψ_2. One possibility is to use two stretched states with the same M_F but opposite molecule orientations $M_N \ell$. Such states are maximally sensitive to variations of the electric field, but polarize quickly, offer good PT violating sensitivities, and are easy to populate with optical pumping. By performing measurements in both $\pm M_F$ states, we can disentangle electric field fluctuations from P, T violating effects. The details of implementation will depend on the excited states available, and their polarization regime in the presence of an E-field. For example, if both ground and excited states are fully polarized, then we must consider ΔM_N selection rules. Finally, if there are stretched states available in the excited state, we can use CPT methods for state preparation and readout, as well as detuned Raman transitions.

Another option is to use so-called *zero g-factor* states, which are time-reversal pairs of $M_F = \pm 1$ states with highly suppressed magnetic sensitivity and large P, T violating sensitivity, discussed in detail in the upcoming section. In ^{174}YbOH, we expect zero g-factor states to generically exist in $N = 1$ at 45 V/cm ($J = 1/2^-, F = 1$) and 62 V/cm ($J = 3/2^-, F = 2$), as well as in $N = 2$ at 299 V/cm ($J = 3/2^+, F = 1$), 318 V/cm ($J = 3/2^+, F = 2$), 350 V/cm ($J = 5/2^-, F = 3$), and 372 V/cm ($J = 5/2^+$). Preparation could be performed by a combination of optical pumping into stretched states and two-photon transitions to $M_F = 0$ states, followed by two-photon transfer to $M_F = \pm 1$ states.

Zero g-factor states are an example of state engineering using applied fields. In Ref. [124], we showed that one can also use external fields to engineer favorable transitions with noise insensitivity

and *PT* violating sensitivity. In the various isotpologues of YbOH, there are many field-insensitive transitions possible, and we direct the reader to Ref. [124] for more details.

5.4 Prototype Measurement with Trapped CaOH Molecules

Parts of this section are adapted from Ref. [403]. This work was performed as part of the PolyEDM collaboration with the Doyle group at Harvard. I spent 2 months working on-site on the project, and continued collaborating virtually for approximately 6 months afterwards.

5.4.1 Overview

Trapped molecules have many advantages for measurements—the most obvious is the increased coherence time, which is on the order of $\gtrsim 1$ s. Another benefit to a trap is easier requirements on field control, as uniformity must be achieved over a small volume $\lesssim 1$ mm^3. A third benefit is the lack of velocity dispersion, providing the ability to apply pulses of optical, microwave, or RF radiation with well defined interaction time. Furthermore, particularly for microwave and RF radiation, there is no concern about the fields leaking into later steps of the experiment, unlike a beam where spatial leakage of a field to different parts of the beamline corresponds to temporal leakage of operations in the sequence. Finally, trapping molecules also provides the possibility of using quantum control and entanglement techniques to improve EDM measurements.

In this Section, we report coherent control of individual quantum states in a polyatomic molecule, calcium monohydroxide (CaOH), and use these techniques to demonstrate a method for searching for the electron electric dipole moment (eEDM). The method starts with preparing ultracold, optically trapped CaOH molecules in a single hyperfine level, after which a static electric field is applied to polarize the molecules. The strength of the polarizing electric field is tuned to obtain near-zero *g*-factor spin states, which have strongly suppressed sensitivity to magnetic field noise while retaining eEDM sensitivity. Microwave pulses are applied to create a coherent superposition of these zero *g*-factor spin states that precess under the influence of an external magnetic field. The precession phase is then read out by a combination of microwave pulses and optical cycling.

We observe spin precession over a range of electric and magnetic fields and characterize the current limitations to the coherence time of the measurement. With readily attainable experimental parameters, coherence times on the order of the state lifetime (>100 ms) could be realistically achieved. We therefore realize the key components of an eEDM measurement in this system. Although the light mass of CaOH precludes a competitive eEDM measurement [408], the protocol demonstrated here is directly transferable to heavier laser-cooled alkaline earth monohydroxides with identical internal level structures, such as SrOH, YbOH, and RaOH, which have significantly enhanced sensitivity to the eEDM [17, 105, 106, 272, 408].
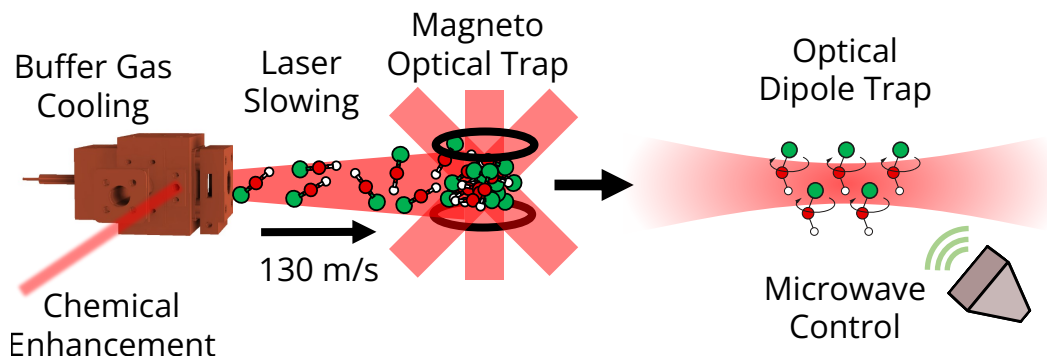
Figure 5.25: Schematic diagram of the CaOH experimental apparatus at Harvard. First, molecules are produced in a 2 stage buffer gas cell by laser ablation of a solid Ca target in the presence of He buffer gas flow. A heated fill line introduced H_2O reagents, and chemical enhancement light stimulates reactions that form CaOH. The molecules exit the cell in a beam, are slowed by lasers, and are trapped in an RF magneto-optical trap (MOT). The molecules are cooled further via sub-Doppler methods, and then loaded into an optical dipole trap (ODT). In the ODT, the molecules are polarized by an electric field, and we perform spin precession using microwave pulse sequences. The left half of the diagram (CBGB, slowing, MOT) was adapted from the CaOH team.

Current EDM bounds rely on specific states in diatomic molecules that have an unusually small g-factor, reducing sensitivity to stray magnetic fields [100, 101]. However, CaOH, like other laser-coolable molecules with structure amenable to eEDM searches [17, 113, 272, 409], has a single valence electron, which results in large magnetic g-factors. In the prototype measurement discussed here, we engineer reduced magnetic sensitivity by using an applied electric field E_Z to tune M_S to a zero-crossing, while maintaining significant eEDM sensitivity Σ. This technique is generic to polyatomic molecules with parity-doublets.

5.4.2 CaOH Apparatus

The CaOH apparatus at Harvard is described in detail in Refs. [108, 200], and here we summarize relevant details. A basic schematic of the experiment is shown in Figure The experiment starts with a CBGB source cooled to 2 K. The buffer gas cell design is a two-stage cell [410], consisting of a "production" cell where ablation and thermalization occur, and a "slowing" cell, which can help reduce the velocity of the resulting molecular beam. While the 4 K cell at Caltech has a rectangular aspect ratio, the CaOH cell is close to a square aspect ratio, with 1-in diameter. Finally, the cell has a $\sim$ 5 mm diameter hole in the back to allow the slowing beams to exit without adding additional heat load. Chemical reactions are enhanced [227] by sending $\sim$800 mW of light into the cell resonant with the $^1S_0 \rightarrow {}^3P_1$ transition in Ca atoms[20].

---

[20]Additionally, during testing, it was found that pre-firing the target with a separate infrared laser, in advance of the ablation, helped with source signal and velocity stability when going to longer repetition rates. This is attributed to desorption of helium by the pre-fired laser, as the optimal time scale for prefiring is approximately after one or two cell emptying times. The removal of helium via pre-firing is thought to help reduce the background gas present that

After exiting the second stage of the cell, the molecules encounter slowing light, which is switched on at an optimized time. This light contains primary cycling light (the $\tilde{X}(000) \to \tilde{A}(000)$ transition) and 11 repumping transitions to return vibrational decays to the optical cycle [108]. The repumps are all spectrally broadened with EOMs to address all velocity classes, and polarization modulated at roughly ~MHz time scale by Pockels cells, to help remix dark states. Downstream is the stainless steel MOT chamber with an RF MOT setup [120, 193, 411]. In the CaOH experiment at Harvard [108], approximately 20,000 molecules are trapped in the MOT, with an RMS size of 0.75 mm and peak number density of 3×10^6/cm^3. We note the MOT magnetic RF coils will later be repurposed to apply electric fields to polarize the molecules. In the MOT, the molecules are at ~1 mK.

The temperature can be lowered further using sub-Doppler cooling methods [115, 120, 400, 412–417]. The CaOH experiment uses two sub-Doppler techniques [109] that are in general complicated and difficult to model. The first technique is Λ-enhanced gray molasses cooling [418–421], which utilizes counter propagating lasers to engineer two-photon resonances that result in velocity selective dark states [412, 416, 417]. Slow and cold molecules are trapped in dark states, while hot and fast molecules perform non-adiabatic transitions to bright states and are further cooled. In CaOH, this technique lowers the free space temperature to 50 µK, and is primarily limited by off-resonant scattering. Next, the cooling light is switched to a different sub-Doppler configuration called single frequency cooling [422], which also relies on dark states. This technique further reduces the scattering rate, resulting in a minimum free space temperature of 20 µK.

Next, the molecules are transferred to an optical dipole trap (ODT) [423]. ODTs are preferable to MOTs, as they apply conservative forces and do not involve constant spontaneous emission. In the CaOH experiment, the ODT is generated by focusing 15 W of off-resonant, 1064 nm light down to a 25 µm waist. Since the laser is red-detuned from relevant electronic transitions, it will generate attractive light shifts at its intensity maxima. Essentially the red-detuned ODT generates an induced dipole that follows the oscillations of the laser field. The ODT loading is performed with the sub-Doppler cooling light still activewhich actually assists with loading molecules into the trap [420, 421]. Further, the cooling light can be used to non-destructively image the molecules (i.e., without losing them from the trap), allowing for shot-to-shot normalization and post-selection.

The ODT light will generally cause differential AC Stark shifts of the molecule levels, similar to the light shifts we encountered with detuned Raman transitions. AC Stark shifts can be calculated

---

can boost the molecular beam as it exits the aperture. On the 4 K experiment at Caltech, we tested pre-firing with the enhancement laser, and it had little impact on molecular production. On the 1 K experiment at Caltech, pre-firing improved signals by a factor of a factor of a few. It is possible the differences are related to cell geometry, temperature, or the helium dynamics of the cell. For example, the emptying times in the 4 K cell are much faster (~1 ms) than the 1 K cell (~10 ms).

using the electric polarizability tensor α, given by:

$$\overleftrightarrow{\alpha} = \frac{2}{\hbar} \sum_{j \neq \psi} \omega_J \frac{\vec{d}|j\rangle\langle j|}{\omega_j^2 - \omega^2} \tag{5.26}$$

where ψ is the ground state of interest, ω is the frequency of the ODT light, and the sum runs over all excited states j. The light shifts are given by the following Hamiltonian:

$$H_{LS} = -\frac{1}{2}\vec{E}(t) \cdot \overleftrightarrow{\alpha} \cdot \vec{E}(t). \tag{5.27}$$

In general, there will be scalar (rank 0), vector (rank 1), and tensor (rank 2) shifts. The scalar shifts are common mode and used to trap the molecules in the 12 MHz deep ODT (the differential shifts are typically 1-10% of this value). The vector shifts arise only in the presence of circular light, and they generate ficticious magnetic fields along the k vector of the light. We will operate with linearly polarized beams, so we ignore this term. Finally, tensor shifts will mimic quadratic Stark shifts from induced dipole moments, shifting $\pm M$ states identically. The formula for scalar and tensor light shifts can be recast into a useful spherical tensor form:

$$H_{LS} = -\frac{1}{4} \sum_{k=0,2} T^k(\alpha) \cdot T^k(E,E) \tag{5.28}$$

where we have excluded $k = 1$ vector light shifts from the sum as their term requires more care. For details on AC Stark shifts and their calculation, we direct the reader to Refs. [424, 425].

Approximately 300 molecules are trapped in the ODT after loading for 80 ms with cooling light [109]. The peak density is $3 \times 10^9/\text{cm}^3$, and the in-trap temperature is 57 μK. This temperature is higher than cooling in free space, as the AC Stark shifts destabilize the dark states that enable effective sub-Doppler cooling.

Finally, when holding the molecules at such low temperature for close to a second, we have to contend with thermal blackbody radiation and the natural lifetime of the $\tilde{X}(010)$ state. Ref. [426] discusses these effects in a detailed investigation of the lifetime of polyatomic molecules in an ODT. They find 300 K blackbody effects limit the total bending mode lifetime at the ~1 s level. They also measure the lifetime from spontaneous emission alone to be $\tau = 720$ ms in CaOH.

5.4.3 State Preparation

The ODT is linearly polarized and its polarization vector $\vec{\epsilon}_{\text{ODT}}$ defines the $\hat{Z}$ axis, along which we also apply magnetic and electric fields, $\vec{B} = B_Z\hat{Z}$ and $\vec{E} = E_Z\hat{Z}$, respectively, as depicted in Figure 1(a). We first non-destructively image the molecules in the ODT for 10 ms as normalization against variation in the number of trapped molecules. The molecules are then optically pumped into the $N = 1^-$ levels of the $\tilde{X}^2\Sigma^+(010)$ vibrational bending mode [109] (Figure 1(c)), and the trap
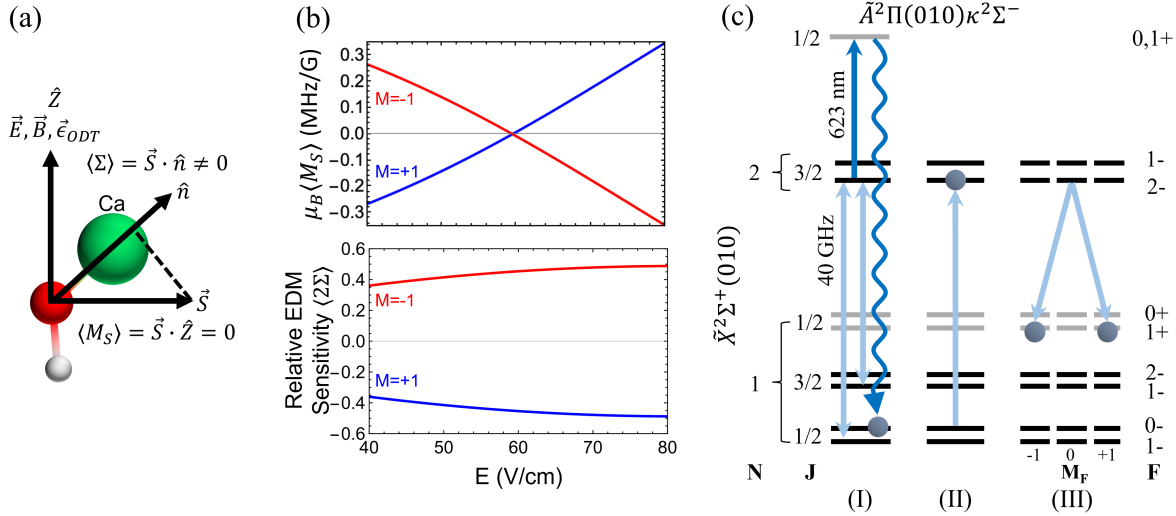
Figure 5.26: Information about the zero g-factor experiment at Harvard University. (a) A geometric picture of the bending molecule at the zero g-factor crossing, showing the electron spin ($\vec{S}$) has a finite projection on the molecule axis ($\hat{n}$), giving eEDM sensitivity. However, the electron spin ($\vec{S}$) is orthogonal to the magnetic field ($\vec{B}$), resulting in suppressed magnetic field insensitivity. (b) The magnetic sensitivity (upper plot) and eEDM sensitivity (lower plot) for a pair of zero g-factor states ($N = 1, J = 1/2^+, F = 1, M_F = \pm 1$) are shown as a function of the applied electric field. (c) Experimental sequence to prepare the eEDM sensitive state. First, the molecules are pumped into a single quantum state ($N = 1, J = 1/2^-, F = 0$) with a combination of microwave drives and optical pumping (I). Next, a microwave π-pulse drives the molecules into the $N = 2, J = 3/2^-, F = 2, M_F = 0$ state (II). Lastly, the eEDM measurement state is prepared as a coherent superposition of the $N = 1, J = 1/2^-, F = 1$ $M_F = \pm 1$ states with a microwave π-pulse (III). The states which are optically detectable with the detection light are shown in black, while those not addressed by the detection light are in gray. Figure reproduced from Ref. [403].

depth is adiabatically lowered by 3.5× to reduce the effect of AC Stark shifts from the trap light and to lower the temperature of the molecules to 34 μK. Any molecules that were not pumped into $N = 1^-$ levels of the bending mode are heated out of the trap with a pulse of resonant laser light.

Once the ODT is loaded, the molecule population is in the $N = 1^-$ manifold of the $\tilde{X}^2\Sigma^+(000)$ state. Population transfer to the $\tilde{X}^2\Sigma^+(010)$ state proceeds by optical cycling with one repumper removed [109]. In detail, the sub-Doppler cooling light is turned on with only the $N'' = 1^-$ repumper addressing $\tilde{X}^2\Sigma^+(010)$ is turned off. We note there is also a repumper addressing $\tilde{X}^2\Sigma^+(010)$ $N'' = 2^-$ that stays on. This repumper is required because the excited state in cycling is always $J' = 1/2^+$ in character, therefore E1 decays are only permitted to ground states with $J'' = 1/2^-$ and $3/2^-$ character. For ground states with parity doubling, such as bending modes, this means both $N'' = 1^-$ and $N'' = 2, J'' = 3/2^-$ manifolds must be addressed during cycling.

Transfer to the bending mode proceeds within 1200 photon scatters, equivalent to ~26 ms at the single frequency scattering rate. The decay pathways into the bending mode are ~80% through

the excited $\tilde{A}$ state and ~20% through the excited $\tilde{B}$ state. We calculate the rotational branching ratio of the decays to the states within $N = 1$ as 21.6% to $J = 3/2^-$ and 78% to $J = 1/2^-$.

Following transfer to the $\tilde{X}^2\Sigma^+(010)(N = 1^-)$ state, the molecular population is initially spread across twelve hyperfine Zeeman sublevels in the spin-rotation components $J = 1/2$ and $J = 3/2$. The mixed state describing the ensemble has statistical weights given by the rotational branching of the excited states. To perform coherent quantum operations, the initial density matrix must be purified. A dissipative process is required to decrease the entropy of the density matrix, and the simplest approach is to use optical pumping, either to remove unwanted population, and/or to gather population in a single state. We also seek a scheme that requires minimal photon scatters, as each photon recoil imparts ~500 nK of energy. In experiments with trapped diatomic metal fluorides, such as CaF, the hyperfine structure is optically resolved, and pumping proceeds by addressing all states but $F = 0$. In metal hydroxides hyperfine structure is *not* optically resolvable, as discussed in Sec. 5.2. If we solely address $J = 3/2^-$ optically, we would still leave population spread out over the M_F sublevels in $J'' = 1/2^-$, $F'' = 1, 0$. Additionally, the two spin-rotation states in $N = 1$ are separated by $\approx 2.5\times$ the optical linewidth, making off-resonant pumping difficult to avoid.

By adding in microwaves to couple the molecules between rotational states, we solve our problems. Microwave linewidths are significantly narrower compared to optical linewidths, often dominated by power broadening. Therefore, with microwaves we can separately resolve the hyperfine states. Further, since microwaves couple population to another rotational state, we can perform our optical pumping there, without worrying about off-resonant excitation of $N = 1$. We note there is no $N = 0$ state as we have $|\ell| = 1$. The nearest rotational level, $N = 2$, is 40 GHz away.

To prepare the molecules in a single hyperfine state, we use a combination of optical pumping and microwave pulses, as shown in Figure 5.26(c). We first apply microwaves from the $(N = 1, J = 3/2^-)$ state up to the $(N = 2, J = 3/2^-)$ state. As this transition is parity-forbidden, we apply a small electric field $E_Z = 7.5$ V/cm to slightly mix the parity of the $N = 1$ levels and provide transition strength. From the $N = 2$ state, we drive an optical transition to the excited $\tilde{A}^2\Pi(010)\kappa^2\Sigma^{(-)}, J = 1/2^+$ state. This state predominately decays to both $F = 0$ (the target state) and $F = 1$ states in the $N = 1, J = 1/2^-$ manifold. After 3 ms of optical pumping, the microwaves are switched to drive the accumulated $N = 1, J = 1/2^-, F = 1$ population to the same $N = 2, J = 3/2^-$ state in $\tilde{X}(010)$, where they are excited by the optical light and pumped into the target $F = 0$ state. Once this optical pumping sequence is complete, we adiabatically ramp the electric field to $E_Z = 150$ V/cm to significantly mix parity, then drive population up to the $N = 2, J = 3/2^-, F = 2, M = 0$ state with a microwave π-pulse (Figure 5.26(c)(II)). We clean out any remaining population in the $N = 1$ state with a depletion laser that resonantly drives population to undetected rotational levels.

(a) ^{40}CaOH $\tilde{X}(010)$ $N = 1$ g-factors

(b) ^{40}CaOH $\tilde{X}(010)$ EDM Shifts
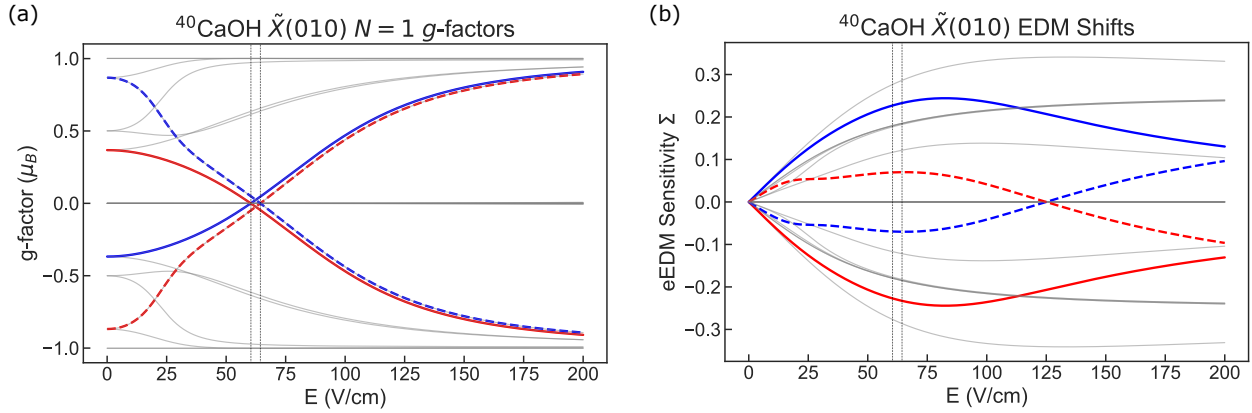
Figure 5.27: Electric field tuning of $N = 1$ zero g-factor states near $B_Z = 0$ in the absence of trap shifts. Blue lines denote $M_F = +1$ states and red lines $M_F = -1$. Solid traces denote the $J = 1/2$ state pair and dashed traces denote the $J = 3/2$ pair. The dotted vertical lines mark the electric field value of the zero g-factor crossing without trap shifts, ≈ 60.5 V/cm for $J = 1/2$ and ≈ 64.4 V/cm for $J = 3/2$. Grayed out traces are other states in the $N = 1$ manifold. (a) The g-factor $g_S \mu_B \langle M_S \rangle$ as a function of the applied electric field. (b) eEDM sensitivity $\langle \Sigma \rangle$ as a function of the applied electric field. A consequence of the Hund's case (b) coupling scheme is that Σ asymptotes to a maximum magnitude of $S/(N(N + 1)) = 1/4$ for fields where the parity doublets are fully mixed but rotational mixing is negligible [117]. For fields where J is not fully mixed, some states can exhibit $|\Sigma| > 1/4$. Figure reproduced from Ref. [403].

5.4.4 Engineering Zero g-Factor States

In $^2\Sigma$ electronic states of linear polyatomic molecules, the spin-rotation interaction, $\gamma \vec{N} \cdot \vec{S}$, couples the molecular rotation N and the electron spin S to form the total angular momentum J. These states are well described in the Hund's case (b) coupled basis. An applied electric field E_Z will interact with the molecular-frame electric dipole moment μ_E, connecting states with opposite parity, $\Delta M_F = 0$, and $\Delta J \leq 1$. When $\mu_E E_Z \gg \gamma$, N and S are uncoupled and well described by their lab frame projections M_N and M_S. However, in the intermediate field regime with $\mu_E E_Z \sim \gamma$, the molecular eigenstates are mixed in both the Hund's case (b) coupled basis and the decoupled basis. M_F remains a good quantum number in the absence of transverse fields. In this regime, $M_F \neq 0$ states with $\langle M_S \rangle = 0$ can arise at specific field values. These states have no first order electron spin magnetic sensitivity, and, unlike $M_F = 0$ clock states, have large eEDM sensitivity near $B_Z = 0$. We refer to these states as *zero g-factor* states [17].

Zero g-factor states arise from avoided level crossings as free field states are mixed by the electric field. One of the crossing states has $\langle M_S \rangle < 0$, the other state has $\langle M_S \rangle > 0$, and both have mixed M_N. The spin-rotation interaction couples the states and lifts the crossing degeneracy, resulting in eigenstates that are superpositions of electron spin up and down with $\langle M_S \rangle = 0$, while retaining non-zero molecular orientation with $\langle \hat{n} \rangle = \langle M_N \ell \rangle \neq 0$. The lab frame projection of $\hat{n}$

ensures that the eEDM interaction in the molecule frame does not rotationally average away, i.e., the eEDM shifts are diagonal.

Zero g-factor states are generically present in the Stark tuning of polyatomic molecules. The reduction of symmetry in a polyatomic molecule allows for rotation about the internuclear axis, resulting in closely spaced doublets of opposite parity. When these doublets are mixed by an applied electric field, they split into $2N+1$ groups of levels representing the values of the molecular orientation $\langle M_N \ell \rangle$. For each N manifold with parity doubling, avoided level crossings generically occur between an $M_N \ell = \pm 1$ Stark manifold and an $M_N \ell = 0$ Stark manifold.

In diatomic molecules without parity-doubling, the existence of zero g-factor states requires an inverted spin rotation structure ($\gamma < 0$), such that the two J states are tuned closer to each other by an electric field. For example, the YbF molecule ($\gamma = -13.4$ MHz [377, 427]) has zero g-factor states at $E \approx 866$ V/cm in the $N = 1$ manifold, while CaF does not. However, since $|\gamma|/B \ll 1$ for most $^2\Sigma$ diatomic molecules, the electric fields that mix spin-rotation states are much less than those that polarize the molecule. Therefore, zero g-factor states occur when the molecule has negligible lab-frame polarization, limiting eEDM sensitivity. For example, the aforementioned states in YbF have $|\langle \Sigma \rangle| \approx 0.006$, which is ~3% the value of Σ in the zero g-factor states used in this work.

To locate zero g-factor crossings and calculate eEDM sensitivities, we model the $\tilde{X}(010)$ level structure using an effective Hamiltonian approach [39, 129, 162]:

$$H_{\text{eff}} = H_{\text{Rot}} + H_{\text{SR}} + H_\ell + H_{\text{Hyp}} + H_{\text{Zeeman}} + H_{\text{Stark}} + H_{\text{ODT}} \tag{5.29a}$$

$$H_{\text{Rot}} = B\left(\vec{N}^2 - \ell^2\right) \tag{5.29b}$$

$$H_{\text{SR}} = \gamma\left(\vec{N} \cdot \vec{S} - N_z S_z\right) \tag{5.29c}$$

$$H_\ell = -q_\ell \left(N_+^2 e^{-i2\phi} + N_-^2 e^{i2\phi}\right) \tag{5.29d}$$

$$H_{\text{Hyp}} = b_F \vec{I} \cdot \vec{S} + \frac{c}{3}\left(3 I_z S_z - \vec{I} \cdot \vec{S}\right) \tag{5.29e}$$

$$H_{\text{Zeeman}} = g_S \mu_B B_Z S_Z \tag{5.29f}$$

$$H_{\text{Stark}} = -\mu_Z E_Z \tag{5.29g}$$

$$H_{\text{ODT}} = -\vec{d} \cdot \vec{E}_{\text{ODT}}. \tag{5.29h}$$

Here, we use a similar Hamilton as Ref. [146]. H_{Rot} is the rotational energy; H_{SR} is the spin-rotation interaction accurate for low-N bending mode levels, with z defined in the molecule frame; H_ℓ is the ℓ-type doubling Hamiltonian, with $\pm$ defined in the molecule frame, ϕ as the nuclear bending coordinate, and using the same phase convention as Ref. [159]; H_{Hyp} is the hyperfine Fermi-contact

and dipolar spin interactions, defined in the molecule frame; H_{Zeeman} describes the interaction of the electron spin magnetic moment with the lab-frame magnetic field; H_{Stark} is the interaction of the Z-component of molecule-frame electric dipole moment μ_E with the lab frame DC electric field, E_Z; and H_{ODT} is the interaction of the molecular dipole moment operator $\vec{d}$ with the electric field of the ODT laser, $\vec{E}_{\text{ODT}} = \mathcal{E}_0/2(\hat{\epsilon}_{\text{ODT}}e^{-i\omega t} + \text{c.c.})$.

To evaluate the molecule frame matrix elements, we follow the techniques outlined in Refs. [39, 129] to transform into the lab frame. The field-free Hamiltonian parameters are taken from Ref. [147], except for the hyperfine parameters, which were determined by the observed line positions to be $b_F = 2.45$ MHz and $c = 2.6$ MHz, similar to those of the $\tilde{X}(000)$ state [375]. We use the same dipole moment, $|\mu| = 1.47$ D, as the $\tilde{X}(000)$ state, determined in Ref. [428]. Matrix elements of H_{ODT} are calculated following Ref. [424] using the 1064 nm dynamic polarizabilities reported in Ref. [109].

For all calculations discussed the ODT is polarized along the laboratory Z axis and the molecules sit at a fixed trap depth of 160 μK (corresponding to the average trap intensity seen by the molecules in the experiment). As detailed in the main text, when the trapping light is aligned with E_Z, it acts like a weak electric field, shifting the zero g-factor crossing by ~ 1 V/cm from the field-free value. If the trapping light polarization is rotated relative to E_Z, tensor light shifts can couple states with $\Delta M_F = \pm 2$ or ± 1 (the linearity of the light ensures there are no $\Delta M_F = \pm 1$ vector shifts) [424]. The effects of this coupling are similar to those of transverse magnetic fields, which we discuss below.

In the current work, we ignore nuclear and rotational Zeeman effects. Specifically, the magnetic sensitivity of CaOH receives small contributions from nuclear spin of the H atom and the rotational magnetic moment of both the electrons and the nuclear framework. While they have not yet been fully characterized, all of these effects will contribute at the $10^{-3}\mu_B$ level or less. These additional g-factors do not depend strongly on the applied electric field, and result in a small shift of the zero g-factor crossing location. Future work characterizing rotational magnetic moments of $\tilde{X}(010)$ states of laser-coolable metal hydroxides can enable more accurate predictions of zero g-factor field values.

In CaOH, each rotational state N supports multiple $M = \pm 1$ pairs of zero g-factor states. The states at finite electric field can be labeled in terms of their adiabatically correlated zero-field quantum numbers $|N, J', F, M\rangle$. In the presence of trap shifts, the zero g-factor states for $N = 1$ occur at $E = 59.6$ V/cm for $|J = 1/2^+, F = 1, M = \pm 1\rangle$ and at $E = 64.1$ V/cm for $|J = 3/2^+, F = 1, M = \pm 1\rangle$. The $J = 1/2, M = 1$ state is a superposition of 47% $M_N \ell = -1$, 50% $M_N \ell = 0$, and 3% $M_N \ell = 1$, while the $J = 3/2, M = 1$ state is 43% $M_N \ell = -1$, 48% $M_N = 0$, and 9% $M_N \ell = 1$. Both states are weak-electric-field seekers, yet the opposite molecule frame
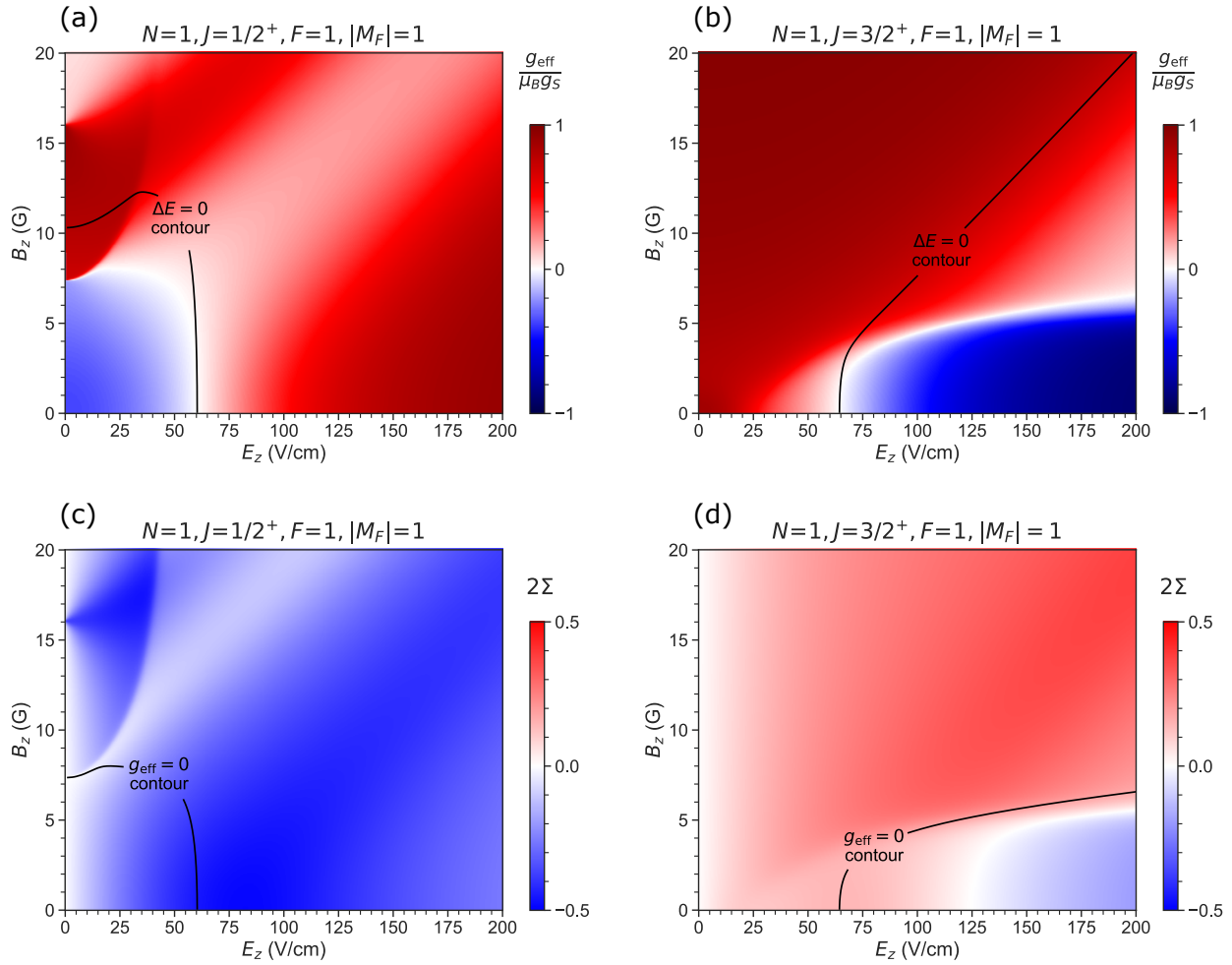
Figure 5.28: Full electric and magnetic characterization of zero g-factor states in the $N = 1$ manifold of CaOH, without trap shifts. (a, b) 2D plots of the effective g-factor difference between two $M = \pm 1$ states, defined by $g_{\mathrm{eff}} = g_S \mu_B \left(\langle M_S \rangle_{M=+1} - \langle M_S \rangle_{M=-1} \right)$. The plotted g-factor is normalized by $g_S \mu_B$. The black line represents the contour where the $M = \pm 1$ levels are nominally degenerate. (c, d) 2D plots of the eEDM sensitivity, $\langle \Sigma \rangle_{M=+1} - \langle \Sigma \rangle_{M=-1}$. The black line represents the $g_{\mathrm{eff}} = 0$ contour.

orientation of the spin results in differences in the value of Σ and the g-factor slope. For CaOH, the magnetic sensitivity and eEDM sensitivity of $N = 1$ zero g-factor states are shown in Fig. 5.27.

By diagonalizing H_{eff} over a grid of (E_Z, B_Z) values, we can obtain 2D plots of g-factors and eEDM sensitivities shown in Fig. 5.28. For generality, we consider the molecular structure in the absence of trap shifts. Using the Z-symmetry of the Hamiltonian, we separately diagonalize each M_F block to avoid degeneracies at $B_Z = 0$. Continuous 2D surfaces for eigenvalues and eigenvectors are obtained by ordering eigenstates at each value of (E, B) according to their adiabatically correlated free field state. The application of an external magnetic field parallel to the electric field results in $\langle M_S \rangle \neq 0$ for an individual zero g-factor state, but the differential value between a zero

g-factor pair can still have $\Delta\langle M_S \rangle = 0$. This differential value means the superposition of a zero g-factor pair can maintain magnetic insensitivity and EDM sensitivity over a range of fields, for example up to $\sim$5 G for the $J = 1/2, N = 1$ pair.

The procedure we use here for identifying zero g-factor states can be generically extended to searching for favorable transitions between states with differing eEDM sensitivities, similar to what has been already demonstrated in a recent proposal to search for ultra-light dark matter using SrOH [146]. In addition, there are also fields of $B_Z \approx 10 - 20$ G and $E_Z \approx 0$ where opposite parity states are tuned to near degeneracy. This is the field regime that has been proposed for precision measurements of parity-violation in optically trapped polyatomic molecules [304].

We note that zero g-factor pairs also occur in $N = 2^-$. The crossings occur around $400 - 500$ V/cm for states correlated with the negative parity manifold. Since many interactions increase in magnitude with larger N, the overall electric field scale of the intermediate regime increases. Additionally, the robustness of zero g-factor states also improves, with some pairs able to maintain $\Delta\langle M_S \rangle = 0$ for magnetic fields up to 40 G. These $N = 2$ pairs also have non-zero eEDM sensitivity for a wide range of magnetic field values.

5.4.4.1   Transverse Field Sensitivity

We now expand our discussion to include the effect of transverse magnetic fields. Their effects can be modeled by adding $B_X S_X$ and $B_Y S_Y$ terms to the effective Hamiltonian, which have the selection rule $\Delta M_F = \pm 1$. For this discussion, we focus on the level structure of the $N = 1, J = 1/2^+$ manifold in CaOH near the zero g-factor crossing at 60.5 V/cm in the absence of trap shifts, shown in Figure 5.29. We note if there were no nuclear spin I, the two zero g-factor states would be $M_J = \pm 1/2$ states separated by $\Delta M = 1$. In such a case these degenerate states would be directly sensitive to transverse fields at first order, thereby reducing the g-factor suppression.

Due to the hyperfine structure from the nuclear spin of the H atom in CaOH, the degenerate $M_F = \pm 1$ states in a zero g-factor pair are coupled by second order transverse field interactions. These interactions are mediated via the $M_F = 0^\pm$ states, where $\pm$ denotes the upper or lower states. Using a Schrieffer–Wolff (a.k.a. Van-Vleck) transformation, we can express the effective Hamiltonian matrix for second order coupling between the $M_F = \pm 1$ states. We write the states as $|M_F\rangle$, and for convenience we take the transverse field to point along X:

$$H_{+1,-1} = -(g_S \mu_B B_X)^2 \left(\frac{\langle -1|S_X|0^+\rangle\langle 0^+|S_X|+1\rangle}{\Delta E_{0^+}} + \frac{\langle -1|S_X|0^-\rangle\langle 0^-|S_X|+1\rangle}{\Delta E_{0^-}} \right). \tag{5.30}$$

Here, $\Delta E_{0^\pm}$ is the energy difference of the $M_F = 0^\pm$ levels from the $M_F = \pm 1$ levels. Our model provides the following values: $\langle 0^-|S_X|+1\rangle = \langle 0^-|S_X|-1\rangle = -0.18$, $\langle 0^+|S_X|+1\rangle = -0.16$, and
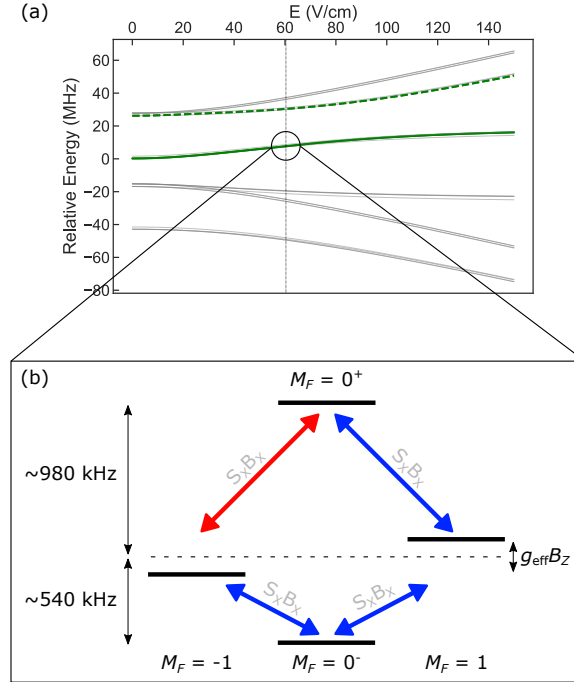
Figure 5.29: Zoomed in diagram of the zero g-factor manifold and its transverse couplings. (a) Stark shifts for the $N = 1$ states in CaOH. The $J = 1/2^+$ zero g-factor states are shown with a solid green line, while the $J = 3/2^+$ zero g-factor states are indicated with a dashed green line. All other levels are grayed out. A vertical dotted line indicates the location of the $J = 1/2^+$ zero g-factor crossing. (b) A zoomed in level diagram of the $J = 1/2^+$ zero g-factor hyperfine manifold. The bias field splitting $g_{\text{eff}}B_Z$ is not to scale. Transverse field couplings are shown with double sided arrows, with blue (red) indicating negative (positive) S_X matrix element.

$\langle 0^+|S_X| - 1\rangle = 0.16$. The difference in sign is a result of Clebsh-Gordon coefficient phases, and only the relative phase is relevant. We also have $\Delta E_{0^+} = 0.98$ MHz and $\Delta E_{0^-} = -0.54$ MHz. The combination of phases precludes the possibility of destructive interference. With these parameters and defining $g_\perp = H_{+1,-1}/B_X$, then eqn. 5.30 evaluates to $(g_S\mu_B B_X)^2(0.086/\text{MHz}) \approx (0.68$ MHz/G$^2)B_X^2$. Our model estimates the transverse sensitivity at $B_X \sim 1$ mG to be $g_\perp\mu_B \sim 7 \times 10^{-4}$ MHz/G, of the same order as the neglected nuclear and rotational Zeeman terms. The suppressed transverse field sensitivity bounds the magnitude of B_Z, which must be large enough to define a quantization axis for the spin, $g_{\text{eff}}B_Z \gg g_\perp B_\perp$.

5.4.4.2 Imperfect Field Reversal

We briefly present a systematic effect involving non-reversing fields in eEDM measurements with zero g-factor states and discuss methods for its mitigation. The electric field dependence of g_{eff} can mimic an eEDM signal when combined with other systematic effects, very much like in $^3\Delta_1$ molecules [11, 101]. When the sign of E_Z is switched, a non-reversing electric field E_{NR} will

cause a g-factor difference of $g_{NR} = (dg_{eff}/dE_Z)E_{NR}$. This will give an additional spin precession signal $g_{NR}B_Z$. By perfectly reversing B_Z as well, this precession signal can be distinguished from a true EDM signal. However, if there is also a non-reversing magnetic field B_{NR}, there will still be a residual EDM signal given by $(dg/dE)E_{NR}B_{NR}$. Using the measured slope of ~0.03 (MHz/G)/(V/cm), and using conservative estimates of $E_{NR} \sim 1$ mV/cm and $B_{NR} \sim 1$ μG, we obtain an estimate precession frequency of ~30 μHz. While this is an order of magnitude smaller than the statistical error for the current best eEDM measurement measurement [67], it is still desirable to devise methods to reduce the effect further.

Performing eEDM measurements at different zero g-factor states can help suppress systematic errors resulting from the above mechanism. For example, the $N = 1, J = 3/2$ zero crossing has a different magnitude for Σ, which can be used to distinguish a true eEDM from a systematic effect. Both $N = 1$ crossings are only separated by ~4 V/cm. Furthermore, the zero g-factor states in $N = 2^-$ can also be used for systematic checks, as they additionally offer different g_{eff} vs E_Z slopes as well as different Σ values. The $N = 2^-$ states can be populated directly by the photon-cycling used to pump into the bending mode.

5.4.5 Ramsey Measurements with Zero g-Factor States

In eEDM measurements with polarized molecules, the electron spin $\vec{S}$ precesses under the influence of an external magnetic field B_Z and the internal electric field of the molecule, $\mathcal{E}_{eff}$, which can be large due to relativistic effects. Time evolution is described by the Hamiltonian

$$
\begin{aligned}
H &= g_S\mu_B B_Z \vec{S} \cdot \hat{Z} - d_e \mathcal{E}_{eff}\vec{S} \cdot \hat{n} \\
&= g_S\mu_B B_Z M_S - d_e \mathcal{E}_{eff}\Sigma.
\end{aligned}
\tag{5.31}
$$

Here, $g_S \approx 2$ is the electron spin g-factor, μ_B is the Bohr magneton, B_Z points along the lab $\hat{Z}$ axis, and the internal field $\mathcal{E}_{eff}$ points along the molecule's internuclear axis $\hat{n}$. We define the quantities $M_S = \vec{S} \cdot \hat{Z}$ and $\Sigma = \vec{S} \cdot \hat{n}$ to describe the electron's magnetic sensitivity and EDM sensitivity, respectively. The effect of the eEDM can be isolated by switching the orientation of the applied magnetic field or, alternatively, by switching internal states to change the sign of M_S or Σ. Performing both switches is a powerful technique for suppressing systematic errors [11, 101].

To perform spin precession in the eEDM sensitive state, we first adiabatically ramp the electric field to a value E_Z, then turn on a small bias magnetic field B_Z. We measure the electron spin precession frequency using a procedure analogous to Ramsey spectroscopy [11, 100]. The molecules are prepared by driving a π-pulse (2.5 μs), with microwaves linearly polarized along the lab $\hat{X}$ axis, into the "bright" superposition state $|B\rangle = (|M = 1\rangle + |M = -1\rangle)/\sqrt{2}$ within the

$N = 1, J = 1/2^+, F = 1, M = \pm 1$ eEDM sensitive manifold (Figure 5.26(c)). The state begins to oscillate between the bright state and the "dark" state $|D\rangle = (|M = 1\rangle - |M = -1\rangle)/\sqrt{2}$ at a rate $\omega_{SP} = \mu_{eff}B_Z$, where the effective magnetic moment $\mu_{eff} = \mu_B g_{eff} = g_S \mu_B (\langle M_S \rangle_{M=1} - \langle M_S \rangle_{M=-1})$ is tuned via the applied electric field E_Z (Figure 5.26(b)). The contribution from the $d_e \mathcal{E}_{eff}$ term in eqn. 5.31 is negligible in CaOH, but could be measured in heavier molecules with much larger $\mathcal{E}_{eff}$. After a given time, a second π-pulse is applied to stop spin precession and transfer the bright state to the optically detectable $N = 2, J = 3/2^-$ level. Once the electric field is ramped down, the population remaining in the eEDM manifold, which has the opposite parity, is not optically detectable. We then image the ODT again and take the ratio of the first and second images. At long spin precession times (> 10 ms), losses from background gas collisions (~ 1 sec), blackbody excitation (~ 1 sec), and the spontaneous lifetime of the bending mode (~ 0.7 sec) lead to an overall loss of signal, as characterized in Ref. [109]. This effect is mitigated with a fixed duration between the first and second images, making the loss independent of the precession time.

To map out the location of the zero g-factor crossing, we perform spin precession measurements at a fixed magnetic field $B_Z = 110$ mG for different electric fields. The spin precession frequency corresponds to an effective g-factor at that electric field. We find that the zero g-factor crossing within the $N = 1, J = 1/2^+, F = 1, M = \pm 1$ eEDM manifold occurs at an electric field of 59.6 V/cm, in agreement with theory calculations described in the Supplemental Material. We note that there is another zero g-factor crossing for the $N = 1, J = 3/2^+, F = 1$ manifold at ≈ 64 V/cm, which has a smaller eEDM sensitivity but the opposite slope of g_{eff} vs. E_Z, thereby providing a powerful resource to reject systematic errors related to imperfect field reversals. We emphasize that while the location of these crossings is dependent on the structure of a specific molecule, their existence is generic in polyatomic molecules, which naturally have parity-doublet structure [17].

A critical component of the spin precession measurement is the coherence time, which sets the sensitivity of an eEDM search. We characterize two dominant limitations that wash out oscillations at long times. Variations in the spin precession frequency can be linearly expanded as $\delta\omega_{SP} = \mu_{eff}(\delta B_Z) + (\delta\mu_{eff})B_Z$. The first term describes magnetic field noise and drift of the applied bias field, given by δB_Z. The second term describes noise and drifts in the g-factor, δg_{eff}, which can arise from instability in the applied electric field, E_Z, or from AC Stark shifts (described below). Drifts in the bias electric field E_Z are found to be negligible in the apparatus.

Decoherence due to magnetic field noise, δB_Z, is independent of the applied magnetic field but is proportional to μ_{eff}, and can be mitigated by operating near the zero g-factor crossing. At an electric field of 90 V/cm, corresponding to a large magnetic moment of $\mu_{eff} = 1.0$ MHz/G, we realize a magnetic field noise-limited coherence time of 0.5 ms at $B_Z \approx 15$ mG. At an electric field of 61.5 V/cm, corresponding to $\mu_{eff} = 0.06$ MHz/G, much closer to the zero g-factor location, we

find a coherence time of 4 ms at the same B_Z.

At higher magnetic fields, the primary limitation to the coherence time is due to AC stark shifts from the optical trapping light. The intense Z-polarized ODT light leads to a shift in the electric field at which the zero g-factor crossing occurs. Due to the finite temperature of the molecules within the trap, they will explore different intensities of trap light and hence have different values of g_{eff}. The spread δg_{eff} causes variation of ω_{SP}, which leads to decoherence. In contrast to the magnetic field noise term, this effect is independent of the electric field E_Z but decreases monotonically with B_Z, which scales the frequency sensitivity to g-factor variations, $\delta \omega_{\text{SP}} = B_Z \delta \mu_{\text{eff}}$. The effect of g-factor broadening is insensitive to the exact value of g_{eff}. Decoherence due to AC Stark shifts can be reduced by cooling the molecules to lower temperatures or by decreasing B_Z. The bias magnetic field can be reduced arbitrarily far until either transverse magnetic fields or magnetic field noise become dominant. From the decoherence rates measured in this work, it is expected that AC Stark shift-limited coherence times ~1 s could be achieved at bias fields of $B_Z \sim 100\ \mu$G. If the molecules could be cooled to a temperature significantly less than the trap depth, this effect would be greatly reduced. Additionally, since the δg_{eff} term is scaled by B_Z, this decoherence can also be reduced by lowering the magnetic field. As the bias magnetic field is reduced, however, the effect of unwanted transverse magnetic fields is increased.

When transverse magnetic fields are dominant, the electron will be quantized along the transverse axis and there is minimal spin precession by the bias B_Z field. The transverse coupling results in eigenstates given by $(|M_F = 1\rangle \pm e^{i\phi}|M_F = -1\rangle)/\sqrt{2}$, where the phase ϕ is set by the direction of $\vec{B}$ in the transverse plane. If $\phi = 0$ or π, only one of these states is bright to the $\hat{X}$-polarized state preparation microwaves, which means the initial state is stationary under the transverse fields. For all other orientations, the transverse field causes spin precession with varying contrast, depending on the specific value of ϕ.

We are able to use transverse spin precesion to measure and zero transverse fields to the mG level. We do so by operating with minimal bias field $B_Z \approx 0$ and operating E_Z near the zero g-factor crossing, such that $g_{\text{eff}} B_Z < g_{\perp} B_{\perp}$. We then apply a small transverse magnetic field to perform transverse spin precession. Here, the dynamics are dominated by the transverse fields rather than the Z fields. We obtain field zeros by iteratively minimizing the precession frequency by tuning the bias fields B_X and B_Y.

It is expected that the longest achievable coherence times will occur for very small g-factors, $g_{\text{eff}} \approx 0$, and very small bias fields, $B_Z \approx 0$. Minimizing B_Z requires reducing the effects of both magnetic field noise and transverse magnetic fields to well below the level of the bias field energy shifts. We cancel the transverse magnetic fields to below 1 mG by maximizing the spin precession period under the influence of transverse B fields only, and actively monitor and feedback on the

magnetic field along each axis to minimize noise and drifts in B_Z. Note that the stainless steel vacuum chamber has no magnetic shielding, leading to high levels of magnetic field noise which would not be present in an apparatus designed for an eEDM search. Even under these conditions, we achieve a coherence time of 30 ms at an electric field of 60.3 V/cm (corresponding to $\mu_{\text{eff}} = 0.02$ MHz/G) and a bias field of $B_Z \approx 2$ mG. However, at such a low bias field, the molecules are sensitive to 60 Hz magnetic field noise present in the unshielded apparatus, which is on the same order as the bias field. Since the experiment is phase stable with respect to the AC line frequency, this 60 Hz magnetic field fluctuation causes a time-dependent spin precession frequency. Nevertheless, our prototype experiment confirms that long coherence times are possible, and any future eEDM experiment would have magnetic shielding that would greatly suppress nefarious magnetic fields from the environment. Such shielding could readily enable coherence times exceeding that of the ~ 0.5 s lifetime of the bending modes of similar linear polyatomic molecules with larger eEDM sensitivity [109].

5.4.6 Conclusion

In summary, we have realized coherent control of optically trapped polyatomic molecules and demonstrated a realistic experimental roadmap for future eEDM measurements. By leveraging the unique features of the quantum levels in polyatomic molecules, we achieve a coherence time of 30 ms for paramagnetic molecules in a stainless steel chamber with no magnetic shielding. With common shielding techniques employed in past EDM experiments, there is a clear path to reducing stray fields and extending coherence times to > 100 ms. At such a level, the dominant limitation becomes the finite lifetime of the bending mode [109]. Even longer coherence times are possible with the right choice of parity doublet states, as found in symmetric or asymmetric top molecules [17, 107, 123, 429].

Following our established roadmap with heavier trapped polyatomic molecules has the potential to provide orders-of-magnitude improvements to current bounds on T violating physics. Using the $\tilde{X}(010)$ study of YbOH from Sec. 4.2, we have identified similar $N = 1$ zero g-factor states for eEDM measurements with significantly improved sensitivity. In addition to the g-factor tuning demonstrated in this work, polyatomic molecules provide the ability to reverse the sign of Σ without reversing M_S - a crucial feature of recent experiments that have greatly improved the limit on the eEDM [10, 11]. For example, in the $N = 1$ manifold of CaOH, there is another zero g-factor crossing at a nearby electric field value, with 69% smaller values of Σ and opposite sign. Since the ratio of eEDM sensitivity to g-factor vs. E_Z slope differs between these two crossings, measurements at both points could be used to suppress systematics due to non-reversing fields coupling to the electric field dependence of the g-factor [11].

We have provided the first experimental demonstration of the advantages of the rich level structure of polyatomic molecules for precision measurements. While we have focused here on spin precession with T-reversed states ($M = \pm 1$), many levels of interest can be favorably engineered for precision measurement experiments. In a recent proposal [304], parity-doublets, magnetically tuned to degeneracy in optically trapped polyatomic molecules, were shown to be advantageous for searches for parity violating physics. In another recent work [146], a microwave clock between rovibrational states in SrOH was proposed as a sensitive probe of ultra-light dark matter, utilizing transitions tuned to electric and/or magnetic insensitivity. Finally, in Ref. [124], we show that EDM sensitive transitions with reduced sensitivity to stray fields can be engineered with application of external fields. In these proposals, and now experimentally demonstrated in our work, coherent control and state engineering in polyatomic molecules can mitigate systematic errors and enable robust searches for new physics.

CHAPTER

6

CONCLUSIONS

Do, or do not. There is no try.

–Yoda

6.1 Overview of Results

This thesis has made major advances to the platform of polyatomic molecules for new physics searches. In polyatomic molecules, angular momentum states J are characterized by a projection in the molecule frame, K, and a projection in the lab frame, M. Both of these projections are odd under time-reversal (T), while the K projection internal to the molecule is odd under parity reversal (P). Therefore, the oriented states of polyatomic molecules offer us intrinsic control over both the P-odd and T-odd degrees of freedom of the system. This is useful when engineering differential measurements to search for effects that violate symmetries, allowing us to perform numerous systematic checks by reversing and reorienting the P, T violating signal (internal co-magnetometry). Indeed, parity doublets are a key feature behind both the ACME and JILA experiments that currently set the best bounds on a possible P, T violating electron electric dipole moment. The power of polyatomic molecules is they can generically combine the parity doublet feature with laser cooling.

Our work focused on YbOH, a linear triatomic molecule with significant new physics sensitivity owing to the heavy Yb nucleus. We have shown that polyatomic YbOH molecules can be produced in large quantities at low temperatures. By optically exciting reactant atoms, we were able to chemically enhance our molecular yield by an order of magnitude [227]. With this chemical

enhancement light, our cryogenic buffer gas beam (CBGB) source produces $\sim 10^{11}$ ground state YbOH molecules inside the cell at ~4 K. The buffer gas flow extracts $\sim 10^{10}$ molecules into a beam traveling at ~200 m/s. Downstream in the beam, we can interrogate $\sim 10^7$ molecules per pulse, with repetition rates up to 10 Hz. Additionally, our CBGB has natural $\tilde{X}(010)$ science state population, with about 10^6 molecules downstream, without optical pumping.

Before we began this work, YbOH had only been characterized in a high temperature study from 2001 [430], with many speculative assignments. In this work, we made significant spectroscopy progress, essentially determining all the necessary spectroscopic information to perform precision measurements with YbOH. We fully characterized the science state of YbOH, the $\tilde{X}^2\Sigma^+(010)$ fundamental bending mode of the ground state [280]. We determined effective Hamiltonian parameters that allow us to accurately model the quantum levels of the $\tilde{X}(010)$ state, in both free-field and in the presence of applied electromagnetic fields. In particular, our study of level tuning by the electric fields illustrates the orientation control over the P, T violating interactions that is afforded by polyatomic molecules. Furthermore, we also characterized the $\tilde{A}(010)$ bending excited state of YbOH. This state shows a rich interplay of spin-orbit and vibronic interactions that results in an emergent level pattern reminiscent of a bent molecule with quenched orbital electronic angular momentum. Finally, we determined optimal states to use for optical pumping into $\tilde{X}(010)$ and for coherently manipulating quantum states in $\tilde{X}(010)$.

We also made significant progress in state preparation and readout schemes for precision measurements with polyatomic molecules. We demonstrated coherent quantum control of YbOH using detuned two-photon transitions, and on the way we re-discovered lessons in atomic physics regarding destructive interference from unresolved hyperfine structure. We showed that control issues related to unresolved hyperfine can be overcome with the appropriate choice of laser polarizations and optical sideband generation scheme. Using our spectroscopy knowledge, we were able to perform a prototype Ramsey interferometry sequence, measuring spin precession between individual quantum states in the presence of a magnetic field. The next step beyond this work is to generalize our Ramsey interferometry protocol to YbOH molecules in the presence of a polarizing electric field. Achieving this milestone would finalize the transition of the YbOH experiment from the prototyping phase to the precision measurement phase.

This work is also broadly applicable beyond YbOH to other linear triatomic molecules useful for precision measurements, such as SrOH [302] and RaOH [272, 431]. The laser induced chemical enhancement we demonstrate is expected to apply to both SrOH and RaOH, given it works for YbOH and CaOH. Further, the path we laid for science state spectroscopy will be the same for other hydroxides. Finally, the two-photon techniques we demonstrate can be generalized to other polyatomic molecules as well, as we do not need to worry about fine-tuning of frequencies.

Additionally, as part of the PolyEDM collaboration, we performed a proof-of-principle Ramsey measurement of ultracold, optically trapped CaOH molecules in the $\tilde{X}(010)$ science state. This work demonstrated the power afforded by laser cooling and trapping polyatomic molecules for precision emasurements. We showed that the parity doublet structure of polyatomic molecules generically gives rise to zero g-factor states with magnetic insensitivity while still retaining new physics sensitivity. We have found these states also exist in YbOH and other linear triatomic molecules. In CaOH, we used zero g-factor states to achieve a nearly 70× reduction of magnetic sensitivity compared to the electron's typical g-factor. In a magnetically unshielded stainless steel chamber, we were able to reach coherence times of order 30 ms, with clear next steps for improvement.

Zero g-factor states are just the tip of the iceberg when it comes to quantum state enegineering of polyatomic molecules precision measurements. In Ref. [124], we showed that we can generically find transitions in polyatomc and diatomic molecules that have favorable magnetic and electric insensitivities. These transitions arise with the application of increasing electric field, as the molecular angular momenta transition from being internally coupled to being decoupled and aligned along the external field. These field insensitive transitions can be driven with RF, microwave, of two-photon techniques, and can retain strong sensitivity to P, T violating effects.

Field insensitive transitions are a generalization of EDM measurements to the rotating frame. The EDM causes differential evolution of $\pm M$ states relative to an oscillating reference clock or drive. When we perform a Ramsey measurement, we work in a rotated basis, where the diagonal EDM shifts now become off-diagonal couplings between spin precession states. EDMs also cause off-diagonal couplings in free field. As a result, we can imagine working in a rotated basis, taking superpositions of opposite parity states.

In free field, the eigenstates are symmetrized, $|JM \pm \mathcal{P}\rangle$, and have well defined parity. Therefore, EDM matrix elements are present on the off diagonals of the Hamiltonian connecting opposite parity states, $\langle JM \pm \mathcal{P}|H_{PT}|JM \mp \mathcal{P}\rangle = E_{PT}$. This is similar to the matrix element for the ordinary molecule frame dipole interaction, $H_E = \vec{D} \cdot \vec{E}_{\text{lab}}$, with the difference being the behavior of H_{PT} under time-reversal. On the other hand, in the presence of an electric field, the parity basis is mixed, and we instead consider the un-symmetrized symmetric top wavefunctions, $|JKM\rangle$. In this basis the EDM is diagonal: $\langle J \pm KM|H_{PT}|J \pm KM\rangle = \pm E_{PT}$.

By the Wigner-Eckart theorem, the EDM matrix elements connect $\Delta M = 0$ and $\Delta J = 0$, and induce a small, P, T violating permanent dipole moment in free field. The T odd behavior of the EDM appears when we compare $+MK$ and $-MK$ states, which have opposite PT-odd coupling matrix element. It is also instructive to consider the diagonal EDM matrix element H_{PT}, as well as the Stark interaction H_E, in the decoupled basis, defined by M_N, M_S, and K. We have

$H_{PT} \propto M_N M_S K$, while $H_E \propto M_N K$. Since only K flips under a parity transformation, both matrix elements are P-odd. However, since K and M flip under a time-reversal transformation, we see only the EDM interaction is also T-odd. In a sense, an EDM measurement is observing the T-odd interference between the parity-odd couplings, H_{PT} and H_E.

In free field, the effect of the EDM coupling between opposite parity states is suppressed by the overall parity splitting $\omega_{\mathcal{P}}$ of the molecule. However, in the frame rotating at the parity energy splitting, denoted $\omega_{\mathcal{P}}$, the EDM interaction could be observed as a coupling in the rotating frame. The catch is that the spin, which is defined in the lab-frame, must also be brought into the rotating frame, such that the EDM interaction does not average out. This is similar to Ref. [69], where the authors propose a rotating frame measurement between hyperfine states driven by an RF magnetic field, with the molecule orientation adiabatically following an applied in phase RF electric field. One can also consider the electric field analogue of this technique, where an RF electric field prepares an opposite parity superposition, and adiabatic following of an RF magnetic field brings the spin into the rotating frame. Such a scheme could have the benefit of not requiring DC electric fields, and only being sensitive to noise in the rotating frame.

6.2 Outlook for YbOH

The odd isotopologue ^{173}YbOH can support a nuclear magnetic quadrupole moment (NMQM) on the Yb nucleus with $I = 3/2$. The NMQM provides us an avenue for sensitivity to hadronic P, T violating physics in paramagnetic systems. Aside from special cases of octupole deformed nuclei, the NMQM is expected to provide a stronger symmetry violating signal than the nuclear Schiff moment, which is partially screened. Currently, the best limit on the MQM of a nucleus is from a measurement of atomic Cs performed in 1989 [432], corresponding to a 95% upper limit of $\mathcal{M} < 2.6 \times 10^{-7} \mu_N R_{Cs} = 1.5 \times 10^{-44}$ A m^3 = $3 \times 10^{-3} \mu_Q$. In the last equality we have defined the nuclear unit for an MQM, $\mu_Q = $ fm μ_N.

In our lab, a science beamline is currently under construction to perform a measurement of the NMQM in ^{173}YbOH. All of the parts have been designed, ordered, assembled, and tested. The electric field plates, fluorescence collection optics, and beamline layout are detailed in Appendix F. The three layers of magnetic shields for the experiment have also been assembled, complete with degaussing electronics. Initial shielding tests indicate a shielding factor of > 100, with the measurement thus far limited primarily by magnetometer zero offsets. Progress is now underway to assemble the beamline within the magnetic shielding. Once closed up, the beamline will allow us to perform Ramsey measurements with a coherence time of $\tau = 1$ ms, limited only by time-of-flight across the 20 cm long interaction region.

We now estimate the new physics sensitivity of YbOH measurements in our apparatus in the

near future. With an optimized source using enriched isotope targets and optical pumping, but also taking into account finite state preparation efficiencies, we assume have available $\sim 10^6$ bending mode ^{173}YbOH molecules downstream in the beam in a single quantum state. Furthermore, we assume 20% optics collection efficiency and 10% PMT efficiency, resulting in $N_{\text{meas}} = 2 \times 10^4$. We additionally assume a repetition rate of 10 Hz and a coherence time of $\tau = 1$ ms. Furthermore, we estimate the differential NMQM energy shift as as $\Delta E = h W_{\mathcal{M}} \mathcal{M} \times 0.2$ [407]. From Refs. [267, 406], we have $W_M \approx -1.07 \times 10^{33}$ Hz/(e cm^2)/c $= -2.3 \times 10^{44}$ Hz/(A m^3) $= -1.13 \times 10^6$ Hz/μ_Q. We can then calculate the MQM sensitivity using the quantum projection noise limit:

$$\delta \mathcal{M} = \frac{\hbar}{2(0.2 \times h W_{\mathcal{M}}) \tau \sqrt{N_p R_p T_{tot}}} \tag{6.1}$$

For the estimates given above, we obtain $\delta \mathcal{M} \approx 1.4 \times 10^{-50}$ A m$^3/\sqrt{\text{day}} = 2.7 \times 10^{-9}$ $\mu_Q/\sqrt{\text{day}}$. We see that we can improve on the Cs limit quite drastically. Even with just 1 hour of data taking, we stand to beat the Cs limit by nearly 6 orders of magnitude.

Since Yb and Cs are different nuclei, such a comparison is not quite accurate. Rather, we must consider the sensitivity of the Yb nucleus to potential P, T violating effects, as discussed in Ref. [267]. There, the authors considered the magnitude of a NMQM in ^{173}YbOH originating from two different P, T violating hadronic effects: the QCD vacuum angle, $\mathcal{M}(\theta) = \theta \times 0.95 \mu_Q$, and the difference in up and down quark chromo-EDMs, $\mathcal{M}(\tilde{d}) = 3.1 \mu_B \times (\tilde{d}_u - \tilde{d}_p)$. On the other hand, current limits [433] are given by $|\theta| < 2.4 \times 10^{-10}$ and $|\tilde{d}_u - \tilde{d}_p| < 6 \times 10^{-27}$ cm. Putting all of these together, in YbOH P, T violating effects should result in values no larger than $\mathcal{M}(\theta) < 2.3 \times 10^{-10} \mu_Q$ and $\mathcal{M}(\tilde{d}) < 3.4 \times 10^{-10} \mu_Q$. Therefore we see our 1 day sensitivity is about an order of magnitude away from being competative with existing limits. While the estimates given have been approximate, they provide excellent motivation to pursue a measurement in ^{173}YbOH. We note we have not discussed potential improvements that could help increase sensitivity, such as implementing laser cooling to reduce beam divergence, using laser slowing to increase the interaction time, and using optical cycling for efficient state preparation and readout.

BIBLIOGRAPHY

[1] G. Aad et al., "Observation of a new particle in the search for the Standard Model Higgs boson with the ATLAS detector at the LHC," Physics Letters B **716**, 1–29 (2012) `10.1016/j.physletb.2012.08.020`.

[2] S. Chatrchyan et al., "Observation of a new boson at a mass of 125 GeV with the CMS experiment at the LHC," Physics Letters B **716**, 30–61 (2012) `10.1016/j.physletb.2012.08.021`.

[3] X. Fan, T. G. Myers, B. A. D. Sukra, and G. Gabrielse, "Measurement of the Electron Magnetic Moment," Physical Review Letters **130**, 071801 (2023) `10.1103/PhysRevLett.130.071801`.

[4] M. Dine and A. Kusenko, "Origin of the matter-antimatter asymmetry," Reviews of Modern Physics **76**, 1–30 (2004).

[5] F. Feruglio, "Pieces of the flavour puzzle," The European Physical Journal. C, Particles and Fields **75**, 373 (2015) `10.1140/epjc/s10052-015-3576-5`.

[6] J. L. Feng, "Naturalness and the Status of Supersymmetry," Annual Review of Nuclear and Particle Science **63**, 351–382 (2013) `10.1146/annurev-nucl-102010-130447`.

[7] T. E. Chupp, P. Fierlinger, M. J. Ramsey-Musolf, and J. T. Singh, "Electric dipole moments of atoms, molecules, nuclei, and particles," Reviews of Modern Physics **91**, 015001 (2019) `10.1103/RevModPhys.91.015001`.

[8] M. Pospelov and A. Ritz, "CKM benchmarks for electron electric dipole moment experiments," Physical Review D **89**, 056006 (2014) `10.1103/PhysRevD.89.056006`.

[9] T. Ibrahim and P. Nath, "$\Mathit{CP}$ violation from the standard model to strings," Reviews of Modern Physics **80**, 577–631 (2008) `10.1103/RevModPhys.80.577`.

[10] T. S. Roussy, L. Caldwell, T. Wright, W. B. Cairncross, Y. Shagam, K. B. Ng, N. Schlossberger, S. Y. Park, A. Wang, J. Ye, and E. A. Cornell, *A new bound on the electron's electric dipole moment*, (Dec. 27, 2022) `10.48550/arXiv.2212.11841`, `http://arxiv.org/abs/2212.11841`, preprint.

[11] ACME Collaboration, "Improved limit on the electric dipole moment of the electron," Nature **562**, 355–360 (2018) `10.1038/s41586-018-0599-8`.

[12]R. Alarcon, J. Alexander, V. Anastassopoulos, T. Aoki, R. Baartman, S. Baeßler, L. Bartoszek, D. H. Beck, F. Bedeschi, R. Berger, M. Berz, H. L. Bethlem, T. Bhattacharya, M. Blaskiewicz, T. Blum, T. Bowcock, A. Borschevsky, K. Brown, D. Budker, S. Burdin, B. C. Casey, G. Casse, G. Cantatore, L. Cheng, T. Chupp, V. Cianciolo, V. Cirigliano, S. M. Clayton, C. Crawford, B. P. Das, H. Davoudiasl, J. de Vries, D. DeMille, D. Denisov, M. V. Diwan, J. M. Doyle, J. Engel, G. Fanourakis, R. Fatemi, B. W. Filippone, V. V. Flambaum, T. Fleig, N. Fomin, W. Fischer, G. Gabrielse, R. F. G. Ruiz, A. Gardikiotis, C. Gatti, A. Geraci, J. Gooding, B. Golub, P. Graham, F. Gray, W. C. Griffith, S. Haciomeroglu, G. Gwinner, S. Hoekstra, G. H. Hoffstaetter, H. Huang, N. R. Hutzler, M. Incagli, T. M. Ito, T. Izubuchi, A. M. Jayich, H. Jeong, D. Kaplan, M. Karuza, D. Kawall, O. Kim, I. Koop, W. Korsch, E. Korobkina, V. Lebedev, J. Lee, S. Lee, R. Lehnert, K. K. H. Leung, C.-Y. Liu, J. Long, A. Lusiani, W. J. Marciano, M. Maroudas, A. Matlashov, N. Matsumoto, R. Mawhorter, F. Meot, E. Mereghetti, J. P. Miller, W. M. Morse, J. Mott, Z. Omarov, L. A. Orozco, C. M. O'Shaughnessy, C. Ozben, S. Park, R. W. Pattie Jr., A. N. Petrov, G. M. Piacentino, B. R. Plaster, B. Podobedov, M. Poelker, D. Pocanic, V. S. Prasannaa, J. Price, M. J. Ramsey-Musolf, D. Raparia, S. Rajendran, M. Reece, A. Reid, S. Rescia, A. Ritz, B. L. Roberts, M. S. Safronova, Y. Sakemi, P. Schmidt-Wellenburg, A. Shindler, Y. K. Semertzidis, A. Silenko, J. T. Singh, L. V. Skripnikov, A. Soni, E. Stephenson, R. Suleiman, A. Sunaga, M. Syphers, S. Syritsyn, M. R. Tarbutt, P. Thoerngren, R. G. E. Timmermans, V. Tishchenko, A. V. Titov, N. Tsoupas, S. Tzamarias, A. Variola, G. Venanzoni, E. Vilella, J. Vossebeld, P. Winter, E. Won, A. Zelenski, T. Zelevinsky, Y. Zhou, and K. Zioutas, *Electric dipole moments and the search for new physics*, (Apr. 4, 2022) `http://arxiv.org/abs/2203.08103`, preprint.

[13]D. DeMille, J. M. Doyle, and A. O. Sushkov, "Probing the frontiers of particle physics with tabletop-scale experiments," Science **357**, 990–994 (2017) `10.1126/science.aal3003`.

[14]M. S. Safronova, D. Budker, D. DeMille, D. F. J. Kimball, A. Derevianko, and C. W. Clark, "Search for new physics with atoms and molecules," Reviews of Modern Physics **90**, 025008 (2018) `10.1103/RevModPhys.90.025008`.

[15]W. B. Cairncross and J. Ye, "Atoms and molecules in the search for time-reversal symmetry violation," Nature Reviews Physics **1**, 510–521 (2019) `10.1038/s42254-019-0080-0`.

[16]X. F. Yang, S. J. Wang, S. G. Wilkins, and R. F. G. Ruiz, "Laser spectroscopy for the study of exotic nuclei," Progress in Particle and Nuclear Physics **129**, 104005 (2023) `10.1016/j.ppnp.2022.104005`.

[17]I. Kozyryev and N. R. Hutzler, "Precision Measurement of Time-Reversal Symmetry Violation with Laser-Cooled Polyatomic Molecules," Physical Review Letters **119**, 133002 (2017) `10.1103/PhysRevLett.119.133002`.

[18]L. Pezzè, A. Smerzi, M. K. Oberthaler, R. Schmied, and P. Treutlein, "Quantum metrology with nonclassical states of atomic ensembles," Reviews of Modern Physics **90**, 035005 (2018) `10.1103/RevModPhys.90.035005`.

[19]M. D. Schwartz, *Quantum Field Theory and the Standard Model* (Cambridge University Press, 2014), 869 pp.

[20]E. Wigner, "On Unitary Representations of the Inhomogeneous Lorentz Group," Annals of Mathematics **40**, 149–204 (1939) `10.2307/1968551`.

[21] Particle Data Group, P. A. Zyla, R. M. Barnett, J. Beringer, O. Dahl, D. A. Dwyer, D. E. Groom, C. .-. Lin, K. S. Lugovsky, E. Pianori, D. J. Robinson, C. G. Wohl, W. .-. Yao, K. Agashe, G. Aielli, B. C. Allanach, C. Amsler, M. Antonelli, E. C. Aschenauer, D. M. Asner, H. Baer, S. Banerjee, L. Baudis, C. W. Bauer, J. J. Beatty, V. I. Belousov, S. Bethke, A. Bettini, O. Biebel, K. M. Black, E. Blucher, O. Buchmuller, V. Burkert, M. A. Bychkov, R. N. Cahn, M. Carena, A. Ceccucci, A. Cerri, D. Chakraborty, R. S. Chivukula, G. Cowan, G. D'Ambrosio, T. Damour, D. de Florian, A. de Gouvêa, T. DeGrand, P. de Jong, G. Dissertori, B. A. Dobrescu, M. D'Onofrio, M. Doser, M. Drees, H. K. Dreiner, P. Eerola, U. Egede, S. Eidelman, J. Ellis, J. Erler, V. V. Ezhela, W. Fetscher, B. D. Fields, B. Foster, A. Freitas, H. Gallagher, L. Garren, H. .-. Gerber, G. Gerbier, T. Gershon, Y. Gershtein, T. Gherghetta, A. A. Godizov, M. C. Gonzalez-Garcia, M. Goodman, C. Grab, A. V. Gritsan, C. Grojean, M. Grünewald, A. Gurtu, T. Gutsche, H. E. Haber, C. Hanhart, S. Hashimoto, Y. Hayato, A. Hebecker, S. Heinemeyer, B. Heltsley, J. J. Hernández-Rey, K. Hikasa, J. Hisano, A. Höcker, J. Holder, A. Holtkamp, J. Huston, T. Hyodo, K. F. Johnson, M. Kado, M. Karliner, U. F. Katz, M. Kenzie, V. A. Khoze, S. R. Klein, E. Klempt, R. V. Kowalewski, F. Krauss, M. Kreps, B. Krusche, Y. Kwon, O. Lahav, J. Laiho, L. P. Lellouch, J. Lesgourgues, A. R. Liddle, Z. Ligeti, C. Lippmann, T. M. Liss, L. Littenberg, C. Lourengo, S. B. Lugovsky, A. Lusiani, Y. Makida, F. Maltoni, T. Mannel, A. V. Manohar, W. J. Marciano, A. Masoni, J. Matthews, U. .-. Meißner, M. Mikhasenko, D. J. Miller, D. Milstead, R. E. Mitchell, K. Mönig, P. Molaro, F. Moortgat, M. Moskovic, K. Nakamura, M. Narain, P. Nason, S. Navas, M. Neubert, P. Nevski, Y. Nir, K. A. Olive, C. Patrignani, J. A. Peacock, S. T. Petcov, V. A. Petrov, A. Pich, A. Piepke, A. Pomarol, S. Profumo, A. Quadt, K. Rabbertz, J. Rademacker, G. Raffelt, H. Ramani, M. Ramsey-Musolf, B. N. Ratcliff, P. Richardson, A. Ringwald, S. Roesler, S. Rolli, A. Romaniouk, L. J. Rosenberg, J. L. Rosner, G. Rybka, M. Ryskin, R. A. Ryutin, Y. Sakai, G. P. Salam, S. Sarkar, F. Sauli, O. Schneider, K. Scholberg, A. J. Schwartz, J. Schwiening, D. Scott, V. Sharma, S. R. Sharpe, T. Shutt, M. Silari, T. Sjöstrand, P. Skands, T. Skwarnicki, G. F. Smoot, A. Soffer, M. S. Sozzi, S. Spanier, C. Spiering, A. Stahl, S. L. Stone, Y. Sumino, T. Sumiyoshi, M. J. Syphers, F. Takahashi, M. Tanabashi, J. Tanaka, M. Taševský, K. Terashi, J. Terning, U. Thoma, R. S. Thorne, L. Tiator, M. Titov, N. P. Tkachenko, D. R. Tovey, K. Trabelsi, P. Urquijo, G. Valencia, R. Van de Water, N. Varelas, G. Venanzoni, L. Verde, M. G. Vincter, P. Vogel, W. Vogelsang, A. Vogt, V. Vorobyev, S. P. Wakely, W. Walkowiak, C. W. Walter, D. Wands, M. O. Wascko, D. H. Weinberg, E. J. Weinberg, M. White, L. R. Wiencke, S. Willocq, C. L. Woody, R. L. Workman, M. Yokoyama, R. Yoshida, G. Zanderighi, G. P. Zeller, O. V. Zenin, R. .-. Zhu, S. .-. Zhu, F. Zimmermann, J. Anderson, T. Basaglia, V. S. Lugovsky, P. Schaffner, and W. Zheng, "Review of Particle Physics," Progress of Theoretical and Experimental Physics **2020**, 083C01 (2020) `10.1093/ptep/ptaa104`.

[22] L. Canetti, M. Drewes, and M. Shaposhnikov, "Matter and antimatter in the universe," New Journal of Physics **14**, 95012 (2012) `10.1088/1367-2630/14/9/095012`.

[23] F. K. Hansen, A. J. Banday, and K. M. Górski, "Testing the cosmological principle of isotropy: local power-spectrum estimates of the WMAP data," Monthly Notices of the Royal Astronomical Society **354**, 641–665 (2004) `10.1111/j.1365-2966.2004.08229.x`.

[24] C. A. P. Bengaly, R. Maartens, N. Randriamiarinarivo, and A. Baloyi, "Testing the cosmological principle in the radio sky," Journal of Cosmology and Astroparticle Physics **2019**, 025 (2019) `10.1088/1475-7516/2019/09/025`.

[25]P. K. Aluri, P. Cea, P. Chingangbam, M.-C. Chu, R. G. Clowes, D. Hutsemékers, J. P. Kochappan, A. M. Lopez, L. Liu, N. C. M. Martens, C. J. A. P. Martins, K. Migkas, E. Ó. Colgáin, P. Pranav, L. Shamir, A. K. Singal, M. M. Sheikh-Jabbari, J. Wagner, S.-J. Wang, D. L. Wiltshire, S. Yeung, L. Yin, and W. Zhao, "Is the observable Universe consistent with the cosmological principle?" Classical and Quantum Gravity **40**, 094001 (2023) `10.1088/1361-6382/acbefc`.

[26]Planck Collaboration, N. Aghanim, Y. Akrami, M. Ashdown, J. Aumont, C. Baccigalupi, M. Ballardini, A. J. Banday, R. B. Barreiro, N. Bartolo, S. Basak, R. Battye, K. Benabed, J. .-. Bernard, M. Bersanelli, P. Bielewicz, J. J. Bock, J. R. Bond, J. Borrill, F. R. Bouchet, F. Boulanger, M. Bucher, C. Burigana, R. C. Butler, E. Calabrese, J. .-. Cardoso, J. Carron, A. Challinor, H. C. Chiang, J. Chluba, L. P. L. Colombo, C. Combet, D. Contreras, B. P. Crill, F. Cuttaia, P. de Bernardis, G. de Zotti, J. Delabrouille, J. .-. Delouis, E. Di Valentino, J. M. Diego, O. Doré, M. Douspis, A. Ducout, X. Dupac, S. Dusini, G. Efstathiou, F. Elsner, T. A. Enßlin, H. K. Eriksen, Y. Fantaye, M. Farhang, J. Fergusson, R. Fernandez-Cobos, F. Finelli, F. Forastieri, M. Frailis, E. Franceschi, A. Frolov, S. Galeotta, S. Galli, K. Ganga, R. T. Génova-Santos, M. Gerbino, T. Ghosh, J. González-Nuevo, K. M. Górski, S. Gratton, A. Gruppuso, J. E. Gudmundsson, J. Hamann, W. Handley, D. Herranz, E. Hivon, Z. Huang, A. H. Jaffe, W. C. Jones, A. Karakci, E. Keihänen, R. Keskitalo, K. Kiiveri, J. Kim, T. S. Kisner, L. Knox, N. Krachmalnicoff, M. Kunz, H. Kurki-Suonio, G. Lagache, J. .-. Lamarre, A. Lasenby, M. Lattanzi, C. R. Lawrence, M. L. Jeune, P. Lemos, J. Lesgourgues, F. Levrier, A. Lewis, M. Liguori, P. B. Lilje, M. Lilley, V. Lindholm, M. López-Caniego, P. M. Lubin, Y. .-. Ma, J. F. Macías-Pérez, G. Maggio, D. Maino, N. Mandolesi, A. Mangilli, A. Marcos-Caballero, M. Maris, P. G. Martin, M. Martinelli, E. Martínez-González, S. Matarrese, N. Mauri, J. D. McEwen, P. R. Meinhold, A. Melchiorri, A. Mennella, M. Migliaccio, M. Millea, S. Mitra, M. .-. Miville-Deschênes, D. Molinari, L. Montier, G. Morgante, A. Moss, P. Natoli, H. U. Nørgaard-Nielsen, L. Pagano, D. Paoletti, B. Partridge, G. Patanchon, H. V. Peiris, F. Perrotta, V. Pettorino, F. Piacentini, L. Polastri, G. Polenta, J. .-. Puget, J. P. Rachen, M. Reinecke, M. Remazeilles, A. Renzi, G. Rocha, C. Rosset, G. Roudier, J. A. Rubiño-Martín, B. Ruiz-Granados, L. Salvati, M. Sandri, M. Savelainen, D. Scott, E. P. S. Shellard, C. Sirignano, G. Sirri, L. D. Spencer, R. Sunyaev, A. .-. Suur-Uski, J. A. Tauber, D. Tavagnacco, M. Tenti, L. Toffolatti, M. Tomasi, T. Trombetti, L. Valenziano, J. Valiviita, B. Van Tent, L. Vibert, P. Vielva, F. Villa, N. Vittorio, B. D. Wandelt, I. K. Wehus, M. White, S. D. M. White, A. Zacchei, and A. Zonca, "Planck 2018 results. VI. Cosmological parameters," 2018.

[27]A. D. Sakharov, "Violation of CP Invariance, C Asymmetry, and Baryon Asymmetry of the Universe," Journal of Experimental and Theoretical Physics Letters **5**, 27–30 (1967).

[28]K. Rummukainen, M. Tsypin, K. Kajantie, M. Laine, and M. Shaposhnikov, "The universality class of the electroweak theory," Nuclear Physics B **532**, 283–314 (1998) `10.1016/S0550-3213(98)00494-5`.

[29]C. Jarlskog, "A basis independent formulation of the connection between quark mass matrices, CP violation and experiment," Zeitschrift für Physik C Particles and Fields **29**, 491–497 (1985) `10.1007/BF01565198`.

[30]F. R. Joaquim, I. Masina, and A. Riotto, "Observable Electron EDM and Leptogenesis," 2007, `10/b5577x`.

[31] S. Pascoli, S. T. Petcov, and A. Riotto, "Leptogenesis and low energy CP-violation in neutrino physics," Nuclear Physics B **774**, 1–52 (2007) `10.1016/j.nuclphysb.2007.02.019`.

[32] A. Pilaftsis, "The little review on leptogenesis," Journal of Physics: Conference Series **171**, 012017 (2009) `10.1088/1742-6596/171/1/012017`.

[33] O. Bertolami, D. Colladay, V. A. Kostelecký, and R. Potting, "CPT violation and baryogenesis," Physics Letters B **395**, 178–183 (1997) `10.1016/S0370-2693(97)00062-2`.

[34] G. A. White, *A Pedagogical Introduction to Electroweak Baryogenesis* (Morgan & Claypool Publishers, Nov. 1, 2016).

[35] I. B. Khriplovich and S. K. Lamoreaux, *CP Violation Without Strangeness* (Springer-Verlag Berlin Heidelberg, Berlin, Heidelberg, 1997), `10.1007/978-3-642-60838-4`.

[36] W. Bernreuther and M. Suzuki, "The electric dipole moment of the electron," Reviews of Modern Physics **63**, 313 (1991) `10.1103/RevModPhys.63.313`.

[37] W. C. Haxton, C.-P. Liu, and M. J. Ramsey-Musolf, "Nuclear anapole moments," Physical Review C **65**, 045502 (2002) `10.1103/PhysRevC.65.045502`.

[38] M. Nowakowski, E. A. Paschos, and J. M. Rodríguez, "All electromagnetic form factors," European Journal of Physics **26**, 545 (2005) `10.1088/0143-0807/26/4/001`.

[39] J. M. Brown and A. Carrington, *Rotational Spectroscopy of Diatomic Molecules*, 1st edition (Cambridge University Press, Cambridge ; New York, 2003), 1046 pp., `10.1017/cbo9780511814808`.

[40] A. C. Vutha and A. Chandra Vutha, "A search for the electric dipole moment of the electron using thorium monoxide" (Yale University, 2011).

[41] N. R. Hutzler, "A New Limit on the Electron Electric Dipole Moment" (Harvard University, 2014).

[42] E. R. Boston and P. G. H. Sandars, "The anapole moments of hydrogenic atoms," Journal of Physics B: Atomic, Molecular and Optical Physics **23**, 2663 (1990) `10.1088/0953-4075/23/15/030`.

[43] F. Boudjema, C. P. Burgess, C. Hamzaoui, and J. A. Robinson, "CP-violating but P-preserving electromagnetic couplings of the $W^{\pm}$ and Z^0," Physical Review D **43**, 3683–3690 (1991) `10.1103/PhysRevD.43.3683`.

[44] J. F. Nieves and P. B. Pal, "Electromagnetic properties of neutral and charged spin-1 particles," Physical Review D **55**, 3118–3130 (1997) `10.1103/PhysRevD.55.3118`.

[45] C. G. Gray, G. Karl, and V. A. Novikov, "Magnetic multipolar contact fields: The anapole and related moments," American Journal of Physics **78**, 936–948 (2010) `10.1119/1.3427412`.

[46] E. B. Graham, J. Pierrus, and R. E. Raab, "Multipole moments and Maxwell's equations," Journal of Physics B: Atomic, Molecular and Optical Physics **25**, 4673 (1992) `10.1088/0953-4075/25/21/030`.

[47] J. D. Jackson, *Classical Electrodynamics Third Edition*, 3rd edition (Wiley, New York, Aug. 14, 1998), 832 pp.

[48] J. H. Smith, E. M. Purcell, and N. F. Ramsey, "Experimental Limit to the Electric Dipole Moment of the Neutron," Phys. Rev. **108**, 120 (1957) `10.1103/PhysRev.108.120`.

[49] M. W. Ahmed, R. Alarcon, A. Aleksandrova, S. Baeßler, L. Barron-Palos, L. M. Bartoszek, D. H. Beck, M. Behzadipour, I. Berkutov, J. Bessuille, M. Blatnik, M. Broering, L. J. Broussard, M. Busch, R. Carr, V. Cianciolo, S. M. Clayton, M. D. Cooper, C. Crawford, S. A. Currie, C. Daurer, R. Dipert, K. Dow, D. Dutta, Y. Efremenko, C. B. Erickson, B. W. Filippone, N. Fomin, H. Gao, R. Golub, C. R. Gould, G. Greene, D. G. Haase, D. Hasell, A. I. Hawari, M. E. Hayden, A. Holley, R. J. Holt, P. R. Huffman, E. Ihloff, S. K. Imam, T. M. Ito, M. Karcz, J. Kelsey, D. P. Kendellen, Y. J. Kim, E. Korobkina, W. Korsch, S. K. Lamoreaux, E. Leggett, K. K. H. Leung, A. Lipman, C. Y. Liu, J. Long, S. W. T. MacDonald, M. Makela, A. Matlashov, J. D. Maxwell, M. Mendenhall, H. O. Meyer, R. G. Milner, P. E. Mueller, N. Nouri, C. M. O'Shaughnessy, C. Osthelder, J. C. Peng, S. I. Penttila, N. S. Phan, B. Plaster, J. C. Ramsey, T. M. Rao, R. P. Redwine, A. Reid, A. Saftah, G. M. Seidel, I. Silvera, S. Slutsky, E. Smith, W. M. Snow, W. Sondheim, S. Sosothikul, T. D. S. Stanislaus, X. Sun, C. M. Swank, Z. Tang, R. T. Dinani, E. Tsentalovich, C. Vidal, W. Wei, C. R. White, S. E. Williamson, L. Yang, W. Yao, and A. R. Young, "A new cryogenic apparatus to search for the neutron electric dipole moment," Journal of Instrumentation **14**, P11017 (2019) `10.1088/1748-0221/14/11/P11017`.

[50] J. E. Kim and G. Carosi, "Axions and the strong CP problem," Reviews of Modern Physics **82**, 557–601 (2010) `10.1103/RevModPhys.82.557`.

[51] J. S. M. Ginges and V. V. Flambaum, "Violations of fundamental symmetries in atoms and tests of unification theories of elementary particles," Physics Reports **397**, 63–154 (2004) `10.1016/j.physrep.2004.03.005`.

[52] M. G. Kozlov and L. N. Labzowsky, "Parity violation effects in diatomics," Journal of Physics B: Atomic, Molecular and Optical Physics **28**, 1933–1961 (1995) `2011042219375100`.

[53] L. I. Schiff, "Measurability of Nuclear Electric Dipole Moments," Physical Review **132**, 2194 (1963) `10/cx6nrx`.

[54] S. Porsev, J. Ginges, and V. Flambaum, "Atomic electric dipole moment induced by the nuclear electric dipole moment: The magnetic moment effect," Physical Review A **83**, 1–7 (2011) `10.1103/PhysRevA.83.042507`.

[55] V. Flambaum and J. Ginges, "Nuclear Schiff moment and time-invariance violation in atoms," Physical Review A **65**, 1–9 (2002) `10.1103/PhysRevA.65.032113`.

[56] C.-P. Liu, M. J. Ramsey-Musolf, W. C. Haxton, R. G. E. Timmermans, and A. E. L. Dieperink, "Atomic electric dipole moments: The Schiff theorem and its corrections," Physical Review C **76**, 035503 (2007) `10.1103/PhysRevC.76.035503`.

[57] V. V. Flambaum, D. DeMille, and M. G. Kozlov, "Time-reversal symmetry violation in molecules induced by nuclear magnetic quadrupole moments," Physical Review Letters **113**, 103003 (2014) `10.1103/PhysRevLett.113.103003`.

[58] P. Sushkov, V. V. V. Flambaum, I. B. B. Khriplovich, O. P. P. Sushkov, V. V. V. Flambaum, and I. B. B. Khriplovich, "Possibility of investigating P- and T-odd nuclear forces in atomic and molecular experiments," Journal of Experimental and Theoretical Physics **60**, 873 (1984) `10.1007/s10824-013-9205-y`.

[59]V. V. Flambaum, D. W. Murray, and S. R. Orton, "Time invariance violating nuclear electric octupole moments," Physical Review C **56**, 2820–2829 (1997) `10.1103/PhysRevC.56.2820`.

[60]P. G. H. Sandars, "The electric dipole moment of an atom," Physics Letters **14**, 194–196 (1965) `10.1016/0031-9163(65)90583-4`.

[61]E. D. Commins, J. D. Jackson, and D. P. DeMille, "The electric dipole moment of the electron: An intuitive explanation for the evasion of Schiff's theorem," American Journal of Physics **75**, 532–536 (2007) `10.1119/1.2710486`.

[62]I. B. Khriplovich, "Fundamental Symmetries and Atomic Physics," Physica Scripta **T112**, 52 (2004) `10.1238/Physica.Topical.112a00052`.

[63]E. D. Commins, J. D. Jackson, and D. P. DeMille, "The electric dipole moment of the electron: An intuitive explanation for the evasion of Schiff's theorem," American Journal of Physics **75**, 532 (2007) `10.1119/1.2710486`.

[64]V. V. Flambaum, D. W. Murray, and S. R. Orton, "Time invariance violating nuclear electric octupole moments," Physical Review C **56**, 2820–2829 (1997) `10.1103/PhysRevC.56.2820`.

[65]B. Graner, Y. Chen, E. G. Lindahl, and B. R. Heckel, "Reduced Limit on the Permanent Electric Dipole Moment of Hg 199," Physical Review Letters **116**, 161601 (2016) `10.1103/PhysRevLett.116.161601`.

[66]O. P. Sushkov and V. V. Flambaum, "Parity breaking effects in diatomic molecules," Journal of Experimental and Theoretical Physics **48**, 608–611 (1978).

[67]Z. Lasner, "Order-of-magnitude-tighter bound on the electron electric dipole moment," PhD thesis (Harvard Uni, 2019), 375 pp.

[68]P. G. H. Sandars, "Measurability of the Proton Electric Dipole Moment," Physical Review Letters **19**, 1396–1398 (1967) `10.1103/PhysRevLett.19.1396`.

[69]M. Verma, A. M. Jayich, and A. C. Vutha, "Electron Electric Dipole Moment Searches Using Clock Transitions in Ultracold Molecules," Physical Review Letters **125**, 153201 (2020) `10.1103/PhysRevLett.125.153201`.

[70]C. J. Ho, J. Lim, B. E. Sauer, and M. R. Tarbutt, "Measuring the nuclear magnetic quadrupole moment in heavy polar molecules," Frontiers in Physics **11**, 1086980 (2023) `10.3389/fphy.2023.1086980`.

[71]W. C. Haxton and E. M. Henley, "Enhanced T -Nonconserving Nuclear Moments," Physical Review Letters **51**, 1937–1940 (1983) `10.1103/PhysRevLett.51.1937`.

[72]V. V. Flambaum, "Spin hedgehog and collective magnetic quadrupole moments induced by parity and time invariance violating interaction," Physics Letters B **320**, 211–215 (1994) `10.1016/0370-2693(94)90646-7`.

[73]V. Spevak and N. Auerbach, "Parity mixing and time reversal violation in nuclei with octupole deformations," Physics Letters B **359**, 254–260 (1995) `10.1016/0370-2693(95)01099-C`.

[74]N. Auerbach, V. V. Flambaum, and V. Spevak, "Collective T - and P -Odd Electromagnetic Moments in Nuclei with Octupole Deformations," Physical Review Letters **76**, 4316–4319 (1996) `10.1103/PhysRevLett.76.4316`.

[75] V. Spevak, N. Auerbach, and V. V. Flambaum, "Enhanced T-odd, P-odd electromagnetic moments in reflection asymmetric nuclei," Physical Review C - Nuclear Physics **56**, 1357–1369 (1997) `10.1103/PhysRevC.56.1357`.

[76] V. V. Flambaum, "Enhancement of parity and time invariance violation in the radium atom," Physical Review A **60**, R2611–R2613 (1999) `10.1103/PhysRevA.60.R2611`.

[77] J. Engel, J. L. Friar, and A. C. Hayes, "Nuclear octupole correlations and the enhancement of atomic time-reversal violation," Physical Review C **61**, 035502 (2000) `10.1103/PhysRevC.61.035502`.

[78] J. Dobaczewski and J. Engel, "Nuclear Time-Reversal Violation and the Schiff Moment of 225Ra," Physical Review Letters **94**, 232502 (2005) `10.1103/PhysRevLett.94.232502`.

[79] N. Auerbach, "Search for electric dipole moments in atoms of radioactive nuclei," Journal of Physics G: Nuclear and Particle Physics **35**, 014040 (2008) `10.1088/0954-3899/35/1/014040`.

[80] B. G. C. Lackenby and V. V. Flambaum, "Time reversal violating Magnetic Quadrupole Moment in heavy deformed nuclei," Physical Review D **98**, 115019 (2018) `10.1103/PhysRevD.98.115019`.

[81] J. Dobaczewski, J. Engel, M. Kortelainen, and P. Becker, "Correlating Schiff Moments in the Light Actinides with Octupole Moments," Physical Review Letters **121**, 232501 (2018) `10.1103/PhysRevLett.121.232501`.

[82] V. V. Flambaum and H. Feldmeier, "Enhanced nuclear Schiff moment in stable and metastable nuclei," 2019.

[83] V. V. Flambaum and A. J. Mansour, "Enhanced magnetic quadrupole moments in nuclei with octupole deformation and their CP-violating effects in molecules," Physical Review C **105**, 065503 (2022) `10.1103/PhysRevC.105.065503`.

[84] F. Dalton, V. V. Flambaum, and A. J. Mansour, "Enhanced Schiff and magnetic quadrupole moments in deformed nuclei and their connection to the search for axion dark matter," Physical Review C **107**, 035502 (2023) `10.1103/PhysRevC.107.035502`.

[85] P. A. Butler and W. Nazarewicz, "Intrinsic reflection asymmetry in atomic nuclei," Reviews of Modern Physics **68**, 349–421 (1996) `10.1103/RevModPhys.68.349`.

[86] R. F. Casten, *Nuclear Structure from a Simple Perspective*, 2nd edition (Oxford University Press, Oxford ; New York, June 21, 2001), 480 pp.

[87] P. A. Butler, "Octupole collectivity in nuclei," Journal of Physics G: Nuclear and Particle Physics **43**, 073002 (2016) `10.1088/0954-3899/43/7/073002`.

[88] P. A. Butler, "Pear-shaped atomic nuclei," Proceedings of the Royal Society A: Mathematical, Physical and Engineering Sciences **476**, 20200202 (2020) `10.1098/rspa.2020.0202`.

[89] M. Chen, T. Li, J. Dobaczewski, and W. Nazarewicz, "Microscopic origin of reflection-asymmetric nuclear shapes," Physical Review C **103**, 034303 (2021) `10.1103/PhysRevC.103.034303`.

[90] M. M. R. Chishti, D. O'Donnell, G. Battaglia, M. Bowry, D. A. Jaroszynski, B. S. N. Singh, M. Scheck, P. Spagnoletti, and J. F. Smith, "Direct measurement of the intrinsic electric dipole moment in pear-shaped thorium-228," Nature Physics **16**, 853–856 (2020) 10.1038/s41567-020-0899-4.

[91] P. A. Butler, L. P. Gaffney, P. Spagnoletti, K. Abrahams, M. Bowry, J. Cederkäll, G. de Angelis, H. De Witte, P. E. Garrett, A. Goldkuhle, C. Henrich, A. Illana, K. Johnston, D. T. Joss, J. M. Keatings, N. A. Kelly, M. Komorowska, J. Konki, T. Kröll, M. Lozano, B. S. Nara Singh, D. O'Donnell, J. Ojala, R. D. Page, L. G. Pedersen, C. Raison, P. Reiter, J. A. Rodriguez, D. Rosiak, S. Rothe, M. Scheck, M. Seidlitz, T. M. Shneidman, B. Siebeck, J. Sinclair, J. F. Smith, M. Stryjczyk, P. Van Duppen, S. Vinals, V. Virtanen, N. Warr, K. Wrzosek-Lipska, and M. Zielińska, "Evolution of Octupole Deformation in Radium Nuclei from Coulomb Excitation of Radioactive 222Ra and 228Ra Beams," Physical Review Letters **124**, 042503 (2020) 10.1103/PhysRevLett.124.042503.

[92] R. K. Sheline, "223Ra - Parity doublets and the case for reflection asymmetry," Physics Letters B **166**, 269–273 (1986) 10.1016/0370-2693(86)90796-3.

[93] R. G. Helmer, M. A. Lee, C. W. Reich, and I. Ahmad, "Intrinsic reflection asymmetry in 225Ra: Additional information from a study of the α-decay scheme of 229Th," Nuclear Physics A **474**, 77–113 (1987) 10.1016/0375-9474(87)90195-3.

[94] P. Yu and N. R. Hutzler, "Probing Fundamental Symmetries of Deformed Nuclei in Symmetric Top Molecules," Physical Review Letters **126**, 023003 (2021) 10.1103/PhysRevLett.126.023003.

[95] J. Engel, M. J. Ramsey-Musolf, and U. van Kolck, "Electric dipole moments of nucleons, nuclei, and atoms: The Standard Model and beyond," Progress in Particle and Nuclear Physics, Fundamental Symmetries in the Era of the LHC **71**, 21–74 (2013) 10.1016/j.ppnp.2013.03.003.

[96] T. Chupp and M. Ramsey-Musolf, "Electric dipole moments: A global analysis," Physical Review C **91**, 035502 (2015) 10.1103/PhysRevC.91.035502.

[97] I. Brivio and M. Trott, "The standard model as an effective field theory," Physics Reports, The Standard Model as an Effective Field Theory **793**, 1–98 (2019) 10.1016/j.physrep.2018.11.002.

[98] C. Cesarotti, Q. Lu, Y. Nakai, A. Parikh, and M. Reece, "Interpreting the Electron EDM Constraint," Journal of High Energy Physics **2019**, 59 (2019) 10.1007/JHEP05(2019)059.

[99] Y. Ema, T. Gao, and M. Pospelov, "Standard Model Prediction for Paramagnetic Electric Dipole Moments," Physical Review Letters **129**, 231801 (2022) 10.1103/PhysRevLett.129.231801.

[100] J. Baron, W. C. Campbell, D. DeMille, J. M. Doyle, G. Gabrielse, Y. V. Gurevich, P. W. Hess, N. R. Hutzler, E. Kirilov, I. Kozyrev, B. R. O'Leary, C. D. Panda, M. F. Parsons, E. S. Petrik, B. Spaun, A. C. Vutha, and A. D. West, "Order of Magnitude Smaller Limit on the Electric Dipole Moment of the Electron," Science **343**, 269–272 (2014) 10.1126/science.1248213.

[101] W. B. Cairncross, D. N. Gresh, M. Grau, K. C. Cossel, T. S. Roussy, Y. Ni, Y. Zhou, J. Ye, and E. A. Cornell, "A precision measurement of the electron's electric dipole moment using trapped molecular ions," Physical Review Letters **0**, 153001 (2017) `10.1103/PhysRevLett.119.153001`.

[102] Y. Zhou, Y. Shagam, W. B. Cairncross, K. B. Ng, T. S. Roussy, T. Grogan, K. Boyce, A. Vigil, M. Pettine, T. Zelevinsky, J. Ye, and E. A. Cornell, "Second-Scale Coherence Measured at the Quantum Projection Noise Limit with Hundreds of Molecular Ions," Physical Review Letters **124**, 053201 (2020) `10.1103/PhysRevLett.124.053201`.

[103] E. S. Shuman, J. F. Barry, and D. Demille, "Laser cooling of a diatomic molecule.," Nature **467**, 820–823 (2010) `10.1038/nature09443`.

[104] J. F. Barry, D. J. McCarron, E. B. Norrgard, M. H. Steinecker, and D. Demille, "Magneto-optical trapping of a diatomic molecule," Nature **512**, 286–289 (2014) `10.1038/nature13634`.

[105] I. Kozyryev, L. Baum, K. Matsuda, B. L. Augenbraun, L. Anderegg, A. P. Sedlack, and J. M. Doyle, "Sisyphus Laser Cooling of a Polyatomic Molecule," Physical Review Letters **118**, `10.1103/PhysRevLett.118.173201` (2017) `10.1103/PhysRevLett.118.173201`.

[106] B. L. Augenbraun, Z. D. Lasner, A. Frenett, H. Sawaoka, C. Miller, T. C. Steimle, and J. M. Doyle, "Laser-cooled polyatomic molecules for improved electron electric dipole moment searches," New Journal of Physics **22**, 022003 (2020) `10.1088/1367-2630/ab687b`.

[107] D. Mitra, N. B. Vilas, C. Hallas, L. Anderegg, B. L. Augenbraun, L. Baum, C. Miller, S. Raval, and J. M. Doyle, "Direct laser cooling of a symmetric top molecule," Science **369**, 1366–1369 (2020) `10.1126/science.abc5357`.

[108] N. B. Vilas, C. Hallas, L. Anderegg, P. Robichaud, A. Winnicki, D. Mitra, and J. M. Doyle, "Magneto-optical trapping and sub-Doppler cooling of a polyatomic molecule," Nature **606**, 70–74 (2022) `10.1038/s41586-022-04620-5`.

[109] C. Hallas, N. B. Vilas, L. Anderegg, P. Robichaud, A. Winnicki, C. Zhang, L. Cheng, and J. M. Doyle, "Optical Trapping of a Polyatomic Molecule in an $\ensuremath{\ell}$-Type Parity Doublet State," Physical Review Letters **130**, 153202 (2023) `10.1103/PhysRevLett.130.153202`.

[110] M. Zeppenfeld, B. G. U. Englert, R. Glöckner, A. Prehn, M. Mielenz, C. Sommer, L. D. van Buuren, M. Motsch, and G. Rempe, "Sisyphus cooling of electrically trapped polyatomic molecules," Nature **491**, 570–573 (2012) `10.1038/nature11595`.

[111] A. Prehn, M. Ibrügger, R. Glöckner, G. Rempe, and M. Zeppenfeld, "Optoelectrical Cooling of Polar Molecules to Submillikelvin Temperatures," Physical Review Letters **116**, 063005 (2016) `10.1103/PhysRevLett.116.063005`.

[112] I. Kozyryev, L. Baum, K. Matsuda, and J. M. Doyle, "Proposal for Laser Cooling of Complex Polyatomic Molecules," ChemPhysChem **17**, 3641–3648 (2016) `10.1002/cphc.201601051`.

[113] T. A. Isaev and R. Berger, "Polyatomic Candidates for Cooling of Molecules with Lasers from Simple Theoretical Concepts," Physical Review Letters **116**, 63006 (2016) `10.1103/PhysRevLett.116.063006`.

[114]P. Yu, A. Lopez, W. A. Goddard, and N. R. Hutzler, "Multivalent optical cycling centers: towards control of polyatomics with multi-electron degrees of freedom," Physical Chemistry Chemical Physics **25**, 154–170 (2023) `10.1039/D2CP03545F`.

[115]M. R. Tarbutt, "Laser cooling of molecules," Contemporary Physics **59**, 356–376 (2018) `10.1080/00107514.2018.1576338`.

[116]K.-i. C. Namiki, J. S. Robinson, and T. C. Steimle, "A spectroscopic study of CaOCH3 using the pump/probe microwave and the molecular beam/optical Stark techniques," The Journal of Chemical Physics **109**, 5283–5289 (1998) `10.1063/1.477146`.

[117]A. Petrov and A. Zakharova, "Sensitivity of the YbOH molecule to PT-odd effects in an external electric field," Physical Review A **105**, L050801 (2022) `10.1103/PhysRevA.105.L050801`.

[118]W. Itano, J. Bergquist, J. Bollinger, J. Gilligan, D. Heinzen, F. Moore, M. Raizen, and D. Wineland, "Quantum projection noise: Population fluctuations in two-level systems," Physical Review A **47**, 3554–3570 (1993) `10.1103/PhysRevA.47.3554`.

[119]A. C. Vutha, "A search for the electric dipole moment of the electron using thorium monoxide,"

[120]T. K. Langin and D. DeMille, "Toward improved loading, cooling, and trapping of molecules in magneto-optical traps," New Journal of Physics **25**, 043005 (2023) `10.1088/1367-2630/acc34d`.

[121]J. J. Burau, P. Aggarwal, K. Mehling, and J. Ye, *Blue-Detuned Magneto-Optical Trap of Molecules*, (Dec. 14, 2022) `10.48550/arXiv.2212.07472`, `http://arxiv.org/abs/2212.07472`, preprint.

[122]Y. Lu, C. M. Holland, and L. W. Cheuk, "Molecular Laser Cooling in a Dynamically Tunable Repulsive Optical Trap," Physical Review Letters **128**, 213201 (2022) `10.1103/PhysRevLett.128.213201`.

[123]B. L. Augenbraun, J. M. Doyle, T. Zelevinsky, and I. Kozyrev, "Molecular Asymmetry and Optical Cycling: Laser Cooling Asymmetric Top Molecules," Physical Review X **10**, 031022 (2020) `10.1103/PhysRevX.10.031022`.

[124]Y. Takahashi, C. Zhang, A. Jadbabaie, and N. R. Hutzler, *Engineering field-insensitive molecular clock transitions for symmetry violation searches*, (Apr. 26, 2023) `10.48550/arXiv.2304.13817`, `http://arxiv.org/abs/2304.13817`, preprint.

[125]T. Manovitz, R. Shaniv, Y. Shapira, R. Ozeri, and N. Akerman, "Precision Measurement of Atomic Isotope Shifts Using a Two-Isotope Entangled State," Physical Review Letters **123**, 203001 (2019) `10.1103/PhysRevLett.123.203001`.

[126]M. Chwalla, K. Kim, T. Monz, P. Schindler, M. Riebe, C. Roos, and R. Blatt, "Precision spectroscopy with two correlated atoms," Applied Physics B **89**, 483–488 (2007) `10.1007/s00340-007-2867-4`.

[127]D. J. Wineland, J. J. Bollinger, W. M. Itano, F. L. Moore, and D. J. Heinzen, "Spin squeezing and reduced quantum noise in spectroscopy," Physical Review A **46**, R6797–R6800 (1992) `10.1103/PhysRevA.46.R6797`.

[128]C. F. Roos, M. Chwalla, K. Kim, M. Riebe, and R. Blatt, "'Designer atoms' for quantum metrology," Nature **443**, 316–319 (2006) `10.1038/nature05101`.

[129]E. Hirota, *High-Resolution Spectroscopy of Transient Molecules* (Springer Berlin Heidelberg, Berlin, Heidelberg, 1985), `10.1007/978-3-642-82477-7`.

[130]R. N. Zare, *Angular Momentum: Understanding Spatial Aspects in Chemistry and Physics*, 1st edition (Wiley-Interscience, New York, Jan. 8, 1991), 368 pp.

[131]D. Budker, D. Kimball, and D. DeMille, *Atomic physics: An exploration through problems and solutions* (Oxford University Press, USA, 2008).

[132]N. R. Hutzler, "A New Limit on the Electron Electric Dipole Moment: Beam Production, Data Interpretation, and Systematics" (2014), 1-322.

[133]K. Gottfried and T.-M. Yan, *Quantum Mechanics: Fundamentals*, red. by R. S. Berry, J. L. Birman, M. P. Silverman, H. E. Stanley, and M. Voloshin, Graduate Texts in Contemporary Physics (Springer New York, New York, NY, 2003), `10.1007/978-0-387-21623-2`.

[134]L. Pauling, *The Nature of the Chemical Bond and the Structure of Molecules and Crystals: An Introduction to Mode*, Third edition (Cornell University Press, Ithaca, NY, Feb. 15, 1960), 644 pp.

[135]W. Demtröder, *Molecular Physics: Theoretical Principles and Experimental Methods* (John Wiley & Sons, Sept. 26, 2008), 487 pp.

[136]A. R. Allouche and M. Aubertfrecon, "A Ligand Field Approach for the Low-Lying States of Ca, Sr, and Ba Monohydroxides," Journal of Molecular Spectroscopy **163**, 599–603 (1994) `10.1006/jmsp.1994.1049`.

[137]A. L. Kaledin, M. C. Heaven, R. W. Field, and L. A. Kaledin, "The Electronic Structure of the Lanthanide Monohalides: A Ligand Field Approach," Journal of Molecular Spectroscopy **179**, 310–319 (1996) `10.1006/jmsp.1996.0209`.

[138]P. Carette and A. Hocquet, "Ligand field calculation of the lower electronic energy levels of the lanthanide monoxides," Journal of Molecular Spectroscopy **131**, 301–324 (1988) `10.1016/0022-2852(88)90241-X`.

[139]B. L. Augenbraun, "Methods for Direct Laser Cooling of Polyatomic Molecules," PhD thesis (Harvard, 2021).

[140]P. R. Bunker and P. Jensen, *Molecular Symmetry and Spectroscopy* (NRC Research Press, 2006), 778 pp.

[141]T. J. Sears, "The calculation of the energy levels of an asymmetric top free radical in a magnetic field," Computer Physics Reports **2**, 1–32 (1984) `10.1016/0167-7977(84)90005-4`.

[142]J. F. Barry, D. J. McCarron, E. B. Norrgard, M. H. Steinecker, and D. DeMille, "Magneto-optical trapping of a diatomic molecule," Nature **512**, 286–289 (2014) `10.1038/nature13634`.

[143]L. Baum, N. B. Vilas, C. Hallas, B. L. Augenbraun, S. Raval, D. Mitra, and J. M. Doyle, "Establishing a nearly closed cycling transition in a polyatomic molecule," Physical Review A **103**, 043111 (2021) `10.1103/PhysRevA.103.043111`.

[144] C. Zhang, B. L. Augenbraun, Z. D. Lasner, N. B. Vilas, J. M. Doyle, and L. Cheng, "Accurate prediction and measurement of vibronic branching ratios for laser cooling linear polyatomic molecules," The Journal of Chemical Physics **155**, 091101 (2021) `10.1063/5.0063611`.

[145] I. Kozyryev, "Laser Cooling and Inelastic Collisions of the Polyatomic Radical SrOH" (Harvard University, 2017).

[146] I. Kozyryev, Z. Lasner, and J. M. Doyle, "Enhanced sensitivity to ultralight bosonic dark matter in the spectra of the linear radical SrOH," Physical Review A **103**, 043313 (2021) `10.1103/PhysRevA.103.043313`.

[147] M. Li and J. A. Coxon, "High-resolution analysis of the fundamental bending vibrations in the $\tilde{A}$ 2Π and $\tilde{X}$ 2Σ+states of CaOH and CaOD: Deperturbation of Renner-Teller, spin-orbit and K-type resonance interactions," The Journal of Chemical Physics **102**, 2663–2674 (1995) `10.1063/1.468643`.

[148] C. di Lauro and I. Mills, "Coriolis interactions about X-Y axes in symmetric tops," Journal of Molecular Spectroscopy **21**, 386–413 (1966) `10.1016/0022-2852(66)90164-0`.

[149] K. Yamada, "Effect of Phase Choices in Rovibrational Wavefunctions on the Labeling of K-and l-Type Doubling in Molecular Energy Levels," Zeitschrift für Naturforschung A **38**, 821–834 (1983) `10.1515/zna-1983-0802`.

[150] W. Quapp and B. P. Winnewisser, "What you thought you already knew about the bending motion of triatomic molecules," Journal of Mathematical Chemistry **14**, 259–285 (1993) `10.1007/BF01164471`.

[151] J. M. Brown, "The Renner-Teller effect: The effective Hamiltonian Approach," in *Computational Molecular Spectroscopy* (John Wiley & Sons, Ltd, 2000), pp. 517–537.

[152] C. Di Lauro, F. Lattanzi, and G. Graner, "The effect of phase conventions on vibration-rotation matrix elements," Journal of Molecular Spectroscopy **143**, 111–136 (1990) `10.1016/0022-2852(90)90265-R`.

[153] C. di Lauro, F. Lattanzi, and G. Graner, "Phase conventions that render all matrix elements of the vibration-rotation Hamiltonian real," Molecular Physics **71**, 1285–1302 (1990) `10.1080/00268979000102491`.

[154] H. H. Nielsen, "The Vibration-Rotation Energies of Molecules," Reviews of Modern Physics **23**, 90–136 (1951) `10.1103/RevModPhys.23.90`.

[155] P. Bernath, *Spectra of Atoms and Molecules* (Oxford University Press, 2005).

[156] J. Brown, "The effective Hamiltonian for the Renner-Teller effect," Journal of Molecular Spectroscopy **68**, 412–422 (1977) `10.1016/0022-2852(77)90245-4`.

[157] N. H. Pilgram, A. Jadbabaie, Y. Zeng, N. R. Hutzler, and T. C. Steimle, "Fine and hyperfine interactions in ^{171} YbOH and ^{173} YbOH," The Journal of Chemical Physics **154**, 244309 (2021) `10.1063/5.0055293`.

[158] J. Brown and H. Uehara, "On the effective Zeeman Hamiltonian for a linear molecule in an orbitally degenerate state," Molecular Physics **24**, 1169–1174 (1972) `10.1080/00268977200102241`.

[159] J. M. Brown, "The rotational dependence of the Renner-Teller interaction: A new term in the effective Hamiltonian for linear triatomic molecules in Π electronic states," Molecular Physics **101**, 3419–3426 (2003) `10.1080/00268970310001645864`.

[160] J. Brown and B. Howard, "An approach to the anomalous commutation relations of rotational angular momenta in molecules," Molecular Physics **31**, 1517–1525 (1976) `10.1080/00268977600101191`.

[161] N. H. Pilgram, "Production and Characterization of Ytterbium Monohydroxide (YbOH) for Next-Generation Parity and Time-Reversal Violating Physics Searches," PhD thesis (California Institute of Technology, 2023), `10.7907/05m0-4g74`.

[162] A. Merer and J. Allegretti, "Rotational Energies of Linear Polyatomic Molecules in Vibrationally Degenerate Levels of Electronic States," Canadian Journal of Physics **49** (1971).

[163] C.-F. Chang and Y.-N. Chiu, "Magnetic Renner Effect: Direct Orbital and Spin Interaction with "Vibrational" Rotation in Linear Triatomic Molecules," The Journal of Chemical Physics **53**, 2186–2195 (1970) `10.1063/1.1674312`.

[164] W. Weltner, *Magnetic Atoms and Molecules* (Dover Publications, New York, Nov. 1, 1989), 436 pp.

[165] J. M. Brown and A. J. Merer, "Lambda-type doubling parameters for molecules in Π electronic states of triplet and higher multiplicity," Journal of Molecular Spectroscopy **74**, 488–494 (1979) `10.1016/0022-2852(79)90172-3`.

[166] J. M. Brown, A.-C. Cheung, and A. J. Merer, "Λ-Type doubling parameters for molecules in Δ electronic states," Journal of Molecular Spectroscopy **124**, 464–475 (1987) `10.1016/0022-2852(87)90157-3`.

[167] J. M. Brown, "K-Type Doubling Parameters for Linear Molecules in Π Electronic States," Journal of Molecular Spectroscopy **56**, 159–162 (1975) `10.1016/0022-2852(75)90212-X`.

[168] M. D. Allen, K. M. Evenson, D. A. Gillett, and J. M. Brown, "Far-Infrared Laser Magnetic Resonance Spectroscopic Study of the v2 Bending Fundamental of the CCN Radical in Its $\tilde{X}^2\Pi_r$ State," Journal of Molecular Spectroscopy **201**, 18–29 (2000) `10.1006/jmsp.2000.8075`.

[169] S. A. Beaton and J. M. Brown, "Laser Excitation Spectroscopy of the Ã3Π–X3Σ Transition of the NCN Radical 2. The v2 hot band," Journal of Molecular Spectroscopy **183**, 347–359 (1997) `10.1006/jmsp.1997.7286`.

[170] R. Renner, "Zur Theorie der Wechselwirkung zwischen Elektronen- und Kernbewegung bei dreiatomigen, stabförmigen Molekülen," Zeitschrift für Physik **92**, 172–193 (1934) `10.1007/BF01350054`.

[171] A. Carrington, A. Fabris, B. Howard, and N. Lucas, "Electron resonance studies of the renner effect: I. Gaseous NCO in its $^2\Pi_{3/2}$ (n=1), $^2\Delta_{5/2}$ (n=2) and $^2\Phi_{7/2}$ (n=3) vibronic states," Molecular Physics **20**, 961–980 (1971) `10.1080/00268977100100971`.

[172] D. Gauyacq and Ch. Jungen, "Orbital angular momentum in triatomic molecules: V. Vibronic corrections and anharmonic effects in linear molecules," Molecular Physics **41**, 383–407 (1980) `10.1080/00268978000102841`.

[173]J. M. Brown and F. Jørgensen, "Vibronic Energy Levels of a Linear Triatomic Molecule in a Degenerate Electronic State: a Unified Treatment of the Renner-Teller Effect," in *Advances in Chemical Physics*, edited by I. Prigogine and S. A. Rice (John Wiley & Sons, Inc., Hoboken, NJ, USA, 1982), pp. 117–180, `10.1002/9780470142769.ch2`.

[174]J. M. Hayes and G. J. Small, "Supersonic Jets, Rotational Cooling, and Analytical Chemistry," Analytical Chemistry **55**, 565A–574A (1983) `10.1021/ac00255a784`.

[175]M. D. Morse, "Supersonic Beam Sources," in *Experimental Methods in the Physical Sciences, vol. 29B: Atomic, Molecular, and Optical Physics*, Vol. 29B, edited by F. B. Dunning and R. G. Hulet (Academic Press, 1996), pp. 21–47, `10.1016/S0076-695X(08)60784-X`.

[176]D. H. Levy, L. Wharton, and R. E. Smalley, "Laser Spectroscopy in Supersonic Jets," in *Chemical and Biochemical Applications of Lasers*, edited by C. B. Moore (Academic Press, 1977), pp. 1–41.

[177]R. F. Garcia Ruiz, R. Berger, J. Billowes, C. L. Binnersley, M. L. Bissell, A. A. Breier, A. J. Brinson, K. Chrysalidis, T. E. Cocolios, B. S. Cooper, K. T. Flanagan, T. F. Giesen, R. P. de Groote, S. Franchoo, F. P. Gustafsson, T. A. Isaev, Á. Koszorús, G. Neyens, H. A. Perrett, C. M. Ricketts, S. Rothe, L. Schweikhard, A. R. Vernon, K. D. A. Wendt, F. Wienholtz, S. G. Wilkins, and X. F. Yang, "Spectroscopy of short-lived radioactive molecules," Nature **581**, 396–400 (2020) `10.1038/s41586-020-2299-4`.

[178]N. R. Hutzler, H. I. Lu, and J. M. Doyle, "The buffer gas beam: An intense, cold, and slow source for atoms and molecules," Chemical Reviews, `10.1021/cr200362u` (2012) `10.1021/cr200362u`.

[179]N. R. Hutzler, M. F. Parsons, Y. V. Gurevich, P. W. Hess, E. Petrik, B. Spaun, A. C. Vutha, D. DeMille, G. Gabrielse, and J. M. Doyle, "A cryogenic beam of refractory, chemically reactive molecules with expansion cooling.," Physical chemistry chemical physics : PCCP **13**, 18976–18985 (2011) `10.1039/c1cp20901a`.

[180]S. Truppe, H. J. Williams, N. J. Fitch, M. Hambach, T. E. Wall, E. A. Hinds, B. E. Sauer, and M. R. Tarbutt, "An intense, cold, velocity-controlled molecular beam by frequency-chirped laser slowing," New Journal of Physics **19**, 22001 (2017) `10.1088/1367-2630/aa5ca2`.

[181]S. Truppe, M. Hambach, S. M. Skoff, N. E. Bulleid, J. S. Bumby, R. J. Hendricks, E. A. Hinds, B. E. Sauer, and M. R. Tarbutt, "A buffer gas beam source for short, intense and slow molecular pulses," Journal of Modern Optics **65**, 246–254 (2018) `10.1080/09500340.2017.1384516`.

[182]L. Anderegg, B. L. Augenbraun, E. Chae, B. Hemmerling, N. R. Hutzler, A. Ravi, A. Collopy, J. Ye, W. Ketterle, and J. M. Doyle, "Radio Frequency Magneto-Optical Trapping of CaF with High Density," Physical Review Letters **119**, 103201 (2017) `10.1103/PhysRevLett.119.103201`.

[183]A. L. Collopy, S. Ding, Y. Wu, I. A. Finneran, L. ïc Anderegg, B. L. Augenbraun, J. M. Doyle, and J. Ye, "3D Magneto-Optical Trap of Yttrium Monoxide," Physical Review Letters **121**, 213201 (2018) `10.1103/PhysRevLett.121.213201`.

[184]S. C. Wright, M. Doppelbauer, S. Hofsäss, H. Christian Schewe, B. Sartakov, G. Meijer, and S. Truppe, "Cryogenic buffer gas beams of AlF, CaF, MgF, YbF, Al, Ca, Yb and NO – a comparison," Molecular Physics **0**, e2146541 (2022) `10.1080/00268976.2022.2146541`.

[185] B. L. Augenbraun, L. Anderegg, C. Hallas, Z. D. Lasner, N. B. Vilas, and J. M. Doyle, *Direct Laser Cooling of Polyatomic Molecules*, (Feb. 20, 2023) `10.48550/arXiv.2302.10161`, `http://arxiv.org/abs/2302.10161`, preprint.

[186] J. Piskorski, D. Patterson, S. Eibenberger, and J. M. Doyle, "Cooling, Spectroscopy and Non-Sticking of trans-Stilbene and Nile Red," ChemPhysChem **15**, 3800–3804 (2014) `10.1002/cphc.201402502`.

[187] Y. Takahashi, D. Shlivko, G. Woolls, and N. R. Hutzler, "Simulation of cryogenic buffer gas beams," Physical Review Research **3**, 023018 (2021) `10.1103/PhysRevResearch.3.023018`.

[188] T. Sizyuk and A. Hassanein, "Scaling mechanisms of vapour/plasma shielding from laser-produced plasmas to magnetic fusion regimes," Nuclear Fusion **54**, 023004 (2014) `10.1088/0029-5515/54/2/023004`.

[189] A. M. Elsied, P. C. Dieffenbach, P. K. Diwakar, and A. Hassanein, "Nanosecond laser-metal ablation at different ambient conditions," Spectrochimica Acta Part B: Atomic Spectroscopy **143**, 26–31 (2018) `10.1016/j.sab.2018.02.012`.

[190] S. M. Skoff, R. J. Hendricks, C. D. J. Sinclair, J. J. Hudson, D. M. Segal, B. E. Sauer, E. A. Hinds, and M. R. Tarbutt, "Diffusion, thermalization, and optical pumping of YbF molecules in a cold buffer-gas cell," Physical Review A **83**, 023418 (2011) `10.1103/PhysRevA.83.023418`.

[191] J. F. Barry, E. S. Shuman, and D. DeMille, "A bright, slow cryogenic molecular beam source for free radicals.," Physical chemistry chemical physics : PCCP **13**, 18936–18947 (2011) `10.1039/c1cp20335e`.

[192] I. Kozyryev, L. Baum, K. Matsuda, P. Olson, B. Hemmerling, and J. M. Doyle, "Collisional relaxation of vibrational states of SrOH with He at 2 K," New Journal of Physics **17**, 045003 (2015) `10.1088/1367-2630/17/4/045003`.

[193] L. Anderegg, "Ultracold Molecules in Optical Arrays: From Laser Cooling to Molecular Collisions," (2020).

[194] M. Sinvani, D. L. Goodstein, and M. W. Cole, "Scattering of low-energy helium atoms from a low-temperature solid surface," Physical Review B **29**, 3905–3907 (1984) `10.1103/PhysRevB.29.3905`.

[195] B. N. Chichkov, C. Momma, S. Nolte, F. von Alvensleben, A. Tünnermann, and A. Tunnermann, "Femtosecond, picosecond and nanosecond laser ablation of solids," Appl. Phys. A **63**, 109–115 (1996) `10.1007/s003390050359`.

[196] A. Bogaerts and Z. Chen, "Nanosecond laser ablation of Cu: modeling of the expansion in He background gas, and comparison with expansion in vacuumPresented at the 2004 Winter Conference on Plasma Spectrochemistry, Fort Lauderdale, Florida, January 5?10, 2004.," Journal of Analytical Atomic Spectrometry **19**, 1169 (2004) `10.1039/b402946a`.

[197] J. Koch, S. Schlamp, T. Rösgen, D. Fliegel, and D. Günther, "Visualization of aerosol particles generated by near infrared nano- and femtosecond laser ablation," Spectrochimica Acta - Part B Atomic Spectroscopy **62**, 20–29 (2007) `10.1016/j.sab.2006.11.006`.

[198] S. B. Wen, X. Mao, R. Greif, and R. E. Russo, "Laser ablation induced vapor plume expansion into a background gas. II. Experimental analysis," Journal of Applied Physics **101**, `10.1063/1.2431085` (2007) `10.1063/1.2431085`.

[199] R. Albrecht, M. Scharwaechter, T. Sixt, L. Hofer, and T. Langen, "Buffer-gas cooling, high-resolution spectroscopy, and optical cycling of barium monofluoride molecules," Physical Review A **101**, 013413 (2020) `10.1103/PhysRevA.101.013413`.

[200] L. Baum, "Laser cooling and 1D magneto-optical trapping of calcium monohydroxide," PhD thesis (Harvard, 2020).

[201] E. P. West, "A Thermochemical Cryogenic Buffer Gas Beam Source of ThO for Measuring the Electric Dipole Moment of the Electron" (ProQuest Dissertations Publishing, 2017).

[202] H. Guo, J. Guo, A. Baker, and C. A. Randall, "Hydrothermal-Assisted Cold Sintering Process: A New Guidance for Low-Temperature Ceramic Sintering," ACS Applied Materials & Interfaces **8**, 20909–20915 (2016) `10.1021/acsami.6b07481`.

[203] H. Guo, A. Baker, J. Guo, and C. A. Randall, "Cold Sintering Process: A Novel Technique for Low-Temperature Ceramic Processing of Ferroelectrics," Journal of the American Ceramic Society **99**, edited by D. Johnson, 3489–3507 (2016) `10.1111/jace.14554`.

[204] J.-P. Maria, X. Kang, R. D. Floyd, E. C. Dickey, H. Guo, J. Guo, A. Baker, S. Funihashi, and C. A. Randall, "Cold sintering: Current status and prospects," Journal of Materials Research **32**, 3205–3218 (2017) `10.1557/jmr.2017.262`.

[205] X. Kang, R. Floyd, S. Lowum, M. Cabral, E. Dickey, and J.-P. Maria, "Mechanism studies of hydrothermal cold sintering of zinc oxide at near room temperature," Journal of the American Ceramic Society **102**, 4459–4469 (2019) `10.1111/jace.16340`.

[206] A. Ndayishimiye, M. Y. Sengul, S. H. Bang, K. Tsuji, K. Takashima, T. Hérisson de Beauvoir, D. Denux, J.-M. Thibaud, A. C. van Duin, C. Elissalde, G. Goglio, and C. A. Randall, "Comparing hydrothermal sintering and cold sintering process: Mechanisms, microstructure, kinetics and chemistry," Journal of the European Ceramic Society **40**, 1312–1324 (2020) `10.1016/j.jeurceramsoc.2019.11.049`.

[207] S. Grasso, M. Biesuz, L. Zoli, G. Taveri, A. I. Duff, D. Ke, A. Jiang, and M. J. Reece, "A review of cold sintering processes," Advances in Applied Ceramics **119**, 115–143 (2020) `10.1080/17436753.2019.1706825`.

[208] A. Ndayishimiye, M. Y. Sengul, T. Sada, S. Dursun, S. H. Bang, Z. A. Grady, K. Tsuji, S. Funahashi, A. C. van Duin, and C. A. Randall, "Roadmap for densification in cold sintering: Chemical pathways," Open Ceramics **2**, 100019 (2020) `10.1016/j.oceram.2020.100019`.

[209] M. Kermani, M. Biesuz, J. Dong, H. Deng, M. Bortolotti, A. Chiappini, M. J. Reece, V. M. Sglavo, C. Hu, and S. Grasso, "Flash cold sintering: Combining water and electricity," Journal of the European Ceramic Society **40**, 6266–6271 (2020) `10.1016/j.jeurceramsoc.2020.06.051`.

[210] J. Dong, M. Kermani, C. Hu, and S. Grasso, "Flash cold sintering of Nb_2O_5: polarity and electrolyte effects," Journal of Asian Ceramic Societies **9**, 934–939 (2021) `10.1080/21870764.2021.1926704`.

[211]S. Lowum, R. Floyd, and J.-P. Maria, "Hydroflux-assisted densification: applying flux crystal growth techniques to cold sintering," Journal of Materials Science **55**, 12747–12760 (2020) `10.1007/s10853-020-04926-7`.

[212]T. Hérisson de Beauvoir and C. Estournès, "Translucent γ-AlOOH and γ-Al2O3 glass-ceramics using the cold sintering process," Scripta Materialia **194**, 113650 (2021) `10.1016/j.scriptamat.2020.113650`.

[213]D. A. Steck and D. Steck, *Quantum and Atom Optics* (2019).

[214]T. Wall, J. Kanem, J. Hudson, B. Sauer, D. Cho, M. Boshier, E. Hinds, and M. Tarbutt, "Lifetime of the A(v'=0) state and Franck-Condon factor of the A-X(0-0) transition of CaF measured by the saturation of laser-induced fluorescence," Physical Review A **78**, 62509 (2008) `10.1103/PhysRevA.78.062509`.

[215]M. Weissbluth, *Atoms and Molecules* (Academic Press, 1978), 742 pp.

[216]M. Auzinsh, D. Budker, and S. Rochester, *Optically polarized atoms: understanding light-atom interactions* (New York : Oxford University Press, Oxford, 2010), 376 pp.

[217]E. T. Mengesha, A. T. Le, T. C. Steimle, L. Cheng, C. Zhang, B. L. Augenbraun, Z. Lasner, and J. Doyle, "Branching Ratios, Radiative Lifetimes, and Transition Dipole Moments for YbOH," The Journal of Physical Chemistry A **124**, 3135–3148 (2020) `10.1021/acs.jpca.0c00850`.

[218]P. Hamilton, "Preliminary results in the search for the electron electric dipole moment in PbO$_*$" (Yale University, 2010).

[219]E. J. Salumbides, K. S. E. Eikema, W. Ubachs, U. Hollenstein, H. Knöckel, and E. Tiemann, "The hyperfine structure of 129 I 2 and 127 I 129 in the B band system," Molecular Physics **104**, 2641–2652 (2006) `10.1080/00268970600747696`.

[220]N. H. Pilgram, A. Jadbabaie, C. J. Conn, and N. R. Hutzler, *Direct measurement of high-lying vibrational repumping transitions for molecular laser cooling*, (Mar. 6, 2023) `http://arxiv.org/abs/2303.03233`, preprint.

[221]G. C. Bjorklund, "Frequency-modulation spectroscopy: a new method for measuring weak absorptions and dispersions," Optics Letters **5**, 15–17 (1980) `10.1364/OL.5.000015`.

[222]M. Gehrtz, E. A. Whittaker, and G. C. Bjorklund, "Quantum-limited laser frequency-modulation spectroscopy," Journal of the Optical Society of America B **2**, 1510 (1985) `10.1364/JOSAB.2.001510`.

[223]G. C. Bjorklund, M. D. Levenson, W. Lenth, and C. Ortiz, "Frequency modulation (FM) spectroscopy: Theory of Lineshapes and Signal-to-Noise Analysis," Applied Physics B **32**, 145–152 (1983) `10/cq5cqv`.

[224]G. E. Hall and S. W. North, "Transient Laser Frequency Modulation Spectroscopy," Annual Review of Physical Chemistry **51**, 243–274 (2000) `10.1146/annurev.physchem.51.1.243`.

[225]G. C. Bjorklund and E. A. Whittaker, "High Sensitivity Frequency Modulation Spectroscopy and the Path to Single Molecule Detection," The Journal of Physical Chemistry A **125**, 8519–8528 (2021) `10.1021/acs.jpca.1c05752`.

[226] N. J. Fitch and M. R. Tarbutt, "Chapter Three - Laser-cooled molecules," in *Advances In Atomic, Molecular, and Optical Physics*, Vol. 70, edited by L. F. Dimauro, H. Perrin, and S. F. Yelin (Academic Press, Jan. 1, 2021), pp. 157–262, `10.1016/bs.aamop.2021.04.003`.

[227] A. Jadbabaie, N. H. Pilgram, J. Kłos, S. Kotochigova, and N. R. Hutzler, "Enhanced molecular yield from a cryogenic buffer gas beam source via excited state chemistry," New Journal of Physics **22**, 022002 (2020) `10.1088/1367-2630/ab6eae`.

[228] C. J. Bowers, D. Budker, E. D. Commins, D. DeMille, S. J. Freedman, A.-T. Nguyen, S.-Q. Shang, and M. Zolotorev, "Experimental investigation of excited-state lifetimes in atomic ytterbium," Physical Review A **53**, 3103–3109 (1996) `10.1103/PhysRevA.53.3103`.

[229] J. C. Whitehead, *Selectivity in Chemical Reactions*, edited by J. C. Whitehead (Springer Netherlands, Dordrecht, 1988), `10.1007/978-94-009-3047-6`.

[230] A. G. UreÑa and R. Vetter, "Dynamics of reactive collisions by optical methods," International Reviews in Physical Chemistry **15**, 375–427 (1996) `10.1080/01442359609353189`.

[231] H. H. Telle, A. González Ureña, and R. J. Donovan, *Laser Chemistry: Spectroscopy, Dynamics and Applications* (John Wiley & Sons Ltd, Jan. 2007), 265-323, `10.5860/CHOICE.45-2619`.

[232] M. Agndez, J. R. Goicoechea, J. Cernicharo, A. Faure, and E. Roueff, "The chemistry of vibrationally excited H2 in the interstellar medium," Astrophysical Journal **713**, 662–670 (2010) `10.1088/0004-637X/713/1/662`.

[233] A. Zanchet, M. Agúndez, V. J. Herrero, A. Aguado, and O. Roncero, "Sulfur chemistry in the interstellar medium: The effect of vibrational excitation of H 2 in the reaction S + +H 2 →sH + +H," Astronomical Journal **146**, `10.1088/0004-6256/146/5/125` (2013) `10.1088/0004-6256/146/5/125`.

[234] R. C. Fortenberry and T. D. Crawford, "Singlet excited states of silicon-containing anions relevant to interstellar chemistry," Journal of Physical Chemistry A **115**, 8119–8124 (2011) `10.1021/jp204844j`.

[235] R. J. Cvetanović, "Excited State Chemistry in the Stratosphere," Canadian Journal of Chemistry **52**, 1452–1464 (1974) `10.1139/v74-217`.

[236] J. R. Wiesenfeld, "Atmospheric Chemistry Involving Electronically Excited Oxygen Atoms," Accounts of Chemical Research **15**, 110–116 (1982) `10.1021/ar00076a003`.

[237] D. R. Glowacki, J. Lockhart, M. A. Blitz, S. J. Klippenstein, M. J. Pilling, S. H. Robertson, and P. W. Seakins, "Interception of excited vibrational quantum states by O2 in atmospheric association reactions," Science **337**, 1066–1069 (2012) `10.1126/science.1224106`.

[238] T. Yang, A. Li, G. K. Chen, C. Xie, A. G. Suits, W. C. Campbell, H. Guo, and E. R. Hudson, "Optical Control of Reactions between Water and Laser-Cooled Be+ Ions," Journal of Physical Chemistry Letters **9**, 3555–3560 (2018) `10.1021/acs.jpclett.8b01437`.

[239] P. F. Bernath, "Gas-phase inorganic chemistry: Monovalent derivatives of calcium and strontium," Science **254**, 665–670 (1991) `10.1126/science.254.5032.665`.

[240]P. F. Bernath, "Spectroscopy and Photochemistry of Polyatomic Alkaline Earth Containing Molecules," in *Advances in Photochemistry*, Vol. 23 (Jan. 5, 1997), pp. 1–62, `10.1002/9780470133545.ch1`.

[241]A. González-Ureña and R. Vetter, "Reactive collisions with excited-state atoms," Journal of the Chemical Society, Faraday Transactions **91**, 389–398 (1995) `10.1039/FT9959100389`.

[242]D. L. King and D. W. Setser, "Reactions of Electronically Excited-State Atoms," Annual Review of Physical Chemistry **27**, 407–442 (1976) `10.1146/annurev.pc.27.100176.002203`.

[243]J. M. Mestdagh, C. Alcaraz, J. Berlande, J. Cuvellier, T. Gustavsson, P. Meynadier, P. De Pujo, O. Sublemontier, J. P. Visticot, D. Of, E. Barium, M. Clusters, J. M. Mestdagh, C. Alcaraz, J. Berlande, J. Cuvellier, T. Gustavsson, P. Meynadier, P. De Pujo, O. Sublemontier, and J. P. Visticot, "Reaction Dynamics of Electronically Excited Barium Atoms With Free Molecules and Molecular Clusters," Laser Chemistry **10**, 389–403 (1990) `10.1155/1990/36585`.

[244]H. F. Davis, A. G. Suits, Y. T. Lee, C. Alcaraz, and J. M. Mestdagh, "State specific reactions of Ba(1S0) and Ba(1D2) with water and methanol," The Journal of Chemical Physics **98**, 9595–9609 (1993) `10.1063/1.464390`.

[245]M. D. Oberlander and J. M. Parson, "Laser excited fluorescence study of reactions of excited Ca and Sr with water and alcohols: Product selectivity and energy disposal," The Journal of Chemical Physics **105**, 5806–5816 (1996) `10.1063/1.472457`.

[246]M. D. Oberlander, R. P. Kampf, and J. M. Parson, "Chemiluminescent reactions of Ca with hydrogen peroxide," Chemical Physics Letters **176**, 385–389 (1991) `10.1016/0009-2614(91)90048-E`.

[247]B. S. Cheong and J. M. Parson, "Chemiluminescent reactions of group 2 (Ca, Sr, and Ba) elements with H 2O2, t-BuOOH, HNO3, and NO2: Reactivities and product state distributions," The Journal of Chemical Physics **100**, 2637–2650 (1994) `10.1063/1.466459`.

[248]R. W. Solarz and S. A. Johnson, "Laser induced fluorescence studies of the reactions of barium (1 S , 3 D) and strontium (1 S , 3 P) with halogenated methanes," The Journal of Chemical Physics **70**, 3592–3599 (1979) `10.1063/1.437962`.

[249]J. M. Teule, M. H. M. Janssen, J. Bulthuis, and S. Stolte, "Laser-induced fluorescence studies of excited Sr reactions: II. Sr(3P1)+CH3F, C2H5F, C2H4F2," The Journal of Chemical Physics **110**, 10792–10802 (1999) `10.1063/1.479022`.

[250]D. Husain, J. Geng, F. Castaño, and M. N. Sanchez Rayo, "Measurements of branching ratios of CaF(A) from the reactions of Ca[4s4p()] with CH3F following pulsed dye-laser excitation of atomic calcium," Journal of Photochemistry and Photobiology A: Chemistry **133**, 1–6 (2000) `10.1016/S1010-6030(00)00211-2`.

[251]J. M. Teule, J. Mes, J. Bulthuis, M. H. M. Janssen, and S. Stolte, "Laser-Induced Fluorescence Studies of Excited Sr Reactions. † 1. Sr(3 P 1) + HF," The Journal of Physical Chemistry A **102**, 9482–9488 (1998) `10.1021/jp981993e`.

[252] M. De Castro, R. Candori, F. Pirani, V. Aquilanti, M. Garay, and A. González Ureña, "Chemiluminescent reactions of excited calcium atoms with HCl and HBr: Selective charge-transfer "harpooning" and synchronized intermediate complex rearrangement," The Journal of Chemical Physics **112**, 770–780 (2000) `10.1063/1.480607`.

[253] K. Okada, M. Wada, L. Boesten, T. Nakamura, I. Katayama, and S. Ohtani, "Acceleration of the chemical reaction of trapped Ca+ ions with H2O molecules by laser excitation," Journal of Physics B: Atomic, Molecular and Optical Physics **36**, 33–46 (2003) `10.1088/0953-4075/36/1/304`.

[254] P. Puri, M. Mills, I. Simbotin, J. A. Montgomery, R. Côté, C. Schneider, A. G. Suits, and E. R. Hudson, "Reaction blockading in a reaction between an excited atom and a charged molecule at low collision energy," Nature Chemistry **11**, 615–621 (2019) `10.1038/s41557-019-0264-3`.

[255] M. Mills, P. Puri, M. Li, S. J. Schowalter, A. Dunning, C. Schneider, S. Kotochigova, and E. R. Hudson, "Engineering Excited-State Interactions at Ultracold Temperatures," Physical Review Letters **122**, 233401 (2019) `10.1103/PhysRevLett.122.233401`.

[256] M. W. Shafer and R. Roy, "Rare-Earth Polymorphism and Phase Equilibria in Rare-Earth Oxide-Water Systems," Journal of the American Ceramic Society **42**, 563–570 (1959) `10.1111/j.1151-2916.1959.tb13574.x`.

[257] M. Ozawa, R. Onoe, and H. Kato, "Formation and decomposition of some rare earth (RE=La, Ce, Pr) hydroxides and oxides by homogeneous precipitation," Journal of Alloys and Compounds, Proceedings of Rare Earths'04 in Nara, Japan **408–412**, 556–559 (2006) `10.1016/j.jallcom.2004.12.073`.

[258] Y. Liu and A. A. Houck, "Quantum electrodynamics near a photonic bandgap," Nature Physics **13**, 1–15 (2016) `10.1038/nphys3834`.

[259] D. Patterson and J. M. Doyle, "Bright, guided molecular beam with hydrodynamic enhancement.," The Journal of Chemical Physics **126**, 154307 (2007) `10.1063/1.2717178`.

[260] S. Brutti, T. Terai, M. Yamawaki, M. Yasumoto, G. Balducci, G. Gigli, and A. Ciccioli, "Mass spectrometric investigation of gaseous YbH, YbO and YbOH molecules," Rapid Communications in Mass Spectrometry **19**, 2251–2258 (2005) `10.1002/rcm.2050`.

[261] B. deB Darwent, *Bond dissociation energies in simple molecules*, NBS NSRDS 31 (National Bureau of Standards, Gaithersburg, MD, 1970), `10.6028/NBS.NSRDS.31`.

[262] T. Helgaker, E. Uggerud, and H. J. A. Jensen, "Integration of the classical equations of motion on ab initio molecular potential energy surfaces using gradients and Hessians: application to translational energy release upon fragmentation," Chemical Physics Letters **173**, 145–150 (1990) `10.1016/0009-2614(90)80068-O`.

[263] J. Lim, J. R. Almond, M. R. Tarbutt, D. T. Nguyen, and T. C. Steimle, "The [557]-X2Σ+ and [561]-X2Σ+ bands of ytterbium fluoride, 174YbF," Journal of Molecular Spectroscopy **338**, 81–90 (2017) `10.1016/j.jms.2017.06.007`.

[264] T. C. Steimle, C. Linton, E. T. Mengesha, X. Bai, and A. T. Le, "Field-free, Stark, and Zeeman spectroscopy of the $\tilde{A}^2\Pi_{1/2} - \tilde{X}^2\Sigma^+$ transition of ytterbium monohydroxide," Physical Review A **100**, 052509 (2019) `10.1103/PhysRevA.100.052509`.

[265] S. M. Skoff, R. J. Hendricks, C. D. J. Sinclair, M. R. Tarbutt, J. J. Hudson, D. M. Segal, B. E. Sauer, and E. A. Hinds, "Doppler-free laser spectroscopy of buffer-gas-cooled molecular radicals," New Journal of Physics **11**, 123026 (2009) `10.1088/1367-2630/11/12/123026`.

[266] W. Bu, T. Chen, G. Lv, and B. Yan, "Cold collision and high-resolution spectroscopy of buffer-gas-cooled BaF molecules," Physical Review A **95**, 032701 (2017) `10.1103/PhysRevA.95.032701`.

[267] D. E. Maison, L. V. Skripnikov, and V. V. Flambaum, "Theoretical study of ^{173}YbOH to search for the nuclear magnetic quadrupole moment," Physical Review A **100**, 032514 (2019) `10.1103/PhysRevA.100.032514`.

[268] H. Wang, A. T. Le, T. C. Steimle, E. A. C. Koskelo, G. Aufderheide, R. Mawhorter, and J.-U. Grabow, "Fine and hyperfine interaction in 173YbF," Physical Review A **100**, 022516 (2019) `10.1103/PhysRevA.100.022516`.

[269] K. Pandey, A. K. Singh, P. V. Kumar, M. V. Suryanarayana, and V. Natarajan, "Isotope shifts and hyperfine structure in the 555.8-nm S1 0 → P3 1 line of Yb," Physical Review A - Atomic, Molecular, and Optical Physics **80**, 022518 (2009) `10.1103/PhysRevA.80.022518`.

[270] R. Santra, K. V. Christ, and C. H. Greene, "Properties of metastable alkaline-earth-metal atoms calculated using an accurate effective core potential," **042510**, 1–10 (2004) `10.1103/PhysRevA.69.042510`.

[271] T. Isaev, S. Hoekstra, and R. Berger, "Laser-cooled RaF as a promising candidate to measure molecular parity violation," Physical Review A **82**, 52521 (2010) `10.1103/PhysRevA.82.052521`.

[272] T. A. Isaev, A. V. Zaitsevskii, and E. Eliav, "Laser-coolable polyatomic molecules with heavy nuclei," Journal of Physics B **50**, 225101 (2017) `10.1088/1361-6455/aa8f34`.

[273] T. Kamiński, R. Tylenda, K. M. Menten, A. Karakas, J. M. Winters, A. A. Breier, K. T. Wong, T. F. Giesen, and N. A. Patel, "Astronomical detection of radioactive molecule 26AlF in the remnant of an ancient explosion," Nature Astronomy **2**, 778–783 (2018) `10.1038/s41550-018-0541-x`.

[274] Y. S. Au, C. B. Connolly, W. Ketterle, and J. M. Doyle, "Properties of the ground 3F2 state and the excited 3P0 state of atomic thorium in cold collisions with 3He," Physical Review A **90**, 32702 (2014) `10.1103/PhysRevA.90.032702`.

[275] M. J. O'Rourke and N. R. Hutzler, "Hypermetallic Polar Molecules for Precision Measurements," Physical Review A **100**, 022502 (2019) `10.1103/PhysRevA.100.022502`.

[276] K. Gaul and R. Berger, "Ab initio study of parity and time-reversal violation in laser-coolable triatomic molecules," 2018.

[277] M. Denis, P. A. B. Haase, R. G. E. Timmermans, E. Eliav, N. R. Hutzler, and A. Borschevsky, "Enhancement factor for the electric dipole moment of the electron in the BaOH and YbOH molecules," Physical Review A **99**, 42512 (2019) `10.1103/PhysRevA.99.042512`.

[278] V. S. Prasannaa, N. Shitara, A. Sakurai, M. Abe, and B. P. Das, "Enhanced sensitivity of the electron electric dipole moment from YbOH: The role of theory," Physical Review A **99**, 62502 (2019) `10.1103/PhysRevA.99.062502`.

[279] M. Yeo, M. T. Hummon, A. L. Collopy, B. Yan, B. Hemmerling, E. Chae, J. M. Doyle, and J. Ye, "Rotational State Microwave Mixing for Laser Cooling of Complex Diatomic Molecules," Physical Review Letters **114**, 223003 (2015) `10.1103/PhysRevLett.114.223003`.

[280] A. Jadbabaie, Y. Takahashi, N. H. Pilgram, C. J. Conn, Y. Zeng, C. Zhang, and N. R. Hutzler, *Characterizing the Fundamental Bending Vibration of a Linear Polyatomic Molecule for Symmetry Violation Searches*, (Jan. 10, 2023) `http://arxiv.org/abs/2301.04124`, preprint.

[281] S. Nakhate, T. C. Steimle, N. H. Pilgram, and N. R. Hutzler, "The pure rotational spectrum of YbOH," Chemical Physics Letters **715**, 105–108 (2019) `10.1016/j.cplett.2018.11.030`.

[282] H. Sawaoka, A. Frenett, A. Nasir, T. Ono, B. L. Augenbraun, T. C. Steimle, and J. M. Doyle, "Zeeman-Sisyphus deceleration for heavy molecules with perturbed excited-state structure," Physical Review A **107**, 022810 (2023) `10.1103/PhysRevA.107.022810`.

[283] D. A. Fletcher, M. A. Anderson, W. L. Barclay, and L. M. Ziurys, "Millimeter-wave spectroscopy of vibrationally excited ground state alkaline-earth hydroxide radicals ($X2\Sigma+$)," The Journal of Chemical Physics **102**, 4334–4339 (1995) `10.1063/1.469482`.

[284] D. A. Gillett, A. L. Cooksy, and J. M. Brown, "Infrared laser magnetic resonance spectroscopy of the $N3$ fundamental and associated hot bands of the NCO free radical," Journal of Molecular Spectroscopy **239**, 190–200 (2006) `10.1016/j.jms.2006.07.005`.

[285] R. F. Curl, P. G. Carrick, and A. J. Merer, "Rotational analysis of the $\tilde{A} \leftarrow \tilde{X}$ system of C_2H," The Journal of Chemical Physics **82**, 3479–3486 (1985) `10.1063/1.448927`.

[286] K. Tanaka, M. Nakamura, M. Shirasaka, A. Sakamoto, K. Harada, and T. Tanaka, "Millimeter-wave spectroscopy of the FeCO radical in the ν_2 and ν_3 vibrationally excited states," The Journal of Chemical Physics **143**, 014303 (2015) `10.1063/1.4923215`.

[287] A. J. Apponi, M. A. Anderson, and L. M. Ziurys, "High resolution spectroscopy of MgOH ($X 2\Sigma+$) in its V2 mode: Further evidence for quasilinearity," The Journal of Chemical Physics **111**, 10919–10925 (1999) `10.1063/1.480455`.

[288] M. A. Brewster and L. M. Ziurys, "Rotational spectroscopy of 3d transition-metal cyanides: Millimeter-wave studies of ZnCN ($X2\Sigma+$)," The Journal of Chemical Physics **117**, 4853–4860 (2002) `10.1063/1.1498466`.

[289] M. A. Flory, Robert. W. Field, and L. M. Ziurys, "The pure rotational spectrum of CrCN ($X 6 \Sigma +$): an unexpected geometry and unusual spin interactions," Molecular Physics **105**, 585–597 (2007) `10.1080/00268970601146872`.

[290] S. Nakhate, T. C. Steimle, N. H. Pilgram, and N. R. Hutzler, "The pure rotational spectrum of YbOH," Chemical Physics Letters **715**, 105–108 (2019) `10.1016/j.cplett.2018.11.030`.

[291] C. Zhang, C. Zhang, L. Cheng, T. C. Steimle, and M. R. Tarbutt, "Inner-shell excitation in the YbF molecule and its impact on laser cooling," Journal of Molecular Spectroscopy **386**, 111625 (2022) `10.1016/j.jms.2022.111625`.

[292]A. Zakharova and A. Petrov, *Impact of the ligand deformation on the PT-violation effects in the YbOH molecule*, (Aug. 15, 2022) `http://arxiv.org/abs/2208.07058`, preprint.

[293]R. Pereira and D. H. Levy, "Observation and spectroscopy of high-lying states of the CaOH radical: Evidence for a bent, covalent state," The Journal of Chemical Physics **105**, 9733–9739 (1996) `10.1063/1.472844`.

[294]P. Presunka and J. Coxon, "High-resolution laser spectroscopy of excited bending vibrations ($\Upsilon2 \leq 2$) of the and electronic states of SrOH: analysis of ℓ-type doubling and ℓ-type resonance," Canadian Journal of Chemistry **71**, 1689–1705 (1993) `10.1139/v93-211`.

[295]G. Herzberg, *Molecular Spectra and Molecular Structure: Volume III. Electronic Spectra and Electronic Structure of Polyatomic Molecules*, 2nd edition (D. Van Nostrand Company, 1966), 745 pp.

[296]P. Bolman and J. Brown, "The Renner-Teller effect and vibronically induced bands in the electronic spectrum of NCO," Chemical Physics Letters **21**, 213–216 (1973) `10.1016/0009-2614(73)80121-6`.

[297]R. N. Dixon and D. A. Ramsay, "Electronic absorption spectrum of the NCS free radical," Canadian Journal of Physics **46**, 2619–2631 (1968) `10.1139/p68-628`.

[298]M. Fukushima and T. Ishiwata, "Low-lying bending vibronic bands of the MgNC $\tilde{A}\Pi2$-$\tilde{X}\Sigma+2$ transition," The Journal of Chemical Physics **127**, 044314 (2007) `10.1063/1.2748769`.

[299]C. N. Jarman and P. F. Bernath, "High resolution laser spectroscopy of the C 2Δ– X$\Sigma+$ transition of CaOH and CaOD: Vibronic coupling and the Renner–Teller effect," The Journal of Chemical Physics **97**, 1711–1718 (1992) `10.1063/1.463158`.

[300]J. A. Coxon, M. G. Li, and P. I. Presunka, "Laser Spectroscopy of the (010)2Σ(+), 2Σ(-)-(000)2$\Sigma+$ Parallel Bands in the $\tilde{A}2\Pi$-$\tilde{X}2\Sigma+$ System of CaOH," Journal of Molecular Spectroscopy **164**, 118–128 (1994) `10.1006/jmsp.1994.1060`.

[301]P. I. Presunka and J. A. Coxon, "Laser spectroscopy of the $\tilde{A}^2\Pi$ - $\tilde{X}\ ^2\Sigma^+$ transition of SrOH: Deperturbation analysis of K-resonance in the v2 = 1 level of the $\tilde{A}^2\Pi$ state," The Journal of Chemical Physics **101**, 201–222 (1994) `10.1063/1.468171`.

[302]Z. Lasner, A. Lunstad, C. Zhang, L. Cheng, and J. M. Doyle, "Vibronic branching ratios for nearly closed rapid photon cycling of SrOH," Physical Review A **106**, L020801 (2022) `10.1103/PhysRevA.106.L020801`.

[303]H. Köppel, W. Domcke, and L. S. Cederbaum, "Theory of vibronic coupling in linear molecules," The Journal of Chemical Physics **74**, 2945–2968 (1981) `10.1063/1.441417`.

[304]E. B. Norrgard, D. S. Barker, S. P. Eckel, J. A. Fedchak, N. N. Klimov, and J. Scherschligt, "Nuclear-spin dependent parity violation in optically trapped polyatomic molecules," Communications Physics **2**, 77 (2019) `10.1038/s42005-019-0181-1`.

[305]G. Herzberg, *Molecular Spectra and Molecular Structure: Volume II. Infrared and Raman Spectra of Polyatomic Molecules*, 2nd edition (D. Van Nostrand Company, 1966).

[306]G. Duxbury and A. Alexander, *High-Resolution Electronic Spectroscopy of Small Molecules*, 1st ed. (CRC Press, Aug. 2, 2017), `10.1201/9781315372815`.

[307] Ch. Jungen, "The Renner-Teller effect revisited 40 years later," Journal of Molecular Spectroscopy **363**, 111172 (2019) `10.1016/j.jms.2019.07.003`.

[308] Ch. Jungen and A. Merer, "Orbital angular momentum in triatomic molecules: I. A general method for calculating the vibronic energy levels of states that become degenerate in the linear molecule (the Renner-Teller effect)," Molecular Physics **40**, 1–23 (1980) `10.1080/00268978000101291`.

[309] J. M. Brown and F. Jørgensen, "Anharmonic corrections for linear triatomic molecules subject to the Rennet-Teller effect," Molecular Physics **47**, 1065–1086 (1982) `10.1080/00268978200100782`.

[310] L. V. Poluyanov and W. Domcke, "The relativistic Renner–Teller effect revisited," Chemical Physics **301**, 111–127 (2004) `10.1016/j.chemphys.2004.02.017`.

[311] S. Mishra, V. Vallet, L. V. Poluyanov, and W. Domcke, "Spectroscopic effects of first-order relativistic vibronic coupling in linear triatomic molecules," The Journal of Chemical Physics **123**, 124104 (2005) `10.1063/1.2018702`.

[312] S.-G. He, H. Li, T. C. Smith, D. J. Clouthier, and A. J. Merer, "The Renner-Teller effect and Sears resonances in the ground state of the GeCH and GeCD free radicals," The Journal of Chemical Physics **119**, 10115–10124 (2003) `10.1063/1.1618219`.

[313] E. Bosch, P. Crozet, A. Ross, and J. Brown, "Fourier Transform Spectra of the E2Πu–X2Πg(3/2) System of CuCl2," Journal of Molecular Spectroscopy **202**, 253–261 (2000) `10.1006/jmsp.2000.8128`.

[314] S.-G. He, D. J. Clouthier, A. G. Adam, and D. W. Tokaryk, "A laser spectroscopic study of the $\tilde{X}\Pi g2$, AΠu2, and $\tilde{B}\Sigma u+2$ states of BS2: Renner–Teller, spin-orbit, and K-resonance effects," The Journal of Chemical Physics **122**, 194314 (2005) `10.1063/1.1898221`.

[315] A. G. Adam, A. J. Merer, and D. M. Steunenberg, "Vibronic perturbations in the $\tilde{A}$ 2Πu–$\tilde{X}$ 2Πg transition of BO2: K-resonance crossings and the onset of chaotic behavior," The Journal of Chemical Physics **92**, 2848–2861 (1990) `10.1063/1.457931`.

[316] J. M. Frye and T. J. Sears, "Measurement of the Renner-Teller effect in X $^2\Pi$ CO_2 $^+$ by diode laser absorption," Molecular Physics **62**, 919–937 (1987) `10.1080/00268978700102671`.

[317] M. Li, "High Resolution Laser Spectroscopy of the A~2Π - X~2Σ+ system of CaOH and CaOD Radicals," PhD thesis (Dalhousie University, 1995).

[318] P. I. Presunka, "High resolution laser excitation and dispersed fluorescence spectroscopy of the alkaline earth monohydroxides: the low-lying electronic states of the CaOH/CaOD and SrOH radicals," PhD thesis (Dalhousie University, 1994).

[319] T. C. Smith, H. Li, D. A. Hostutler, D. J. Clouthier, and A. J. Merer, "Orbital angular momentum (Renner–Teller) effects in the Πi2 ground state of silicon methylidyne (SiCH)," The Journal of Chemical Physics **114**, 725–734 (2001) `10.1063/1.1331316`.

[320] F. Northrup and T. J. Sears, "Renner-Teller, spin-orbit and Fermi-resonance interactions in X ^{2} Π NCS investigated by LIF spectroscopy," Molecular Physics **71**, 45–64 (1990) `10.1080/00268979000101631`.

[321] M. Wu and T. J. Sears, "Stimulated emission pumping spectroscopy of $^2\Sigma$ and $^2\pi$ vibronic levels in $[\tilde{X}](v_1 v_2 0)\,^2\pi$ NCO," Molecular Physics **82**, 503–521 (1994) `10.1080/00268979400100374`.

[322] M. Li and J. A. Coxon, "The First Excited Ca–C–C Bending Vibration Levels in theÃ2Π and X2Σ+States of the CaCCH Radical: The Renner–Teller Effect andK-type Resonance," Journal of Molecular Spectroscopy **180**, 287–297 (1996) `10.1006/jmsp.1996.0251`.

[323] J. Tang and S. Saito, "Microwave spectroscopy of the HCCS and DCCS radicals ($\tilde{X}\,^2\Pi_i$) in excited vibronic states: A study of the Renner–Teller effect," The Journal of Chemical Physics **105**, 8020–8033 (1996) `10.1063/1.472715`.

[324] M. Sommavilla and F. Merkt, "Pulsed-Field-Ionization Zero-Kinetic-Energy (PFI-ZEKE) Photoelectron Spectroscopic Study of the Renner-Teller Effect in the Ã+ 2Π State of OCS+," The Journal of Physical Chemistry A **108**, 9970–9978 (2004) `10.1021/jp0478458`.

[325] J. Li, H. Li, and Y. Mo, "Renner-Teller Effect, Spin-Orbit Coupling, and Fermi Resonance in BrCN$^+$ ($\tilde{X}\,^2\Pi$): A Combined Experimental and Theoretical Study," The Journal of Physical Chemistry A **114**, 9973–9980 (2010) `10.1021/jp1039332`.

[326] M. Pernpointner and F. Salopiata, "A four-component quadratic vibronic coupling approach to the Renner–Teller effect in linear triatomic molecules. The , manifold of BrCN+ and ClCN+," Journal of Physics B: Atomic, Molecular and Optical Physics **46**, 125101 (2013) `10.1088/0953-4075/46/12/125101`.

[327] M. Biczysko and R. Tarroni, "Renner–Teller interactions coupled to large spin–orbit splittings: The BrCN+ case," Chemical Physics Letters **415**, 223–229 (2005) `10.1016/j.cplett.2005.09.004`.

[328] J. H. D. Eland, P. Baltzer, M. Lundqvist, B. Wannberg, and L. Karlsson, "Vibrational structure of the BrCN+ ion from high resolution photoelectron spectroscopy," Chemical Physics **212**, 457–469 (1996) `10.1016/S0301-0104(96)00197-8`.

[329] M. Allan and J. P. Maier, "The emission spectra of ClCN+, BrCN+, ICN+ radical cations: ~B2Π→~X2Π and ~A2Σ+ → ~X2Π band systems," Chemical Physics Letters **41**, 231–235 (1976) `10.1016/0009-2614(76)80799-3`.

[330] M. Araki, T. Ito, S. Hoshino, and K. Tsukiyama, "Rotationally resolved gas-phase spectrum of the $\tilde{A}$ 2Σ+– $\tilde{X}$ 2Π3/2 electronic transition for the cyanogen halide radical cation ICN+," Journal of Molecular Spectroscopy **388**, 111675 (2022) `10.1016/j.jms.2022.111675`.

[331] J. Eland, P. Baltzer, L. Karlsson, and B. Wannberg, "The photoelectron spectrum of iodine cyanide, ICN," Chemical Physics **222**, 229–240 (1997) `10.1016/S0301-0104(97)00214-0`.

[332] J. Brown, J. Hougen, K.-P. Huber, J. Johns, I. Kopp, H. Lefebvre-Brion, A. Merer, D. Ramsay, J. Rostas, and R. Zare, "The labeling of parity doublet levels in linear molecules," Journal of Molecular Spectroscopy **55**, 500–503 (1975) `10.1016/0022-2852(75)90291-X`.

[333] S. A. Beaton, Y. Ito, and J. M. Brown, "Laser Excitation Spectroscopy of the Ã3Π–X3Σ- Transition of the NCN Radical 1. The (0-0) hot band," Journal of Molecular Spectroscopy **178**, 99–107 (1996) `10.1006/jmsp.1996.0162`.

[334] A. Carrington, D. H. Levy, and T. A. Miller, "Electron Resonance of Gaseous Diatomic Molecules," in *Advances in Chemical Physics*, edited by I. Prigogine and S. A. Rice (John Wiley & Sons, Inc., Hoboken, NJ, USA, 1970), pp. 149–248, `10.1002/9780470143650.ch4`.

[335] T. D. Persinger, J. Han, A. T. Le, T. C. Steimle, and M. C. Heaven, "Electronic spectroscopy and ionization potentials for YbOH and YbOCH 3," Physical Review A **107**, 032810 (2023) `10.1103/PhysRevA.107.032810`.

[336] G. Herzberg, *Molecular Spectra and Molecular Structure: Volume I. Spectra of Diatomic Molecules*, 2nd edition (D. Van Nostrand Company, 1964).

[337] T. D. Persinger, J. Han, A. T. Le, T. C. Steimle, and M. C. Heaven, "Direct observation of the Yb (4 f 13 6 s 2) F states and accurate determination of the YbF ionization energy," Physical Review A **106**, 062804 (2022) `10.1103/PhysRevA.106.062804`.

[338] B. A. Woody and L. Lynds, "Frequency-modulated laser absorption spectroscopy of the HF fourth overtone," Applied Optics **25**, 2148 (1986) `10.1364/AO.25.002148`.

[339] C. Linton, A. Le, A. Adam, E. Mengesha, and T. Steimle, "HIGH RESOLUTION LASER IN-DUCED FLUORESCENCE AND ZEEMAN EFFECT IN THE [18.6]1.5-X$^2\Sigma^+$ TRANSITION OF YbOH," in Proceedings of the 2021 International Symposium on Molecular Spectroscopy (June 24, 2021), pp. 1–1, `10.15278/isms.2021.FL05`.

[340] J. Lim, J. R. Almond, M. R. Tarbutt, D. T. Nguyen, and T. C. Steimle, "The [557]-X2Σ+ and [561]-X2Σ+ bands of ytterbium fluoride, 174YbF," Journal of Molecular Spectroscopy **338**, 81–90 (2017) `10.1016/j.jms.2017.06.007`.

[341] A. M. Souza, G. A. Álvarez, and D. Suter, "Robust dynamical decoupling," Philosophical Transactions of the Royal Society A: Mathematical, Physical and Engineering Sciences **370**, 4748–4769 (2012) `10.1098/rsta.2011.0355`.

[342] D. J. Wineland, J. J. Bollinger, W. M. Itano, and D. J. Heinzen, "Squeezed atomic states and projection noise in spectroscopy," Physical Review A **50**, 67–88 (1994) `10.1103/PhysRevA.50.67`.

[343] A. C. Vutha, M. Horbatsch, and E. A. Hessels, "Orientation-dependent hyperfine structure of polar molecules in a rare-gas matrix: A scheme for measuring the electron electric dipole moment," Physical Review A **98**, 032513 (2018) `10.1103/PhysRevA.98.032513`.

[344] G. Edvinsson and A. Lagerqvist, "Rotational analysis of yellow and near infrared bands in ThO," Physica Scripta **30**, 309–320 (1984) `10/c4b5hh`.

[345] A. C. Vutha, B. Spaun, Y. V. Gurevich, N. R. Hutzler, E. Kirilov, J. M. Doyle, G. Gabrielse, and D. DeMille, "Magnetic and electric dipole moments of the H3Delta1 state in ThO," Physical Review A **84**, 34502 (2011) `10.1103/PhysRevA.84.034502`.

[346] M. Grau, "Measuring the Electron Electric Dipole Moment with Trapped Molecular Ions," PhD thesis (University of Colorado, Boulder, 2016).

[347] K. B. Whaley and J. C. Light, "Rotating-frame transformations: A new approximation for multiphoton absorption and dissociation in laser fields," Physical Review A **29**, 1188–1207 (1984) `10.1103/PhysRevA.29.1188`.

[348]D. J. Berkeland and M. G. Boshier, "Destabilization of dark states and optical spectroscopy in Zeeman-degenerate atomic systems," Physical Review A **65**, 033413 (2002) `10.1103/PhysRevA.65.033413`.

[349]K. Wenz, "Nuclear Schiff Moment Search in Thallium Fluoride Molecular Beam: Rotational Cooling,"

[350]H. R. Gray, R. M. Whitley, and C. R. Stroud, "Coherent trapping of atomic populations," Optics Letters **3**, 218 (1978) `10.1364/ol.3.000218`.

[351]F. Renzoni, W. Maichen, L. Windholz, and E. Arimondo, "Coherent population trapping with losses observed on the Hanle effect of the D 1 sodium line," Physical Review A **55**, 3710–3718 (1997) `10.1103/PhysRevA.55.3710`.

[352]T. Zanon, S. Guerandel, E. De Clercq, D. Holleville, N. Dimarcq, and A. Clairon, "High contrast ramsey fringes with coherent-population-Trapping pulses in a double lambda atomic system," Physical Review Letters **94**, `10.1103/PhysRevLett.94.193002` (2005) `10.1103/PhysRevLett.94.193002`.

[353]A. Huss, R. Lammegger, L. Windholz, E. Alipieva, S. Gateva, L. Petrov, E. Taskova, and G. Todorov, "Polarization-dependent sensitivity of level-crossing, coherent-population-trapping resonances to stray magnetic fields," Journal of the Optical Society of America B **23**, 1729 (2006) `10.1364/JOSAB.23.001729`.

[354]Y. Zhang, S. Qu, and S. Gu, "Spin-polarized dark state free CPT state preparation with co-propagating left and right circularly polarized lasers," Optics Express **20**, 6400 (2012) `10.1364/OE.20.006400`.

[355]P. Yun, F. Tricot, C. E. Calosso, S. Micalizio, B. François, R. Boudot, S. Guérandel, and E. de Clercq, "High-Performance Coherent Population Trapping Clock with Polarization Modulation," Physical Review Applied **7**, 014018 (2017) `10.1103/PhysRevApplied.7.014018`.

[356]J. D. Elgin, T. P. Heavner, J. Kitching, E. A. Donley, J. Denney, and E. A. Salim, "A cold-atom beam clock based on coherent population trapping," Applied Physics Letters **115**, 033503 (2019) `10.1063/1.5087119`.

[357]J. R. Morris and B. W. Shore, "Reduction of degenerate two-level excitation to independent two-state systems," Physical Review A **27**, 906–912 (1983) `10.1103/PhysRevA.27.906`.

[358]E. Arimondo, "Relaxation processes in coherent-population trapping," Physical Review A **54**, 2216–2223 (1996) `10.1103/PhysRevA.54.2216`.

[359]D. V. Kosachiov, B. G. Matisov, and Y. V. Rozhdestvensky, "Coherent phenomena in multilevel systems with closed interaction contour," Journal of Physics B: Atomic, Molecular and Optical Physics **25**, 2473–2488 (1992) `10.1088/0953-4075/25/11/005`.

[360]F. Renzoni, A. Lindner, and E. Arimondo, "Coherent population trapping in open systems: A coupled/noncoupled-state analysis," Physical Review A - Atomic, Molecular, and Optical Physics **60**, 450–455 (1999) `10.1103/PhysRevA.60.450`.

[361]F. Renzoni and E. Arimondo, "Depopulation and repopulation pumping in coherent population trapping," Europhysics Letters **46**, 716–721 (1999) `10.1209/epl/i1999-00324-1`.

[362] L. Windholz, "Coherent Population Trapping in Open and Closed Systems," Acta Physica Polonica A **97**, 259–274 (2000) `10.12693/APhysPolA.97.259`.

[363] L. Windholz, "Coherent Population Trapping in Multi-Level Atomic Systems," Physica Scripta **T95**, 81 (2001) `10.1238/Physica.Topical.095a00081`.

[364] E. Arimondo, "Laser Phase Spectroscopy in Closed-Loop Multilevel Schemes," in *Exploring the World with the Laser*, edited by D. Meschede, T. Udem, and T. Esslinger (Springer International Publishing, Cham, 2018), pp. 665–677, `10.1007/978-3-319-64346-5_36`.

[365] V. Milner and Y. Prior, "Multilevel Dark States: Coherent Population Trapping with Elliptically Polarized Incoherent Light," Physical Review Letters **80**, 940–943 (1998) `10.1103/PhysRevLett.80.940`.

[366] A. V. Ta, "Elliptic dark states: Explicit invariant form," **91**, 9 (2000).

[367] N. V. Vitanov, Z. Kis, and B. W. Shore, "Coherent excitation of a degenerate two-level system by an elliptically polarized laser pulse," Physical Review A **68**, 063414 (2003) `10.1103/PhysRevA.68.063414`.

[368] A. V. Taichenachev, V. I. Yudin, V. L. Velichansky, A. S. Zibrov, and S. A. Zibrov, "Pure superposition states of atoms generated by a bichromatic elliptically polarized field," Physical Review A **73**, 013812 (2006) `10.1103/PhysRevA.73.013812`.

[369] K. Nasyrov, S. Cartaleva, N. Petrov, V. Biancalana, Y. Dancheva, E. Mariotti, and L. Moi, "Coherent population trapping resonances in Cs atoms excited by elliptically polarized light," Physical Review A **74**, 013811 (2006) `10.1103/PhysRevA.74.013811`.

[370] K. Bergmann, H. Theuer, and B. W. Shore, "Coherent population transfer among quantum states of atoms and molecules," Reviews of Modern Physics **70**, 1003–1025 (1998) `10.1103/RevModPhys.70.1003`.

[371] K. Bergmann, H.-C. Nägerl, C. Panda, G. Gabrielse, E. Miloglyadov, M. Quack, G. Seyfang, G. Wichmann, S. Ospelkaus, A. Kuhn, S. Longhi, A. Szameit, P. Pirro, B. Hillebrands, X.-F. Zhu, J. Zhu, M. Drewsen, W. K. Hensinger, S. Weidt, T. Halfmann, H.-L. Wang, G. S. Paraoanu, N. V. Vitanov, J. Mompart, T. Busch, T. J. Barnum, D. D. Grimes, R. W. Field, M. G. Raizen, E. Narevicius, M. Auzinsh, D. Budker, A. Pálffy, and C. H. Keitel, "Roadmap on STIRAP applications," Journal of Physics B: Atomic, Molecular and Optical Physics **52**, 202001 (2019) `10.1088/1361-6455/ab3995`.

[372] M. Auzinsh, D. Budker, and S. M. Rochester, "Light-induced polarization effects in atoms with partially resolved hyperfine structure and applications to absorption, fluorescence, and nonlinear magneto-optical rotation," Physical Review A **80**, 053406 (2009) `10.1103/PhysRevA.80.053406`.

[373] B. W. Shore, "Two-state behavior in N-state quantum systems: The Morris–Shore transformation reviewed," Journal of Modern Optics **61**, 787–815 (2014) `10.1080/09500340.2013.837205`.

[374] K. N. Zlatanov, G. S. Vasilev, and N. V. Vitanov, "Morris-Shore transformation for non-degenerate systems," Physical Review A **102**, 063113 (2020) `10.1103/PhysRevA.102.063113`.

[375] C. Scurlock, D. Fletcher, and T. Steimle, "Hyperfine Structure in the (0,0,0) X $2\Sigma+$ State of CaOH Observed by Pump/Probe Microwave-Optical Double Resonance," Journal of Molecular Spectroscopy **159**, 350–356 (1993) `10.1006/jmsp.1993.1133`.

[376] D. A. Fletcher, K. Y. Jung, C. T. Scurlock, and T. C. Steimle, "Molecular beam pump/probe microwave-optical double resonance using a laser ablation source," The Journal of Chemical Physics **98**, 1837 (1993) `10/d82xsm`.

[377] C. S. Dickinson, J. A. Coxon, N. R. Walker, and M. C. L. Gerry, "Fourier transform microwave spectroscopy of the $\Sigma+2$ ground states of YbX (X=F, Cl, Br): Characterization of hyperfine effects and determination of the molecular geometries," The Journal of Chemical Physics **115**, 6979–6989 (2001) `10.1063/1.1404146`.

[378] L. B. Knight Jr., W. C. Easley, W. Weltner Jr., and M. Wilson, "Hyperfine Interaction and Chemical Bonding in MgF, CaF, SrF, and BaF molecules," The Journal of Chemical Physics **54**, 322–329 (2003) `10.1063/1.1674610`.

[379] S. Burchesky, L. Anderegg, Y. Bao, S. S. Yu, E. Chae, W. Ketterle, K.-K. Ni, and J. M. Doyle, "Rotational Coherence Times of Polar Molecules in Optical Tweezers," Physical Review Letters **127**, 123202 (2021) `10.1103/PhysRevLett.127.123202`.

[380] L. Anderegg, S. Burchesky, Y. Bao, S. S. Yu, T. Karman, E. Chae, K.-K. Ni, W. Ketterle, and J. M. Doyle, "Observation of microwave shielding of ultracold molecules," Science **373**, 779–782 (2021) `10.1126/science.abg9502`.

[381] E. Breschi, G. Kazakov, R. Lammegger, G. Mileti, B. Matisov, and L. Windholz, "Quantitative study of the destructive quantum-interference effect on coherent population trapping," Physical Review A **79**, 063837 (2009) `10.1103/PhysRevA.79.063837`.

[382] J. S. Jackson and D. S. Durfee, "Magneto-Optical Trap Field Characterization with the Directional Hanle Effect," Scientific Reports **9**, 8896 (2019) `10.1038/s41598-019-45324-7`.

[383] J. Trujillo-Bueno, *Atomic Polarization and the Hanle Effect*, (Feb. 18, 2002) `http://arxiv.org/abs/astro-ph/0202328`, preprint.

[384] P. Zhou and S. Swain, "Hanle fluorescence spectra of an atom with a J g =0⇆ J e =1 transition," Physical Review A **55**, 717–724 (1997) `10.1103/PhysRevA.55.717`.

[385] A. Kastler, "The Hanle effect and its use for the measurements of very small magnetic fields," Nuclear Instruments and Methods **110**, 259–265 (1973) `10.1016/0029-554X(73)90698-8`.

[386] H. Azizbekyan, S. Shmavonyan, A. Khanbekyan, M. Movsisyan, and A. Papoyan, "High-speed optical three-axis vector magnetometry based on nonlinear Hanle effect in rubidium vapor," Optical Engineering **56**, 074104 (2017) `10.1117/1.OE.56.7.074104`.

[387] J. O. Stenflo, "History of Solar Magnetic Fields Since George Ellery Hale," Space Science Reviews **210**, 5–35 (2017) `10.1007/s11214-015-0198-z`.

[388] A. Fabricant, I. Novikova, and G. Bison, "How to build a magnetometer with thermal atomic vapor: a tutorial," New Journal of Physics **25**, 025001 (2023) `10.1088/1367-2630/acb840`.

[389] M. Zielonkowski, J. Steiger, U. Schünemann, M. DeKieviet, and R. Grimm, "Optically induced spin precession and echo in an atomic beam," Physical Review A **58**, 3993–3998 (1998) `10.1103/PhysRevA.58.3993`.

[390] O. Grasdijk, O. Timgren, J. Kastelic, T. Wright, S. Lamoreaux, D. DeMille, K. Wenz, M. Aitken, T. Zelevinsky, T. Winick, and D. Kawall, "CeNTREX: a new search for time-reversal symmetry violation in the 205Tl nucleus," Quantum Science and Technology **6**, 044007 (2021) `10.1088/2058-9565/abdca3`.

[391] J. J. Hudson, D. M. Kara, I. J. Smallman, B. E. Sauer, M. R. Tarbutt, and E. A. Hinds, "Improved measurement of the shape of the electron," Nature **473**, 493–496 (2011) `10.1038/nature10104`.

[392] S. M. Freund, M. Römheld, and T. Oka, "Infrared-Radio-Frequency Two-Photon and Multiphoton Lamb Dips for CH$_{3}$F," Physical Review Letters **35**, 1497–1500 (1975) `10.1103/PhysRevLett.35.1497`.

[393] F. Lang, P. v d Straten, B. Brandstätter, G. Thalhammer, K. Winkler, P. S. Julienne, R. Grimm, and J. Hecker Denschlag, "Cruising through molecular bound-state manifolds with radiofrequency," Nature Physics **4**, 223–226 (2008) `10.1038/nphys838`.

[394] S. H. Autler and C. H. Townes, "Stark Effect in Rapidly Varying Fields," Physical Review **100**, 703–722 (1955) `10.1103/PhysRev.100.703`.

[395] P. J. Lee, B. B. Blinov, K. Brickman, L. Deslauriers, M. J. Madsen, R. Miller, D. L. Moehring, D. Stick, and C. Monroe, "Atomic qubit manipulations with an electro-optic modulator," Optics Letters **28**, 1582–1584 (2003) `10.1364/OL.28.001582`.

[396] E. A. Donley, T. P. Heavner, F. Levi, M. O. Tataw, and S. R. Jefferts, "Double-pass acousto-optic modulator system," Review of Scientific Instruments **76**, 063112 (2005) `10.1063/1.1930095`.

[397] E. Brion, L. H. Pedersen, and K. Mølmer, "Adiabatic elimination in a lambda system," Journal of Physics A: Mathematical and Theoretical **40**, 1033–1043 (2007) `10.1088/1751-8113/40/5/011`.

[398] I. Dotsenko, W. Alt, S. Kuhr, D. Schrader, M. Müller, Y. Miroshnychenko, V. Gomer, A. Rauschenbeutel, and D. Meschede, "Application of electro-optically generated light fields for Raman spectroscopy of trapped cesium atoms," Applied Physics B **78**, 711–717 (2004) `10.1007/s00340-004-1467-9`.

[399] H. Levine, D. Bluvstein, A. Keesling, T. T. Wang, S. Ebadi, G. Semeghini, A. Omran, M. Greiner, V. Vuletić, and M. D. Lukin, "Dispersive optical systems for scalable Raman driving of hyperfine qubits," Physical Review A **105**, 032618 (2022) `10.1103/PhysRevA.105.032618`.

[400] J. A. Devlin and M. R. Tarbutt, "Three-dimensional Doppler, polarization-gradient, and magneto-optical forces for atoms and molecules with dark states," New Journal of Physics **18**, 123017 (2016) `10.1088/1367-2630/18/12/123017`.

[401] J. A. Devlin and M. R. Tarbutt, "Laser cooling and magneto-optical trapping of molecules analyzed using optical Bloch equations and the Fokker-Planck-Kramers equation," Physical Review A **98**, `10.1103/PhysRevA.98.063415` (2018) `10.1103/PhysRevA.98.063415`.

[402]"Open quantum systems," in *Quantum Measurement and Control*, edited by G. J. Milburn and H. M. Wiseman (Cambridge University Press, Cambridge, 2009), pp. 97–147, `10.1017/CBO9780511813948.004`.

[403]L. Anderegg, N. B. Vilas, C. Hallas, P. Robichaud, A. Jadbabaie, J. M. Doyle, and N. R. Hutzler, *Quantum Control of Trapped Polyatomic Molecules for eEDM Searches*, (Jan. 20, 2023) `http://arxiv.org/abs/2301.08656`, preprint.

[404]E. B. Norrgard, D. S. Barker, S. Eckel, J. A. Fedchak, N. N. Klimov, and J. Scherschligt, "Nuclear-spin dependent parity violation in optically trapped polyatomic molecules," Communications Physics **2**, 77 (2019) `10.1038/s42005-019-0181-1`.

[405]D. E. Maison, L. V. Skripnikov, and V. V. Flambaum, "Theoretical study of YbOH 173 to search for the nuclear magnetic quadrupole moment," Physical Review A **100**, 032514 (2019) `10.1103/PhysRevA.100.032514`.

[406]M. Denis, Y. Hao, E. Eliav, N. R. Hutzler, M. K. Nayak, R. G. E. Timmermans, and A. Borschesvky, "Enhanced P,T-violating nuclear magnetic quadrupole moment effects in laser-coolable molecules," The Journal of Chemical Physics **152**, 084303 (2020) `10.1063/1.5141065`.

[407]I. Kurchavov and A. Petrov, "P , T -odd energy shifts of the ^{173}YbOH molecule," Physical Review A **106**, 062806 (2022) `10.1103/PhysRevA.106.062806`.

[408]K. Gaul and R. Berger, "Ab initio study of parity and time-reversal violation in laser-coolable triatomic molecules," Physical Review A **101**, 012508 (2020) `10.1103/PhysRevA.101.012508`.

[409]I. Kozyrev, L. Baum, K. Matsuda, and J. M. Doyle, "Proposal for Laser Cooling of Complex Polyatomic Molecules," ChemPhysChem **17**, 3641–3648 (2016) `10.1002/cphc.201601051`.

[410]H.-I. Lu, J. Rasmussen, M. J. Wright, D. Patterson, and J. M. Doyle, "A cold and slow molecular beam," Physical Chemistry Chemical Physics **13**, 18986–18990 (2011) `10.1039/c1cp21206k`.

[411]E. B. Norrgard, D. J. McCarron, M. H. Steinecker, M. R. Tarbutt, and D. DeMille, "Submillikelvin Dipolar Molecules in a Radio-Frequency Magneto-Optical Trap," Physical Review Letters **116**, 1–6 (2016) `10.1103/PhysRevLett.116.063004`.

[412]C. N. Cohen-Tannoudji, "Nobel Lecture: Manipulating atoms with photons," Reviews of Modern Physics **70**, 707–719 (1998) `10.1103/RevModPhys.70.707`.

[413]J. Dalibard and C. Cohen-Tannoudji, "Laser cooling below the Doppler limit by polarization gradients: simple theoretical models," JOSA B **6**, 2023–2045 (1989) `10.1364/JOSAB.6.002023`.

[414]C. Cohen-Tannoudji, "Laser cooling and trapping of neutral atoms: theory," Physics Reports **219**, 153–164 (1992) `10.1016/0370-1573(92)90133-K`.

[415]O. Emile, R. Kaiser, C. Gerz, H. Wallis, A. Aspect, and C. Cohen-Tannoudji, "Magnetically assisted Sisyphus effect," Journal de Physique II **3**, 1709 (1993) `10.1051/jp2:1993226`.

[416] A. Aspect, E. Arimondo, R. Kaiser, N. Vansteenkiste, and C. Cohen-Tannoudji, "Laser Cooling below the One-Photon Recoil Energy by Velocity-Selective Coherent Population Trapping," Physical Review Letters **61**, 826–829 (1988) `10.1103/PhysRevLett.61.826`.

[417] M. S. Shahriar, P. R. Hemmer, M. G. Prentiss, P. Marte, J. Mervis, D. P. Katz, N. P. Bigelow, and T. Cai, "Continuous polarization-gradient precooling-assisted velocity-selective coherent population trapping," Physical Review A **48**, R4035–R4038 (1993) `10.1103/PhysRevA.48.R4035`.

[418] D. Boiron, A. Michaud, P. Lemonde, Y. Castin, C. Salomon, S. Weyers, K. Szymaniec, L. Cognet, and A. Clairon, "Laser cooling of cesium atoms in gray optical molasses down to 1.1 μK," Physical Review A **53**, R3734–R3737 (1996) `10.1103/PhysRevA.53.R3734`.

[419] A. T. Grier, I. Ferrier-Barbut, B. S. Rem, M. Delehaye, L. Khaykovich, F. Chevy, and C. Salomon, "Λ -enhanced sub-Doppler cooling of lithium atoms in D 1 gray molasses," Physical Review A **87**, 063411 (2013) `10.1103/PhysRevA.87.063411`.

[420] L. W. Cheuk, L. Anderegg, B. L. Augenbraun, Y. Bao, S. Burchesky, W. Ketterle, and J. M. Doyle, "Λ-Enhanced Imaging of Molecules in an Optical Trap," Physical Review Letters **121**, 83201 (2018) `10.1103/PhysRevLett.121.083201`.

[421] T. K. Langin, V. Jorapur, Y. Zhu, Q. Wang, and D. DeMille, "Polarization Enhanced Deep Optical Dipole Trapping of Λ-Cooled Polar Molecules," Physical Review Letters **127**, 163201 (2021) `10.1103/PhysRevLett.127.163201`.

[422] L. Caldwell, J. A. Devlin, H. J. Williams, N. J. Fitch, E. A. Hinds, B. E. Sauer, and M. R. Tarbutt, "Deep Laser Cooling and Efficient Magnetic Compression of Molecules," Physical Review Letters **123**, 033202 (2019) `10.1103/PhysRevLett.123.033202`.

[423] H. J. Metcalf and P. van der Straten, *Laser Cooling and Trapping* (Springer-Verlag, 1999).

[424] L. Caldwell and M. R. Tarbutt, "Sideband cooling of molecules in optical traps," Physical Review Research **2**, 013251 (2020) `10.1103/PhysRevResearch.2.013251`.

[425] L. Caldwell, "Deep laser cooling and coherent control of molecules," PhD thesis (Imperial College London, Feb. 2020), 163 pp.

[426] N. B. Vilas, C. Hallas, L. Anderegg, P. Robichaud, C. Zhang, S. Dawley, L. Cheng, and J. M. Doyle, *Blackbody thermalization and vibrational lifetimes of trapped polyatomic molecules*, (Mar. 16, 2023) `http://arxiv.org/abs/2303.09424`, preprint.

[427] B. E. Sauer, J. Wang, and E. A. Hinds, "Laser-rf double resonance spectroscopy of 174YbF in the X2Σ+ state: Spin-rotation, hyperfine interactions, and the electric dipole moment," J. Chem. Phys. **105**, 7412 (1996) `10.1063/1.472569`.

[428] T. C. Steimle, D. A. Fletcher, K. Y. Jung, and C. T. Scurlock, "A supersonic molecular beam optical Stark study of CaOH and SrOH," The Journal of Chemical Physics **96**, 2556–2564 (1992) `10.1063/1.462007`.

[429] B. L. Augenbraun, Z. D. Lasner, A. Frenett, H. Sawaoka, A. T. Le, J. M. Doyle, and T. C. Steimle, "Observation and laser spectroscopy of ytterbium monomethoxide, $YbOCH_3$," Physical Review A **103**, 022814 (2021) `10.1103/PhysRevA.103.022814`.

[430]T. C. Melville and J. A. Coxon, "The visible laser excitation spectrum of YbOH: The Ã2Π-$\tilde{X}$2Σ+ transition," Journal of Chemical Physics **115**, 6974–6978 (2001) `10.1063/1.1404145`.

[431]A. Zakharova and A. Petrov, "P , T -odd effects for the RaOH molecule in the excited vibrational state," Physical Review A **103**, 032819 (2021) `10.1103/PhysRevA.103.032819`.

[432]S. A. Murthy, D. Krause, Z. L. Li, and L. R. Hunter, "New limits on the electron electric dipole moment from cesium," Physical Review Letters **63**, 965–968 (1989) `10.1103/PhysRevLett.63.965`.

[433]M. D. Swallows, T. H. Loftus, W. C. Griffith, B. R. Heckel, E. N. Fortson, and M. V. Romalis, "Techniques used to search for a permanent electric dipole moment of the 199 Hg atom and the implications for CP violation," Physical Review A **87**, 012102 (2013) `10.1103/PhysRevA.87.012102`.

[434]V. Perevalov, O. Sulakshina, and J.-L. Teffo, "Phase conventions for the rovibrational levels of linear molecules," Journal of Molecular Spectroscopy **155**, 433–435 (1992) `10.1016/0022-2852(92)90536-W`.

[435]C. di Lauro and F. Lattanzi, "PHASE ANGLES IN THE MATRIX ELEMENTS OF MOLEC-ULAR SPECTROSCOPY," in D. Papoušek, *Advanced Series in Physical Chemistry*, Vol. 9 (WORLD SCIENTIFIC, Oct. 1997), pp. 352–395, `10.1142/9789814261500_0006`.

[436]J. J. Sakurai and J. J. Napolitano, *Modern Quantum Mechanics* (Pearson, 2010).

[437]R. Mulliken, "Notation for spectra of diatomic molecules," The Physical Review **36**, 611–629 (1930) `10/bhh4fk`.

[438]J. M. Brown, I. Kopp, C. Malmberg, and B. Rydh, "An Analysis of Hyperfine Interactions in the Electronic Spectrum of AIF," Physica Scripta **17**, 55–67 (1978) `10.1088/0031-8949/17/2/003`.

[439]Z. Morbi, C. Zhao, and P. F. Bernath, "A high-resolution analysis of the $\tilde{C}$ 2A1–$\tilde{X}$ 2A1 transition of CaNH2: Pure precession in polyatomic molecules," The Journal of Chemical Physics **106**, 4860–4868 (1997) `10.1063/1.473535`.

[440]E. B. Norrgard, E. R. Edwards, D. J. McCarron, M. H. Steinecker, D. DeMille, S. S. Alam, S. K. Peck, N. S. Wadia, and L. R. Hunter, "Hyperfine Structure of the B3Pi1 State and Predictions of Optical Cycling Behavior in the X-B transition of TlF," Physical Review A **95**, 62506 (2017) `10.1103/PhysRevA.95.062506`.

[441]M. D. Allen, K. M. Evenson, and J. M. Brown, "High-resolution spectroscopic measurements of the v5 bending vibration-rotation band of HCCN in its $\tilde{X}$3Σ- state at 129 cm-1," Journal of Molecular Spectroscopy **209**, 143–164 (2001) `10.1006/jmsp.2001.8387`.

A

MATRIX ELEMENTS

I should think that you Jedi would
have more respect for the
difference between knowledge
and...wisdom.

–Dexter Jettster

In this section we provide some helpful information for factorizing and evaluating matrix elements of composite angular momenta in rotating molecules. We follow Brown and Carrington [39] and Hirota [129] primarily, and rely on some of the basic molecular structure discussions from Ch. 2.

A.1 Basis States

The basis vectors are labeled by a series of quantum numbers, which describe the eigenvalue of an associated operator. The basis vectors are tensor products across the electronic, vibrational, and rotational degrees of freedom:

$$|\psi_{\text{elec}}\rangle \otimes |\psi_{\text{vib}}\rangle \otimes |\psi_{\text{rot}}\rangle. \tag{A.1}$$

The electronic state is approximated by a sum over the spherical harmonics:

$$|\psi_{\text{elec}}\rangle = |\Lambda\rangle = \sum_L F_L Y_{L,\Lambda}(\theta, \phi). \tag{A.2}$$

Here, $\theta \in [0, \pi]$ and $\phi \in [0, 2\pi)$ are spherical coordinates angles defined in the molecule frame, and F_L are wavefunction amplitudes. For example, a Σ^+ state can be a linear combination of $c_1 s\sigma + c_2 p\sigma + \ldots$ with amplitudes c_1, c_2, etc.

For a linear triatomic molecule, the vibrational state is written as:

$$|\psi_{\text{vib}}\rangle = |v_1, v_2^{\ell}, v_3\rangle = |v_1\rangle \otimes |v_2, \ell\rangle \otimes |v_3\rangle. \tag{A.3}$$

The states of the symmetric stretching vibrations, v_1 and v_3, are described, to first order, by the 1-D harmonic oscillator wavefunctions. Meanwhile, the eigenstates of the 2-D harmonic oscillator wavefunction are provided in Ch 2, Sec. 2.1.7. The relevant form is given by:

$$|v_2, \ell\rangle = \frac{1}{\sqrt{2\pi}} e^{i\ell\phi} \Psi_{v_2,\ell}(q). \tag{A.4}$$

Here, $\ell = \vec{G} \cdot \hat{n}$, and $q = q_2 = \sqrt{q_{2x}^2 + q_{2y}^2}$, where (q_{2x}, q_{2y}) are the dimensionless normal coordinates of the bending mode, and $\phi = \tan^{-1}(q_2/q_1)$ is the bending angle associated with the normal mode. The function $\Psi_{v_2,\ell}$ is given in the main text. Using the phase convention $\delta_\ell = 0$ (see Sec. A.2), we have $\Psi_{v_2,\ell} = \Psi_{v_2,-\ell}$.

Finally, the rotational state is given in term of the symmetric top wavefunctions. The choice of symmetric top wavefunction depends on the Hund's case in use. For Hund's case (a), we have:

$$|\psi_{\text{rot}}\rangle_{(a)} = |S, \Sigma\rangle \otimes |J, P, M\rangle \tag{A.5}$$

where $P = \Sigma + \Lambda + \ell = \vec{J} \cdot \hat{n}$, and the spin $\Sigma = \vec{S} \cdot \hat{n}$ is defined in the molecule frame. The projection $M = J \cdot \hat{Z}$ is defined in the lab frame. We note J and all angular momenta containing J have anomalous commutation relations when evaluated in the molecule frame, while S is not anomalous.

For Hund's case (b), we instead have the symmetric top states $|N, M_N, K\rangle$, with $K = \Lambda + \ell = \vec{N} \cdot \hat{n}$ for linear molecules. This state is then coupled (using Clebsch-Gordan coefficients) to the space-fixed (a.k.a. defined in the lab frame) spin state $|S, M_S\rangle$ to obtain the Hund's case (b) states [160]:

$$
\begin{aligned}
|\psi_{\text{rot}}\rangle_{(b)} &= |N, K, S, J, M\rangle \\
&= \sum_{M_N, M_S} (-1)^{N-S+M} \sqrt{2J+1} \begin{pmatrix} N & S & J \\ M_N & M_S & -M \end{pmatrix} |N, M_N, K\rangle |S, M_S\rangle.
\end{aligned} \tag{A.6}
$$

The molecule frame components of N and all angular momenta containing N have anomalous commutation relations.

Special care must be taken when converting between the two bases, as the molecule frame defined components of $\vec{N}$ and $\vec{S}$ do not commute in case (b). The conversion is derived in Ref. [160], and we provide it here for reference:

$$|N, K, S, J, M\rangle = \sum_{\Sigma, P} (-1)^{N-S+P} \sqrt{2N+1} \begin{pmatrix} J & S & N \\ P & -\Sigma & -K \end{pmatrix} |S, \Sigma\rangle |J, P, M\rangle. \qquad (A.7)$$

Nuclear spins can be added using standard coupling of angular momenta with Clebsch-Gordan coefficients. Their molecule frame quantities are never anomalous. The total angular momentum is then generically written as F. For example, in Hund's case ($b_{\beta S}$), we have:

$$|N, K, S, J, I, F, M\rangle = (-1)^{I-J+M} \sqrt{2F+1}$$
$$\times \sum_{M_J, M_I} \begin{pmatrix} J & I & F \\ M_J & M_I & -M_F \end{pmatrix} |N, K, S, J, M_J\rangle |I, M_I\rangle. \qquad (A.8)$$

A.2   Parity, Time-Reversal, and Phase Conventions

We now describe the symmetry properties of molecular states transforming under discrete symmetries of Parity ($\mathcal{P}$) and Time-reversal ($\mathcal{T}$) symmetries[1]. These transformation properties are very useful, not only for symmetry violation searches, but also to understand the behavior the molecular state in general. In particular, the electric dipole operator, involved in electronic transitions as well as the Stark effect, is $\mathcal{P}$ odd. Throughout this section, we deal with various choices of phase conventions, resulting in factors such as $e^{i\delta}$. We note these phases δ are always chosen such that the factor is real ($\delta = n\pi$, n integer), and they only affect the off-diagonal matrix elements. Therefore the phases have no impact on the eigenenergies, however they can change the phase of Hamiltonian parameters or relative phases of wavefunctions.

A.2.1   Parity

We begin the total molecular state, given in Hund's case (a) by:

$$\Psi_{\Lambda, \ell, \Sigma, P} = |\Lambda; v, \ell; S, \Sigma; J, P, M\rangle. \qquad (A.9)$$

Later we can generalize to include the hyperfine spins. Generalization to Hund's case (b) is performed by dropping the S, Σ ket and performing the replacements $P \to K, J \to N$.

First, we discuss the behavior of Ψ under a parity transformation, $\mathcal{P} : f(X, Y, Z) \to f(-X, -Y, -Z)$, where f is a function of the space-fixed axes X, Y, Z. This operator is also referred to as space-fixed inversion, denoted E^*. For this section, we will use E^* to avoid confusing the projection quantum number P with the parity operator $\mathcal{P}$. Continuing, we have a few properties

---

[1]We denote these operations with different scripts to help distinguish from other symbols we use in this section.

of the parity operation: first, $(E*)^2 = 1$, which means for a state of well-defined parity, $E^*\Psi = \pm\Psi$. Further, we notice that we can obtain E^* by first reflecting about a plane in space, and then rotating by π about an axis perpendicular to the reflection plane. In the language of group theory, we can write $E^* = \sigma_{ij}R_k(\pi)$, where σ is the reflection through the plane defined by axes i, j, and $R_k(\pi)$ is a π rotation about the third axis k. Often, we are interested in the effect of E^* on the molecule frame wavefunctions, which are functions of the molecule frame $f(x, y, z)$, and naturally have the symmetry axis $\hat{n} = \hat{z}$. We note that while the angular momenta $\vec{J}$ are invariant under E^*, their projections on $\hat{n}$ *will* generically flip under E^*, as $\hat{n}$ is parity odd. The action of E^* is to reflect the *electronic and vibrational* coordinates about a plane containing $\hat{n}$, and then rotate the molecule frame by π about an axis perpendicular to the reflection plane.

At this point we pause to note there are multiple conventions for defining the action of E^* on molecular states. One convention, followed by Brown and Carrington [39] and Hirota [129], is to define $E^* = \sigma_{xz}R_y(\pi)$. This is the convention we use in this thesis, and is also used in Ref. [149]. These authors show that the effect of E^* on the Euler angles defining the molecule frame is given by $(\phi, \theta, \xi) \xrightarrow{E^*} (\pi+\phi, \pi-\theta, \pi-\xi)$. Further, they go on to show that for a function f defined in the molecule frame, such as the electronic or vibrational wavefunction, E^* is equivalent to $f(x, y, z) \xrightarrow{E^*} f(x, -, y, z)$. Since these authors are interested in the behavior of the internal molecule frame wavefunctions, which do not depend on the orientation of the molecule frame, these authors just consider the action of σ_{xz} when considering E^*.

Meanwhile, there is a separate convention given in Bunker and Jensen [140] and Zare [130]. In this convention, $E^* = \sigma_{yz}R_x(\pi)$. The resulting effect on functions of the molecule frame axes is given by $f(x, y, z) \xrightarrow{E^*} f(-x, y, z)$. We do not use this convention, but provide it for completeness.

We now present how the individual molecular wavefunction components transform under E^*. First, we begin with the symmetric top wavefunction $|J, P, M\rangle$. The most general form of the transformation includes a phase factor $e^{iP\delta_P}$, which we will return to shortly. In general we have [39, 129, 140, 149, 152, 153, 434, 435]:

$$R_x(\pi)|J, P, M\rangle = (-1)^J e^{-2iP\delta_P}|J, -P, M\rangle \tag{A.10}$$

$$R_y(\pi)|J, P, M\rangle = (-1)^{J-P} e^{-2iP\delta_P}|J, -P, M\rangle. \tag{A.11}$$

We see that M does not change, as $\vec{J}$ is parity even (see Ch. 1) and remains fixed in space. However, since $\hat{n}$ is just a vector, it will reverse under E^*, and causing the projection P to also reverse. Now we discuss the phase convention δ_P. This phase is related to the convention used to define the symmetric top wavefunctions and the action of the ladder operators $J_{X,Y}$ in the lab frame and $J_{x,y}$ in the molecule frame. The overwhelmingly accepted phase choice is that the matrix elements of J_X and J_x are real and positive, known as the Condon and Shortley phase, which takes $\delta_P = 0$. We use

this phase choice everywhere in this thesis. As a result, since we use $R_y(\pi)$, we have the following behavior under space-fixed inversion: $|J, P, M\rangle \xrightarrow{E^*} (-1)^{J-P}|J, -P, M\rangle$, agreeing with Refs. [39, 129].

Now we move on to considering the transformation properties of the vibrational state $|v, \ell\rangle$ under E^*. We follow closely the discussion in Refs. [129, 148, 149, 152, 153, 434]. We note that Ref. [149] is very helpful, but unfortunately defines the vibrational ladder operators containing both q and p with an extra factor of $\mp i$ compared to all other references. Continuing, the action of E^* is equivalent to just considering the reflection of the vibrational coordinates in a plane containing $\hat{n}$. We therefore have:

$$\begin{aligned} \sigma_{xz}|v, \ell\rangle &= e^{-2i\ell\delta_\ell}|v, -\ell\rangle \\ \sigma_{yz}|v, \ell\rangle &= -e^{-2i\ell\delta_\ell}|v, -\ell\rangle. \end{aligned} \tag{A.12}$$

Here we have introduced the the phase factor $\delta_\ell = n\pi/2$ for n integer[2]. This phase factor has consequences for the raising and lowering operators $q_\pm$ as well. In this thesis, we follow Brown [151] and Hirota [129], who take $\delta_\ell = 0$. As a result, using σ_{xz} for space-fixed inversion, we have $E^*|v, \ell\rangle = |v, -\ell\rangle$.

Continuing, we finally consider the effect of E^* on $|S, \Sigma\rangle$ and $|\Lambda\rangle$. Following Refs. [39, 129, 130], we have:

$$\begin{aligned} \sigma_{xz}|S, \Sigma\rangle &= (-1)^{S-\Sigma}|S, -\Sigma\rangle \\ \sigma_{yz}|S, \Sigma\rangle &= (-1)^{S}|S, -\Sigma\rangle \end{aligned} \tag{A.13}$$

where we have used the Condon and Shortley phase convention. Finally, for $|\Lambda\rangle$, we follow Refs. [39, 129], where the Λ wavefunction is written as a sum over spherical harmonics. This results in the following transformation properties under E^*:

$$\begin{aligned} \sigma_{xz}|\Lambda\rangle &= (-1)^{s+\Lambda}|S, -\Lambda\rangle \\ \sigma_{yz}|S, \Sigma\rangle &= (-1)^{s}|S, -\Lambda\rangle \end{aligned} \tag{A.14}$$

where $s = 1$ for Σ^- states and $s = 0$ for all other states.

Putting everything together, and taking $\delta_P = 0$ but leaving δ_ℓ, we obtain the full behavior of Ψ under space-fixed inversion $E^* = \sigma_{xz}R_y(\pi)$ as [39, 129, 434]:

$$\begin{aligned} E^*\Psi_{\Lambda,\ell,\Sigma,P} &= (-1)^{J-P}(-1)^{S-\Sigma}(-1)^{\Lambda+s}e^{-2i\ell\delta_\ell}\Psi_{-\Lambda,-\ell,-\Sigma,-P} \\ &= (-1)^{J-S-\ell+s}\Psi_{-\Lambda,-\ell,-\Sigma,-P} \end{aligned} \tag{A.15}$$

where in the second line we write $P = \Sigma + \ell + \Lambda$, set $\delta_\ell = 0$, and using $S = |\Sigma|$, we rewrite $S - 2\Sigma = -S$. This is the parity phase factor we use throughout this thesis, and is used by

---

[2]Comparing to the notation in Ref. [149], we have $2\delta_\ell = \xi - \eta - \pi$.

Brown [151] and Hirota [129]. Unfortunately, this choice means the definition of parity changes upon exciting odd number of ℓ quanta, and interactions that cause $\Delta\ell = \pm 1$ will mix symmetric and anti-symmetric parity superpositions, which we deal with in Ch. 4, Sec. 4.2. An alternative parity convention that does not mix symmetric and anti-symmetric levels is provided in Ref. [434]. The authors there propose taking $\delta_\ell = \pi/2$, which would cancel the extra factor of ℓ in the phase factor, making the definition of parity independent of of ℓ. However, we note that such a choice would modify the behavior of the $q_\pm$ matrix elements. We end our parity discussion by noting that the behavior of the wavefunction under a parity transformation is intimately related to the sign of off-diagonal parity doubling operators that can flip projection quantum numbers and cause parity splittings. We return to this point in Sec. 2.2.3.

A.2.2 Time-Reversal

Now we briefly mention the transformation properties under time-reversal, $\mathcal{T}$. Often, this operator is written as θ in the literature. We note that $\mathcal{T}$ is anti-unitary [19, 130, 133, 135, 140, 152, 435], which means it performs complex conjugation. For a general angular momentum state $|J, M\rangle$, we have [133, 140, 436]:

$$\mathcal{T}|J, M\rangle = (-1)^M |J, -M\rangle \tag{A.16}$$

$$\mathcal{T}^2|J, M\rangle = (-1)^{2M}|J, M\rangle. \tag{A.17}$$

These results can be applied to both $|S, \Sigma\rangle$ and $|\Lambda\rangle$. We see that half-integer angular momenta have $\mathcal{T}^2 = -1$, while integer angular momenta have $\mathcal{T}^2 = +1$. We note there is a phase choice hidden here for half-integer systems, and the general form is actually given by $\mathcal{T}|J, M\rangle = \eta_T (-1)^{J-M}|J, -M\rangle$. Authors take $\eta_T = i^{2J}$ to establish correspondence with the integer case, where $\mathcal{T}|J, M\rangle = (-1)^M |J, -M\rangle$, which can be derived from the properties of the spherical harmonics upon complex conjugation. An alternative choice is $\eta_T = 1$, which results in the phase factor $(-1)^{J-M}$. In the end the difference is just a factor of $(-1)^J$.

For the symmetric top wavefunctions, both P and M reverse under $\mathcal{T}$, giving us [39, 152, 435, 436]:

$$\mathcal{T}|J, P, M\rangle = (-1)^{M-P} e^{2iJ\eta_J}|J, -P, -M\rangle. \tag{A.18}$$

We note there is yet another phase choice made here, the factor of η_J. Following Brown and Carrington [39], we always choose $\eta_J = 0$.

Finally, for the vibrational state, we have [152, 435]:

$$\mathcal{T}|v, \ell\rangle = e^{2iv\delta_v}|v, -\ell\rangle \tag{A.19}$$

where we have encountered another phase factor, δ_v. It turns out both δ_v and δ_ℓ determine the phase relations of the $q_\pm$ ladder operators [149, 152]. Our choice of $\delta_\ell = 0$ and use of real, positive

$q_\pm$ matrix elements means we take $\delta_v = 0$ as well, and so $\mathcal{T}|v, \ell\rangle = |v, -\ell\rangle$. If we were to follow the alternative phase convention in Ref. [434] with $\delta_\ell = \pi/2$, we would also have to take $\delta_v = \pi/2$ to ensure the action of the $F^{\pm(\pm)}$ vibrational ladder operators are real. This would also have the consequence of adding a $(-1)^v$ phase factor in the time-reversal of $|v, \ell\rangle$. We do not follow this convention, but mention it for completeness.

Finally, we mention the time-reversal property of spherical tensor operators $T_p^k(A)$, with A some operator, which is derived in Ref. [130] by considering the Hermitian conjugate $(T_q^k)^\dagger$. We obtain:

$$\mathcal{T}T_p^k(A)\mathcal{T} = (-1)^p T_{-p}^k(A). \tag{A.20}$$

We see the spherical tensors transform analogously to the spherical harmonics under $\mathcal{T}$. This shows that raising and lowering ladder operators are not Hermitian, as they transform into each other under $\mathcal{T}$. This also gives us an intuition for the anomalous commutation relations of the molecule, where $J_\pm^{(mol)}$ seem to be reversed in their behavior. In the fixed lab frame, we see the molecule rotating one way, but in the fixed molecule frame, the lab seems to rotate in the opposite direction. Finally, Zare shows that the above relation implies $\langle J||T^k||J'\rangle^* = (-1)^{J'-J}\langle J'||T^k||J\rangle$.

A.2.3 Electronic Parity Doubling

There is an accepted convention for Λ-doubling, which was laid out by Mulliken and Christy [437]. The convention is reiterated by Brown in [165] and Brown and Carrington in [39]. This convention is given by

$$\langle \Lambda = \pm 1|e^{\pm 2i\phi_e}|\Lambda' = \mp 1\rangle = -1 \times \delta_{\Lambda,\Lambda'\pm 2}. \tag{A.21}$$

Here, $e^{\pm i\phi_e}$ is a raising/lowering operator with ϕ_e the azimuthal angle of the electrons. In this convention, a positive q_e electronic Λ-doubling parameter in a $^1\Pi$ state corresponds to the $(-1)^J$ parity level lying above the $(-1)^{J+1}$ parity level. In other words, the + parity state is below the − parity state for $J = 1$. In the YbOH $\tilde{A}$ state, $p_e + 2q_e$ is negative, and the − parity state is below the + parity state. This phase choice also manifests in the signs of the Λ-doubling Hamiltonian. When written in Hund's case (a), the $J_\pm S_\pm$ terms have a positive prefactor, and the $J_\pm J_\pm$ terms have a negative prefactor. For this work, we drop the $J_\pm J_\pm$ term in $\tilde{A}$ as its contribution is negligible.

Now we derive the Λ phase convention, following arguments from [129] and [39]. We begin by expanding $|\Lambda\rangle$ in terms of spherical harmonics:

$$|\Lambda\rangle = \sum_L F_L Y_{L\Lambda}(\theta_e, \phi_e) = \sum_L \frac{F_L}{\sqrt{2\pi}} e^{i\Lambda\phi_e} \Theta_{L\Lambda}(\theta_e). \tag{A.22}$$

Here, $\sum_L |F_L|^2 = 1$, and $\Theta_{L\Lambda}(\theta_e)$ is proportional to the associated Legendre functions $P_L^\Lambda(\cos\theta_e)$.

$$\Theta_{l,m}(\theta) = (-1)^m \sqrt{\frac{2l+1}{2} \frac{(l-m)!}{(l+m)!}} P_l^m(\cos\theta) \quad \text{for } m \geq 0 \tag{A.23}$$
$$= (-1)^m \Theta_{l,-m}(\theta) \quad \text{for } m < 0.$$

Note the function $\Theta_{L\Lambda}$ satisfies $\Theta_{L,-|\Lambda|} = (-1)^\Lambda \Theta_{L,|\Lambda|}$. This is the origin of this specific phase-convention.

Now we can evaluate the left hand side of eqn. A.21

$$\langle \Lambda | e^{\pm 2i\phi_e} | \Lambda' \rangle = \int \sin\theta_e d\theta_e d\phi_e \sum_{L,L'} F_L^* F_{L'} Y_{L\Lambda}(\theta_e, \phi_e)^* e^{\pm 2i\phi_e} Y_{L'\Lambda'}(\theta_e, \phi_e)$$
$$= \sum_{L,L'} F_L^* F_{L'} \delta_{\Lambda,\Lambda'\pm 2} \int \sin\theta_e d\theta_e (-1)^{\Lambda'\pm 2} \Theta_{L,-\Lambda'\mp 2}(\theta_e) \Theta_{L',\Lambda'}(\theta_e) \tag{A.24}$$

where we substitute $Y_{L,\Lambda}(\theta_e, \phi_e)^* = (-1)^\Lambda Y_{L,-\Lambda}(\theta_e, \phi_e)$ and performed the ϕ_e integral taking advantage of the orthogonality of exponential functions.

Now we simplify the integrand by noting we are interested in $\Lambda = \pm 1, \Lambda' = \mp 1$. This allows us to write $-\Lambda' \mp 2 = \Lambda'$. Then the remaining θ_e integral can be performed by using the orthogonality relations of the associated Legendre polynomials, which results in

$$\langle \Lambda = \pm 1 | e^{\pm 2i\phi_e} | \Lambda' = \mp 1 \rangle = \delta_{\Lambda,\Lambda'\pm 2} \sum_L |F_L|^2 (-1)^{\Lambda'} = -1 \times \delta_{\Lambda,\Lambda'\pm 2} \tag{A.25}$$

where we have substituted $|\Lambda| = 1$ in the last line and used the fact that $|F_L|^2$ is normalized.

We also note that the behavior of $Y_{L\Lambda}$ upon the transformation $\Lambda \to -\Lambda$ gives the parity properties of $|\Lambda\rangle$. The action of space-fixed inversion, i.e. the parity operator $\mathcal{P}$, is equivalent to a reflection σ_{xz} of the xz plane of the molecule. This can be derived by considering the effect of space-fixed inversion on the Euler angles relating the molecule and lab frames. Therefore we have:

$$\mathcal{P} Y_{L,\Lambda}(\theta_e, \phi_e) = \sigma_{xz} Y_{L,\Lambda}(\theta_e, \phi_e)$$
$$= Y_{L,\Lambda}(\theta_e, 2\pi - \phi_e)$$
$$= Y_{L,\Lambda}(\theta_e, \phi_e)^* \tag{A.26}$$
$$= (-1)^\Lambda Y_{L,-\Lambda}(\theta_e, \phi_e).$$

This recovers the result $\mathcal{P} |\Lambda\rangle = (-1)^\Lambda |-\Lambda\rangle$ (note a Σ^- state has an extra factor of (-1) that we do not consider).

For the full parity of the rotational wavefunction, the action of $\mathcal{P}$ must also be computed on the spin and rotational wavefunctions, which also reverse the projection quantum numbers and

contribute parity phases of $(-1)^{S-\Sigma}$ and $(-1)^{J-\Omega}$ respectively. The combination of all phase factors gives the complete case (a) parity phase without bending motion: $(-1)^{\Lambda+S-\Sigma+J-\Omega} = (-1)^{J-S}$, where we have used $|\Sigma| = S$ and $\Omega = \Lambda + \Sigma$ to simplify the exponent.

A.2.4   Vibrational Parity Doubling

For the derivation of the parity phase and matrix elements involving ℓ, we follow Ref. [129], which uses the vibrational phase conventions established by by Di Lauro and Mills [148].

The wavefunction for an isotropic 2D harmonic oscillator may be written as:

$$|v_2, \ell\rangle = \frac{1}{\sqrt{2\pi}} e^{i\ell\phi_n} \Psi_{v_2,\ell}(q). \tag{A.27}$$

Here, $q = \sqrt{q_1^2 + q_2^2}$, where (q_1, q_2) are the dimensionless, doubly-degenerate normal coordinates of the bending mode, and $\phi_n = \tan^{-1}(q_2/q_1)$ is the azimuthal angle of the bending nuclear framework. The function $\Psi_{v_2,\ell}$ is given by [148]:

$$\Psi_{v,\ell}(q) = (-1)^{(v+|\ell|)/2} N_{v,\ell} q^{|\ell|} e^{-q^2/2} L^{|\ell|}_{(v+|\ell|)/2}(q^2). \tag{A.28}$$

Here, $N_{v,\ell}$ is a normalization factor and $L^k_n(x)$ is an associated Laguerre polynomial.

The function satisfies $\sigma_{xz}\Psi_{v_2,|\ell|} = e^{-2i\ell\delta_\ell}\Psi_{v_2,-|\ell|}$. We now take $\delta_\ell = 0$ to obtain the result at the end of this section. If we were to take $\delta_\ell = \pi/2$, we would instead obtain the same result as for Λ doubling.

With $\delta_\ell = 0$ and $\Psi_{v_2,|\ell|} = \Psi_{v_2,-|\ell|}$, we now consider the matrix elements between $\ell = \pm 1$ states:

$$\langle\ell|e^{\pm 2i\phi_n}|\ell'\rangle = \int \mathrm{d}q\mathrm{d}\phi \frac{1}{2\pi} e^{-i\ell\phi_n}\Psi_{v,\ell}(q)e^{\pm 2i\phi_n}e^{i\ell'\phi_n}\Psi_{v,\ell'}(q). \tag{A.29}$$

The integration bounds are taken for $q \geq 0$ and $2\pi > q \geq 0$. The ϕ_n integral is evaluated with the orthogonality of complex exponential functions and enforces $\delta_{\ell,\ell'+2}$.

Restricting our attention to $\ell = \pm 1$ states, the $\Psi_{v,\ell}(q)$ functions depend only on $|\ell|$, and do not add an additional phase. As a result we can evaluate the remaining $\mathrm{d}q$ integral using the orthogonality relations of the associated Laguerre polynomials. We are left with

$$\langle\ell|e^{\pm 2i\phi_n}|\ell'\rangle = 1 \times \delta_{\ell,\ell'\pm 2}. \tag{A.30}$$

The difference between parity phase factors for ℓ and Λ can be traced to the difference in phase between $\Psi_{v\ell}(q)$ and $\Theta_{L\Lambda}(\theta_e)$ upon space-fixed inversion. By considering the behavior of the wavefunctions under $\phi_n \to 2\pi - \phi_n$, we see the radial q part is unaffected, giving us $\mathcal{P}|v_2, \ell\rangle = |v_2, -\ell\rangle$. When combined with rotational and spin parity phase factors, we then obtain the complete parity phase $(-1)^{J-S-\ell}$.

A.3 Additional Effective Hamiltonian Details

A.3.1 N and R Formalisms

The next discussion is inspired by Section 7.5.3 of Ref. [39]. In the effective Hamiltonian picture, we sometimes use R to represent the rotation of the molecules. However, R contains matrix elements of $L_\perp$ and $L_\perp^2$, as well as $G_{\ell\perp}$ and $G_{\ell\perp}^2$. Using the effective Hamiltonian, we can deal with the $L_\perp$ like terms, and in practice spectroscopists simply drop the $L_\perp^2$ like terms. This is called the "R^2 formalism." Another approach is also possible, called the "N^2 formalism." Once we have performed a transformation to an effective Hamiltonian, we can instead consider $\vec{N} = \vec{J} - \vec{S}$, which has no contributions from L or G_ℓ, and therefore all the matrix elements act within our subspace $\psi^{(0)}$. The rotational Hamiltonian in Hund's case (b) then becomes just $B\vec{N}^2$, while in case (a) we have $B(\vec{J} - \vec{S})^2$.

The two formalisms describe equivalent physics. However, their energy origins differ, as a result of different offsets from the rotational Hamiltonian. This means there are also differences in the centrifugal correction terms as well between the two formalisms. Consider the case (a) rotation Hamiltonian, $B(\vec{J} - \vec{S})^2$. If we expand this out, we obtain almost the same form as the R^2 approach in eq. 2.32, if we drop the $L_\perp$ and $L_\perp^2$ terms in the R^2 approach. However, we see there is still a different energy offset between the two formulations. Specifically, in the $\vec{N}^2$ formulation, we have a rotational energy offset of $-2J_z S_z$, while in the $\vec{R}^2$ formulation the offset is $-2J_z^2 - 2\Sigma^2 = -2J_z S_z - (L_z + G_{\ell z})^2$. Therefore, the two Hamiltonians differ in their electronic origins by the value $-(L_z + G_{\ell z})^2 = -K^2$. We can connect the two formalisms by writing $\vec{R} = N_x \hat{x} + N_y \hat{y} + (N_z - K)\hat{z}$. For formulae on how to convert the centrifugal and higher distortion parameters between the two approaches, see Ref. [39], Sec. 7.5.3.

In this thesis, we use the R^2 formalism. This is primarily because the paper performing spectroscopy on the YbOH origin band, $\tilde{X}^2\Sigma^+(000) \rightarrow \tilde{A}^2\Pi_{1/2}(000)$, used the R^2 form, with matrix elements[3] taken from the Appendix of Ref. [438]. As an aside, we note the R^2 formalism in case (b) generates a rotational Hamiltonian of the form $B(\vec{N}^2 - K^2)$, which satisfyingly correlates with the form of the symmetric top Hamiltonian in eq. 2.17.

A.3.2 Pure Precession

Here we describe a method for estimating the off-diagonal matrix elements of L_x and L_y, known as the Van Vleck *pure precession hypothesis* [39]. Essentially, if our molecular orbital has strong atomic character, we can think of the electronic wavefunction as a linear combination of spherical harmonics, $|\Lambda\rangle = \sum_L c_L Y_{L,\Lambda}$, with coefficients c_L. These spherical harmonics are taken to represent atomic orbitals with principle quantum number n, angular momentum l, and projection λ. In such a

---

[3]Note there is a typo in the H_{sr} matrix element in the Appendix. The authors have written $\Sigma^2 - S(S+1)$, but the correct form is $\Omega\Sigma - S(S+1)$ for a diatomic. For a $^2\Sigma$ state with $\Omega = \Sigma$, the typo has no effect.

case, the matrix elements of $L_\perp$ can be approximated as $l_\pm|n, l, \lambda\rangle = \sqrt{l(l+1) - \lambda(\lambda\pm)}||n, l, \lambda\pm 1\rangle$. The pure precession hypothesis has been shown to be a reasonable approximation in CaOH [147], SrOH [301], and even non-linear CaNH$_2$ [439]; it is no coincidence that such atom-like electronic orbitals have been found to be laser-coolable. We note the pure precession approximation will always break down at some level, and it is least applicable is when there is significant mixing of the electronic configuration of the molecule.

A.3.3 Hamiltonian Transformations

The mathematical formulation of the effective Hamiltonian derivation is that of degenerate perturbation theory with a Hamiltonian $H = H^{(0)} + V$, with V a perturbation. In a sense, we consider all of the states within $\psi^{(0)}$ to be a degenerate subspace governed by $H^{(0)}$, and consider couplings by V to states outside of our subspace at various orders of perturbation theory. The external subspaces are labeled as $\psi^{(\alpha)}$. The procedure is detailed in Ref. [39], Ch. 7, and is reproduced in Ref. [161]. The degenerate perturbation theory approach is equivalent up to third order with the contact transformation approach, also referred to as Van Vleck transformations [39], or Schrieffer-Wolff transformations. Essentially, these transformations all amount to performing a unitary transformation on the Hamiltonian given by $U = e^{iS}$, where S is Hermitian, and can be chosen such that the transformed Hamiltonian is only has diagonal matrix elements of V to first order. By repeated application of unitaries e^{iS_n}, we can chose the S_n such that the Hamiltonian is diagonal in V up to order n. We denote the various orders of the Hamiltonian after the contact transformations as $\tilde{H}_1, \tilde{H}_2, \ldots$. Matrix elements of these transformed Hamiltonians have the following forms [39] between two states i, j within $\psi^{(0)}$:

$$\langle\psi^{(0)}, i|\tilde{H}_0|\psi^{(0)}, j\rangle = E^{(0)} \tag{A.31}$$

$$\langle\psi^{(0)}, i|\tilde{H}_1|\psi^{(0)}, j\rangle = \langle\psi^{(0)}, i|V|\psi^{(0)}, j\rangle \tag{A.32}$$

$$\langle\psi^{(0)}, i|\tilde{H}_2|\psi^{(0)}, j\rangle = \sum_{\psi^{(\alpha)}\neq\psi^{(0)}} \sum_k \frac{\langle\psi^{(0)}, i|V|\psi^{(\alpha)}, k\rangle\langle\psi^{(\alpha)}, k|V|\psi^{(0)}, j\rangle}{E^{(0)} - E^{(\alpha)}}. \tag{A.33}$$

Here, $E^{(0)}$ is the vibronic origin of $\psi^{(0)}$, only dependent on the electronic and vibrational state, while $E^{(\alpha)}$ is the vibronic origin of a distant state $\psi^{(\alpha)}$ that perturbs our subspace of interest. The index k labels states in other subspaces. We note that V can contain many different terms that can all contribute cross-interactions. In other words, for $V = \sum_m V_m$, at second order we must consider $\langle V_m\rangle\langle V_n\rangle$ for all m and n. The third order and higher forms can be found in Ch. 7 of Ref. [39].

A.4 Evaluating Matrix Elements

Matrix elements are most easily evaluated for spherical tensor operators. These operators can be defined in the lab frame, denoted with a subscript p (T_p^k) or the molecule frame, denoted with

subscript q (T_q^k). For operators involving anomalous commutation, such as $\vec{J}$ or $\vec{N}$, we evaluate the operator in the lab frame. Depending on our basis, operators involving spin are more easily evaluated in the lab or molecule frame. To transform between the two frames for some operator A, we use the following formulae:

$$
\begin{aligned}
T_p^k(A) &= \sum_q \mathcal{D}_{p,q}^{(k)}(\omega)^* T_q^k(A) \\
T_q^k(A) &= \sum_p (-1)^{p-q} \mathcal{D}_{-p,-q}^{(k)}(\omega)^* T_p^k(A) \\
&= (-1)^q \sum_p (-1)^p \mathcal{D}_{-p,-q}^{(k)}(\omega)^* T_{-p}^k(A) \\
&= (-1)^q \mathcal{D}_{\cdot,-q}^{(k)}(\omega)^* \cdot T^k(A).
\end{aligned}
$$

(A.34)

In the last line, we have introduced notation $\mathcal{D}_{\cdot,-q}^{(k)}(\omega)^*$, which represents a tensor that is reduced in the lab-frame and not the molecule-frame. This notation informs us that the dot product sum is taken over the lab components, p. Writing the Wigner rotation as a dot product is useful when dealing with Hamiltonian operators expressed in the molecule frame.

Every matrix element begins unfactorized in both lab and molecule frames. The first step is to use the Wigner-Eckart theorem to factorize out the lab frame angular momentum projection, M. For example, if the total angular momentum is F, for any arbitrary operator, we have:

$$
\begin{aligned}
\langle \ldots, F, M | T_p^k(A_1, A_2, \ldots) | F', M', \ldots \rangle = \\
(-1)^{F-M} \begin{pmatrix} F & k & F' \\ -M & p & -M' \end{pmatrix} \langle \ldots, F || T^k(A_1, A_2, \ldots) || F', \ldots \rangle
\end{aligned}
$$

(A.35)

Here, $\langle \ldots F || T^k || F' \ldots \rangle$ is the reduced matrix element, which does not dependent on M. The selection rules of the 3j symbol are useful for determining the action of an operator at a glance. For example, rank $k > 0$ can mix $\Delta F \neq 0$. In free-field, we have rotational symmetry, which means F is conserved and the M sublevels are degenerate. Therefore, all free-field matrix element operators are scalars, $k = 0$, and represented as dot products. The molecule frame quantities are given as dot products with the D-matrices, as written above. Dot products can be written as a rank $k = 0$ composite spherical tensor operator:

$$
T_{p=0}^{k_{12}=0}(A_1, A_2) = \frac{(-1)^k}{\sqrt{2k+1}} T^k(A_1) \cdot T^k(A_2)
$$

(A.36)

The dot product is the rank $k = 0$ example of a composite spherical tensor operator. Such operators can be constructed from other operators using Clebsch-Gordan coefficients, essentially analogous to coupling two angular momenta. The formula for their construction is given in Brown

and Carrington eq. 5.165. The equivalent formula in Hirota (tab. 2.4, 2) has a typo in the 3j symbol's lower row.

The Wigner-Eckart theorem can be used for any rank to factorize the M dependence of the operator. For a rank $k = 0$ operator such as the dot product, the form after the Wigner-Eckart theorem can be simplified further:

$$
\begin{aligned}
\langle \ldots F, M | T_{p=0}^{k=0}(A_1, A_2) | \ldots F', M' \rangle &= (-1)^{F-M} \begin{pmatrix} F & 0 & F' \\ -M & 0 & M' \end{pmatrix} \\
&= \delta_{F,F'} \delta_{M,M'} \frac{1}{\sqrt{2F+1}} \\
&\times \langle \ldots F || T^0(A_1, A_2) || F' \ldots \rangle
\end{aligned}
\tag{A.37}
$$

Where we have expanded the Wigner 3j symbol using its analytic form. We have simplified $(-1)^{2F-2M} = 1$, as even though F and M can be half-integer, their difference is always an integer, and such a phase factor squared is always positive. In general, we have to be careful with half-integer angular momenta in phase factors, which can arise when coupling I or S. Some quantities are always integer valued, such as anything to do with orbital angular momentum: N, Λ, ℓ. Also the rank k of a spherical tensor operator is an integer.

When the spin S is defined in the molecule frame (Hund's case (a)), we can also use the Wigner-Eckart theorem to evaluate the spin matrix elements in the molecule frame, as the operators $T^1(S)_{q=\pm 1}$ follow normal commutation relations. Applying the Wigner-Eckart theorem on the spin in the molecule frame factorizes out the dependence of the projection Σ. As always, we caution that a similar evaluation of the molecule frame $T_{q=\pm 1}^1(J)$ operators will give the *wrong answer* due to anomalous commutation. The solution for these operators is to transform them to the lab-frame.

When we apply electromagnetic fields, we break the rotational symmetry of space. If the fields are only in one direction, we can take that direction to be the $\hat{Z}$ axis. The operators can be generically of higher rank, $k \geq 1$. By the Wigner-Eckart theorem, higher rank operators can mix F. However, if we maintain cylindrical symmetry about $\hat{Z}$, the projection of our applied field is always $p = 0$, and the operators will not mix M. Only when we have field projections $p \neq 0$ do we also mix M sublevels.

Now that we have factored out the M sublevel dependence, all that is left is to deal with the reduced matrix element. Eventually, we want to arrive at the form $\langle J_i || T^k(A_i) || J_i' \rangle$, where the subscript indicates the operator A_i acts on J_i. However, often the angular momentum states are composite states of coupled angular momenta, and look like: $|(J_1, J_2)J_3, \ldots (J_i, J_j)J_k \ldots\rangle$. In order to evaluate an operator acting on an J_i, we must first factor out the dependence on J_k. To factorize these matrix elements, we use tools from angular momentum algebra.

1) Matrix elements of a composite tensor operator acting on two different systems (Brown and Carrington eq. 5.169, Hirota tab. 2.4, 6ii). One system is J_1 with operator A_1, the other is J_2 with operator A_2, and the total angular momentum is $\vec{J}_3 = \vec{J}_1 + \vec{J}_2$, and the combiend operator is $T^{k_{12}}(A_1, A_2) = T^{k_1}(A_1) \times T^{k_2}(A_2)$. The factorization is then given by:

$$\langle J_1, J_2, J_{12} || T^k_{12}(A_1, A_2) || J'_1, J'_2, J'_{12}\rangle =$$

$$\sqrt{(2J_{12}+1)(2J'_{12}+1)(2k_{12}+1)}$$

$$\times \begin{Bmatrix} J_{12} & J'_{12} & k_{12} \\ J_1 & J'_1 & k_1 \\ J_2 & J'_2 & k_2 \end{Bmatrix} \tag{A.38}$$

$$\times \langle J_1 || T^{k_1}(A_1) || J'_1 \rangle \langle J_2 || T^{k_2}(A_2) || J'_2 \rangle.$$

This formula uses the Wigner 9j symbol (see Ref. [39], Ch. 5), which, like the 3j and 6j symbols, is just a way of keeping track of Clebsch-Gordan coefficients and angular momentum coupling. Many other formulae can be obtained from eq. A.38, as the 9j symbol reduces to a 6j symbol when one of its arguments is zero (see Brown and Carrington eq. 5.94). When comparing formulae, we emphasize it is important to be aware that the 3j, 6j, and 9j symbols have certain symmetries that allow for certain interchanges of rows and columns–for details, see Ref. [39].

2) The Spectator Theorem (Brown and Carrington eq. 5.174, Hirota tab. 2.4, iv), a name first coined in Ref. [440]. This formula factorizes a matrix element that only acts on one component of a coupled angular momentum, for example A_1 acting only on J_1. The formula can be obtained[4] by setting $T^{k_2}(A_2) = 1$ and $k_2 = 0$ in eq. A.38. The spectator theorem for A_1 is given by:

$$\langle J_1, J_2, J_{12} || T^k(A_1) || J'_1 J'_2 J'_{12}\rangle = \delta_{J_2,J'_2}(-1)^{J'_{12}+J_1+J_2+k}\sqrt{(2J_{12}+1)(2J'_{12}+1)}$$

$$\times \begin{Bmatrix} J'_1 & J'_{12} & J_2 \\ J_{12} & J_1 & k \end{Bmatrix} \langle J_1 || T^k(A_1) || J_1 \rangle \tag{A.39}$$

On the other hand, if the operator of interest is A_2, and acts on J_2, we instead have (Brown and Carrington eq. 5.175, Hirota tab. 2.4, iv):

$$\langle J_1, J_2, J_{12} || T^k(A_2) || J'_1 J'_2 J'_{12}\rangle = \delta_{J_1,J'_2}(-1)^{J_{12}+J_1+J'_2+k}\sqrt{(2J_{12}+1)(2J'_{12}+1)}$$

$$\times \begin{Bmatrix} J'_2 & J'_{12} & J_1 \\ J_{12} & J_2 & k \end{Bmatrix} \langle J_2 || T^k(A_2) || J_2 \rangle \tag{A.40}$$

Notice the difference in phase factor compared to the J_1 case. This distinction is important when combining multiple terms that act on different components of the coupled angular momentum, i.e.

---

[4]The reduced matrix element for 1 is given by $\langle j || 1 || j' \rangle = \delta_{j,j'}\sqrt{2j+1}$.

studying the Zeeman effect in hyperfine coupled states. As long as we are always consistent with which angular momenta is J_1 and which is J_2, the order of coupling does not matter for the end result.

3) Matrix element of a dot product acting on two different systems (Brown and Carrington eq. 5.140). This is the special case of eq. A.38 with $k_{12} = 0$ and keeping track of the difference in normalization between $T^0(A_1, A_2)$ and $T^k(A_1) \cdot T^k(A_2)$. The formula is given by:

$$\langle J_1, J_2, J_{12} || T^k(A_1) \cdot T^k(A_2) || J_1', J_2', J_{12}' \rangle =$$

$$\delta_{J_{12}, J_{12}'} \sqrt{2J_{12} + 1}(-1)^{J_1' + J_2 + J_{12}} \begin{Bmatrix} J_1' & J_2' & J \\ J_2 & J_1 & k \end{Bmatrix} \quad \text{(A.41)}$$

$$\times \langle J_1 || T^k(A_1) || J_1' \rangle \langle J_2 || T^k(A_2) || J_2' \rangle.$$

We can combine this equation with the Wigner-Eckart theorem (eq. A.41) to obtain the same formula as Brown and Carrington eq. 5.173.

4) Matrix element of a composite tensor operator formed from non-commuting operators acting on the same system (Brown and Carrington eq. 5.142, Hirota tab. 2.4, 6i). So far we have worked with operators A_1 and A_2 acting on separate systems, which commute with each other. However, sometimes we must work with coupled operators $T^{k_1}(A_1)$ and $T^{k_2}(B_1)$, which both act on the same subsystem J, and may not commute with each other. We can use the following formula to factorize the matrix element:

$$\langle J || T^k(A_1, B_1) || J' \rangle =$$

$$\sqrt{2k + 1}(-1)^{J + J' + k} \sum_{\eta'', J''} \begin{Bmatrix} k_1 & k_2 & k \\ J & J' & J'' \end{Bmatrix} \quad \text{(A.42)}$$

$$\langle \eta, J || T^{k_1}(A_1) || \eta'', J'' \rangle \langle \eta'', J'' || T^{k_2}(B_1) || \eta', J' \rangle$$

Here, η represents all other quantum numbers. This formula can be used in combination with the spectator theorem to deal with $T^k(A_1, B_1)$ acting on one part (J_1) of a combined angular momentum (J_3). We caution the reader from using Brown and Carrington eq. 5.177, which seems to be missing the extra factors from the spectator theorem. However, using the normalization of the dot product as a tensor operator and simplifying the 6j symbols analytically (Appendix D of Ref. [39]), we obtain Brown and Carrington eq. 5.178 by combining Wigner-Eckart, Spectator Theorem, and eq. A.42.

5) Switching the coupling scheme of a composite operator. Often it is useful to rewrite a composite operator in terms of a different coupling scheme. We imagine we have three spherical tensor operators, $T^1(A)$, $T^1(B)$, and $T^2(C)$. These operators can be combined to form a scalar $k = 0$ composite operator in multiple ways, which can be related to each other as follows:

$$T^2(C) \cdot T^2(A, B) = -\sqrt{\frac{5}{3}} T^1(A) \cdot T^1(C^2, B) \quad \text{(A.43)}$$

Here, $T^1(C^2, B)$ is the rank 1 tensor formed by coupling $T^2(C)$ and $T^1(B)$. This result is derived in Brown and Carrington eq. 8.459. We use this relationship when evaluating hyperfine matrix elements, as well as matrix elements involving the MQM [70].

6) Evaluating reduced matrix elements. The goal of factorizing the matrix element is to obtain terms of the form $\langle J||T^k(J)||J'\rangle$, with J an arbitrary angular momentum. These terms can be evaluated by looking up their form, given for arbitrary k in Brown and Carrington eq. 5.134. However it is instructive to run through the derivation of the reduced matrix element (provided in both Brown and Carrington and Hirota), for example for $T^1(J)$. Using the Wigner-Eckart theorem, we have:

$$\langle J, M|T^1_p(J)|J', M'\rangle = (-1)^{J-M} \begin{pmatrix} J & 1 & J' \\ -M & p & M' \end{pmatrix} \langle J||T^k(J)||J'\rangle. \tag{A.44}$$

We now consider the specific case when $p = 0$, where the operator becomes $T^1_0(J) = J_Z$. Our states are eigenstates of J_Z, so we can evaluate the matrix element as $\langle J, M|J_Z|J', M'\rangle = \delta_{J,J'}\delta_{M,M'}M$. Setting this equal to the form obtained from the Wigner-Eckart theorem, simplifying the 3j with analytic formulae (see Appendix C of Ref. [39]), we can then solve for the reduced matrix element as:

$$\langle J||T^1(J)||J'\rangle = \delta_{J,J'}\sqrt{J(J+1)(2J+1)}. \tag{A.45}$$

This approach can be generalized to higher rank k. For example, for $T^2(J)$, we obtain:

$$\langle J||T^2(J)||J'\rangle = \delta_{J,J'}\frac{(2J-1)J}{\sqrt{6}\begin{pmatrix} J & 2 & J \\ J & 0 & J \end{pmatrix}}. \tag{A.46}$$

Deriving reduced matrix elements shows how the unfactorized matrix element for all $2k+1$ components of a spherical tensor operator is proportional to a single value, the matrix element of the operator along the $\hat{Z}$ axis. This allows for the matrix element of different operators, A and B, to be related by the ratio of their reduced matrix elements, known as the replacement theorem (see Brown and Carrington eq. 5.135).

Finally, we will often encounter the reduced matrix element of the Wigner D-matrix, $\mathcal{D}^{(k)}_{p,q}(\omega)^*$. The D-matrix acts on both the lab and molecule frame projections of the symmetric top state. Since we have used the Wigner-Eckart theorem to factorize out the M dependence, the matrix element is written as $\langle J, P||\mathcal{D}^{(k)}_{.,q}||J', P\rangle$ and is referred to as "reduced in the lab-frame" [440]. Here, $P = \vec{J} \cdot \hat{n}$, and indicates the molecule-frame projection of the symmetric top wavefunction. The reduced matrix element is given by (Brown and Carrington eq. 5.186):

$$\langle J, P||\mathcal{D}^{(k)}_{.,q}||J', P'\rangle = (-1)^{J-P}\sqrt{(2J+1)(2J'+1)}\begin{pmatrix} J & k & J' \\ -P & q & P' \end{pmatrix}. \tag{A.47}$$

Here we have provided the reduced matrix element for Hund's case (a) symmetric top states. The form for Hund's case (b) is analogous, and obtained by replacing $J \to N$ and $P \to K$.

A.5 Sample Matrix Elements

This section provides a non-exhaustive list of some sample matrix elements. We use the phase factors detailed in the earlier section on phase conventions. Many other matrix elements can be found in Brown and Carrington [39], Hirota [129], and the Appendix of Ref. [438].

A.5.1 Without Hyperfine

The following matrix elements are given without hyperfine structure in Hund's case (b), which is relevant for the $\tilde{X}(010)$ bending mode with optical resolution.

The operator associated with γ_G, axial spin-rotation:

$$\langle \ell; N, S, J, M | T_{q=0}^1(N) T_{q=0}^1(S) | \ell'; N', S, J', M' \rangle$$

$$= \delta_{J,J'} \delta_{N,N'} \delta_{M,M'} \delta_{\ell,\ell'} \times \ell$$

$$\times (-1)^{J+N'+S} \begin{Bmatrix} N & S & J \\ S & N & 1 \end{Bmatrix}$$

$$\times (-1)^{N-\ell} \begin{pmatrix} N & 1 & N \\ -\ell & 0 & \ell \end{pmatrix} (2N+1)$$

$$\times \sqrt{S(S+1)(2S+1)}$$

(A.48)

The operator associated with p_G, parity-dependent spin-rotation:

$$\langle \ell; N, S, J, M | T_{2q}^2(N,S) e^{-2iq\phi} | \ell'; N', S, J', M' \rangle$$

$$= \delta_{J,J'} \delta_{N,N'} \delta_{M,M'} \delta_{\ell,\ell'+2q}$$

$$\times (-1)^{J+N+S} \sqrt{\frac{5}{2}} \begin{Bmatrix} N & S & J \\ S & N & 1 \end{Bmatrix}$$

$$\times \sqrt{S(S+1)(2S+1)}$$

$$\times \sqrt{3} \begin{Bmatrix} 2 & 1 & 1 \\ N & N & N \end{Bmatrix} \sqrt{N(N+1)(2N+1)}$$

$$\times (-1)^{N-\ell} \begin{pmatrix} N & 2 & N \\ -\ell & 2q & \ell \end{pmatrix} (2N+1)$$

$$\times \sqrt{S(S+1)(2S+1)}$$

(A.49)

The operator associated with q_G, rotational ℓ-doubling:

$$\langle \ell; N, S, J, M | T_{2q}^2(N, N) e^{-2iq\phi} | \ell'; N', S, J', M' \rangle$$

$$= \delta_{J,J'} \delta_{N,N'} \delta_{M,M'} \delta_{\ell,\ell'+2q}$$

$$\times (-1)^{J+N+S} \begin{Bmatrix} N & J & S \\ J & N & 0 \end{Bmatrix}$$

$$\times \sqrt{5} \begin{Bmatrix} 2 & 2 & 0 \\ N & N & N \end{Bmatrix} \tag{A.50}$$

$$\times \frac{1}{2\sqrt{6}} \sqrt{(2N-1)(2N)(2N+1)(2N+2)(2N+3)}$$

$$\times (-1)^{N-\ell} \begin{pmatrix} N & 2 & N \\ -\ell & 2q & \ell \end{pmatrix} (2N+1)$$

The operator associated with the lab-frame projection molecule frame dipole moment ($D_{\text{mol}} = \langle \ell; N || T_{q=0}^1(d) || \ell; N \rangle$), useful for Stark shifts:

$$\langle \ell; N, S, J, M | T_p^1(d) | \ell'; N', S, J', M' \rangle$$

$$= (-1)^{J-M} \begin{pmatrix} J & 1 & J' \\ -M & p & M' \end{pmatrix}$$

$$\times (-1)^{J'+N+S+1} \sqrt{(2J+1)(2J'+1)} \begin{Bmatrix} N' & J' & S \\ J & N & 1 \end{Bmatrix} \tag{A.51}$$

$$\times (-1)^{N-\ell} \sqrt{(2N+1)(2N'+1)} \begin{pmatrix} N & 1 & N' \\ -\ell & 0 & \ell' \end{pmatrix}$$

$$\times \langle \ell; N || T_{q=0}^1(d) || \ell; N \rangle$$

The operator associated with the lab-frame projection of the spin, useful for Zeeman shifts:

$$\langle \ell; N, S, J, M | T_p^1(S) | \ell'; N', S, J', M' \rangle$$

$$= \delta_{\ell,\ell'} (-1)^{J-M} \begin{pmatrix} J & 1 & J' \\ -M & p & M' \end{pmatrix}$$

$$\times (-1)^{J+N+S+1} \sqrt{(2J+1)(2J'+1)} \begin{Bmatrix} S & J' & N \\ J & S & 1 \end{Bmatrix} \tag{A.52}$$

$$\times \sqrt{S(S+1)(2S+1)}$$

The following matrix element is given in Hund's case (a), and describes the electronic Λ-

doubling term, $p_e + 2q_e$:

$$\langle \Lambda; S, \Sigma; J, \Omega, M | e^{2iq\theta} T_{2q}^2 (J, S) | \Lambda'; S, \Sigma'; J', \Omega', M' \rangle$$

$$= \delta_{J,J'} \delta_{M,M'} \delta_{\Lambda+2q,\Lambda'}$$

$$\times (-1)^{J-\Omega} \begin{pmatrix} J & 1 & J \\ -\Omega & -q & \Omega' \end{pmatrix} \sqrt{J(J+1)(2J+1)} \qquad \text{(A.53)}$$

$$\times (-1)^{S-\Sigma} \begin{pmatrix} S & 1 & S \\ -\Sigma & q & \Sigma' \end{pmatrix} \sqrt{S(S+1)(2S+1)}$$

Finally, we reproduce the Hund's case (a) formula for the transition dipole moment (TDM) in the E1 (dipole) approximation:

$$\langle \ell; \Lambda; S, \Sigma; J, P, M | T_p^1(d) | \ell'; \Lambda'; S, \Sigma'; J', P', M' \rangle$$

$$= \delta_{\Sigma,\Sigma'} \delta_{\ell,\ell'}$$

$$\times (-1)^{J-M} \begin{pmatrix} J & 1 & J' \\ -M & p & M' \end{pmatrix}$$

$$\times \sqrt{(2J+1)(2J'+1)} (-1)^{J-M} \qquad \text{(A.54)}$$

$$\times \sum_q \begin{pmatrix} J & 1 & J' \\ -P & q & P' \end{pmatrix} \delta_{\Lambda,\Lambda'+q}$$

$$\times \langle \Lambda || T_q^1(d) || \Lambda' \rangle$$

The last term is the reduced matrix element encoding the transition dipole integral between two electronic states.

A.5.2 With Hyperfine

We provide some example matrix elements in Hund's case (b$_{\beta J}$), relevant to hyperfine interactions. When evaluating these matrix elements, we emphasize we must be consistent with the order of coupling N and S to form J.

The matrix element for the Fermi contact interaction, proportional to the constant b_F:

$$\langle K; N, S, J, I, F, M | T^1(I) \cdot T^1(S) | K'; N', S, J', I, F', M' \rangle =$$

$$\delta_{F,F'} \delta_{M,M'} \delta_{N,N'} \delta_{K,K'}$$

$$\times (-1)^{J'+F+I} \begin{Bmatrix} J' & I & F \\ I & J & 1 \end{Bmatrix}$$

$$\times (-1)^{J+N+S+1} \sqrt{(2J'+1)(2J+1)} \begin{Bmatrix} S & J' & N \\ J & S & 1 \end{Bmatrix} \qquad \text{(A.55)}$$

$$\times \sqrt{S(S+1)(2S+1)I(I+1)(2I+1)}$$

The matrix element for the isotropic electron spin-nuclear spin dipolar interaction, proportional to the constant c:

$$\langle K; N, S, J, I, F, M | T^2_{q=0}(I, S) | K'; N', S, J', I, F', M' \rangle =$$

$$- \delta_{F,F'} \delta_{M,M'} \sqrt{\frac{5}{3}} (-1)^{F+I+J+N-K} \begin{Bmatrix} I & J' & F \\ J & I & 1 \end{Bmatrix}$$

$$\times \sqrt{(2I+1)(I+1)I} \sqrt{(2S+1)(S+1)S}$$

$$\times \sqrt{3(2J+1)(2J'+1)} \begin{Bmatrix} S & N' & J' \\ 1 & 2 & 1 \\ S & N & J \end{Bmatrix}$$

$$\times \begin{pmatrix} N & 2 & N' \\ -K & 0 & K' \end{pmatrix} \sqrt{(2N+1)(2N'+1)}$$

(A.56)

We note the electron spin magnitude S and nuclear spin magnitude I do not change in the effective Hamiltonian for a single vibronic state.

The matrix element for the electron spin projection on the lab-frame, useful for modeling the Zeeman interaction:

$$\langle K; N, S, J, I, F, M | T^1_{p=0}(S) | K'; N', S, J', I, F', M' \rangle =$$

$$= \delta_{K,K'} \delta_{M,M'} \delta_{N,N'} (-1)^{F-M} \begin{pmatrix} F & 1 & F' \\ -M & 0 & M' \end{pmatrix}$$

$$\times (-1)^{F'+J+I+1} \sqrt{(2F+1)(2F'+1)} \begin{Bmatrix} J' & F' & I \\ F & J & 1 \end{Bmatrix}$$

(A.57)

$$\times (-1)^{J+N+S+1} \sqrt{(2J+1)(2J'+1)} \begin{Bmatrix} S & J' & N \\ J & S & 1 \end{Bmatrix}$$

$$\times \sqrt{S(S+1)(2S+1)}$$

And finally, the matrix element for the molecule frame dipole moment projection on the

lab-frame, useful for modeling Stark shifts:

$$\langle K; N, S, J, I, F, M | T^1_{p=0}(d) | K'; N', S, J', I, F', M' \rangle =$$

$$= \delta_{K,K'} \delta_{M,M'} (-1)^{F-M} \begin{pmatrix} F & 1 & F' \\ -M & 0 & M' \end{pmatrix}$$

$$\times (-1)^{F'+J+I+1} \sqrt{(2F+1)(2F'+1)} \begin{Bmatrix} J' & F' & I \\ F & J & 1 \end{Bmatrix}$$

$$\times (-1)^{J'+N+S+1} \sqrt{(2J+1)(2J'+1)} \begin{Bmatrix} N' & J' & S \\ J & N & 1 \end{Bmatrix}$$

$$\times (-1)^{N-K} \sqrt{(2N+1)(2N'+1)} \begin{pmatrix} N & 1 & N' \\ -K & 0 & K' \end{pmatrix}$$

(A.58)

B

MAGNETIC FIELD CALIBRATION WITH THE HANLE EFFECT

Well if droids could think, there'd
be none of us here, would there?
                    –Obi-Wan Kenobi

We often wish to characterize and calibrate the magnetic field magnitude in the beamline. We do this by both measuring the field with a magnetometer when the vacuum chamber is vented, and by using the response of atomic Yb in the cryogenic buffer gas beam (CBGB). Specifically, we use the Hanle effect in the excited $^3P_1$ state. Briefly, the Hanle effect uses the rotation of angular momentum polarization, either in the ground or excited state, to perform magnetometry [382, 385]. Semiclassically, the excited state Hanle effect can be thought of as observing the magnetic rotation of the excited state magnetic dipole using the spatial and polarization anisotropy of the decay fluorescence. Therefore, as we will see, excited state magnetometry is limited in resolution by the excited state lifetime.

To perform magnetometry, we first excite Yb atoms on the $^1S_0 \rightarrow ^3P_1$ transition, with a ~870 ns lifetime. The even isotopes of Yb lack hyperfine structure in their ground state, and the population initially begins entirely in a pure $J = 0, M = 0$ state. Therefore the polarization of the excitation light uniquely determines the excited state sublevel. By time reversal symmetry, the polarization of the decay fluorescence is also indicative of the excited state sublevel.

Consider excitation with linearly polarized light. In the quantization axis aligned with the light, the atom is excited to the $J = 1, M = 0$ sublevel. In the language of density matrix polarization moments, the excited state has angular momentum alignment. Since the $^3P_1$ state has a $\approx 1.5\mu_B$ magnetic dipole moment, this alignment can interact with ambient magnetic fields.

Magnetic fields along the excitation light polarization only cause phase evolution of the excited state. This phase has no physical impact in the case we consider here. However, magnetic fields transverse to the light polarization axis couple states with $\Delta M = \pm 1$, causing population transfer to other M levels. In the angular momentum probability surface picture, magnetic fields cause angular momentum rotation about the field axis, which can rotate the transition dipole and change the allowed fluorescence decays.

Due to the existence of a single $M = 0$ ground state, the excited $M = 0$ and $M = \pm 1$ levels exhibit significantly different angular fluorescence distributions. In particular, the $M = 0$ excited state can only decay by emission of linearly polarized photon. The emission pattern for a $\Delta M = 0$ decay mirrors that of a linearly oscillating charge. We can semi-classically understand this connection by considering the superposition of an s and p_z atomic orbitals, with projection $M = 0$ for both states. The resulting superposition has an oscillating dipole moment, which generates optical radiation. In particular, there is no emission along the transition dipole oscillation axis, as light can only have transverse polarization. In the case of the radiating atom, the excited $M = 0$ state does not emit fluorescence along the quantization axis, which we have chosen to coincide with the light polarization axis.

In the absence of ambient magnetic fields, a PMT or camera placed along the axis of the light polarization should not detect any fluorescence photons. It is important to emphasize this effect is particularly clear in the special case of states with a single ground state. For example, the odd isotopes of Yb have additional ground states due to nuclear spin orientation, and so the value of ΔM for fluorescence decays is not as tightly constrained. This effect is important to consider when performing isotope spectroscopy on Yb atoms, as well as other $^1S_0$ states without hyperfine structure.

The presence of transverse fields causes the excited state angular momentum polarization to rotate before decaying. This rotation, equivalently population transfer to other $M \neq 0$ states, makes possible the emission of fluorescence along the axis of the excitation light polarization. Therefore, when exciting an $M = 0$ state, the magnitude of fluorescence detected by a PMT along the excitation polarization axis serves as a proxy for the strength of transverse magnetic fields.

The sensitivity of this method is proportional to the lifetime and magnetic moment of the excited state. The magnetic interaction sets a timescale for Lamor precession of the excited state,

$\omega_L = g\mu_B B$. If this timescale is shorter than the excited state radiative decay rate, $\gamma = 1/\tau$, the fluorescence decays will not be very sensitive to the magnetic field. On the other hand, if the field interaction is too fast, $\omega_L \gg \gamma$, the oscillating excited states will dephase due to the variation in the exact decay times, and the fluorescence becomes de-polarized. When $\omega_L \sim \gamma$, we can observe magnetic rotation of the excited state in the fluorescence polarization.

In the directional Hanle effect, we observe a fluorescence feature as we scan the applied magnetic field. The feature is described by a Lorentzian with a full-width half maximum (FWHM) of [382, 385]

$$B_{\text{FWHM}} = \frac{\gamma}{\omega_L} = \frac{1}{\tau g \mu_B}. \tag{B.1}$$

Therefore, with longer lifetimes or with larger g-factors, we can achieve more sensitive magnetometry. However, for a beam experiment, if the lifetime is too long, the atoms will travel an appreciable distance while in the excited state, sampling a large and inhomogenous ambient field distribution.

For Yb, the ~870 ns lifetime of the $^3P_1$ state and the g-factor $g = 1.5$ means the FWHM of the Hanle feature is $B \approx 87$ mG. In practice, the center of this Hanle feature can be determined to an accuracy of roughly ~10 mG.

C

Bending Angle Estimates

Luke, you're going to find that
many of the truths we cling to
depend greatly on our own point of
view.

–Obi-Wan Kenobi

C.1   From Parity Doubling

As mentioned in Ch. 4, the additional γ_G and p_G terms describing $\tilde{X}(010)$ mean that we can draw an analogy between picturing $\tilde{X}(010)$ as a dynamically bending linear molecule and a bent asymmetric molecule. This correspondence is possible in cases with significant vibronic mixing, and is detailed in Ref. [441], where HCCN in the ν_5 bending mode was modeled as an asymmetric rotor. Ignoring centrifugal corrections, we have the following correspondence: $B \rightarrow \frac{1}{2}(B_b + B_c)$, $q_G \rightarrow -\frac{1}{2}(B_b - B_c)$, $\gamma_G \rightarrow \epsilon_{aa}$, $\gamma \rightarrow \frac{1}{2}(\epsilon_{bb} + \epsilon_{cc})$, $p_G \rightarrow \frac{1}{2}(\epsilon_{bb} - \epsilon_{cc})$. Here, $\epsilon_{\alpha\beta}$ is the generalized spin-rotation tensor, B_b and B_c represent the rotational constants of the b and c axes of the asymmetric rotor, with $c = y$ pointing out of the plane of the bent molecule and $b = x$ pointing perpendicular to the Yb-O bond and in the plane of the bent molecule. The remaining axis a is identified with the z axis of the molecule, pointing along the Yb-O bond.

Using this correspondence, we can estimate the H bending angle θ relative to the Yb-O bond. We define this angle as the deviation from linearity, i.e. $\theta = 0$ is the nominally linear YbOH configuration.

First, we fix $r_{\text{YbO}} = 2.0397$ Å and $r_{\text{OH}} = 0.9270$ Å as in the ground $\tilde{X}(000)$ state [290], and we assume the O atom does not bend. These approximations treat the bonds as infinitely stiff, which is reasonable for the O-H bond with high stretching frequency, but will likely breakdown for the Yb-O bond. We then construct and diagonalize the moment of inertia tensor for the three masses, and solve for the value of θ that satisfies $q_G = -\frac{1}{2}(B_b - B_c)$. We obtain $\langle\theta\rangle \approx 32°$ for the bending angle in YbOH $\tilde{X}(010)$.

Alternatively, the bending angle can be approximated by equating the vibrational bending energy of the linear molecule to the rotational energy about the $a = z$ axis of a nearly prolate bent rotor: $\omega_2 \approx 2B_a$. Making the harmonic approximation $\omega_2 \approx T_0$ and diagonalizing the moment of inertia tensor, we obtain $\langle\theta\rangle \approx 22°$.

These two approximations provide a picture of bending YbOH with $\langle\theta\rangle \approx 22°–32°$. In comparison, in CaOH approximating the bending potential as harmonic and using the Virial theorem, we obtain a bending angle of $\langle\theta\rangle \approx 10°$ [147]. We note that in all of these cases, a large bending angle may not correspond to a large normal coordinate deviation q–that is, the potential is expected to remain harmonic.

C.2   From Hyperfine

We use the value obtained in Ch. 5, $c_{(010)} = 3.49(38)$ MHz, and the value from Ref. [290], $c_{(000)} = 2.46(48)$ MHz, with parentheses indicating 2-σ error bars. Recall the c term can be written as [39, 157]:

$$c \propto \left\langle \frac{3\cos\theta'^2 - 1}{r^3} \right\rangle \tag{C.1}$$

Here, r is the separation between the electron and nuclear spin, and θ' is the angle between the separation vector and the internuclear axis. We use a prime to distinguish this angle from the bending angle, θ.

To make an estimate, we fix the bond lengths and assume the bending motion only consists of only the H bending off axis. We will parameterize the bending angle relative to the internuclear axis as θ, where $\theta = 0$ corresponds to the linear limit. Further, we assume the electron spin is fixed at the Yb nucleus. We can then compute the ratio of c values as:

$$\frac{c_{(010)}}{c_{(000)}} \approx \frac{(r_{\text{YbO}} + r_{\text{OH}})^3 \left(4r_{\text{YbO}}^2 + r_{\text{OH}}^2 + 8r_{\text{YbO}}r_{\text{OH}}\cos\theta + 3r_{\text{OH}}^2\cos(2\theta)\right)}{4\left(r_{\text{YbO}}^2 + r_{\text{OH}}^2 + 2r_{\text{YbO}}r_{\text{OH}}\cos\theta\right)^{5/2}} \tag{C.2}$$

We fix the bond lengths to the $\tilde{X}(000)$ values[1] from Ref. [290], which are $r_{\text{Yb-O}} = 2.0397$ Å and $r_{\text{O-H}} = 0.9270$ Å. Using the experimentally determined ratio $c_{(010)}/c_{(000)} \approx 1.42 \pm 0.18$, we obtain

---

[1]Only the Yb-O bond distance is determined from data. The O-H bond distance is assumed to be the same as BaOH.

$\theta \approx 75°{}^{+10°}_{-15°}$. This corresponds to quite a significant bending angle, and we caution the reader from interpreting this number further. Clearly our approximations of stiff bonds and non-bending O atom are breaking down.

D

LINE LIST

What about the Droid attack on the
Wookiees?

–Ki-Adi-Mundi

D.1   Science State Lines

The lines are listed in Tables D.1 and D.2. Transition notation is given in Sec. 4.1.3.

Table D.1: Observed lines, ground states quantum numbers $(N'', J'', \mathcal{P}'')$, excited states quantum numbers $(J', \mathcal{P}')$, observed positions, and residuals of $\tilde{X}^2\Sigma^+(010) \to \tilde{A}^2\Pi_{1/2}(000)$ band of YbOH. Line notation is described in Sec. 4.1.3. There are in total 38 lines assigned to 39 transitions as the $^Q R_{12}^-(1)$ and $^P Q_{12}^-(5)$ lines are overlapped. The R lines are on the next page. The fit residual is 6.1 MHz.

Line	$N'', J'', \mathcal{P}''$	$J', \mathcal{P}'$	Obs. (cm^{-1})	Obs. - Calc. (MHz)
$^O P_{12}^+$	2, 3/2, +	1/2, −	17002.4883	4.4
	3, 5/2, +	3/2, −	17002.4312	−7.4
	4, 7/2, +	5/2, −	17000.6512	−2.7
$^O P_{12}^-$	2, 3/2, −	1/2, +	17002.9232	−0.1
	3, 5/2, −	3/2, +	17001.5614	14.9
$^P P_{11}^+$	1, 3/2, +	1/2, −	17003.4683	−0.2
	3, 7/2, +	5/2, −	17002.6114	1.7
	5, 11/2, +	9/2, −	17001.8212	12.2
$^P P_{11}^-$	1, 3/2, −	1/2, +	17003.9070	−2.2
	2, 5/2, −	3/2, +	17003.0314	−3.6
	4, 9/2, −	7/2, +	17002.2076	−4.8
$^P Q_{12}^+$	2, 3/2, +	3/2, −	17003.9039	−8.8
	3, 5/2, +	5/2, −	17002.6012	−5.8
	5, 9/2, +	9/2, −	17001.8046	12.7
$^P Q_{12}^-$	1, 1/2, −	1/2, +	17003.9053	−5.8
	2, 3/2, −	3/2, +	17003.0250	−5.0
	3, 5/2, −	5/2, +	17003.9208	−5.3
	5, 9/2, −	9/2, +	17004.0076	13.3
$^Q Q_{11}^+$	1, 3/2, +	3/2, −	17004.8846	3.3
	3, 7/2, +	7/2, −	17005.9150	−13.0
	5, 11/2, +	11/2, −	17007.0123	−3.5
$^Q Q_{11}^-$	1, 3/2, −	3/2, +	17004.0091	5.5
	2, 5/2, −	5/2, +	17005.3917	−0.7
	4, 9/2, −	9/2, +	17006.4556	−1.6

E

POLARIZATION MOMENTS

Chewie! Take the professor in the
back and plug him into the
hyperdrive.

–Han Solo

This discussion follows Ref. [216]. Angular momentum polarization refers to the creation of an anisotropic distribution for the direction of an angular momentum J in space. For now, consider a single J level with degenerate sublevels, M. The molecular state is described by a density matrix:

$$\rho = \rho_{ij} \sum_{ij} |J, M_i\rangle\langle J, M_j| \tag{E.1}$$

Note, we use a density matrix to allow us to incorporate coherent and incoherent polarization, in other words to consider both pure and mixed states. We also note that the density matrix can be represented in real space as an angular distribution, $\rho(\theta, \phi)$. Physically, such a distribution encodes the probability of measuring the angular momentum J pointing along a given direction, (θ, ϕ).

The state vectors $|J, M\rangle$ transform under rotations according to the Wigner D-matrices, typically as trigonometric functions of the Euler rotation angles. Naturally, we can instead cast the density matrix in terms of spherical tensor operators, which transform in a standard manner under rotations (in particular, z rotations just add a phase). This is equivalent to performing a multipole expansion of the density matrix $\rho(\theta, \phi)$. The density matrix can therefore be written in a spherical form:

$$\rho_q^k \propto \sum_{M_i, M_j = -J}^{J} \langle J, M_i; k, q | J M_j \rangle \rho_{ij} \tag{E.2}$$

The various ρ_q^k components in the multipole expansion of the density matrix are referred to as the polarization moments. The interpretation of these moments is useful in understanding angular momentum polarization.

Consider first the lowest order multipole, ρ_0^0. This is proportional to the total population summed over all the M states; essentially the scaled trace of the density matrix. If a molecular state occupies an equal distribution of all M, the angular momentum distribution is isotropic as the spherical harmonics are complete. This is referred to as an unpolarized sample, and it only has non-zero ρ_0^0.

The next multipole, ρ_q^1, describes the angular momentum *orientation*. An oriented angular momentum behaves like a single headed arrow, in analogy with a magnetic dipole moment: if the angular momentum is fixed to an associated magnetic dipole moment, a non-zero orientation is analogous to a non-zero magnetization, i.e. there is some axis n with $\langle J_n \rangle \neq 0$. The quantity ρ_0^1 describes longitudinal orientation, while the $\rho_{\pm 1}^1$ components describe transverse orientations. Typically, oriented states can be formed by absorption/optical pumping of a sample using circularly polarized light, the polarization vector of which can be naturally decomposed into a spherical basis.

The last multipole we will consider is ρ_q^2, which describes the angular momentum *alignment* (also referred to as a quadrupole moment). Whereas orientation describes a vector direction in space, alignment describes a plane in space along which the angular momentum probability is distributed, and an aligned angular momentum behaves like a double headed arrow. Alignment describes population in equal mixtures of $\pm M$ sublevels, while orientation describes an asymmetry in the M population distribution. The superposition state used by the ACME and JILA experiments is a state with non-zero alignment but zero orientation: in other words for some axis n, $\langle J_n \rangle = 0$, but $\langle J_n^2 \rangle \neq 0$.

There are of course higher order moments, but for our purposes we will not consider them. We will only note that the existence of a given rank k of angular momentum polarization requires coherence between states separated by $\Delta M = k$ when written in any rotated frame. This is another way to think of the multipole moments: they characterize the spatial coherence of angular momentum states that is invariant under rotation.

Finally, we often visualize the density matrix using an angular momentum probability surface. This 3-D probability surface is defined as $P_\rho(\theta, \phi) = \langle J, M_{(\theta, \phi)} = J | \rho(\theta, \phi) | J, M_{(\theta, \phi)} = J \rangle$, where $M_{(\theta, \phi)} = \vec{J} \cdot \hat{r}$, where $\hat{r}$ is the unit vector pointing along (θ, ϕ). This expectation value represents

the probability of measuring the largest possible angular momentum projection, J, pointing along a given direction $\hat{r}$. The distribution P_ρ provides powerful, intuitive insight into the behavior of angular momenta under applied fields. For example, a magnetic field simply rotates P_ρ about the field axis. Meanwhile electric fields cause inversion of any orientation in P_ρ, and converting angular momentum orientation to alignment. Further details can be found in Ref. [216].

<div style="text-align: right">

A P P E N D I X

F

</div>

MQM Science Chamber Designs

Who's more foolish, the fool or the
fool who follows him?
          –Obi-Wan Kenobi

In this appendix we provide information about the science chamber made to perform measurements of the nuclear magnetic quadrupole moment (NMQM) in ^{173}YbOH.

F.1   Layout

The science chamber is constructed by connecting together two 9x9x9 inch, IdealVacuum modular, cubic vacuum chambers. Each cube consists of an aluminum frame with titanium helicoils, and each exterior face of the frame has an aluminum plate attached with titanium fasteners and sealed with an o-ring. Some plates have feedthroughs to allow for molecule beam access, optical access, and electrical access. The use of titanium fasteners and helicoils ensures no residual magnetism[1]. Unlike most of the prototype vacuum chambers used in this thesis, the interior of the MQM science chamber is *not* painted black with Alion MH2200, as it contains manganese ferrite and is measurably magnetic.

An annotated render of the chamber design is shown in Figure F.1. We provide information here on the components inside the science chamber, namely the electric field plates and the fluorescence collection optics.

---

[1]We initially tried brass C260 fasteners, which are also non-magnetic, but Yuiki Takahashi and Chi Zhang found the chamber was leaky.
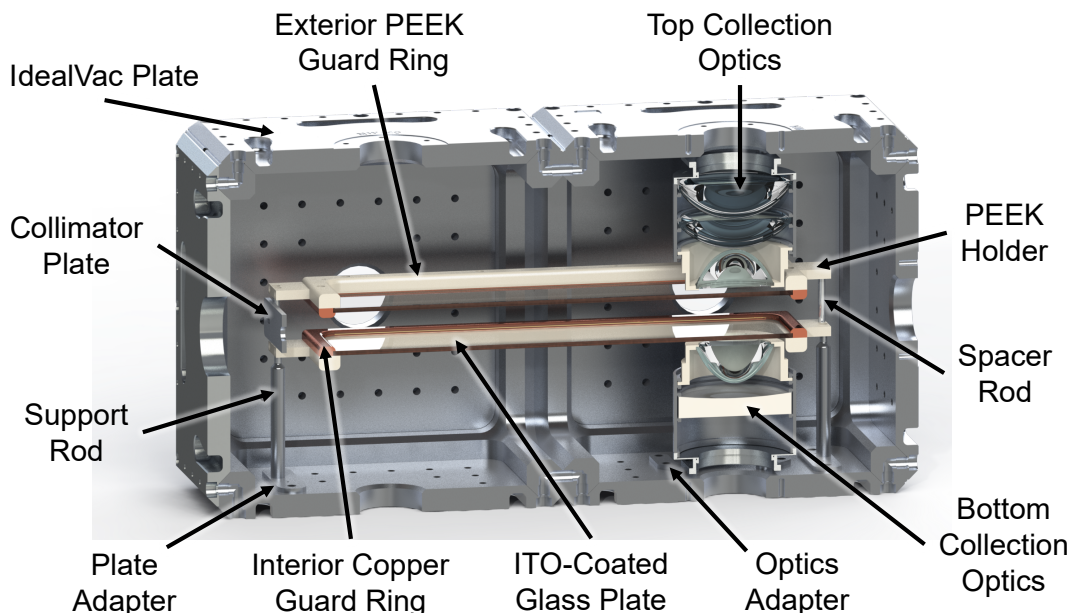
Figure F.1: Annotated render of a cut-away view of the MQM science chamber. The molecule beam travels from left to right. Unless stated otherwise, all parts are aluminum 6061 construction. The bottom collection optics retroreflects the fluorescence light. The top collection optics focuses the light into a light pipe, not pictured.

The field plates themselves are Pilkington Optiwhite glass, with dimensions 4-inch wide, 12-inch long, and 0.118-inch (3 mm) thick. One side of the plates is coated with a ~30.2 nm layer of Indium Tin Oxide (ITO), which is a conductor. The ITO layer has a specified sheet resistance of 100 Ω. According to the manufacturer, Delta Technologies, the ITO transmission is ≈87% around 577 nm. The conductor sides of the plates are separated by 1 inch in the design.

To secure the plates, they are sandwiched between an interior and exterior guard ring. The interior guard ring is of copper construction. Since copper can oxidize, the copper is coated with a 1 μ-inch thick layer of gold[2]. The gold-coated interior guard ring presents a smooth conductive surface for the molecule beam passing through the chamber[3]. The ITO side of the glass plate rests on the lip of the interior guard ring, and is secured via PEEK set screws pushing down on the non-conductive glass side. The set screws are threaded through the PEEK exterior guard ring.

The PEEK exterior guard ring is attached to the interior guard ring via PEEK fasteners that screw into the copper. We used PEEK for the exterior guard ring construction to avoid large fields at corners and near the collection optics. Other than the set screws securing the glass, there is no direct contact of the PEEK exterior guard ring with the glass plate. While most of the fasteners connecting the interior and exterior guard rings are PEEK, at least two fasteners per plate

---

[2]Coating performed by AOTCO inc. with no intermediate nickel layer.
[3]We avoid line of sight from the molecules to insulating surfaces, which can build up patch potentials.

are titanium, providing a conductive path that allows us to apply voltages to the ITO glass and separately monitor the voltage.

The exterior guard ring has threaded holes on the sides used to connect and affix the guard ring to the chamber. On the short sides of the exterior guard ring, we attach a PEEK holder using titanium fasteners. Initially, we used vented PEEK fasteners, but the PEEK on PEEK contact was too slippery and did not provide sufficient rigidity. Since the titanium fasteners are not vented, we vented the threads by drilling small vent holes into the top of the PEEK guard ring[4]. The PEEK holders have counterbored holes for spacer rods to fix the distance between the two plates, as well as support rods holding up the entire two-plate apparatus. For these connections, we also reverted to titanium fasteners, and added vent holes in the spacer and support rods after the fact.

The spacer rods and the PEEK holders set the interior distance between the two ITO coated plates to be 1 inch. The PEEK holders have a handedness (left/right), owing to the different diameters of the support and spacer rods; the spacer rods are connected to the exterior holes, while the support rods are connected to the interior holes. The support rods have fillets to reduce stray electric fields from corners, and are designed to center the molecule beam between the two glass plates. The support rods connect to the hole pattern of the IdealVac chamber via PEEK set screws threading into aluminum adapter plates, which have 1/8-inch thickness.

In the front of the plate assembly, the molecule beam is collimated by a collimating plate with a 3/8-inch diameter collimating hole. The hole is countersunk to redirect colliding gas particles away from the interaction region. The collimator plate is attached via slotted holes to commercial aluminum shaft collars that clamp onto the spacer rods. The combination of slotted holes and movable shaft collars allow the adjustments of the collimator position.

While the plates are separated by a 1-inch vertical distance, the clear space between the plates is limited to 0.75 inch by the interior guard rings. This clear aperture allows us to send laser beams, through the gap between the plates, to prepare and readout the molecules. There are two regions for transverse laser access, separated by a horizontal distance of 9 inches. For a 200 m/s molecule beam, this gives us a coherence time of $\approx$1.1 ms.

In the downstream optical region, we will readout the molecules with laser-induced fluorescence. We have two collection optics stacks to collect as much of the fluorescence as possible. All lenses are anti-reflection (AR)-coated. The bottom optics stack[5] consists of a $f = 52$ mm aspheric lens with a 50 mm diameter, and an $f = 150$ mm concave retro-reflecting mirror with a 75 mm diameter. The aim of the bottom stack is to reflect fluorescence back through the top optics

---

[4]The holes are not shown in the technical drawing. They were made with a no. 50 drill bit.
[5]Asphere: CVI LAG-52.0-33.0-C -SLMF-400-700; Mirror: ThorLabs CM750-150-E02.

stack. The top optics stack[6] consists of the same $f = 52$ mm asphere, but followed by two 75-inch diameter plano-convex lenses, a $f = 100$ mm lens and a $f = 85$ mm lens. The lenses focus the collected fluorescence into a 3/4-inch diameter light pipe (not shown), which transports the light out of the chamber and eventually to a photo-multiplier tube.

The aspheric lenses are held in a custom PEEK lens tube, secured via EPO-TEK 302-3M optical epoxy. We use PEEK for this lens tube to reduce stray electric fields that would arise when bringing metal parts close to the field plates. The flat face of the aspheric lens is 3.5 mm away from the exterior face of the glass plates. The PEEK lens tube is then secured to a commercial, aluminum lens tube[7] with 3-inch diameter. The aluminum lens tube is unanodized to prevent trapped volumes. The PEEK lens tube and the rest of the optics are secured inside the aluminum lens tube using anodized retaining rings, which prevent galling with the unanodized threads. Small holes are drilled into the side of the aluminum lens tube to prevent trapped volumes. The 3-inch lens tube is connected to IdealVacuum chamber using two unanodized aluminum adapters[8], followed by a custom, 1/8-inch thick aluminum adapter to connect to the IdealVac plate hole pattern. This adapter is similar to that used to connect the support rod to the chamber.

To simulate the collection optics performance, we use the ray-tracing software LightTools. Optics part designs are obtained either from the internal LightTools library or by downloading 3-D CAD files from vendors and setting the appropriate materials composition to obtain the correct index of refraction. We model the molecules as a uniform cylindrical volume of emitters, with 3/8-inch diameter and 3/8-inch length, representing the size of the laser beam cross section with the molecular beam. The collection efficiency is defined as the fraction of emitted rays that make it to the exit face of the 3/4-in diameter light pipe. Simulations indicate the collection efficiency is 19.4% with an optimal light pipe distance of 24.6 mm, measured from the light pipe entrance face to the flat side of the LA1740-A lens in the top collection optics stack[9]. The final simulations track both transmitted and reflected rays, and include quarter-wave AR coating, Fresnel losses, finite ITO transmission with angle dependence[10] and finite apertures from the lens tube mounting. Without the retro-reflecting optics, the simulated efficiency is 13.6%. We can compare these values to the efficiencies for collecting the fluorescence from a point source, which are 22.1% with the retro-reflector and 14.4% without. Sample simulation results are shown in Figure F.2

F.2 Technical Drawings

---

[6]Asphere: CVI LAG-52.0-33.0-C -SLMF-400-700; PCX lenses: ThorLabs LA1238-A, ThorLabs LA1740-A.

[7]ThorLabs SM3L20, unanodized. The retaining rings are SM3RR.

[8]ThorLabs SM3A2 and SM2F1.

[9]Alternatively, a distance of 7.3 mm (in the exterior direction) from the face of the IdealVacuum frame.

[10]We use the internal LightTools coating library to model the ITO surface, which has ~82% transmission on normal incidence at 577 nm.
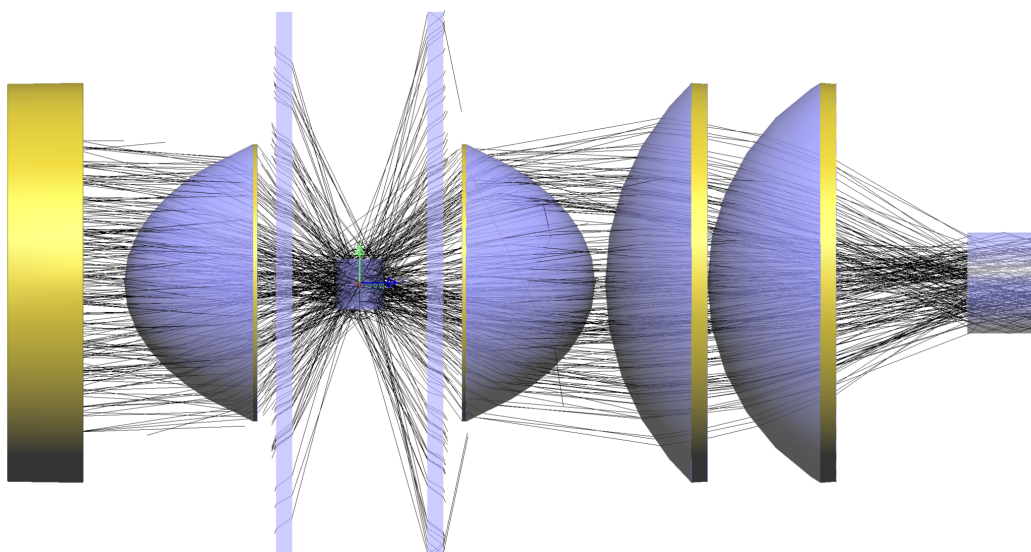
Figure F.2: Simulations of the fluorescence collection setup for the science chamber. Simulations were performed using LightTools. The diagram here only shows transmitted and totally-internally reflected rays. See main text for details.
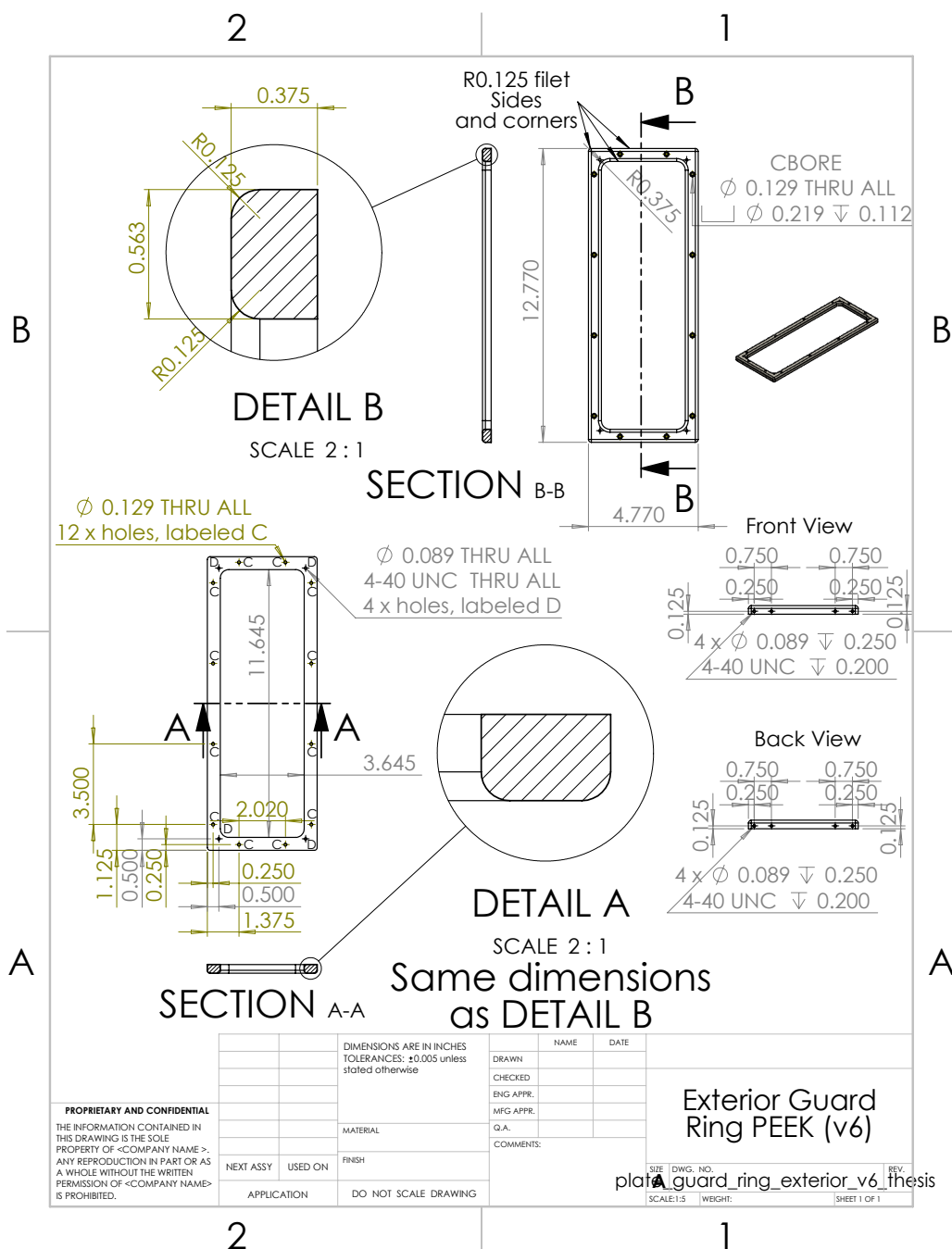
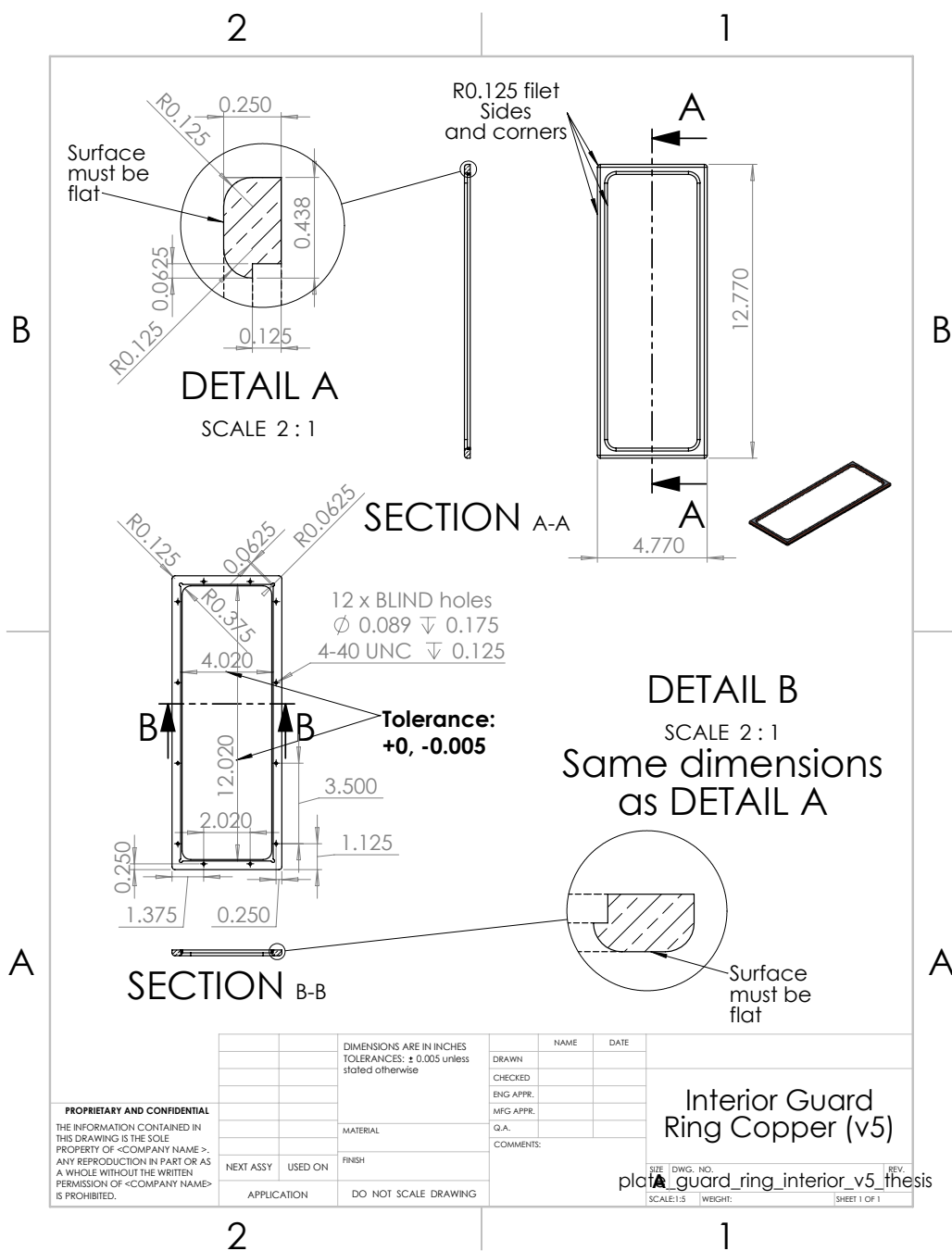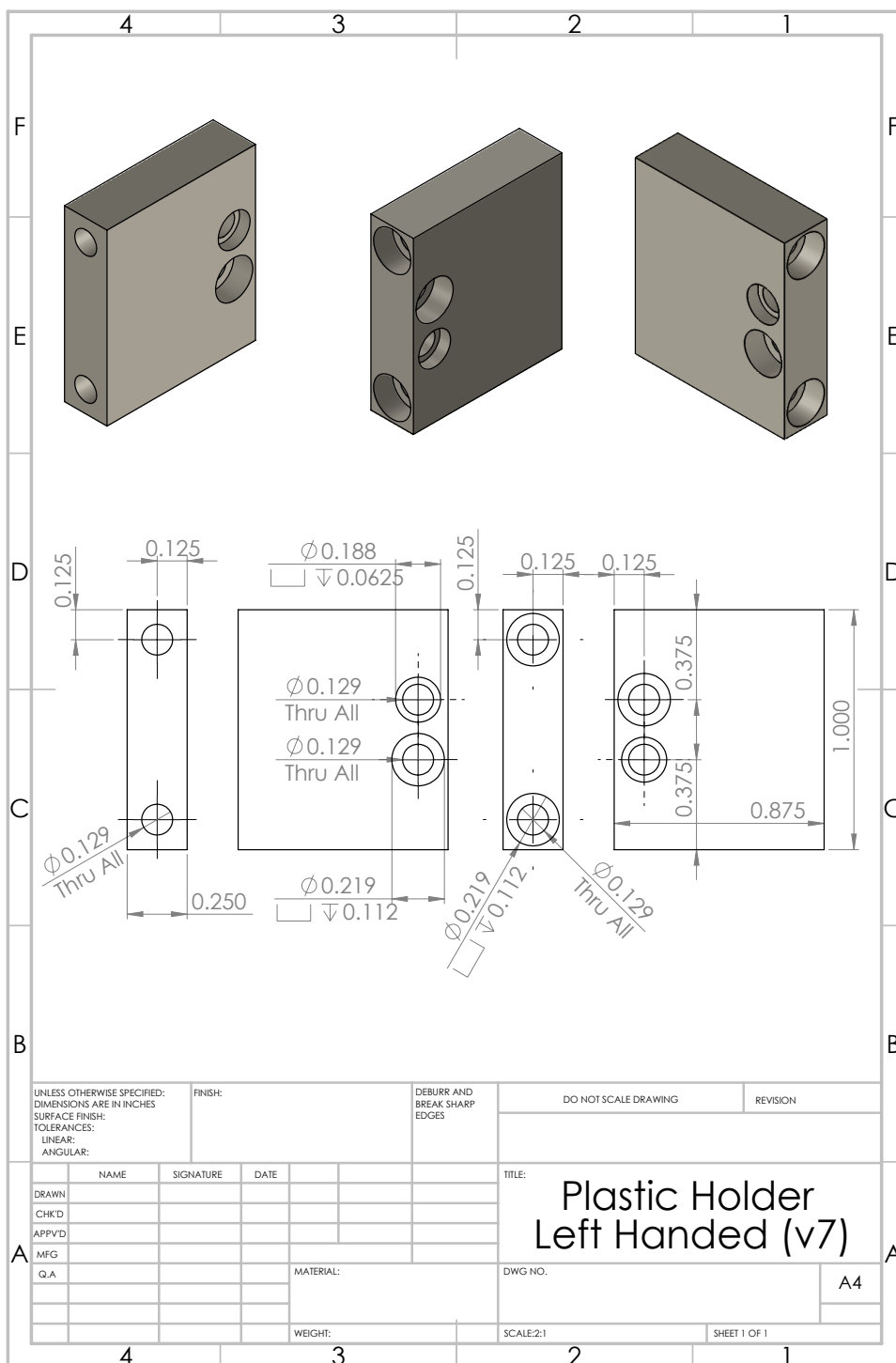Figure F.3: Design of the exterior PEEK guard ring holding the E-field plates. See main text for details.

321

Figure F.4: Design of the interior copper guard ring holding the E-field plates. See main text for details.

Figure F.5: Design of the left-handed PEEK holder connecting the exterior guard ring to the support and spacer rods. See main text for details.
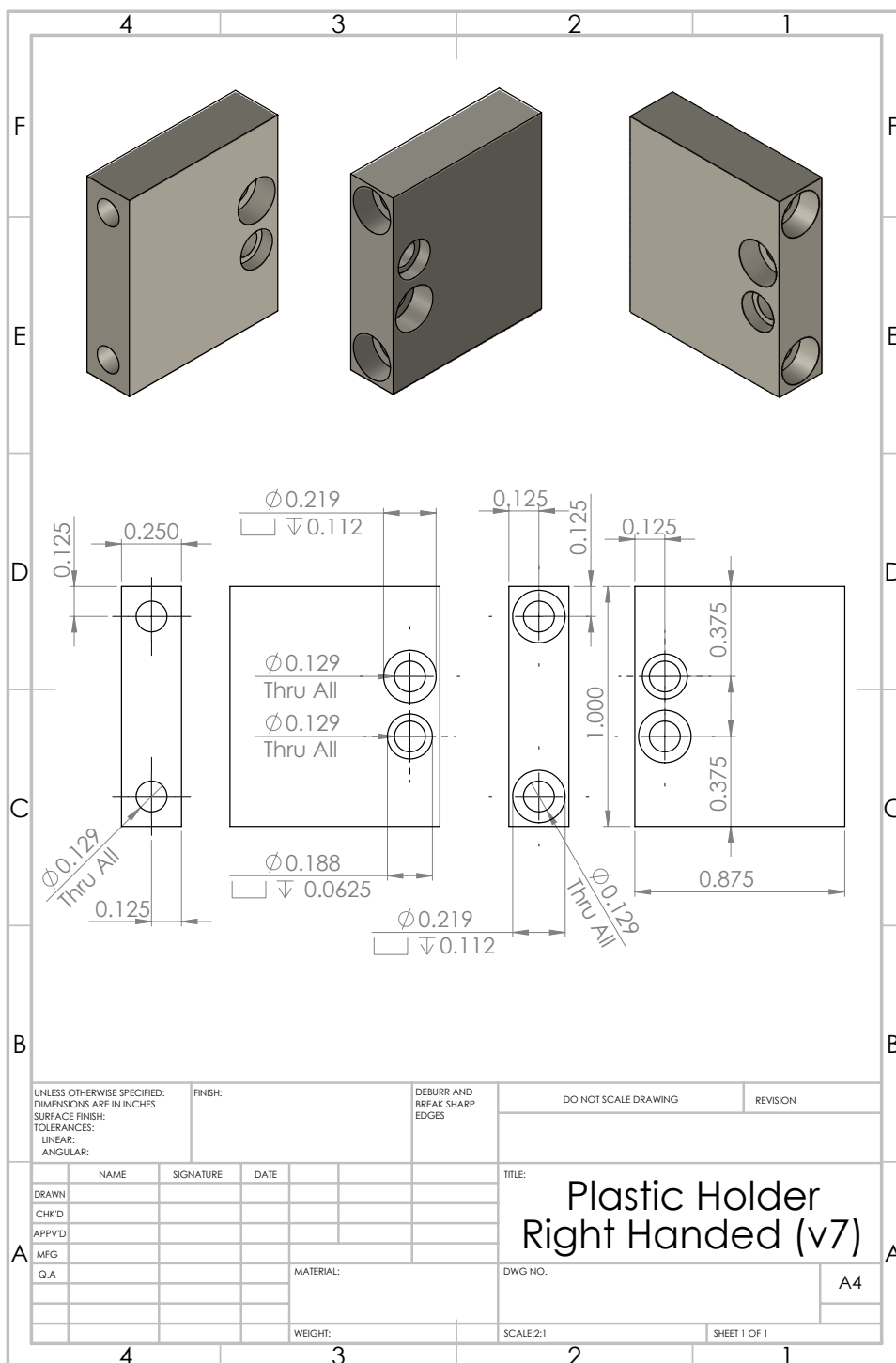
Figure F.6: Design of the right-handed PEEK holder connecting the exterior guard ring to the support and spacer rods. See main text for details.
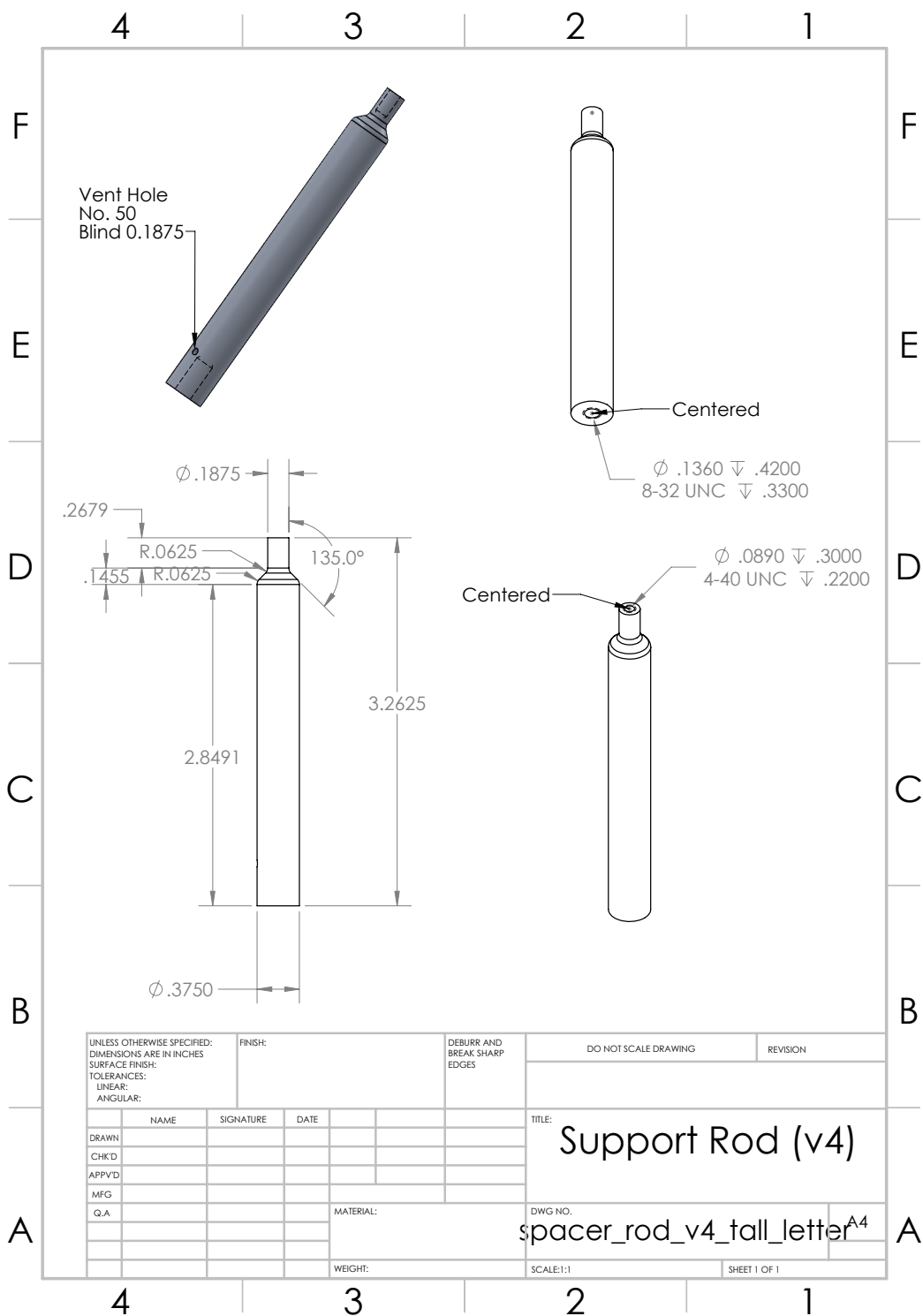
Figure F.7: Design of the support rods holding up the E-field plates. See main text for details.
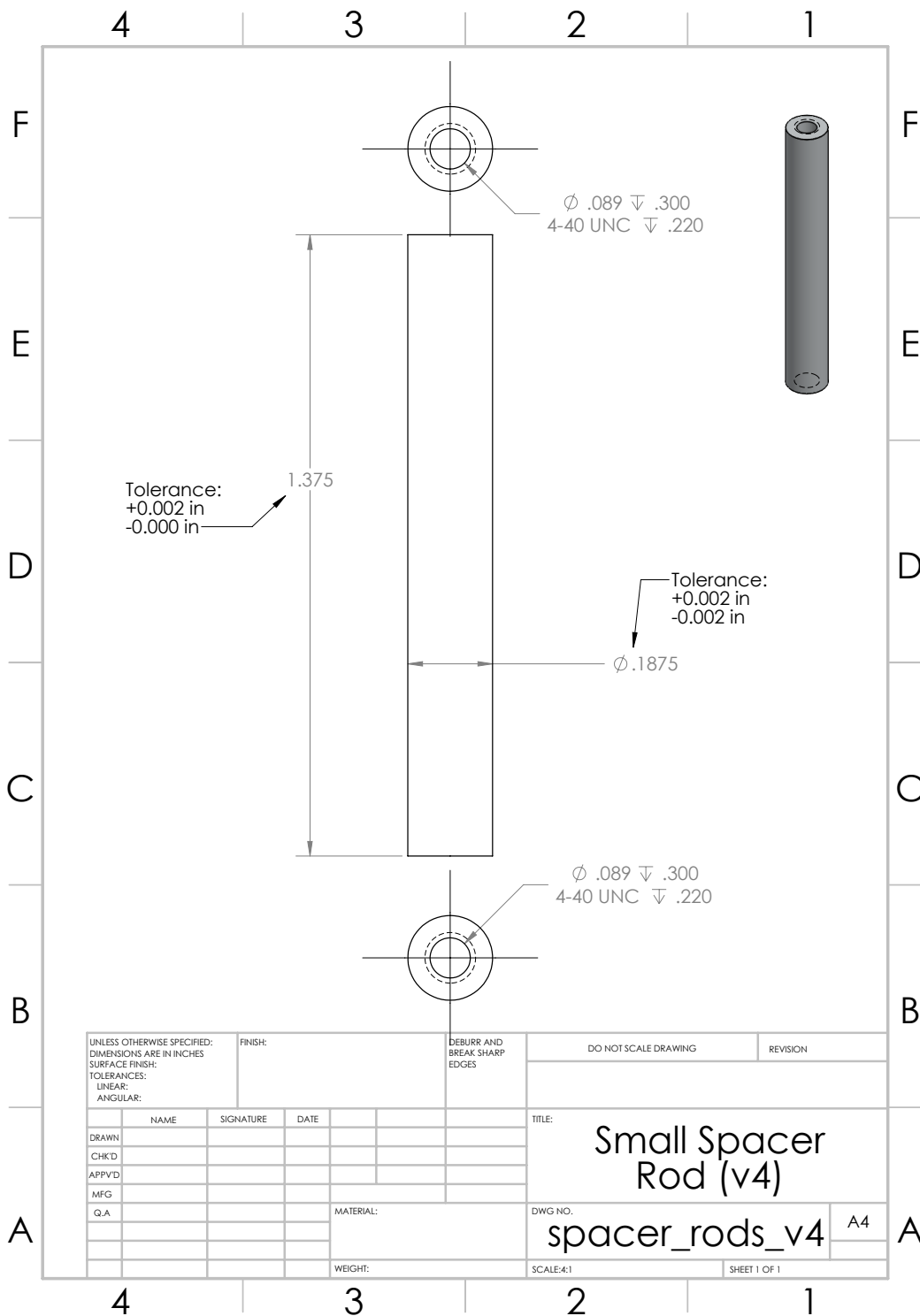
4   3   2   1

F   F

∅ .089 ⊼ .300
4-40 UNC ⊼ .220

E   E

Tolerance:
+0.002 in
-0.000 in

1.375

D   D

Tolerance:
+0.002 in
-0.002 in

∅ .1875

C   C

∅ .089 ⊼ .300
4-40 UNC ⊼ .220

B   B

UNLESS OTHERWISE SPECIFIED: DIMENSIONS ARE IN INCHES SURFACE FINISH: TOLERANCES: LINEAR: ANGULAR:	FINISH:		DEBURR AND BREAK SHARP EDGES	DO NOT SCALE DRAWING		REVISION

	NAME	SIGNATURE	DATE			TITLE:	
DRAWN						Small Spacer Rod (v4)	
CHK'D							
APPV'D							
MFG							
Q.A			MATERIAL:		DWG NO. spacer_rods_v4	A4	
			WEIGHT:		SCALE:4:1	SHEET 1 OF 1	

A   A

4   3   2   1

Figure F.8: Design of the spacer rods that separate the two E-field plates. See main text for details.
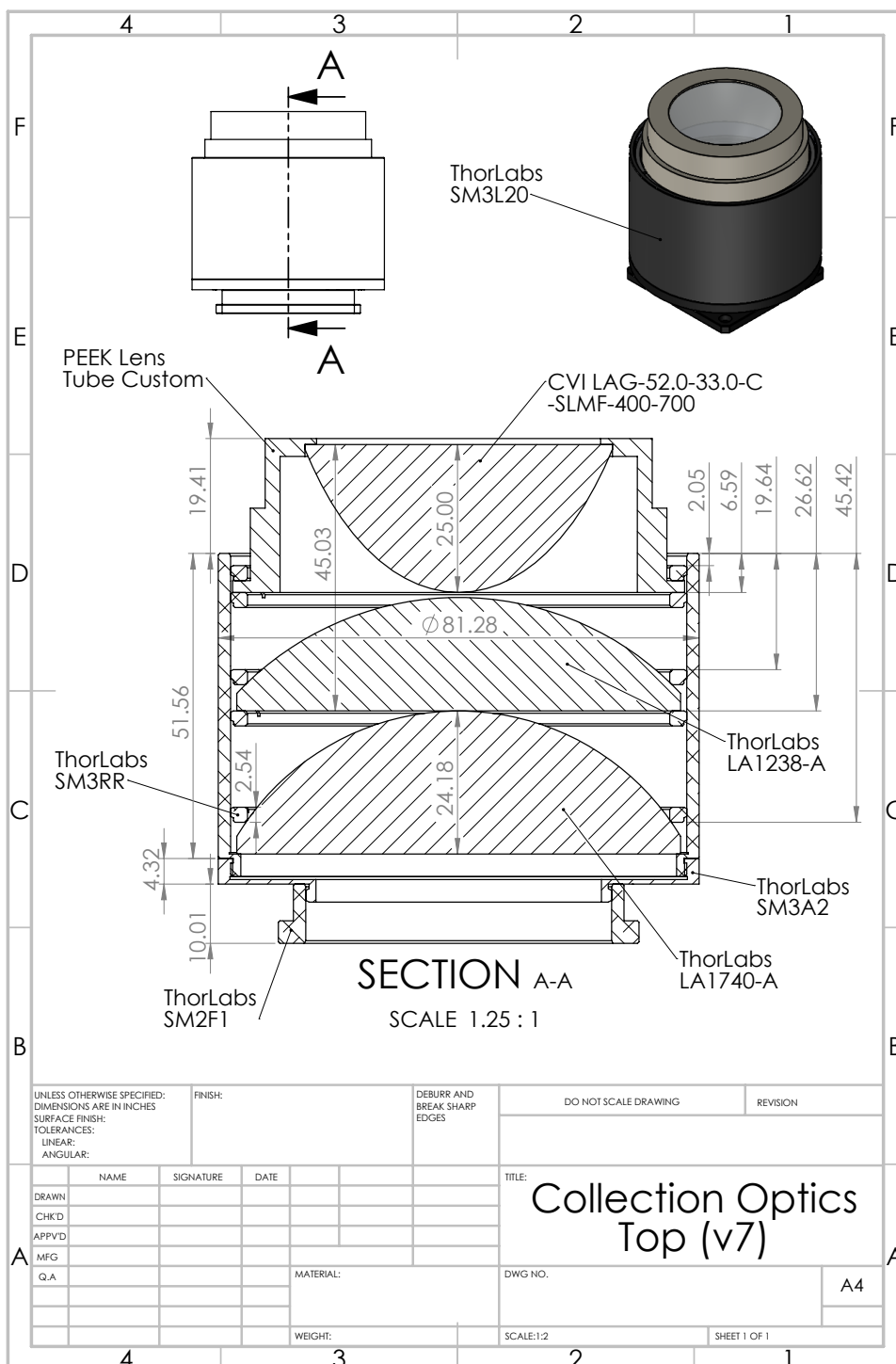
Figure F.9: Design of the top collection optics stack. Light pipe not shown. ll lens tubes are not black anodized. See main text for details.
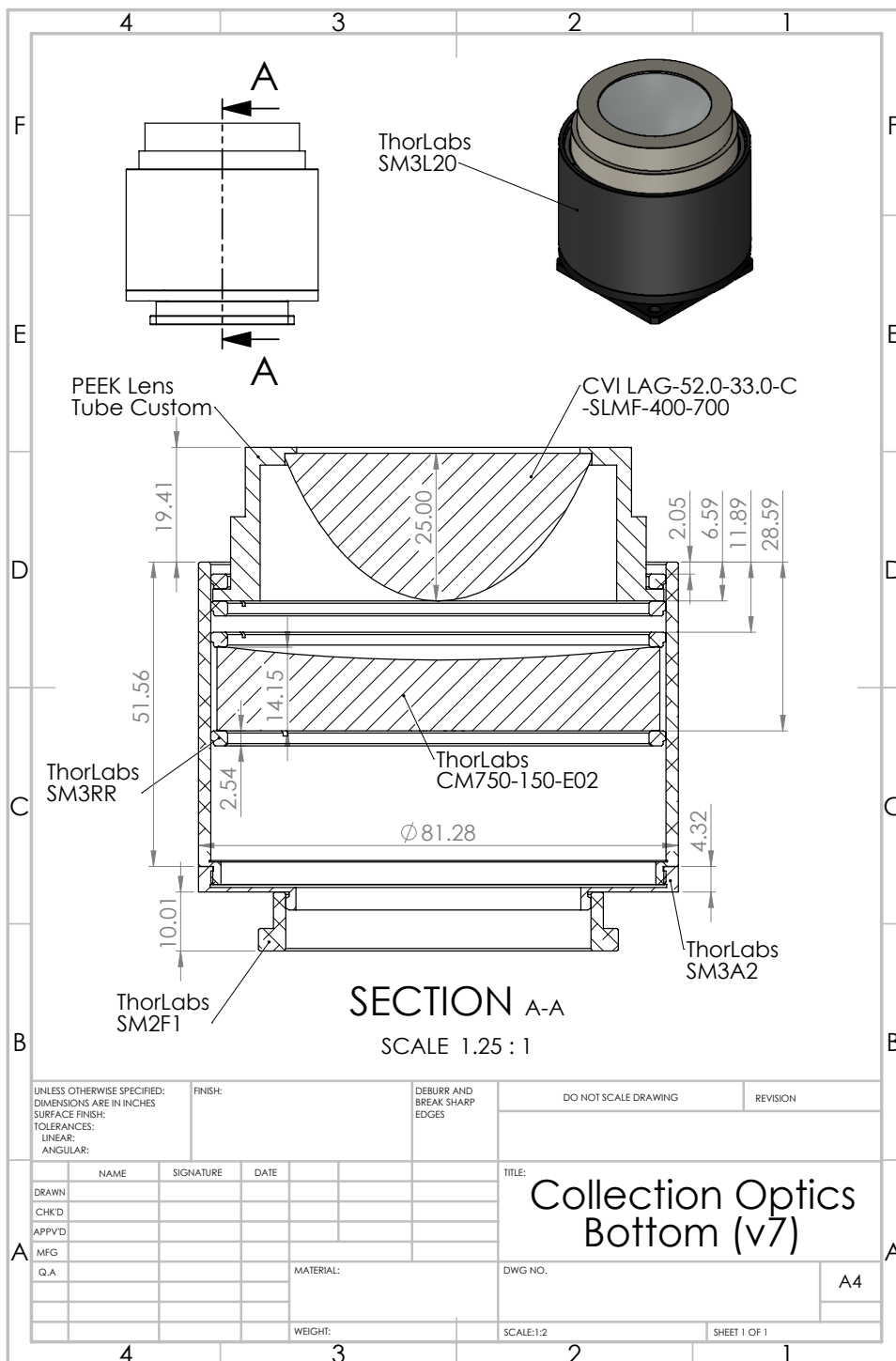
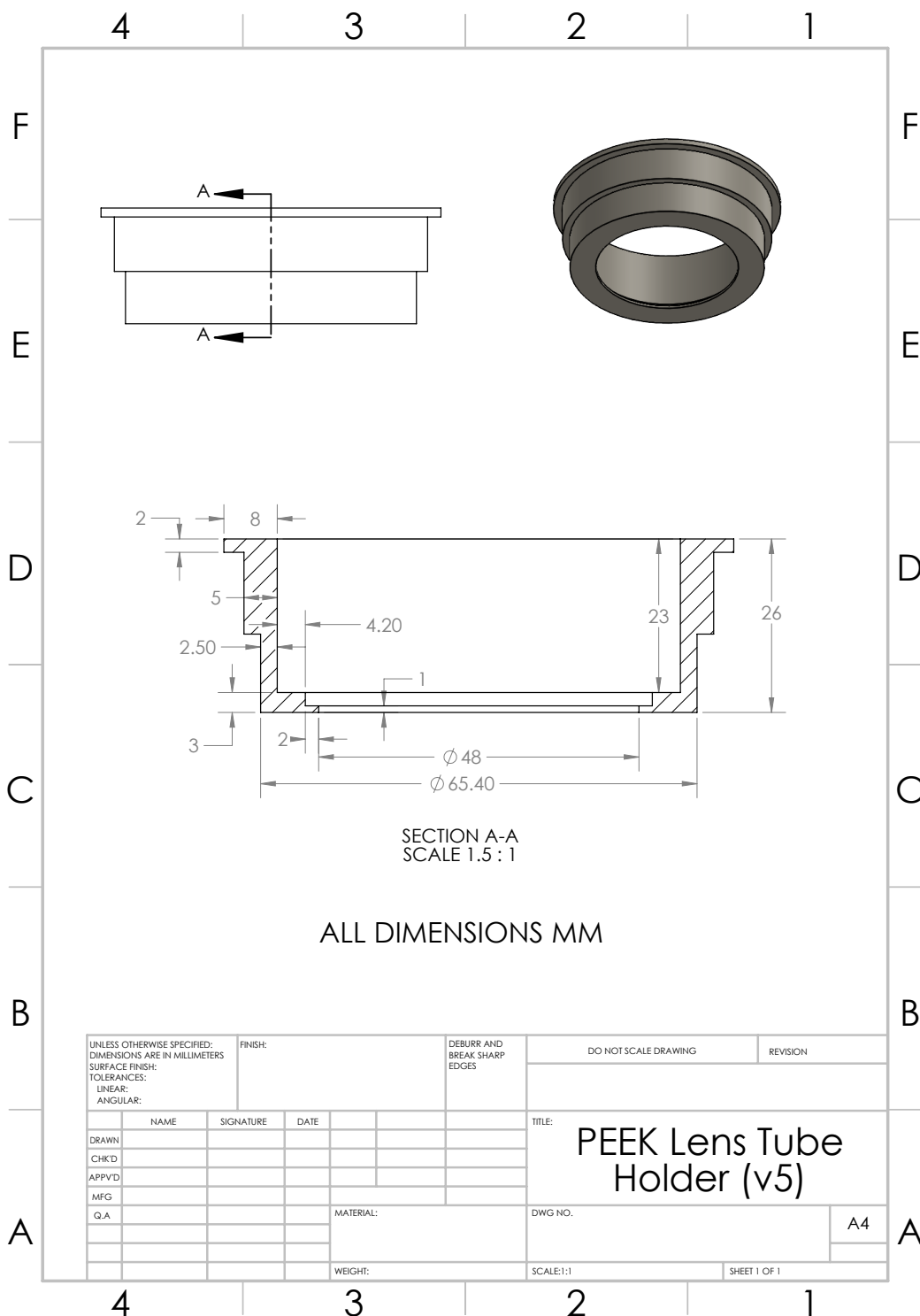Figure F.10: Design of the bottom retro-reflecting optics stack. See main text for details.

Figure F.11: Design of the PEEK lens tube holder for the collection optics stacks. See main text for details.
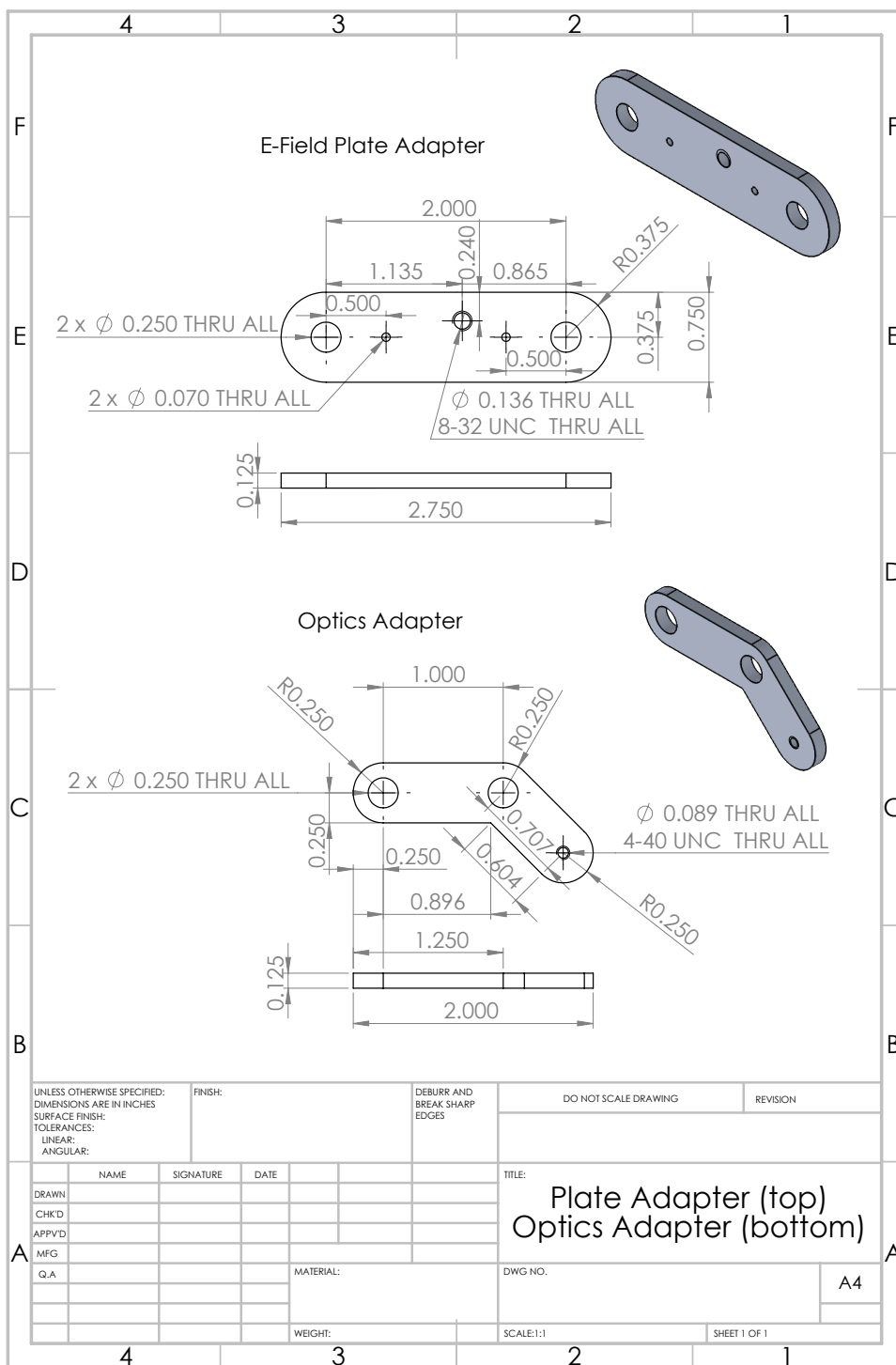
329

Figure F.12: Design of the aluminum adapter plates connecting the support rods to the IdealVac chamber hole pattern (top, E-field plate adapter), and connecting the optics stacks to the IdealVac chamber hole pattern (bottom, optics adapter). See main text for details.